ornl

OAK RIDGE NATIONAL LABORATORY

LOCKHEED MARTIN

ORNL/TM-12924

Ceramic Technology Project
Semiannual Progress Report for
April 1994 Through September 1994

Prepared for
U.S. Department of Energy
Assistant Secretary for
Energy Efficiency and Renewable Energy
Office of Transportation Technologies
Propulsion System Materials Program

CERAMIC TECHNOLOGY PROJECT

DISTRIBUTION OF THIS DOCUMENT IS UNLIMITED

MASTER

DISCLAIMER

Portions of this document may be illegible in electronic image products. Images are produced from the best available original document.

Metals and Ceramics Division

CERAMIC TECHNOLOGY PROJECT
SEMIANNUAL PROGRESS REPORT FOR
APRIL 1994 THROUGH SEPTEMBER 1994

D. R. Johnson
Project Manager

Date Published: June 1995

REPORTS PREVIOUSLY ISSUED

ORNL/TM-9325	Period March 1983-September 1983
ORNL/TM-9466	Period October 1983-March 1984
ORNL/TM-9497	Period April 1984-September 1984
ORNL/TM-9673	Period October 1984-March 1985
ORNL/IM-9947	Period April 1985-September 1985
ORNL/TM-10079	Period October 1985-March 1986
ORNL/TM-10308	Period April 1986-September 1986
ORNL/TM-10469	Period October 1986-March 1987
ORNL/TM-10705	Period April 1987-September 1987
ORNL/TM-10838	Period October 1987-March 1988
ORNL/TM-11116	Period April 1988-September 1988
ORNL/TM-11239	Period October 1988-March 1989
ORNL/TM-11489	Period April 1989-September 1989
ORNL/TM-11586	Period October 1989-March 1990
ORNL/TM-11719	Period April 1990-September 1990
ORNL/TM-11859	Period October 1990-March 1991
ORNL/TM-11984	Period April 1991-September 1991
ORNL/TM-12133	Period October 1991-March 1992
ORNL/TM-12363	Period April 1992-September 1992
ORNL/TM-12428	Period October 1992-March 1993
ORNL/TM-12674	Period April 1993-September 1993
ORNL/TM-12778	Period October 1993-March 1994

CONTENTS

CERAMIC TECHNOLOGY PROJECT SEMIANNUAL PROGRESS REPORT FOR OCTOBER 1993 THROUGH MARCH 1994

SUMMARY

The Ceramic Technology Project was originally developed by the Department of Energy's Office of Transportation Systems (OTS) in Energy Efficiency and Renewable Energy. This project, part of the OTS's Materials Development Program, was developed to meet the ceramic technology requirements of the OTS's automotive technology programs.

Significant accomplishments in fabricating ceramic components for the Department of Energy (DOE), National Aeronautics and Space Administration (NASA), and Department of Defense (DoD) advanced heat engine programs have provided evidence that the operation of ceramic parts in high-temperature engine environments is feasible. However, these programs have also demonstrated that additional research is needed in materials and processing development, design methodology, and data base and life prediction before industry will have a sufficient technology base from which to produce reliable cost-effective ceramic engine components commercially.

An assessment of needs was completed, and a five-year project plan was developed with extensive input from private industry. In July 1990, the original plan was updated through the estimated completion of development in 1993. The original objective of the project was to develop the industrial technology base required for reliable ceramics for application in advanced automotive heat engines.

During the course of the Ceramic Technology Project, remarkable progress has been made in the development of reliable structural ceramics. However, further work is needed to reduce the cost of ceramics to facilitate their commercial introduction, especially in the highly cost-sensitive automotive market. To this end, the direction of the Ceramic Technology Project is now shifting toward reducing the cost of ceramics to facilitate commercial introduction of ceramic components for near-term engine applications. In response to extensive input from industry, the plan is to extend the engine types which were previously supported (advanced gas turbine and low-heat-rejection diesel engines) to include near-term (5-10 years) applications in conventional automobile and diesel truck engines. To facilitate the rapid transfer of this technology to U.S. industry, the major portion of the work is being done in the ceramic industry, with technological support from government laboratories, other industrial laboratories, and universities.

A systematic approach to reducing the cost of components is envisioned. The work elements are as follows: economic cost modeling, ceramic machining, powder synthesis, alternative forming and densification processes, yield improvement, system design studies, standards development, low-expansion ceramics, and testing and data base development.

This project is managed by ORNL for the Office of Transportation Technologies, Propulsion System Materials Program, and is closely coordinated with complementary ceramics tasks funded by other DOE offices, NASA, DoD, and industry. A joint DOE and NASA technical plan has been established, with DOE focus on automotive applications and NASA focus on aerospace applications. A common work breakdown structure (WBS) was developed to facilitate coordination. The work described in this report is organized according to the following WBS project elements:

0.0   Project Management and Coordination

1.0   Materials and Processing

      1.1   Monolithics
      1.2   Ceramic Composites
      1.3   Thermal and Wear Coatings
      1.4   Joining
      1.5   Ceramic Machining

2.0   Materials Design Methodology

      2.1   Modeling
      2.2   Contact Interfaces
      2.3   New Concepts

3.0   Data Base and Life Prediction

      3.1   Structural Qualification
      3.2   Time-Dependent Behavior
      3.3   Environmental Effects
      3.4   Fracture Mechanics
      3.5   Nondestructive Evaluation Development

4.0   Technology Transfer

      4.1   Technology Transfer

This report includes contributions from all currently active project participants. The contributions are arranged according to the work breakdown structure outline.

0.0 PROJECT MANAGEMENT AND COORDINATION

D. R. Johnson
Oak Ridge National Laboratory

Objective/scope

This task includes the technical management of the project in accordance with the project plans and management plan approved by the Department of Energy (DOE) Oak Ridge Operations Office, and the Office of Transportation Technologies. This task includes preparation of annual field work proposals, initiation and management of subcontracts and interagency agreements, and management of ORNL technical tasks. Monthly management reports and bimonthly reports are provided to DOE; highlights and semiannual technical reports are provided to DOE and program participants. In addition, the program is coordinated with interfacing programs sponsored by other DOE offices and federal agencies, including the National Aeronautics and Space Administration (NASA) and the Department of Defense (DoD). This coordination is accomplished by participation in DOE and NASA joint management meetings, annual interagency heat engine ceramics coordination meetings, DOE contractor coordination meetings, and DOE Energy Materials Coordinating Committee (EMaCC) meetings, as well as special coordination meetings.

1.0 MATERIALS AND PROCESSING

INTRODUCTION

This portion of the project is identified as project element 1.0 within the work breakdown structure (WBS). It contains five subelements: (1) Monolithics, (2) Ceramic Composites, (3) Thermal and Wear Coatings, (4) Joining, and (5) Ceramic Machining. Ceramic research conducted within the Monolithics subelement currently includes work activities on low cost Si_3N_4 powder, green state ceramic fabrication, characterization, and densification, and on structural, mechanical, and physical properties of these ceramics. Research conducted within the Ceramic Composites subelement currently includes silicon nitride and oxide-based composites. Research conducted in the Thermal and Wear Coatings subelement is currently limited to oxide-based coatings and involves coating synthesis, characterization, and determination of the mechanical and physical properties of the coatings. Research conducted in the Joining subelement currently includes studies of processes to produce strong, stable joints between zirconia ceramics and iron-base alloys. As part of an expanded effort to reduce the cost of ceramic components, a new initiative in cost effective machining has been started.

A major objective of the research in the Materials and Processing project element is to systematically advance the understanding of the relationships between ceramic raw materials such as powders and reactant gases, the processing variables involved in producing the ceramic materials, and the resultant microstructures and physical and mechanical properties of the ceramic materials. Success in meeting this objective will provide U.S. companies with new or improved ways for producing economical, highly reliable ceramic components for advanced heat engines.

1.1 MONOLITHICS

1.1.2 Silicon Nitride

Characterization of Attrition Milled Silicon Nitride Powder
S. G. Malghan, P. T. Pei and D. B. Minor
(National Institute of Standards and Technology)

Objective/Scope

Currently, the starting materials in the manufacture of silicon nitride ceramic components are fine powders. These fine sized powders tend to form agglomerates due to the Van der Waals attractive forces. For improved reliability in the manufacture of ceramic components, the agglomerates in the powders should be eliminated since they form defects. In addition, the powders should have an appropriate range of size distribution and specific surface area for achieving a near-theoretical density of the ceramic after densification. These factors necessitate the use of powder milling as one of the major powder processing unit operations. Therefore, milling of powders is an integral unit operation in the manufacture of silicon nitride components for advanced energy applications. The production and use of these powders require the use of efficient milling techniques and understanding of characteristics of the milled powders in a given environment. High energy attrition milling appears to offer significant advantages over conventional tumbling and vibratory mills.

The major objectives of this project are: 1. establish repeatability of particle size distribution and other relevant characteristics of slurries milled in a high energy agitation mill (HEAM); 2. determine processing and densification characteristics of powders milled in HEAM; and 3. compare properties of powder, and resulting ceramic obtained by milling in the HEAM vs. vibratory ball mill in a collaborative project with Norton Company.

Technical Progress

Two activities in progress during the reporting period were: surface chemistry of yttria and milling of silicon nitride to achieve high solids loading. In the first activity, we have completed a study of aging of yttrium powders in the presence of a supporting electrolyte and a polymethacrylate dispersant. The primary goal of these studies is to develop an understanding of yttrium oxide interaction with the silicon nitride slurry system in the high energy agitation ball mill (HEAM). In the presence of sodium nitrate as a supporting electrolyte, the pH_{iep} of the aged powder decreases steadily as a function of time up to 16 hours and no further decrease was observed beyond this period. The initial pH_{iep} of 13.4 at 30 min aging decreased to 8.4 after 16 hr aging. These results indicate that surface hydrolysis continued to take place during this period and a stable surface was reached in about 16 hours. In the presence of sodium perchlorate, an electrolyte that does not exhibit any tendency to specifically adsorb, the pH_{iep} values were of the same order as that found in the absence of perchlorate. In the presence of 375 ppm polymethacrylate dispersant, the shift in the pH_{iep} was narrowed. At 30 min aging, the pH_{iep} was at 9.6 which decreased to 7.8 after 16 hr aging. The narrowing of the shift in the pH_{iep} after aging in the presence of the polymethacrylate is probably due to the

adsorption and the resultant surface modification. However, the fact that the pH_{iep} is undergoing changes as a function of time in the presence of the polymethacrylate shows that the surface hydrolysis of yttria is continuing to dominate. If the adsorbed layer of polymethacrylate were to dominate the surface interactions, then the pH_{iep} would be in the range of pH 4.5, and in addition pH_{iep} would not change as a function of aging time. The next task was to examine adsorption isotherms for this system in the presence of polymethacrylate to identify suitable regions for improved aging characteristics. In the study of yttria surface chemistry, adsorption isotherms were obtained at 1 h and 24 h adsorption of Darvan C. The adsorption was found to increase as a function of bulk concentration and reached a plateau at about 300 ppm with respect to the powder weight. At 1 h, approximately 55% of the total dispersant added was adsorbed. However, almost 50% of this total amount had desorbed when the slurry was aged for 24 h. Therefore, during milling tests to retain effective dispersion, the yttria containing silicon nitride slurries should not be aged beyond a few hours.

In the second activity on milling of a silicon nitride powder as applied to gel casting, we conducted a few tests. The primary purpose of these tests were to prepare a slip containing 50% vol. suspension for gel casting of UBE SNE-10 powder. The procedure for the addition of surfactants was modified compared to that in the first test conducted in collaboration with Dr. Mark Janney, Oak Ridge National Laboratory. The major change to the procedure was in the addition of gel forming components and dispersants at the beginning of the milling period. The concentrations and order of additions were kept the same as in the previous test. In addition, rotor speed was decreased to 1800 rpm, while the slip flow rate was decreased to 200 cm^3/min. These changes were expected to promote deagglomeration while preventing the primary particles fracture. The milling proceeded very well for 45 min when the slip suddenly formed a gel. At this time no initiator was added. Though the test could not be completed, we identified several items. First of all, we could have loaded the slip with 50% vol. if the slip had not formed the gel. Second, in spite of the significantly reduced rotor speed, the final specific surface area of the powder was 13 m^2/g, which is much greater than desired. The causes of gel forming without the addition of a initiator are not clear. Some of the suspected causes are local temperature rise due to high shearing action, and high turbulence in the mill. We are planning to conduct follow-up tests after collecting sufficient information on the gel formation.

Through a related study at NIST, we had identified a different approach to the development of improved dispersions by enhancing the adsorption of polymethacrylate dispersant. This procedure consists of adsorption of the dispersant in the acidic region at an approximate pH of 4.0 followed by deagglomeration and suspension preparation at pH 9.5. We have been able to obtain better dispersions than that obtained by the conventional method of adsorption and dispersion at pH 9.5 on a large number of powders. The purpose of these milling tests was to evaulate the improved dispersion procedure to prepare dense suspensions using the

current composition of Ube silicon nitride powders containing 4% by weight Y_2O_3. Initial slurries were prepared at pH 4.0 containing approximately 45% wt. powder and the entire amount of dispersant. When the pH was increased to 9.5, the slurry as expected became very thin. The remaining powder was added to this suspension in the usual manner. When the entire powder to make up to 80% by weight was added, the slurry was much thicker than that of the conventionally prepared slurry. Another problem with this slurry was its inability to reach 80% by weight in one test. The tests conducted until now have clearly indicated that unless we are able to load close to 65% by weight of powder into the slurry before milling is initiated, we will have different problems. We are studying the results in more detail to overcome some of the these problems.

The current composition of silicon nitride powder constitutes a fixed ratio of SNE-3, SNE-5, and SNE-10, and a 4% wt. of yttria powder. Our goal in these tests was to determine the likelihood of increasing the solids loading to higher than 80% by weight by feeding the coarse (SNE-3 and 5) and fine (SNE-10) powders in a sequential manner rather than feeding a combined mixture of the three powders. The logic behind this thinking is that SNE-10 powder, being highly agglomerated, would require a longer deagglomeration time and a larger quantity of water due to its high specific surface area. On the other hand, both SNE-3 and 5 would require a smaller quantity of water due to their relatively lower specific surface area.

In one test, the SNE-3 and 5 powders were added first in the mixing stage, while the SNE-10 was added as milling proceeded. In a subsequent test, the order of addition was reversed by adding the SNE-10 first, followed by the addition of a mixture of SNE-3 and 5. In the first test, no significant advantage was evident compared to that of adding a mixture of all three powders. In fact, the slip was more viscous by adding the powders in a sequential manner. In the second test, by the time all the SNE-10 was added in the mixing stage, the slip was highly viscous and we were unable to add additional powder. The primary outcome of these tests is that the order of addition of the constituent powders has no advantages, in fact, the addition of mixture of the powders is more beneficial.

Recently, we have contacted Dow Chemical Company to obtain a batch of their silicon nitride powder. The purpose of obtaining this new powder is to evaluate the potential of obtaining higher solids loading and to assess the response of other silicon nitride powders produced by different synthesis methods to high energy agitation milling. The Dow Chemical Company has agreed to send a 14 kg batch of their powder. We will coordinate with Dow in obtaining surface chemistry and milling data on this powder. Primarily, we will characterize for surface oxide composition and reasons for a low isoelectric point of this powder. Subsequently, we will conduct milling tests and collaborate with Dow and others to evaluate the milled slips.

Status of Milestones

Milestone 111809 will be completed by March 1, 1995.

Communications/Visits

None

Publications

An Assessment of Repeatability in the Milling of Silicon Nitride Powders in a High Energy Agitation Ball Mill, S. G. Malghan, D. Minor P. Pei and S. Schiller, AIChE Proc., August 1994.

Microwave Sintering of Silicon Nitride

J. O. Kiggans, T. N. Tiegs, E. M. Sabolsky, Jon-Paul Maria, C. C. Davisson,
and M. F. Iskander (Oak Ridge National Laboratory)

Objective/Scope

The objective of this research element is to identify those aspects of microwave processing of silicon nitride that might (1) accelerate densification, (2) permit sintering to high density with much lower levels of sintering aids, (3) lower the sintering temperature, or (4) produce unique microstructures. The investigation of microstructure development is being performed on dense silicon nitride materials annealed in the microwave furnace. The sintering of silicon nitride involves two approaches. The first approach comprises heating of silicon nitride and sialon powder compositions in the 2.45- or 28-GHz units. The second approach uses reaction-bonded silicon nitride as the starting material and is done entirely in the 2.45-GHz microwave furnace.

Technical Highlights

Scaleup of Sintered Reaction-Bonded Silicon Nitride (SRBSN). The primary focus of the microwave sintering work during this working period has been the determination of the proper conditions for the scaleup of the SRBSN process via microwave heating. Previous experiments showed that not only the samples, but also the sample crucible, had to be heated during microwave heating to achieve uniform processing. The focus of the research during the present reporting period has been the development of new crucible materials to provide uniform heating for the microwave processing of SRBSN. These microwave crucibles must have the following properties: (1) chemical compatibility to SRBSN; (2) temperature capability to 1800°C; (3) durability for repeated use; (4) strength suitable for large crucibles, with low creep at elevated temperatures; (5) low mass to reduce the total load on the microwave energy absorbed; and (6) lack of a sudden, strong change in the dielectric properties during the heating cycle.

The first material tested for microwave processing of SRBSN using microwave-suscepting crucibles was "Crystar" SiC. This material is relatively cheap, is chemically compatible with SRBSN, and can be heated to 1800°C without apparent deterioration. As in early tests, bucket tappets purchased form Cremer Forchung Institute were used as test samples. The microwave processing of the bucket tappets was done in a 500-L cylindrical multimode cavity equipped with a 6-kW, 2.45-GHz power supply. The bucket-tappet samples were stacked in three layers of nine samples each in a 7 x 7 x 5 in. crucible constructed from 0.25-in.-thick "Crystar" SiC plates as shown in Fig. 1. The sample crucible was insulated by silicon nitride packing powder in a fiberboard box, as previously described. Type "C" thermocouples were inserted between the samples in the bottom layer of buckets and directly under the crucible to measure the respective temperatures inside and outside of the crucible. The microwave furnace was evacuated and backfilled with nitrogen and purged with flowing nitrogen during the experiment. The final processing condition was a 1625°C dwell for 1 h. The microwave power input to the cavity was also recorded during heating cycle.

ORNL-DWG 95-5862

CROSS-SECTIONAL VIEW OF
FRONT OF INSULATION CASKET

FIBERBOARD BOX

POWDER INSULATION

BUCKET TAPPET SAMPLES

SiC INNER CRUCIBLE

TYPE "C" THERMOCOUPLE

7.5 IN.

7 IN.

13 IN.

11 IN.

5 IN.

13 IN.
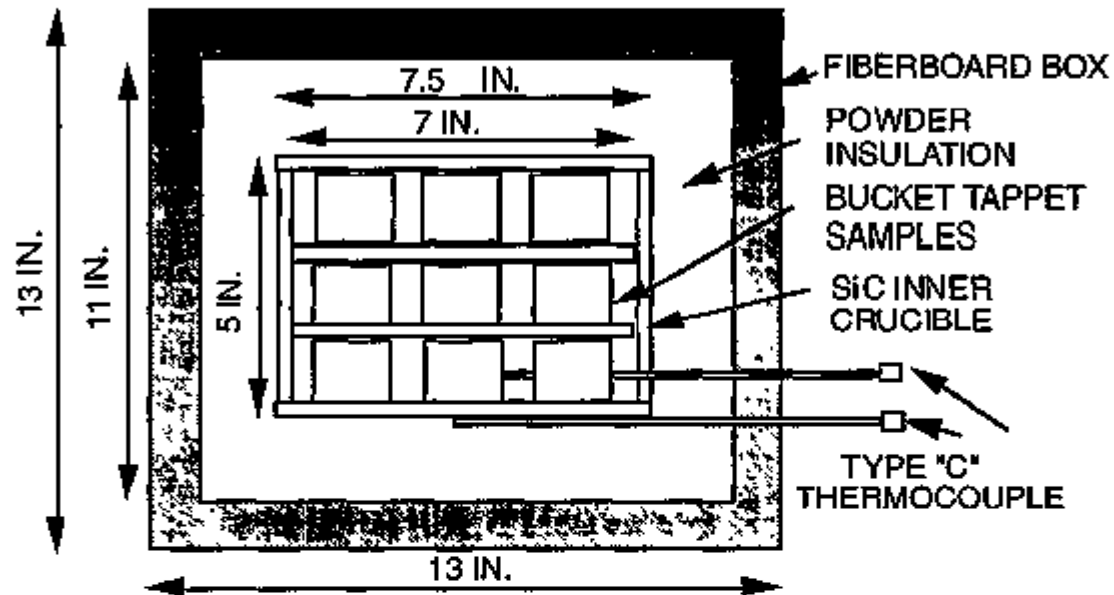
TOP VIEW (LID OFF CRUCIBLE)

FIBERBOARD BOX

POWDER INSULATION

SiC INNER CRUCIBLE

BUCKET TAPPET SAMPLES

INNER BN SETTER PLATE
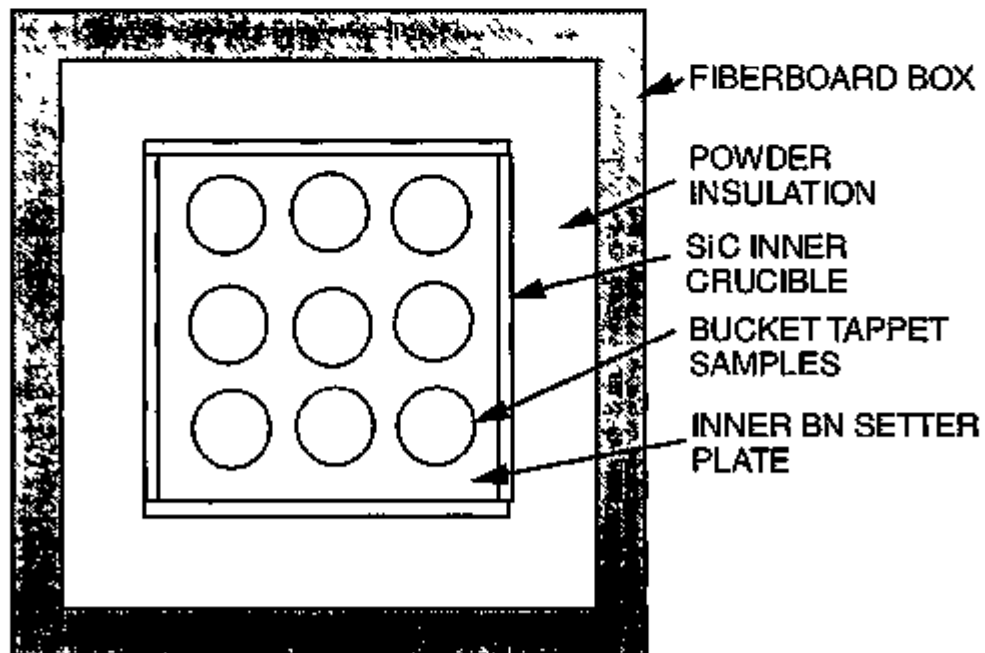
Fig. 1. Sintered Reaction-Bonded Silicon Nitride bucket tappets processed in a "Crystar" SiC crucible using microwave heating.

Partial success was achieved in this experiment since the samples nitrided evenly, independent of their positions in the crucible. A photo of the nitrided parts is shown in Fig. 2. The standard deviation of the weight gain was ± 0.31 g. The temperatures of the crucible and the parts were within 10 °C of each other throughout the run; however, the crucible absorbed too much of the available microwave power. A peak power of 5 kW was required to reach the final temperature of 1625°C due to the lossy nature of the "Crystar" SiC at the 2.45-GHz microwave frequency. This high-power absorption rules out the use of crucibles made solely of "Crystar" SiC. One should be able to make a crucible with a defined energy absorption by adjusting the amount of absorbing material in the crucible by adjusting the density of the crucible. Crucibles made of Si_3N_4 with sintering aids such as Y_2O_3 and SiO_2, along with the SiC microwave absorber, should act as a good system to test this idea.

Two sets of experiments were performed to determine the proper combination of Si_3N_4 and SiC to be incorporated in the crucibles used for the microwave processing of SRBSN. The first set of experiments was designed to measure the effect of varying the concentration of the SiC in the crucible materials on the microwave power absorption by these materials. Powder mixtures were made consisting of Ube E-03 Si_3N_4 and 5 wt % sintering aids combined with either 0, 10, 20, 30, 40, and 50 wt % Stark A-10 SiC. The mixtures were gelcast in a 15 wt % solution of the methacrylamide monomer/methylene bisacrylamide corsslinker (MAM/MBAM) 6:1 system into discs (2 in. diam by 0.5 in. thick) which were then dried, air fired to remove the organic gelcast agents, and then sintered in nitrogen at 1800°C for 4 h in a graphite-element furnace. Sets of two each of the discs of a given SiC composition were then insulated as shown in Fig. 3 and heated in the ORNL 500-L microwave furnace in nitrogen to a final temperature of 1450°C. Figure 4 shows the graphs of the microwave power required to heat the sets of discs composed of 20, 30, 40, and 50 wt % SiC at 5°C/min. to 1450°C and also a representative temperature plot. The data for the 10 vol % SiC samples are not shown since the heating was too erratic with this low SiC content. The other power curves show the large differences in power required for the varying concentrations of SiC in each crucible material.

Although the first set of experiments gave basic information on the effect of SiC concentrations on microwave heating, it did not indicate which SiC concentration would be suitable for processing of SRBSN using microwave heating. A second set of experiments was run to help answer this question. Gelcast crucibles, 2 in. diam by 3 in. tall by 0.2 in. thick, were made with the 10, 30, and 50 wt % SiC crucible materials. These crucibles were processed in the same manner as the discs of the first experiment set. TM-145 bars, 0.25 in. thick by 0.25 in. wide by 1.25 in. long, were placed inside these crucibles as shown in Fig. 3. The bars were nitrided in the microwave furnace to a final processing condition of 1450°C for 1 h. The location of each sample inside the crucibles was noted, and the weight of each sample was measured before and after processing to evaluate the processing uniformity. Processing in the crucible consisting of 10 wt % SiC additive was very nonuniform. There was a lower weight gain for samples located on the inner edge of the crucible, indicating that there was too much heat loss at the crucible surface. Processing in the crucible containing 30 wt % SiC resulted in more uniform processing. However, the most uniform heating was obtained with the crucible containing 50 wt % SiC. The standard deviation was ±0.07%. It should also be noted that this is the first time nitridation experiments have been done using an insulation setup in which there was no Si_3N_4 packing powder used for additional insulation. Thus, a simple insulation setup lacking powder insulation is possible for microwave-assisted nitridation.
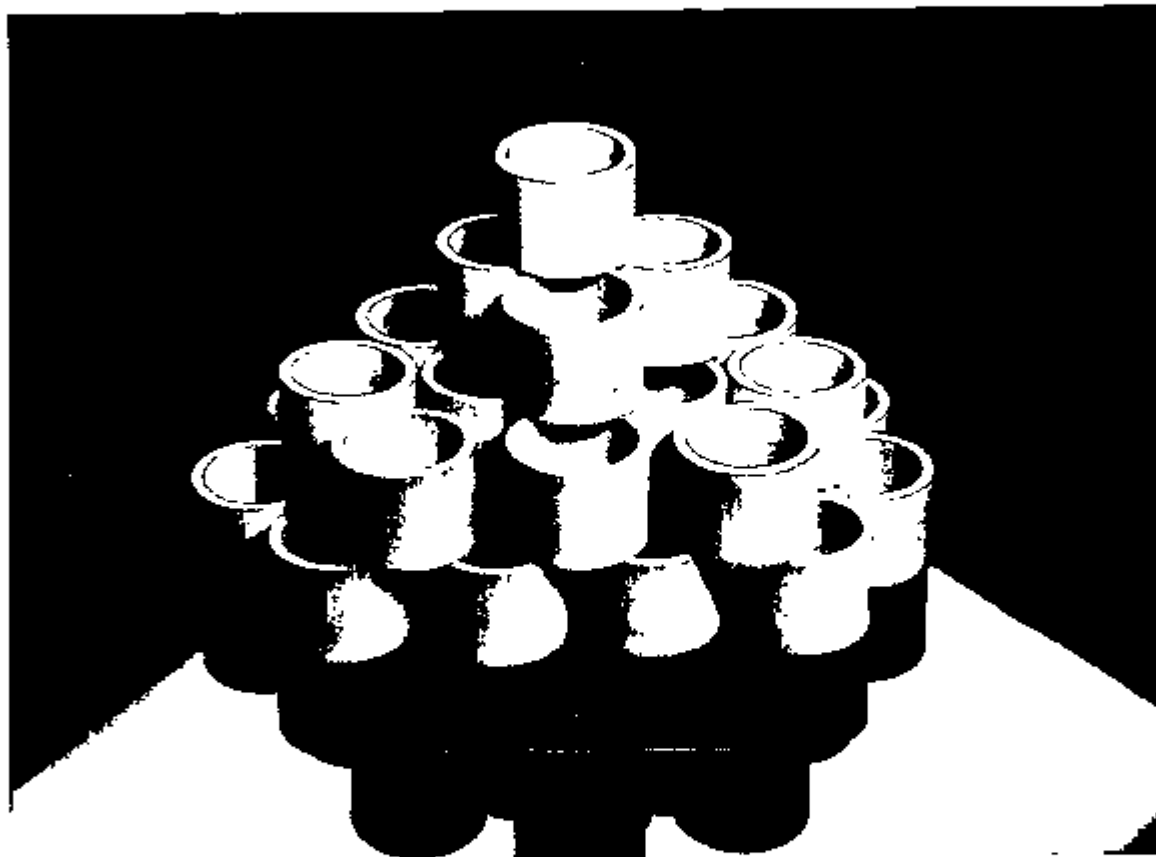
Fig. 2. Sintered Reaction-Bonded Silicon Nitride bucket tappets processed in a "Crystar" SiC crucible using microwave heating.

ORNL-DWG 95-5863

Alumina fiberboard

Type C
thermocouple

Samples

BN plate
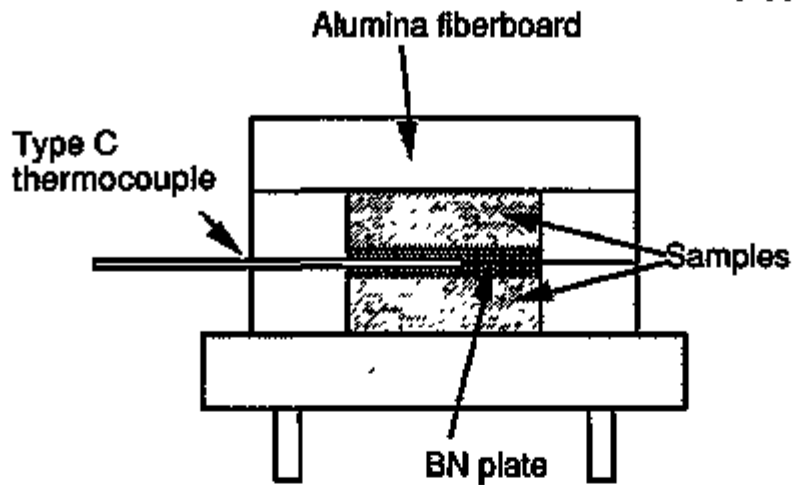
Fig. 3. Insulation setup for determining the microwave power
required to heat test discs containing different amounts of SiC.

ORNL-DWG 95-5864
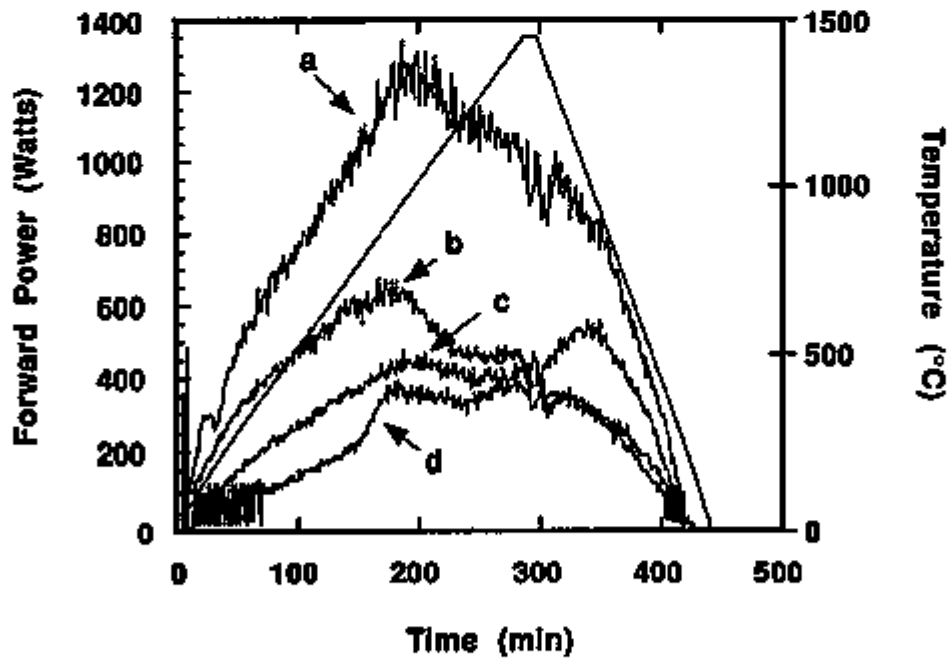
Fig. 4. Microwave power required for different crucible materials containing:
(a) 20 wt % SiC, (b) 30 wt % SiC, (c) 40 wt % SiC, and (d) 50 wt % SiC.

Finally, an experiment was performed to ensure that not only nitridation (1450°C), but also sintering, could be accomplished using these new crucibles. For this test, TM-145 test bars were placed in a 50 wt % SiC crucible as in the previous experiment. This crucible was packed in a 2-in.-thick layer of Si_3N_4 packing powder inside an alumina fiberboard box. Figure 5 shows the temperature measured between the samples inside the crucible and the temperature measured outside and under the crucible. Note, there is approximately a 100°C temperature difference between the inside sample and outside the sample crucible at the peak 1800°C temperature. The microwave power needed for this processing run was very low, since the low mass crucible did not present a significant heat load. The standard deviation in the densities was ±0.08 g/cm^3. The next step in the project was to design and construct the first scaleup crucible to test the hybrid crucible with larger numbers of samples.

Two possible crucible designs were considered for scaleup work. The first design was a cylindrical crucible. The second design was a box-type crucible. The box-shaped crucible was chosen for several reasons: (1) the exterior fiber insulation casket used in microwave heating is of a box construction, so the use of the box geometry for the inner hybrid crucible should allow more uniform insulation of microwave-heated samples; (2) the box shape should be more easily made, since the walls, top, and bottom can be made as separate panels, which can then be joined (also, the separate panels can be of different compositions; and (3) the box design should be more easily scaled up, since a larger crucible can be built from multiple tiles.

The design for the first scaleup crucible is shown in Fig. 6. The inner diameter of the crucible is a 7-in. cube with individual panels 0.25 in. thick. This crucible can accommodate 4 layers with 9 to 16 bucket tappet samples per layer, depending on the spacing allowed between samples. The outer walls of the crucible are composed of Si_3N_4 with 40 wt % SiC and 5.0 wt % sintering aids to provide heating along the periphery of the samples. The top, bottom, and three inner shelves are composed of Si_3N_4 with 5 wt % sintering aids and no SiC, since hybrid heat should not be needed in these areas of the crucible.

ORNL-DWG 95-5865
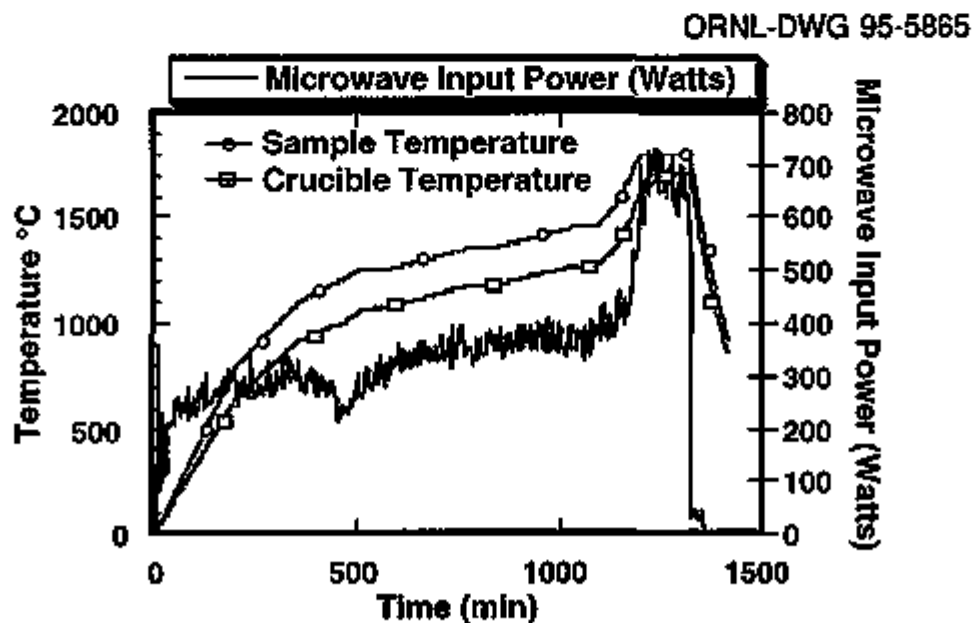
Fig. 5. Power-temperature curve for the nitridation and sintering of TM-145 materials in a silicon nitride crucible containing 50 wt % SiC.

ORNL-DWG 95-5866

Front View of Hybrid Crucible

7.2 in.

Si3N4-Si
Exterior Wall

Bucket Tappet
Samples

Si3N4 Setter
Shelves

7.0 in.

7.2 in.

Top View of Single Layer of Samples
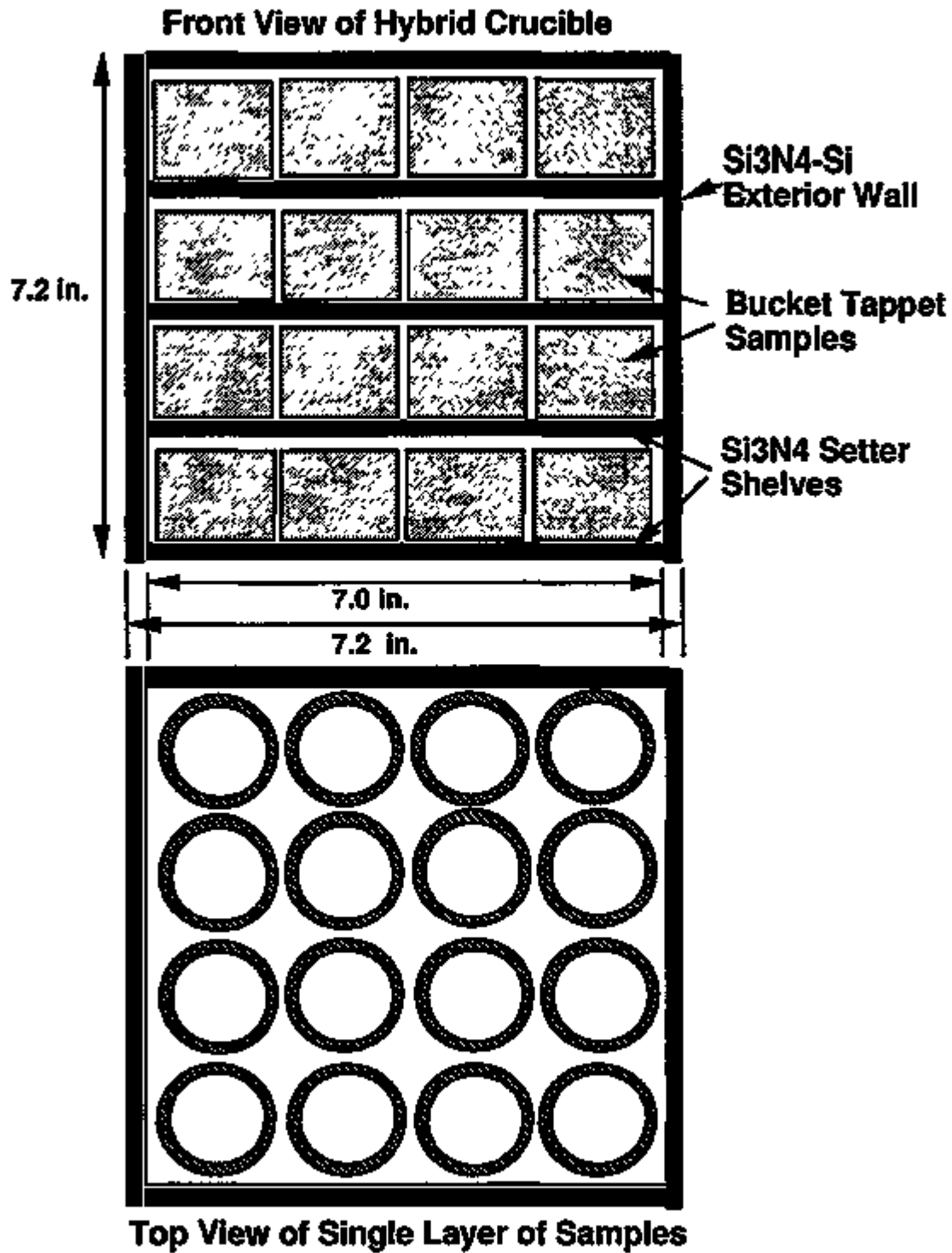
Fig. 6.   Hybrid crucible for microwave processing of Sintered Reaction-Bonded
Silicon Nitride.

Two methods were tested for making the panels for the hybrid crucibles. The first method tested was slip-casting using a 8.5 x 8.5 x 0.4 in. size plaster-of-paris mold. Several attempts were made to slip-cast slurries consisting of 95 wt % Ube-ESP Si_3N_4, 4 wt % Y_2O_3, 1 wt % SiO_2, 0.4 wt % Darvan 821A, 0.6 wt % PVP K-15, and 0.5 wt % Carbowax 1000. The resulting cast plates cracked during initial drying in the molds. Also, these materials bonded to the molds and were difficult to remove. This method for making the plates for the crucible walls was rejected, since the technical problems associated with this method and the weakness of the resulting product did not look promising.

The second method tested for making the panels for the hybrid crucible, which was successful, was the gelcasting method. An 8 x 8 x 0.25 in. casting mold was made, which consisted of two glass plates separated by a 1-in.-wide by 0.25-in.-thick rubber gasket. The first crucible plates to be made were those for the top, bottom, and inner shelves of the crucible. Gelcasting slurries containing 45 vol % powder consisting of 95 wt % Ube-E03 Si_3N_4, 4 wt % Y_2O_3, 1 wt % SiO_2, 0.4 wt % Darvan 821A, and 0.6 wt % PVP K-15 were made utilizing the MAM/MBAM 6:1 gel system. Initial tests with slurries showed that 0.1 μL of tetramethylethylenediamine (TEMED) and 0.5 μL of 10 wt % ammonium persulfate (APS) were optimal for producing gels that did not clump on mixing but which showed even gelling after a (1-h) incubation at 60°C. The plates made by this method were dried at 92% relative humidity for 1 d, at room humidity conditions for 1 d, and then for 4 h at 40°C. The plates were then cut to 7.5 by 7.5 in. size, packed in silicon nitride packing powder in graphite crucibles, and both debindered and sintered in a single run in a graphite furnace at the final conditions of 1800°C for 2 h in flowing nitrogen. The final density of these plates was approximately 2.0 g/cm^3. As mentioned in the previous discussion, a second set of crucible plates was needed for the side walls of the crucible. Gelcasting slurries were made containing 45 vol % powder consisting of 55 wt % Ube-E03 Si_3N_4, 40 wt % Starck A-10 SiC, 4.2 wt % Y_2O_3, 0.8 wt % SiO_2, 0.4 wt % Darvan 821A, 0.6 wt % PVP K-15, and 0.3 wt % tetramethylammonium hydroxide utilizing both the MAM/MBAM 6:1 gel system and later, the MAM/PEG 3:1 system. The pH of slurries was 12.8. The MAM/MBAM gel system did not work well. The gel slurries clumped badly on the addition of even small amounts of the initiator. This resulted in uneven gelling at 60°C, producing gels that cracked during drying. The MAM/PEG system produced very different results. The slurries did not clump on the addition of APS and gelled evenly at 60°C. The gelled plates were dried without cracking. The drying, debindering, and sintering were conducted using the same conditions as the first set of crucible plates. The final density of this set of plates averaged 1.9 g/cm^3. Future work will include tests performed with the crucible built from the gelcast plates.

Insulation Panel Development

The second area of research, which was begun during the last bimonthly period of this semiannual, was work on the development of Si_3N_4 insulation panels to replace the packing powders used as insulation in microwave processing. Several approaches have been taken toward this initiative. Approach one consisted of pressing silicon powders containing Si_3N_4 seed at very low pressures and then bonding the powders together by nitridation to form porous RBSN panels. RBSN materials are transparent to microwaves and, if the porosity is sufficient, can act as insulation. A powder blend consisting of 80 wt % silicon (Elkem metallurgical grade) and 20 wt % Ube-E03 Si_3N_4 was pressed to a pressure of 0.25 psi in a 7.5 x 7.5 x 1 in. graphite die, which was coated with boron nitride. The 0.5-in.-thick pressed plate was fired on a 15-h nitridation cycle to a final condition of 1450°C for 2 h in flowing nitrogen. The nitridation of the silicon appeared to be quite even; however, there was minor cracking in the final plate. The density was

1.2 g/cm³. The cracking in the plate was the result of uneven pressing, and a more suitable die for pressing large plates is being fabricated. A second method tested for making Si₃N₄ insulation boards was using the gelcasting technique. A gelcasting slurry was made containing 40 vol % powder consisting of 62 wt % Ube-E03 Si₃N₄, 26.7 wt % SiO₂, 11.1 wt % Fortel carbon fibers, 0.4 wt % Darvan 821A, and 0.6 wt % PVP K-15 utilizing the MAM/MBAM 6:1 gel system. Experiments showed that 5 μL of Temed and 10 μL of APS per 1 g of slurry were required to gel this material at 60°C. Following gelling, the 2-in.-diam by 0.5-in.-thick test samples were dried and then heated to 600°C for 1 h to remove the carbon fibers. The test discs were then sintered in a graphite furnace at the final conditions of 1800°C for 2 h in flowing nitrogen. The resultant discs had a density of 0.9 g/cm³. Both methods for making insulation panels looked promising, although as expected, the densities of the panels were higher than the 0.4 g/cm³ density of loose powder insulation.

Modeling work in support of crucible development

As early attempts were in progress to develop hybrid crucibles for the microwave processing of SRBSN, it became apparent that computer modeling would be necessary to help resolve the proper dielectric composition of crucibles. In response to this need, a subcontract was established with the University of Utah, with Dr. Magdy Iskander as the principal investigator to perform this modeling. This subcontract includes measuring the dielectric properties of both samples and insulation materials used in the SRBSN scaleup experiments and the eventual integration of these measurements into heating models.

One of the first tasks in this subcontract involved measurement of the dielectric properties of some of the materials used in our microwave heating studies. Table 1 shows the values for dielectric constant, e', and the dielectric loss factor, e", as measured by the cavity perturbation method and/or also the open probe method for the various crucible materials,

Table 1. Dielectric property measurements for different crucible compositions and for the TM-145 silicon material. E' is the dielectric constant and e" is the dielectric loss factor.

Material	Additive	Open end probe data		Cavity perturbation data	
		e'	e"	e'	e"
UBE-03 Si3N4	none	3.45	0.05	3.25	0.014
UBE-03 Si3N4	10 wt % SiC	2.48	0.08	2.92	0.04
UBE-03 Si3N4	20 wt % SiC	4.49	0.15	4.93	0.05
UBE-03 Si3N4	30 wt % SiC	4.97	0.17	5.27	0.061
UBE-03 Si3N4	40 wt % SiC	5.44	0.29	5.49	0.093
UBE-03 Si3N4	50 wt % SiC	8.74	0.53	12	0.4
TM-145*	none	ND	ND	7.9	1.52

*Si with 10% Si₃N₄, 9% Y₂O₃, 3% Al₂O₃, and 2% SiO₂.

insulation, and samples used in various microwave processing experiments. Note, the open probe method is primarily used as a method of verification for the e' value and is not accurate for measuring the e" values. This dielectric property data will be used in future computer modeling studies to help formulate strategies for microwave processing of SRBSN. These data are also being used to calculate the maximum crucible wall thickness acceptable for given crucible compositions.

Microwave annealing experiments

Several experiments were performed during this period involving the microwave annealing of SRBSN and sintered silicon nitride (SSN). Experimental details and results will be presented in future reports.

Problems

None.

Publications

None.

Status of Milestones

Milestone 112407 has been completed in the current reporting period.

Communications/Visits/Travel

Travel by T. N. Tiegs to the Eighth CIMTEC World Ceramics Conference in Florence, Italy, to give an invited lecture entitled "Microwave Sintering of Ceramics."

A poster entitled "Studies on the Scaleup of the Microwave-Assisted Nitridation and Sintering of Reaction-Bonded Silicon Nitride," by J. O. Kiggans, T. N. Tiegs, H. D. Kimrey, and Jon-Paul Maria was presented by R. B. Schultz at the 5th International Symposium on Ceramic Materials and Components for Engines, Shanghai, China, May 29 - June 1, 1994.

Development of a High Quality, Low Cost Silicon Nitride Powder
D. F. Carroll, G. A. Cochran, C. L. Conner, S. D. Dunmead, G. A. Eisman,
J. Hwang, and A. W. Weimer (The Dow Chemical Company)

OBJECTIVE/SCOPE

The objective of this program is to scale a carbothermal nitridation process to the pilot plant level for the production of a high quality, low cost silicon nitride powder. The tasks of this program are designed to 1) determine the relationships between raw material precursors, reactor conditions and post-processing on the characteristics of carbothermal powder produced in the intermediate scale reactor, 2) scale the process to a pilot plant stage and 3) identify those characteristics which yield a sinterable powder that can be pressureless sintered into dense, high strength components. The results of the above tasks will be utilized in the latter stages of the program when high quality, low cost silicon nitride powder is produced in our pilot plant facility.

TECHNICAL PROGRESS

TASK 2.0 Process Development and Process Scale-up

During this reporting period, a significant amount of time was spent on improving the process at the pilot plant level. Equipment modifications were carried out as was the installation of new equipment. In particular, in order to be able to produce a homogeneous lot in large quantities, a ribbon blender was added as a final unit operation in the process. This addition allows for the blending of smaller batches of powder into a final batch of approximately a quarter of a metric ton in size. The blending of hundreds of pounds of powder was carried out in this unit in order to prepare the final deliverable. The powder properties of a 338 lb batch after blending are presented in Table I.

Table I
Powder Properties

Wt. lbs	Carbon wt%	Oxygen wt%	Nitrogen wt%	Fe ppm	Al ppm	Ca ppm	Mg ppm	D10 microns	D50 microns	D90 microns	S.A. m^2/g
55.00	0.4675	1.932	40.49	35	76	49	138	0.38	0.83	2.14	9.609
55.00	0.4692	1.895	40.30	35	52	49	112	0.38	0.83	2.25	9.469
55.00	0.4685	1.902	40.12	33	50	53	145	0.38	0.83	2.17	9.604
55.00	0.4643	1.910	39.82	36	70	46	130	0.38	0.83	2.23	9.689
55.00	0.4622	1.896	39.94	38	58	49	100	0.39	0.85	2.29	9.565
63.75	0.4703	1.907	40.23	47	50	50	123	0.39	0.85	2.26	9.551

338.75 TOTAL

| Average | 0.4671 | 1.907 | 40.15 | 38 | 59 | 49 | 125 | 0.38 | 0.84 | 2.22 | 9.580 |

The powder which was produced in the process was utilized for the 10 kg May deliverable, fabrication of MOR test bars, and the final contract deliverable of 100 kg. In addition to the final product properties reported above in Table I, run data associated with the generation of the powder are presented in Figures 1 and 2. Specifically, crude oxygen vs. time is plotted in Fig. 1 while final residual oxygen's and carbon's are presented in Fig. 2.

Figure 1
Run CSN-175

CRUDE OXYGEN VS. TIME

Figure 2

FINAL OXYGEN & CARBON
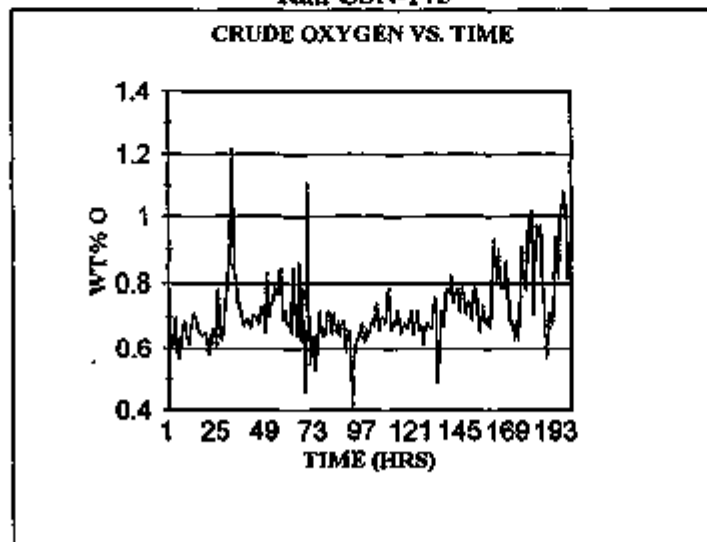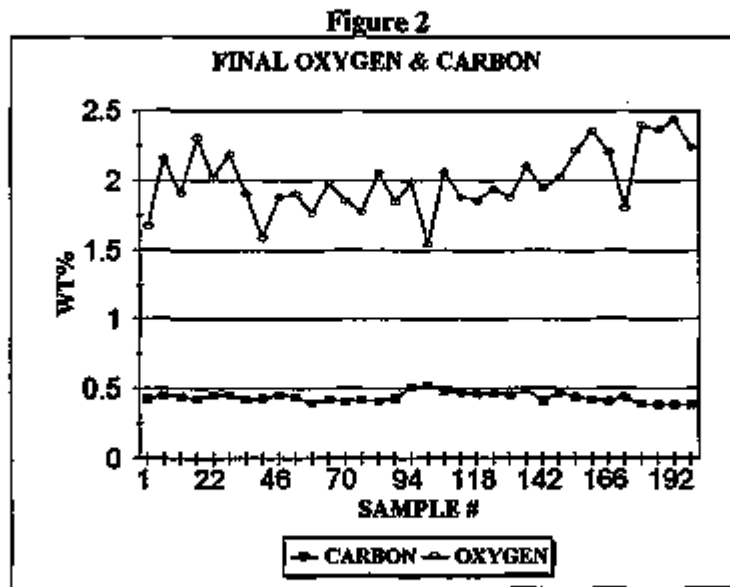
In addition to the installation of a blender, process equipment evaluations continued during the period. In particular, a piece of equipment which could be utilized in the processing of precursor material was identified and tested. Hundreds of pounds of starting material were processed through the new equipment and then returned to the program for incorporation into the process.

Prior to the production of the final powder deliverable, a series of tests were carried out in order to further refine the operating window and conditions during the reaction. The overall objective was to maximize the throughput while at the same time impacting the product quality as little as possible. As a result, a designed experiment was carried out which focused on the key process variables. The major factors were the throughput of material out of the reactor, flow rate, and temperature. The responses were residual oxygen and residual carbon content. The results of the study are still in an evaluation phase but indicate that the throughput can be significantly enhanced and still not impact overall product quality.

Task 3.1 Powder Characterization

The ten kilograms of carbothermal silicon nitride powder, produced in Task 2.0 and delivered to MMES in May, was characterized in order to determine the powder properties. The results of this analysis are summarized in Table I. This lot of carbothermal silicon nitride had an oxygen content of 1.70 wt.% and a carbon content of 0.49 wt.%. The specific surface area and average particle size was measured to be 9.3 m2/g and 0.84 μm, respectively. The metallic and non-metallic impurity levels were found to be very low and well within specifications.

Table II. Powder Properties of 10 kg Lot of Carbothermal
Powder Delivered to MMES in May.

Property	Deliverable	Goals
Oxygen (wt.%)	1.70	<2.5
Carbon (wt.%)	0.49	<0.6
Al (ppm)	ND(50)	<1300
Fe (ppm)	26	<2000
Ca (ppm)	44	<1000
Na (ppm)	ND (400)	<10
Mg (ppm)	ND (100)	<50
K (ppm)	ND (5)	<10
Cl (ppm)	ND (10)	<100
S (ppm)	ND (20)	<100
F (ppm)	NM	<100
Surface Area (m2/g)	9.3	5-20
Alpha (wt.%)	>95	>90
d50 (μm)	0.84	<0.8

ND( ) - not detectable at detection limit indicated in parenthesis
NM - not measured

Task 3.2 Powder Sinterability

Experiments were initiated to examine the alpha to beta transformation behavior in our carbothermal powder. Initial results indicate that the rate of alpha to beta transformation in our baseline carbothermal powder maybe slightly slower than a similar composition made with a di-imide Si3N4 powder. Recent results have shown the rate of alpha to beta transformation can be controlled, surpassing that of the di-imide powder by varying one of the raw material additives used to make the carbothermal Si3N4 powder. The effect of varying the rate of alpha to beta transformation on the properties of carbothermal silicon nitride components is currently under investigation.

Task 3.4 Suspension Development/TASK 3.5 Greenware Formation and Part Densification

Work continues in the areas of slip aging, slip pH and casting conditions on greenware characteristics.

A series of slips, prepared by attrition milling, were aged for various times and their pH monitored. Greenware was then cast from the aged slip, dried and fired. In general, the greenware density and fired density decreased with decreasing slip pH, especially when the pH dropped below 9.7. During the aging process, the slip pH initially decreased reaching a stable level after about 6 hours. The initial quick drop in pH was due to a rise in slip temperature. As a result, slips, which were not aged prior to slip casting, generally produced greenware that warped or cracked during sintering. This type of behavior was attributed to a density gradient caused by the initial pH change. Control of slip pH and temperature during milling was found to be important in preparing high quality greenware.

On casting conditions, three approaches were examined— regular slip casting, vacuum casting, and pressure casting. In vacuum casting, the slip was under atmospheric nitrogen pressure and the gypsum mold was placed under vacuum. In pressure casting, a nitrogen pressure of 80 to 120 psi was applied on top of slip to cast the greenware component. Green and fired densities of the pressure cast pieces were normally 1 to 2 % lower than regular slip-cast and vacuum cast pieces. The rate of casting was at least 5 times faster for the pressure casting method than either the regular or vacuum casting methods.

During this reporting session, slip cast greenware was also fabricated from the 10 kg lot of carbothermal powder sent to MMES in May of 1994. The greenware was slip-cast using our baseline procedure for the Y_2O_3-Al_2O_3-SiO_2 sintering formulation. These plates were then pressureless sintered into components for the mechanical property evaluation and deliverables required in Task 3.7. A total of 7 plates were sintered with an average density of 98.8±0.3%.

Task 3.6 Part Fabrication at AlliedSignal Ceramic Component Division

An independent evaluation of the quality of the carbothermal silicon nitride powder was also conducted by Allied Signal Ceramics Components (ASCC) in Torrance, CA. This evaluation consisted of substituting the carbothermal powder into their standard process for making the GS44 grade of silicon nitride. In this evaluation, the carbothermal powder was mixed into a slip with a solids loading of 70 wt.% using their proprietary formulation. The slip was then cast into greenware 3/4-1" thick with a green density of ~60%. The greenware was then densified using a gas-pressure sintering method. The final density of the sintered component was > 99% of theoretical density. The component was then machined into mechanical test bars to measure the room and high temperature strength, Weibull modulus and fracture toughness. Table III is a summary of the mechanical property results for the Dow carbothermal silicon nitride powder. For comparison, the mechanical properties for their standard GS44 formulation are also included. The results indicate that the carbothermal powder can be substituted into their standard process and yield components with mechanical properties similar or slightly better than their standard material. The room temperature strength, Weibull modulus and fracture toughness of the component made with carbothermal silicon nitride powder were measured to be 1008 MPa, 20.5 and 7.25 MPa-m$^{1/2}$, respectively. At elevated temperatures, the carbothermal silicon nitride component was found to exhibit higher mechanical strength than their standard material. At 900°C, an improvement in average fracture strength of ~25% to 917 MPa was observed.

Table III. Mechanical property results of the GS44 formulation made by ASCC using Dow carbothermal Si3N4 powder and a standard commercially available Si3N4 powder.

Property	GS44 Formulation Made With	
	Dow Carbothermal Si3N4	Standard Si3N4 Powder
Strength (MPa)		
@ 25°C	1008	1050
@900°C	917	715
@1100°C	684	655
Weibull Modulus	20.5	20-35
Fracture Toughness (MPa-m$^{1/2}$)	7.25	8.25

Task 3.7 Part Characterization

The sintered plates produced in Task 3.5, from the same powder lot used in the 10 kg deliverable to MMES, were machined into a total of forty-nine 3 x 4 x 45 mm flexure specimens for mechanical property analysis. Twenty-four of these specimens were tested according to the ASTM C1161 standard for measuring four point bend strengths. The average fracture strength and Weibull modulus of this material were measured to be 875±100 MPa and 10, respectively. The fracture strengths were found to exceed the >800 MPa goal required by the contract. The Weibull modulus was measured to be 10 which is an improvement over our previous results in the last semi-annual report. It is expected that with further processing improvements the Weibull modulus can be increased, surpassing the 15 goal of the contract. As part of a July deliverable, twenty-five of these specimens were sent to MMES for their evaluation.

STATUS OF MILESTONES
All milestones are on schedule.

PUBLICATIONS
Dr. D.F. Carroll presented a paper on the current program at the American Ceramic Society National Mtg. held in Indianapolis, IN., April 1994.

COMMUNICATION/TRAVEL
Drs. C. Conner and D. Carroll visited Norton/St. Gobain Ceramics in July.
Dr. C. Conner visited AlliedSignal Ceramic Components to review the evaluation of the Dow powder.
Dr. G. Eisman and Mr. P.R. Stoesser visited MMES for a project update in July.

PATENT ACTIVITY
None

Cost Effective Sintering of Silicon Nitride Ceramics (SIU-C)
D. E. Wittmer, Southern Illinois University, Carbondale, IL 62901

Objective/Scope

The purpose of this work is to investigate the potential of cost effective sintering of Si_3N_4 through the development of continuous sintering techniques and the use of lower cost Si_3N_4 powders and sintering aids.

Technical Highlights

Task 1.   **Refine Economic Model and Design for Chosen Furnace Configuration**

This task was completed as reported in a previous semiannual report.

Task 2.   **Continue evaluation of sintering parameters on properties of selected Si_3N_4 compositions**

Continuous Sintering

During this reporting period, the CVI belt furnace with the tungsten hot-zone was used to finish the continuous sintering trials for A2Y6, A4Y6, and A2Y8 UBE E-10 Si_3N_4 compositions with and without β-Si_3N_4 seeding. The sintering temperatures of 1675, 1725 and 1750°C for sintering times of 90 min. and 1700°C for sintering times of 30, 60 and 90 min were completed. The physical property measurements, XRD analyses and microstructural analyses were also completed. Tables I and II summarize the 4-point flexural strength results, Table III summarizes the fracture toughness results, and Table IV summarizes the XRD results obtained for these compositions for the respective sintering times and temperatures.

From this data it was determined that seeding marginally reduced the strength for the A4Y6 and A2Y8 formulations, while increasing the strength slightly at lower sintering temperatures for the A2Y6 formulation. Seeding did not appear to have much effect on the fracture toughness (determined by the strength method) for the A4Y6 and A2Y8 formulations, but did appear to somewhat increase the fracture toughness for the A2Y6 formulation.

Although the strength and fracture toughness results did not show any conclusive benefit of seeding, XRD and microstructural analyses showed that seeding does promote the $\alpha \rightarrow \beta$ transformation and enhance the growth of the β-phase. Microstructural analyses also revealed that the β-phase distribution appeared to be more uniform for the unseeded A4Y6 and A2Y8 formulations. Seeding of these formulations produced much

larger β-grains which appeared to be less uniformly distributed. These effects may be the result of using a slightly larger β-seed than used in previous work.

The information obtained from this portion of the subcontract was the basis for one Master's thesis completed during this reporting period. The results of this thesis will be presented at the Annual Conference on Composites and Advanced Ceramic Materials at Cocoa Beach, FL in January, 1995 and will also be published in the conference proceedings. Copies of this thesis have been forwarded to the Program Manager and Project Monitor.

High Temperature Testing

The second bench top testing machine dedicated to elevated temperature testing was received and installed at SIU-C. A furnace fixture was designed and installed which will allow testing up to $1500°C$. During preliminary testing of the furnace and loading fixture, it was determined that the load cell on the test frame was getting too hot during testing to obtain accurate data. The loading fixture was redesigned and materials were ordered from Coors Ceramics to finish rebuilding the test fixture. The alumina loading ram received from Coors was out-of-specification and was returned to Coors for replacement. The replacement has recently been received and subjected to low temperature load evaluation. The test system is now ready for elevated temperature testing.

Improved Processing

Previously it was reported that the processing temperature can have a significant effect on the viscosity of silicon nitride slurries. Depending on the processing method, it is possible to produce a hysteresis behavior in the viscosity as a function of temperature. This research is aimed at determining if this hysteresis behavior will produce a measurable effect on the physical properties and microstructure.

During this reporting period, the A4Y6-E10 formulation (at 30 and 40 vol.%) was processed in the Turbomill under "Hot" (25 °C) and "Cold" (10 °C) conditions to determine the effects of process temperature and slurry aging on green density, sintered density, strength, and microstructure. Some disks were pressure cast directly from the Turbomill after milling for 2 h and then the remaining slurry was aged for 24 h before the remainder of the slurry was cast. These disks were dried, isopressed and sintered in the belt furnace at Centorr/Vacuum Industries. The sintered disks were all >99% of theoretical density. Four-point flexural strength and fracture toughness (strength method) were measured on Type B test bars. Polished test bars for all processing conditions were microwave plasma etched by techniques resulting from an experimentally designed test matrix, and the respective microstructures examined by SEM.

The results indicate a distinct relationship between processing conditions, green density and flexural strength. It appears that the "Cold" processed 30 vol% composition

without aging has the highest average flexural strength and that slurries processing at higher solids loading under both "Hot" and "Cold" conditions produce sintered material with lower flexural strength. Microstructural results indicated that higher solids loading, higher processing temperature, and aging produced a greater degree of agglomeration which is likely responsible for the decreased flexural strength observed. Fracture toughness (strength method) did not appear to be affected by the processing conditions. The strength results are shown in Figure 1 and the fracture toughness results are given in Figure 2.

Task 3. Continue Evaluation of Low Cost Si_3N_4 Powder

As previously reported, the primary goal of this task is to work with the low cost Si_3N_4 powder presently being produced by Dow Chemical Company, under contract to DoE through Martin Marietta Energy Systems, Inc.. A 5 kg sample the Dow Chemical Company Si_3N_4 powder sent to ORNL as part of the May 1994 delivery has been received at SIU-C. This powder is currently being evaluated in A2Y6, A2Y8, A4Y6, and A4Y13 formulations. These compositions have been prepared by Turbomilling as 30 vol% aqueous suspensions, followed by pressure casting, drying, isopressing, and continuous sintering. The density results are given in Table V and the four-point flexural strength results are given in Table VI. These results indicate that it is possible to produce high-density, high-strength materials from this powder. Similar experiments are planned for the Si_3N_4 powder lot which is the final deliverable under Dow Chemical Company's contract.

Task 4. Design and Construct Prototype Belt Furnace

During this reporting period, the prototype Model 44-BF belt furnace was constructed. The furnace has been designed with interchangeable graphite and tungsten hot zones and an innovative SiC link belt. The furnace also has three retractable thermocouples, three over-temperature thermocouples and three 2-color optical pyrometers. The control thermocouples are used with the tungsten hot zone and the pyrometers are used with the graphite hot zone. Preliminary testing with the graphite hot zone was conducted to >2200°C under flowing N_2. Minor design changes were required that necessitated some rework of the hot zone. The design modifications have been made and the furnace is presently being retested with the graphite hot zone. The furnace is now scheduled for delivery to SIU-C in January or February 1995.

Status of Milestones

1.	Refine Economic Model and Design for Chosen Furnace Configuration	Completed
2.	Continue Evaluation of Sintering Parameters on Properties of Selected Si_3N_4 Compositions	On Schedule Continuing
3.	Continue Evaluation of Low Cost Si_3N_4 Powders	On Schedule Continuing
4.	Design and construct prototype belt furnace	On Schedule New Target

Communications/Visits/Travel

D.E. Wittmer, V. A. Knapp, J.J. Conover, and B. Rodely to Annual ACS Meeting in Indianapolis, IN, April 24-27, 1994.

Problems Encountered

Material for high-temperature testing fixture was delayed by Coors.

Publications

V. A. Knapp, D. E. Wittmer, J. J. Conover and C. W..Miller, Jr.,"Microwave Plasma Etching of Si_3N_4," Ceramic Engineering and Science Proceedings, 15 [5] 1118-1127 (1994).

J. J. Conover, " Continuous Sintering of Self-Reinforced Silicon Nitride Containing Reduced Amounts of Sintering Aids," M.S. Thesis, SIU-C, Carbondale, IL August 1994.

V. A. Knapp, "The Effect of Slurry Processing Temperature on Silicon Nitride Properties and Microstructural Development," M.S. Thesis, SIU-C, Carbondale, IL (in review).

Presentations

V.A. Knapp and D.E. Wittmer, "Effect of Processing Temperature on the Viscosity of Silicon Nitride Slurries," Annual American Ceramic Society Meeting, Indianapolis, IN , April 24-27, 1994.

Table I. Summary of flexural strength measurements for belt sintered Si3N4 compositions sintered for 90 minutes at various temperatures.

Temperature	Flexural Strength (MPa)					
(°C)	A4Y6	A4Y6-S	A2Y8	A2Y8-S	A2Y6	A2Y6-S
1750	906	869	1053	929	918	879
1725	952	761	953	978	854	920
1700	890	748	948	966	778	820

-S indicates 5 wt.% β-Si_3N_4 seeded composition

Table II. Summary of flexural strength measurements for belt sintered Si3N4 compositions sintered for 1700°C for various times.

Time	Flexural Strength (MPa)					
(min)	A4Y6	A4Y6-S	A2Y8	A2Y8-S	A2Y6	A2Y6-S
90	890	748	948	966	778	820
60	715	786	875	952	820	685
30	857	741	714	904	741	701

-S indicates 5 wt.% β-Si_3N_4 seeded composition

Table III. Summary of fracture toughness results (strength method) for continuously sintered Si_3N_4.

Composition	Fracture Toughness (MPa-m$^{\frac{1}{2}}$)	Fracture Toughness (MPa-m$^{\frac{1}{2}}$)
	Range for 90 min. sinter	Range for 1700°C sinter
A4Y6	6.6-5.7	5.9-6.6
A4Y6-S	6.6-5.7	6.0-6.6
A2Y8	6.5-6.9	5.0-5.4
A2Y8-S	6.5-6.7	6.1-6.5
A2Y6	5.8-6.5	4.8-5.8
A2Y6-S	6.2-6.5	5.2-6.2

-S indicates 5 wt.% β-Si_3N_4 seeded composition

Table IV. Results of XRD analysis.

Sintering Temperature	Sintering Time	Residual α-Si_3N_4 Content (%)					
(°C)	(min)	A4Y6	A4Y6-S	A2Y8	A2Y8-S	A2Y6	A2Y6-S
1750	90	ND	ND	ND	ND	ND	ND
1725	90	ND	ND	ND	ND	ND	ND
1700	90	ND	ND	ND	ND	ND	ND
1700	60	ND	ND	ND	ND	4.3	ND
1700	30	ND	ND	14	12	17	4.6

-S indicates 5 wt.% β-Si_3N_4 seeded composition
ND = None Detected

Table V. Density of Belt Sintered Compositions Processed with
Dow Chemical Company Si_3N_4.

Composition	Sintering Temp.	Time (min)		
		30	60	90
		% of Theoretical Density		
A2Y6	1775	93.7	--	--
	1750	93.4	93.7	--
	1725	95	94.2	93.8
	1700	--	--	94.2
A2Y6 Oxidized @600C/2h	1725	--	94	93.2

Composition	Sintering Temp.	Time (min)		
		30	60	90
		% of Theoretical Density		
A2Y8	1775	97.6	--	--
	1750	97.1	97.4	--
	1725	95.5	96.6	--
	1700	--	95.2	97.3
	1675	--	93.4	--
A2Y8 Oxidized @600C/2h	1725	--	96.8	96.8

Table V. Density of Belt Sintered Compositions Processed with
Dow Chemical Company Si_3N_4 (continued).

Composition	Sintering Temp.	Time (min)		
		30	60	90
		% of Theoretical Density		
A4Y6	1775	91.9	--	--
	1750	94.2	92.2	--
	1725	96.2	95.5	--
	1700	96.8	96.5	95.7
	1675	--	97	--
A4Y6 Oxidized @600C/2h	1725	--	94.1	93.3

Composition	Sintering Temp.	Time (min)		
		30	60	90
		% of Theoretical Density		
A4Y13	1750	98.9	--	--
	1725	99.2	--	--
	1700	99.4	99.4	99.4
	1675	--	99.4	--
A4Y13 Oxidized @600C/2h	1700	99.4	--	99.4

Table VI. Flexural Strength of Belt Sintered Compositions
Processed with Dow Chemical Company Si_3N_4.

Composition	Sintering Temp.	Time (min)		
		30	60	90
		4-Point Flexural Strength		
A2Y6	1775	---	--	--
	1750	--	--	--
	1725	714	800	904
	1700	--	--	838
A2Y6 Oxidized @600C/2h	1725	--	--	--

Composition	Sintering Temp.	Time (min)		
		30	60	90
		4-Point Flexural Strength		
A2Y8	1775	831	--	--
	1750	826	910	--
	1725	808	838	--
	1700	--	--	830
	1675	--	--	--
A2Y8 Oxidized @600C/2h	1725	--	816	833
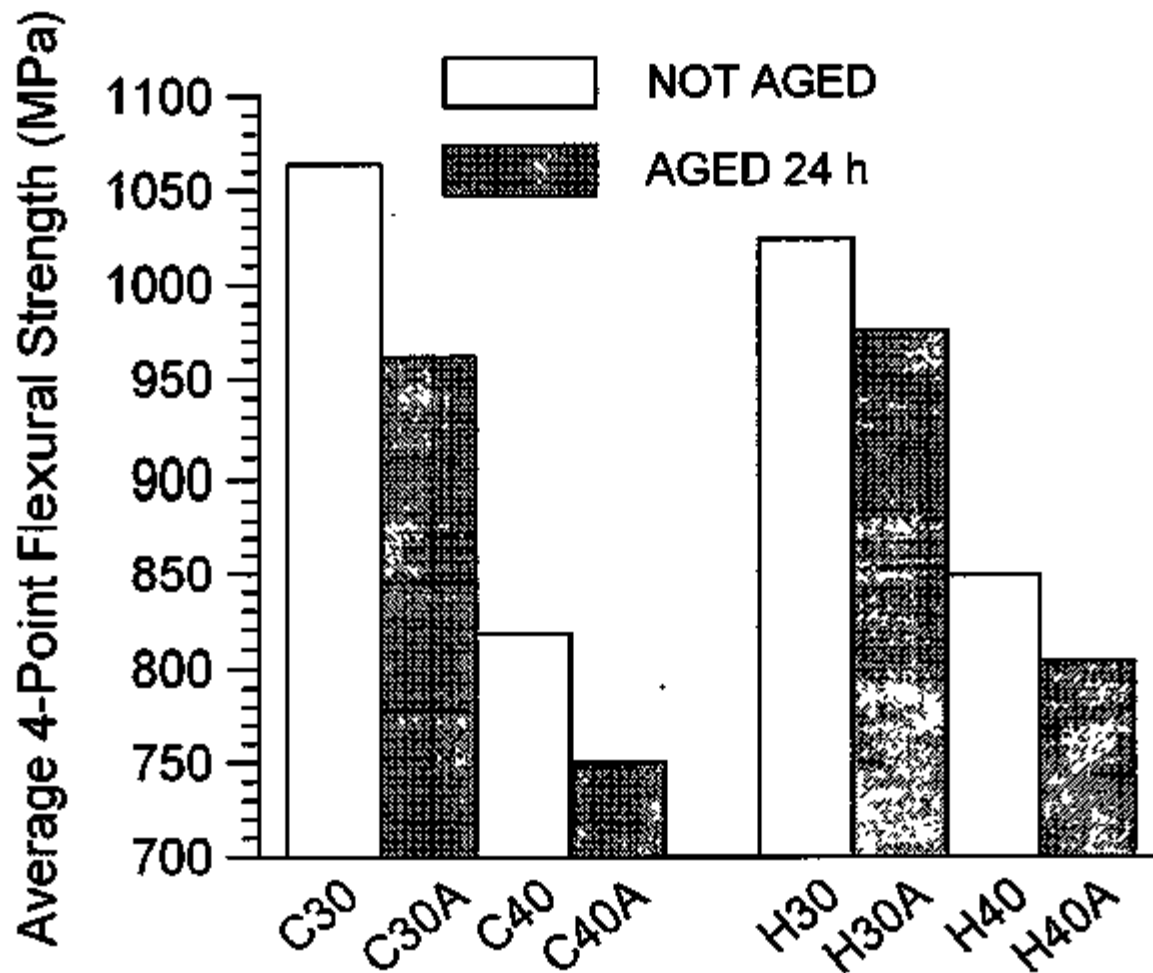
Figure 1 Average 4-point flexural strength for A4Y6 E-10 Si_3N_4 continuously sintered at 1750 °C for 90 min. (C and H represent processing at 10 and 25 °C, respectively, 30 and 40 are the vol.% solid loadings, and A stands for 24 h aging).
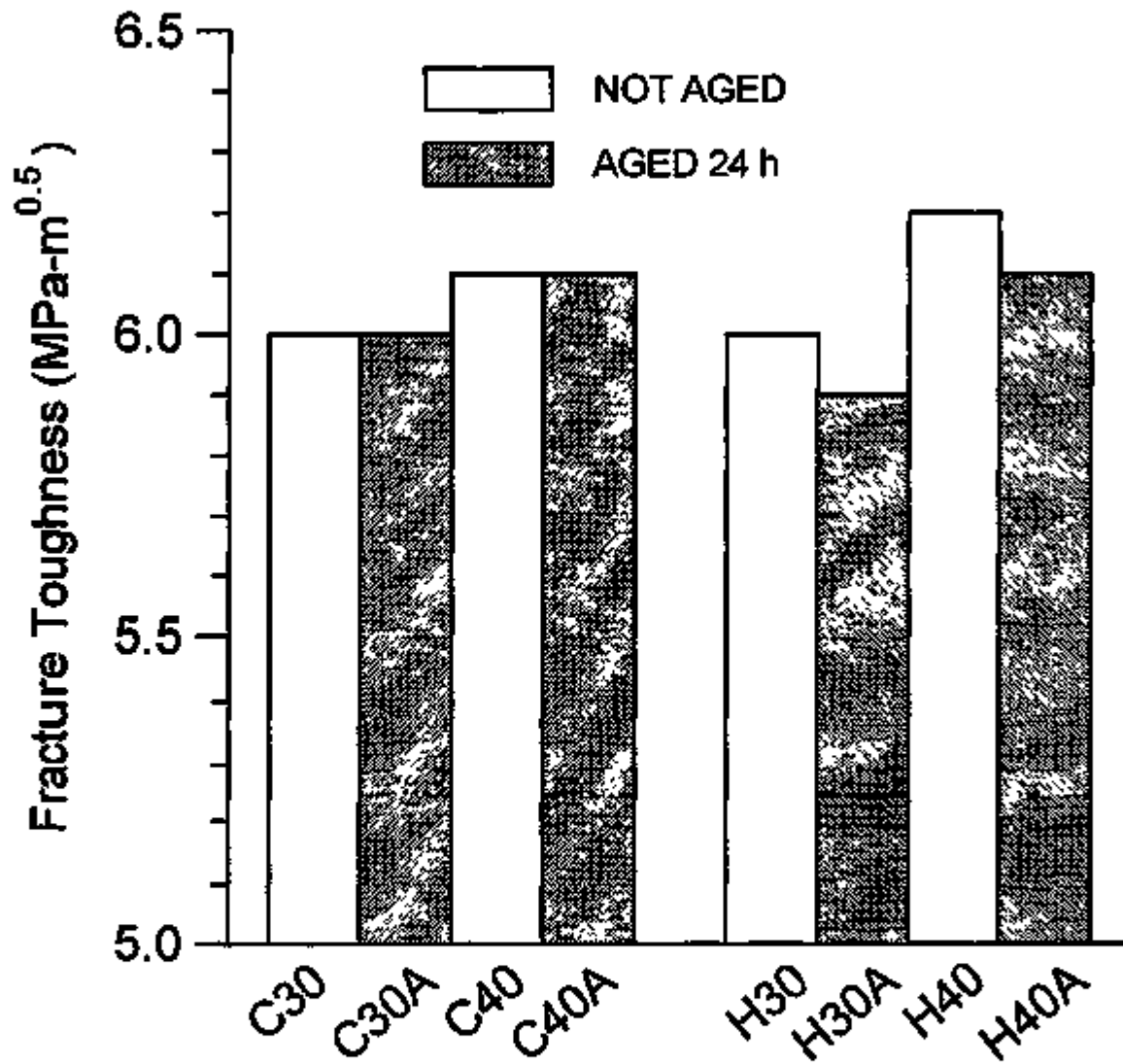
Figure 2. Average fracture toughness (strength method) for A4Y6 E-10 Si_3N_4 continuously sintered at 1750 °C for 90 min. (C and H represent processing at 10 and 25 °C, respectively, 30 and 40 are the vol.% solid loadings, and A stands for 24 h aging).

1.1.4 Processing of Monolithics

Improved Processing
V.K. Pujari, D.M. Tracey, M.R. Foley, A.B. Hardy, S.J. Lombardo, P.J. Pelletier, L.C.Sales, R.L. Yeckley (Norton Company)

OBJECTIVE/SCOPE

The goals of this contract are to develop and demonstrate significant improvements in processing methods, process controls, and nondestructive evaluation (NDE) which can be commercially implemented to produce high reliability silicon nitride components for advanced heat engine applications at temperatures to 1370°C. Achievement of these goals shall be sought through:
- Reliability optimization of aqueous colloidal forming using highly loaded suspensions and glass encapsulated HIP'ing.
- Application of the high reliability colloidal processing technique to a gas pressure sinterable (GPS) composition.
- Demonstration of representative complex component fabrication in both the HIP and GPS systems.

TECHNICAL HIGHLIGHTS

TASK 1: Forming Using Highly Loaded Suspensions and HIP'ing

Completed

TASK 2:   High Reliability Colloidal Processing of GPS Composition

The final batch (S012) of NCX5400 was prepared according to the route developed in the course of the program. Five techniques were used to facilitate the processing of S012:
1)   Temperature Control
2)   pH Control
3)   Surfactant Additions
4)   Form of MgO Addition
5) Si_3N_4 Powder Size Distribution

Approaches 1-4 address the solubility and, hence, dissolution of the magnesium sintering aid into Mg divalent cations. Controlling temperature and pH during milling seems to lower the magnesium ion concentration. The use of surfactants also inhibits the dissolution reactions of the sintering aid into the divalent cations. In addition, some chemical forms have an inherently lower solubility than MgO. Finally, controlling the size distribution of the Si_3N_4 powder leads to better powder packing.

In the early stages of the program, cast green densities of 1.2 - 1.4 g/cc and solids loadings of < 60 weight percent were obtained. Using the 5 approaches outlined above, however, green densities above 2.0 g/cc were attained. Furthermore, the slurry could be concentrated to > 70 w/% and densified to > 99% of theoretical density.

A summary of the progress is given in Table 1.

Table 1:

Batch	Filtered	Concentrated Weight % Solids	Green Density (g/cc)	Fired Density % TD
S001	-	51	1.3	>99
S008	very fine	41	1.3	98.5
S010	medium	40	2.2	96
S012	very fine	72	2.0	>99

Batch S012 simultaneously achieved colloidal stability (as evidenced by the filtration step and concentration to 72 weight percent) and high green and fired density.

Cast tensile rods and CIP'ed tiles from S012 were air fired and then densified according to the GPS cycle. Test specimens were machined following the machining procedure developed in the Processing Phase I program.

Tensile and flexure strength and toughness data are given in Table 2.

Table 2: NCX5400 Strength and Toughness Data

	Tensile Strength (MPa)	Flexure Strength (MPa)	K_{IC} (MPa m$^{1/2}$)
Mean	625	773	8.28
S.D.	103	46	0.38
Characteristic Strength	667	775	
Weibull Modulus	7.0	20	

The tensile strength data were obtained from 27 buttonhead tensile specimens. Of the 27 rods tested, 13 failed from flaws located in the volume of the sample and 14 failed from surface flaws.

In Phase 1 of the program, it was demonstrated that the intrinsic flaw population was best described by a 3 parameter Weibull distribution. Since only a sampling of flaw origins for NCX5400 was determined, this grouping of the flaws cannot be performed in this case. The entire flaw population - both volume and surface - was therefore analyzed according to both 2- and 3- parameter Weibull statistics. As seen in Figure 1, both 2- and 3- parameter distributions describe the data ($r^2 = 0.970$ and $r^2 = 0.979$, respectively) reasonably well.

The strength performance of NCX5400 as compared to other silicon nitride materials is displayed in Figure 2 in which the tensile strength is plotted versus the flexure strength. Material with superior volume properties lie in the upper half of the graph; materials with superior surface properties lie in the lower half. NCX5400 is seen to be equivalent in tension to other gas-pressure sintered materials such as SN253 and NGK. Since the objective of this program was to demonstrate reliable volume properties, this can be assessed by observing how near to the upper half of the graph a material falls. NCX5400 is seen to be the 3rd best material after NCX5102 and SN253.
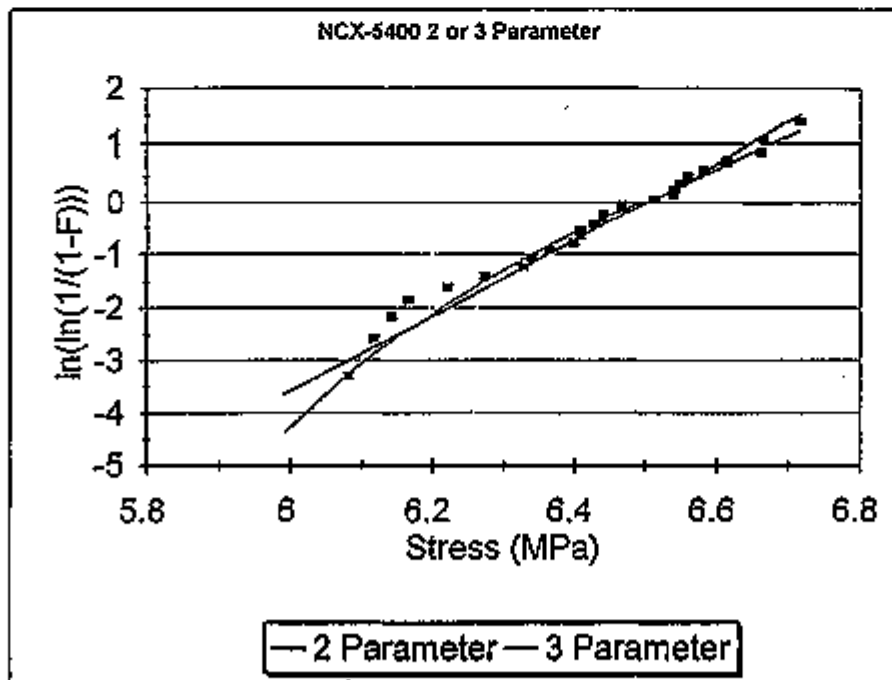
Figure 1: Weibull Plots of NCX5400 Tensile Strength Data
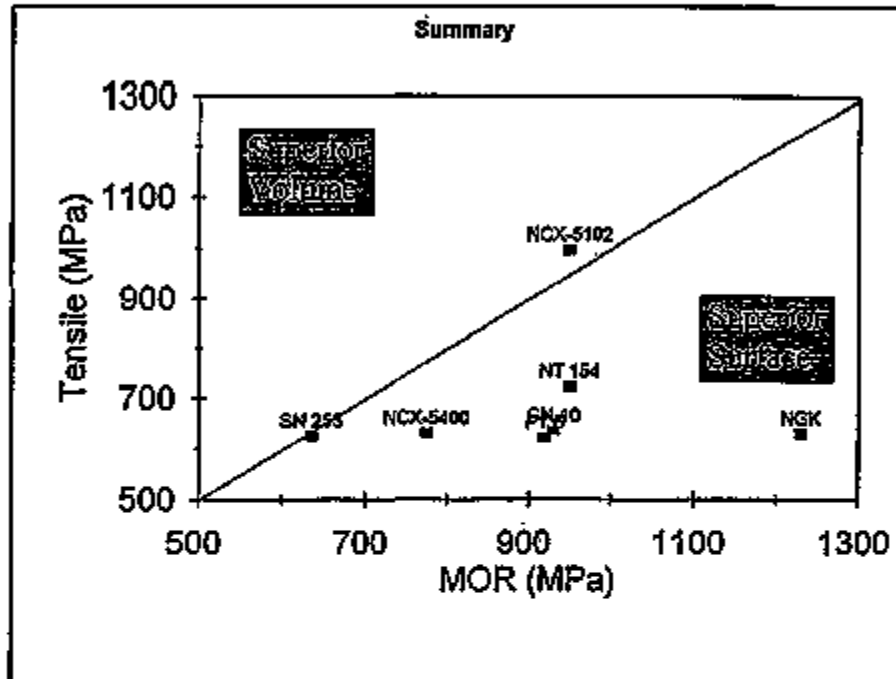
Figure 2:   Tensile vs. Flexure Strength of NCX5400 and Other Silicon Nitride
              Material.

TASK 3: Complex Shape Demonstration

Consistent with the objective of this task, complex shape forming
capability of the NCX5102 slurry was evaluated. Using the standard operating
procedure (SOP) of the closed loop process, a 15 kg batch of NCX5102 slurry
was milled, filtered and subsequently concentrated to a solids loading 72 w %.
Shape forming capability of this slurry was evaluated by pressure casting a
complex shape vane designed for an APU. Castings were performed using a
standard mold being utilized currently by NAC (Norton Advanced Ceramics) for
prototype production of these components.

Net shape castings were produced crack free with NCX5102 slurry with
and without binder addition. The quality of the NCX5102 castings were found to
be equivalent to that produced by the prototype process involving conventional
powder processing and agglomerated powder.

Presence/absence of cracks and surface pits were examined both in the green and dense (HIP'ed) states. Frequency of presence/absence of cracks was found to be equivalent compared to the conventional process. However, presence of surface pits in the HIP'ed component were minimized due to the use of non agglomerated powder in the closed loop NCX5102 process. Of course, the most significant advantage of the NCX5102 castings is the superior (20-30% higher) inherent tensile strength established earlier in Phase I of this program.

REFERENCES

None

STATUS OF MILESTONES

All milestones on schedule.

PUBLICATIONS / PRESENTATIONS

None

PROBLEMS ENCOUNTERED

None

Improved Processing

S. D. Nunn, O. O. Omatete, C. A. Walls, D. L. Barker, R. E. Simpson, M. D. Teske, and J. A. Horn
(Oak Ridge National Laboratory)

Objective/Scope

The objective of this research element is to determine and develop the reliability of selected advanced ceramic processing methods. This program is to be conducted on a scale that will permit the potential for manufacturing use of candidate processes to be evaluated. The emphasis is on silicon nitride. Issues of practicality; safety, hygiene, and environmental issues; and in-process testing methods are to be addressed in addition to technical feasibility. The methodology includes selection of candidate processes and evaluation of their range of applicability to various kinds of commercially available ceramic powders.

Technical Highlights

I.   Silicon Nitride Gelcasting - Dow Powder

Dow Chemical Co. is developing a low-cost silicon nitride powder under W.B.S. Element 1.1.2.5 of the Ceramic Technology Project. As part of the evaluation of this powder, we will be conducting experiments to characterize its behavior in gelcasting.

Initial gelcasting trials indicate that the Dow silicon nitride has considerably different dispersion characteristics when compared to UBE E-10 silicon nitride which has a similar particle size and surface area. Slurries prepared in the MAM/MBAM system became too viscous for gelcast processing at solids loadings above about 40 vol %. The dispersing aids used were GAF PVP K-15 and Darvan 821A. The 40 vol % slurries formed satisfactory gelcast bodies, but a higher solids loading is desirable.

A study was initiated to evaluate the dispersion of the Dow powder using a variety of commercially available dispersing aids. More than 20 dispersing agents were evaluated to determine their effectiveness in dispersing the Dow silicon nitride powder in water. After the initial screening tests in dilute powder slurries, six of these dispersing aids were identified for further evaluation. Gelcasting slurries containing 40 vol % powder were prepared to compare the dispersion characteristics under normal processing conditions. One of the dispersing aids, Hypermer KD-2, was significantly more effective than the others at reducing the viscosity of the slurry. Two additional dispersing aids which were suggested by Dow have been received and will be evaluated during the next reporting period.

A gelcasting batch of the Dow silicon nitride powder was prepared using the Hypermer KD-2 dispersing aid. The solids content in the batch was limited to 40 vol % to maintain sufficient fluidity for deairing and casting. Two flat plate samples were cast from the batch for evaluation of sintering behavior. Yttria and alumina were added to the batch as sintering aids. The samples looked good after the drying and binder burnout procedures; however, both plates cracked during the sintering run. Additional samples are being prepared to determine the cause of the cracking problem.

II.   Sintered Reaction-Bonded Silicon Nitride (SRBSN) Gelcasting

Previous results showed that the porosity which developed during gelling of yttria- and lanthana-containing SRBSN compositions was eliminated when the slurries were aged

for 1 h at 60°C or aged overnight at room temperature prior to the normal milling step. Elimination of this problem has allowed preparation of SRBSN materials with compositions similar to high-strength sintered silicon nitride.

Samples were prepared for nitriding and sintering studies. The sample composition was formulated to result in 4.56 wt % yttria and 3.44 wt % alumina in a silicon nitride matrix after nitridation. Plate samples were cast from several identical batches of gelcast silicon. All of the batches utilized the acrylic acid gelling system which has been described in earlier reports. The density of the samples was measured after firing, and 4-point bend test bars were machined from the plates for strength measurement. The characterization results are summarized in Table 1.

Table 1. Characteristics of gelcast sintered reaction-bonded silicon nitride samples

Sample No.	Nitridation (%)	Fired density		Strength (MPa)	Weibull modulus
		(g/cc)	(%)		
1	92.0	3.15	96.5	497 ± 71	8.0
2	91.5	3.17	97.1	560 ± 88	7.3
3	83.8	3.17	97.2	489 ± 58	9.8
4	83.8	3.19	97.8	595 ± 74	9.3
5	89.9	3.21	98.3	430 ± 54	9.2

The percent nitridation was calculated based on the amount of silicon in the starting composition of the samples and the weight gain after completing the nitriding run. Samples 1, 2, and 4 had a 1-h hold at 1450°C at the end of the nitriding cycle, while sample 3 began cooling down immediately after reaching 1450°C. Sample 5 had a slower ramp rate from 1350°C to the final nitriding temperature of 1450°C. All of the samples were fired at 1800°C for 2 h under a 25 psia overpressure of nitrogen. Although the degree of nitridation showed considerable variation, the fired densities were all quite similar. The variation in 4-point bend strengths is shown graphically in Fig. 1. The strengths do not correlate with fired density or percent nitridation, and additional tests are planned to try to clarify the important characteristics controlling the strength.
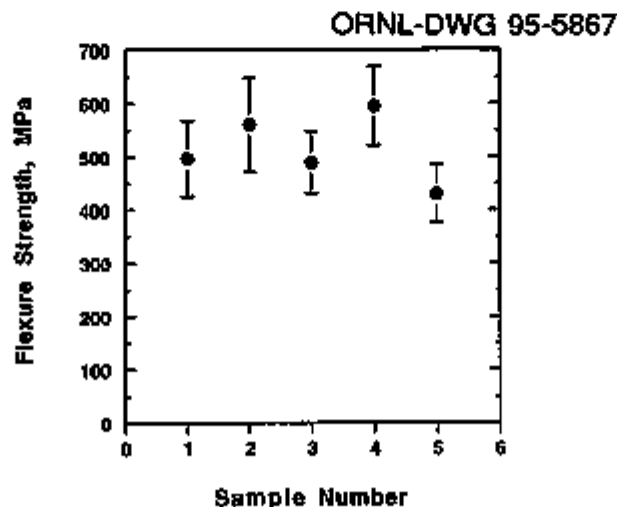
ORNL-DWG 95-5867

Fig. 1. Four-point flexure strength of gelcast Sintered Reaction-Bonded Silicon Nitride (SRBSN) samples.

III. Rheometric Characterization of Gels

Rheometric measurements are being made to obtain quantitative characterization of gels and the gelling process. Complex viscosity measurements of premix solutions (no ceramic powder additions) were made using a high-torque rheometer in oscillatory mode. The premix solutions contained a total of 15 wt % methacrylamide (MAM) monomer plus methylene bisacrylamide (MBAM) crosslinker in water. The monomer-to-crosslinker ratio was varied along with the gelling temperature and the initiator (10 wt % ammonium persulfate in water, APS) and catalyst (tetramethylethylenediamine, TEMED) additions as shown in Table 2. This resulted in a total of 27 combinations which were evaluated. Measurements were made at a frequency of 1 Hz and 10% amplitude.

Table 2. Variations in premix formulation, gelling temperatures, and additions

MAM/MBAM[a] ratio	Gelling temperature (°C)	APS/TEMED[b] additions (μL/μL)/mL of premix
9:1	60	20/2/1
6:1	40	10/1/1
3:1	25	5/0.5/1

[a]MAM/MBAM = methacrylamide monomer/methylene bisacrylamide crosslinker.
[b]APS/TEMED = ammonium persulfate/tetramethylethylenediamine.

Figure 2 shows a typical rheogram which was obtained for a MAM/MBAM ratio of 6:1, a gelling temperature of 40°C, and initiator/catalyst additions of 10 and 1 μL, respectively, per milliliter of premix solution. Generally, the viscosity and the elastic modulus increased by five to six orders of magnitude as the solutions gelled. The small phase angle, delta (δ), indicates that the gels are highly elastic. In all cases, the gelation time decreased with increasing levels of initiator. However, the initiator levels had no significant effect on the modulus and the viscosity of the gels. The gelation temperature appeared to have the most significant effect; the gelation times were decreased sharply with increasing temperature, and surprisingly, the viscosity, modulus, and phase angle all decreased with increasing temperature. These findings show that the gels formed at lower temperatures had higher elastic and viscous moduli than those formed at higher temperatures. These findings will be explored in more detail in future studies.

IV. Drying of Gelcast Green Bodies

The drying characteristics of gelcast bodies are being evaluated in the controlled temperature and humidity chamber. An analytical balance has been incorporated in the system to allow continuous monitoring of weight changes during the drying process. Sample dimensions are measured periodically. Data on the weight, temperature, and humidity are being logged and stored on a computer. Trial runs have been carried out in the humidity chamber where varying temperatures and relative humidities have been programmed into the controller. These runs indicate that both hardware and software problems still exist. However, it is anticipated that the problems will be solved soon and that data for drying under controlled conditions will be available to define the optimum drying conditions for gelcast materials.

V. Golden Technologies Cooperative Research and Development Agreement (CRADA)

A CRADA has been signed with Golden Technologies to evaluate the gelcasting of aluminum titanate to form exhaust port liners. The work plan includes development of an appropriate gelcasting slurry, casting of simple test shapes for firing and characterization, and casting of a more complex shape to demonstrate the process for the intended application.

ORNL-DWG 95-5868
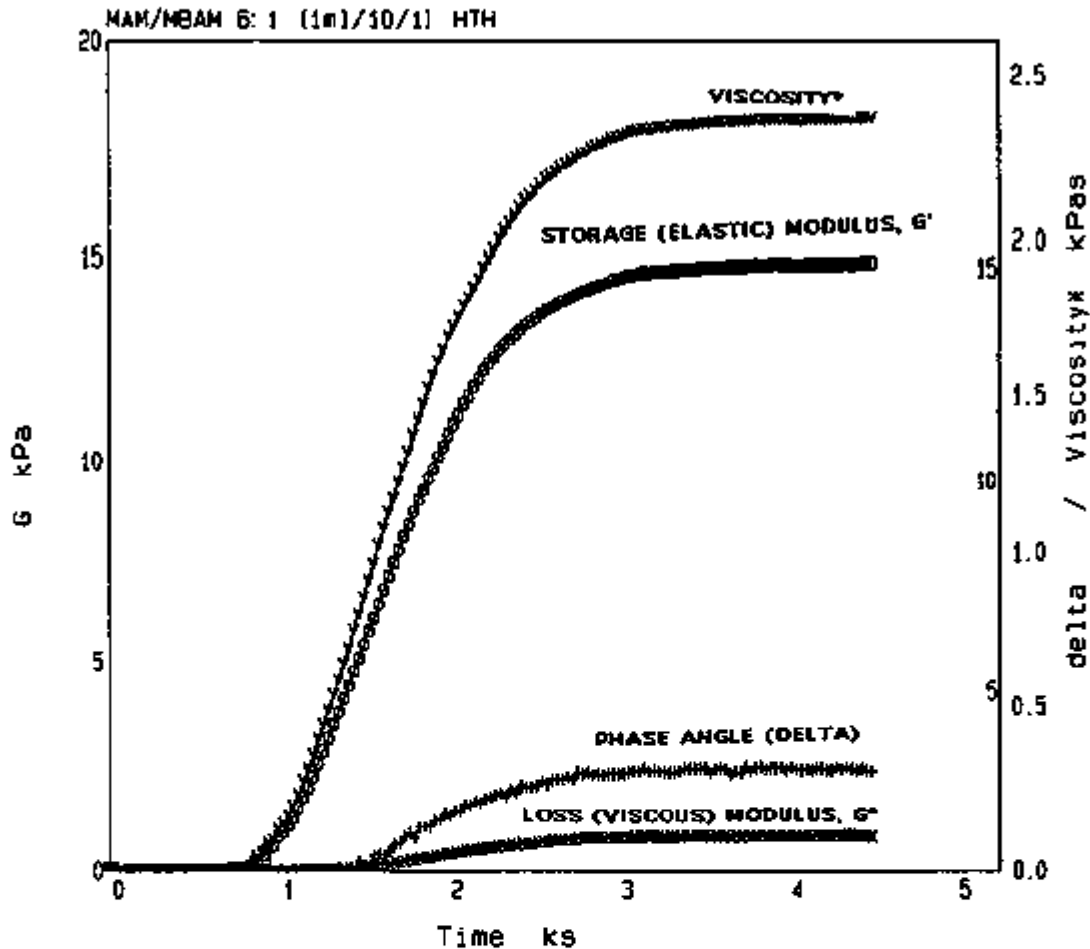
Fig. 2. Rheogram of standard premix solution (6:1) at 40°C and initiation level of 1 mL premix/10 µL ammonium persulfate/1 µL tetramethylethylenediamine.

Initial gelcasting trials using Golden's slip-casting slurry formulation in the MAM/MBAM gelcasting system showed good gelling properties but poor drying characteristics. Additives in the slurry formula apparently sealed off the pore structure at the surface of the cast samples during the early stages of drying and strongly inhibited drying of the bulk material. The individual starting materials were shipped from Golden to prepare an alternate aluminum titanate composition for gelcasting which eliminated some of the organic additives that had been used in the original formulation. Using the altered formula, the slurries showed good viscosity and gelling characteristics and dried at rates similar to other gelcast materials.

Samples in both plate and tubular form were cast and fired. The density of the samples fired at ORNL was somewhat less than that observed in firings of the baseline material at Golden. Particle size measurement of the milled slurry showed a particle size distribution which was coarser than baseline slip-casting material. Samples were sent to Golden for evaluation and comparison. Their evaluation showed results in agreement with the findings obtained at ORNL. It is believed that correction of the particle size distribution will improve the fired density. Approaches for improving the milling of the aluminum titanate powder composition were discussed, and alternative milling procedures will be evaluated during the next reporting period.

<u>Status of Milestones</u>

On schedule.

<u>Publications and Presentations</u>

S. D. Nunn, O. O. Omatete, C. A. Walls, and D. L. Barker, "Aqueous Gelcasting of Ceramic Materials," Paper SVIII-66-94, presented at the 96th Annual Meeting of the American Ceramic Society, Indianapolis, Ind., April 24-27, 1994.

S. D. Nunn, O. O. Omatete, C. A. Walls, and D. L. Barker, "Tensile Strength of Dried Gelcast Green Bodies," *Ceram. Eng. Sci. Proc.* 15 [4], 493-98 (1994).

1.2 CERAMIC COMPOSITES

1.2.2 Silicon Nitride Matrix

Optimization of Mechanical Properties of Silicon Nitride Ceramics
K. J. Lee and T. Y. Tien (The University of Michigan)

Objective/Scope

The objective of this project is to investigate a two-phase silicon nitride ceramics whose compositions consisting β-Si_3N_4, α'-SiAlON and a grain boundary phase. We have shown that the β-Si_3N_4 + α'-SiAlON ceramics consists of elongated β-Si_3N_4 grains and equiaxed α'-SiAlON grains. The intertwining of the elongated β-Si_3N_4 grains and equiaxed α'-SiAlON grains gives this material its superior mechanical properties. However, these materials can only be sintered using transient liquid and the liquid phase will be consumed at the later stage of sintering process. Therefore, it is difficult to develop desirable morphology of the silicon nitride phases. When another compounds are added as sintering additives, stable liquid will be formed during sintering. This condition will allow the silicon nitride phases to develop their desired morphology which will give these ceramics superior mechanical properties. Garnet ($Y_3Al_5O_{12}$) was selected for this purpose. The system β-Si_3N_4 - α'-SiAlON - $Y_3Al_5O_{12}$ will be studied.

Technical Highlights

In order to select optimum compositions for densification, melting behavior in the system has to be determined. Composition points were calculated in the composition triangle β-Si_3N_4 + α'-SiAlON + YAG. The compositions investigated are shown in Fig. 1. Batches were prepared by using Si_3N_4, AlN, Al_2O_3 and Y_2O_3 as starting materials. Powders were mixed under acetone, cold-pressed into pellets, and sintered under the pressure of 10 atm N_2. Melting behavior of these compositions will be determined.

Status of Milestones
On schedule.

Communications/Visits/Travel
None.
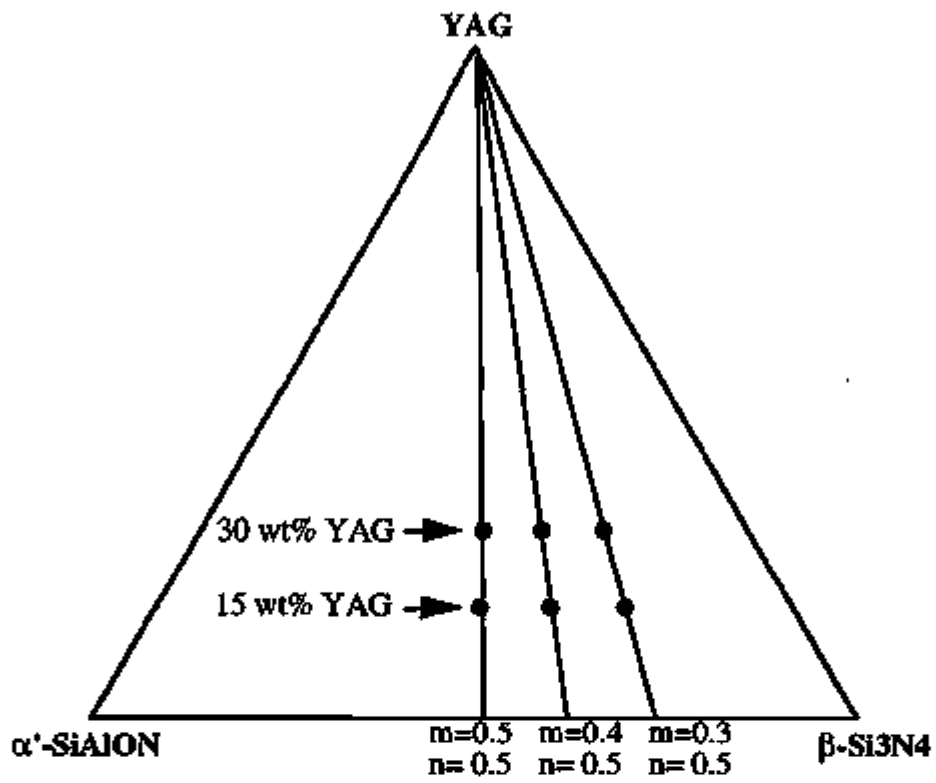
Problems Encountered
None.

Fig.1 Composition triangle in α'-SiAlON - β-Si3N4 - YAG system.

Microstructure Optimization of SRBSN
S. F. Kuang, K. J. Lee, and T. Y. Tien (The University of Michigan)

Objective/Scope

Sintered reaction bonded silicon nitride is one of the most cost effective method for producing silicon nitride ceramics in large quantities. However this method involves the nitridation of the starting metallic silicon particles and post nitridation sintering which make the control of the microstructure difficult. The purpose of this project is to develop a process to obtain green compacts with uniform pore distribution. Nitridation process will also be optimized to produce uniform microstructure. Post nitridation sintering will also be studied to develop optimum morphology of the β-Si$_3$N$_4$ grains.

Technical Highlights:

Silicon powders were obtained from Oak Ridge National Laboratory. Particle size distribution of the "as received powder" was measured, and the average particle size was 2.25μm, which was also confirmed by the SEM photo. The relationship between the average particle size and attrition milling time is shown in Figure 1. Attrition milling time for 2 hours was used for our experiment. After 2 hours of milling, the average particle size is about 0.96μm. The particle size distribution curves before and after the attrition milling are shown in Fig. 2.

Composition containing 67.85% Si + 0.23% SiO$_2$ + 14.51% α-Si$_3$N$_4$ + 13.06% Y$_2$O$_3$ + 4.35% Al$_2$O$_3$ (Weight) was chosen for this study. The mixed powder was attrition milled for 2 hours with isopropyl alcohol in an alumina jar using alumina milling balls. The surfactant (PVP K-30) was also added to the milling.

To determine the best rheological condition for pressure casting, the viscosity of the slurry was measured with a cone/plate viscometer. Slurries with different solid content were made. Surfactant content which gave the lowest viscosity, and hence the best casting condition, was obtained. Figure 3 shows the relation between viscosity and PVP concentration. A common minimum with 5 (g PVP/100g Powder) is seen at various solid contents, therefore it was used for subsequent work.

Discs were made by pressure casting. Different pressure-time program were used for preparation of green bodies. Pores size distributions will be measured using mercury porosimeter. Green compacts will be delivered to Terry Tieg in ORNL for nitridation.

Status of Milestones
On schedule

Communications/Visits/Travel
None

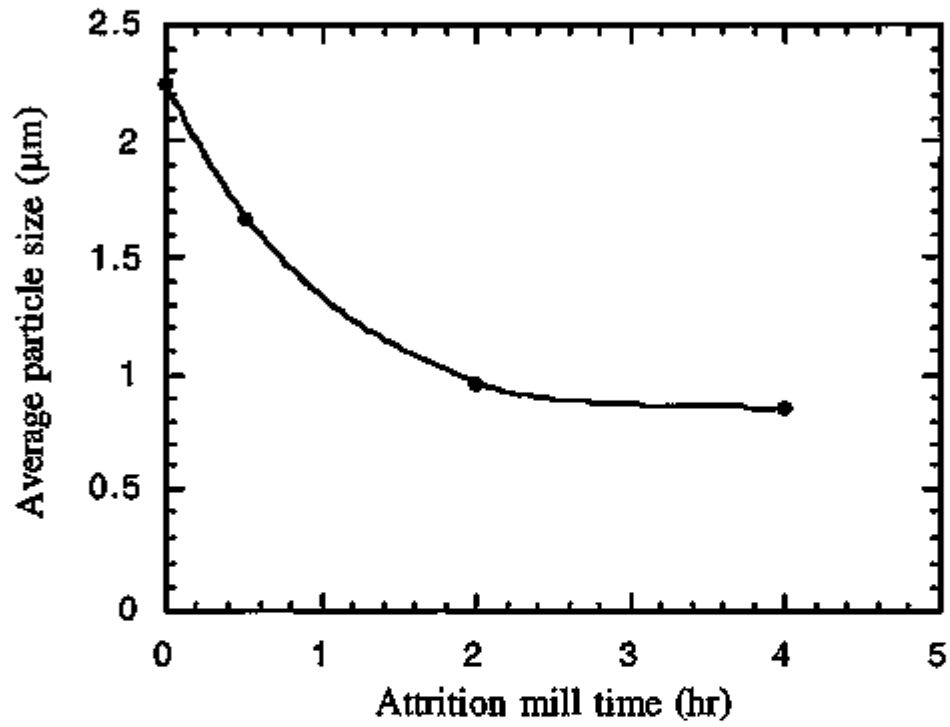### Problems Encountered
None

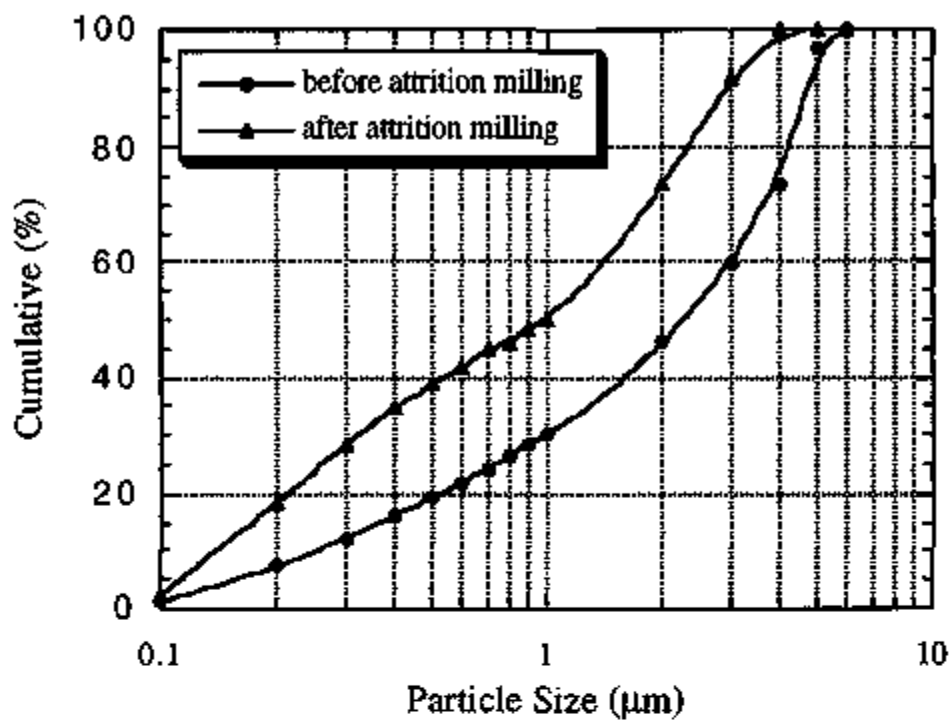Fig. 1   Relationship between average particle size and attrition milling time

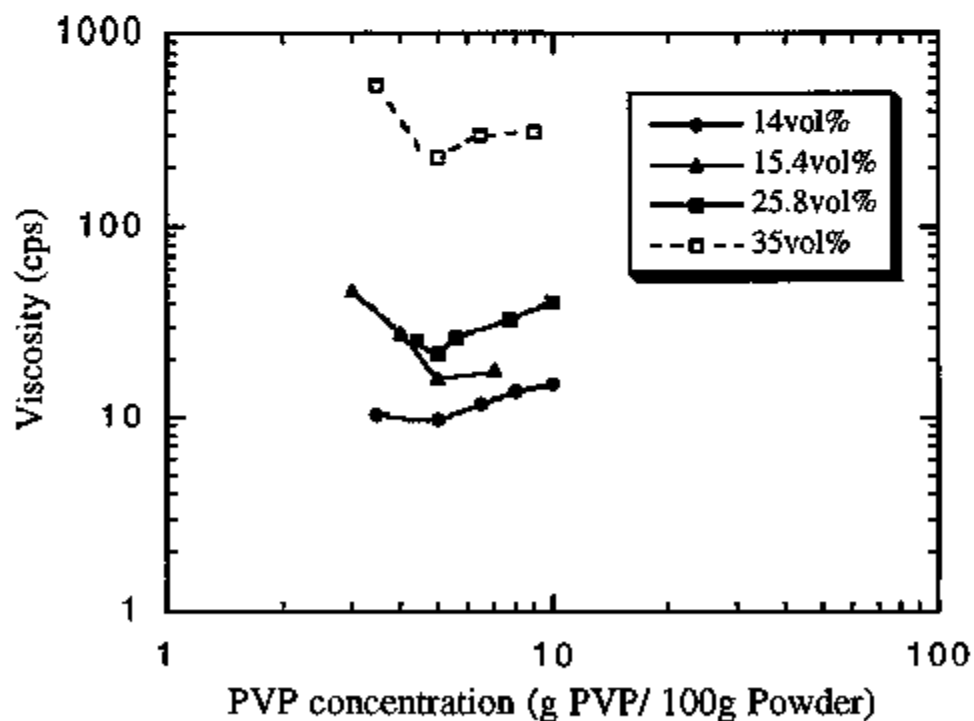Fig. 2 Particle size distribution of powder before and after attrition milling (2hr)

Fig. 3 Viscosity variation with PVP concentration at different solid contents

Characterization of Grain Boundary Phases in Silicon Nitride Ceramics
I. M. Peterson and T. Y. Tien (The University of Michigan)

Objective/Scope

The objective of this investigation is to develop silicon nitride ceramics with high flexural strength, high fracture toughness and superior creep resistance. The fiber-like structure of the β-Si$_3$N$_4$ grains can be obtained by sintering the silicon nitride ceramics at high temperature under high nitrogen pressure. The composition of the sintering additives will affect the microstructural development, grain boundary characteristics, and hence, the mechanical properties. The grain boundary phases have never been synthesized separately and their properties have never been studied. The goal of this project is to synthesize and characterize the grain boundary phase and to understand the relationships between the nature of the grain boundary phase and the properties of silicon nitride ceramics. It is believed that with a thorough understanding of these relationships, ceramics with optimum mechanical properties can be obtained.

The energy required to propagate an intergranular crack depends on the residual stress present at the grain boundary , the strength of the bonding along the interface, and the intrinsic toughness of the grain boundary phase. The residual stress can be controlled by tailoring the thermal expansion coefficient mismatch between the silicon nitride and the grain boundary phase. The intrinsic toughness of the grain boundary phase is dependent on both the chemistry and the morphology of the grain boundary phase.

This report contains the first measurements of the residual stress caused by thermal expansion mismatch betweeen the grain boundary phase and silicon nitride. The stresses were measured by both x-ray and neutron diffraction methods at ORNL.

Technical Highlights

Both x-ray and neutron diffraction techniques rely on the shift in the positions of the diffraction peaks caused by distortion in the crystal lattice. For example, if the lattice is under compression, the interplanar lattice spacing will decrease, which will shift the peak position to higher angles. Residual stresses are determined from the difference in lattice spacing between an unstressed reference sample and a stressed sample. The strain in any particular direction can be determined from the lattice spacing [1] :

$$\varepsilon_{hkl} = \frac{d - d_0}{d_0} \qquad (1)$$

where:

ε_{hkl} is the strain in direction [h k l],
d is the measured lattice spacing along direction [h k l]
and d0 is the lattice spacing in the unstressed sample along
direction [h k l]

Silicon nitride samples with different volume percentages of two different sintering aids were prepared, as shown in Table I. The sintering aids were two different alkaline earth

aluminosilicate compositions: 2 MgO: 2 Al$_2$O$_3$: 5 SiO$_2$ and 2 BaO: 2 Al$_2$O$_3$: 5 SiO$_2$.

The oxide powders were attrition milled with silicon nitride for four hours . The sintering schedules are shown in Table II . The samples were all densified by gas pressure sintering under 10 atmospheres of nitrogen. The samples were quenched by turning off the power to the furnace. The sample containing 10 volume % BaO- was sintered at a higher temperature than the others to avoid the crystallization of its refractory grain boundary phase. The sample containing 25 volume % barium aluminosilicate underwent further heat treatment o crystallize the grain boundary phase, as shown in Table II.

The samples were polished to 0.1 μm. After polishing, the samples were annealed at 1500°C for one hour to remove the polishing stresses. X-ray diffraction was used to determine the phases present.

The compositions and thermal expansion coefficients of the grain boundary phases are shown in Table III. (The thermal expansion coefficient of Si$_3$N$_4$ is 3.0 x 10^{-6}/°C.)

In silicon nitride, the (233)/(323) peak and the (451/541) /(720/270) peaks were used for the neutron diffraction measurements of strain . The wavelength was 1.4178 angstroms.The pattern from 80°<2Θ<150°was also obtained for each sample.

For the x-ray measurements of strain , the (233)/(323) peak was used. The wavelength was CuKα at 1.5406 angstroms. Tilt angles of 0°, 45° and 90° did not detect any significant macrostresses. The pattern from 130°<2Θ<155° was also obtained for each sample.

The thermal expansion coefficient of both grain boundary phases was higher than that of silicon nitride, so a sompressive stress in the silicon nitride would be expected . As expected from theory, the amount of compressive strain in the silicon nitride increased as the thermal expansion coefficient of the grain boundary phase increased. The amount of compressive strain in the silicon nitride also increased as the volume fraction of the grain boundary phase increased. The strains measured using the (233)/(323) peak are shown in Table IV. The lattice strains are listed in Table IV, along with the standard deviation (± σ) of the measurement. The strains along the a and c axes obtained using Rietveld refinement of the neutron scattering data are also listed.The stresses were calculated from the measured strains using x-ray elastic constants measured by Tanaka et al .[2] The Young's moduli and Poisson's ratio for the [323] direction are E $_{323}$ = 305 GPa and v= 0.26. Figure 1 shows the stresses calculated using Eshelby's inclusion theory, along with the stresses calculated from the strains measured using x-ray and neutron diffraction. The stresses found from both diffraction techniques are much higher than the calculated stresses. The calculated stresses are too low because the silicon nitride grains are close enough together for their stress fields to interact, which imposes additional constraints on the deformation in the glass. The model assumes no interactions between the particles. The stresses found from the x-ray data are about 100 MPa smaller than those found from the neutron data. The lower stress values found by x-ray diffraction probably indicate surface relaxation.

T. Watkins performed the x-ray diffraction residual stress measurements. X.L. Wang performed the neutron diffraction stress measurements.

References

1. X. L. Wang, C. R. Hubbard, K. B. Alexander and P. F. Becher, " Neutron Diffraction Measurements of the Residual Stresses in Al_2O_3-ZrO_2 (CeO_2) Ceramic Composites", *J. Am. Cer. Soc.*, **77** , 1569-75 (1994)

2. K. Tanaka, Y. Yamamuto and K. Suzuki, "Elastic Constants of Ceramics from X-Ray Residual Stress Measurement" pp 328-335 *International Conference on Residual Stresses, ICRS2*, ed. by G. Beck, S. Denis and A. Simon , *Proceedings of the Second International Conference on Residual Stresses,* Nancy, France, 1988, Elsevier Science Publishers Inc., Essex, England (1989)

Status of Milestones
On schedule

Communications/Visits/Travel
Visit to Oak Ridge National Lab from 8/8/94 - 8/12/94 to use x-ray and neutron diffraction instruments.

Problems Encountered
None

Publications

Accepted for publication:

Huang, Z. K., Nunn, S.D., Peterson, I.M. and Tien, T.Y. " Formation of N-Phase and Phase Relationships in MgO-Si_2N_2O-Al_2O_3 System"
in the Journal of the American Ceramic Society

TABLE I Sintering Aids

Sample	Sintering Aid	Volume % Sintering Aid
5 MgAlSi	2 MgO: 2 Al_2O_3: 5 SiO_2	5
15 MgAlSi	2 MgO: 2 Al_2O_3: 5 SiO_2	15
10 BaAlSi	2 BaO: 2 Al_2O_3: 5 SiO_2	10
25 BaAlSi (crystallized)	2 BaO: 2 Al_2O_3: 5 SiO_2	25

Table II- Sintering Schedules - Multi - Step Sintering and Annealing

Sample	STEP 1	STEP 2	STEP 3
5 MgAlSi	1640°C (3 hrs)	1840°C (3 hrs)	1640°C (2 hrs)
15 MgAlSi	1640°C (3 hrs)	1840°C (3 hrs)	1640°C (2 hrs)
10 BaAlSi	1640°C (3 hrs)	1940°C (3 hrs)	
25 BaAlSi	1640°C (3 hrs)	1840°C (3 hrs)	1640°C (2 hrs)

Crystallization

25 BaAlSi	1450°C (6 hrs)

Annealing

5 MgAlSi	1500°C (1 hr)
15 MgAlSi	1500°C (1 hr)
10 BaAlSi	1500°C (1 hr)
25 BaAlSi	1500°C (1 hr)

Table III - Compositions and thermal expansion coefficients of the grain boundary phases

MgO (mol %)	BaO (mol %)	Al_2O_3 (mol %)	SiO_2 (mol %)	Si_3N_4 (mol %)	$\alpha \times 10^6/°C$
0.20	0	0.21	0.51	0.08	3.4
0	0.20	0.21	0.51	0.08	7.3

Crystalline Grain Boundary Phases

$BaAl_2Si_2O_8$ (Hexacelsian) $8 \times 10^{-6}/°C$

Table IV - Lattice Strains Measured by X-Ray and Neutron Diffraction

Sample	Grain boundary	X-ray $\varepsilon (\pm\sigma)$	Neutron* $\varepsilon (\pm\sigma)$	Neutron (Rtvld) $\varepsilon_a, \varepsilon_c$
5 MgAlSi	Glass	0 (standard)	0 (standard)	0, 0 (standard)
15 MgAlSi	Glass	-2.96×10^{-4} $(\pm 0.04 \times 10^{-4})$	-4.50×10^{-4} $(\pm 0.11 \times 10^{-4})$	$\varepsilon_a = -3.0 * 10^{-4}$ $\varepsilon_c = -5.5 * 10^{-4}$
10 BaAlSi	Glass	-4.95×10^{-4} $(\pm 0.04 \times 10^{-4})$		
25 BaAlSi	Crystalline	-8.41×10^{-4} $(\pm 0.05 \times 10^{-4})$	-9.18×10^{-4} $(\pm 0.11 \times 10^{-4})$	

* (323)/(233) pe

Table V- Elastic Properties Used in Calculations

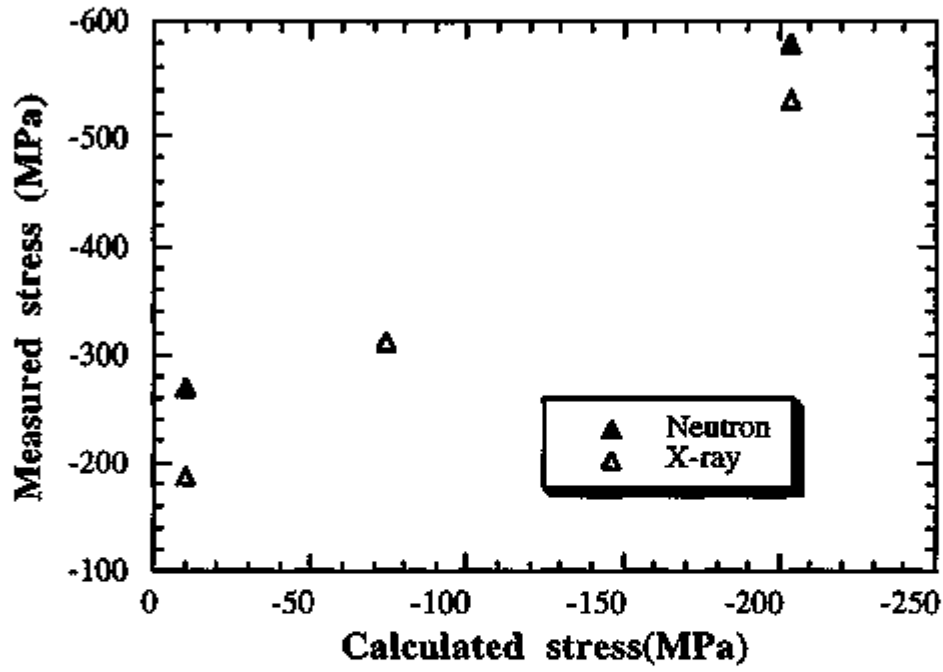|	Silicon Nitride	Glass
E, GPa	305	100
ν	0.26	0.3

Figure 1- Comparison between calculated and measured residual stresses

Development of Silicon Nitride Ceramic Materials with Elongated Grain Microstructures Exhibiting High Fracture Toughness Phase II
H. Yeh, J. Wimmer, C-W. Li, and J. Yamanis (AlliedSignal Inc.)

Objective/Scope

Under Phase I, an *in situ* reinforced (ISR) silicon nitride material (AS800) with elongated grain microstructure has been developed. It was accomplished through composition and processing optimization of a material which had initially been developed at AlliedSignal. The objective of this follow-on effort (Phase II) is to expand the AS800 material property database to meet the requirements for heat engine applications and to build on Phase I results to further improve material properties and processing. To accomplish this objective, a three-task effort shall be conducted over a two-year period. The technical effort was initiated in March 1994.

The AS800 material developed under Phase I (crystallized Composition 2) shall be the baseline for Phase II. Based on the property values measured under Phase I, AS800 is suitable for heat engine applications. However, in order for the material to be considered for these applications, a more comprehensive data base is required for life prediction and other design needs. A typical test matrix recommended by an engine company shall be conducted under Task 1—Expanded Characterization of AS800. The test matrix includes more comprehensive testing of mechanical and thermal properties from room temperature to 2500°F. In addition, an established cyclic oxidation durability test will also be conducted to determine the long-term durability of the material in a simulated gas turbine environment. Most of the tests shall be performed on the baseline material using fully machined test bars, which represent the bulk properties of the material.

For net-shape formed components, the as-processed surface properties are critical. Due to its rougher surface texture and the exposure to the sintering environment, the as-processed surface properties of a silicon nitride part are known to be inferior to the bulk properties. Under Task 2--As-Processed Material Surface Property Improvement, the baseline material surface property shall be characterized and then various techniques shall be investigated to improve the as-processed surface properties.

Although AS800 is densified by a relatively economical technique (gas pressure sintering), compared to glass encapsulation HIP, there is a need to further reduce the cost of densification. The densification process developed under Phase I was primarily aimed at achieving the property goals, without addressing fabrication cost reduction issues. Under Task 3--Lower Cost Fabrication, the green processing procedures and the densification process shall be scaled up and further optimized to reduce the cost without degrading the properties.

TASK 1--EXPANDED CHARACTERIZATION OF AS800

The objective of this task is to conduct a comprehensive test matrix of mechanical properties for crystallized Composition 2. The test matrix includes tensile, flexural strengths, tensile stress rupture, and toughness from RT through 2500°F, and cyclic oxidation durability test in a simulated engine environment. In addition, elastic and thermal properties from RT through 2500°F shall be measured.

The initial effort of this task was to demonstrate process and property reproducibility in large plates (Approximately 5" x 9" x 1") suitable for machining into button-head tensile test specimens. (Plate size fabricated in Phase I efforts were mostly 2" x 3" x .75") After the reproducibility has been demonstrated, a large number of 5" x 9" plates are being fabricated and then machined into various test specimens, including 140 button-head tensile specimens.

The reproducibility demonstration effort was completed during this reporting period, and the results showed that the baseline process and properties are reproducible. Thus, fabrication of the large plates for tensile and other test specimens was initiated, and is still in progress. To date a total of sixty (60) tensile specimens have been fabricated and the fabrication of the remaining tensile and other test specimens will be completed in the next reporting period.

TASK 2 -- AS-PROCESSED SURFACE PROPERTY IMPROVEMENT

The objective of this task is to improve the as-processed surface properties of crystallized Composition 2. The initial efforts conducted in this reporting period included establishing baseline as-processed surface properties and evaluating the effects of several alternate sintering procedures on the as-processed surface properties. The alternate sintering procedures explored included powder bed, wrapping the green AS800 samples with Si_3N_4 tapes, surrounding the sample with Si_3N_4 tape fragments, and crucible types (chemistry). Samples achieving 99.5% theoretical or higher densities were evaluated. For screening purposes, flexural strengths, based on a limited test results (5 - 8 tests at room and 2 - 3 at an elevated temperature), were the major properties measured to evaluate the effect of the experimental processing techniques. On selected samples, additional characterization were conducted which included stress rupture, indentation toughness and X-ray diffraction (XRD) phase analysis on the as-processed surfaces.

The results obtained to date suggest that among the techniques evaluated, the use of Type II crucibles has the highest potential to produce a significant improvement in as-processed surface properties, as well as being a viable production method. Thus, two additional plates were fabricated using Type II crucibles for a more complete characterization. These plates were sintered to 99.8% theoretical density and their surfaces showed the typical dark-gray color. The room temperature flexural strengths and the corresponding fracture origins are listed in Table 1. The average strength is 103.1±8.1 ksi or 711± MPa (vs. program goal of 770 MPa) and the Weibull modulus calculated from the maximum likelihood method is 16.1 (vs. the program goal of 20). Most of the fracture origins are either large grains or surface, except the two lowest strengths. One is a pore and the other an inclusion, which were both green forming related. If the two bars fractured from green processing related origins were eliminated, the Weibull modulus will be increased to 19.4. The 1200°C and 1370°C strengths (average of two tests) are 596±17 and 538±21 MPa, respectively, which met the program goals. The additional characterization to be conducted early in the next reporting period includes stress rupture and indentation toughness.

Table 1 - Room Temperature As-Processed Surface Strength

Specimen Number	Strength		Fracture Origin
	ksi	MPa	
1	85.0	586	Pore
2	88.0	607	Black Inclusion
3	93.8	647	Surface
4	95.8	661	"
5	97.4	672	Large Grain
6	99.5	686	"
7	99.9	689	Surface
8	102.2	705	Large Grain
9	103.7	715	"
10	104.5	721	Surface
11	105.0	724	Large Grain
12	106.2	732	Surface
13	107.2	739	Surface
14	107.4	741	Large Grain
15	108.7	749	Surface
16	109.1	752	"
17	109.7	756	"
18	110.4	761	"
19	111.6	769	Large Grain
20	117.2	808	Surface
Ave.	103.1±8.1	711±56	

TASK 3 - LOWER COST FABRICATION

The objective of this task is to lower the fabrication cost by scaling up the green forming process (primarily milling/slip preparation process) and the sintering/crystallization process from laboratory scale to production scale. Milling/slip preparation will be scaled up by a factor of six (6); sintering capacity will be increased more than ten (10) times from a small size furnace to a new production size furnace for AS800.

1) Milling/Slip Preparation Scale Up

The initial work conducted in preparation for the actual scale up effort, was to evaluate the effect of not cleaning the mill jar and media after each use. This experiment was performed using the baseline laboratory size mill jar, assuming that the results are applicable to the large scale mill. The current baseline procedure calls for cleaning the mill jar and media immediately after use so that the next batch of material would not be affected by the residues left from the previous batch. The cleaning procedure is time consuming and labor intensive, thus costly. It is desirable to eliminate the cleaning step without affecting the final properties of the material fabricated continuously in a production mode. Two iterations of experiments for a total of six mill jars of materials have been processed through densification/crystallization. Each iteration consists of preparing a batch of slip starting with using a cleaned mill jar/media to prepare a batch of AS800 slip using the baseline procedure, followed by preparing two additional batches of AS800 in the second and third days without cleaning the mill jar/media. The slips were cast into 2" x 3" plates. In each iteration, the slip batches are designated as Day 1, Day 2 and Day 3, respectively. The key green processing characteristics such as slip viscosity, specific gravity and green density were monitored. The data did not exhibit any detectable effect of mill jar/media not being cleaned. All materials were sintered to near full density (>99.5% Theoretical) using the baseline sintering cycle.

Standard 2" x 3" plates from one of the iterations have been machined into test bars and have been tested for room and elevated temperature strengths. Table 2 summarizes the results. Although there seems to have a slight decrease in room temperature strengths as milling day increased; however the difference in average strength is not statistically significant and the strength scattering range is within that of the data base of baseline AS800 at Ceramic Components. Thus, based on the data obtained to date, it is concluded that not cleaning the mill jar/media has negligible effect on the AS800 material. However, an effort will be made to continuously monitor the effect of not cleaning mill jar/media as more slip batches are made in the remainder of this program.

Two batches of materials have been prepared with the production size mill, using the baseline slip preparation procedure, except the mill size; both batches were started with cleaned mill jar/media. The slip properties were within the statistical control limits for the AS800 slip prepared using the laboratory size mill. The standard 2" x 3" plates cast from those two batches achieved near full density (>99.5% theoretical) using the baseline sintering cycle. These plates are now being machined into flexure test bars for mechanical property characterization.

Table 2 - Mill Jar/Media Cleaning Effect on Strength
(Average Strength)

Milling Day	Room Temperature* (Min/Max)		1400°C** (Min/Max)	
	ksi	MPa	ksi	MPa
Day 1(Cleaned)	104.8±9.2 (82.2/115.5)	722.4±63.4 (567.0/803.5)	70.9 (62.2/76.0)	488.9 (428.9/524.0)
Day 2 (Uncleaned)	102.5±4.7 (96.4/109.2)	706.9±32.1 (664.9/753.0)	79.2 (69.3/86.9)	546.1 (477.8/599.2)
Day 3 (Uncleaned)	101.7±4.4 (93.6/108.7)	701.3±30.4 (645.1/749.6)	72.4 (70.7/74.3)	499.2 (489.5/512.3)

* Average of 15 test bars
** Average of 3 test bars

2) Sintering Scale Up

The new production size sintering furnace has been installed and new large size crucibles have been purchased for the furnace. Six (6) test runs have been made using the baseline sintering cycle. In these test runs, standard 2" x 3" and 5" x 9" AS800 plates were placed in different size and type of crucibles, including the new large crucibles and the ones used previously in the smaller furnace. The results showed that the AS800 plates, both large and small, could achieve the required >99.5% theoretical density with the same surface characteristics as those sintered in the baseline smaller furnace, if the crucible is well conditioned. Based on the density data, the temperature distribution in the furnace appeared to be quite uniform. The densified plates are now being machined into test bars to compared the mechanical properties with those sintered in baseline smaller furnace.

Communications/Visits/Travel

None.

Problems Encountered

None

Publications

None

1.2.3 Oxide Matrix

Dispersion-Toughened Ceramic Composite
T. N. Tiegs, S. D. Nunn, P. A. Menchhofer, D. L. Barker, E. D. Larson,
T. L. Beavers, and C. A. Walls (Oak Ridge National Laboratory)

Objective/Scope

Initially, this work involved development and characterization of SiC whisker-reinforced ceramic composites for improved mechanical performance. To date, most of the efforts involving SiC whisker-reinforced alumina, mullite, silicon nitride, and sialon have been completed. In addition, studies of whisker-growth processes were initiated to improve the mechanical properties of SiC whiskers by reducing their flaw sizes and, thereby, improving the mechanical properties of the composites. Currently, in situ acicular grain growth is being investigated to improve fracture toughness of silicon nitride materials.

Technical Highlights

In-Situ Toughening of Silicon Nitride by Microstructure Development

Characterization of As-Fabricated Surfaces Formed During Gas Pressure Sintering (GPS) - During GPS at elevated temperatures, silicon nitride materials exhibit weight losses due to decomposition and loss of Si, N, and SiO. To minimize weight losses, samples are typically packed in powders that create a protective atmosphere. At temperatures >1825°C, nitrogen gas overpressures must also be used, in addition to packing powders, to suppress the decomposition of Si_3N_4 so that materials can be densified. Pressures of 1 to 10 MPa (10 to 100 atm) are usually required, and sintering additives are still needed.

The decomposition of the silicon nitride leads to a reaction layer at the surface of the parts. The thickness of the reaction zone can be quite variable with visible differences up to 2 mm from the surface common. For optimum mechanical properties, these reaction layers are machined off. It is well established that machining represents a major portion of the cost of silicon nitride parts, and efforts are under way to reduce its impact on the economics of these materials for engine applications. Consequently, it is desirable to minimize the reaction layers and thereby minimize the machining necessary. The ultimate goal would be to eliminate the reaction zone completely and use as-fabricated surfaces.

Some initial results on the observed changes in flexural strength as material is machined off of the as-processed sample surfaces are shown in Figs. 1 and 2 for the two compositions. Also shown are the strength changes that occur when a 10-kg diamond indent is made on the tensile surface of the test bar. Interestingly, all of the strengths of the Si_3N_4-6% Y_2O_3-2% Al_2O_3 materials are reduced to about the same level even though the as-sintered and as-machined surface strengths are considerably different. In the case of the Si_3N_4-$Sr_2La_4Yb_4(SiO_4)_6O_2$ samples, the indented strength of the as-sintered surface was higher than the indented strength for the machined surfaces. Thus, one can conclude that the damage tolerance of as-sintered surfaces from GPS silicon nitride is as good or better than machined surfaces. Variations in the fracture toughness and indent hardness are also observed across the compositional and physical gradients as shown in Figs. 3 and 4, respectively.
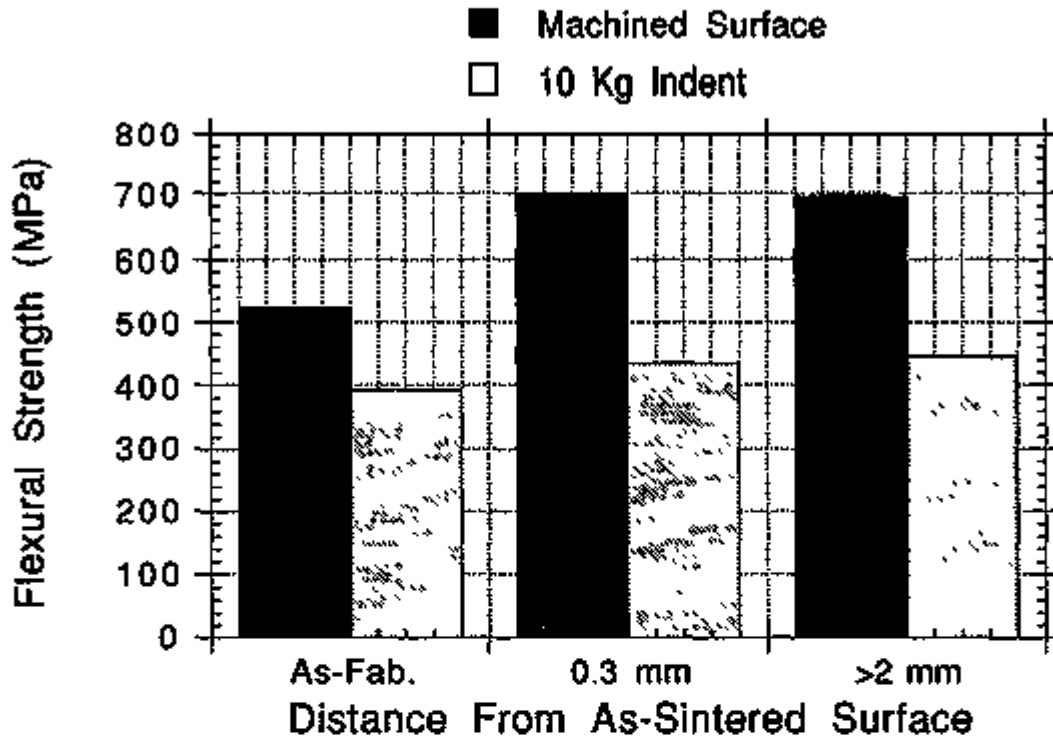
Fig. 1. Flexural strength of gas pressure sintered Si3N4-6% Y2O3-2% Al2O3 as a function of material removed from the as-sintered surface.
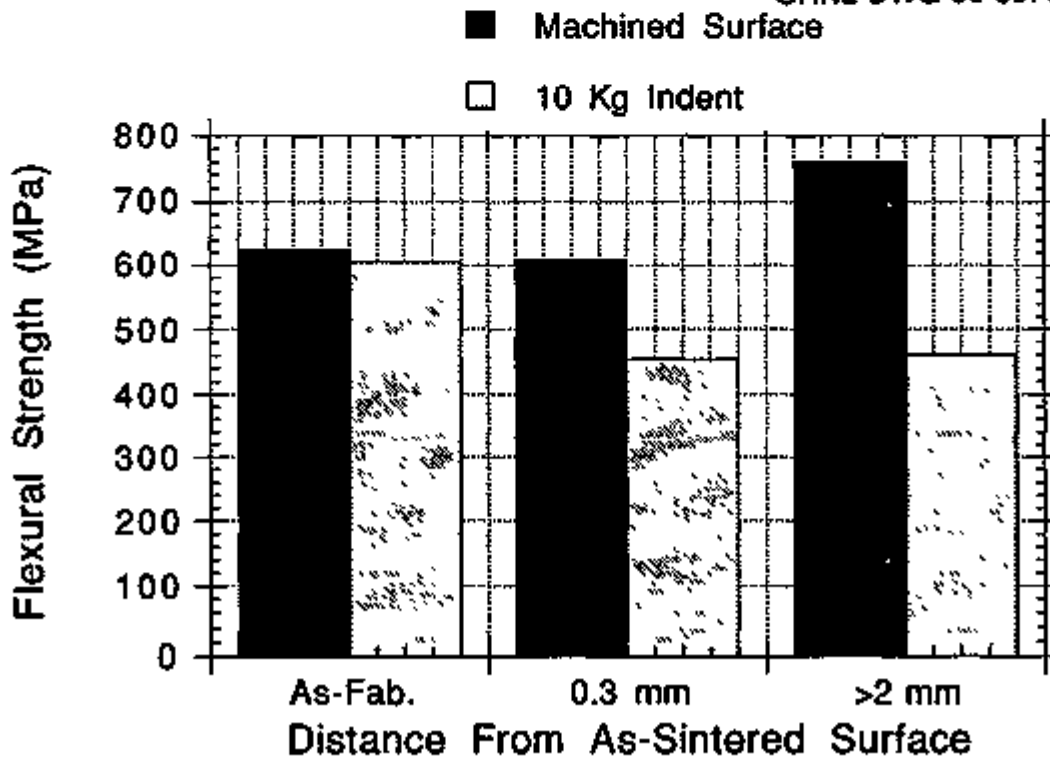
Fig. 2. Flexural strength of gas pressure sintered Si3N4-Sr2La4Yb4(SiO4)6O2 as a function of material removed from the as-sintered surface.

ORNL-DWG 95-5871

— ⊖ - 6% Y2O3-2% Al2O3

- -■- - Si3N4-Yb2O3-La2O3-SrO

Fig. 3. Variation in indent fracture toughness as a function of distance from the as-sintered surface.

ORNL-DWG 95-5872

— ⊖ - 6% Y2O3-2% Al2O3

- -■- - Si3N4-Yb2O3-La2O3-SrO

Fig. 4. Variation in indent hardness as a function of distance from the as-sintered surface.

Microstructural differences can be observed between material near the as-sintered surfaces compared to the bulk material as shown in Figs. 5 and 6. Near the as-sintered surface, large β-Si_3N_4 grains can be observed, whereas at distances ≥ 0.5 mm from the surface, grain sizes typical of the bulk material (>2 mm) are observed. At intermed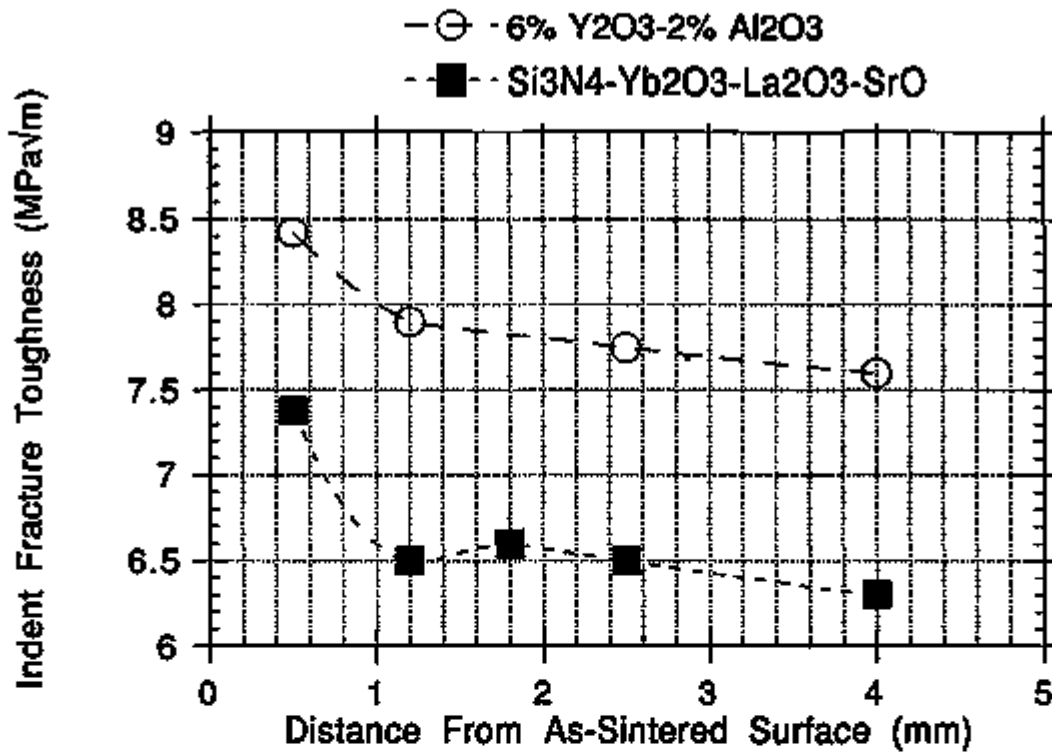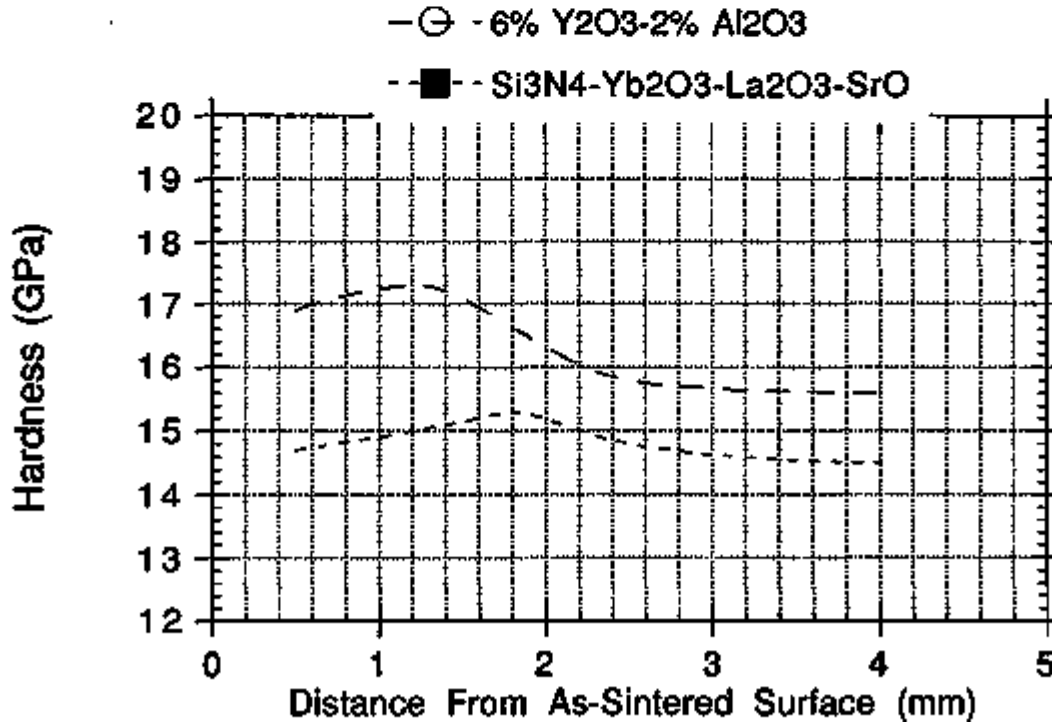iate distances from the surface, intermediate grain sizes can be seen. The large grains near the as-sintered surfaces are the reason for the lower observed strengths and increase in fracture toughness. Also, the damage tolerance is related to the larger grain sizes and higher fracture toughness near the as-sintered surface.

Microstructure Development During GPS - During GPS at elevated temperatures, silicon nitride materials exhibit elongated grain growth which leads to materials with high fracture toughness. A study was initiated to examine the effects of GPS processing parameters on the densification and mechanical properties of silicon nitride materials to maximize the fracture toughness. Important parameters affecting the microstructural development include the sintering temperatures, sintering times, and heating rates. Because a number of variables were to be studied, a Taguchi experimental array was formulated to assess the impact of each of the variables on a two-step GPS process. For each of the conditions, two compositions of silicon nitride with different intergranular phases were tested. These compositions are Si_3N_4-6% Y_2O_3-2% Al_2O_3, and Si_3N_4-$Sr_2La_4Yb_4(SiO_4)_6O_2$ (at 8 equiv % oxygen).

Fabrication and testing of the specimens has been completed with the densification, flexural strength, and fracture toughness results given in Tables 1 and 2 for the two different compositions. Initially, the high heating rate was to be 50°C/min in the Taguchi experimental array. However, during the first two sintering runs at this high heating rate, severe cracking of the samples with the Si_3N_4-6% Y_2O_3-2% Al_2O_3 composition occurred. Consequently, the high heating rate for the Taguchi experimental array was decreased to 25°C so intact samples could be obtained. As shown, high densities were achieved for all of the samples in the Taguchi array. Consequently, no significant effects on the densification were due to the processing conditions chosen. The conditions had been selected to obtain high densities so the effects on the flexural strength and fracture toughness could be better determined.

Analyses of the results for optimizing the processing conditions to maximize the flexural strength and fracture toughness are shown in Tables 3 and 4. For the Si_3N_4-6% Y_2O_3-2% Al_2O_3 samples, only moderate effects were observed for the processing conditions in the experimental array. For the strength, the most important conditions appeared to be the final sintering temperature and the initial sintering time as illustrated in Figs. 7 and 8, respectively. The fracture toughness for the Si_3N_4-6% Y_2O_3-2% Al_2O_3 samples was most affected by the initial sintering temperature as shown in Fig. 9.

The Si_3N_4-$Sr_2La_4Yb_4(SiO_4)_6O_2$ samples showed significantly more deviation in the flexural strength and fracture toughness results depending on the processing conditions. The most significant factor affecting the flexural strength was the final sintering temperature as shown in Fig. 10. The analysis indicated that temperatures ≥ 1900°C were required to achieve high strength values. The fracture toughness was significantly dependent on several factors including initial and final sintering temperature plus the heating rate to the initial sintering temperature. These effects are shown in Figs. 11, 12, and 13, respectively. More analysis will be required to determine exactly why the lower initial sintering temperature improves the fracture toughness, but it probably related to the nucleation and growth of the β-Si_3N_4 grains during the initial densification stages. The final temperature results indicate that the higher temperatures result in larger grain sizes

Microstructural Differences Across Compositional Gradient
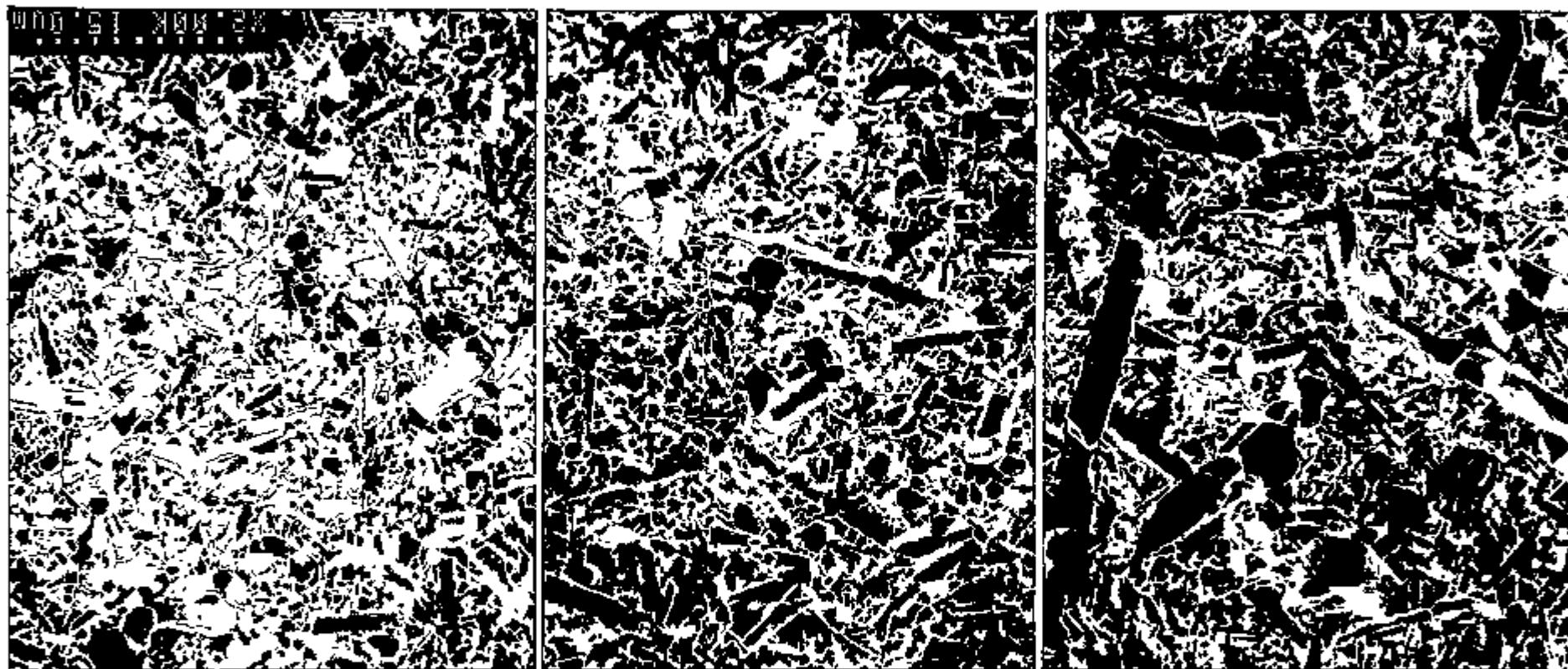
**Near As-Sintered
Surface**

**~0.5 mm From
As-Sintered Surface**

**>2 mm From
As-Sintered Surface**

- **Si_3N_4-6% Y_2O_3-2% Al_2O_3**

Fig. 5. Fracture surfaces of Si_3N_4-6% Y_2O_3-2% Al_2O_3 at various distances from the as-sintered surface.

Microstructural Differences Across Compositional Gradient
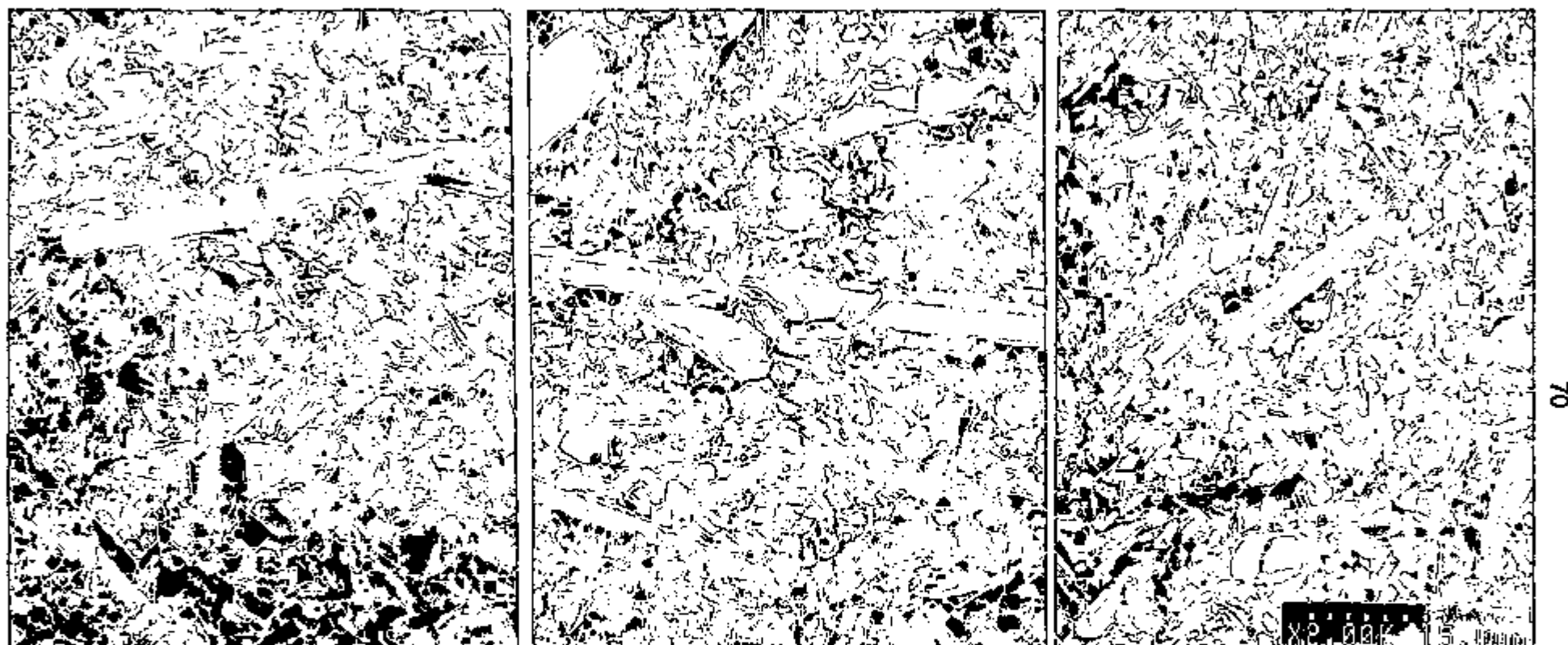
**Near As-Sintered
Surface**

**~0.1 mm From
As-Sintered Surface**

**~0.5 mm From
As-Sintered Surface**

•Si$_3$N$_4$-Sr$_2$La$_4$Yb$_4$(SiO$_4$)$_6$O$_2$ (8 Equiv % Oxygen)

Fig. 6. Fracture surfaces of Si$_3$N$_4$-Sr$_2$La$_4$Yb$_4$(SiO$_4$)$_6$O$_2$ at various distances from the as-sintered surface.

Table 1. Taguchi experimental design array for optimization of densification parameters to obtain silicon nitride ceramics with improved mechanical properties. (Composition is Si_3N_4-6% Y_2O_3-2% Al_2O_3, and the design is a L_8 (4^1 x 2^4); only the first eight tests were used in the Taguchi evaluation.)

Test No.	Final sinter. temp. (°C)	Initial sinter. temp. (°C)	Initial sinter. time (h)[a]	Final sinter. time (h)	Heating rate to initial sinter. temp. (°C/min)	Sintered density (g/cm³, % T.D.)	Flexural strength (MPa)	Fracture toughness (MPa√m)
1	2000	1900	2 (Min.)	2	25	3.24, 99.4	679 ± 41	8.4 ± 0.3
2	2000	1950	2.5 (Min. + 1)	1	10	3.24, 99.4	749 ± 49	8.0 ± 0.1
3	1950	1900	2 (Min.)	1	10	3.24, 99.3	542 ± 37	8.3 ± 0.1
4	1950	1950	2.5 (Min. + 1)	2	25	3.21, 98.6	817 ± 62	8.0 ± 0.2
5	1900	1900	3 (Min. + 1)	2	10	3.25, 99.6	627 ± 52	8.2 ± 0.2
6	1900	1950	1.5 (Min.)	1	25	3.24, 99.5	651 ± 87	7.5 ± 0.3
7	1850	1900	3 (Min. + 1)	1	25	3.23, 99.1	662 ± 37	8.2 ± 0.1
8	1850	1950	1.5 (Min.)	2	10	3.22, 98.9	653 ± 65	8.0 ± 0.6
9	2000	1900	2 (Min.)	0.1	25	3.22, 98.7	653 ± 65	7.9 ± 0.4
10	1900	1950	1.5 (Min.)	1	50	3.22, 98.7	464 ± 55	8.1 ± 0.1

[a] Minimum time to obtain closed porosity (1900°C - 2 h; 1950°C - 1.5 h) with either no further hold time or a 1-h additional hold time. Times defined as minimum (Min.) or minimum plus 1 h (Min. + 1).

Table 2. Taguchi experimental design array for optimization of densification parameters to obtain silicon nitride ceramics with improved mechanical properties. (Composition is Si_3N_4-$Sr_2La_4Yb_4(SiO_4)_6O_2$ (at 8 equiv % oxygen), and the design is a L_8 (4^1 x 2^4); only the first eight tests were used in the Taguchi evaluation.)

Test No.	Final sinter. temp. (°C)	Initial sinter. temp. (°C)	Initial sinter. time (h)[a]	Final sinter. time (h)	Heating rate to initial sinter. temp. (°C/min)	Sintered density (g/cm³, % T.D.)	Flexural strength (MPa)	Fracture toughness (MPa√m)
1	2000	1900	2 (Min.)	2	25	3.51, 100.0	607 ± 160	7.0 ± 0.3
2	2000	1950	2.5 (Min. + 1)	1	10	3.50, 100.0	574 ± 47	5.7 ± 0.5
3	1950	1900	2 (Min.)	1	10	3.30, 94.2	•••	6.1
4	1950	1950	2.5 (Min. + 1)	2	25	3.48, 99.2	503 ± 43	5.0 ± 0.5
5	1900	1900	3 (Min. + 1)	2	10	3.50, 100.0	550 ± 42	7.5 ± 0.7
6	1900	1950	1.5 (Min.)	1	25	3.46, 98.8	--	4.7
7	1850	1900	3 (Min. + 1)	1	25	3.47, 99.1	396 ± 52	4.3 ± 0.2
8	1850	1950	1.5 (Min.)	2	10	3.42, 97.7	362 ± 38	4.6 ± 0.1
9	2000	1900	2 (Min.)	0.1	25	3.52, 100.0	580 ± 57	7.4 ± 0.1
10	1900	1950	1.5 (Min.)	1	50	3.31, 95.1	428 ± 47	4.9 ± 0.2

[a] Minimum time to obtain closed porosity (1900°C - 2 h; 1950°C - 1.5 h) with either no further hold time or a 1-h additional hold time. Times defined as minimum (Min.) or minimum plus 1 h (Min. + 1).

Table 3. Optimum sintering conditions to maximize flexural strength and fracture toughness of Si_3N_4-6% Y_2O_3-2% Al_2O_3 during gas pressure sintering.

Sintering condition variable	Optimum condition to maximize strength	Variable significance	Optimum condition to maximize toughness	Variable significance	Combined optimum conditions
Final sinter. temp. (°C)	2000°C	Moderate	2000°C	Very low	2000°C
Initial sinter. temp. (°C)	1950°C	Moderate	1900°C	Moderate	1900°C
Initial sinter. time (h)[a]	3 (Min. + 1)	Moderate	Either	None	2 (Min.)
Final sinter. time (h)	2	Low	2	Very low	2
Heating rate to initial sinter. temp. (°C/min)	25°C/min	Moderate	10°C/min	Very low	25°C/min

[a] Minimum time to obtain closed porosity (1900°C - 2 h; 1950°C - 1.5 h) with either no further hold time or a 1-h additional hold time. Times defined as minimum (Min.) or minimum plus 1 h (Min. + 1).

Table 4. Optimum sintering conditions to maximize flexural strength and fracture toughness of Si_3N_4-$Sr_2La_4Yb_4(SiO_4)_6O_2$ (at 8 equiv % oxygen) during gas pressure sintering.

Sintering condition variable	Optimum condition to maximize strength	Variable significance	Optimum condition to maximize toughness	Variable significance	Combined optimum conditions
Final sinter. temp. (°C)	2000°C	High	2000°C	Moderate	2000°C
Initial sinter. temp. (°C)	1900°C	Moderate	1900°C	High	1900°C
Initial sinter. time (h)[a]	3 (Min. + 1)	Low	2 (Min.)	Moderate	2 (Min.)
Final sinter. time (h)	2	Low	2	Moderate	2
Heating rate to initial sinter. temp. (°C/min)	25°C/min	Very low	10°C/min	High	10°C/min

[a] Minimum time to obtain closed porosity (1900°C - 2 h; 1950°C - 1.5 h) with either no further hold time or a 1-h additional hold time. Times defined as minimum (Min.) or minimum plus 1 h (Min. + 1).

ORNL-DWG 95-5873
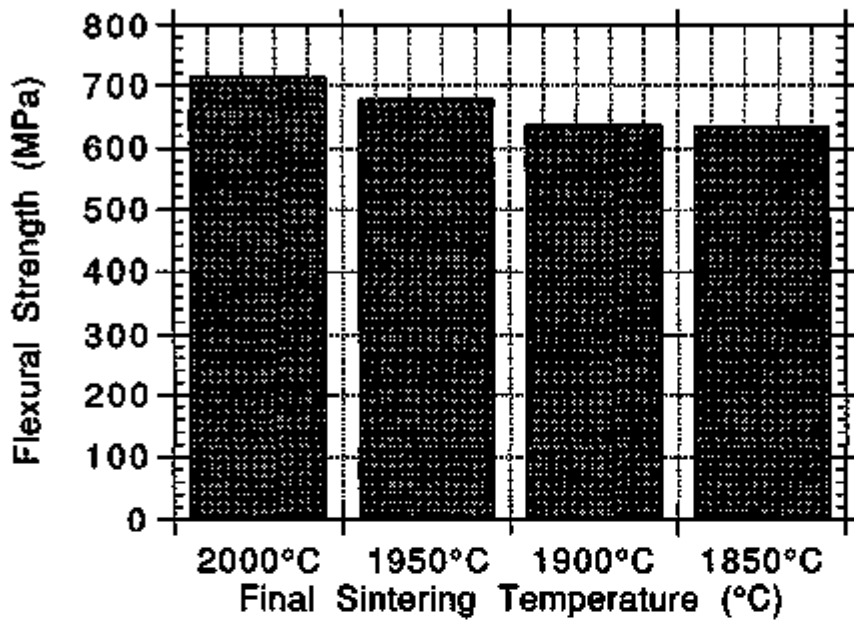
Fig. 7. Effect of final sintering temperature on the average flexural strength of gas pressure sintered Si_3N_4-6% Y_2O_3-2% Al_2O_3.

ORNL-DWG 95-5874
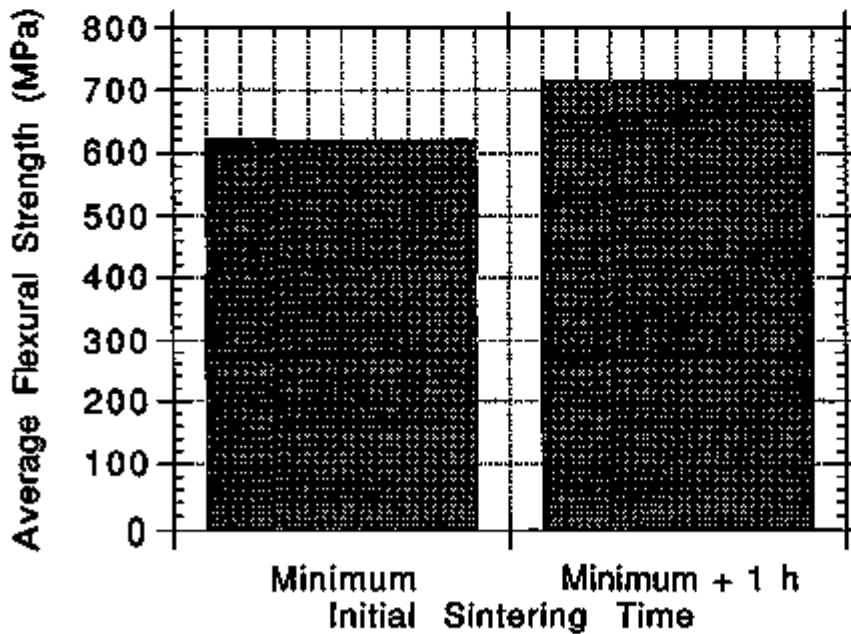
Fig. 8. Effect of initial sintering time on the average flexural strength of gas pressure sintered Si_3N_4-6% Y_2O_3-2% Al_2O_3.

ORNL-DWG 95-5875
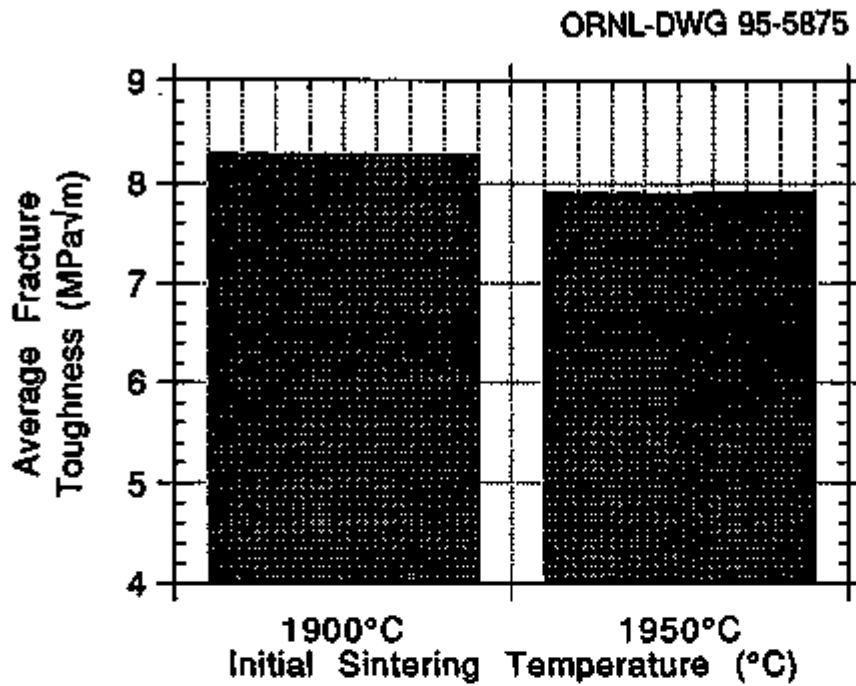
Fig. 9. Effect of initial sintering temperature on the average fracture toughness of gas pressure sintered Si_3N_4-6% Y_2O_3-2% Al_2O_3.

ORNL-DWG 95-5876
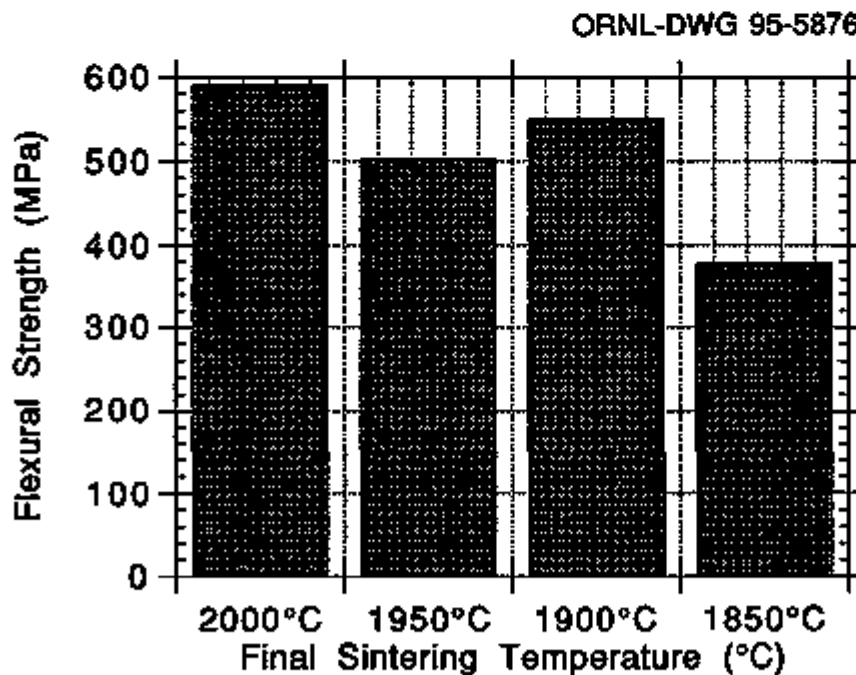
Fig. 10. Effect of final sintering temperature on the average flexural strength of gas pressure sintered Si_3N_4-$Sr_2La_4Yb_4(SiO_4)_6O_2$ (at 8 equiv % oxygen).

ORNL-DWG 95-5877

Fig. 11. Effect of initial sintering temperature on the average fracture toughness of gas pressure sintered Si_3N_4-$Sr_2La_4Yb_4(SiO_4)_6O_2$ (at 8 equiv % oxygen).
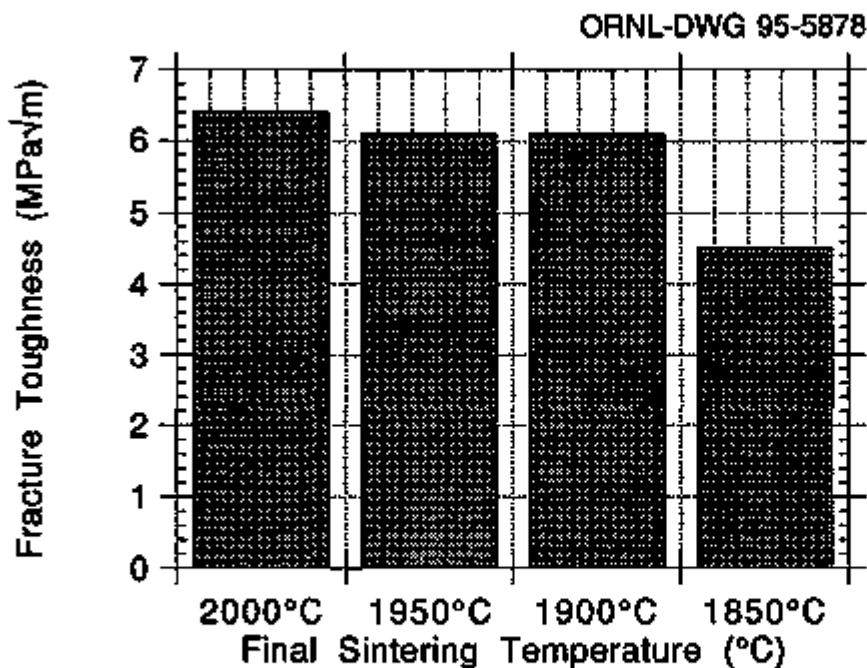
ORNL-DWG 95-5878

Fig. 12. Effect of final sintering temperature on the average fracture toughness of gas pressure sintered Si_3N_4-$Sr_2La_4Yb_4(SiO_4)_6O_2$ (at 8 equiv % oxygen).

ORNL-DWG 95-5879

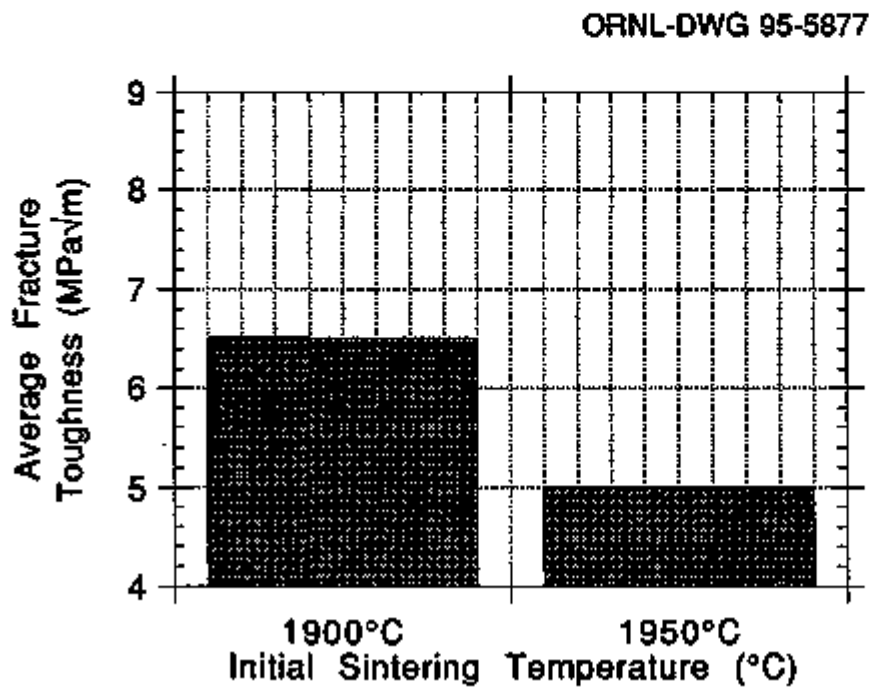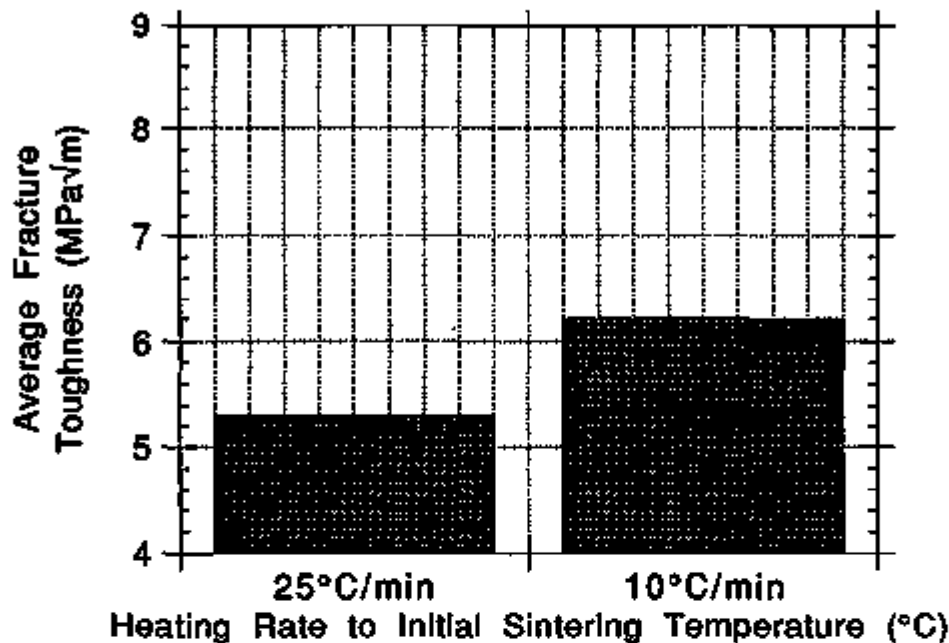Fig. 13. Effect of heating to initial sintering temperature on the average fracture toughness of gas pressure sintered Si_3N_4-$Sr_2La_4Yb_4(SiO_4)_6O_2$ (at 8 equiv % oxygen).

and increased fracture toughness. As with the initial sintering temperature, the improved fracture toughness with the slower initial heating rate is probably related to the early $ß$-Si_3N_4 growth during sintering.

Cooperative Research and Development Agreement (CRADA) - Materials and Electrochemical Research Corp.

The CRADA with Materials and Electrochemical Research Corp. (MER) is currently in progress. The test matrix is shown in Tables 5 and 6. Materials are being made with different starting α/$ß$-Si_3N_4 ratios and with the addition of sintering aids as coatings instead of powders. The samples will be sintered by GPS using the optimum densification parameters developed for high-toughness materials in the ORNL program.

Materials with different starting α/$ß$-Si_3N_4 ratios and with the addition of sintering aids as coatings instead of powders have been received from MER. They are presently being pressed and isopressed into samples suitable for sintering. Powder batches have also been made at ORNL with different starting $ß$-Si_3N_4 types and sizes. The samples will be sintered by GPS using the optimum densification parameters developed for high-toughness materials in the ORNL program. The $ß$-Si_3N_4 seed was produced by heating various combinations of Si_3N_4 powders and Y_2O_3 as shown in Table 7. The powders were milled together and the fired at 1700°C for 4 h to produce the $ß$-phase materials.

Table 5. Test matrix to determine effects of ß-Si$_3$N$_4$ content and type for samples fabricated at ORNL.

Test No.	Grain boundary phase composition	Rare earth addition	ß-Si$_3$N$_4$ content (%)	ß-Si$_3$N$_4$ seed source
1	Sr$_2$La$_4$Yb$_4$(SiO$_4$)$_6$O$_2$ (8 equiv % O)	Powder	0	--
2	Sr$_2$La$_4$Yb$_4$(SiO$_4$)$_6$O$_2$ (8 equiv % O)	Powder	25	ORNL #1
3	Sr$_2$La$_4$Yb$_4$(SiO$_4$)$_6$O$_2$ (8 equiv % O)	Powder	25	ORNL #2
4	Sr$_2$La$_4$Yb$_4$(SiO$_4$)$_6$O$_2$ (8 equiv % O)	Powder	25	ORNL #3
5	Sr$_2$La$_4$Yb$_4$(SiO$_4$)$_6$O$_2$ (8 equiv % O)	Powder	25	ORNL #4
6	Sr$_2$La$_4$Yb$_4$(SiO$_4$)$_6$O$_2$ (8 equiv % O)	Powder	25	Shin-Etsu
7	Sr$_2$La$_4$Yb$_4$(SiO$_4$)$_6$O$_2$ (8 equiv % O)	Powder	50	ORNL #1
8	Sr$_2$La$_4$Yb$_4$(SiO$_4$)$_6$O$_2$ (8 equiv % O)	Powder	5	ORNL #1
9	Y$_2$Si$_2$O$_7$ (5 equiv% O)	Powder	0	--
10	Y$_2$Si$_2$O$_7$ (5 equiv % O)	Powder	25	ORNL #1

Table 6. Test matrix to determine effects of ß-Si$_3$N$_4$ content and rare addition method for samples fabricated at Materials and Electrochemical Research Corp.

Test No.	Composition	Rare earth addition	ß-Si$_3$N$_4$ content (%)	ß-Si$_3$N$_4$ seed source
1	4 % Nd$_2$O$_3$-1% Al$_2$O$_3$	Powder	0	Shin-Etsu
2	4 % Nd$_2$O$_3$-1% Al$_2$O$_3$	Coating	25	Shin-Etsu
3	4 % Nd$_2$O$_3$-1% Al$_2$O$_3$	Coating	25	Shin-Etsu
4	4 % Nd$_2$O$_3$-1% Al$_2$O$_3$	Coating	50	Shin-Etsu
5	4 % Nd$_2$O$_3$-1% Al$_2$O$_3$	Coating	75	Shin-Etsu
6	4 % Y$_2$O$_3$-1% Al$_2$O$_3$	Powder	0	Shin-Etsu
7	4 % Y$_2$O$_3$-1% Al$_2$O$_3$	Coating	0	Shin-Etsu
8	Y$_2$Si$_2$O$_7$ (5 equiv % O)	Powder	0	Shin-Etsu
9	Y$_2$Si$_2$O$_7$ (5 equiv % O)	Coating	0	Shin-Etsu
10	Y$_2$Si$_2$O$_7$ (5 equiv % O)	Coating	25	Shin-Etsu

Table 7. Fabrication of ß-Si$_3$N$_4$ seed at Oak Ridge National Laboratory.

ß-Si$_3$N$_4$ seed fabrication number	Starting Si$_3$N$_4$ powder	Y$_2$O$_3$ addition	ß-Si$_3$N$_4$ content (%)
ORNL #1	Ube E-10	0.7 wt % (as nitrate)	93
ORNL #2	Ube E-10	1 wt % (powder)	100
ORNL #3	Ube E-03	1 wt % (powder)	78
ORNL #4	Starck S1	1 wt % (powder)	100

Status of Milestones

Milestone 123115 - "Optimize the gas-pressure sintering process to fabricate high-toughness silicon nitride with refractory grain boundary phases" was completed on schedule during the current reporting period.

Communications/Visits/Travel

Travel by T. N. Tiegs on April 24-27, 1994, to the American Ceramic Society Annual Meeting in Indianapolis, Ind., to present a talk entitled, "Characterization and Properties of As-Processed Surfaces of Gas-Pressure Sintered Silicon Nitride."

Travel by T. N. Tiegs on June 24, 1994, to Cremer Forschungsinstitut GMBH & Co., Rödental, Germany, to discuss development of silicon nitride for engine applications.

Travel by T. N. Tiegs on June 27, 1994, to Asea Brown Boveri AG, Heidelberg, Germany, to discuss development of ceramics for advanced gas turbine engine applications.

Problems Encountered

Problems with the temperature control on the GPS furnace have caused some delay in fabrication of the samples for the optimization of the processing parameters.

Publications

None.

1.2.4 Low Expansion Materials

Characterization and Testing of Low-Expansion Ceramic Materials
S. Subramaniam and D. P. Stinton (Oak Ridge National Laboratory)

Objective/Scope

Insulated exhaust portliners are needed in advanced diesel engines to increase engine fuel efficiency by increasing the combustion temperatures and reducing the combustion heat that is lost through the head and into the water cooling system. Low-expansion materials have potential for this application due to their very low thermal conductivity, extraordinary thermal shock resistance, and reduction of attachment stresses. Thermal shock resistance is critical because the shape of the portliners requires that they be cast into the metallic cylinder head. Functioning exhaust portliners are inaccessible after they are cast into cylinder heads and, hence, must not require maintenance for the life of the head (~1 million miles). Contracts have been placed with Golden Technologies, Inc., formerly Coors Ceramics Co., and LoTEC, Inc., to develop cost-effective processes for the fabrication of portliners. Coors is investigating Al_2TiO_5 and $Ca_{1-x}Mg_xZr_4P_6O_{24}$, while LoTEC is investigating $Ba_{1+x}Zr_4P_{6-2x}Si_{2x}O_{24}$ (BaZPS) and $Ca_{1-x}Sr_xZr_4P_6O_{24}$. ORNL is assisting Golden Technologies and LoTEC with the characterization and evaluation of their compositions.

Technical Highlights

A systematic investigation of the mechanical and thermal properties of BaZPS ceramics as a function of composition (Si at. %) and grain size has been initiated. Five compositions ($x = 0$, 0.175, 0.25, 0.375, and 0.500) were synthesized from stoichiometric proportions of the reagent grade oxides using a solid-state reaction method and were sintered at 1600°C for 3000 min. To determine the influence of the grain size, three compositions ($x = 0$, 0.175, and 0.500) were additionally sintered for 30 and 300 min to result in smaller grain-sized samples. In this report, dilatometric measurements of BaZPS with $x = 0$ (BS0), 0.175 (BS17), 0.25 (BS25), 0.375 (BS37), and 0.5 (BS50) sintered at 1600°C for 3000 min are presented. In addition, electron microprobe analysis results of the BaZPS compositions and the high-temperature X-ray diffraction (XRD) results of BaZPS with $x = 0.25$ are discussed.

The bulk linear thermal expansion of BaZPS compositions was determined using a computer-controlled dual push rod dilatometer made by Theta Industries, Inc. The thermal expansion was measured at heating and cooling rates of 3°C/min from room temperature to 1250°C. Isothermal holds were maintained during heating and cooling ramps at 500, 1000, and 1250°C for 20 min. A sapphire rod with a length of 25 mm was used as the reference material, and the BaZPS sintered samples used were $25 \times 4 \times 3$ mm.

Dilatometric measurements were made for each of the five BaZPS compositions, and the dilatometric curves are shown in Fig. 1. The BS compositions with $x = 0$ and 0.5 exhibited a large amount of hysterisis and may be attributed to their high thermal expansion anisotropy behavior. The bulk linear thermal expansion coefficient initially increased ($x = 0.175$) and then decreased with increasing Si content in the BaZPS composition. The bulk linear thermal expansion coefficient was negative for BS50.

It is interesting to note that BS0 expands only slightly above 900°C and the high-temperature XRD work indicated that few low-angle peaks of BS0 disappeared above 900°C. Also, a slope change in the expansion is observed for all the BaZPS compositions during the
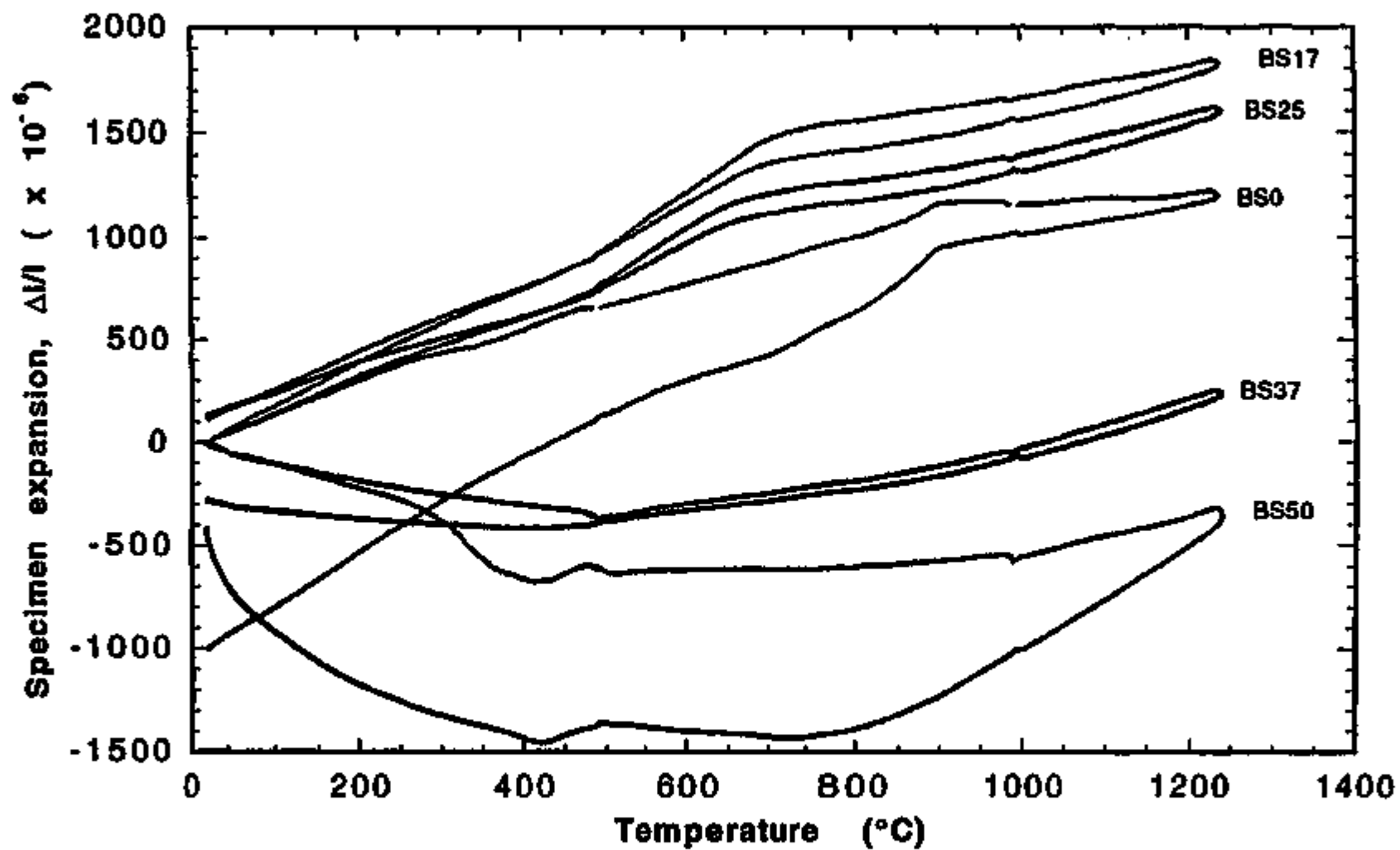
Fig. 1. Thermal expansion curves for BaZPS compositions.

heating cycle. For example, BS0 shows a slope change at 900°C, and BS17 exhibits a slope change at 700°C, thus possibly suggesting that all the BaZPS compositions experience phase transitions. Also, the slope change occurs at a lower temperature with increasing Si content, suggesting a possible relationship between phase transition temperature and Si content.

Electron microprobe analysis was performed on the BaZPS compositions using a Jeol Superprobe 733 electron microprobe operating at 20 kV and a 10-nA reference current. A detailed description of the sample preparation and experimental procedure is found in the bimonthly report (August 1994). The matrix composition, as well as that of the secondary phase(s), if present, was determined for the prepared BaZPS samples. Theoretical wt (%) values for the constituents in the BaZPS compositions and the microprobe analysis for the final BaZPS compositions are presented in Tables 1 and 2, respectively. From the two tables, it is clear that the constituent wt (%) in the synthesized compositions matches well with the theoretical wt (%) of the constituents. Few second-phase particles were observed in all the BaZPS compositions with the exception of BS37.

Table 1. Theoretical weight percent of the constituents
in $Ba_{1+x}Zr_4P_{6-2x}Si_{2x}O_{24}$ compositions

x value in $Ba_{1+x}Zr_4P_{6-2x}Si_{2x}O_{24}$	wt%				
	Ba	Zr	P	Si	O
0.000	12.81	34.04	17.34	0.00	35.81
0.175	14.74	33.32	15.98	0.89	35.07
0.250	15.54	33.02	15.42	1.27	34.75
0.375	16.84	32.54	14.50	1.88	34.24
0.500	18.10	32.07	13.61	2.47	33.75

Table 2. Microprobe analysis of the constituents in the synthesized
$Ba_{1+x}Zr_4P_{6-2x}Si_{2x}O_{24}$ compositions

x value in $Ba_{1+x}Zr_4P_{6-2x}Si_{2x}O_{24}$	wt%				
	Ba	Zr	P	Si	O
0.000	12.6	33.5	17.8	0.00	36.1
0.175	14.6	32.1	15.8	0.89	36.6
0.250	14.9	32.1	15.5	1.0	36.5
0.375	16.4	32.3	15.0	1.8	34.5
0.500	16.8	31.8	14.5	2.0	34.9

High-temperature XRD was carried out on BS25 using a Scintag PAD X θ/θ diffractometer (Scintag, Inc.) equipped with a constant potential X-ray generator operating at 45 kV/40 mA with a Cu target, an Edmund Buehler high-temperature XRD furnace with a beryllium window and Pt/Rh heating strip, and a liquid-N_2-cooled germanium single-crystal solid-state detector. The sample preparation, experimental and data analysis procedure is described in detail in the bimonthly report (October 1994).

Figures 2 and 3 summarize the variation of unit cell paramters, "a" and "c", and the unit-cell volume with temperature. It is observed that the "a" parameter and the unit cell volume increased with increasing temperature. However, the "c" parameter initially increased, then decreased at 600°C, and again increased with increasing temperature. Also, the "a" parameter increased substantially at 600°C. The trends seem to indicate that BaZPS with x = 0.25 may undergo a phase transition between 400 and 800°C. The thermal expansion curve of BaZPS with x = 0.25 was reported earlier, and it undergoes a slope change at around 650°C, thus supporting the possibility of a phase transition.

Milestones

On schedule.

Communications/Visits/Travel

D. P. Stinton and S. Y. Limaye visited Volvo Flygmotor AB (Tröllhatan, Sweden) April 11, 1994, to discuss the application of low-expansion materials as catalyst supports and regenerators in turbine-powered hybrid vehicles.

D. P. Stinton and S. Y. Limaye visited The Swedish Ceramic Institute (SCI) in Gothenburg, Sweden, on April 12, 1994, to discuss the use of low-expansion ceramics as insulating portliners in diesel engines. Volvo Technological Development and Saab Scania support the work at SCI and had representatives at these meetings.

D. P. Stinton and S. Y. Limaye visited MAN Technology in Munich, Germany, on April 14, 1994, to discuss the application of low-expansion ceramics as insulating port liners in diesel engines.

D. P. Stinton and S. Subramaniam attended the 96th Annual Meeting of the American Ceramic Society on April 24-27, 1994, in Indianapolis, Indiana. Both Stinton and Subramaniam participated in a 3-day Symposium on Low-Expansion Ceramics at the meeting.

D. P. Stinton attended the Ceramic Technology Quarterly Review Meeting at DOE Headquarters in Washington, D.C., and the USAMP Ceramics DIvision Meeting in Detroit, Michigan, during the period of June 7-9, 1994.

D. P. Stinton attended a meeting in Salt Lake City, Utah, on August 8 and 9, 1994 to review LoTEC's contract on low-expansion ceramics. Debbie Haught of DOE attended the review and participated in discussions about work to be performed during Phase II of LoTEC's contract.

D. P. Stinton attended a meeting at Golden, Colorado, on August 10, 1994, to review the Golden Technologies, Inc., contract on low-expansion ceramics. Debbie Haught from DOE and Santosh Limaye from LoTEC also attended the review.
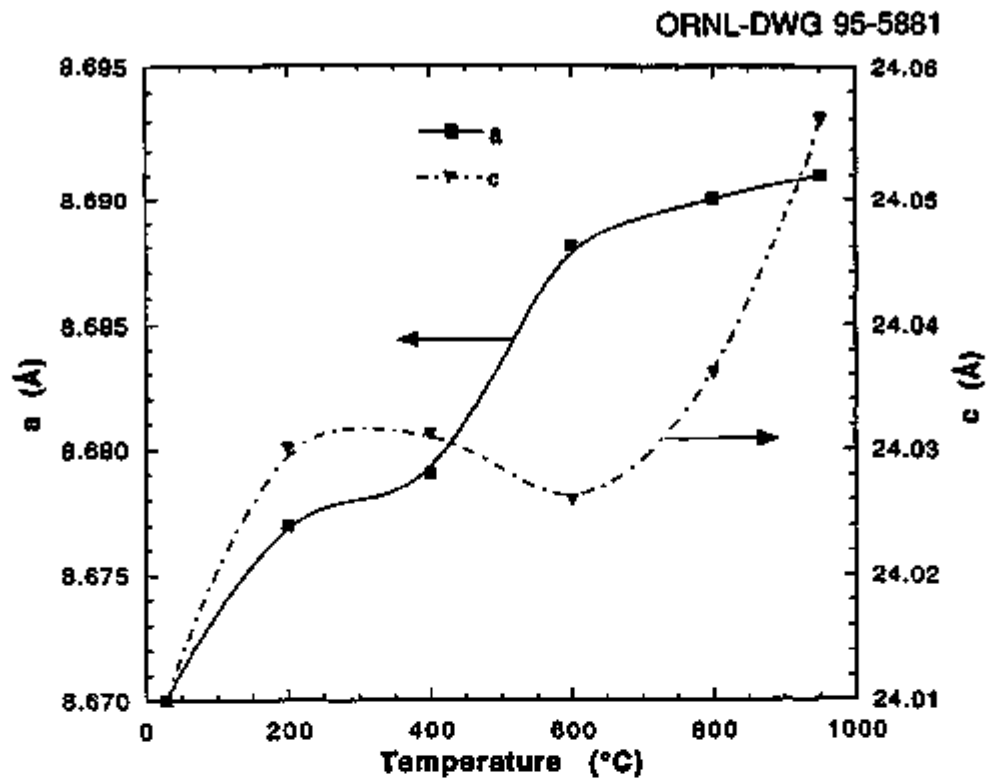
ORNL-DWG 95-5881

Fig. 2. Variation of unit-cell parameters "a" and "c" of BS25 with temperature.

ORNL-DWG 95-5882
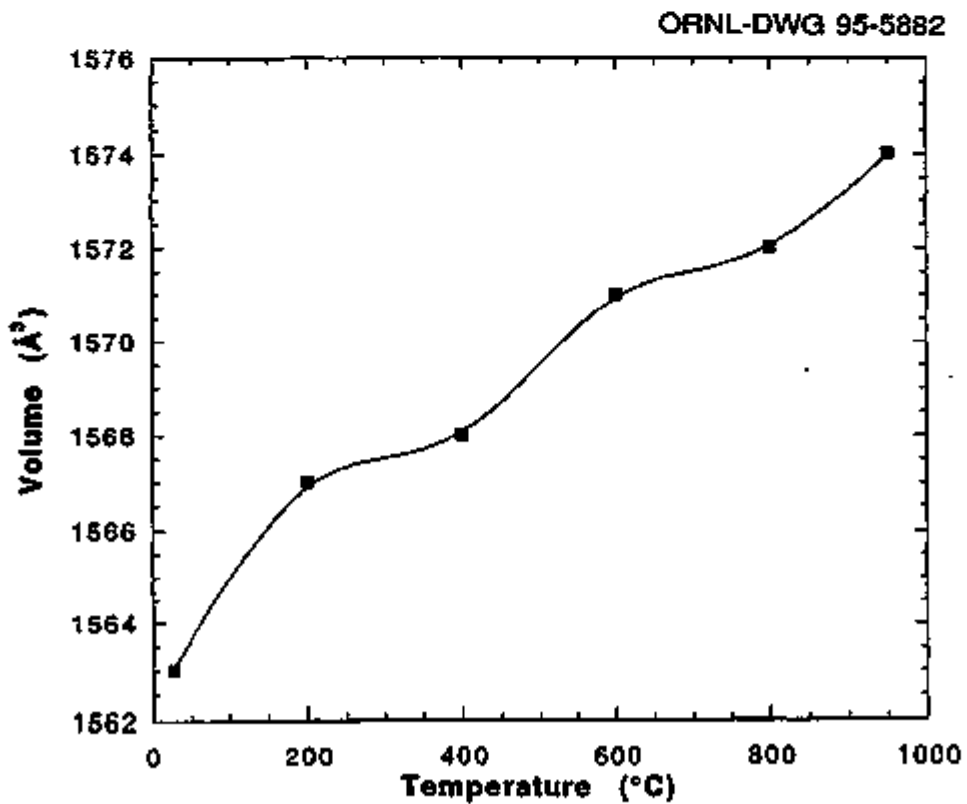
Fig. 3. The unit-cell volume for BS25 increased with increasing temperature.

D. P. Stinton traveled to Peoria, Illinois, on September 20, 1994, with Santosh Limaye of LoTEC to discuss the use of NZP ceramics in diesel engines. The mechanical and physical properties of two NZP compositions (Ca + Sr and Ba + Si) were summarized.

Problems Encountered

None.

Publications/Presentations

A presentation entitled "Thermal and Mechanical Behavior of $Ba_{1+x}Zr_4P_{6-2x}Si_{2x}O_{24}$," authored by S. Shanmugham, D. P. Stinton, C. R. Hubbard, O. B. Cavin, K. L. More, S. Y. Limaye, and N. H. Packan, was presented at the American Ceramics Society 96th Annual Meeting at Indianapolis, Ind., on April 24-27, 1994.

A paper entitled "Thermal and Mechanical Behavior of $Ba_{1+x}Zr_4P_{6-2x}Si_{2x}O_{24}$," authored by S. Shanmugham, D. P. Stinton, C. R. Hubbard, O. B. Cavin, K. L. More, S. Y. Limaye, and N. H. Packan, was accepted for publication in the Low Expansion Symposium Proceedings for the symposium held at the American Ceramics Society 96th Annual Meeting at Indianapolis, Ind., on April 24-27, 1994.

A paper entitled "Synthesis and Cell Refinement of $Ba_{0.5+x/2}Zr_2P_{3-x}Si_xO_{12}$ with $x = 0.25$ and 0.375" was published in *J. Materl. Sci. Lett.* 13 (1994).

A paper entitled "Powder Synthesis, Sintering and Characterization of $Ba_{1+x}Zr_4P_{6-2x}Si_{2x}O_{24}$ - A Low Thermal Expansion System" was submitted for publication to *Scr. Metall.*

Development of NZP Ceramic-Based "Cast-in-Place" Diesel Engine Port Liners
Rama Nageswaran and Santosh Y. Limaye (LoTEC, Inc.)

Objective/Scope

The overall objective of this Phase I research program was to develop sodium-zirconium-phosphate (NZP) ceramic based "cast-in-place" diesel engine port liners. Specific objectives were: (1) Materials requirement analysis, (2) Successful demonstration of metal casting around the ceramic, (3) Cost-effective processes development, and (4) Development of high temperature database (stability, thermal cycling, thermal shock etc.).

Technical Progress

Characterization of the BSX and CSX series of compositions which LoTEC is developing as possible candidate materials for "cast-in-place" diesel engine port liners was nearly completed. This report will discuss the results obtained to this point. In addition, the following processes: (i) Gel-casting, (ii) Ultrasonic-based NDE, and (iii) Acoustic Emission-based Microcrack detection; and some new NZP-type compositions were further developed.

MATERIALS CHARACTERIZATION

Bulk Linear Thermal Expansion:

The stability of some of these ceramic materials, when subjected to thermal cycling, was determined. Thermal expansion was measured on as-sintered specimens and thermally-cycled specimens, after 1 and 250 cycles to 1000°C. The compositional series tested were: BSX $(Ba_{1+x}Zr_4P_{6-2x}Si_{2x}O_{24})$; x=0.0, 0.25 and 0.5, and CSX $(Ca_{1-x}Sr_xZr_4P_6O_{24})$; x=0.25 and 0.5. In addition, thermal expansion measurements were made on as-sintered and cycled specimens of Al_2TiO_5 and CM40 $(Ca_{0.6}Mg_{0.4}Zr_4P_6O_{24})$.

The isotropic compositions (BS25, CS50 and CM40) have little or no microcracking associated with cooling from either the sintering temperature or the heat treatment temperature. Without the presence of microcracking there is very little thermal hysteresis and thus very reproducible thermal expansion curves. The results of the expansion measurements are given in Figures 1-3.

All the anisotropic compositions (BS0, BS50, CS25 and Al_2TiO_5) microcrack upon cooling from the sintering temperature and thus have thermal expansion curves with varying amounts of hysteresis. Also, there is substantial variation in the measured bulk linear thermal expansion, when comparing measurements made on as-sintered specimens to measurements made on thermally cycled specimens. This variation in thermal expansion will be discussed in the succeeding sections. Results of measurements for the above compositions are given in Figures 4-7.

Flexural Strength

The room temperature flexural strength was determined for all the compositions of this study, both in the as-sintered condition and after thermal cycling to 2 different temperatures - 1000°C and 1250°C. Tables 1 and 2 summarize the results. Thermal cycling to 1250°C was described in an earlier report and thermal cycling to 1000°C followed similar procedures. All of the tested compositions have good thermal stability when subjected to thermal cycling as discerned from measuring weight loss. Figure 8 shows the normalized weight loss of the BSX and CSX series of compositions. The weight loss has been normalized to the weight of the specimens after 1 thermal cycle to 1250°C. Weight loss with repeated cycling is less than 0.5 percent. The anisotropic compositions have greater open porosity than the isotropic compositions, therefore, their initial weight loss after 1 thermal cycle is relatively high. But this is only due to driving off absorbed moisture and organic solvents used in the specimen grinding process.

The flexural strength of the compositions under study does not degrade with thermal cycling to either 1000°C or 1250°C. Figures 9(a) and (b) present this situation graphically. What can be noted is that the flexural strength of the isotropic compositions, BS-25 and CS-50, are substantially higher than those of the anisotropic compositions. This is due to the absence of microcracks. As the degree of anisotropy increases the flexural strength decreases. This can be seen in Fig.9(b), which is a plot of data for the CSX series.

Microstructure:

Scanning Electron Microscopy (SEM) was used to evaluate structural changes in the various compositions due to thermal cycling to 1250°C in room air. The test specimens were broken Modulus of Rupture (MOR) bars whose fracture surfaces were examined in both as-sintered condition and after subjecting to 250 cycles between R.T. and 1250°C. The thermal cycling process consisted of placing the fractured bars in crucibles made from the corresponding [NZP] compositions and placing the crucibles in a furnace, and heat-treating according to the following schedule:

1250°C 0.5 hr.   1250°C 0.5 hr.

1 hr.   2.5 hrs.   1 hr.   2.5 hrs.

R.T.   75°C   75°C
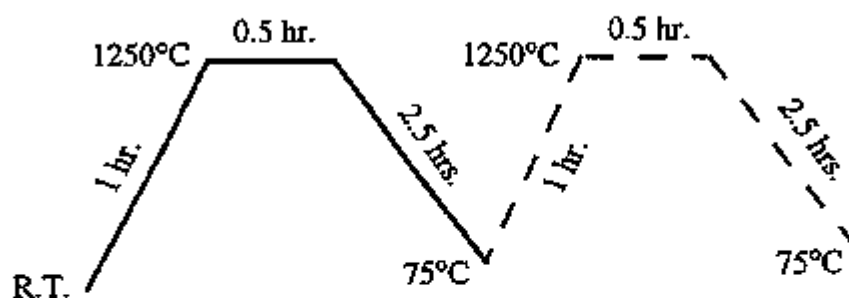
Figures 10 to 14 compare the microstructure (morphology) of the as-sintered specimens with the specimens cycled 250 times for the studied compositions. In the BSX series, there are two anisotropic compositions - BS-0 and BS-50 (Figs.10, 12) - with either positive or negative bulk thermal expansion, respectively, and one isotropic composition - BS-25 (Fig.11) - with a very low positive bulk thermal expansion. Evidence of microcracking is seen in the anisotropic compositions, both in the as-sintered and thermally cycled condition. This microcracking accounts for the low mechanical strengths of the anisotropic compositions, discussed earlier in this report. There is little evidence of microcracking in the BS-25 specimen even after 250 cycles to 1250°C. The observed porosity is consistent with the 85-90% theoretically dense specimens. An unexpected but significant feature of the microstructures is the fine porosity (cavitation) developed in the anisotropic compositions, BS-0 and BS-50, when subjected to thermal cycling. It is believed that this porosity, which has a similar appearance to that found in tensile creep specimens, is due to the anisotropic axial thermal expansion and the internal stresses developed between individual grains during thermal cycling. However, cavitation is not evident in the BS-25 specimen.

The microstructures of the CSX series specimens yielded results similar to those of the BSX compositions (see Figs.13 and 14). Again, microcracking and cavity formation were found in the anisotropic CS-25 material while there was no evidence of microcracking or cavity formation in the isotropic CS-50 composition.

Environmental Effects (Moisture, Humidity etc.). As stated before there was substantial variation in bulk thermal expansion of anisotropic, microcracked compositions. Upon cooling from the sintering temperature, the ceramic microcracks due to the stresses associated with the anisotropic axial thermal expansion of the individual ceramic grains. The microcracks are further opened by the absorption of moisture from either the air or when the ceramic is ground into test specimens in a manner similar to stress corrosion cracking observed in other ceramic materials. When the test specimen is reheated during the thermal expansion measurement the absorbed moisture is driven off and the microcracks close. Further heating promotes microcrack healing.

Taken together this explains the apparent lower bulk thermal expansion obtained for the as sintered and ground specimens. If the subsequent thermal expansion measurements are made shortly after the heat treatment, before any substantial amount of moisture is reabsorbed, consistent results should be obtained. This view finds corroboration in the almost identical expansion curves of an anisotropic material, such as CS-25, subjected to 1 and 250 thermal cycles between room temperature and 1000°C or 1250°C (these results were presented in an earlier report).

To test the hypothesis that it is moisture that promotes crack opening, the following experiments were performed. An anisotropic (CS-25) specimen was heated and cooled in a dilatometer surrounded by an inert (helium) atmosphere. When the specimen reached an equilibrium length during cooling (close to room temperature), the helium atmosphere was displaced by dry air. Next, air with controlled relative humidity was allowed to surround the specimen. With each increase in relative humidity there was a corresponding increase in specimen length. Finally, the dilatometer was carefully opened and water was dripped on to the specimen; this resulted in a sharp increase in the specimen length. The results of this experiment are shown in Figure 15.

The above said experiment was performed using an isotropic behavior (CS-50) specimen. Since the isotropic material returns to its original length by the time it cools down to room temperature and there are not any microcracks present to open up, moisture had virtually no effect on the CS-50 specimen. To determine if the other anisotropic compositions like BS-0 and BS-50 exhibited similar behavior as that of the CS-25 specimen, they were heated and cooled in the dilatometer, which was then followed by controlled application of drops of water. The results obtained for all the anisotropic materials - BS-0, BS-50 and CS-25 - are shown in Fig.16 and contrasted with that for isotropic BS-25. Figures 17(a) and (b) (results derived from verisimilar experiments) provide a closer look into the moisture-assisted microcracking behavior of the BS-0 material.

To determine if there was any chemical change (hydration) associated with the absorption of water, powder X-ray diffraction analysis was performed on CS-25 powders. A sintered test specimen was crushed to form a fine powder. A portion of this powder was heated to 1000°C to drive of any moisture present and then X-rayed. A similar amount of powder was mixed with water, allowed to dry and then subjected to XRD. The powder diffraction patterns for the two samples are shown in Fig.18. It was not possible to detect any secondary phases.

Ultrasonic NDE Technique:

A "dry coupling", direct contact transmission mode ultrasonic technique was tested and adapted for quality checks on finished NZP ceramic parts. As can be seen from Fig. 19, the

technique employs dry coupling transmitting and receiving transducers[§] between which the test material (NZP ceramic) is inserted. The transducers used were W-series transducers capable of operating in the frequency range <50 kHz to >25 MHz and designed for velocity measurements and high resolution testing. A PR35 ultrasonic pulser/receiver[¶] acted as the source and transmitter of electric pulses which were recorded and analyzed using a Cathode Ray Oscilloscope (CRO).

Parameters monitored were the time of flight, longitudinal wave velocity, and amplitude and number of pulses. This information was then processed for comparison with that of a standard. Deviations of the observed/measured parameters of the test sample from the standard were interpreted to be due to defects. In order to ascertain the technique's reliability, some of the seemingly defective samples were dissected to examine for defects. It was found that this technique gave a fairly accurate indication of the presence of flaws. (Accordingly, this NDE method of flaw detection has been incorporated into LoTEC's quality control procedures.)

Gel Casting:

This high potential near-net shape forming technique is being adapted to the fabrication of NZP ceramic based diesel engine port-liners and other components. Processing steps involved in the gel casting of NZP ceramics have been summarized in the flow chart of Fig. 20. Despite its advantages with respect to speed of forming and high green strength of the cast and dried part, several areas of this technique still need further examination; for instance, viscosity of the gel at the time of casting (which depends on the amount of solids loading), idle time between casting and gelation, flowing due to self weight of the semi-dry part after removal from the molds, and burn-out of the polymer. All of these areas will be adequately addressed during Phase II work.

Microcracking Investigation by Acoustic Emission :

Using carefully selected wave guides, acoustic signal activity ("counts") emitted by test specimens were recorded. Initial tests consisted of recording acoustic emissions during heat-up of a specimen to and cool-down from 1000°C. A Locan 320 system which was capable of detecting signals in the range of 3 kHz to 1.2 MHz with amplitudes up to 80 dBel was used for detection of acoustic activities. The number of counts recorded was attempted to be correlated to the extent of microcracking in the specimen. It was observed that while no significant acoustic emission could be registered during heating, the opposite was true during cooling (specially below 350°C); which is in agreement with previous experimental observations. These experiments also indicated that the

---

§ Ultran Laboratories, Inc., Boalsburg, PA 16827-0719.

¶ JSR Ultrasonic Measurement Systems Pittsford, NY 14534.

number of acoustic emission counts is a function of the maximum temperature to which the samples are heated. More work on acoustic emission based detection of microcracking is continuing.

New NZP materials:

As stated in the original proposal, three more NZP systems where chosen for this study.

$$Ca_{1+x}Zr_4P_{6-2x}Si_{2x}O_{24} \text{ (CSX)} \qquad (x = 0.1, 0.25, 0.37)$$
$$Sr_{1+x}Zr_4P_{6-2x}Si_{2x}O_{24} \text{ (SSX)} \qquad (x = 0.1, 0.25, 0.37)$$
$$Ca_{(1+x)/2}Sr_{(1+x)/2}Zr_4P_{6-2x}Si_{2x}O_{24} \text{ (CS'X)} \quad (x = 0.1, 0.25, 0.37)$$

Three compositions (given above) in each system were synthesized by the same method used to prepare the BSX and CSX compositions. Stoichiometric amounts of the appropriate precursors (after taking into account the LOI for a specific composition) were mixed, ball milled in alcohol for 20 hrs, dried in air and calcined for 6 hrs at 1200°C. Calcined powders were then subjected to XRD analysis. The XRD data indicated that the calcined material contained only the NZP phase in most compositions and, in a few, minor amounts of ZrP_2O_7 which typically disappeared after sintering. Detailed characterization of some of these compositions for their properties and potential as low thermal expansion materials will be conducted in coming months.

Future Work

Immediate future work would focus on furthering the ongoing tasks, specially those related to development of alternative cost-effective fabrication processes. Work on the first FEA iteration for establishing material requirements and optimization of the compliant layer is underway. Specimens and components of the CS-50 material are being fabricated to perform remaining characterization.

Status of milestones : Program on schedule.

Communications/Visits/Travel :

1)   T.B. Jackson, S.Y. Limaye, and W.D. Porter, "Effect of Thermal Cycling on the Physical and Mechanical Properties of [NZP] Ceramics," Presented at the 96th meeting of the American Ceramic Society, Indianapolis, IN, April 24-28, 1994.

2)   T.B. Jackson and W.D. Porter, "Environmental Microcracking of [NZP] Type Ceramics," Presented at the 96th meeting of the American Ceramic Society, Indianapolis, IN, April 24-28, 1994.

3) S. Y. Limaye (LoTec, Inc.) and Dave Stinton (Oak Ridge National Lab) visited the Technical Center at Caterpillar, Inc. on September 20th.

4) S. Y. Limaye (LoTec, Inc.), D. Haught (Department of Energy) and Dave Stinton (Oak Ridge National Lab) visited Penn State University on October 5th.

Publications :

1) T.B. Jackson, S.Y. Limaye, and W.D. Porter, "Effect of Thermal Cycling on the Physical and Mechanical Properties of [NZP] Ceramics," to be published in the proceedings of the 96th Meeting of the American Ceramic Society, Indianapolis, IN, April 24-28, 1994.

2) T.B. Jackson and W.D. Porter, "Environmental Microcracking of [NZP] Type Ceramics," to be published in the proceedings of the 96th Meeting of the American Ceramic Society, Indianapolis, IN, April 24-28, 1994.

References : None.

Tables 1 and 2. Summary of the room temperature flexural strengths of as-sintered and thermally-cycled (1250°C) BSX and CSX materials.

Thermal Cycling between R.T and 1250°C				
Composition (BSX and CSX)	Flexure strength (MPa)			
	As Sintered	1 Cycle	25 Cycles	250 Cycles
BS-0	40.13 ± 10.85	46.52 ± 6.34	46.90 ± 2.24	44.25 ± 3.29
BS-17	49.76 ± 5.61	46.53 ± 4.90	-	46.49 ± 4.95
BS-25	84.20 ± 7.61	81.43 ± 12.51	88.19 ± 3.03	75.92 ± 5.95
BS-37.5	46.13 ± 4.13	46.82 ± 6.59	48.99 ± 6.17	45.14 ± 6.16
BS-50	45.55 ± 3.48	42.50 ± 3.61	49.19 ± 6.70	41.21 ± 4.76
CS-25	36.87 ± 7.55	37.47 ± 5.36	42.02 ± 4.73	37.95 ± 7.26
CS-37.5	58.41 ± 6.82	53.88 ± 5.57	57.60 ± 4.73	54.90 ± 5.17
CS-50	75.52 ± 4.83	69.81 ± 4.91	67.88 ± 1.62	70.16 ± 3.86

Thermal Cycling between R.T and 1000°C				
Composition (BSX and CSX)	Flexure strength (MPa)			
	As Sintered	1 Cycle	25 Cycles	250 Cycles
BS-0	40.13 ± 10.85	46.38 ± 13.20	38.73 ± 4.62	34.80 ± 8.37
BS-17	49.76 ± 5.61			46.22 ± 5.48
BS-25	84.20 ± 7.61	83.93 ± 10.99	78.45 ± 12.26	79.52 ± 10.87
BS-37.5	46.13 ± 4.13	48.33 ± 4.94	43.65 ± 5.81	46.64 ± 8.03
BS-50	45.55 ± 3.48	41.55 ± 3.85	39.16 ± 4.03	46.19 ± 4.00
CS-25	36.87 ± 7.55	44.98 ± 8.33	41.42 ± 8.24	43.73 ± 7.23
CS-37.5	58.41 ± 6.82	63.77 ± 7.22	55.60 ± 4.59	58.69 ± 6.01
CS-50	75.52 ± 4.83	76.21 ± 9.30	67.21 ± 10.41	66.70 ± 5.82

Figure 1. Effect of thermal cycling on the bulk linear thermal expansion of BS25 material.

Figure 2. Effect of thermal cycling on the bulk linear thermal expansion of CS50 material.

Figure 3. Effect of thermal cycling on the bulk linear thermal expansion of CM40 material.
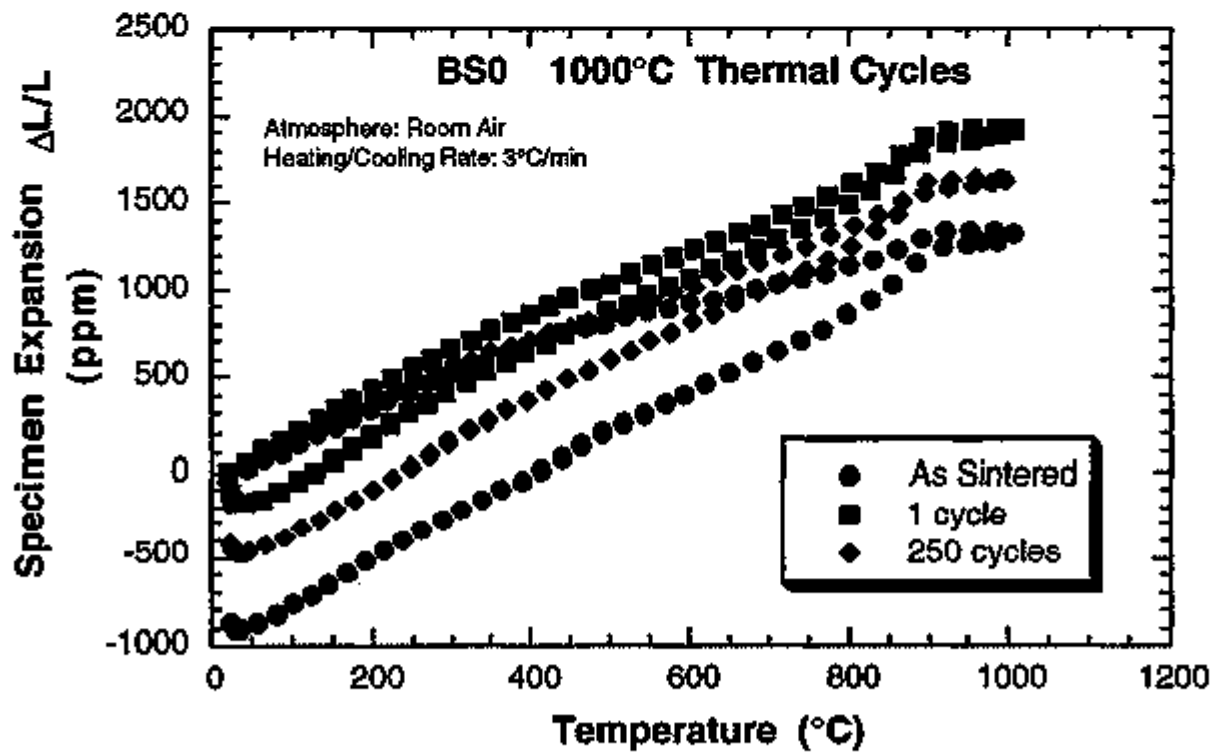
Figure 4. Effect of thermal cycling on the bulk linear thermal expansion of BS0 material.
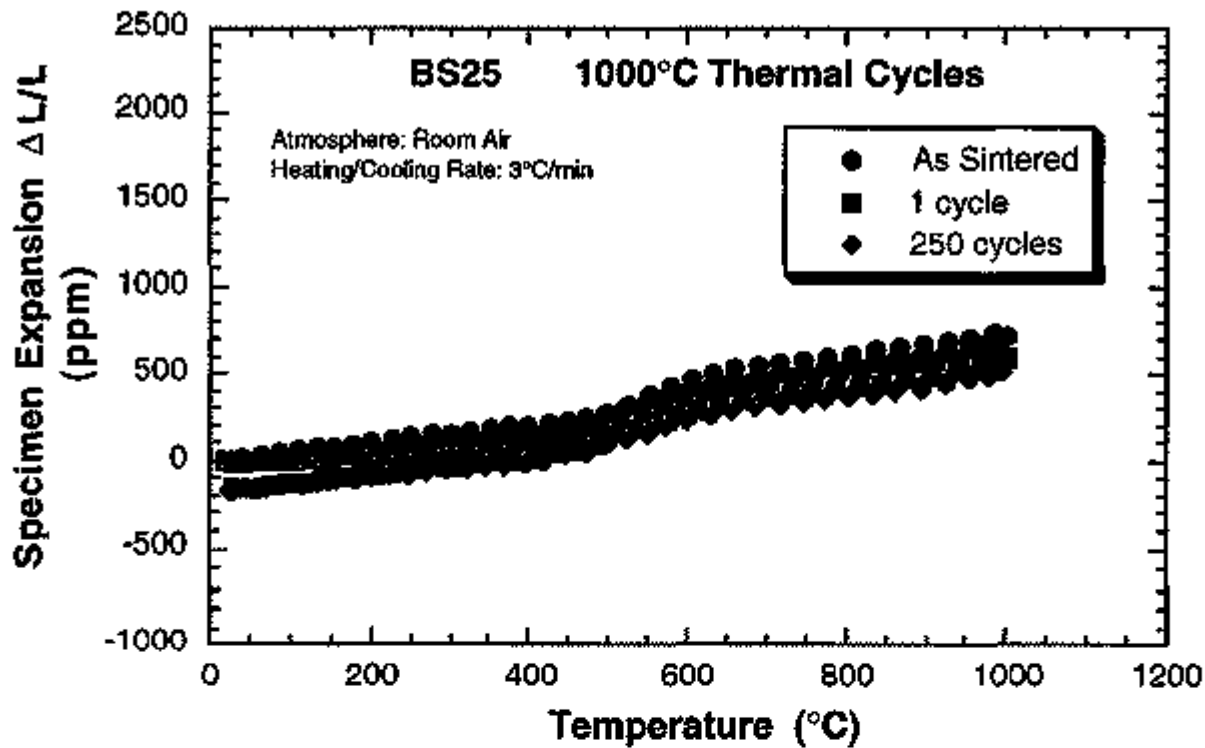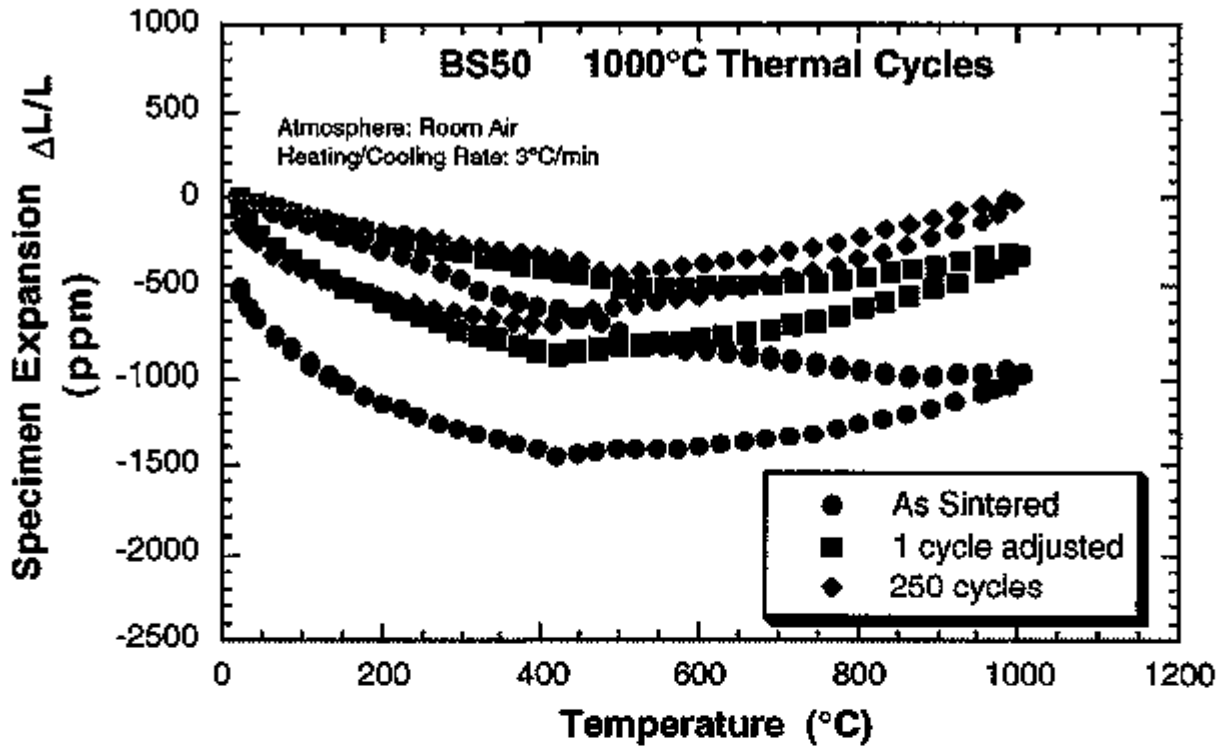
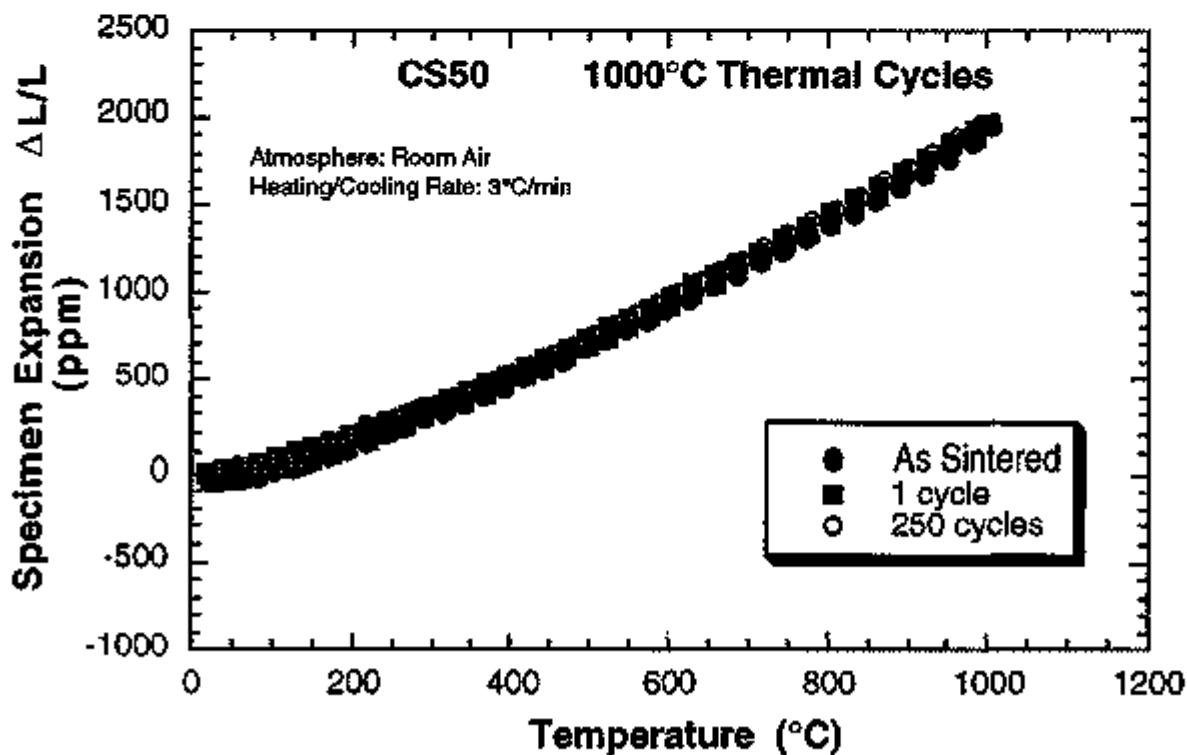Figure 5. Effect of thermal cycling on the bulk linear thermal expansion of BS50 material.
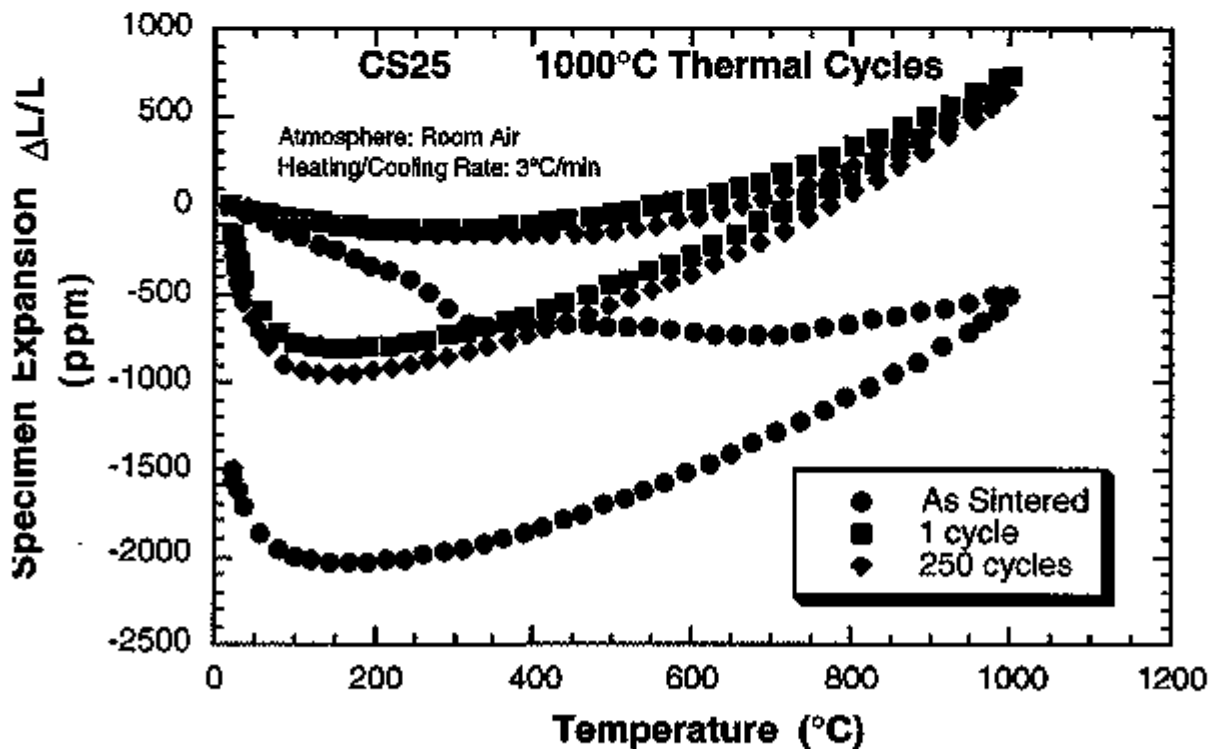
Figure 6. Effect of thermal cycling on the bulk linear thermal expansion of CS25 material.
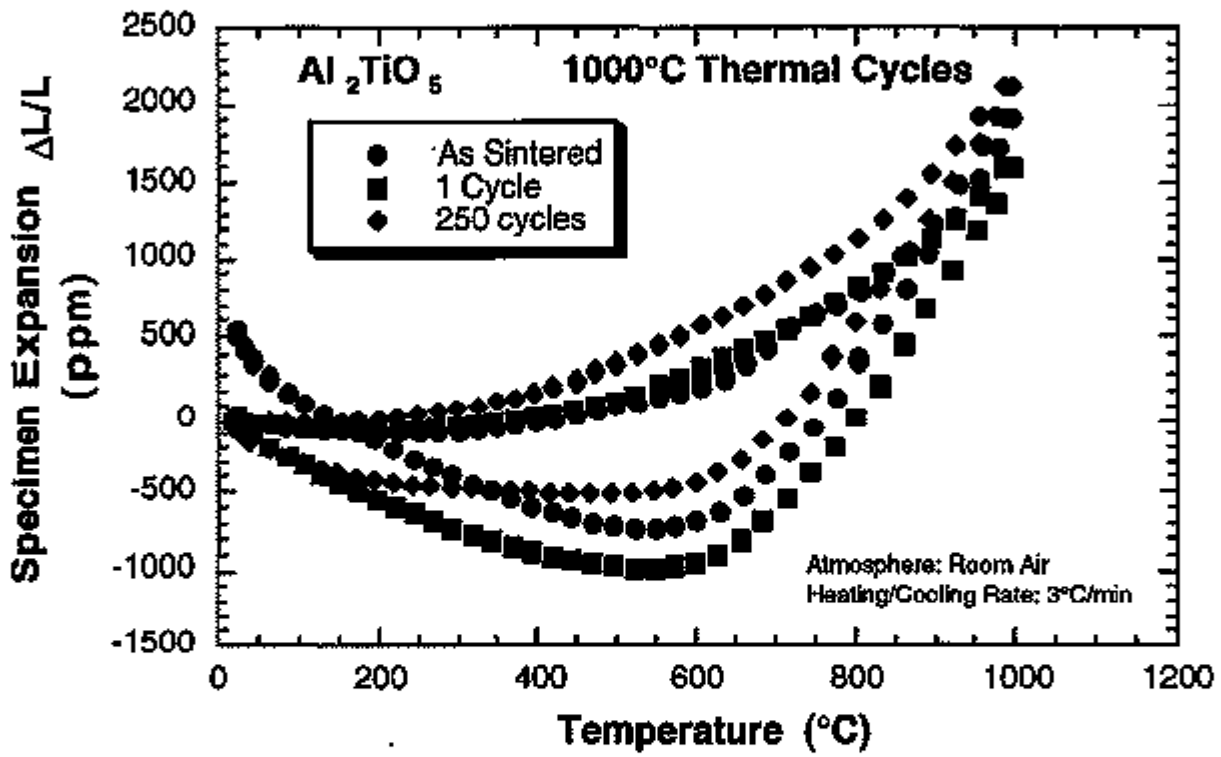
Figure 7. Effect of thermal cycling on the bulk linear thermal expansion of Al$_2$TiO$_5$ material.
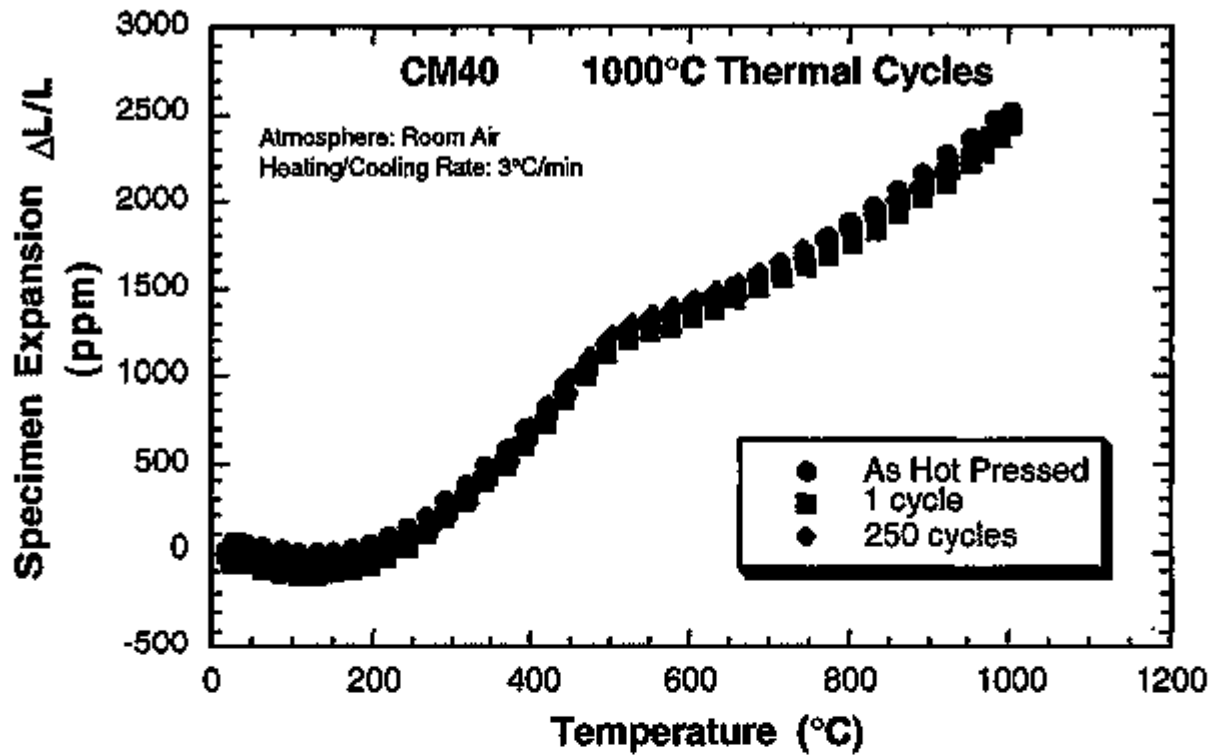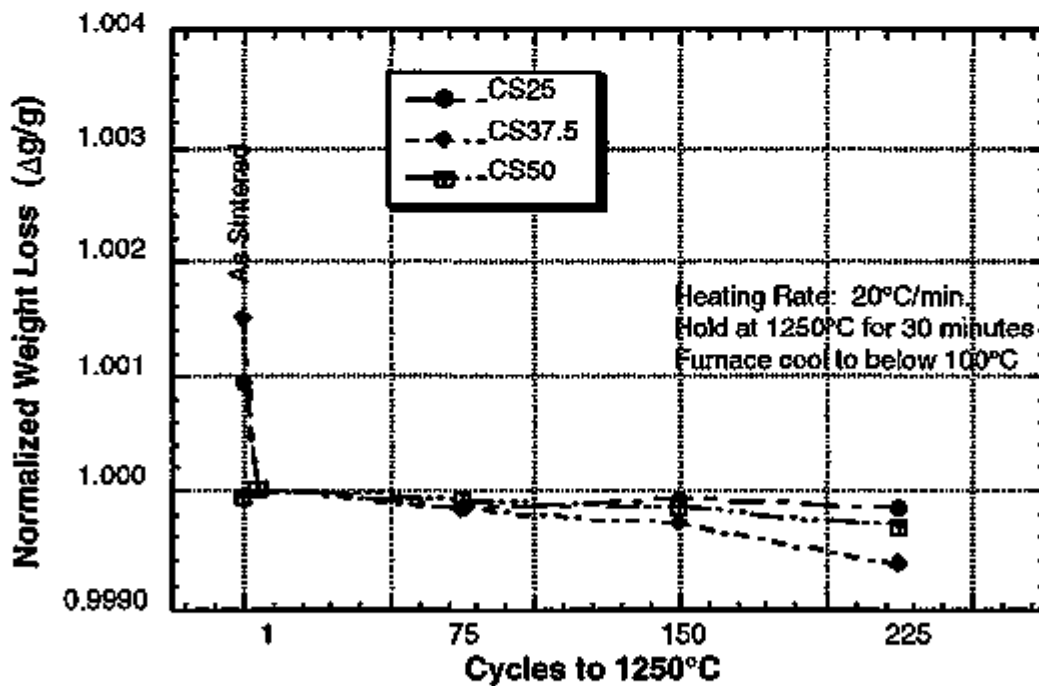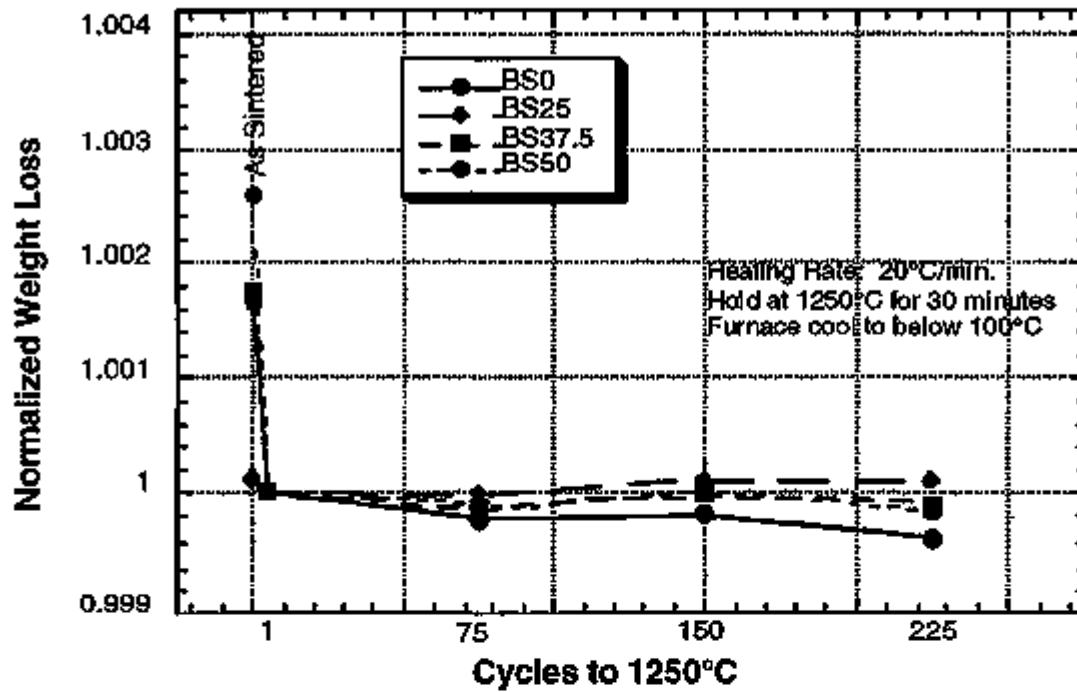
Figures 8(a) and (b). Normalized weight loss as a function of cycles to 1250°C for the (a) BSX and (b) CSX compositions.
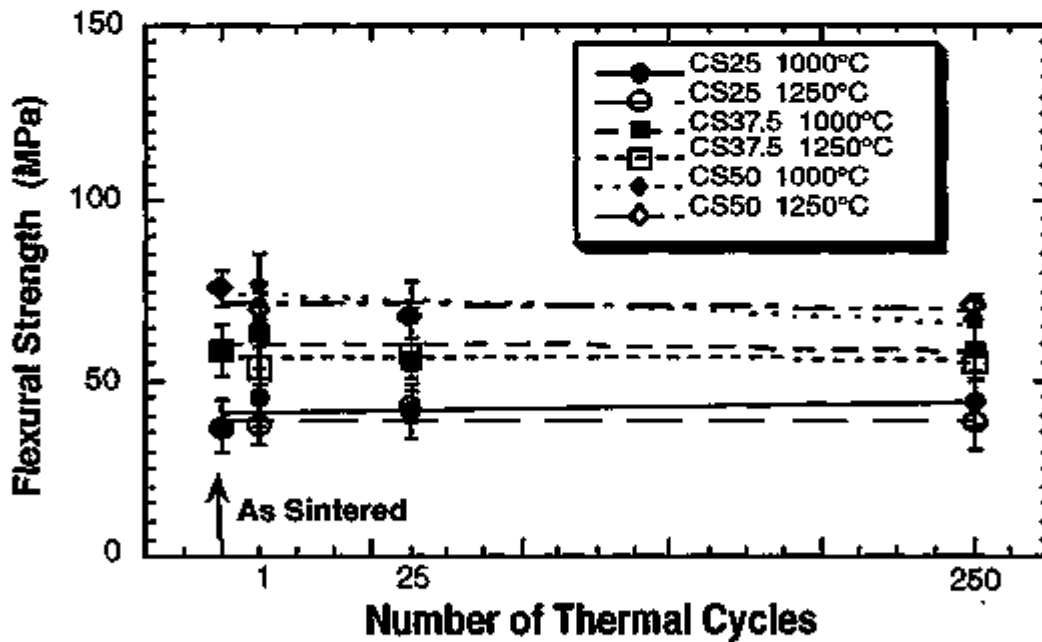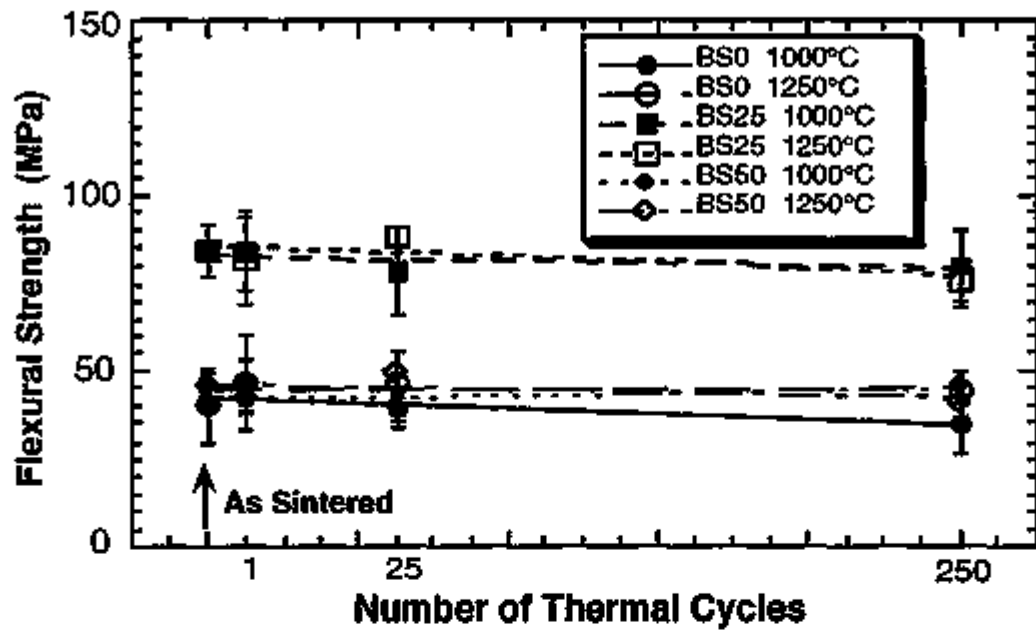
Figure 9(a) and (b). Flexure strength vs. Number of thermal cycles for the (a) BSX and (b) CSX compositions.

534

BS-0

$BaZr_4P_6O_{24}$
As Sintered
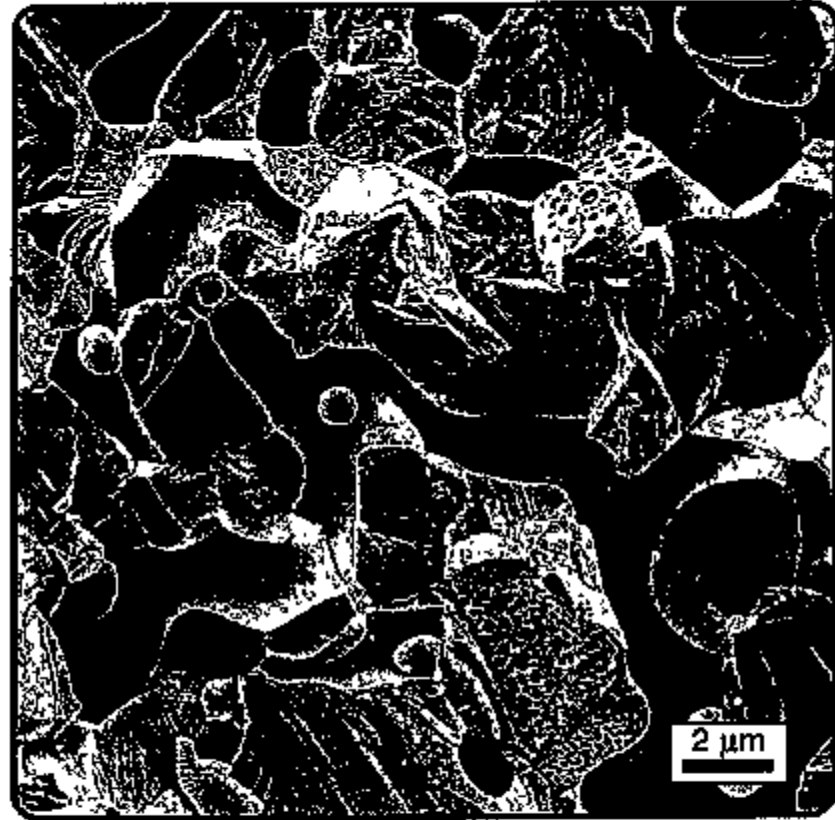
569

BS-0

$BaZr_4P_6O_{24}$
250 Cycles to 1250°C

Figure 10. SEM fracture surface microstructures of (a) as-sintered and (b) thermally cycled (250 cycles to 1250°C) BS-0 specimens.

BS-25

$Ba_{1.25}Zr_4P_{5.5}Si_{0.5}O_{24}$
As Sintered
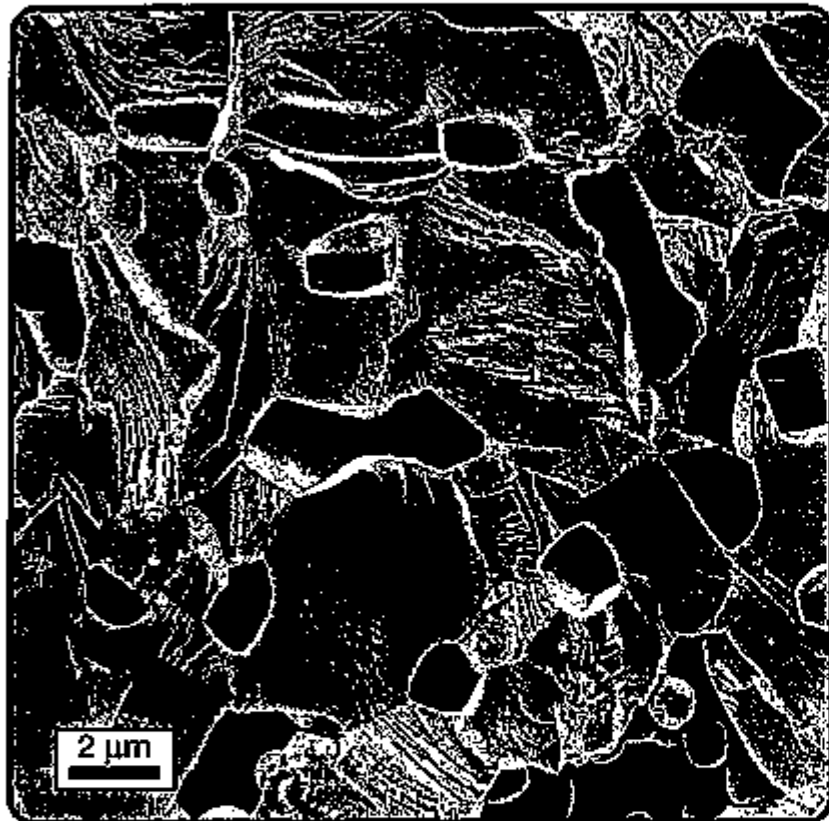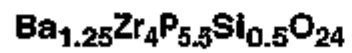
BS-25
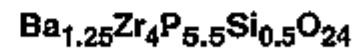
$Ba_{1.25}Zr_4P_{5.5}Si_{0.5}O_{24}$
250 Cycles to 1250°C

Figure 11. SEM fracture surface microstructures of (a) as-sintered and (b) thermally cycled (250 cycles to 1250°C) BS-25 specimens.
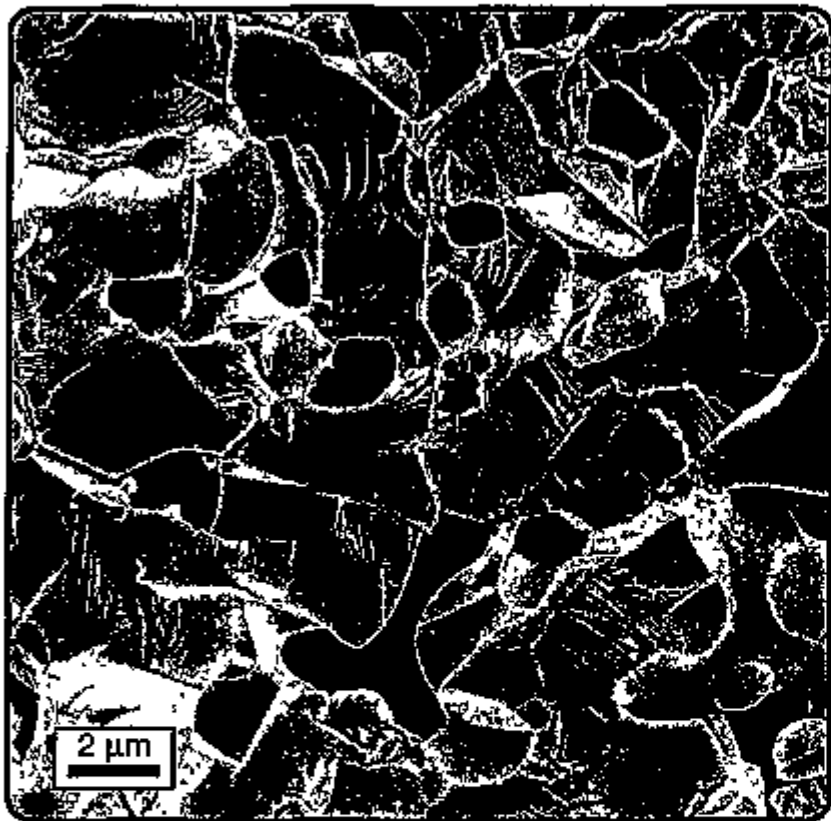
BS-50

$Ba_{1.5}Zr_4P_5SiO_{24}$

As Sintered
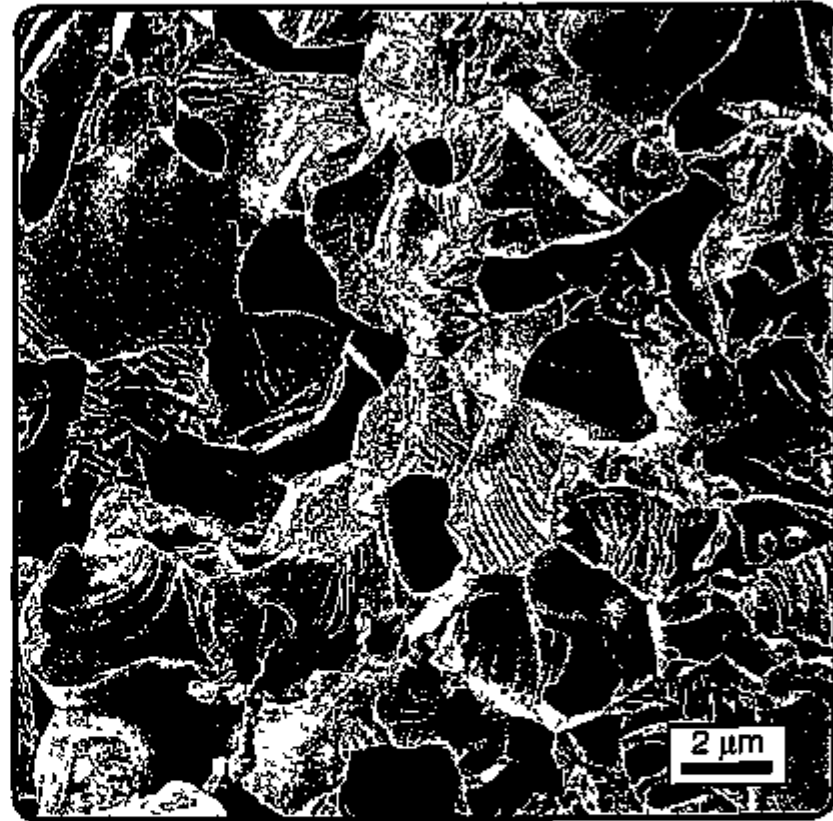
BS-50

$Ba_{1.5}Zr_4P_5SiO_{24}$

250 Cycles to 1250°C

Figure 12. SEM fracture surface microstructures of (a) as-sintered and (b) thermally cycled (250 cycles to 1250°C) BS-50 specimens.

CS-25

$Ca_{0.75}Sr_{0.25}Zr_4P_6O_{24}$

As Sintered

CS-25

$Ca_{0.75}Sr_{0.25}Zr_4P_6O_{24}$
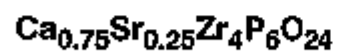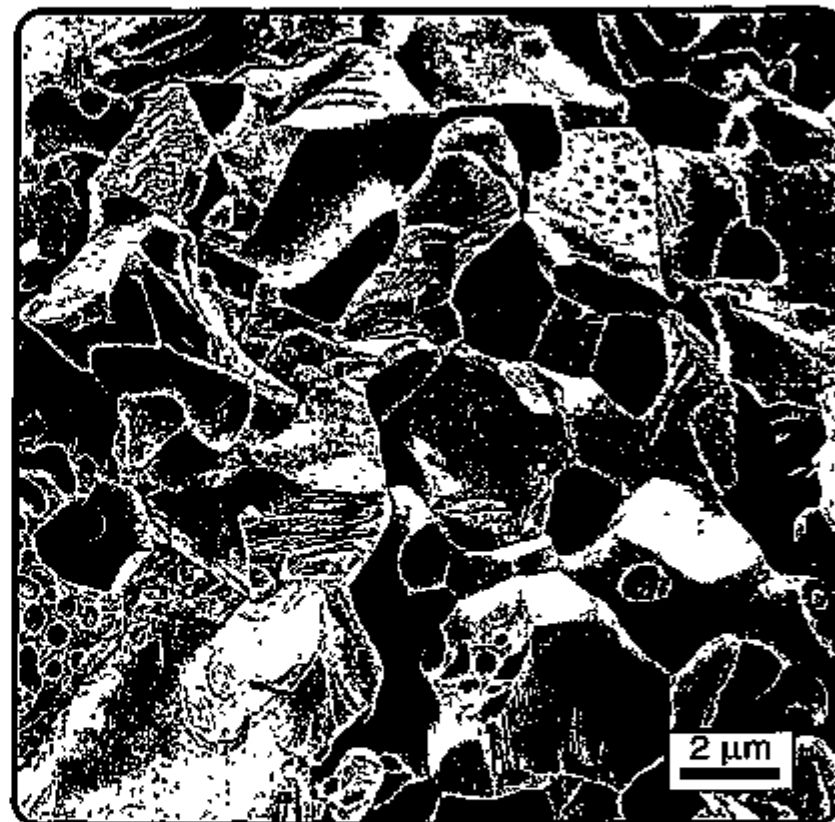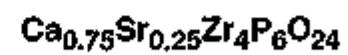
250 Cycles to 1250°C

Figure 13. SEM fracture surface microstructures of (a) as-sintered and (b) thermally cycled (250 cycles to 1250°C) CS-25 specimens.
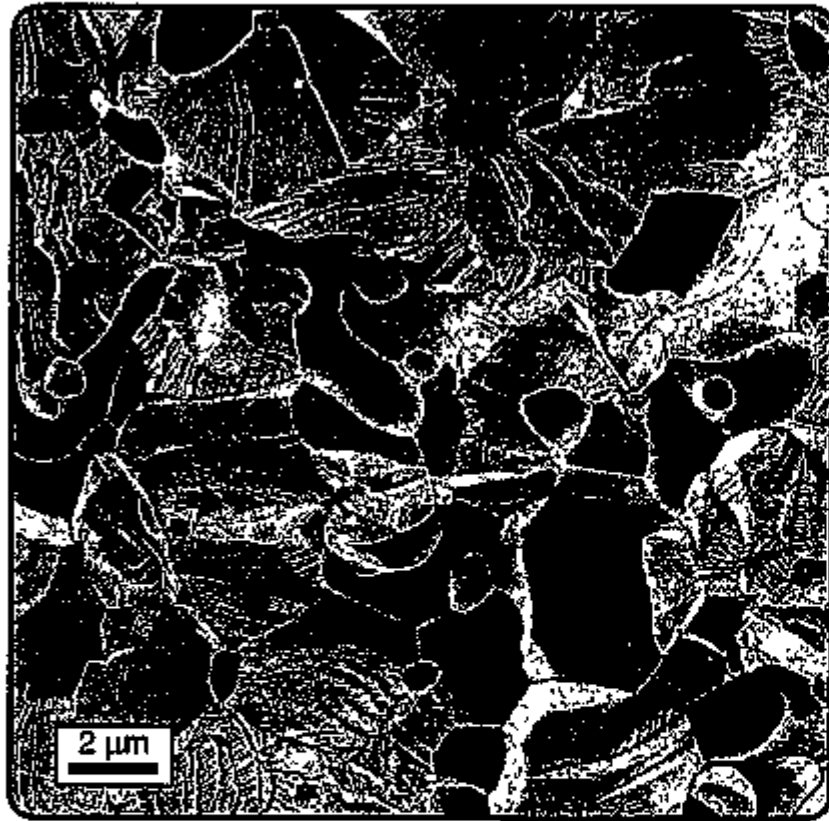
CS-50

$Ca_{0.5}Sr_{0.5}Zr_4P_6O_{24}$
As Sintered

CS-50

$Ca_{0.5}Sr_{0.5}Zr_4P_6O_{24}$
250 Cycles to 1250°C

Figure 14. SEM fracture surface microstructures of (a) as-sintered and (b) thermally cycled (250 cycles to 1250°C) CS-50 specimens.
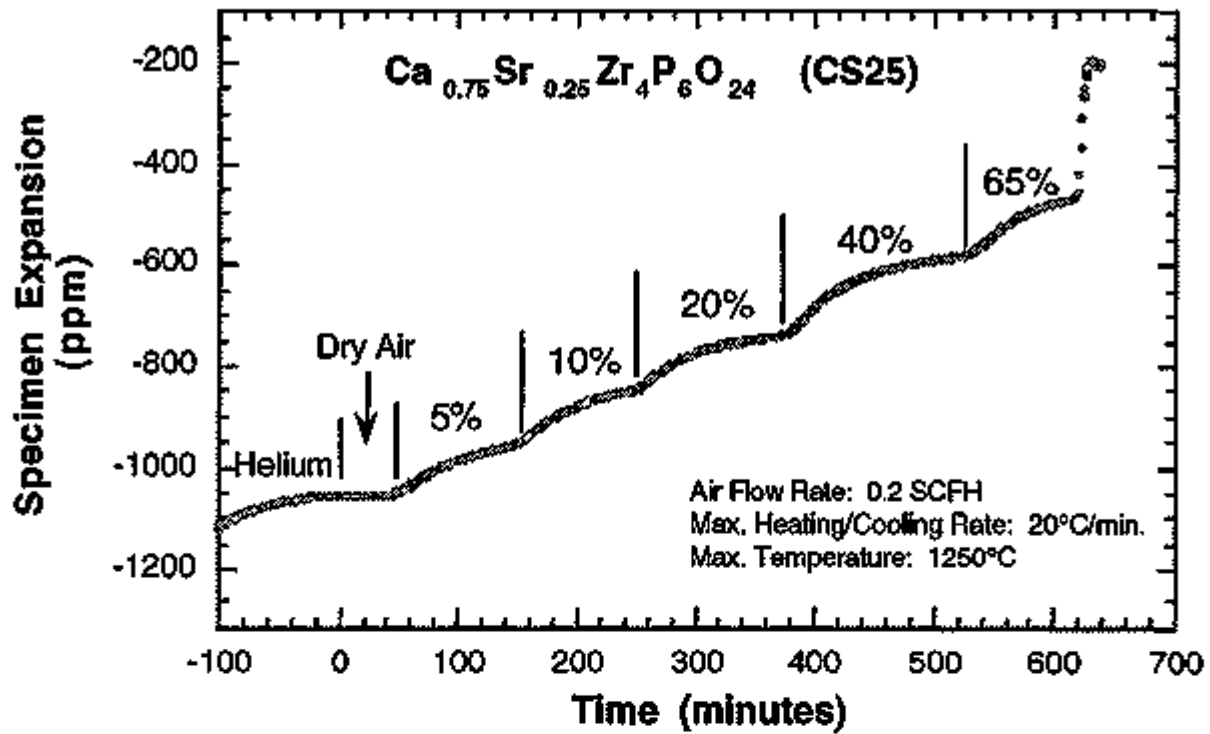
Figure 15. Moisture-assisted microcracking of anisotropic composition CS-25.
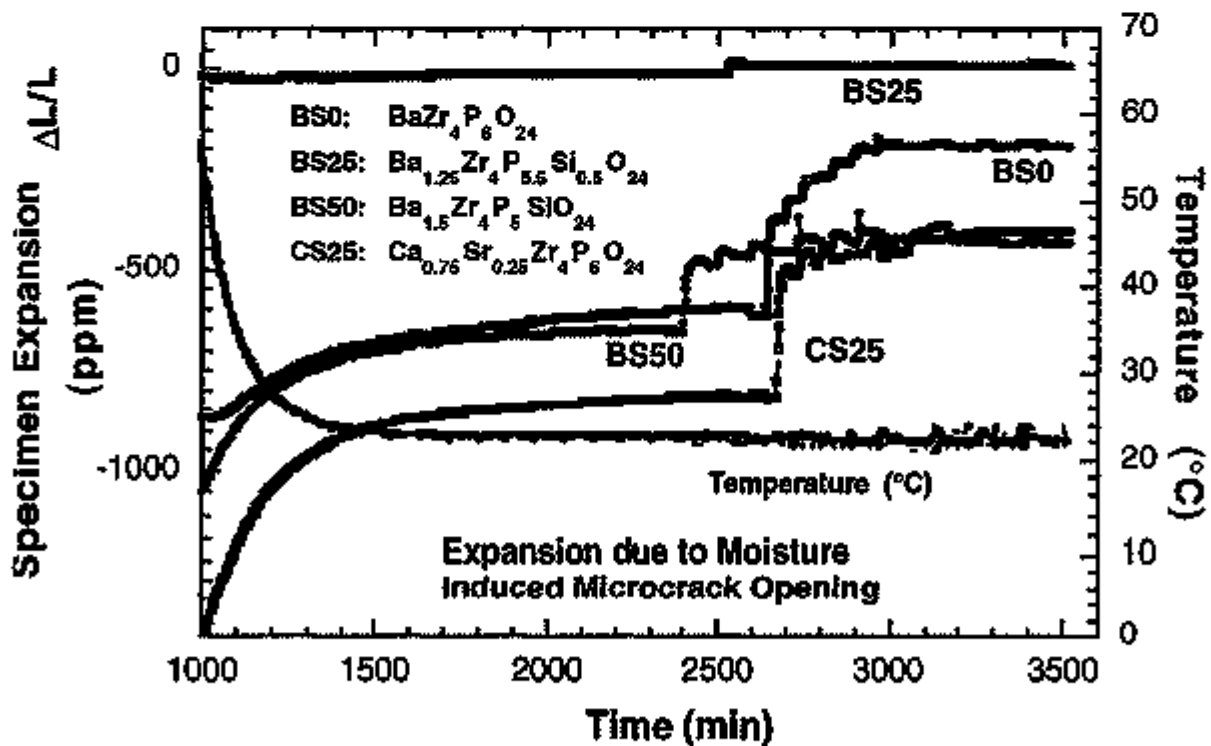
Figure 16. Environmental Effect of Room Temperature Expansion of selected NZP compositions.
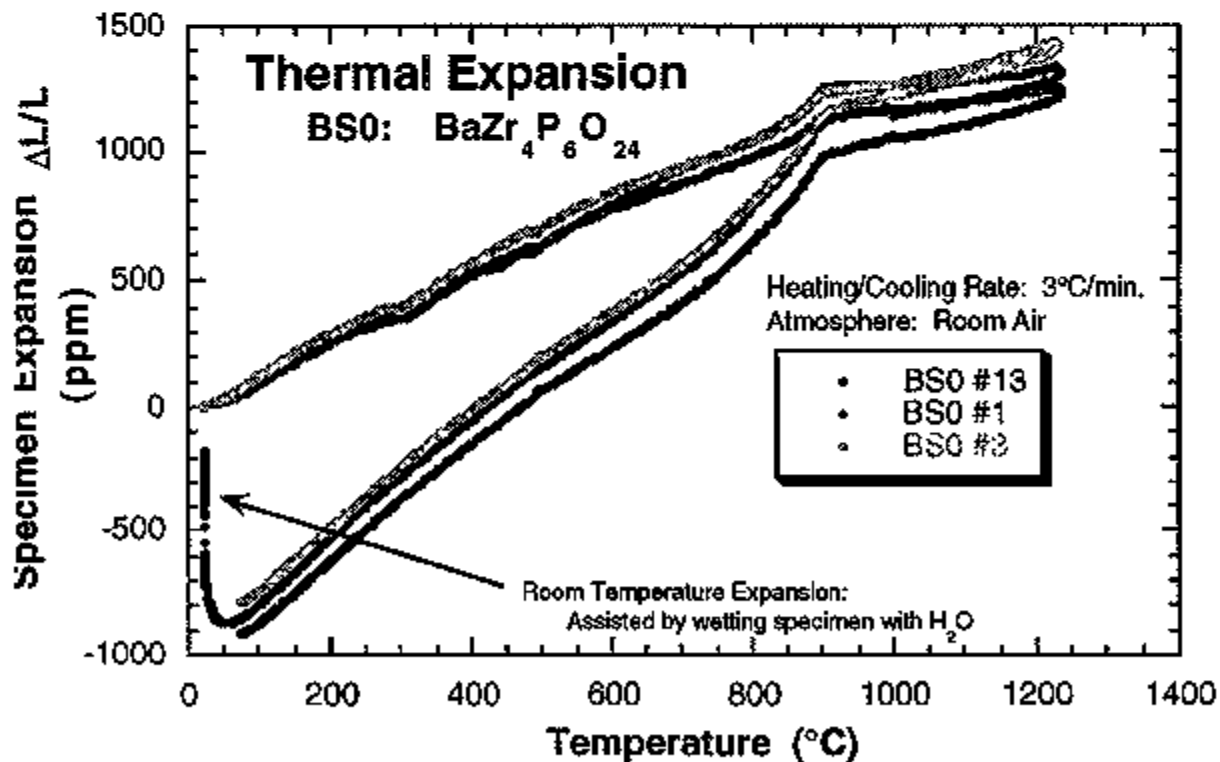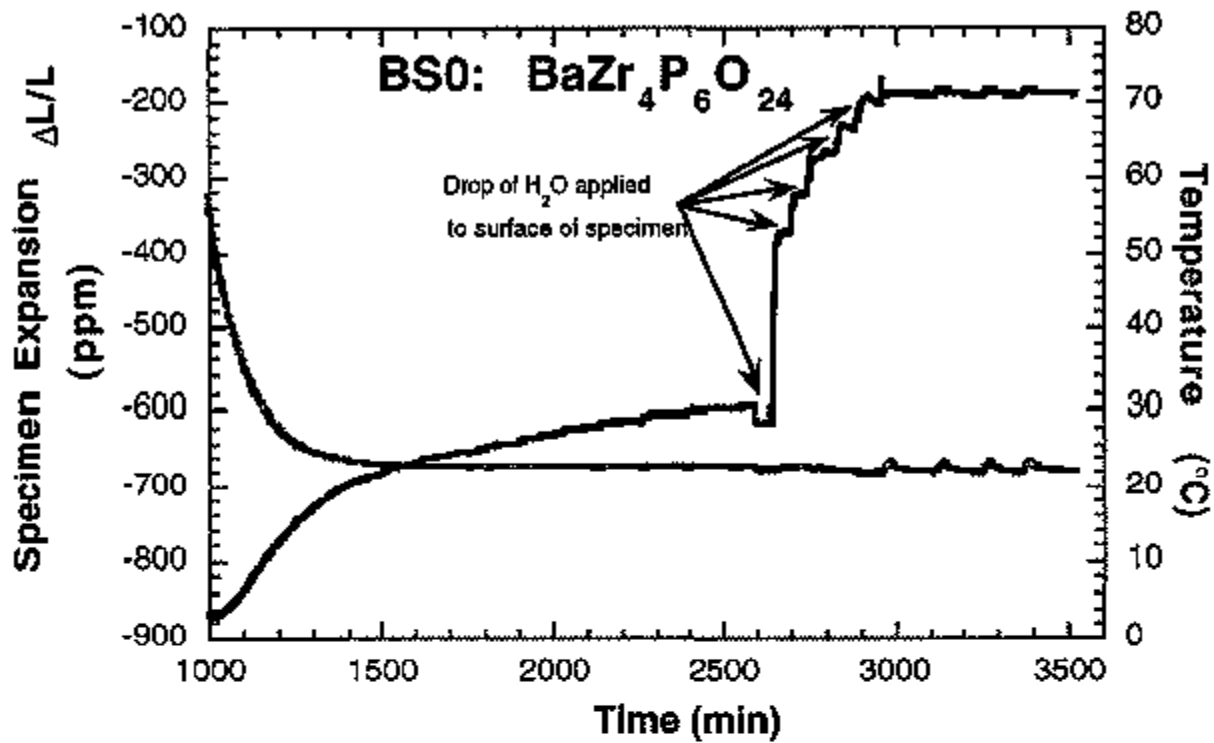
Figure 17(a) and (b). Environmental Effects on Room Temperature Expansion of BS0.
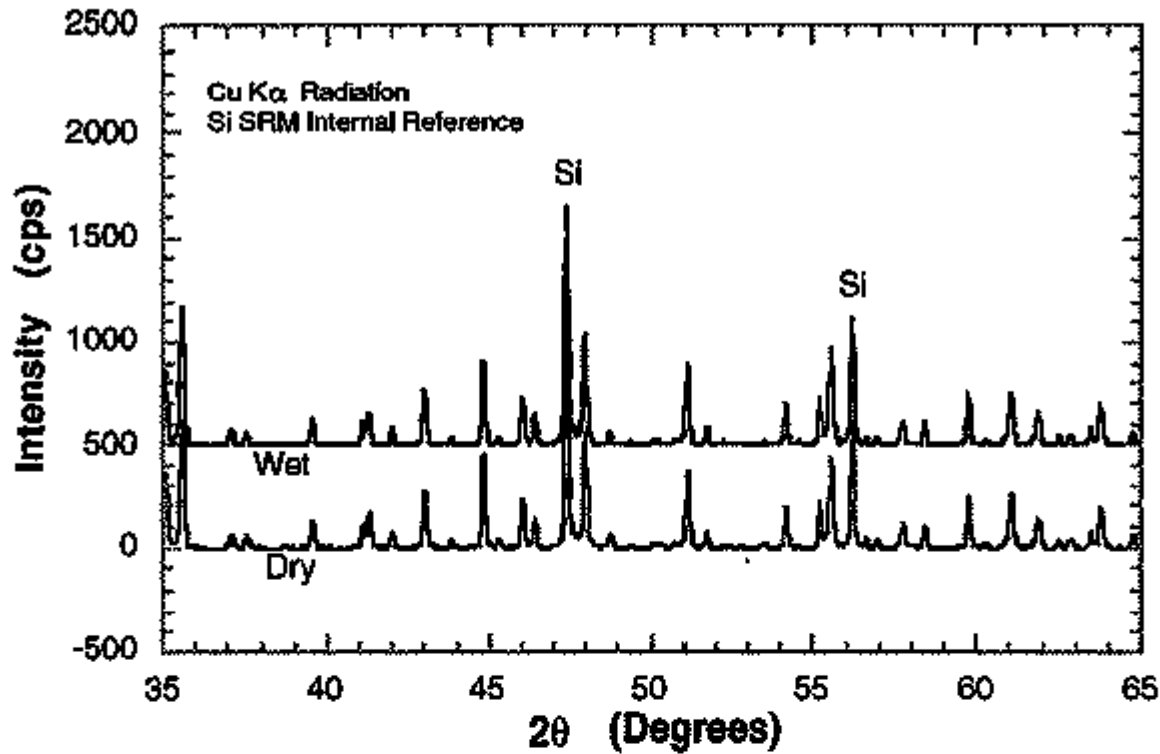
Figure 18. Powder X-ray diffraction patterns of "As-Sintered" and "Moisture-treated" CS-25.
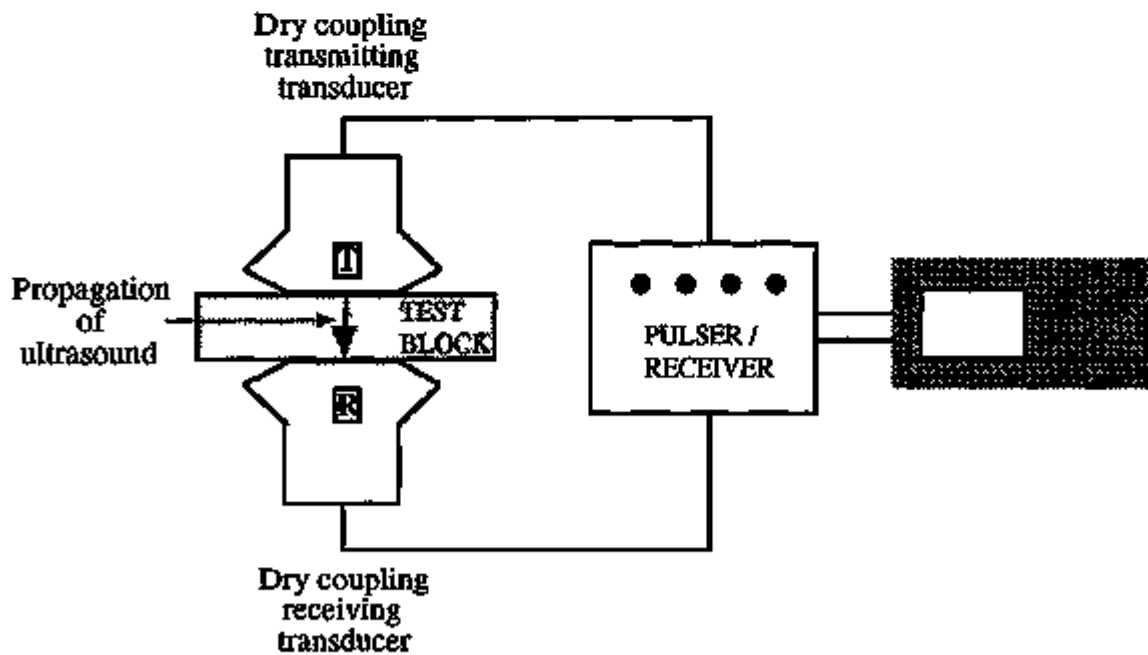
Figure 19. Schematic diagram of the ultrasonic NDE set-up used for flaw detection.

```
        ┌─────────────────────┐
        │   Pre-mixed Slurry  │
        └─────────────────────┘
                   │
                   ▼
        ┌─────────────────────┐
        │  Degassing of Slurry│
        └─────────────────────┘
                   │
┌──────────────┐   │
│   CATALYST   │───┤
└──────────────┘   │
                   ▼
        ┌─────────────────────┐
        │  Stirring for 5 mins.│
        └─────────────────────┘
                   │
                   │              ┌──────────────┐
                   ├──────────────│   INITIATOR  │
                   │              └──────────────┘
                   ▼
        ┌─────────────────────┐
        │ Slow Stirring for 5 mins.│
        └─────────────────────┘
                   │
                   ▼
        ┌─────────────────────┐
        │      Degassing      │
        └─────────────────────┘
                   │
                   ▼
        ┌─────────────────────┐
        │  Pouring of Gel-Slip│
        └─────────────────────┘
```
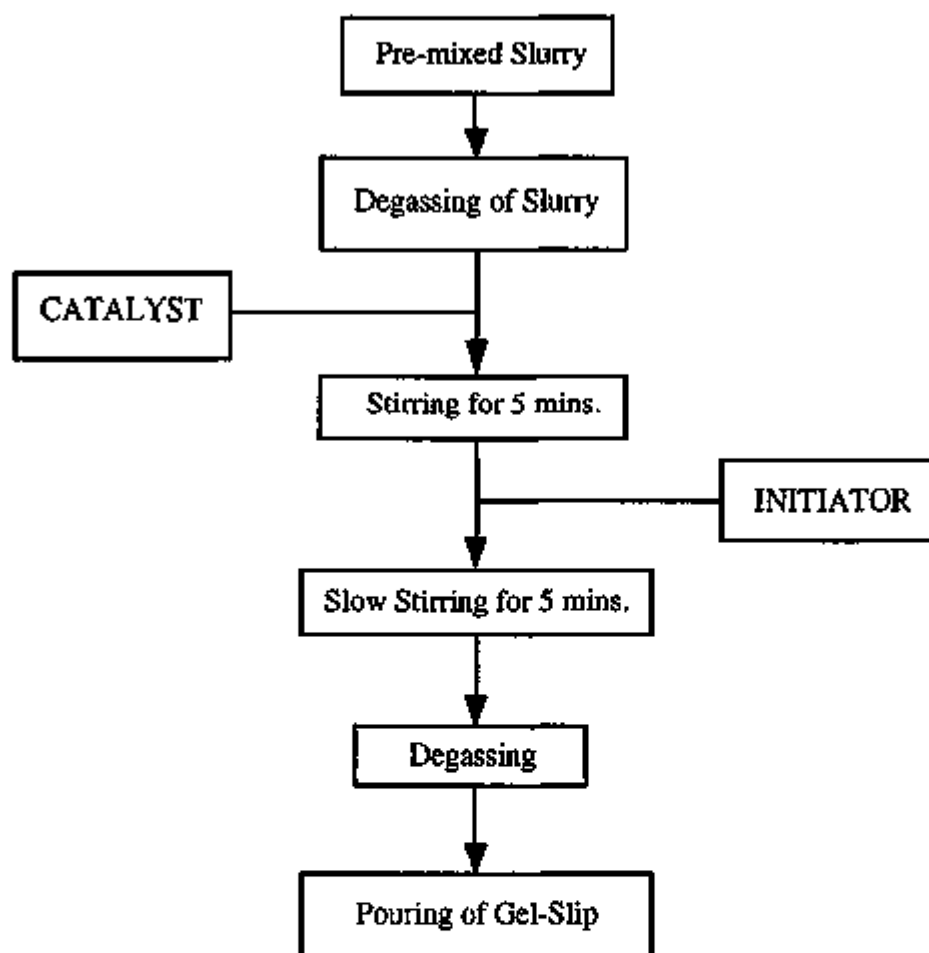
Figure 20. Schematic layout of the sequence involved in gel-casting procedure.

1.3 THERMAL AND WEAR COATINGS

Fabrication and Testing of Corrosion-Resistant Coatings
W. Y. Lee, Y. W. Bae, and D. P. Stinton (Oak Ridge National Laboratory)

Objective/Scope

Sodium corrosion of SiC and Si_3N_4 components in gas turbine engines is a potentially serious problem. The outer surfaces of SiC and Si_3N_4 parts oxidize at high temperatures to form an SiO_2 layer which inhibits further oxidation. However, sodium which is present in high-temperature combustion atmospheres reacts with the SiO_2 layer, such that it is no longer protective. The objective of this program is to develop a coating that will protect the underlying SiC or Si_3N_4 from sodium corrosion and provide simultaneous oxidation protection. To evaluate the behavior of potential materials such as stabilized ZrO_2 or HfO_2, TiO_2, $Al_2O_3 \bullet TiO_2$, and Ta_2O_5 in sodium-containing atmospheres, the corrosion resistance of hot-pressed samples of these materials will first be evaluated. A chemical vapor deposition (CVD) process will be developed for the application of the most promising coatings. The effect of the combustion environment upon coating characteristics such as microstructure, strength, adherence, and other properties will then be evaluated.

Technical Progress

(1)   Thermal Expansion Behavior of Ta_2O_5 Powder

It was previously reported that, when the Ta_2O_5-CVD process was tailored to produce a well-coalesced, void-free coating microstructure, the presence of very fine microcracks was observed on the coating surface. This microcracking behavior was somewhat unexpected since Ta_2O_5 and Si_3N_4 were reported to have similar coefficients of thermal expansion (CTE) when measured by dilatometry, which is a bulk technique. For example, the linear CTE of Si_3N_4 and Ta_2O_5 measured by dilatometry is about 3.0×10^{-6} and 3.1 to 3.6×10^{-6} K^{-1}, respectively. It was hence speculated that Ta_2O_5 might be a highly anisotropic material, which could be susceptible to microcracking upon thermal exposure. A high-temperature X-ray diffraction (XRD) study was conducted to verify this hypothesis.

Ta$_2$O$_5$ powder was used for the XRD analysis. A small amount of platinum was added to the powder sample as an internal standard. XRD patterns were obtained using a Scintag PAD X diffractometer in vacuum over the scan range of 14 to 90° 2θ at a rate of 1°/min at 27, 300, 500, 800, 1000, 1250, and 1500°C during heating and at 27° after cooling. Heating and cooling rates were 20°C/min. The diffraction patterns obtained up to 1000°C are shown in Fig. 1.

ORNL-DWG 95-5883
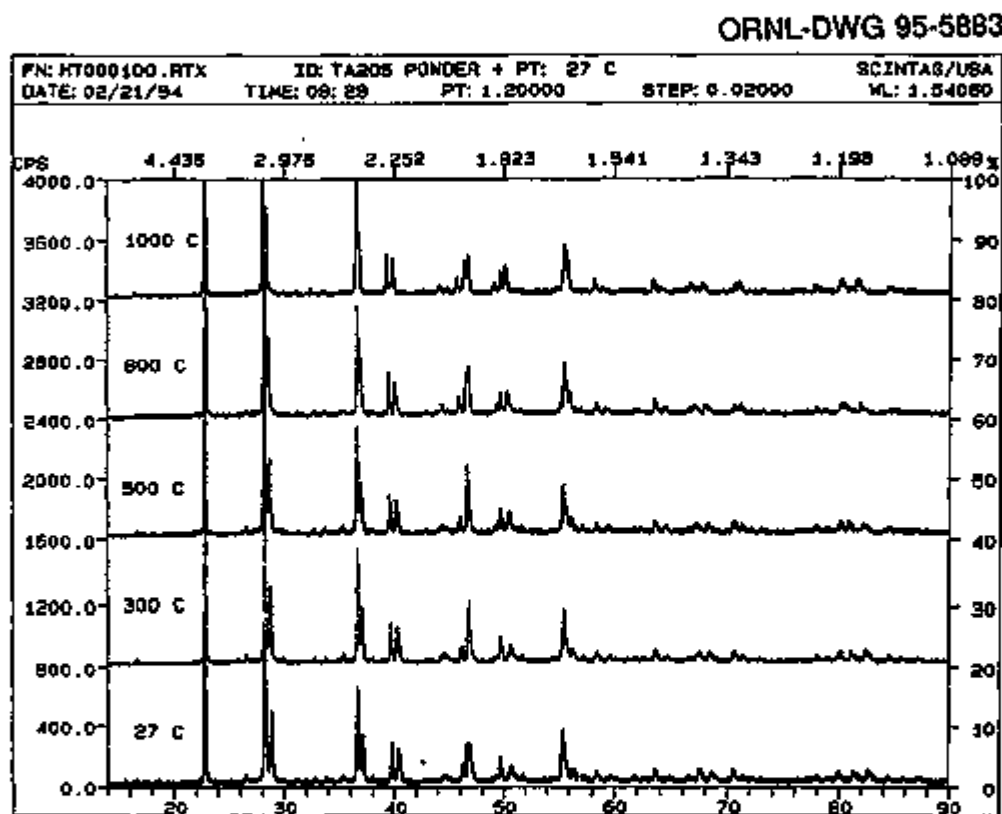
Fig. 1.   X-ray diffraction patterns of Ta$_2$O$_5$ powder
obtained at various temperatures.

Ta$_2$O$_5$ has an orthorhombic crystal structure at room temperature and is triclinic above 1380°C. Also, it is known that Ta$_2$O$_5$ undergoes a metastable transition at 320°C to a monoclinic form which inverts to tetragonal at 920°C. In the present study, the diffraction patterns obtained between 27 and 1000°C were indexed based on an orthorhombic unit cell with P2$_1$2$_1$2 space group. Background correction and K$_{\alpha2}$ peak stripping were performed on the XRD patterns, and the peak position and intensities were determined using a profile fitting program. The observed peaks

were then calibrated using the certified peak positions for the Pt internal standard in order to correct for possible instrumental and sample mounting aberrations. The crystal system and approximate unit-cell parameters were entered, and the cell parameters were refined using a lattice parameter refinement program. The calculated unit-cell parameters are tabulated in Table 1 and are plotted as a function of temperature in Figs. 2 and 3.

Table 1. Calculated unit-cell parameters of Ta_2O_5

Temp. (°C)	a (Å)	b (Å)	c (Å)	Volume (Å³)
27	6.175	40.18	3.922	973.1
300	6.203	40.35	3.864	971.2
500	6.228	40.32	3.887	976.4
800	6.248	40.33	3.885	979.3
1000	6.252	40.43	3.883	981.8

ORNL-DWG 95-5884
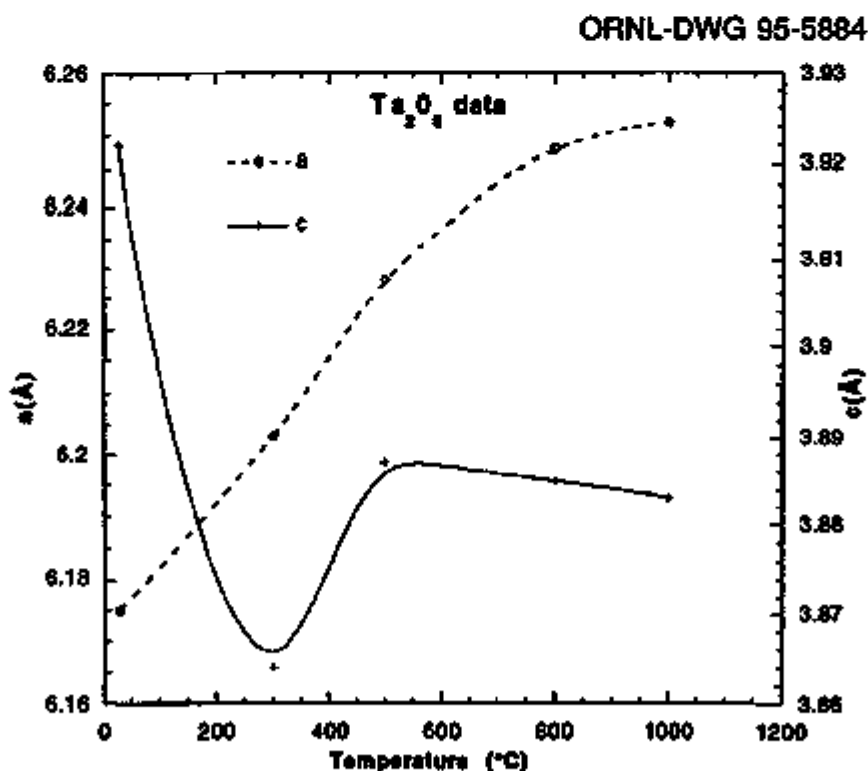
Fig. 2. Thermal expansion of "a" and "c" parameters.

ORNL-DWG 95-5885
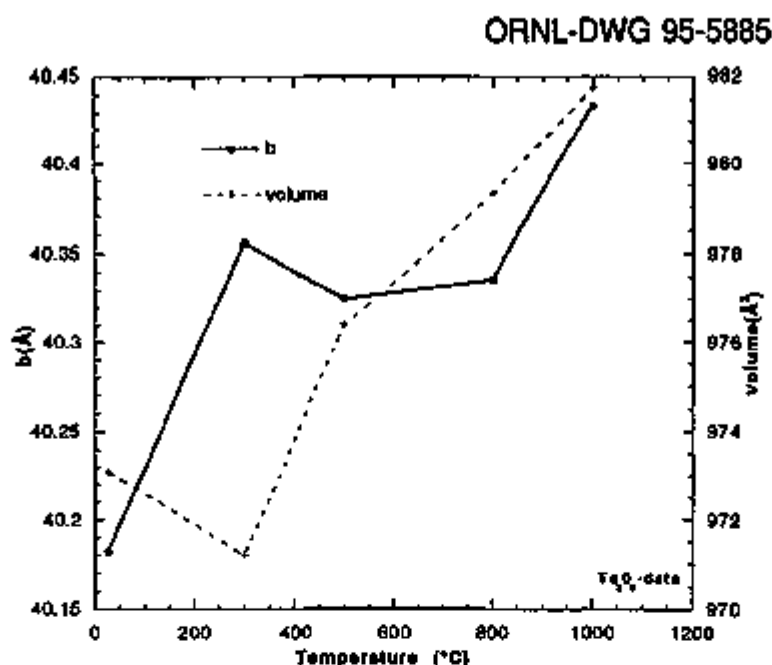
Fig. 3. Thermal expansion of "b" parameter and unit volume.

Figure 2 shows that the "a" parameter increased fairly linearly with temperature. On the other hand, the expansion behavior of the "b" and "c" parameters was nonlinear, as shown in Figs. 2 and 3. However, in considering the entire temperature range, the "b" parameter generally increased with increased temperature while the "c" parameter decreased. The unit-cell volume initially decreased, then increased with increasing temperature. The XRD patterns in Fig. 1 show that the diffraction peaks around $2\theta = 47°$ merged to one peak at 300°C but remained as two distinct peaks below 300 and above 500°C. These results, along with the observed trends in lattice expansion, seemed to indicate that there was a phase transition between 27 and 500°C.

The linear CTE calculated from the XRD data is 12.82×10^{-6} for "a", 6.39×10^{-6} for "b", and -10.22×10^{-6} for "c". Also, the average bulk linear CTE is 3.00×10^{-6}, which compares favorably to the dilatometric values reported for hot-pressed Ta_2O_5. The degree of anisotropy of Ta_2O_5 (e.g., $|\alpha_a-\alpha_c|$) is 23.04×10^{-6} K^{-1}, which is comparable to that of $NaZr_2P_3O_{12}$, a low-expansion ceramic which is known to extensively microcrack due to high thermal expansion anisotropy.

It is also plausible that, since the CVD Ta_2O_5 coating was typically deposited with a strong preferred orientation along the (001) plane, the "c" direction in individual Ta_2O_5 grains in the coating was preferentially aligned perpendicular to the substrate surface. Therefore, as an approximation, the thermal expansion of the coating in the direction parallel to the substrate was considerably higher than that of Si_3N_4. Therefore, upon cooling after deposition, the coating would be under tension, possibly causing the formation of microcracks.

(2)   Corrosion Test of Ta_2O_5 Coating

Since the Ta_2O_5-CVD process has been tailored to produce a well-coalesced, void-free coating microstructure, the stability of the Ta_2O_5 coating deposited on hot-isostatically pressed Si_3N_4 substrates (GN10, AlliedSignal) has been tested in oxidative and corrosive environments. As discussed in the previous semi-annual report, the coated structure was observed to be relatively stable up to 1300°C in oxidation. However, it appeared that the Ta_2O_5-Si_3N_4 system became unstable in the $Na_2SO_4 + O_2$ environment at 1000°C because Ta_2O_5 and Na_2SO_4 reacted rapidly to form $NaTaO_3$ within 5 h of exposure. In this section, results from the $Na_2SO_4 + O_2$ tests conducted for 25 and 100 h and from a burner rig test performed at AlliedSignal Engines are discussed.

Figure 4 shows a cross-section image and X-ray maps of a Ta_2O_5-coated Si_3N_4 substrate which was subjected to the 25-h corrosion test. The presence of two distinct corroded layers was observed. The top layer was about 10 μm thick and rich in Ta and also contained Na and O. Note that the appearance of some Si in this layer in Fig. 4 was a spectral artifact as discussed in the earlier report. The bottom layer was about 40 to 50 μm thick and consisted of Na, Si, O, Y, Ta, and bubbles. Figure 5 shows that the top layer was removed upon washing the specimen in warm distilled water. The XRD pattern shown in Fig. 6(b) confirmed that the crystalline portion of the top (removed) layer was $NaTaO_3$. Note that the peak near 32° in Fig. 6(b) could not be appropriately assigned.

The development of the second layer in the corroded structure was somewhat difficult to understand. This layer was amorphous since it was transparent to XRD [i.e., all the diffraction peaks in

Fig. 4. Backscattered cross-section image and elemental X-ray maps of Ta_2O_5-coated Si_3N_4 after corrosion in $Na_2SO_4 + O_2$ at 1000°C for 25 h before washing.

Fig. 5. Backscattered cross-section image and elemental X-ray maps of Ta$_2$O$_5$-coated Si$_3$N$_4$ after corrosion in Na$_2$SO$_4$ + O$_2$ at 1000°C for 25 h after washing.
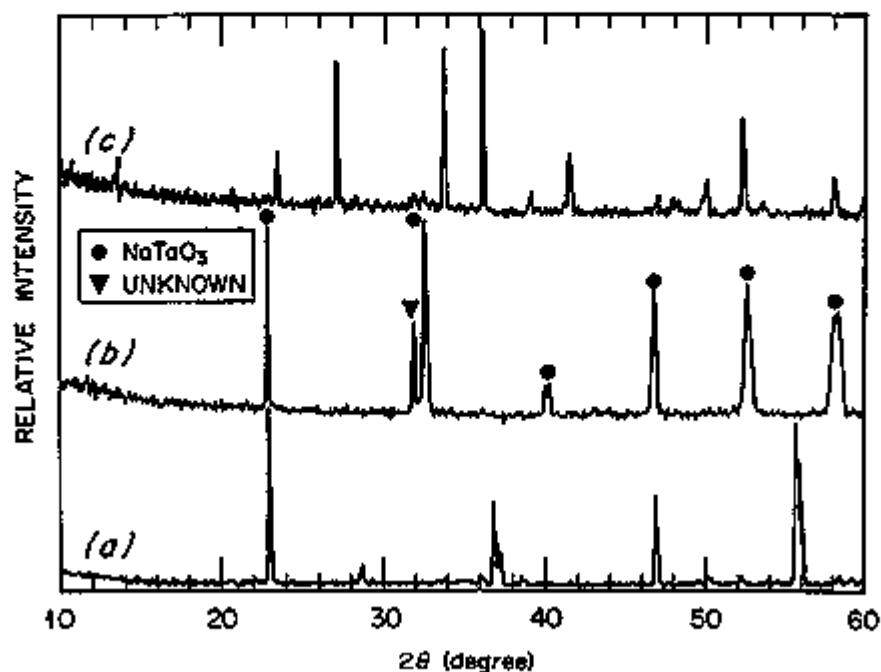
Fig. 6. X-ray diffraction patterns of Ta_2O_5-coated Si_3N_4:
(a) as-deposited; (b) after corrosion in $Na_2SO_4 + O_2$
at 1000°C for 25 h, but prior to washing in water;
and (c) after washing.

Fig. 6(c) were attributed to Si_3N_4]. The layer was not soluble in
water and contained Ta, Na, Si, O, Y, and bubbles. The presence of
the bubbles in this layer indicated that a gaseous species, perhaps N_2,
was rapidly released as a reaction by-product below the substrate
surface and was locally encapsulated to form the bubbles. It was
also possible that $NaTaO_3$ (s) and Si_3N_4 (s) reacted to produce the
amorphous phase containing Ta, Na, Si, and O and to release N_2 (g) as
a by-product. The presence of Y in the reaction layer suggested
that the Si_3N_4 structure was penetrated by the $NaTaO_3$ phase. It
seemed that the amorphous phase was molten under the corrosion
conditions because of the following observations: extensive bubble
formation, highly curved surface contours, and relatively large depth
of penetration (40 to 50 μm). This speculation cannot be verified
since no phase diagram exists for the Ta-Na-Si-O system. If the
amorphous intermediate layer was somewhat molten and the surface
layer containing $NaTaO_3$ was solid at 1000°C, the observed bubble
formation might be easier to comprehend.

After the 100-h treatment, the formation of $NaTaO_3$ and cristobalite on the surface of the sample was indicated by XRD [see Fig. 7(b)]. The $NaTaO_3$ layer and the cristobalite phase were removed from the substrate upon washing [Fig. 7(c)]. Figure 8 shows the presence of an amorphous layer containing bubbles, which was not removed by washing. Although the microscopic appearance of this layer was somewhat similar to that observed after the 25-h treatment, the chemical composition of the two layers was fairly different. For example, the layer formed after 100 h of exposure did not contain Ta, unlike the layer exposed for 25 h. The 100-h sample lost much more weight than the 25-h sample (10.7 vs 0.8 mg). These data implied that the formation mechanism of the corrosion region became different between the 25- to 100-h exposures.

In order to obtain more realistic corrosion data, three NT154 Si_3N_4 flexure bars (10.2 x 1.3 x 0.6 cm) were coated with CVD Ta_2O_5, and two of the coated bars were tested using a burner rig at AlliedSignal. The burner rig test was conducted using Jet A fuel

ORNL-DWG 94-11303
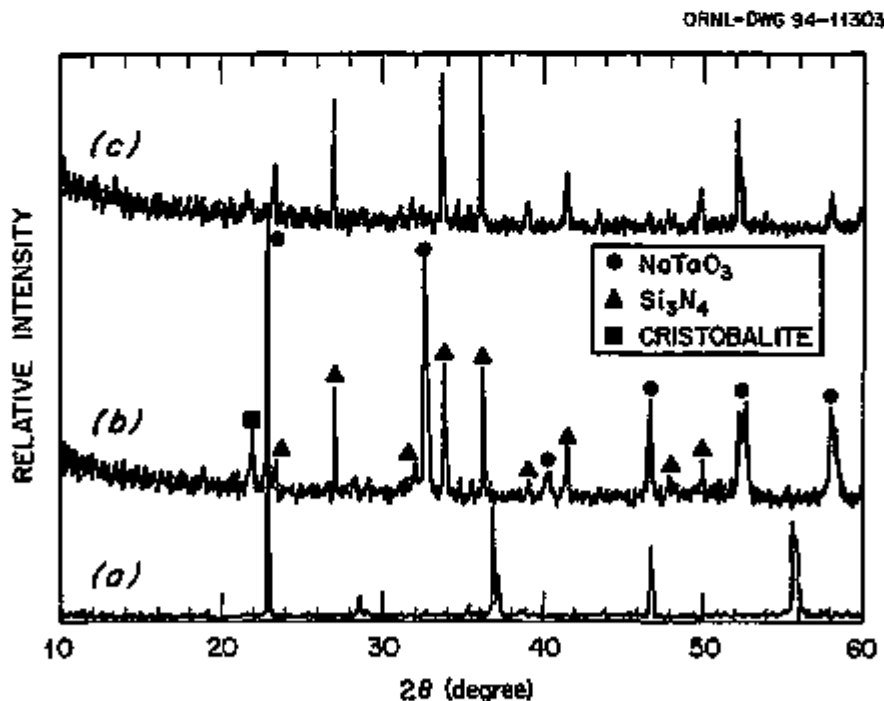
Fig. 7. X-ray diffraction patterns of Ta_2O_5-coated Si_3N_4: (a) as-deposited; (b) after corrosion in $Na_2SO_4 + O_2$ at 1000°C for 100 h, but prior to washing in water; and (c) after washing.
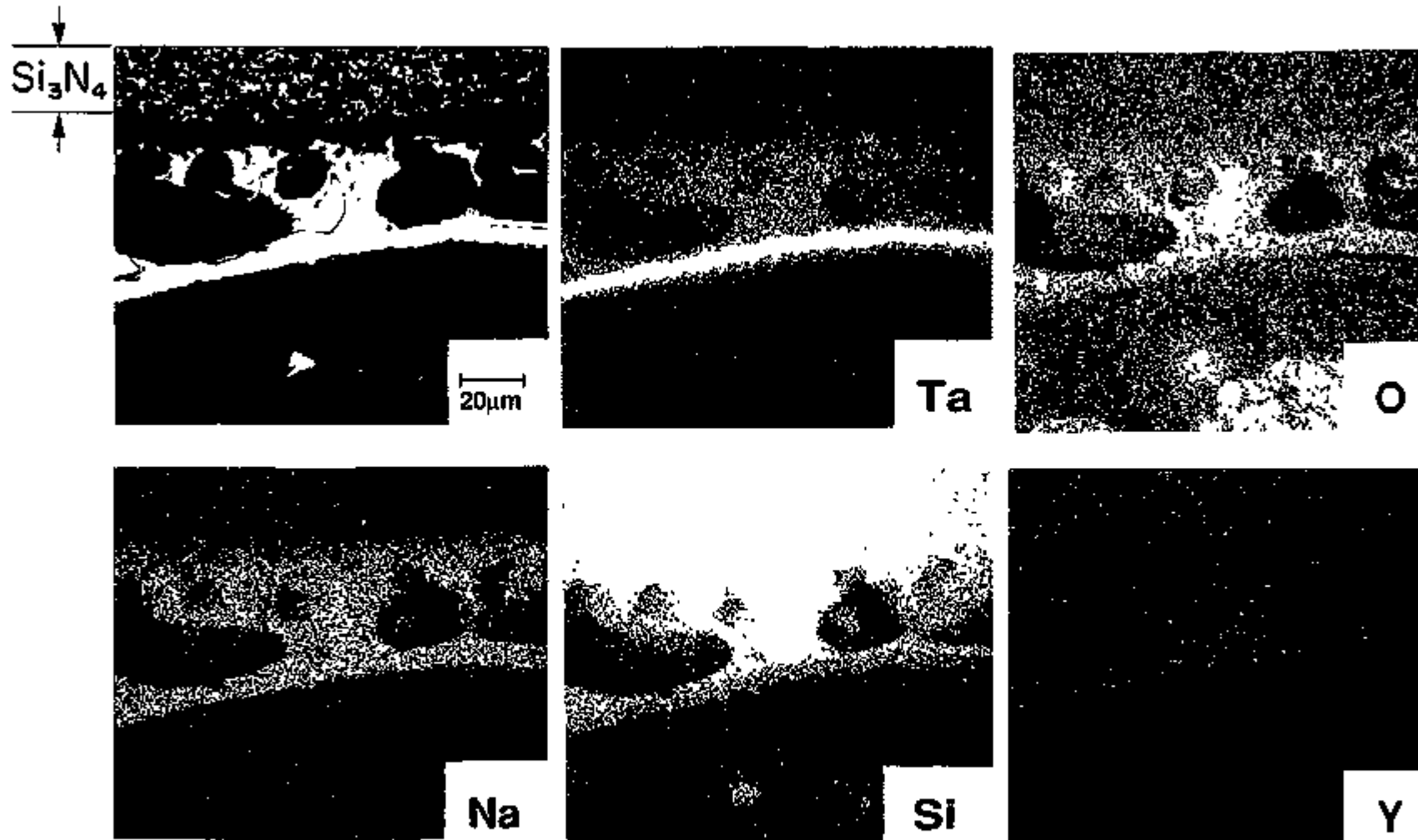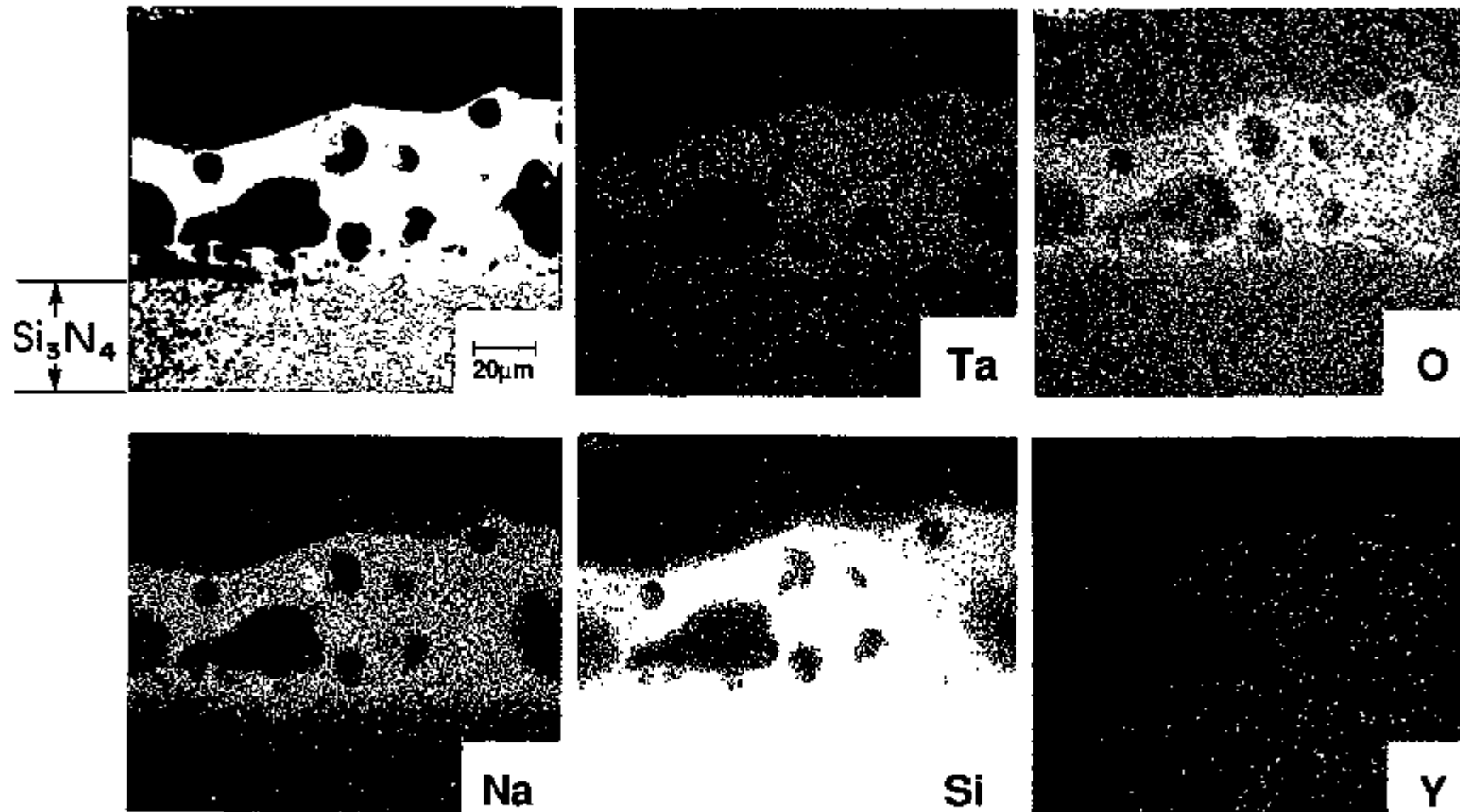
ORNL–PHOTO 5211–94
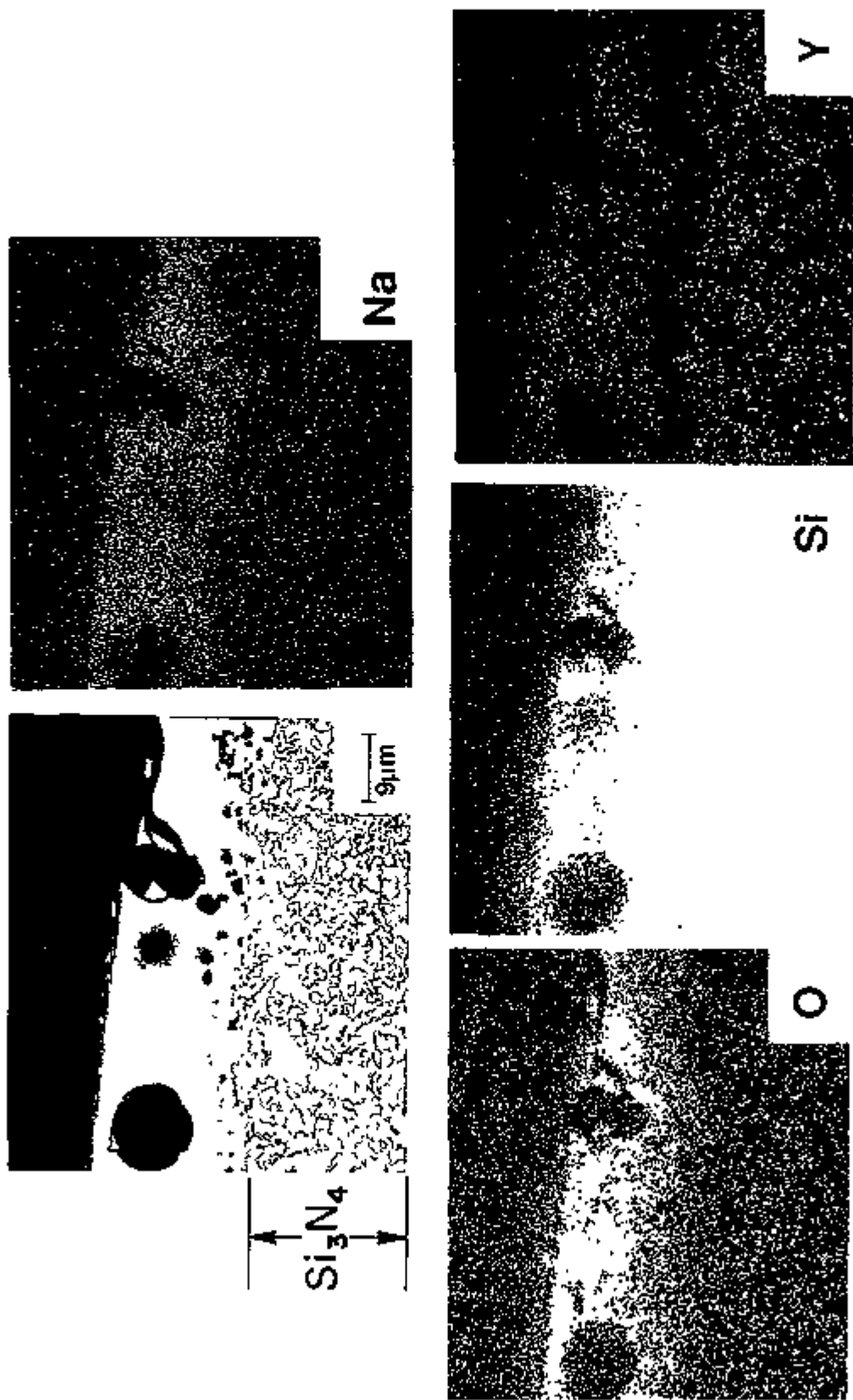
Fig. 8. Backscattered cross-section image and elemental X-ray maps of Ta_2O_5-coated Si_3N_4 after corrosion in $Na_2SO_4 + O_2$ at 1000°C for 100 h after washing.

(0.035% sulfur) at a fuel-to-air ratio of 0.06 with 5 ppm synthetic sea salt (ASTM Specification D1141-52) at 101 kPa. The test lasted for 100 h and consisted of the following thermal cycle: 27 min at 1052°C followed by 3 min of forced air cool. The exposed specimens were broken at room temperature in four-point flexure to assess the effect of corrosion on flexural strength.

Figure 9 shows a photograph of two corroded NT154 Si_3N_4 specimens which were coated with Ta_2O_5. For comparison, a coated NT154 sample which was not exposed to the burner rig test is also shown. As tabulated in Table 2, the flexure strength of the coated NT154 specimens was significantly reduced after the burner rig test, but the level of strength reduction was similar to that measured from uncoated NT154 specimens subjected to the same test. The visual appearance of the coated and uncoated specimens after the corrosion test was basically identical. The fracture surfaces of the coated and uncoated flexure specimens were also examined at magnifications up to 40x. For all coated and uncoated specimens, crack initiation occurred on the corroded surface. Note that, prior to flexure testing, the glassy silicate corrosion products observed on the exposed surface were removed from the compression surface and loading pin locations on the tensile surface. It was probable that, in the initial thermal cycling stage of the burner rig test, the coating was spalled off from the substrates as the coating layer was being converted to $NaTaO_3$.

Table 2. Flexure strength of chemical vapor deposited
Ta_2O_5 coated and uncoated NT154 specimens

Sample No.	Coating	Burner rig exposure	Flexure strength (MPa)
10	Uncoated	Yes	501
11	Uncoated	Yes	541
52	Coated	Yes	516
53	Coated	Yes	501
19	Coated	No	858
12	Uncoated	No	861
188	Uncoated	No	988

ORNL-PHOTO 5208-94
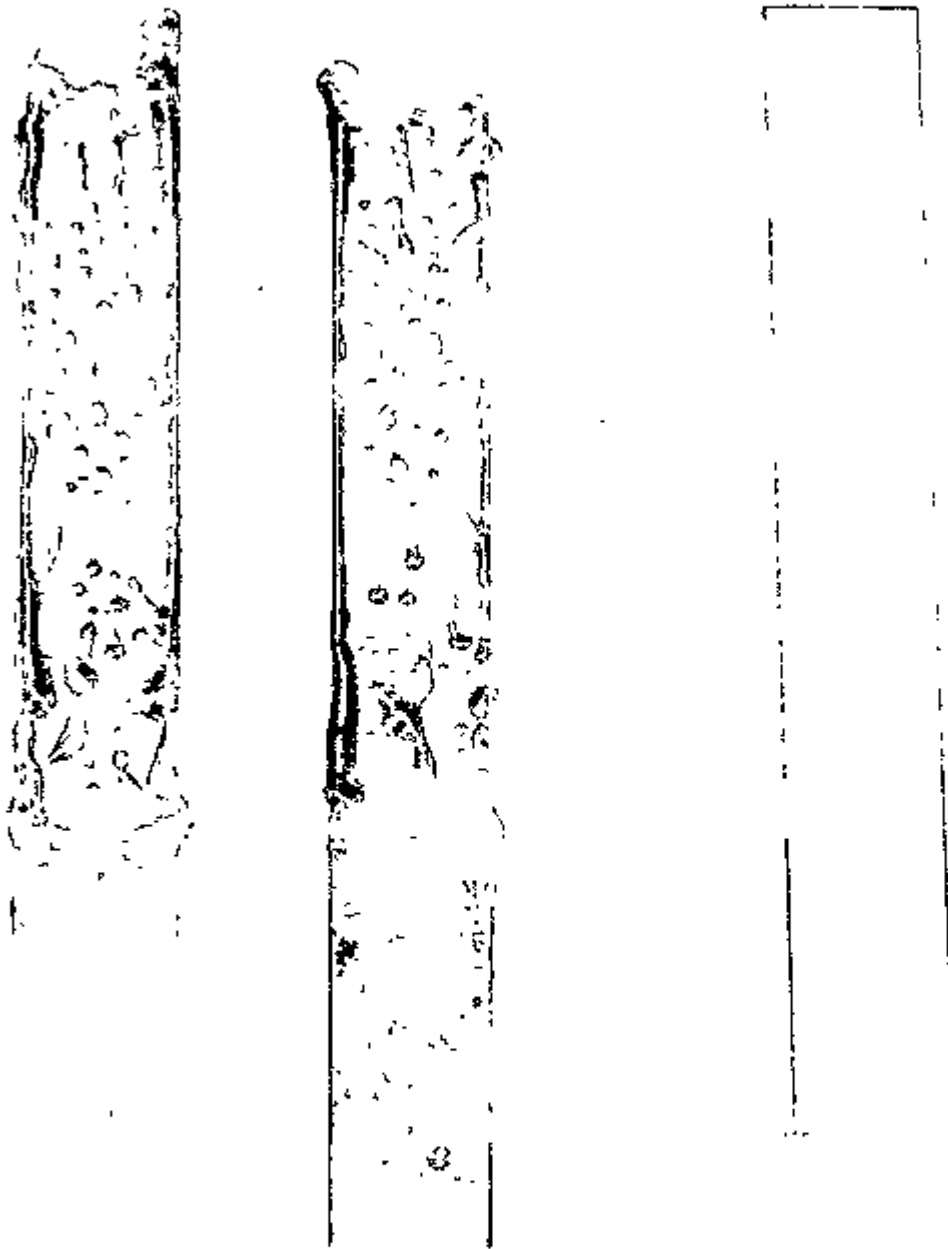
Fig. 9.   Two NT154 specimens coated with Ta_2O_5 after corrosion
along with one coated sample which was not exposed.

(3)   Corrosion Resistance of Other Coating Candidates

GN10 Si_3N_4 substrates, which were coated with CVD mullite recently developed at Boston University, were delivered to ORNL. The coated specimens will be corrosion tested in the next reporting period.

The corrosion resistance of low-expansion ceramic materials such as $Ba_{1+x}Zr_4P_{6-2x}Si_{2x}O_{24}$, $Ca_{1-x}Sr_xZr_4P_6O_{24}$, and Al_2TiO_5 + mullite has been tested in an $Na_2SO_4 + O_2$ environment for 100 h at 1000°C. XRD and weight measurement data indicated that $Ca_{1-x}Sr_xZr_4P_6O_{24}$ performed relatively well.   The samples are being further characterized by metallography and electron microprobe.

Status of Milestones

On schedule.

Communications/Visits/Travel

W. Y. Lee presented a paper entitled "Na_2SO_4-Induced Corrosion of Si_3N_4 Coated with Chemically Vapor Deposited Ta_2O_5" at the 8th Annual Conference on Fossil Energy Materials, which was held on May 11, 1994, in Oak Ridge, Tenn. The co-authors of the paper were Y. W. Bae and D. P. Stinton of ORNL and T. E. Strangman of AlliedSignal Engines.

W. Y. Lee, Y. W. Bae, and D. P. Stinton met with T. E. Strangman of AlliedSignal Engines and R. A. Miller of NASA-Lewis Research Center on May 12, 1994, at ORNL. The purpose of the meeting was to discuss the possible integration of ORNL's CVD capability and NASA's recent success in depositing a thermal-shock-resistant mullite coating by plasma spraying. It was agreed that several hybrid coating concepts will be pursued in the hope of developing a more robust, multilayer corrosion protection system for Si_3N_4 turbine components. One of the concepts involves using a thin CVD Al_2O_3 coating as a top coat for the plasma-sprayed (or electron beam physical vapor deposited) mullite coating since the corrosion resistance of pure Al_2O_3 is intrinsically superior to that of mullite. The adhesion of the thin Al_2O_3 coating structure to the mullite surface will be critically evaluated as a function of the surface morphology and porosity level of the mullite surface.

Problems Encountered

Based on the experimental results obtained so far, it is apparent that the Ta_2O_5-Si_3N_4 system becomes unstable in the $Na_2SO_4 + O_2$ environment at 1000°C because (1) Ta_2O_5 and Na_2SO_4 react rapidly to form $NaTaO_3$ and (2) subsequently, $NaTaO_3$ interacts destructively with the underlying Si_3N_4 structure. Furthermore, Ta_2O_5 exhibited highly anisotropic thermal expansion behavior and, hence, was found to be susceptible to microcracking. On the promising side, the Ta_2O_5-coated structure is relatively stable up to 1300°C in oxidation. Other coating candidates are currently being examined. For example, the corrosion resistance of CVD mullite, recently developed by V. Sarin of Boston University, will be tested at ORNL as mentioned earlier. Also, the corrosion resistance of newly developed low-expansion ceramics such as $Ba_{1+x}Zr_4P_{6-2x}Si_{2x}O_{24}$, $Ca_{1-x}Sr_xZr_4P_6O_{24}$, and Al_2TiO_5 + mullite is being examined. In parallel to these corrosion studies, the aforementioned hybrid coating concepts are being explored with AlliedSignal and NASA-Lewis.

Publications

Two manuscripts entitled "Na_2SO_4-Induced Corrosion of Si_3N_4 Coated with Chemically Vapor Deposited Ta_2O_5" and "Effects of Temperature and Reagent Concentration on the Morphology of Chemically Vapor Deposited β-Ta_2O_5" were submitted for publication in *J. Am. Ceram. Soc.*

Development of Adherent Coatings to Reduce Contact Stress Damage of Ceramics

V. K. Sarin (Boston University)

Objective/Scope

The development of oxidation/corrosion resistant, high toughness, adherent coating configurations for silicon based ceramic substrates for use in advanced gas turbine engines.

Technical Progress

CVD experiments were performed to grow $Al_2O_3-SiO_2$ codeposited coatings from $AlCl_3-SiCl_4-CO_2-H_2$ mixtures. Initial parameters for experimentation were chosen from equilibrium thermodynamic analysis and the corresponding CVD phase diagrams that were constructed. This was discussed in detail in the previous semiannual report. CVD phase plots show that a combination of Al_2O_3, mullite, and SiO_2 phases can be obtained at low concentrations of $AlCl_3$ and $SiCl_4$. All the processing was done at $1000°C$ and 75 torr. The relative mole fractions of $AlCl_3/SiCl_4$ were varied keeping the amount of CO_2 and H_2 constant throughout.

Figure 1 shows a typical $Al_2O_3-SiO_2$ coating on a SiC substrate. The coatings were extremely non-uniform in composition. The composition within each sample varied from silica rich coatings(Al:Si ~ 1:5) to alumina rich coatings (Al:Si ~ 5:1). Figure 2 shows the surface morphology and figure 3 the energy dispersion spectra of several areas of the coating. Figure 4 shows an EDS line scan performed on a coating across the substrate that shows increasing amount of Al and decreasing amount of Si to the right. The coatings however were mostly silica rich in general with decreasing amount of Al species radially outward in the reactor. Nucleation in the gas phase was also observed. This powder contained mostly Al and very little Si(Al:Si ~ 5:1). This points out that $AlCl_3$ reacts much more readily with the water gas than $SiCl_4$. It can also be said that the Al_2O_3 deposition is mostly in the mass transport controlled regime, where as the deposition of SiO_2 is mostly surface reaction controlled. Gas mixing and flow patterns may have also contributed to the non-uniformity.

Process conditions (temperature and pressure) were adjusted so that formation of both Al_2O_3 and SiO_2 is in the surface reaction controlled regime thus avoiding homogeneous nucleation from the vapor phase. Reactant flow rates and fixturing was also altered to obtain coatings with uniform composition and thickness. Further optimization of the process resulted in CVD mullite coatings. Figure 5 shows a scanning electron micrograph of a typical mullite coating on a Si_3N_4 substrate. X-ray diffraction analysis confirms that the only crystalline phase present in the coating is mullite. Figure 6 shows the x-ray diffraction pattern. The coating is uniform, with a fine grained, equiaxed structure. There is some agglomeration of grains seen on the surface. This, however is not believed to have originated from the substrate surface, but instead is formed on the surface of the coating. The coating appears to be very dense. There were no cracks observed on the surface of the coating. Transmission electron microscopy was carried out to further analyze the mullite coatings. Figure 7 shows a brightfield transmission electron micrograph of a typical mullite coating. The coating starts with relatively small equiaxed grains near the substrate surface and then grows into large, mostly columnar grains. Figure 8 shows the electron diffraction pattern obtained on the coating. This further confirms the findings of the x-ray diffraction analysis.

When higher mole fractions of the chlorides was used in the experiment, there was a considerable amount of powder observed in the reactor. Figure 9 shows micrographs of typical powder observed in the chamber. The particle size is approximately 100 nm. The only crystalline phase found in the powder was mullite as confirmed by x-ray diffraction (Figure 10), though the powder had a composition different from that of mullite as shown by the EDS analysis in Figure 11. The excess Si in the powder is believed to be in the form of amorphous silica.

Further experimentation is necessary to correlate the microstructure of the coating to the process parameters. Samples were sent for initial corrosion resistance evaluation at ORNL. The coatings will be optimized through an iterative process of processing, characterization, and testing.

Status of Milestones

	Schedule	Status
Task 1: Optimize process parameters of codeposited mullite coatings to obtain desired structure/properties	6/95	On Schedule
Task 2: Coating Characterization	10/95	On Schedule
Task 3: Testing	11/95	On Schedule
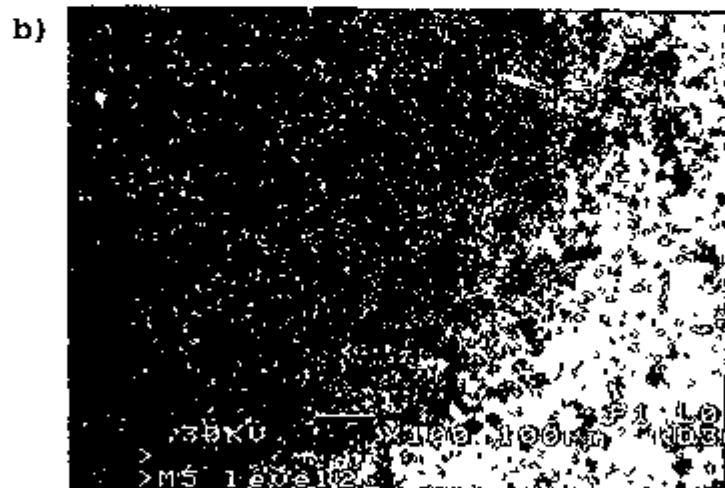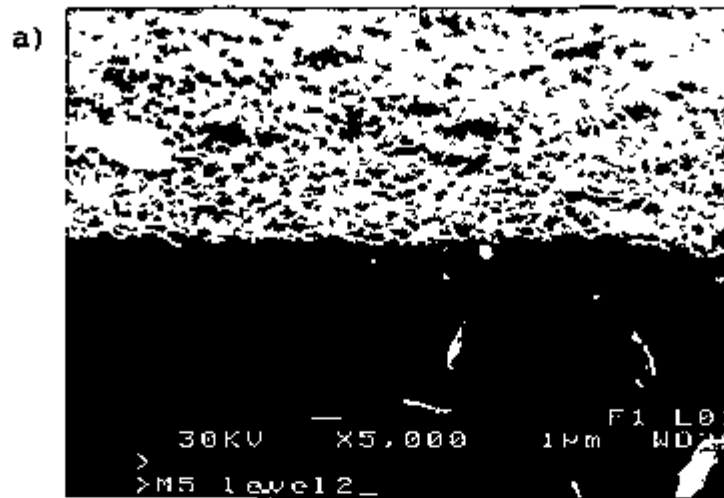
Figure 1: Al$_2$O$_3$-SiO$_2$ codeposited coating on SiC — a)cross-section, and b) surface
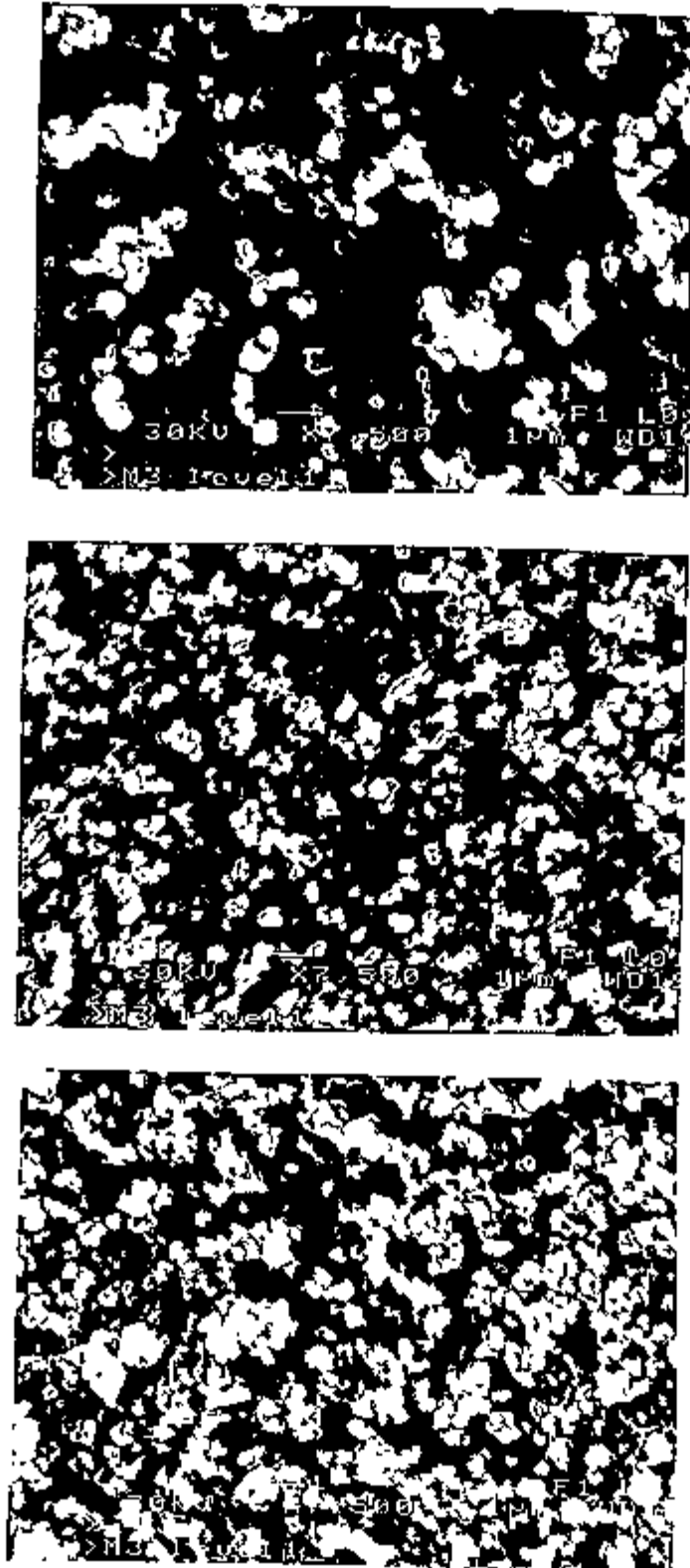
Figure 2: Surface morphology of the codeposited coating on SiC at different points in the coating.

10-Jun-1994 14:34:28

M3 on Ni level 1 center 5kv
vert= 5000 counts Disp= 1

Preset=   50 secs
Elapsed=   50 secs

Si

Al

S

ELEMENT & LINE	WEIGHT PERCENT	ATOMIC PERCENT*
Al KA	31.41	32.28
Si KA	68.59	67.72
Ni KA	0.00	0.00

← 0.000   Range= 10.230 keV   5.130 →
Integral 6 =   4121

Figure 3 a: Energy dipersion spectra on Al_2O_3-SiO_2 coating on a Ni substrate − Al:Si atomic ratio 1:2.1

10-Jun-1994 14:57:55

M3 on Ni level 1 corner2 5kv
vert= 5000 counts Disp= 1

Preset=   50 secs
Elapsed=   50 secs

Al

Si

ELEMENT & LINE	WEIGHT PERCENT	ATOMIC PERCENT*
Al KA	74.79	76.02
Si KA	23.90	23.34

← 0.000   Range= 10.230 keV   5.130 →
Integral 0 =   5953

Figure 3 b: Energy dipersion spectra on Al_2O_3-SiO_2 coating on a Ni substrate − Al:Si atomic ratio 3.25:1

```
12-Jun-1994 18:05:35

M3 level2 corner2   Element Search List    Preset=      50 secs
Vert=   20000 counts  Disp= 1              Elapsed=     50 secs


                                 ELEMENT    WEIGHT     ATOMIC
                                 & LINE     PERCENT    PERCENT*

                    Al           Al KA      81.20      81.81
                                 Si KA      18.80      18.19
                                 Ni KA       0.00       0.00


                    Si


    |1      |2      |3      |4      |5      |6      |7      |8      |9
 ←  0.000     Range=    20.460 keV                              9.460 →
                                      Integral 0  =          84217
```

Figure 3 c: Energy dipersion spectra on Al_2O_3-SiO_2 coating on a Ni substrate - Al:Si atomic ratio 4.5:1

Figure 4: EDS line scan of a Al_2O_3-SiO_2 coating on a Ni substrate
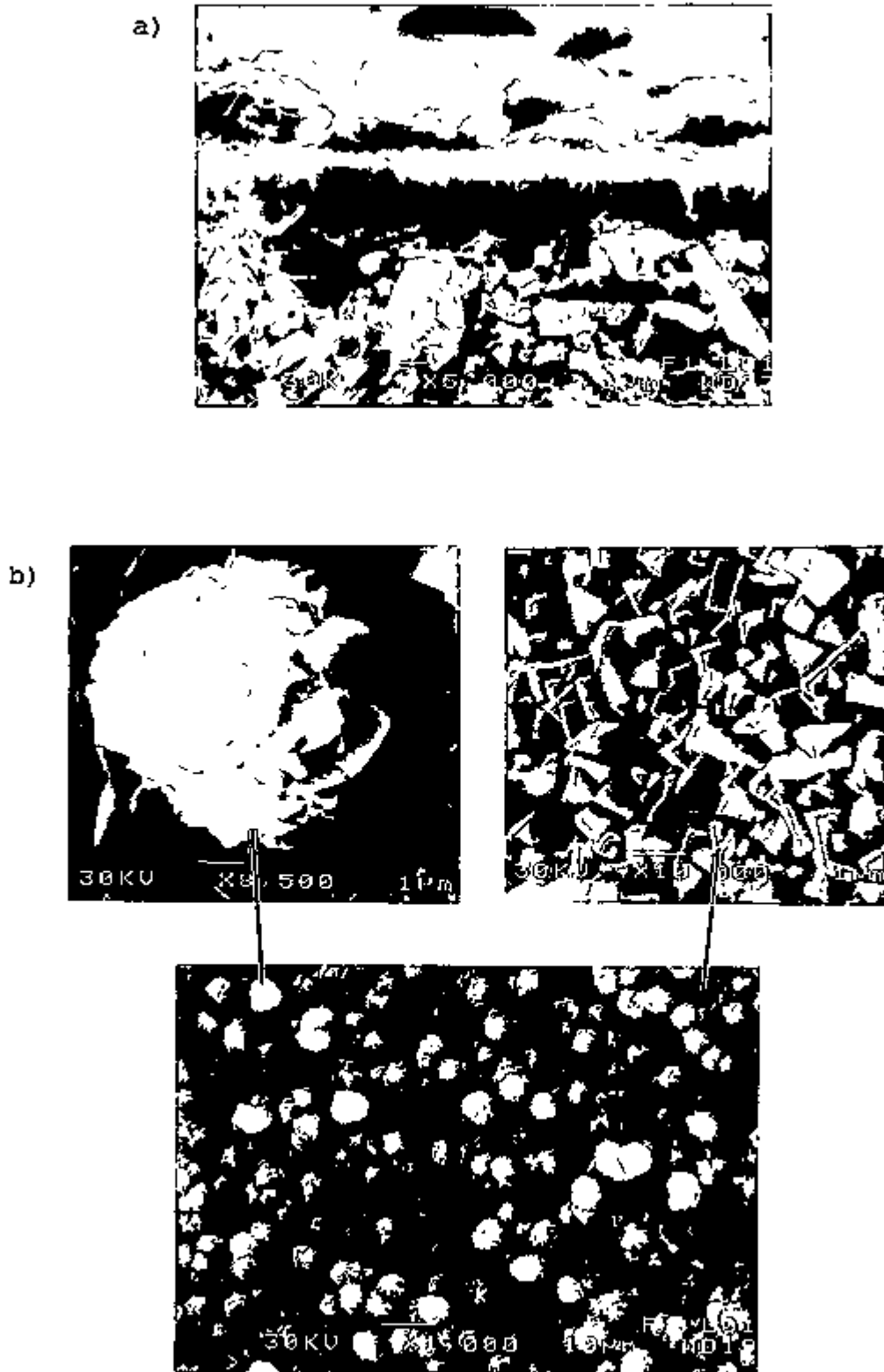
Figure 5: Scanning electron micrographs of a typical mullite coating on a Si_3N_4 substrate: a) cross-section, b) surface
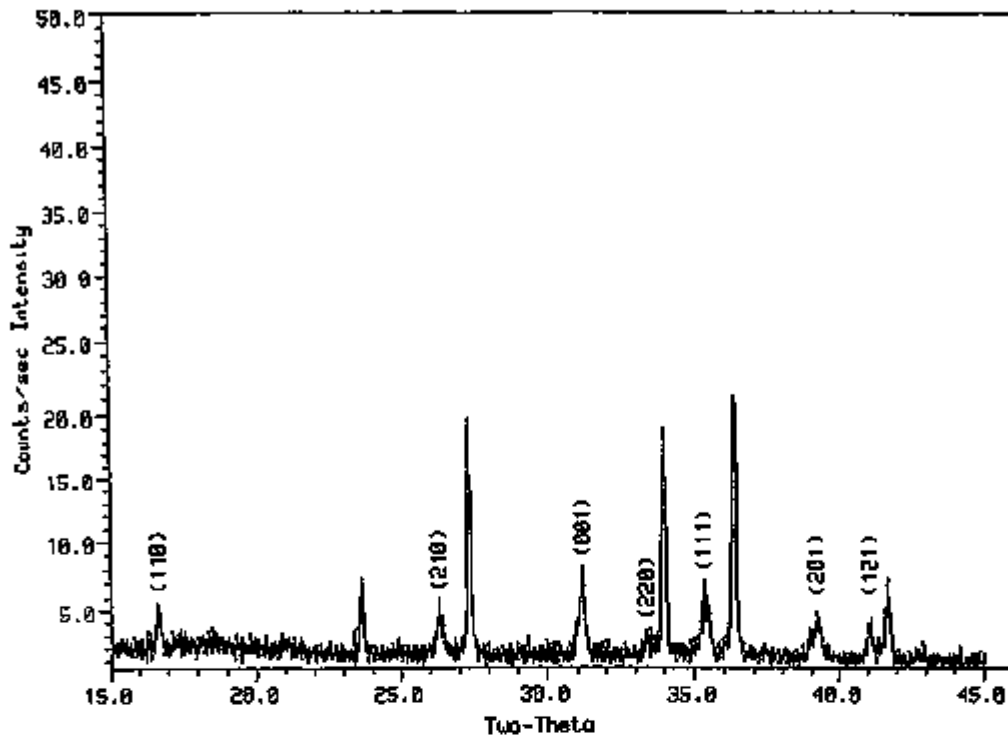
Figure 6: X-ray diffraction pattern of mullite coating on Si₃N₄
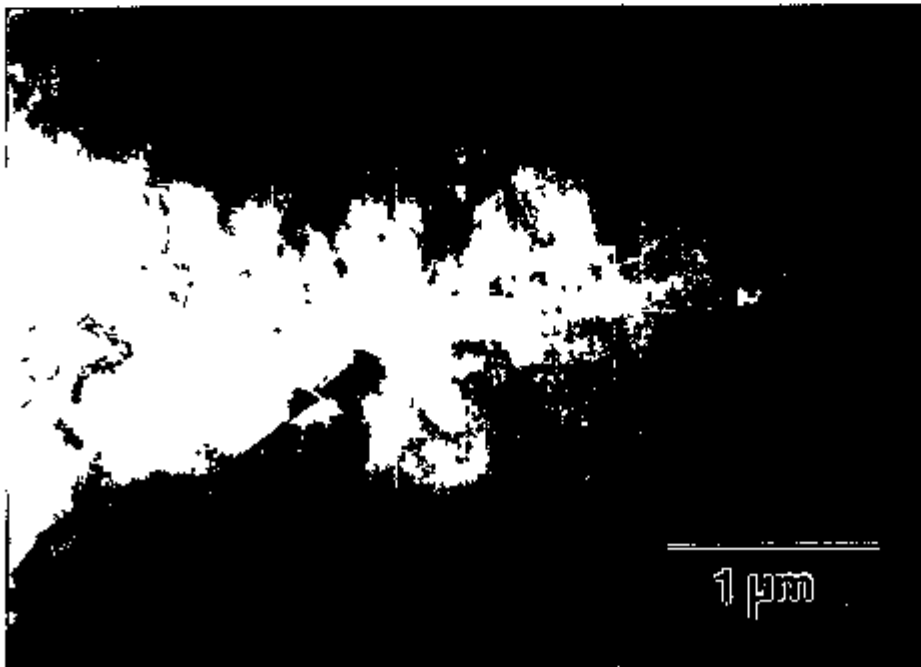
Figure 7: Brightfield transmission electron micrograph of CVD mullite coating on a Si₃N₄ substrate
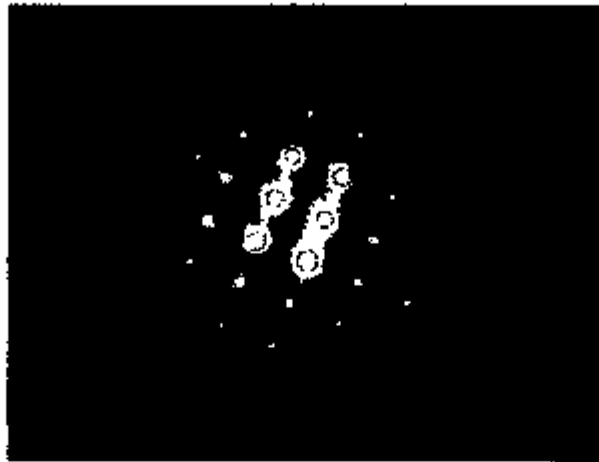
Figure 8: Electron diffraction pattern of a mullite coating grown via CVD
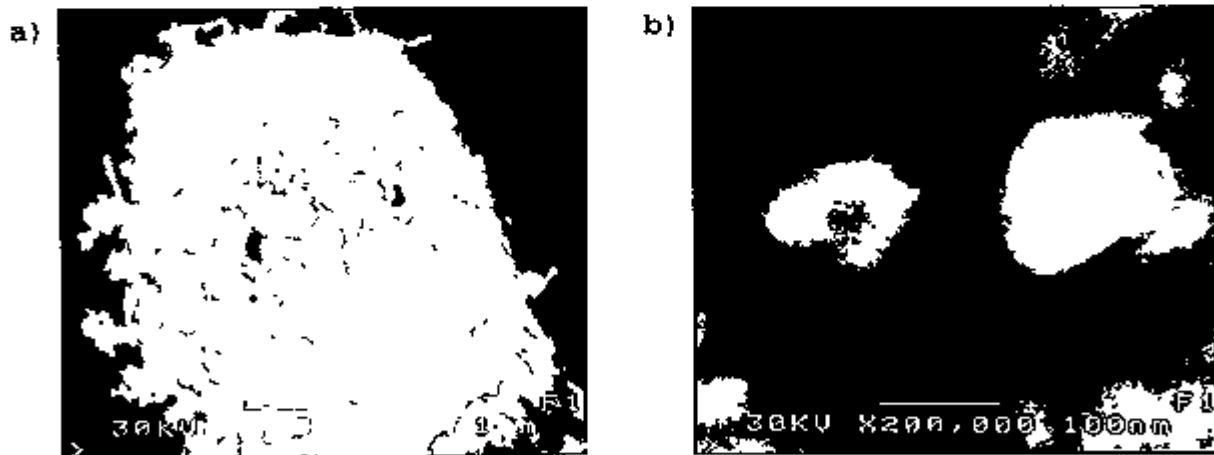
Figure 9: Scanning electron micrographs of mullite powder observed in the CVD reactor: a) agglomerate, b) particle
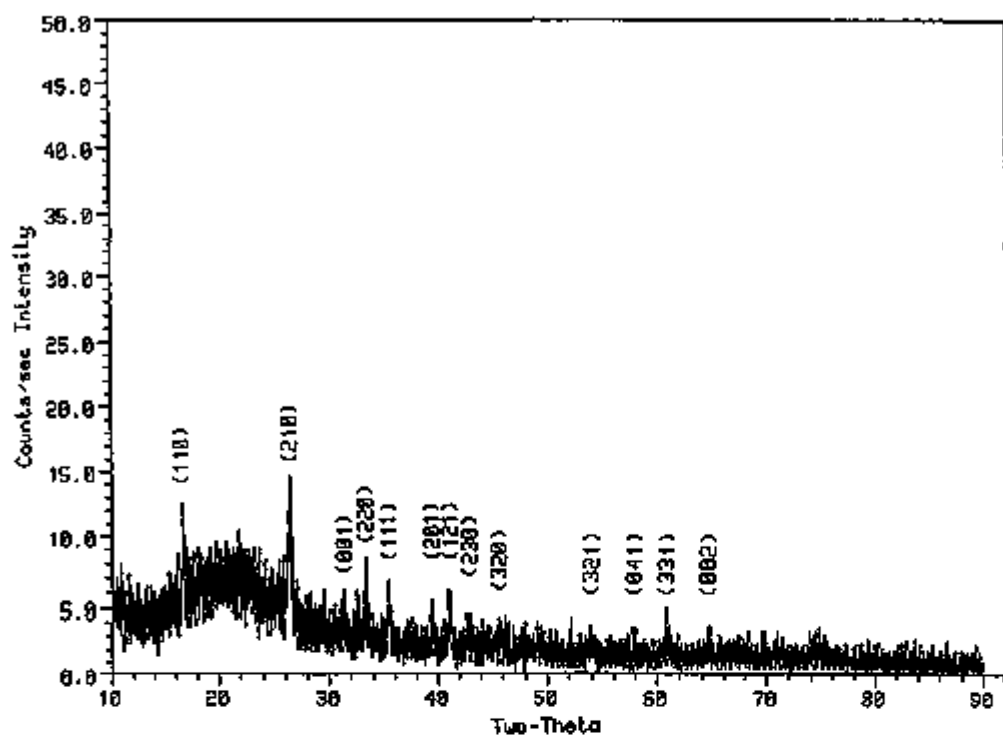
Figure 10: X-ray diffraction pattern of mullite powder
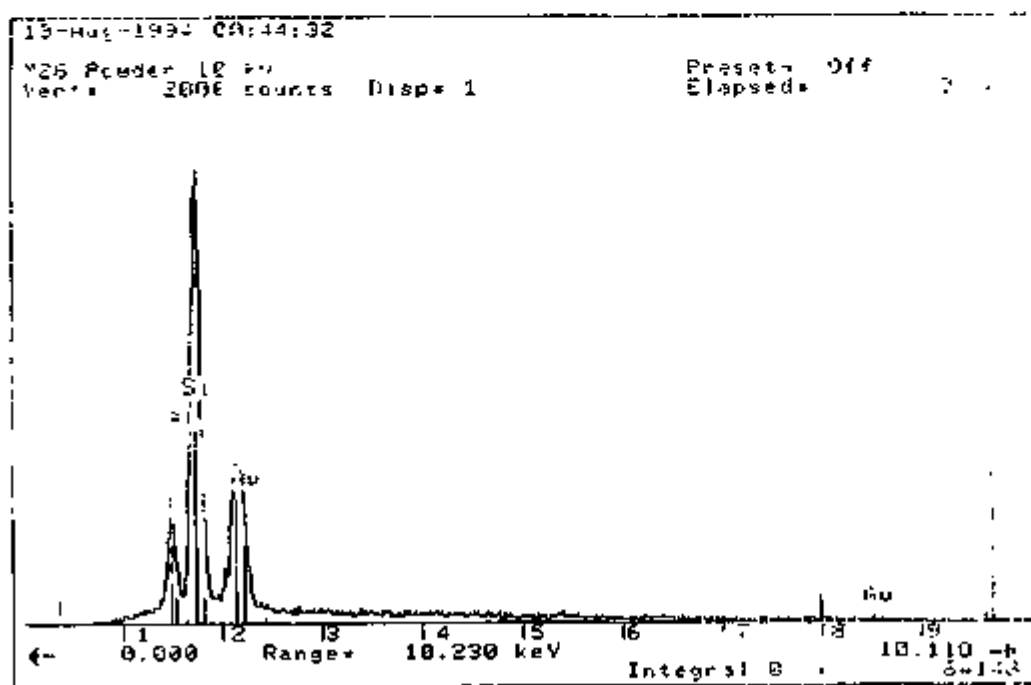
Figure 11: Energy dispersion spectrum analysis of CVD mullite powder

Thick Thermal Barrier Coating (TTBC) Systems for Low Heat Rejection Diesel Engines
M. B. Beardsley (Caterpillar Inc.)

Objective/Scope

The objective of this program is to advance the fundamental understanding of thick thermal barrier coating systems for application to low heat rejection diesel engine combustion chambers. Previous reviews of thermal barrier coating technology concluded that the current level of understanding of coating system behavior is inadequate and the lack of fundamental understanding may impeded the application of TBC's to diesel engines. (Ref. 1)

Areas of TTBC technology being examined in this program include powder characteristics and chemistry; bond coat composition; coating design, microstructure, and thickness as they affect properties, durability, and reliability; and TTBC "aging" effects (microstructural and property changes) under diesel engine operating conditions.

Technical Progress

TTBC POWDERS

Fifteen TTBC ceramic powders are being evaluated. These powders were selected to investigate the effects of different chemistries, different manufacturing methods, lot-to-lot variations, different suppliers and varying impurity levels, Table 1. The results of the powder characterization for chemistry, particle size distribution, surface area, crystallographic phases, apparent density and Hall flow have been report previously (Ref. 2). In the chemical analysis, it was found that the three spray dried and sintered materials to be used in the impurity study (lots 34850, 34992, and 34993) range from low levels of alumina and silica (34992), low alumina and mid-level silica (34850), to high alumina and silica (34993). The chemistries of the powders produced by different manufacturing methods (HOSP proprietary Metco process, spray dried, spray dried and sintered, fused and crushed, and sol gel materials) also show slightly differing ranges of impurities reflecting the different manufacturing methods.

The particle size distributions of the fifteen materials showed small variations in the mean and size ranges. The surface areas of the powders do show a wide range even for similarly manufactured powders (lots 34850, 34992, 34993 and lots 34243, 34302, 34547).

Each of the fifteen materials has been sprayed using 36 parameters selected by a design of experiments (DOE) to determine the effects of primary gas (Ar and N2), primary gas flow rate, voltage, arc current, powder feed rate, carrier gas flow rate, and spraying distance. The deposition efficiency, density, and thermal conductivity of the resulting coatings were measured. A coating with a high deposition efficiency and low thermal conductivity is

desired from an economic standpoint. An optimum combination of thermal conductivity and deposition efficiency was found for each lot of powder in follow-on experiments and deposition parameters were chosen for full characterization.

The resulting thermal conductivity and deposition efficiency for each of the powders sprayed with optimized parameters have been determined and are compared to the baseline coating (lot 34547, 8% yttria-zirconia, HOSP) in Figure 1. Several of the powders exhibit a lower thermal conductivity than the baseline coating with the 20% yttria-zirconia and spray dried 8% yttria-zirconia having both lower thermal conductivity and higher deposition efficiency. The higher thermal conductivity of materials such as the calcium titanate may be balanced by its higher deposition efficiency. Whether the higher deposition efficiency balances the higher thermal conductivity (which results in needing a thicker coating to achieve similar thermal conductance) is a component design question..

Strengths of the optimized coatings were determined using 4-point bending specimens. The tensile strength was determined using free standing coatings made by spraying onto mild steel substrates which were subsequently removed by chemical etching. The compressive strengths of the coatings were determined using composite specimens of ceramic coated onto stainless steel substrates, tested with the coating in compression and the steel in tension. The strength of the coating was determined from an elastic bi-material analysis of the resulting failure of the coating in compression. The strengths of the coatings compared to the baseline coating are shown in Figure 2.

Although initial comparison of the materials would appear to be straight forward from these results, the results of aging tests of the materials will be necessary to insure that these trends in properties remain after long term exposure to a diesel environment. Some comparisons can be made, such as the comparison between for lot-to-lot variation.

The three lots of 8% yttria-zirconia HOSP materials have similar thermal conductivity, deposition efficiency, and strengths for the parameters selected (all three lots were sprayed with the same parameters). In order to achieve this, the parameters were selected for robustness.. The three lots of material were sprayed with four sets of parameters and the thermal conductivity and deposition parameters measured. In two of the three sets, the deposition of the lots A and B were one third of the deposition of the baseline material. The spray parameters for any given chemistry and specified particle size should be chosen based on the robustness of the parameters over a range of lots rather than on the results from one or two lots of the material.

An axial fatigue test to determine the high cycle fatigue behavior of TTBCs has been developed at the University of Illinois (Ref. 4). A fatigue test apparatus has been designed and initial test work performed which demonstrates the ability to provide a routine method of axial testing of coatings. The test fixture replaces the normal load frame and fixtures used to transmit the hydraulic oil loading to the sample with the TTBC specimen itself.

The TTBC specimen is a composite metal/coating with stainless steel ends. The coating is sprayed onto a mild steel center tube section onto which the stainless steel ends are press fit. The specimen is then machined. After machining, the specimen is placed in an acid bath which etches the mild steel away leaving the TTBC attached to the stainless steel ends. Plugs are then installed in the ends and the composite specimen is loaded in the test fixture where the hydraulic oil pressurizes each end to apply the load. Since oil transmits the load, bending loads are minimized. This test fixture as been modified to allow piston ends to be attached to the specimen which allows tensile loading as well as compressive loading of the specimen.

A TTBC coating previously tested at room temperature in compression using this method resulted in a stress-life curve as shown in Figure 3. This data matches previous fatigue data for this material obtained in 4-point bending, but long life data was obtained with this test method (Ref. 3). Tensile data for this coating has also been generated using the modified axial test fixture resulting in a stress-life curve as shown in Figure 4.

In addition to the room temperature data, specimens have recently been tested at 800 C with surprising results. At high temperature, the TTBC exhibits much higher fatigue strength, Figure 5. This behavior is currently thought to be due to sintering of the splat structure of the TTBC at the high temperature (Ref. 4).

Testing of the TTBC using tension/ compression cycling has been conducted using the modified test fixture. The goal of this work was to investigate the failure mechanisms of the coating and to determine if tensile and compressive fatigue damage would interact to influence the resulting life of the coating. Coating samples were run with various mean compressive loads and constant tensile loading approximately equal to 90% of the tensile strength of the coating. As shown in Figure 6, there is no interaction of the tensile and compressive load. The material fails in tension at the life predicted by the tensile curve. This indicates that there are two differing failure mechanisms for the TTBC in tension and compression.

Status of Milestones

All milestones are on schedule.

Publications

None

References

1. R. A. Miller, "Assessment of Fundamental Materials Needs for Thick Thermal Barrier Coatings (TTBC's) for Truck Diesel Engines", DOE/NASA/21749-1, NASA TM-103130, May 1990.

2. M. B. Beardsley, "Thick Thermal Barrier Coatings", Proceedings of the Annual Automotive Technology Development Contractors' Coordination Meeting 1993, pg. 213.

3. R. C. Brink, "Material Property Evaluation of Thick Thermal Barrier Coating Systems", 89-ICD-13, The American Society of Mechanical Engineers, 1989.

4. K. F. Wesling, D. F. Socie, and M. B. Beardsley, "Fatigue of Thick Thermal Barrier Coatings", J. Am. Ceram. Soc., 77[7], 1994, pg. 1863-1868.

Table 1. TTBC Powders Selected

MATERIAL	MFG METHOD	SUPPLIER	LOT NO
8% Yttria-Zirconia	HOSP	METCO	34847-1
20% Yttria-Zirconia	Spray Dried	METCO	34106-2
24% Ceria-Zirconia	HOSP	METCO	34209-3
Calcium Titanate	Spray Dried	METCO	34849-4
Mullite	Fused & Crushed	METCO	34542-5

DIFFERENT MANUFACTURING METHODS

8% Yttria-Zirconia	Sprayed Dried	METCO	32678-6
8% Yttria-Zirconia	Spray Dried & Sintered	METCO	34850-7
8% Yttria-Zirconia	Fused & Crushed	Norton	291-8
8% Yttria-Zirconia	SOL GEL	METCO	34440-9

DIFFERENT SUPPLIERS

8% Yttria-Zirconia	Sprayed/Compact/Sintered	Zircoa	
8% Yttria-Zirconia	Spray Dried & Sintered	METCO	3803A89011

LOT-TO-LOT VARIATIONS

8% Yttria-Zirconia	HOSP	METCO	
8% Yttria-Zirconia	HOSP	METCO	34193-13

IMPURITIES

8% Yttria-Zirconia	Spray Dried & Sintered	METCO	34992-14
8% Yttria-Zirconia	Spray Dried & Sintered	METCO	34993-15

COMPARISON OF T.C. & % DE
% DIFFERENTIAL
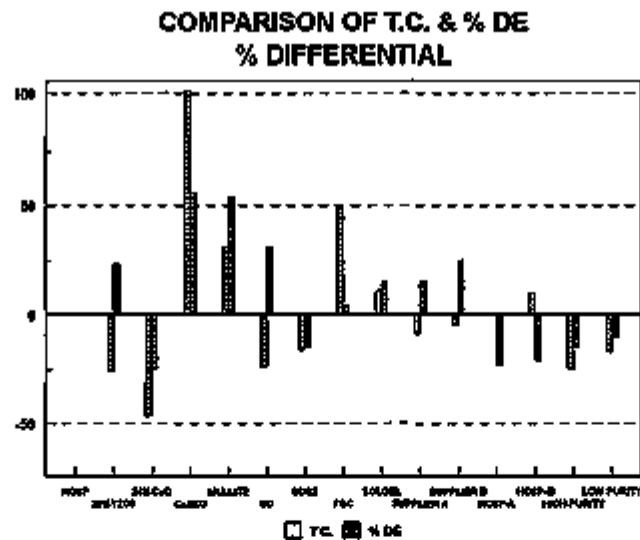
Figure 1. Comparison of the thermal conductivity and deposition efficiency of the coatings to the baseline 8% yttria-zirconia, HOSP material.

COMPARISON OF STRENGTH TO BASELINE
% DIFFERENTIAL
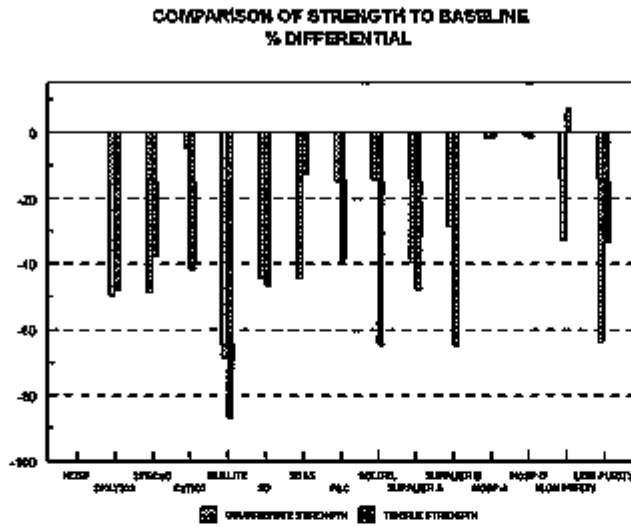
Figure 2. Comparison of the tensile and compressive strengths of the coatings to the baseline 8% yttria-zirconia, HOSP material.

ROOM TEMPERATURE AXIAL FATIGUE
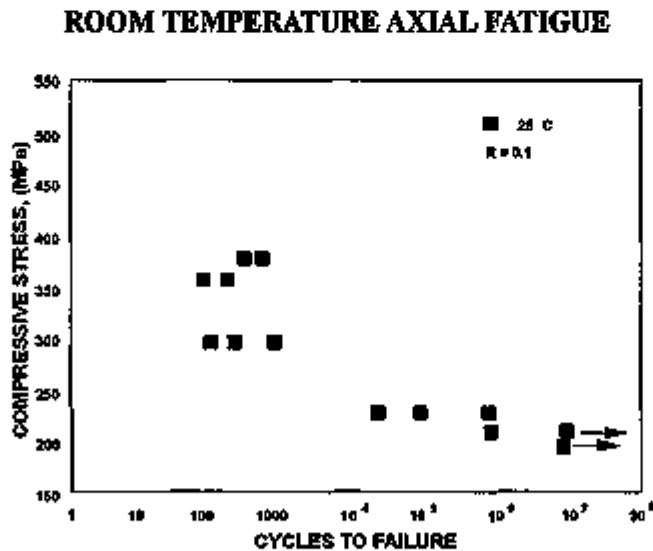
Figure 3. Room temperature compressive fatigue data for TTBC showing long life data.
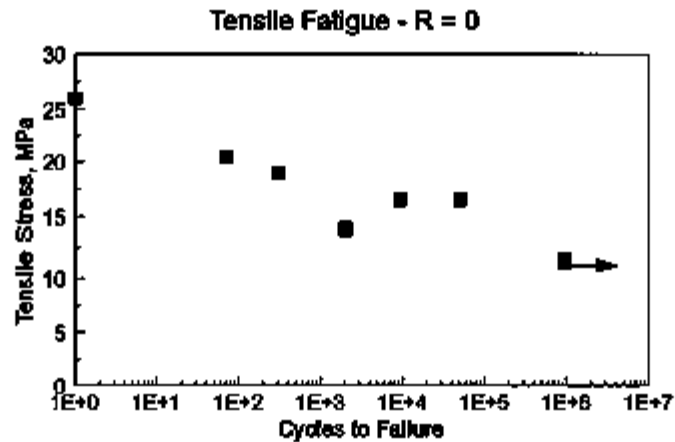
Tensile Fatigue - R = 0

Figure 4. Room temperature tensile fatigue data for TTBC

HIGH TEMPERATURE FATIGUE BEHAVIOR
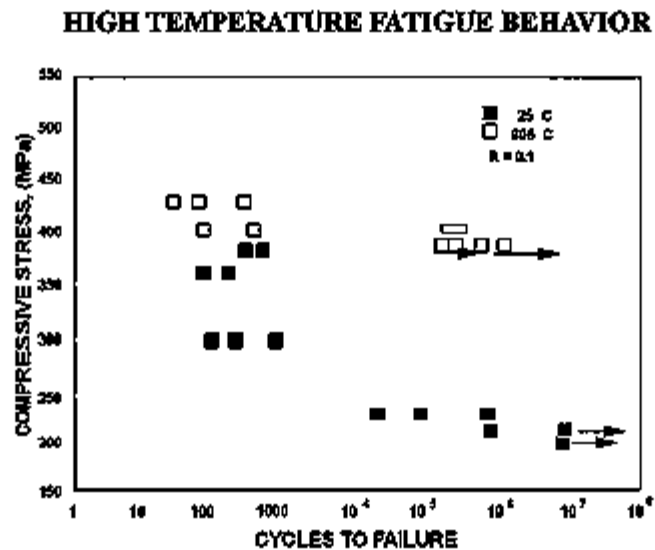
Figure 5. Compressive fatigue data for TTBC showing strengthening of the TTBC at the 800 C test temperature thought to be due to sintering of the splat structure of the TTBC.
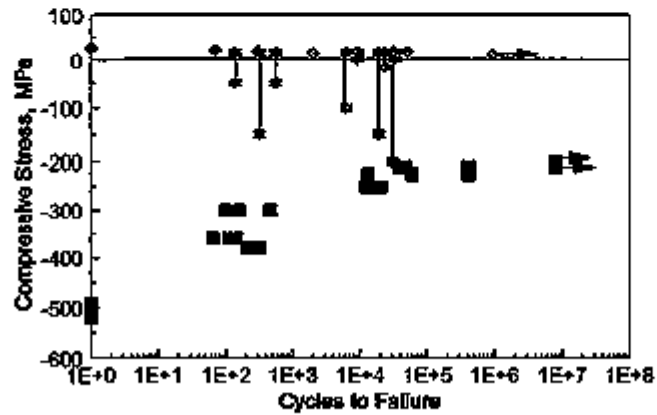
Figure 6. Tensile (diamonds), compressive (squares), and tensile/compressive (stars) fatigue data for TTBC showing that the failure occurs at the tensile fatigue limit independent of the applied compressive stress.

1.4 JOINING

1.4.1 Ceramic-Metals Joints

Joining of Ceramics for Heat Engine Applications
M. L. Santella (Oak Ridge National Laboratory)

Objective/Scope

The objective of this task is to develop strong, reliable joints containing ceramic components for applications in advanced heat engines. The overall emphasis of this task is on studying the brazing characteristics of silicon nitride and silicon carbide. The techniques of direct brazing as well as vapor coating ceramics to circumvent wetting problems are being applied to these materials. The planned activities during FY 1994 will include continuing the study of both the high-temperature brazing of silicon nitride and the mechanical behavior of braze joints. The work will encompass further evaluation and application of an analysis package and approach developed specifically for silicon nitride-to-metal braze joints and evaluating nonmetallic bonding materials for joining silicon nitride.

Technical Highlights

Ceramic-to-metal brazing: Finite element analysis of a poppet valve configured with a ceramic head and a metal stem was completed using properties for several combinations of ceramics and metals. This work showed that the most effective way to control residual stresses in these ceramic-to-metal joints is to minimize the expansion mismatch between the structural materials used.

An illustration of the true scale deformation that results from the property mismatches is given in Fig. 1 for the case of an Incoloy 909 stem/Si_3N_4 head and in Fig. 2 for the case of a Ti stem/Si_3N_4 head. These figures show the same general area at a similar magnification factor. In both cases, the left boundary of the stem and braze layer was aligned with the Si_3N_4 boundary at 830°C. The displacement of these boundaries to the right, relative to the Si_3N_4 boundary, occurs because of the greater contraction of the metals during cooling to ambient temperature. Figures 1 and 2 show that the braze layers experience severe deformation. The large relative displacements of the metals produce large residual stresses in the Si_3N_4. For the Incoloy stem, the analysis predicts that a large volume of the Si_3N_4 experiences residual stresses (maximum principal stress) above 200 MPa with localized regions reaching values above 350 MPa. The volume of stressed material is similar for the Ti stem, but the maximum residual stress value predicted is near 400 MPa. The higher residual stress found for the Ti case results, primarily, from its slightly higher thermal expansion coefficient compared to that of Incoloy 909; see Table 1.

No relatively common, low-cost engineering alloys have thermal expansion coefficients in the range of Si_3N_4. Feasible structural metals which are nearest are alloys of

ORNL-DWG 95-5886

Ceramic

True scale deformation

Braze

Stem
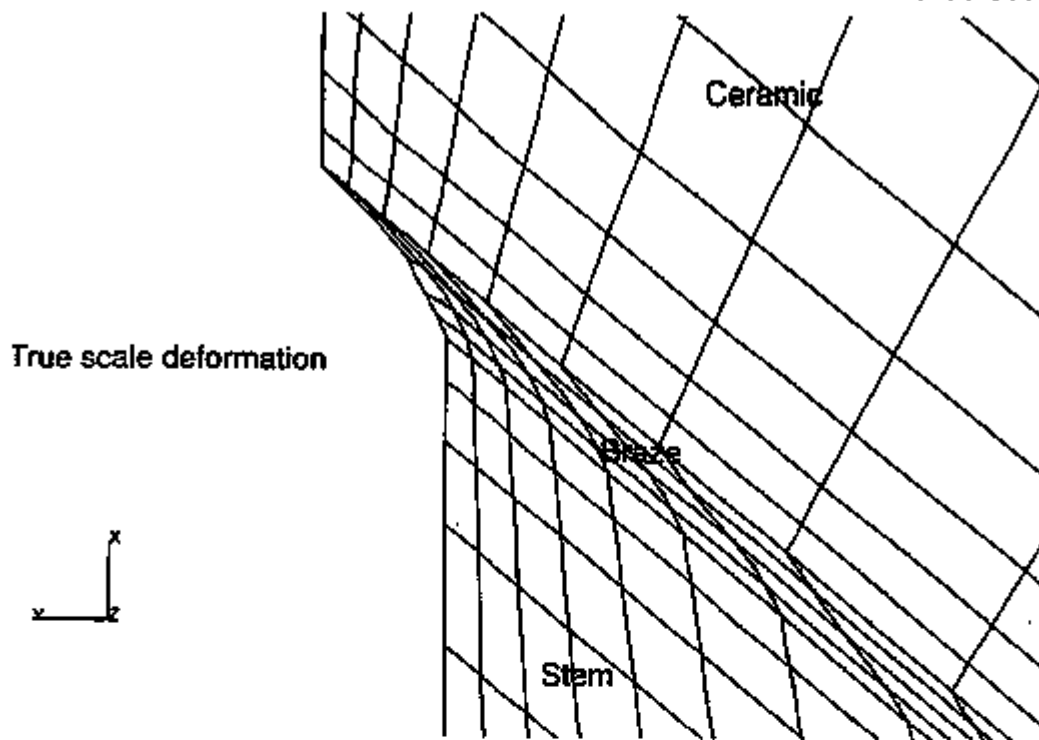
Fig. 1. True scale deformation illustrating relative displacements produced during cooling of Si$_3$N$_4$-to-Incoloy 909 braze joint from 830°C to ambient temperature.

ORNL-DWG 95-5887

Ti-SiN

True Scale Deformation
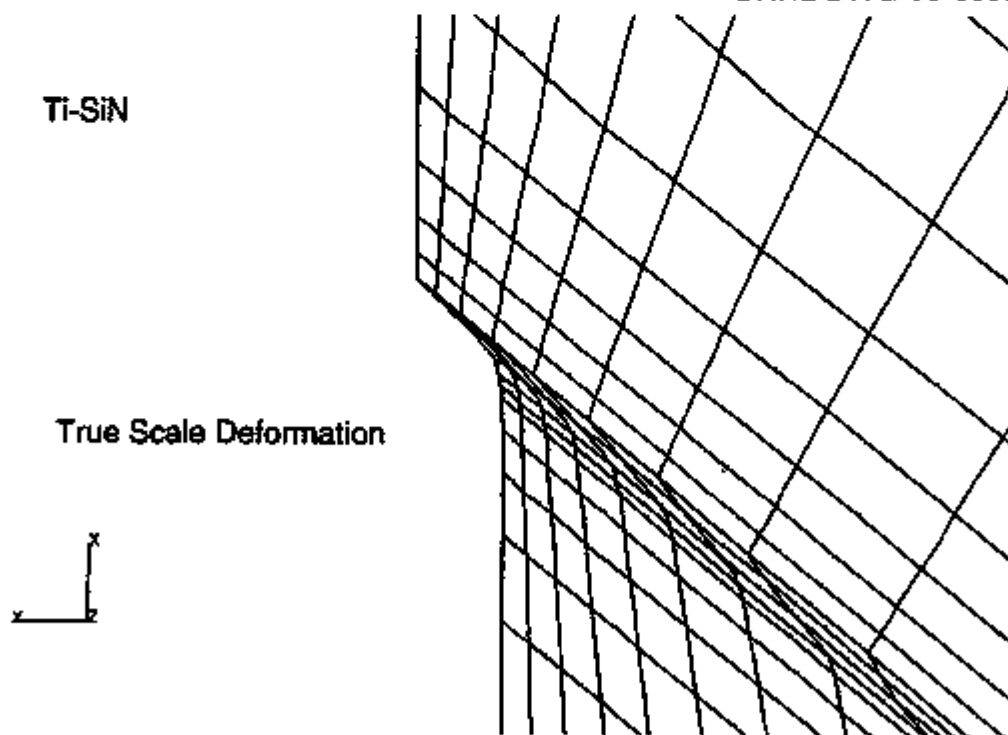
Fig. 2. True scale deformation illustrating relative displacements produced during cooling of Si$_3$N$_4$-to-Ti alloy braze joint from 830°C to ambient temperature.

Table 1. Thermal expanison coefficients for materials
used for analysis of ceramic-metal joints

	α_i (ppm/°C) at temperature								
Alloy	25	100	200	300	400	500	600	700	800
Incoloy	8.0	8.0	8.0	7.5	7.5	8.3	9.5	10.5	12.0
near-α Ti	8.9	9.5	10.2	10.7	11.1	11.4	11.6	11.6	11.6
Si_3N_4	0.8	1.6	2.4	2.9	3.0	3.2	3.3	3.4	3.6
PS-ZrO_2	10.6	10.6	10.6	10.6	10.6	10.6	10.6	10.6	10.6

tungsten or molybdenum, but they are undesirable because of their density, cost, and mechanical properties. Metal-matrix composites offer some potential for better matching of thermal expansion properties, but they have several disadvantages including limited availability and relatively high cost. Nevertheless, the option of using a refractory alloy for the stem is still under consideration for a proof-of-concept demonstration. Redesigning the valve to improve the residual stress situation for Si_3N_4 is another possible approach which could be pursued at a later time.

The approach being followed presently is based on selecting a ceramic and metal which have a relatively good match of thermal expansion properties. The materials selected are partially-stabilized ZrO_2 and Ti. The thermal expansion coefficient of PS-ZrO_2 is linear with temperature up to about 1050°C and is also given in Table 1. An illustration of the true scale deformation that results when the material properties of ZrO_2 and Ti are applied to the finite element model of the poppet valve is shown in Fig. 3. In this case, very little relative displacement between components is predicted. This results in residual stresses that are relatively low in magnitude and confined to relatively small volumes in the ZrO_2. The analysis results indicate that the probability of making a useable valve of this design from these materials is reasonably high.

Based on the latest analysis results, both MgO- and Y_2O_3-stabilized ZrO_2 were acquired from Coors, and an alloy used for Ti valves was also obtained. Trials to establish braze processing were begun using a commercially available filler metal known to bond well to oxide ceramics. The filler metal used in initial trials was Ticusil® (WESGO: 68.8 Ag-26.7 Cu-4.5 Ti wt %) which has a liquidus temperature of 850°C. Surprisingly, this alloy did not produce acceptable ZrO_2-Ti joints, either for the Ti alloy or for commercially pure Ti. Additional experiments showed that good joints of the ZrO_2 bonded to itself could be made with Ticusil, indicating that the difficulty of obtaining acceptable ZrO_2-Ti joints was a result of reaction of the filler metal with the Ti. The evaluation of other filler metals is continuing.

ORNL-DWG 95-5888

Ti-Zirconia

True Scale Deformation
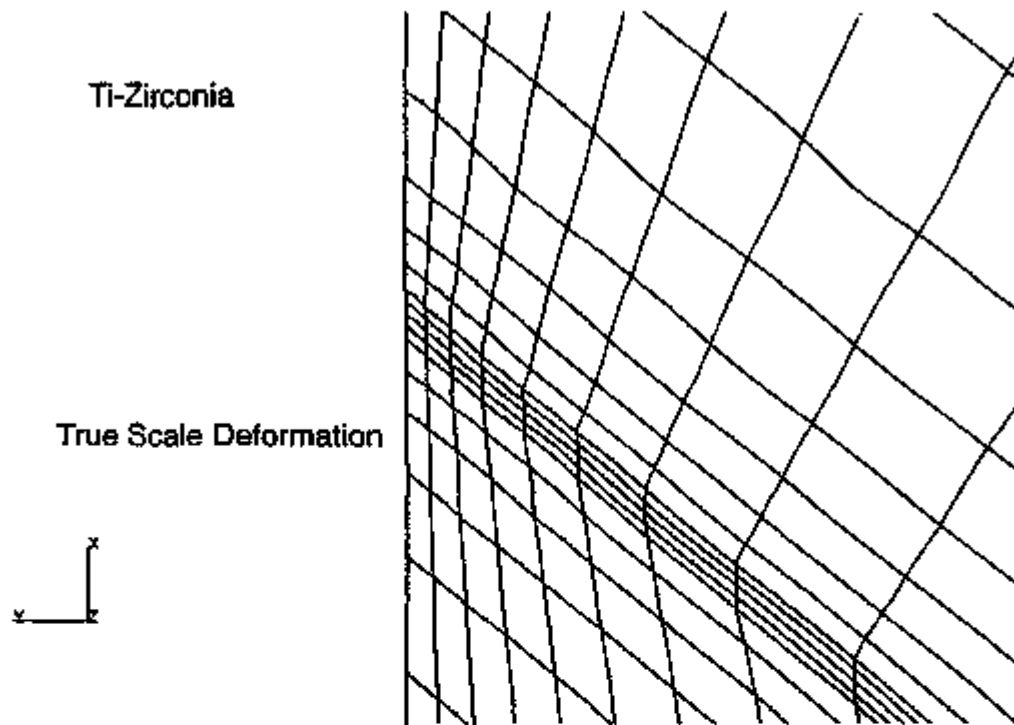
Fig. 3. True scale deformation illustrating relative displacements produced during cooling of PS-ZrO$_2$-Ti braze joint from 830°C to ambient temperature.

Status of Milestones

On schedule.

Publications

A talk entitled, "Si$_3$N$_4$-Metal Joining: Review of Work Sponsored by the Ceramic Technology Project," was presented at a bimonthly ATTAP coordination meeting held at Allison Engine Company, Indianapolis, Ind., on September 29, 1994.

Unpublished work

None.

1.5 CERAMIC MACHINING

Cost-Effective Ceramic Machining
P. J. Blau (Oak Ridge National Laboratory)

Objective/Scope

The objective of this effort is to develop, in conjunction with U.S. Industry, advanced technologies and the associated scientific and economic concepts necessary to reduce the costs associated with the machining of structural ceramics, especially as related to the use of these materials in energy-efficient, low-emissions transportation systems. This effort consists of subcontracts to industry and in-house research at ORNL, Argonne National Laboratory, and the National Institute of Standards and Technology. Progress reports for other than the ORNL in-house research portion of this work may be found elsewhere in this publication. The five subtasks in this effort are:

1. Environmental Safety and Health Aspects of Ceramic Machining
2. Technology Assessment and Future Needs
3. Advanced Machining Methods Development
4. Ceramic Machinability and Related Performance
5. Structure and Surface Quality of Machined Ceramics

ORNL in-house activities are aimed at two technical areas: (1) investigating the effects of machining practices on the durability of ceramics for valve and valve seat applications and (2) understanding and characterizing the detailed nature of machining-induced surface and sub-surface damage and their evolution in advanced ceramic materials using a range of analytical tools. The latter includes such methods as non-contact surface profiling, atomic force microscopy of ground surfaces, and scanning acoustic microscopy to detect subsurface flaws.

Technical Highlights

a. **Study of Electrolytic In-Process Wheel Dressing.** Dr. B. P. Bandyopadhyay, University of North Dakota, conducted a 3-month study of electrolytic in-process dressing (ELID) methods for grinding ceramics on a visit to the laboratory of Prof. Ohmuri of the Institute of Physical and Chemical Research (RIKEN), Tokyo, Japan. Dr. Ohmuri is an inventor and developer of the ELID technique which provides dressing of cast-iron fiber-bonded (CIFB) superabrasive grinding wheels during the actual machining operation. Two types of silicon nitride specimens were ground: SRBSN (Eaton Corporation materials) and a Kyocera silicon nitride material. The effects of speed, feed-rate, and diamond concentration were investigated. A final report has been submitted and is being reviewed prior to its publication as an ORNL technical report, probably by early 1995.

b. **Workshop on Cost-Effective Machining of Ceramics.** A workshop on Cost-Effective Machining of Ceramics was organized and conducted jointly by the

Defense Programs Centers for Manufacturing Technology, the High-Temperature Materials Laboratory Program, and the Cost-Effective Ceramic Machining effort. The 3-day workshop was conducted at the Y-12 Plant and ORNL on August 23-25, 1994. There were over 60 attendees. The first day consisted of presentations by industry participants in Defense Programs Cooperative Research and Development Agreements (CRADAs). These included: Keith Fisher, Coors Electronics Products Group; Nabil Hakim, Detroit Diesel Corporation; and John Kohls, Cincinnati Milacron. The second day consisted of the following talks by participants in the Cost-Effective Ceramic Machining effort:

Development of a Next -Generation Grinding Wheel
R. H. Licht, Norton Advanced Ceramics Company

Chemically-Assisted Grinding of Ceramics
S. M. Hsu, National Institute of Standards and Technology

Grinding Optimization Project at NIST
L. K. Ives, National Institute of Standards and Technology

High-Speed, Low-Damage Grinding of Silicon Nitride
J. A. Kovach, Eaton Corporation

Development of a Grindability Test for Ceramics
K. Costello, Chand Kare Technical Ceramics

Subsurface Grinding Flaw Detection by Laser Scattering
S. Steckenrider, Argonne National Laboratory

Investigation of Ceramic Surface Structure and Performance
P. J. Blau, Oak Ridge National Laboratory

The third day consisted of a tour and demonstrations of ceramic machining-related capabilities at the High-Temperature Materials Laboratory (HTML).

        c. **Phase II of High-Speed, Low-Damage (HSLD) Grinding.** The success of the Eaton Corporation/University of Massachusetts feasibility study of the use of high surface speeds to grind ceramics (Phase I) has led to a follow-on effort whose purpose is to develop the means by which the HSLD method can be effectively implemented in a production line environment. In addition to the engineering issues, technical issues will involve development of a deeper understanding of the partitioning of the heat between the workpiece and the grinding wheel. Studies at the University of Massachusetts will supplement the Eaton Corporation implementation work to provide a balanced effort which links basic concepts with the practical problems of ceramic manufacturing.

Future Plans

A new request for proposals (RFP) for a competitive subcontract on grinding wheel technology has been prepared and an evaluation team assembled to evaluate proposals. The RFP will be released in early November 1994.

The Next-Generation Grinding Wheel Project will be concluding with the delivery of six 8-in.-diam wheels to ORNL for evaluation. A few of the wheels will be evaluated at the HTML, and some will be sent to interested companies for additional third-party testing on silicon nitride ceramics. If the wheels prove to be better than existing commercial grinding wheels, a follow-on program to scaleup and further evaluate the wheels on cylindrical grinders will be considered.

Status of Milestones

On schedule.

Communications/Visitors/Travel

A host of visitors from industry, academia, and other government laboratories attended the workshop on "Cost-Effective Grinding of Ceramics" held August 23-25, 1994, at the Y-12 Plant, Oak Ridge, Tenn.

P. J. Blau attended the American Ceramic Society Basic Science Division Fall Meeting, Louisville, Ky., September 25-28, 1994, and presented a paper entitled "Defining and Measuring the Grindability of Structural Ceramics" in the session on Critical Standards for Ceramic Manufacturing.

Problems encountered

None.

Publications/Presentations

1. S. Srinivasan, P. J. Blau, and J. L. Bjerke, "Effect of Machining Residual Stresses on the Repetitive Impact Behavior of Silicon Nitride," accepted for publication by *J. Mater. Res.* (1994).

2. P. J. Blau and W. A. Simpson, Jr., "Applications of Scanning Acoustic Microscopy in Analyzing Wear and Single Point Abrasion Damage," accepted for publication by *Wear* (1994).

3. J. A. Kovach and S. Malkin, High-Speed, Low-Damage Grinding of Advanced Ceramics, Phase I - Final Report, to be published as an ORNL tech. report.

4. B. P. Bandyopadhyay, <u>Highly Efficient and Precision Grinding of Ceramic Parts by Electrolytic in Process Dressing (ELID) Grinding</u>, final report, in review for later publication as an ORNL tech. report, 1994.

5. P. J. Blau, "Defining and Measuring the Grindability of Structural Ceramics," invited presentation at the American Ceramic Society Basic Science Division Fall Meeting, Louisville, Ky., September 25-28, 1994.

6. <u>Proceedings of the Cost-Effective Machining of Ceramics Workshop</u>, to be published as a Y-12 report in fall 1994 (summary of presentations from the August 1994 workshop).

Innovative Grinding Wheel Design
for Cost-Effective Machining of Advanced Ceramics

R.H. Licht, S. Ramanath, M. Simpson and E. Lilley (Norton Company)

Objective/Scope

The objectives of the Phase I program are: to define requirements, design, develop and evaluate a next-generation grinding wheel for cost-effective cylindrical grinding of advanced ceramics.

Ceramic machining, predominantly diamond grinding, is a major cost factor in advanced ceramics manufacturing. The abrasive wheel performance significantly influences the grinding costs. Additionally, the quality of the grinding operation greatly affects ceramic surface integrity, tolerance and manufacturing yield.

This program is a cooperative effort involving three Norton groups. The Norton Company Superabrasives Division will design and develop a novel metal bond system, and perform the wheel tests at the Norton World Grinding Technology Center. Norton Diamond Film Division will conduct a parallel and complementary research and development effort that incorporates a chemical vapor deposition (CVD) diamond film wheel system. The Northboro Research and Development Center (NRDC) will supply ceramic specimens for the grinding tests, and evaluate surface integrity in the ground ceramics.

The parallel path approach will be carried out in Task 1, Analysis of Required Grinding Wheel Characteristics. This task will involve the design of the bond with respect to mechanical and thermal characteristics, and the selection of the diamond grit. Task 1 will culminate in a small-wheel screening test involving controlled feed plunge grinding of sialon test disks.

Task 2, Design and Prototype Development, will down-select to a few wheel types for further design and optimization. Eight-inch (203 mm) diameter prototype wheels will be tested in a cylindrical mode, grinding ceramic rod specimens similar in geometry to valve stems. Grinding wheel performance will be assessed on three types of ceramic specimens: NC-520 sialon, NCX-5102 HIP'ed silicon nitride and AZ67H zirconia toughened alumina. Wheels will be evaluated for grinding parameters such as stock removal rate, wheel wear, G ratio, and grinding power. Additionally, the grinding wheel influence on ceramic surface integrity characteristics such as surface finish, damage and retained strength will be evaluated.

Technical Progress

TASK 1: Analysis of Grinding Wheel Requirements

Status Overview - Task 1 was planned to include a small wheel screening test utilizing a parallel path approach: Superabrasive metal-type bond and CVD diamond wheel. The higher risk CVD approach was to be a feasibility study, and was not planned for continuation into Task 2, Design and Prototype Development. In this period, the Task 1 design, screening test and data analysis, were completed for both approaches, and Task 2 has been initiated for the Superabrasive approach. The initial CVD wheel test in Task 1 led to some wheel redesign described under Task 1.2, which is in progress.

Task 1.1: Requirements Definition and Experimental Design

Completed and reported last period.

Task 1.2: Screening Test Wheel Manufacturing

Superabrasive Wheels -- A total of approximately 70 superabrasive wheels were manufactured for Task 1 in experimental metal bond systems. The experimental variables included: level of bond porosity, type of pore inducers, bond composition, diamond type, diamond concentration, wheel processing methods and processing conditions. The wheel dimensions were 76 mm X 13 mm thick X 22 mm hole (3" X 0.5" X 0.875").

Approximately 45 of the wheels were tested in the grinding test described in Task 1.3. We encountered manufacturing problems during the fabrication of some of the wheel variables and these out of specification wheels were not tested.

CVD Diamond Wheels - In this period, we assembled and tested our first prototype CVD diamond wheel. The wheel design and assembly is described below.

The wheel design consists of abrasive elements arranged azimuthally and axially around the periphery of a 75 mm diameter grinding wheel. Axial spacing of each element was approximately 50 μm and the total assembly produced a wheel approximately 8 mm thick. Figure 1 shows a view of one of the elements. It was photochemically machined from 30 μm molybdenum sheet. The elements were held in place by an epoxy impregnation after the wheel was assembled. A detailed view of the Mo teeth on one element is shown in Figure 2. The teeth were each 25 μm wide at the OD with a slight taper, and coated on all surfaces with approximately 10 μm thick CVD diamond using a dc plasma torch. Thus, abrasive elements of approximately 45-50 μm cross sections were created, simulating a 320 grit abrasive.

The CVD diamond wheel design was modified after the initial screening test (reported under Task 1.3). During this period the design work for a modified substrate for the CVD coating process was completed, and the substrates were ordered for coating and evaluation in the next two month period. The wheel substrate was modified from an array of segments to a full wheel rim preform, necessitating modifications to the coating apparatus. The new substrates were ordered and completed. The design has changed from an array of segments to a full wheel rim, necessitating modifications to the coating apparatus.

Several wheel preforms were coated with CVD diamond under different deposition conditions. Unlike the initial deposition trial, we pre-nucleated diamond on the preform before diamond coating. This pre-nucleation was to increase nucleation density, thereby reducing grain size and increasing the strength of the diamond coating.

We plan to perform pre-screening cut-off grinding tests on these thin wheel preforms prior to selection of the optimum deposition condition. If grinding performance is favorable, we may fabricate a full thickness wheel from preform layers for evaluation in the cylindrical plunge mode screening test.
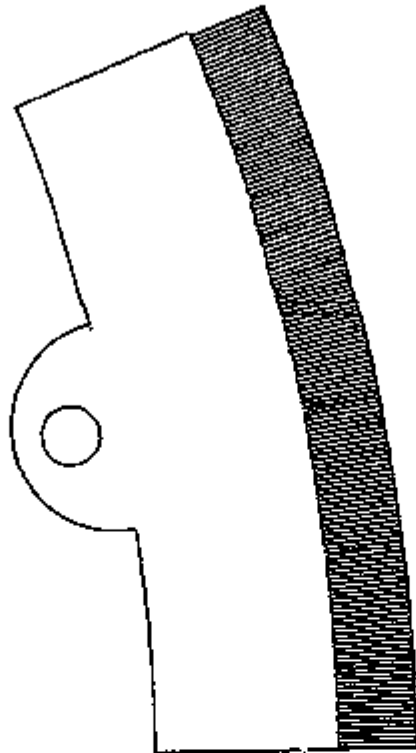
Figure 1 : Abrasive element from the CVD wheel
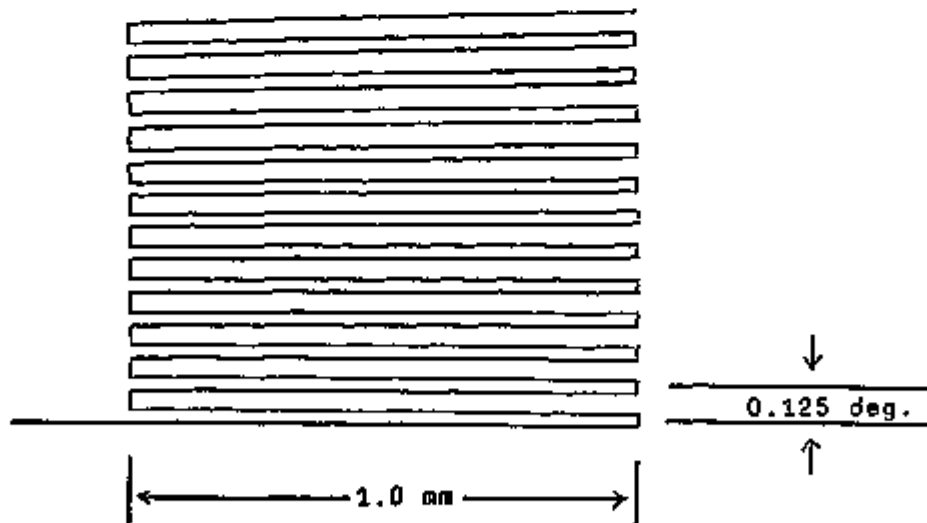
Figure 2 : Details of the Mo teeth on the abrasive element. Thickness of the teeth are approximately 25 μm, distance between teeth centers are 80 μm.

Task 1.3: Screening Wheel Grinding Test and Data Analysis

Grinding Test Description - The screening tests of the 76 mm wheels were completed. The screening test was done in a plunge grinding mode on an instrumented Okuma CNC cylindrical grinder at controlled feed rates. The sialon ceramic workpieces were 112 mm diameter rings x 70 mm ID x 6 mm thick mounted on a specially designed and manufactured arbor that, in turn, was located and mounted precisely on the machine. Thus, it was possible to remove the workpiece together with the arbor for the periodic examination of the ground surface, and to put it back on the machine at the same location. To maximize the testing data, we conducted short grinds at two material removal rates on all wheels followed by longer runs on a selected few wheels. Figure 3 shows the ceramic specimen and mounting assembly. Figure 4 is the Okuma grinder test set-up showing the ceramic specimen, the 76 mm test wheel showing the wear zone and the dressing wheel.

A harmonic response ("hammer") test, of the Okuma cylindrical grinder was conducted with the help the University of Connecticut. The objective of this exercise was to determine the susceptibility of the machine to produce chatter on ground workpiece and make any modifications if needed. Chatter is caused by a grinding machine that is too compliant for a given operating condition. The harmonic response test determines the stability limit defined by the equation

$$-(1/2k_W + 1/2k_S + 1/k) = Re_m$$

Where k_W is the cutting coefficient, k_S is the wear coefficient and k is the contact stiffness and Re_m is the maximum negative real point on the machine curve. The maximum negative real point, Re_m, is determined during the test and, for stability, checked to see if it is greater than the sum of the various factors on the left hand side of the equation.

Preliminary results indicated that the grinding system had adequate stiffness for testing with 3" wheels in all directions. Experimentally, there was no tendency for chatter in all our tests. The University of Connecticut submitted their report on the "Hammer Test". The test indicated that the spindle stiffness is very high in all directions, except one. However, in this direction the stiffness is of acceptable value, as evidenced by the lack of chatter on the workpiece in all our tests at up to 8.6 mm^3/s/mm (0.8 in^3/min./in.).

Superabrasive Wheel Screening Test Grinding Results - We evaluated approximately 45, 76 mm (3") diameter screening wheels at various plunge conditions grinding sialon disks. Our objective was to identify some experimental specifications for grinding wheels that would grind with low power and forces, provide acceptable wheel life and have less tendency of wheel loading. In summary, we demonstrated excellent grinding results on many experimental bonds. As predicted from earlier bond wear and strengths tests (Task 1.1), many experimental metal bonds exhibited intermediate grinding action between the standard resin and metal bonds. These experimental bonds had significantly superior grinding results over the standard B80 resin bond wheels. The standard commercial metal bonds tended to be too hard acting for ceramic plunge grinding and demonstrated high power consumption and loading. Examples of grinding results are discussed below.

Figures 5a-d are data for a series of experimental bonds made from a standard metal bond wheel with different levels of induced porosity (wheels #12, #15 and #5, in the direction
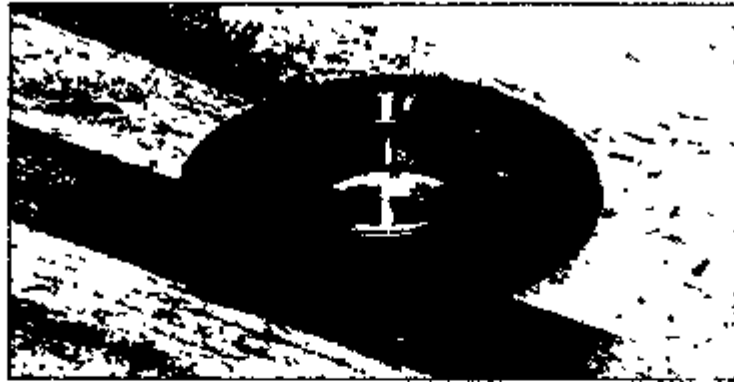
Figure 3. Sialon disk specimen and mounting assembly for screening test.
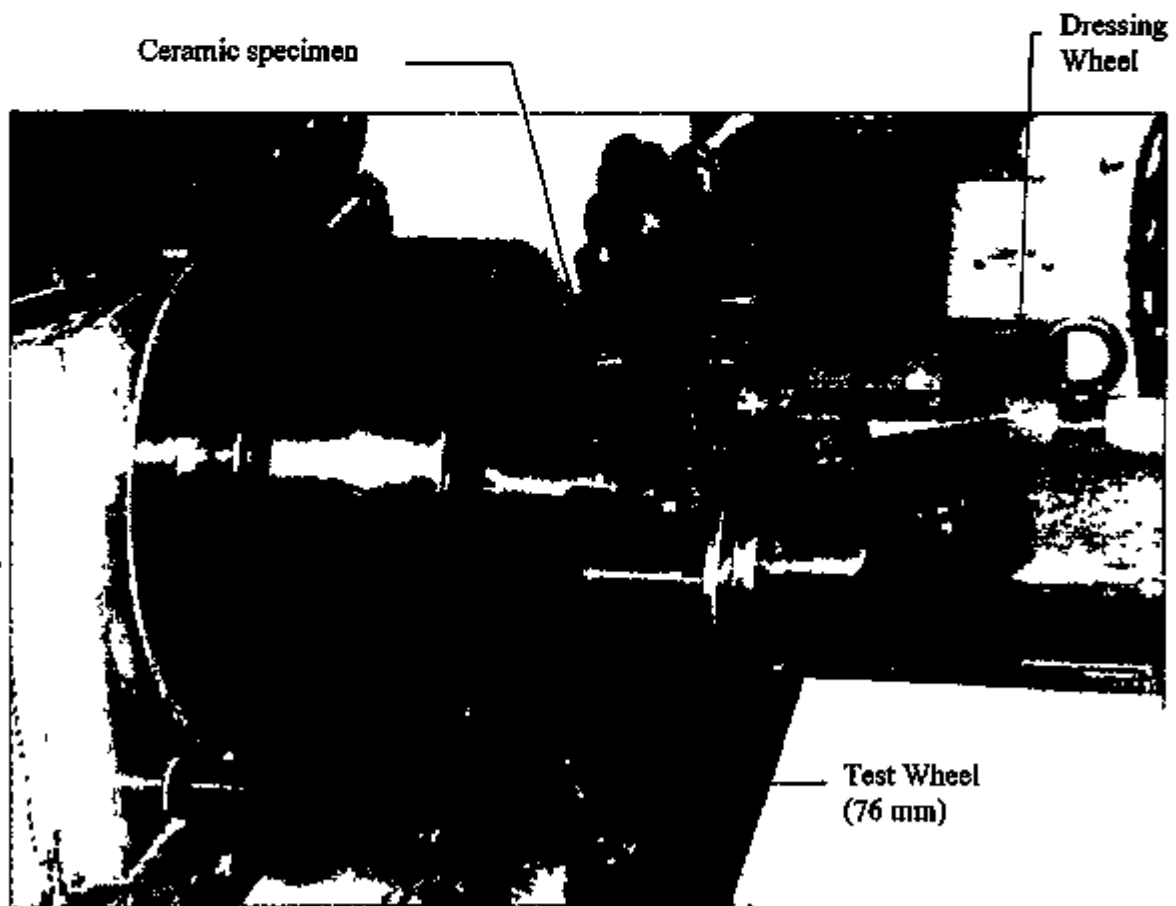
Figure 4. Okuma cylindrical grinder plunge screening test.

Figure 5a
RELATIVE SPINDLE POWER VS STOCK REMOVED

Figure 5b
RELATIVE GRINDING RATIO VS STOCK REMOVED

Figure 5c
RELATIVE NORMAL FORCE VS STOCK REMOVED

Figure 5d
RELATIVE TANGENTIAL FORCE VS STOCK REMOVED

154
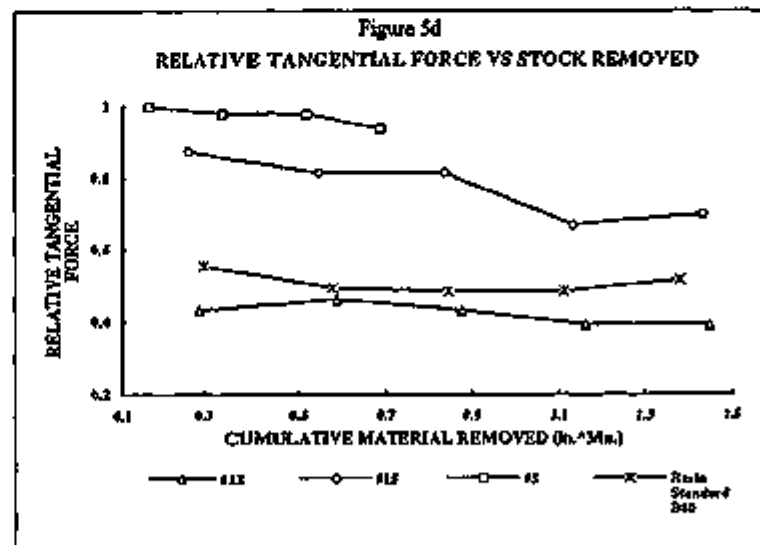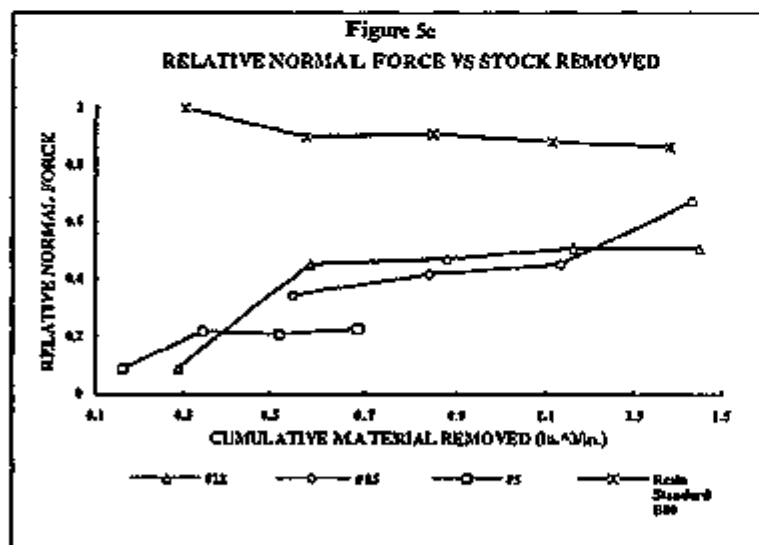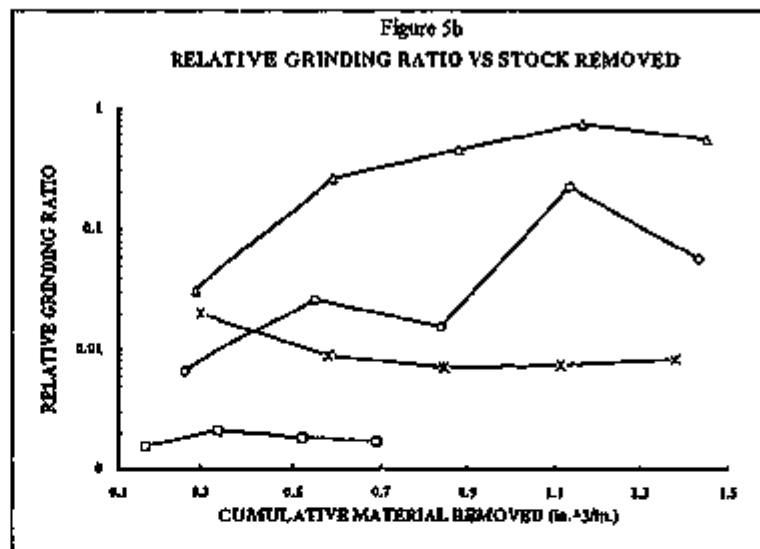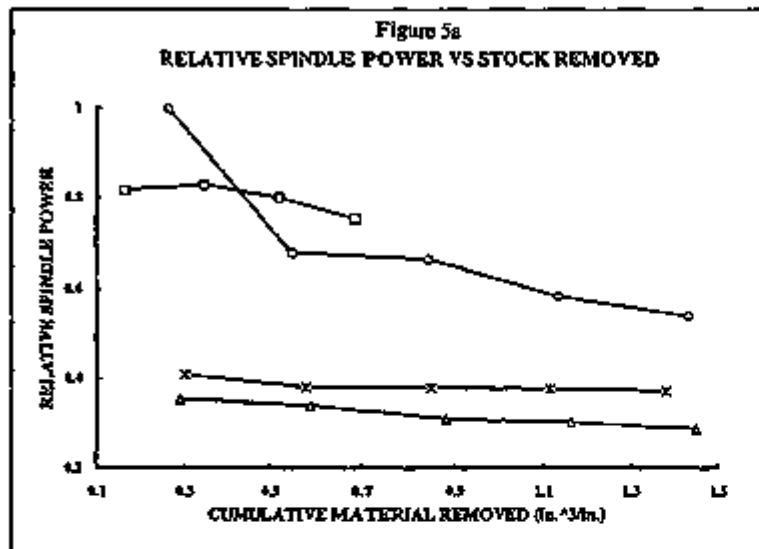
of increasing porosity). A standard resin B80 wheel, commonly used for grinding of ceramics, is also shown for reference. The material removal rate was set at (0.8 in^3/min./in.). The grinding tests on these were also done at low removal rates of 4.3 mm^3/s/mm (0.4 in^3/min./in.) and the results were similar, although the differences were less pronounced. Figures 5a, b, c, d] plot the relative spindle power, grinding ratio, normal force and tangential force, respectively, versus cumulative material removed (or grinding time). Wheel #12, with the lowest level of induced porosity, was the best wheel in this group. This wheel drew lower power than the resin wheel and had over an order of magnitude higher grinding ratio (ratio of material removal rate to wheel wear rate) compared to the standard resin bond wheel. Higher levels of porosity tended to lower normal grinding forces but decreased wheel life significantly. The standard metal bond that these experimental bonds were based (not shown) had severe loading, causing sudden increases in forces and power levels. While these experimental bonds, especially #12, showed good results, other compositions that were tested subsequently led to better grinding performances in terms of lower spindle power and less tendencies for wheel loading.

Figures 6a-d are another series of experimental metal bonds and includes a standard resin (B80) and a standard metal (DM 17) bond. This series of 7 experimental bonds plotted in Figure 6 represents both the inclusion of a pore inducer (PI2) at different levels, and a compositional change to the standard metal bond. Pore inducers were an attempt to give better controlled wear and less tendency for wheel loading. Bonds with the highest levels of pore inducers caused manufacturing problems and these wheels were not tested. Metal composition changes were designed to modify the strength and ductility of the bond. In this series, wheel #25 was considered the most promising composition. This wheel ground at low forces and power and had grinding ratios significantly superior to the standard resin bond. While this wheel did not have the highest grinding ratio of the experimental bonds, it demonstrated reduced wheel loading tendency due to controlled breakdown of the bond. The poor performance of the resin bond was attributed to excess abrasive wear and bond rubbing at these high removal rates. Note the standard metal bond, while showing high grinding ratios, had a dramatic drop in grinding ratio and rise in force and power at about 7.5 in.^{3}/in. cumulative material removed. This indicated severe loading and the need for dressing. Many experimental bonds were able to grind effectively up to 28 in.^{3}/in. (> 3.5 times the stock removal) when the test was ended. This illustrates the superiority of this experimental series.

Several other compositions (not shown here) were tried including different levels of hexagonal boron nitride and graphite as solid lubricants. These wheels exhibited some manufacturability problems and/or had poor grinding performance results, such as high spindle power and unacceptable wheel wear.

Identification of superior bond systems can be masked by incorrect selection to diamond type and content. Therefore, we evaluated different abrasives and abrasive concentrations in many experimental bonds.

Figure 7 shows the effect of three different diamond types in a metal bond that showed promising results in earlier tests. D1 (#35) was an uncoated diamond type while D2 and D3 have metal coatings on them to enhance adhesion between diamond and bond. The coated diamonds improved the wheel life as shown in the relative grinding ratio plot, with minor differences in spindle power, but also generated higher normal grinding forces compared to uncoated diamonds. There was also evidence of wear flats on the coated diamonds. Grinding

Figure 6a

RELATIVE SPINDLE POWER VS STOCK REMOVED

Figure 6b

RELATIVE GRINDING RATIO VS STOCK REMOVED

Figure 6c

RELATIVE NORMAL FORCE VS STOCK REMOVED

Figure 6d

RELATIVE TANGENTIAL FORCE VS STOCK REMOVED

Figure 7

Effect of diamond types on grinding performance
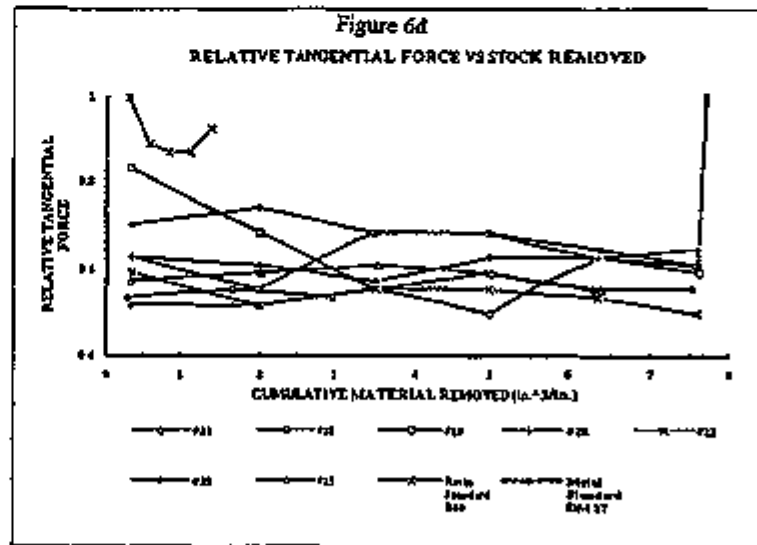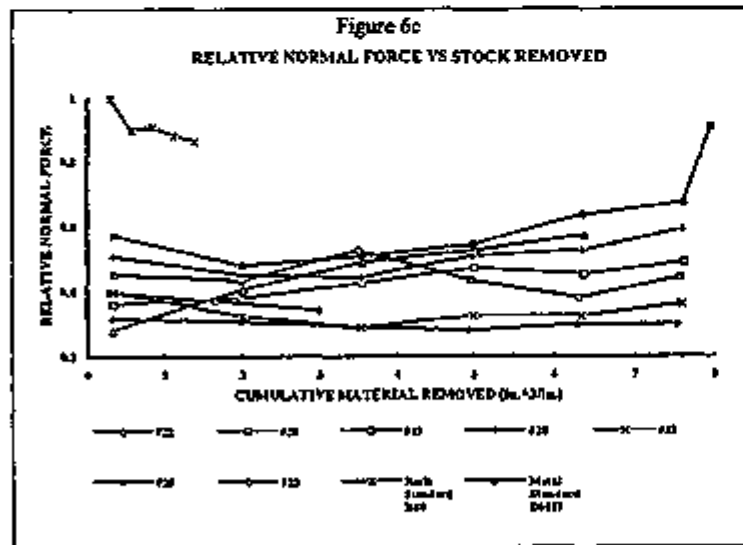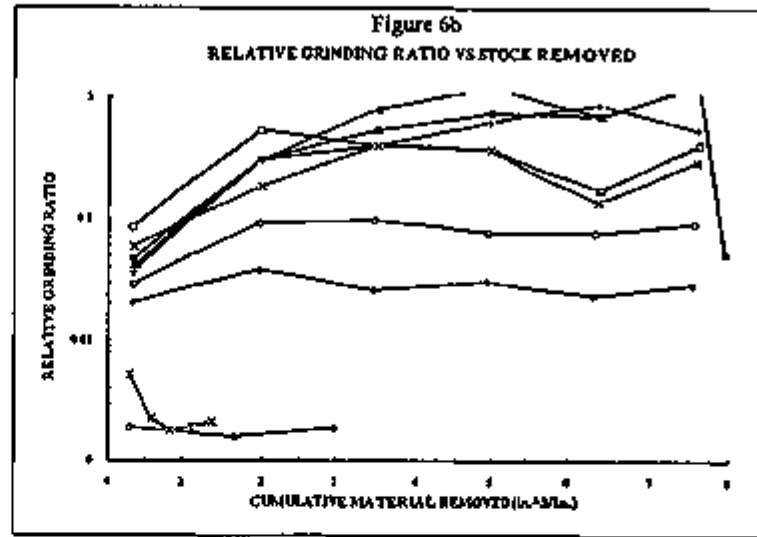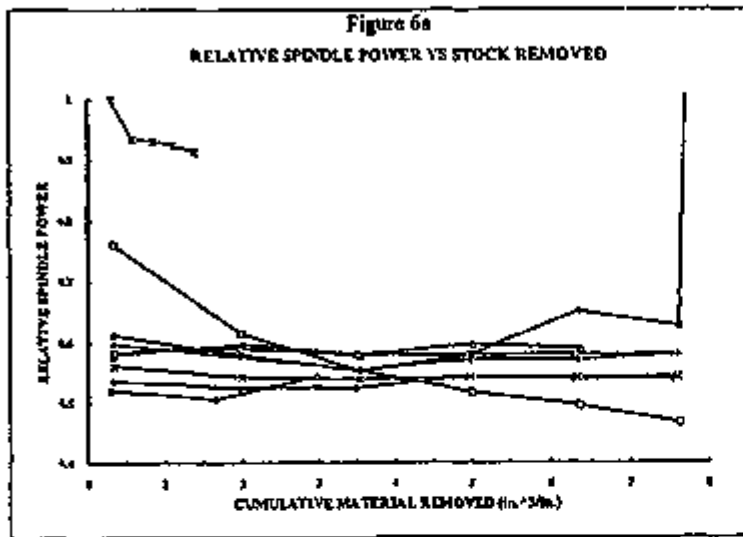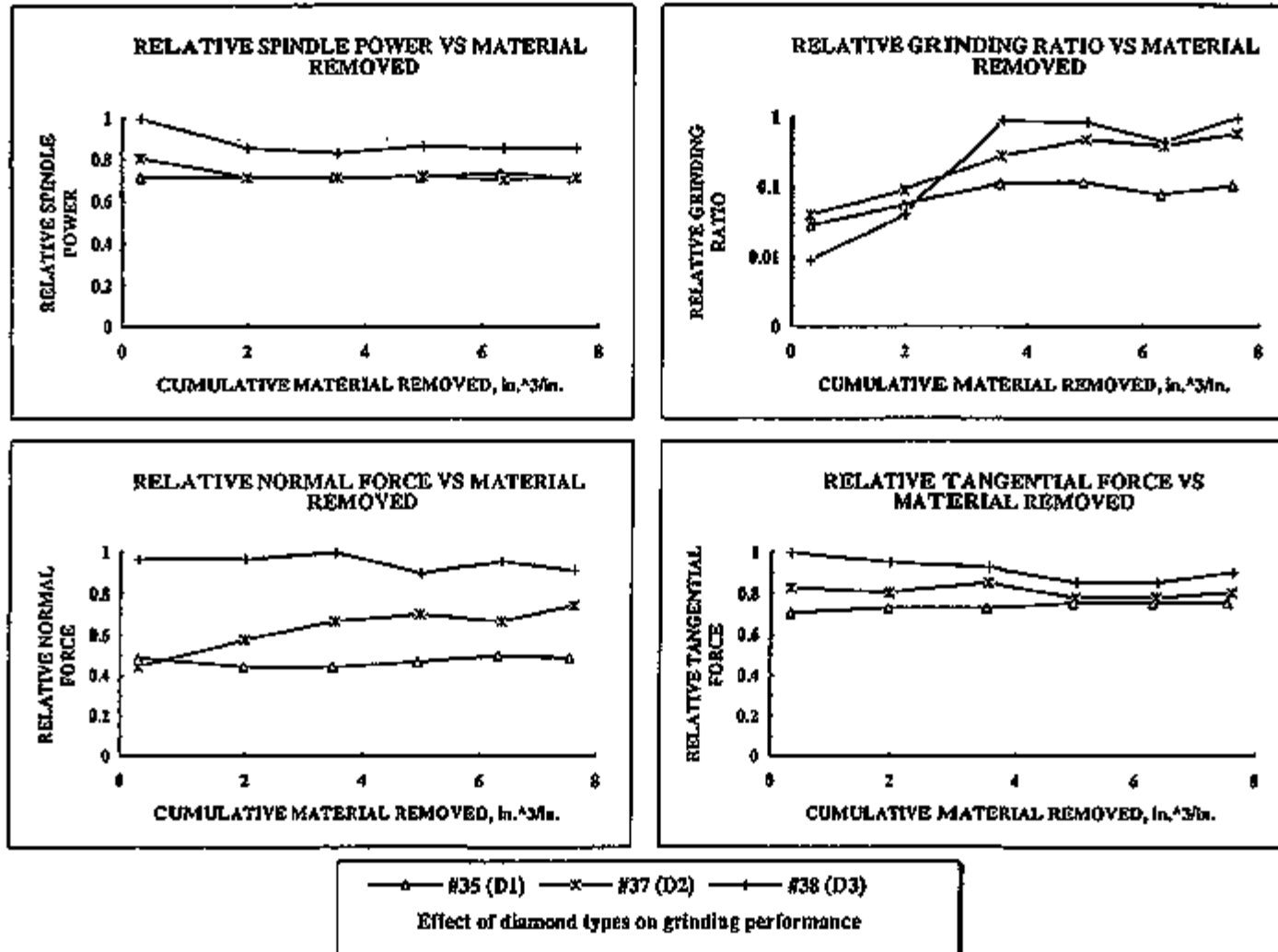
with diamonds having wear flats ("dull" diamonds) generate higher normal grinding forces compared to sharp diamonds leading to more grinding damage on the ceramic. The results also suggest that the bond wear and abrasive grit wear rates were not well balanced for these coated abrasive-bond combinations. A better bond would release the abrasives sooner and would also lower the grinding ratio values. The recommended diamond type may be adjusted after we complete grinding damage assessments in Tasks 1 and 2.

Three different diamond concentrations (100 = 25 volume percent) were tested and an example of the grinding ratio results are shown in Figure 8. Higher diamond concentrations (within the range of test conditions) resulted in enhanced wheel life. The optimum concentration would be decided after considering other factors such as spindle power, grinding forces, frequency of truing, etc.

The grinding ratio versus bond hardness for a set of wheels containing the same metal alloy composition but different levels of pore inducer PI2 is shown in Figure 9. The hardness dropped with increasing levels of pore inducer PI2, as did the Grinding Ratio, leading to a good correlation between hardness and Grinding Ratio for a given metal bond composition.

Figure 10 summarizes much of the screening test grinding data on sialon disks. These plots compare the grinding performance of standard resin, metal and experimental bonds at 2-3 cut rates for one type of friable abrasive. Note that the data presented in Figures 5 and 6 above are for the higher metal removal rate (0.8in.^{3}/min.,in.). The relative performance of the resin bond is somewhat improved at the lower material removal rate as expected. The metal bonded wheels required frequent dressing, using a SiC abrasive stick, at all conditions. For improved grinding performance an order of magnitude enhancement in grinding ratio values is needed relative to the resin bond. This is due to resin bond's rapid breakdown at high stock removal rates. Such a breakdown necessitates frequent regeneration of the wheel profile and hence increases machining cost. The shaded regions in Figure 10 represent the range of values for spindle power, grinding ratio and grinding forces generated with some of the experimental metal bonds. These experimental bonds generally had significantly higher grinding ratio than the standard resin bond and comparable to the metal bond, yet the force and power requirements were more favorable than both standard bond systems.

In conclusion, the screening tests identified very promising wheel specifications that performed superior to standard resin and metal bonded wheels. We met the Task 1 objective to identify improved wheel compositions for manufacturing scale-up to 203 mm wheels in Task 2. The required characteristics of such wheels are: (1) to grind with equal or lower power than the current resin bond (B80) used for ceramic grinding, (2) to wear in a controlled manner in order to expose sharp cutting points and maintain good grinding action (as opposed to the conventional standard metal bonds), and (3) to provide satisfactory wheel life values between those of existing standard metal and resin bonds.

CVD Diamond Wheel Screening Test Grinding Results - The first CVD diamond wheel was tested on the Okuma CNC cylindrical grinding machine in a plunge grinding mode. The workpiece material was the standard sialon used for the Superabrasive wheel screening tests, except that the disk was 3.8 mm thick. The thinner ceramic disk was to compensate for the slightly thinner CVD wheel, thereby avoiding possible edge effects in the plunge test. The screening test conditions were as follows:

Figure 8

RELATIVE GRINDING RATIO VS DIAMOND
CONCENTRATRION

Figure 9

RELATIVE GRINDING RATIO VS RELATIVE HARDNESS
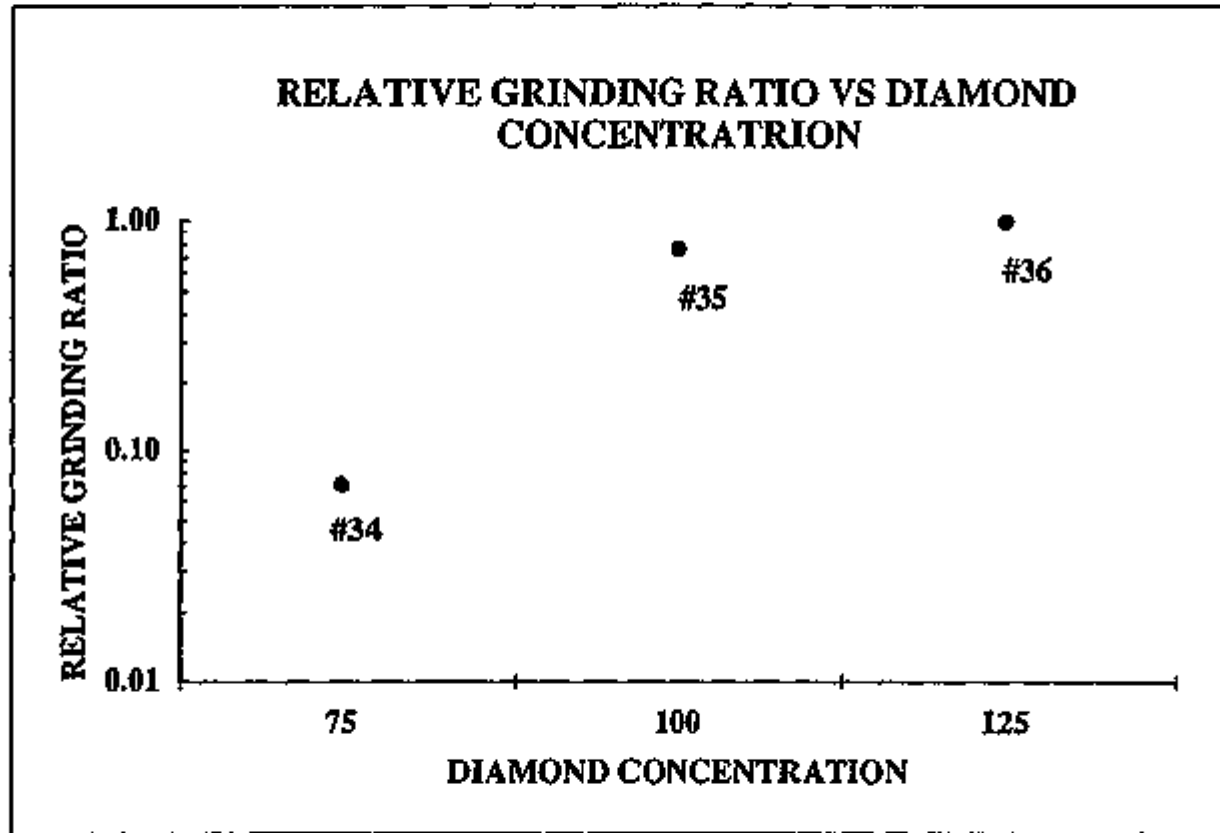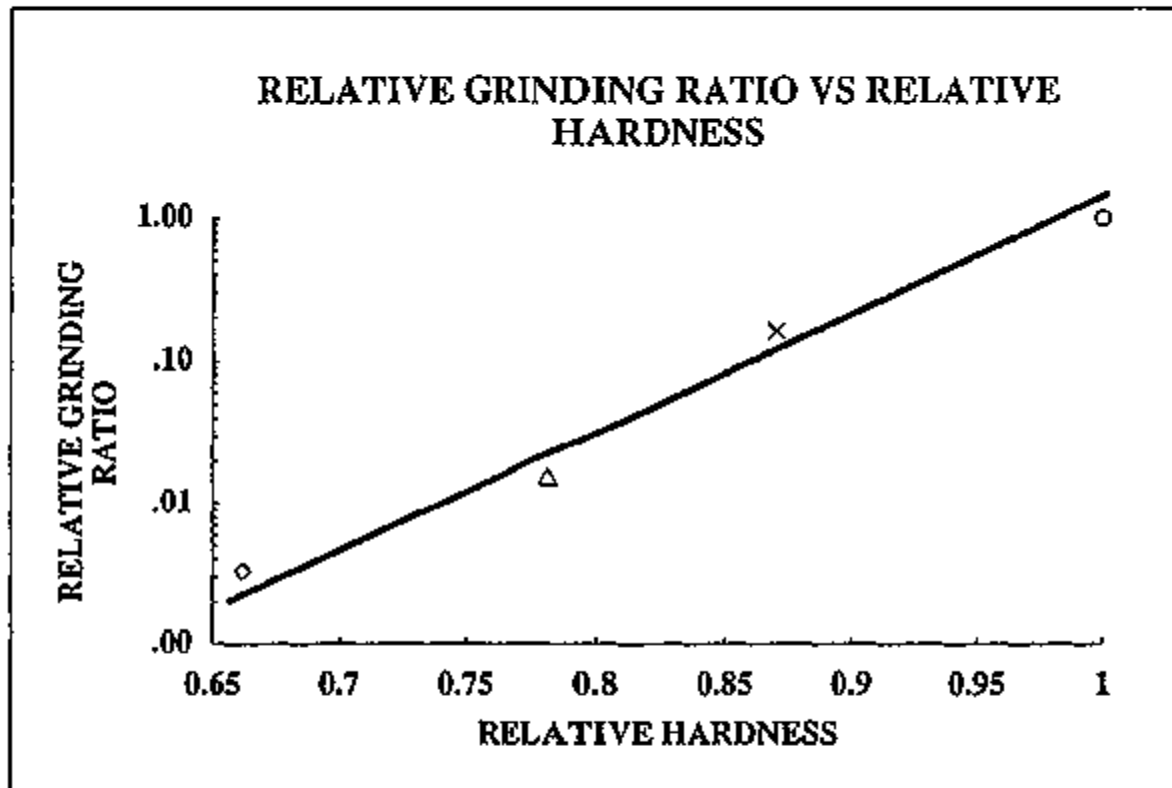
#28 (0%)   #22 (15%)   #44 (20%)   #46 (25%)

Effect of Pore Inducer PI2 (0 to 25%) on Relative Grinding Ratio

Figure 10

RELATIVE SPINDLE POWER VS MATERIAL REMOVAL RATE

RELATIVE NORMAL FORCE VS MATERIAL REMOVAL RATE

RELATIVE GRINDING RATIO VS MATERIAL REMOVAL RATE

RELATIVE TANGENTIAL FORCE VS MATERIAL REMOVAL RATE

• Resin Standard (HB0)   ⌂ Metal Standard (DM17)
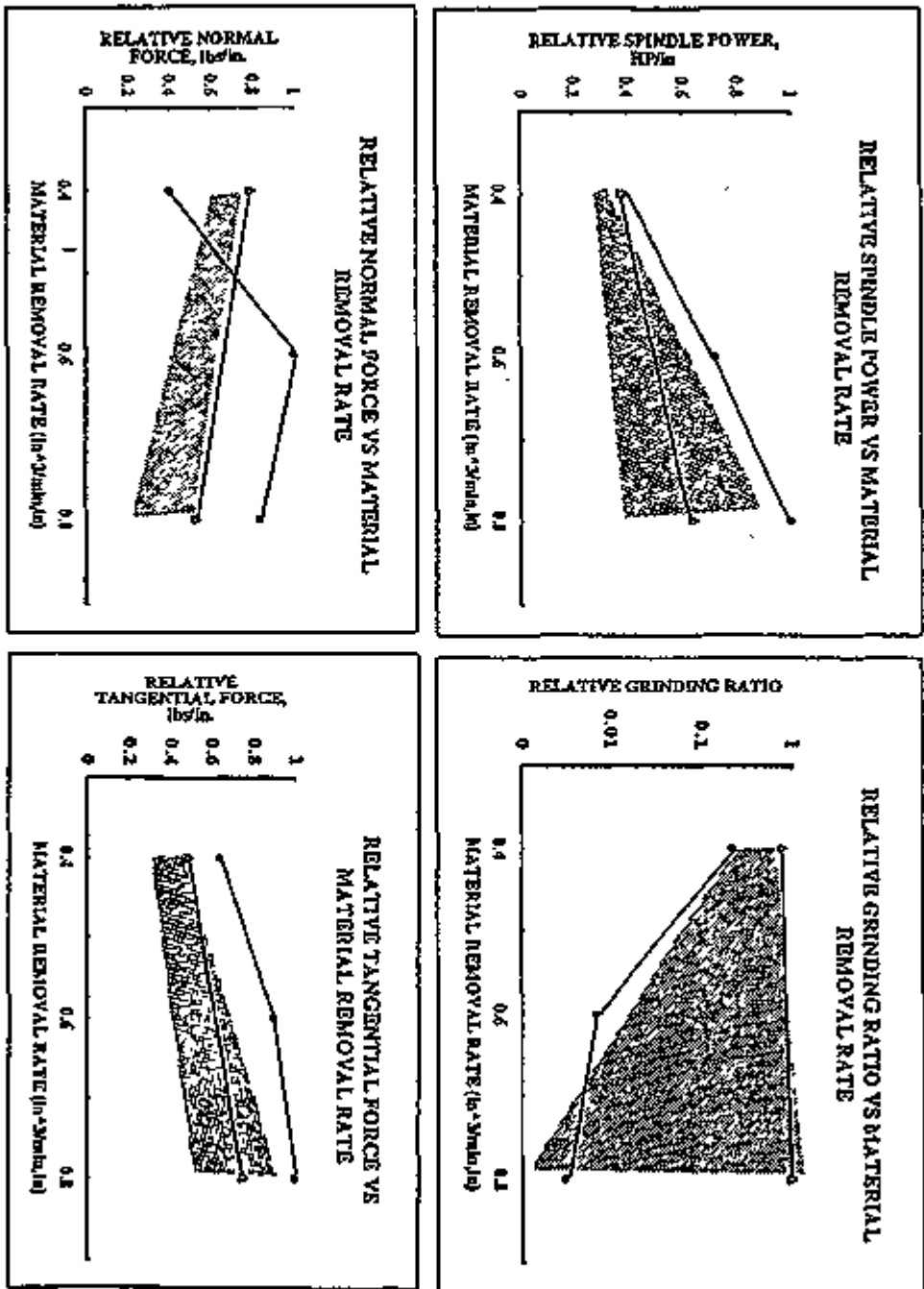
Surface speed: 32 m/s (6252 sfpm)
Infeed rate: 12 μm/s

    The CVD grinding test was disappointing and the configuration was unable to grind effectively. As the wheel encountered the workpiece, the normal force on the workpiece rose rapidly. After 20 seconds F_n exceeded 500 N and the test was terminated to avoid damage to the grinding machine.

    Optical inspection of the workpiece and the wheel showed little stock removal from the workpiece and significant burning of the wheel face. We observed also radial cracks in the wheel face, which were also probably caused by overheating.

    Figure 11 shows a scanning electron micrograph of one tooth in the CVD wheel after use. In the center of the picture the molybdenum core of the tooth is visible; the outer end of the tooth core is below the picture. Residual diamond coating is visible over the upper end of the tooth. The rest of the material is the epoxy matrix: the white highlights are instrument artifacts caused by charging of the non-conducting regions.
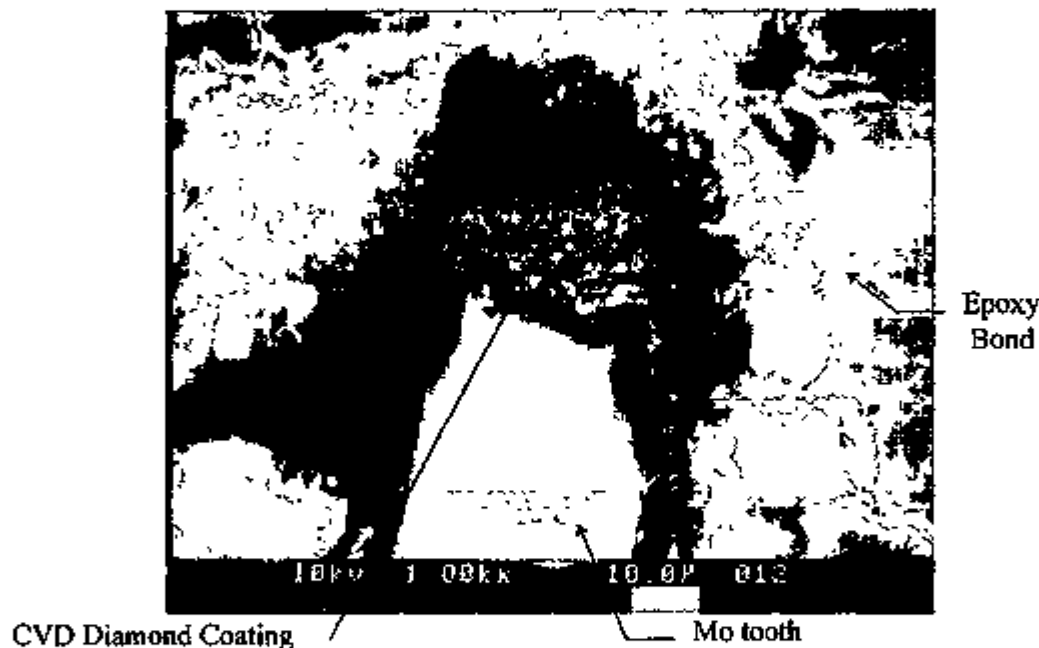
Figure 11. Scanning electron micrograph of a CVD diamond grinding wheel tooth after plunge grinding test.

    The micrograph suggests that diamond tended to crack way from the tooth cores well below the tip of the tooth. We postulate two reasons for this. First, the strength of the diamond and its bond to the molybdenum may have been insufficient. Second, the long aspect ratio of the tooth and the large difference in flexural modulus between molybdenum, diamond and epoxy (perhaps a factor of 500) may permit the tooth to flex in a manner that led to premature cracking of the diamond. Although we did not appreciate their significance at the time, (after truing, but before testing, the wheel) there was evidence of azimuthal cracks in the diamond down to the

visible limit (approximately 100 μm below the surface of the wheel). Figure 11 shows azimuthal cracks in the Mo tooth. We believe that the reason why the wheel did not grind effectively in the test was that diamond prematurely spalled away from the teeth.

The results indicated a need for significant modification to the wheel system design. We prepared modified wheel designs that will both, improve the system stiffness characteristics, and adjust the CVD process conditions to improve diamond characteristics and adhesion. Details of the CVD diamond wheel redesign were discussed above under Task 1.2. We will test thin plunge wheels on sialon samples to confirm that grinding action is achieved. If successful, a full thickness plunge grinding wheel may be fabricated and tested in the conventional screening test conditions.

NRDC Ceramics Support, Analysis of Grinding Damage - Optical microscopy did not reveal grinding cracks in the screening test disks. Selected disks are being prepared for compression "C-Ring" mechanical tests. These tests will evaluate the strength of the ground OD. For the "C-Ring" test, tensile stresses will be parallel to the grinding direction. Dye penetrant evaluation will be done before testing.

More comprehensive flexure testing is scheduled for the Task 2 rods. Stresses generated during flexural testing will be normal to the grinding direction, which is more meaningful for a cylindrical grinding damage evaluation.

TASK 2: Design and Prototype Development

Task 2.1: Final Superabrasive Wheel Experimental Design

Based on the results of Task 1, the Task 2 experimental design was completed. The test wheel specifications were selected from a short list, determined from the screening tests of 76 mm (3") diameter wheels in Task 1. Approximately 6 wheel variables were selected for further study. The variables included metal composition, induced porosity level, diamond concentration and type. The standard wheel for this test was the standard resin bond product.

Task 2.2: Fabrication of 203 mm (8") Wheels and Ceramic Specimens

We encountered some expected manufacturing problems in the scale-up from 76 mm to 203 mm diameter wheels for some of the experimental bonds. These wheels did not meet quality specifications of the original screening test wheels. Some of these specifications are being modified and re-made. However, four experimental wheels met design specifications and were successfully tested.

We completed all the required ceramic rod specimens this period. Three types of ceramics are scheduled to be tested in Task 2, NCX-520 sialon (tested in Task 1), NCX-5102 HIP'ed silicon nitride, and AZ67HS zirconia toughened alumina (ZTA). The rod dimensions were approximately 27 mm diameter X 79 mm long. The sialon and HIP'ed Si_3N_4 rods were fabricated and characterized at the Northboro Research and Development Center. As reported last period, the ZTA rods were fabricated by Norton Advanced Ceramics, (Export, PA).

Task 2.3: Grinding Evaluation of 8" Wheels

The grinding tests using 203 mm (8") experimental wheels on NCX-520 sialon are in progress. While the data is being analyzed, preliminary 203 mm wheel test results show that two experimental metal bond specifications are potential candidates to significantly improve the grinding of advanced ceramic materials.

Grinding Test Description - The grinding test is being performed on the instrumented Okuma cylindrical grinder in Norton's World Grinding Technology Center. The ceramic rods, 27 mm diameter by approximately 79 mm long, are being tested in both the cylindrical plunge mode and transverse mode. The grinding test was designed to provide flexure test rods of the final 6.35 mm diameter ground in the transverse mode for subsequent evaluation of machining damage. For each test wheel, the initial 27 mm rod was plunge ground, using 6.35 mm of wheel width, to 6.9 mm diameter. The rod was then indexed by 6.35 mm axially and plunge ground again. This sequence was repeated nine times per rod and several rods per wheel specification. Within a given plunge, the removal rate was maintained at the desired level by increasing the work speed and radial infeed, periodically. The power, forces, wheel wear and rod surface finish were measured. The rods were subsequently transverse ground in one direction, at a depth/pass of 0.013 mm, to the final 6.35 mm diameter. Figure 12 shows typical rods after grinding tests displaying the original and final diameters (the large diameter end was held in the chuck). These test rods were sent to NRDC for flexure strength and grinding damage evaluation.
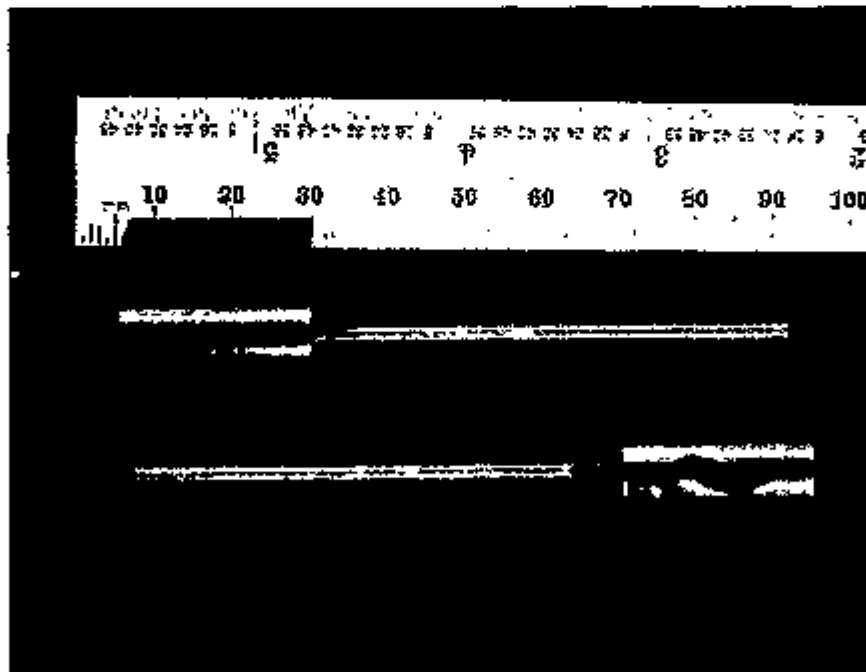
Figure 12. Sialon specimens after cylindrical grinding test and prior to flexural strength testing. Specimens = ~79 mm long. Original diameter = 25.4 mm. Final diameter = 6.35 mm.

Preliminary Grinding Results - To date, two wheels demonstrated grinding ratio values an order of magnitude better than the current resin products. Additionally, the power consumed by these metal bonded wheels were up to 30% lower than that of the resin bonded wheels at those removal rates, primarily due to their better abrasive grit retention.

The experimental metal bonded wheels could also be dressed easily with an abrasive stick, if and when needed. In order to lower the power and noise levels during the grinding tests, the diamond wheels required periodic dressing with an abrasive stick. The experimental wheels required approximately 75% less dressing than the standard resin bond tested at the tested grinding rates. The resin bonded wheel needed dressing approximately every fifth plunge grind compared to every twentieth grind for the best experimental metal bonded wheels. In the case of the resin bonded wheel, the grinding action appeared to knockout the abrasives too frequently, necessitating a dressing operation that would erode the bond and expose new abrasive grits for grinding. Conversely, stick dressing at higher power and noise levels in the metal bonds was necessary to release the worn, flat abrasives that were held too long, and erode and expose sharp new grits. This mechanism was confirmed by visual examination of the wheels by optical microscopy prior to dressing, which showed significant abrasive pullout in the resin bonded wheel. The wheel wear rates of resin bonded wheels were constant while that of the experimental metal bonded wheels decreased with time, again confirming this hypothesis that the abrasives are held well in metal bonds. Unlike the laborious dressing of standard commercial metal bonds, stick dressing of these experimental metal bonds required minimal effort, leading to a drop in grinding force and power levels to their original levels.

All test wheels contained 320 grit diamond abrasives. At the relatively high test removal rates, the surface roughness value of workpieces plunge ground with the resin bonded wheel remained nearly constant at approximately 0.4 μm Ra due to the continuous release of worn abrasives. The roughness of the ceramic workpieces ground by the experimental metal bonded wheels were initially similar, but tended to increase gradually up to about 0.7 μm Ra with grinding time. Release of worn grits by dressing improved the finish and brought it to original levels. Surface finish after the transverse grind tests were constant at about 0.43 μm and 0.51 μm Ra for the resin and metal bonds respectively.

Additional 203 mm diameter test wheels are being manufactured for testing on sialon rods. Selected experimental wheels and the resin bonded standard will also be evaluated grinding NCX-5102 HIP'ed silicon nitride and AZ 67H zirconia toughened alumina.

Status of Milestones

Milestone 1.1. Requirements Definition and Experimental Design -- Completed

Milestone 1.2. Screening Test Wheel Manufacturing -- Completed for Superabrasive wheels.

Milestone 1.3-4. Screening Wheel Test and Data Analysis -- Completed for Superabrasive wheels and first CVD wheel. CVD wheel reiterations and testing rescheduled.

Milestone 2.1. Final Superabrasive Wheel Experimental Design -- Completed

Milestone 2.2. Fabrication of 8" Wheels and Ceramic Specimens -- Completed. Some 8" wheel specifications are being remade.

Milestone 2.3. Grinding Evaluation -- In Progress, On Schedule

Milestone 2.4. Fabrication of Wheels for MMES -- On Schedule

Communications/Visits/Travel

Trevor Howes and George Bailey, University of Connecticut CGRD visited Norton Company World Grinding Technology Center to perform Harmonic Response (Hammer) Test.

R. H. Licht and E. Lilley to the Cost-Effective Machining of Ceramics Workshop (CEMOC), Oak Ridge, TN, August 23-25, 1994.

Publications/Presentations

Development of the Next Generation Grinding Wheel, R. H. Licht, S. Ramanath, M. Simpson, E. Lilley, Presented at the CEMOC Workshop, August 24, 1994.

Cost-Effective Method for Determining the Grindability of Ceramics
C. Guo, R. H. Chand, and N. Krishnan (Chand Kare Technical Ceramics, Inc.)

1   Objective/Scope

The objective of this program is to develop a cost-effective method to determine the grindability of ceramics leading to cost-effective methods for machining such ceramics. In this first phase of activity, Chand Kare Technical Ceramics is engaged in directing its efforts towards review of literature related to ceramic grinding, development of a variable definition of grindability, design of grindability test experiments, and design of a ceramics grindability test system (CGTS). The grindability study underway also includes establishment of correlation between the grindability number and the conventional grinding practices.

2   Technical Highlights

The technical progress to date is summarized by activities in the attached Milestone Schedule. The remainder of this section describes activity during the past six months which includes literature review, design and fabrication of the test machine, preparation of test specimen, screening of suitable diamond belts, and initial grindability test results.

2.1   Literature Search and Study

Planned literature search and study have been completed. Of course, any new development in this area will be followed.

2.2   Selection of Diamond Belt

Structurally, there are two types of diamond belts available. In one structure, diamond grits are deposited on the base material in a form of a series of diamond cluster. We call it cluster-type belt. Extensive investigation about this type belt has revealed that it is not suitable to grindability test application. First of all, this type of belt was designed for polishing which means that the diamond grits are very fine. The coarsest available grit size is 30 microns which is not suitable for material removal as required in grindability test.

For the second type of belt, the diamond grits are randomly deposited on the base material. The belt manufacturer can supply belt with very coarse grit size (up to 100 mesh size) which is suitable for grinding with much higher material removal rate. This belt is chosen for grindability test.

In order to test the grinding capability of the chosen belt, a preliminary test rig was developed. The test rig was mounted on a milling machine. An aluminum wheel was mounted on the spindle (where the milling cutter used to be mounted) and was used to drive the diamond belt. Another wheel was vertically mounted on the work table to support the belt and apply tension to the belt. The belt tension was adjusted by moving the work table. The belt speed was varied by changing the spindle speed. Various ceramic bars were forced against the belt manually while the belt was running at different speeds. Preliminary tests have shown that the selected belt is capable of grinding various commercially available ceramic materials.

2.3   Development of the Test Machine

The development of the grindability test machine has been completed. An illustrative sketch of the test machine is given in Figure 1 to show the mechanisms of its operation. The machine is designed to measure the material removal rate under controlled force grinding. This
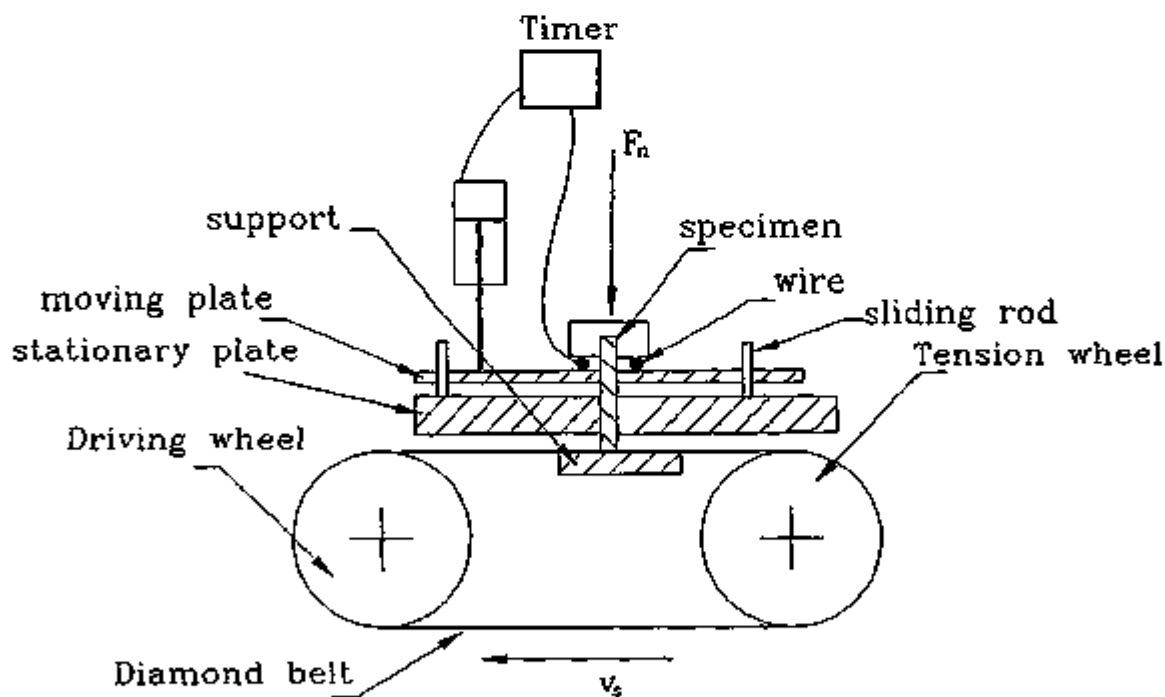
Figure 1   A sketch of the test machine

material removal rate will be used to measure the grindability of a ceramic material after it is normalized by the applied normal grinding force per unit area of contact and the belt speed used.

This normalized material removal rate can also be further used to correlate belt grinding with wheel grinding, controlled force grinding with controlled infeed grinding, which is planned for the next year.

The test machine consists of a diamond belt driving, adjusting, and tension unit, a specimen positioning, holding, and indexing unit, a controlled force application unit, a fast feed and fast retract unit, a coolant supply unit, a timing unit, and a machine base. Belt dimensions are chosen to be: 30 inches long and 2 inches wide. The belt speed is around 4,500 feet/min (22.86 m/sec). The belt is driven by an electric motor of 1 horse power. A stationary platen is placed beneath the belt to overcome the grinding force. The specimen is forced to the platen portion of the belt under a controlled force. After grinding a predetermined period of time, the specimen is retracted quickly. For the next test, the specimen is indexed across the belt width to utilize a new portion of belt surface.

The belt tension is adjusted using a preloaded spring with a mechanism for quick belt change over. A mechanism is also designed to adjust parallelness between the center of the driving wheel and the center of the idle wheel. The purpose of this adjustment is to maintain a newly installed belt to the center of the contact wheel. The fast feed speed of the specimen toward the belt is controlled with an air cylinder. A coolant supply system is incorporated with the test machine to accomplish wet grinding operation. A timing system is also incorporated with the test machine to account the actual grinding time. A desired grinding time can be programmed into the timer.

Controlled force is accomplished by adding weights which is considered to be simple and reliable. Other options were also considered. With pneumatic cylinder, load cannot be maintained to a constant value if pressure fluctuation exists in the air line. Also, the availability of pressurized air may impose limitation. If hydraulic cylinder is chosen, a hydraulic system is needed for the test machine which can make the machine complex for desktop application. One of the limitations of torque control motor is that the torque output varies during one motor revolution. This variation will be more evident when the motor is running at low speeds. In our application, the infeed is very small, especially with hard to grind materials which requires that the motor run at very low speeds. The weight option turns out to be the simplest and most reliable method.

The operation of the test machine is as follows (see Figure 1): After a specimen of known length is mounted and the machine is started, the air cylinder will lower the moving plate at the preadjusted speed. As soon as the specimen contacts the belt (grinding begins), the circuit is broken and the timer starts counting down from the programmed cycle time. When the cycle time is over, the air cylinder fast retracts the specimen. This completes one test. The specimen is then removed and measured for stock removal.

An overview of the test machine is given in Figure 2. A view of the system without the base is given in Figure 3. Top, left and front views of the machine are given in Figures 4, 5 and 6 respectively.
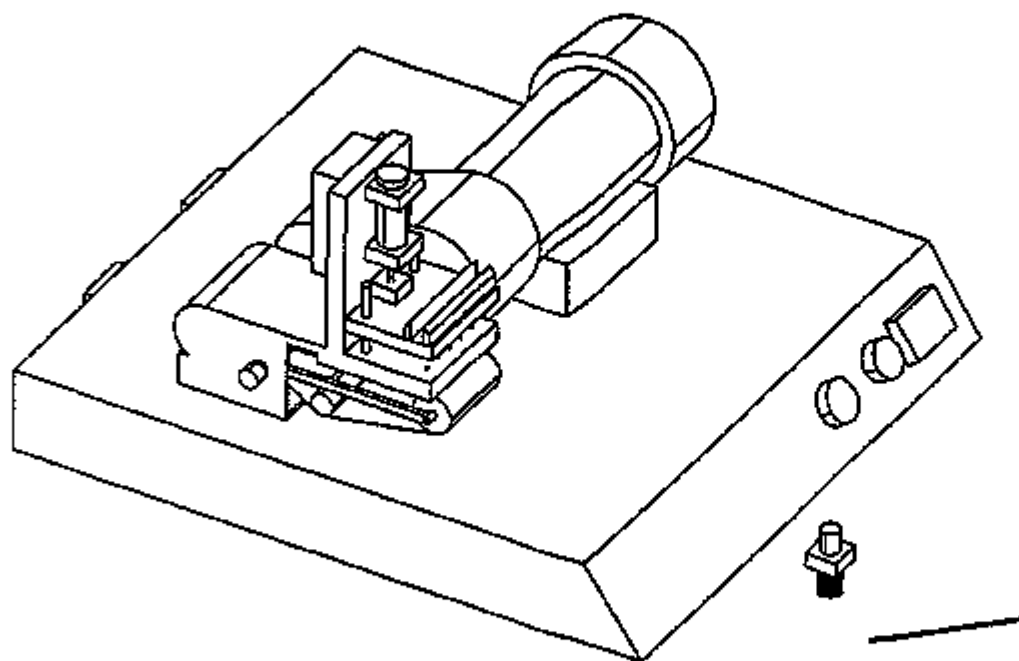
Figure 2   An overview of the test machine
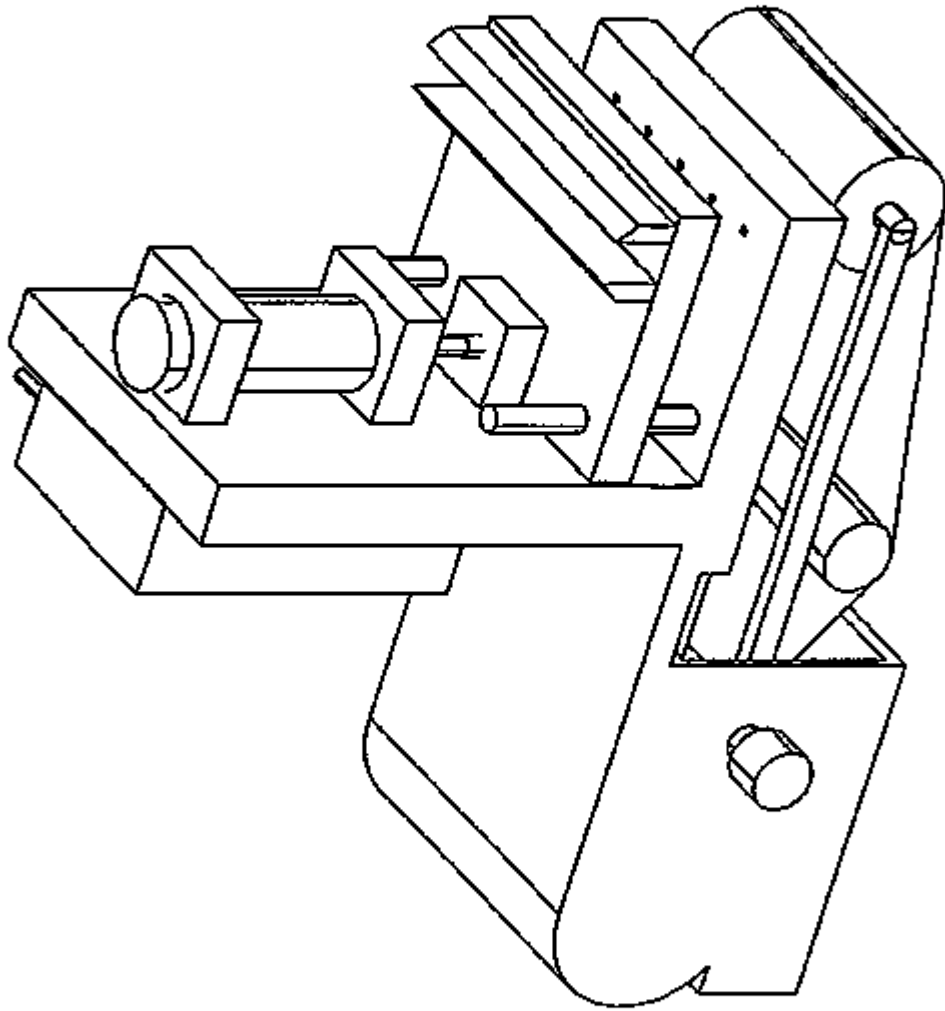
Figure 3 View of the test machine without the base
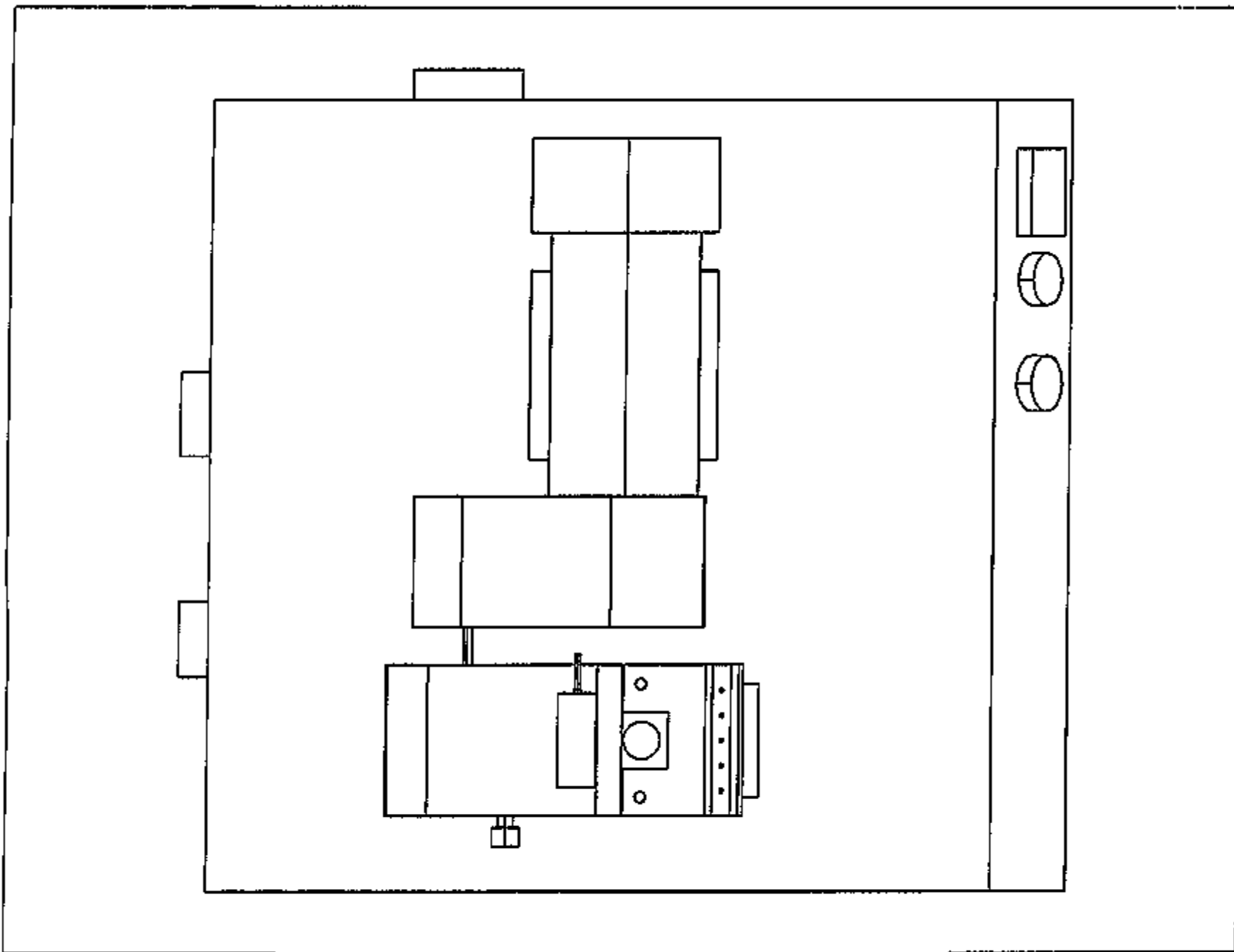
Figure 4   Top view of the test machine

172
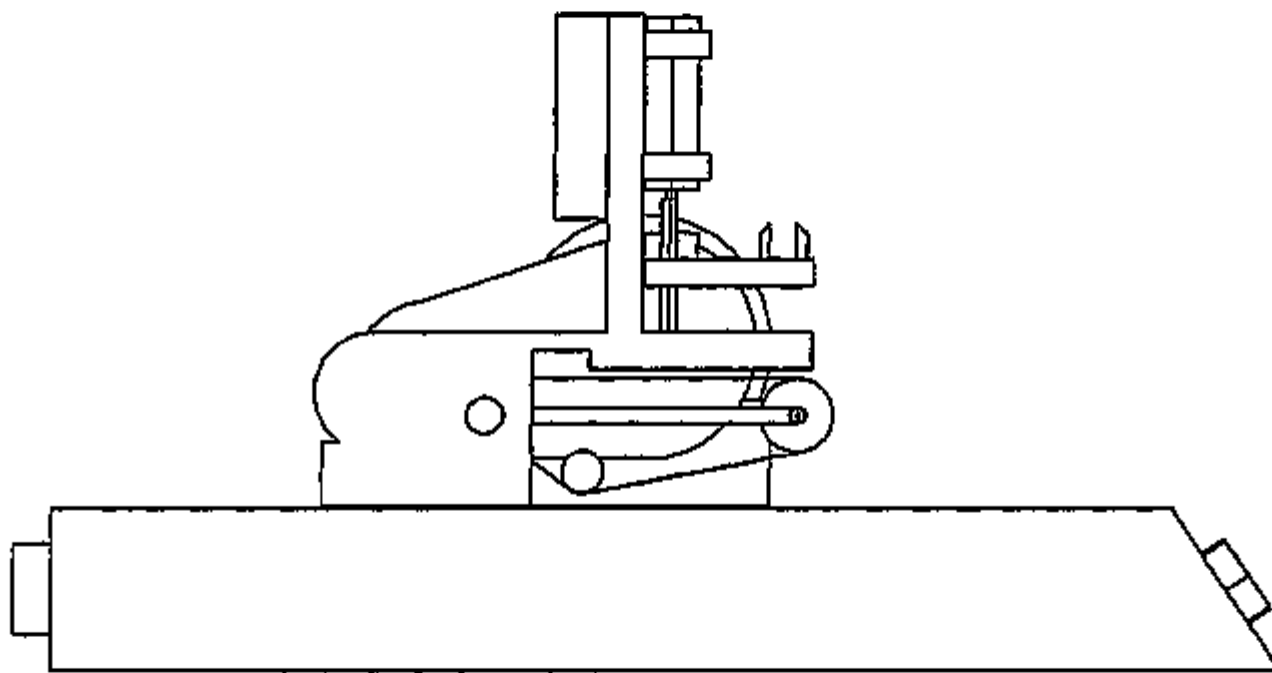
Figure 5 Left view of the test machine
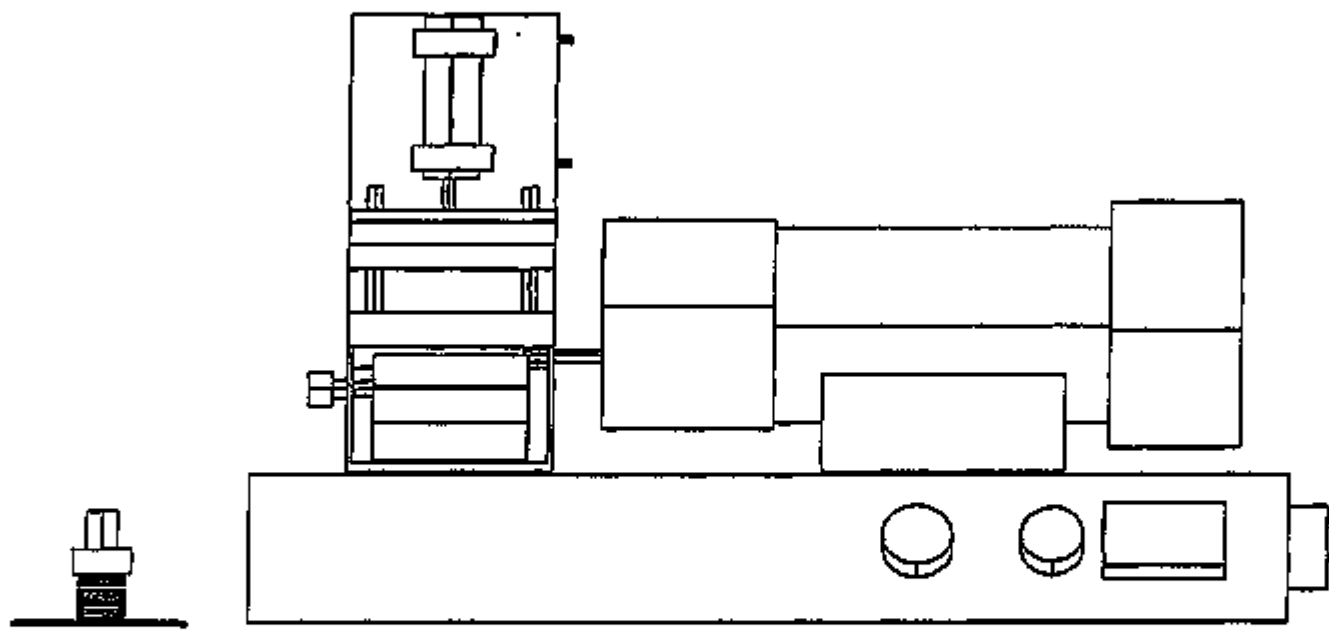
Figure 6   Front view of the test machine

2.4 Preparation of Test Specimen

Specification of standard MOR bars (3 by 4 mm cross section) is chosen as the technical requirements for specimen used to test grindability of ceramic materials. Eight ceramic materials were requested from various material suppliers around the country. For the first set of tests, ten MOR bars from each material were manufactured.

List of Materials to be Tested

Silicon Nitride: GS44	Allied Signal Ceramic Components	
Silicon Nitride: GN10	Allied Signal Ceramic Components	
Silicon Carbide: Hexoloy SA	Carborundum	
Silicon Carbide: CVD	Morton Advanced Materials	
Aluminum Oxide: WESGO 99.8	WESGO	
Aluminum Oxide: Coors AD 99.8	COORS	(Not received yet)
Silicon Carbide	Norton Company	(Not received yet)
Silicon Nitride	Norton Company	(Not received yet)
Ziconia	Norton Company	(Not received yet)

2.5 Initial Grindability Test

In the original design, the specimen was mounted on a slide which was supposed to move up and down freely. But some initial tests have showed that the variation of the friction drag of the slides has significant influence on stock removal. Three different MOR bars were ground for 15 seconds under a load of 450 grams with both a coarser belt (100 grit size) and a finer belt (220 grit size). The results are summarized in Table 1.

Table 1 Initial test result

Coarser belt (100 grit size)				
Material	Initial length (IN)	Final length (IN)	Amount removed (IN)	Normalized infeed rate (mm/sec)
1	1.969	1.933	0.036	0.166
2	1.851	1.643	0.207	0.954
3	1.997	1.720	0.277	1.277
Finer belt (220 grit size)				
Material	Initial length (IN)	Final length (IN)	Amount removed (IN)	Normalized infeed rate (mm/sec)
1	1.933	1.919	0.014	0.065
2	1.643	1.560	0.083	0.382
3	1.720	1.603	0.117	0.539

2.6   Preliminary Grindability Test

After the modification of the test machine, more tests were conducted. Test conditions are as follows:

Test Condition

Belt speed: 22.86 m/s (4500 SFPM)
Load: 1000 grams
Specimen: 3×4 mm MOR bar
Wet grinding: $Q=0.5$ gal/min
Cycle time: 30 seconds

For the preliminary test, five ceramic materials were tested. Some results of stock removal are given in Figure 7. The average removal rates is given in Figure 8. It can be seen that 0.227 inches was removed for WESGO aluminum oxide, 0.189 inches for Carborundum Hexoloy SiC, 0.147 inches for Morton CVD SiC, 0.043 inches for Allied Signal silicon nitride GS44, and 0.041 inches for Allied Signal silicon nitride GN10. If WESGO aluminum oxide is chosen as reference material, the grindability of the tested materials will appear as shown in Figure 9. From this preliminary test, it can be seen that silicon nitrides, silicon carbides, and aluminum oxides have very different grindability. More tests are planned to distinguish the differences in grindability of materials from the same group, such as various silicon nitrides.
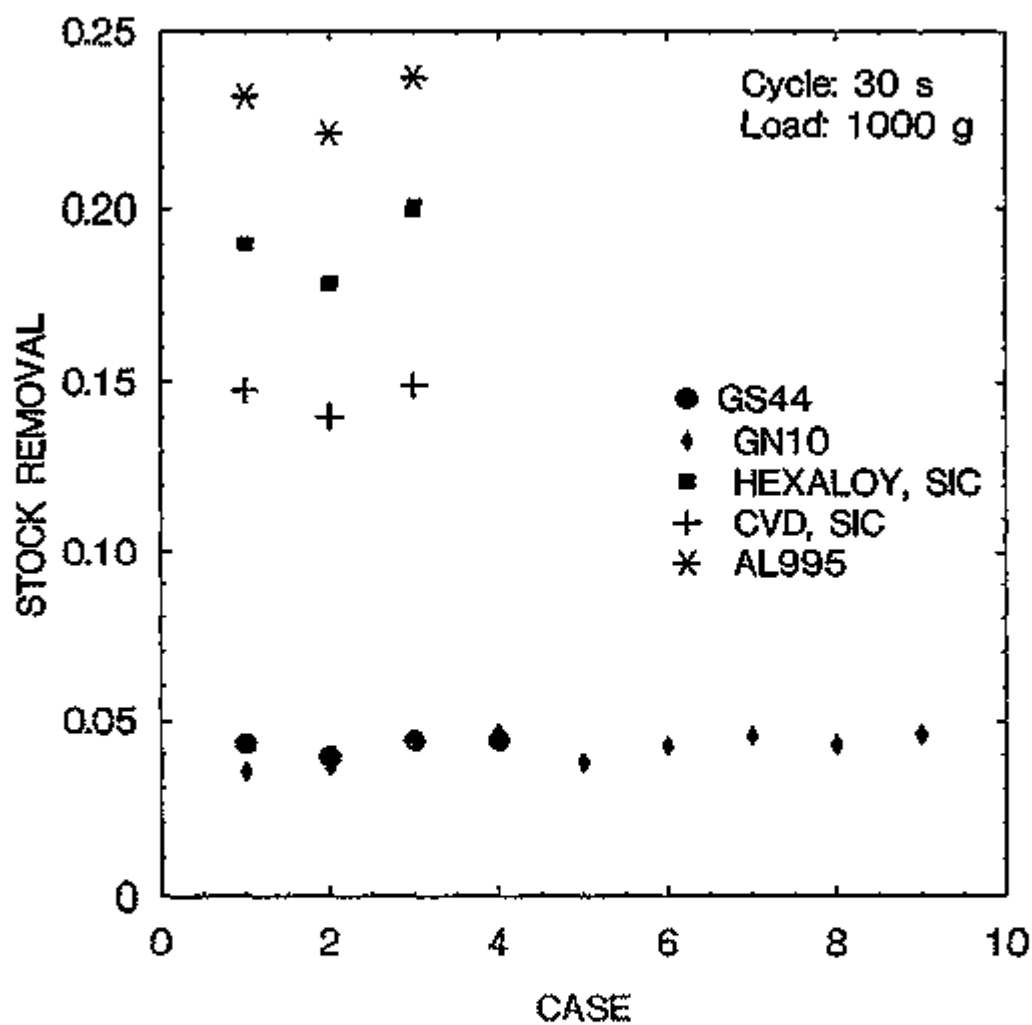
Figure 7   Stock removal for various materials tested
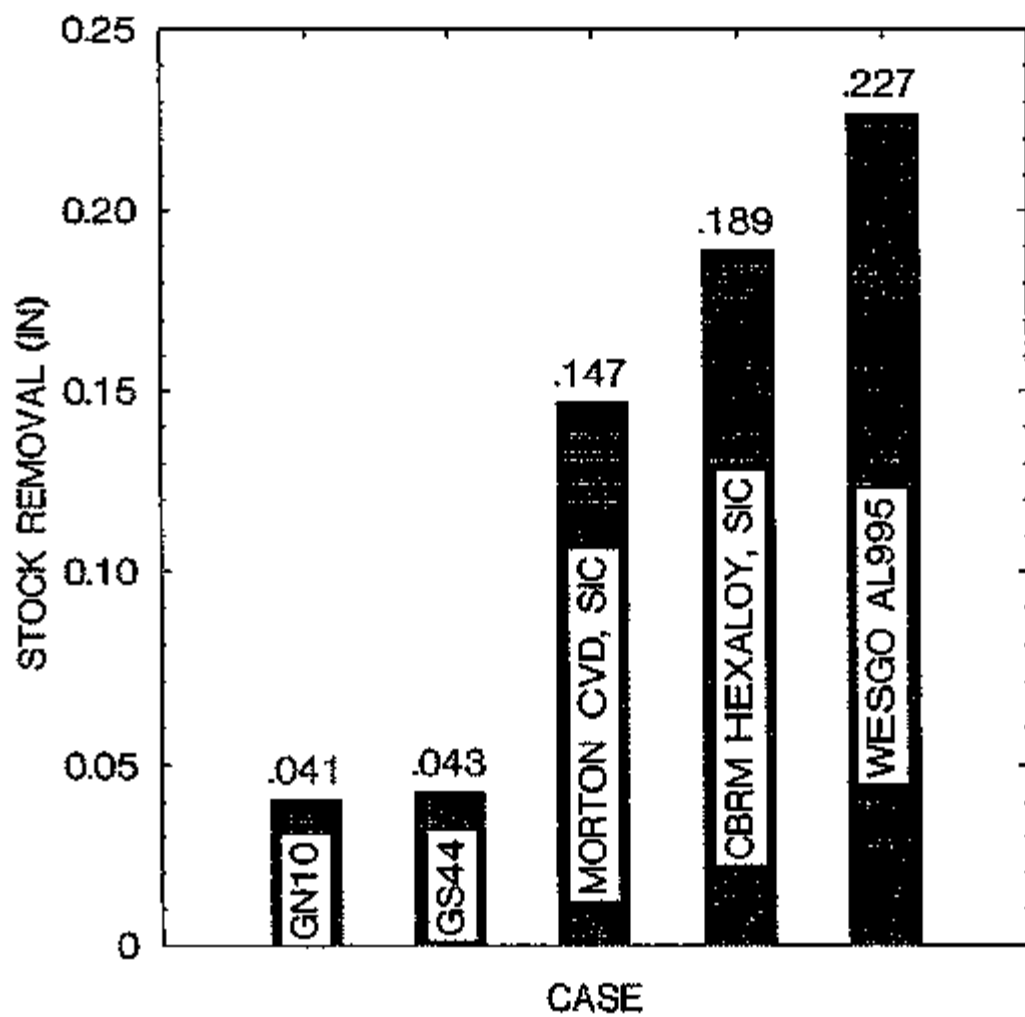
Figure 8   Average stock removal for various materials tested
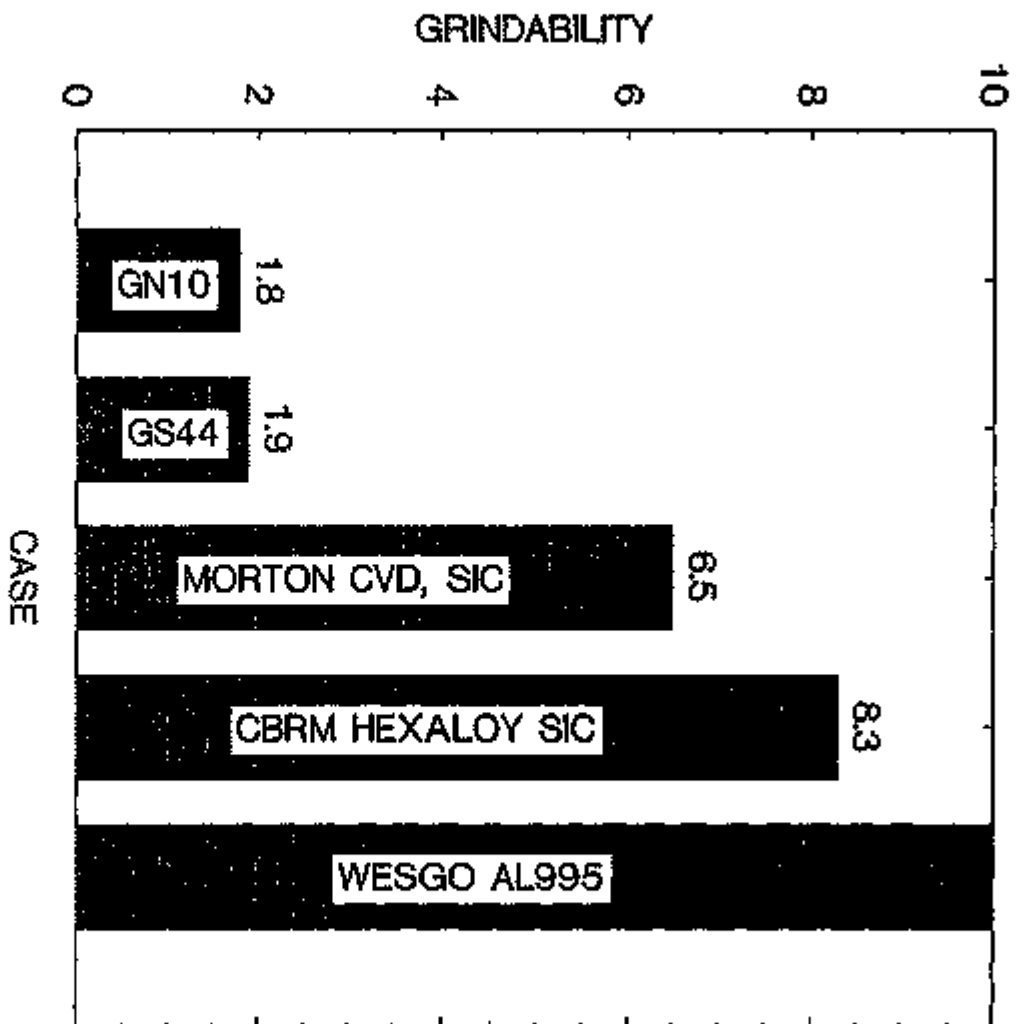
Figure 9 Grindability for various materials tested

GRINDABILITY

CASE

GN10 1.8

GS44 1.9

MORTON CVD, SIC 6.5

CBRM HEXALOY SIC 8.3

WESGO AL995

3   <u>Status of Milestones</u>

See the attached updated Milestone schedule.

4   <u>Communications/Visits/Travel</u>

On October 24, 1994, Mr Keith Costello and Mr. Natesh Krishnan attended a meeting at Oak Ridge National Laboratory. Mr. Keith Costello also did a presentation at the meeting about the program progress and the definition of the grindability.

5   <u>Problems Encountered</u>

None

6   <u>Publications</u>

A paper titled "Cost Effective Method to Determine the Grindability of Ceramic Materials" was submitted to Automobile Technology Development Contractors Coordinating Meeting, which will be presented at the conference by Mr. Changsheng Guo.

MILESTONE SCHEDULE

TASK	1993	1994	1995	B	O	A
	O N D	J F M A M J J A S O N D	J F M A M J J A S			
Literature Review	■■■■■■■■■■■■■■					
● Search	■■■■■■■■■■■■■■					
● Study	■■■■■■■■■■■■■■					
Planning	■■■■■					
● M. schedule	■■					
● G. definition	■■					
● CGTS style	■■■■					
Design	■■■■■■■					
● Level 1	■■					
● Level 2	■■■					
● Level 3	■■■					
Procurment	■■■ □□					
Fabrication	■■■■■■■■					
Experiments	■■■■■■■ □					
● Planning	■■■■					
● Specimen	■■					
● Belts	■■■					
● Testing	■■■ □					
Analysis	■■■ □					
Dsgn upgrade	□□					
Cnst upgrade	□□					
Correlation	■ □□					
Finalization	□					
● Testing	□					
● Mannual	□					
Report	■■■■■■■■■■■■ □□□□□□□□□□					
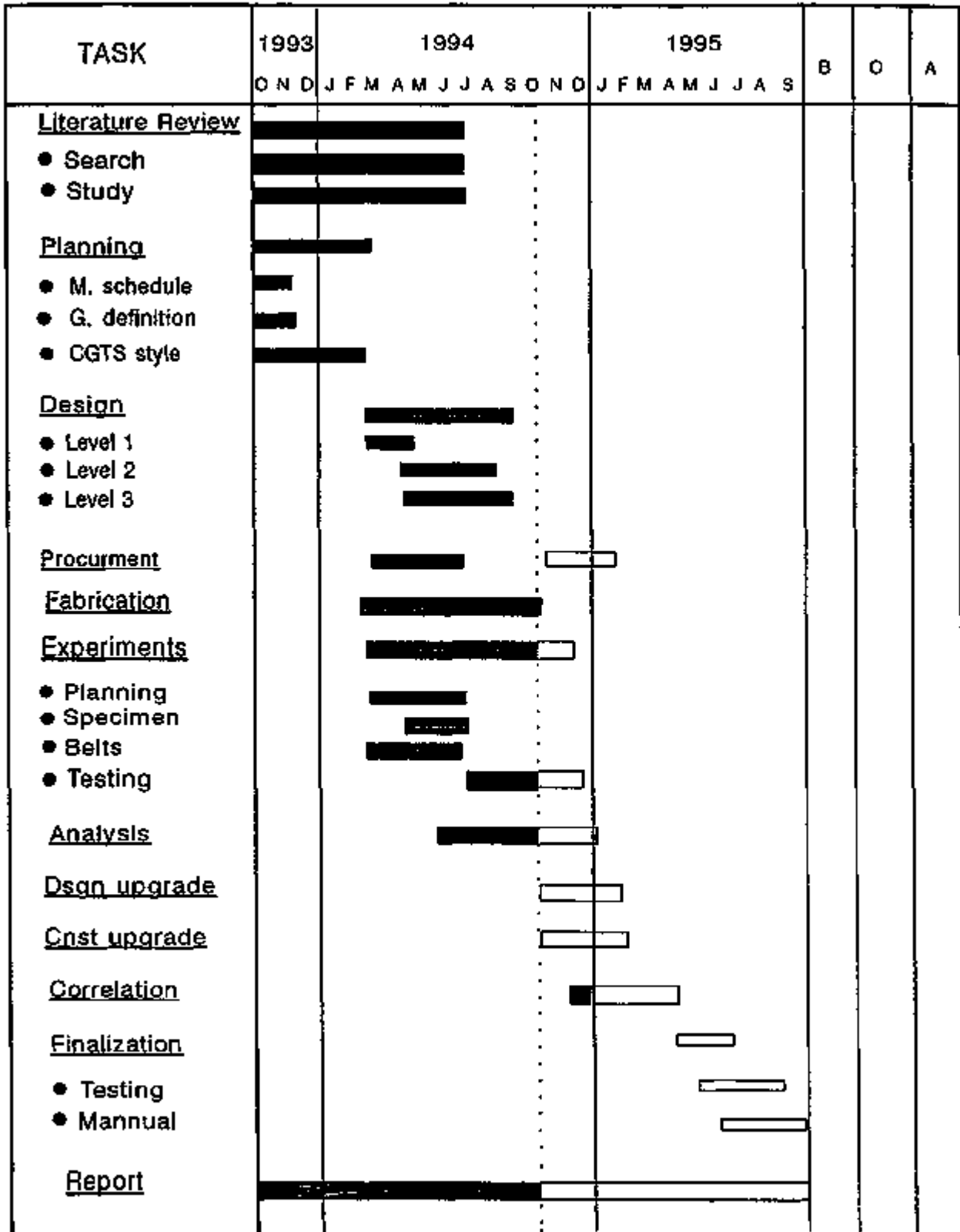
■■■■■■■■■■ To date

□□□□□□□□□□ Future

Grinding Optimization for Advanced Ceramics

Lewis K. Ives, Said Jahanmir, R. Gettings, and L. Wei
(National Institute of Standards and Technology)

Objective/Scope

The overall objective of this project is to develop guidelines and recommendations for grinding optimization of advanced structural ceramics to achieve minimum cost and maximum reliability. The following steps are being taken to achieve the objective: conduct grinding experiments jointly with industrial participants, determine effect of grinding parameters on machining damage and strength, elucidate mechanisms of material removal and damage formation, evaluate several damage detection techniques, and transfer data and information to industry in computerized database format.

Background

The goal of the ceramic machining program at NIST is to provide measurement methods, data, and mechanistic information needed by industry to develop innovative cost-effective methods for machining advanced structural ceramics. Research projects are carried out jointly with industry and academic institutions under the auspices of the Ceramic Machining Consortium. Currently, the consortium has twenty members - Ceradyne, Inc.; Cincinnati Milacron, Inc.; Corning, Inc.; Dow Chemical Company; Eaton Corporation; Eonic, Inc.; Ford Motor Company; General Electric Company; General Motors Corporation; Georgia Institute of Technology; Norton Company; SAC International, Ltd.; Stevens Institute of Technology; Texas A&M University; Torrington Company; Tower Oil and Technology Company; University of Maryland; University of Rochester; W. R. Grace & Company; and West Advanced Ceramics, Inc. Consortium members participate in these projects by providing materials, testing, advice, and other in-kind contributions. Funding for the projects, in addition to the DOE - Ceramic Technology Project, is provided by the NIST - Ceramics Division and the NIST - Standard Reference Data Program. Highlights of the projects that are funded in part by DOE are described below.

Technical Progress

Introduction

Grinding with diamond wheels is the most prevalent method of machining advanced ceramics. This machining method is highly complex and its optimization

requires detailed knowledge of many interdependent factors. The major elements of a grinding system are the grinding wheel, the grinding fluid, the machine tool, and the workpiece. Each of these is associated with several parameters that can influence the grinding process. For example, the type of diamond grit, its size and concentration, as well as the bonding material control the behavior of the grinding wheel. The chemical and physical properties of the grinding fluid, and method of delivery to the grinding zone contribute to the grinding rate and the quality of finished surface. The variables used in grinding such as feed rate and wheel surface speed, and the machine tool characteristics such as stiffness and vibration are major factors in grinding. The workpiece material and its properties are important factors in the selection of the grinding parameters since each material responds differently to the grinding action.

Optimization of the grinding process consists of finding the most appropriate set (or sets) of parameters to be used for each material such that a maximum machining rate is obtained and at the same time relevant performance parameters such as strength and/or surface roughness are maintained at the required level. This objective requires data and information on the effect of grinding parameters on material removal rate, strength, surface roughness, surface integrity, residual stress and others. In addition to these data, detailed information on the mechanisms of material removal processes, and reliable methods for damage detection are required.

Grinding Optimization

The primary focus of the program is on determining the relationship between grinding conditions and grinding induced surface damage. In general, surface and subsurface cracks are the most important form of machining damage in ceramics, and in other brittle materials as well. At the present time there is no suitable non-destructive means for characterizing machining damage and relating the damage characterization measurements to performance. Instead, a performance test is conducted to assess the effects of machining damage. In this program a flexure test utilizing the four-point bending configuration is used to determine the influence of grinding conditions and the related damage on flexure strength. Details of the flexure test procedure which is being employed are described in ASTM Standard C1161.

Once the grindability data is obtained and carefully evaluated, it will be incorporated in a PC database which will be available on floppy disks. In addition to strength data, data on surface roughness, grinding forces, and wheel wear will be included in the database. The design and search structure of the database program were formulated by NIST with technical guidance from Consortium members.

Currently, work is underway to generate grindability data for three different silicon nitride ceramics. They consist of a reaction bonded material (RBSN), a sintered reaction bonded material (SRBSN), and a sintered material (SSN). In addition to being prepared by different processing methods, the materials differ in composition, microstructure and mechanical properties. The SRBSN and SSN materials are homogeneous, low porosity, high strength ceramics while the RBSN material has a relatively high porosity and comparatively low strength. Selection of the materials (provided by consortium

members), choice of grinding parameters, and the general approach taken in the present test program were established by two preliminary series of tests described in previous reports. The present effort can therefore be treated as the third phase of a program to develop grindability data for the selected materials.

Four test parameters with two values for each were chosen for evaluation. These parameters are given in Table 1. Three of the parameters, down feed, table speed, and wheel grit size, are grinding variables which can have a direct effect on the introduction of damage. The fourth parameter, grinding direction, concerns the anisotropy of the damage introduced by the reciprocating grinding method employed, and the sensitivity of the flexure test to that anisotropy. Thus, it is generally found that the plane of microcracks introduced by grinding tends to lie parallel to the direction of grinding. The greatest sensitivity to these microcracks is observed when the tensile axis of the four-point-bend flexure test specimen is perpendicular to the plane of the microcracks and the corresponding grinding direction. Therefore, the greatest sensitivity to grinding damage is expected when the grinding direction is perpendicular to the long axis of the test specimen, and the least sensitivity when grinding is parallel to the long axis of the test specimen.

Table 1. ASSIGNED VARIED PARAMETERS

CONDITION	1	2
TABLE SPEED	0.025 m/s (4.9 ft./min.)	0.125 m/s (24.6 ft./min.)
DOWN FEED	0.050 mm (0.002 in.)	0.125 mm (0.005 in.)
WHEEL GRIT	140/170	80/100
GRINDING DIRECTION	Longitudinal	Transverse

To evaluate the three silicon nitride ceramics for all combinations of these parameters would require 1440 specimens, recognizing that 30 specimens for each condition are needed for reliable Weibull statistical evaluation. Eight consortium

members agreed to conduct grinding experiments. However, for each member to evaluate all combinations of conditions would be prohibitively expensive, both in terms of the number of specimens required and the amount of time necessary for grinding and testing. A design of experiments approach was taken resulting in a test matrix that required each member to assess four combinations of conditions for each of the three silicon nitride materials. This reduced the required number of specimens to 2880 (360 per member). The design incorporated two repetitions of each combination of conditions by two different members, thereby providing for an evaluation of experimental reproducibility. Additionally, two members have volunteered to carry out optional tests which will examine certain conditions that lie outside the bounds of the formal test framework. These optional experiments include an investigation of creep feed grinding , the measurement of grinding forces, and the determination of grinding wheel wear. An outline of the basic steps to execute the planned grinding experiment is as follows:

- Obtain billets of silicon nitride materials and prepare 3000 flexure test bars according to the procedures and specifications in ASTM Standard C1161-90. The bar dimensions are those prescribed in the ASTM Standard for a B-size bar (3.0 mm thick by 4.0 mm wide by 45+ mm in length), except the thickness is set at 3.125 mm to allow for material removal during experimental grinding. In addition, chamfers are not ground on the edges of the face which will be subjected to experimental grinding. This face is the tensile face in the flexure test.

- Numbered each specimen to identify batch, billet, and location in the billet. To minimize the possible bias associated with the variation in specimen properties due to systematic batch-to-batch or other preparation differences, randomly select specimens in sets of 30 for assignment to the participating consortium members.

- Prepare detailed instructions for each participant describing grinder setup, specimen mounting, wheel mounting and dressing, and data reporting. Package each set of specimens together with the assigned grinding conditions and ship to each participant.

- Together with the specimens, deliver to each participant two specially prepared resin-bond diamond-grit grinding wheels (140/170 grit and 80/100 grit prepared by one consortium member under controlled conditions for this project).

- Each participant conducts grinding according to instructions.

- Final two chamfers are applied to experimentally ground face by a single.

- Flexure strength tests and fractographic examination conducted at NIST.

- Surface roughness measured at NIST.

- Statistical evaluation of data done at NIST.

- Data introduced into database.

At the end of this reporting period, six members had completed their assigned grinding tasks and flexure tests have been carried out at NIST on these specimens. Preliminary Weibull statistical evaluation had also been carried out using a maximum likelihood fitting method with unbiasing to determine characteristic strength and Weibull modulus for each material and combination of grinding conditions. Typical Weibull plots are shown in Fig. 1 and 2. The fit to the Weibull probability curve is seen to be very good in Fig. 1, while for Fig. 2 the fit is relatively poor at low strength values. Although good fit does not necessarily signify that failure was due only to a single flaw population, for the case of Fig. 1 fractographic examination indicated that all failures could be associated with machining induced microcracks. For Fig. 2, failures were found to be associated with machining flaws and with inherent inclusions. It is clear that in the assessment of the influence of machining damage on flexure strength, account must be taken of the flaw population that is responsible for failure.

WEIBULL PLOT FOR SSN (TEST 2-10)

CONDITIONS: TABLE SPEED = 0.025 m/s (4.9 (L/min.)
DOWN FEED = 0.125 mm (0.005 in.)
WHEEL GRIT = 140/170
DIRECTION = Transverse

σ_θ = 478 MPa
m = 25.8

PROBABILITY OF FAILURE, %

FRACTURE STRESS, MPa
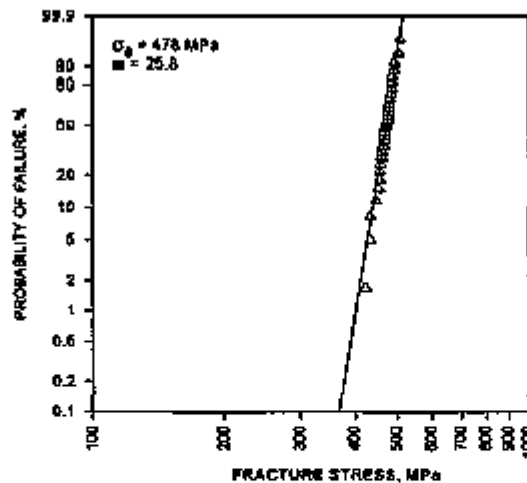
Figure 1. Weibull plot of strength data for the SSN material for one combination of grinding conditions
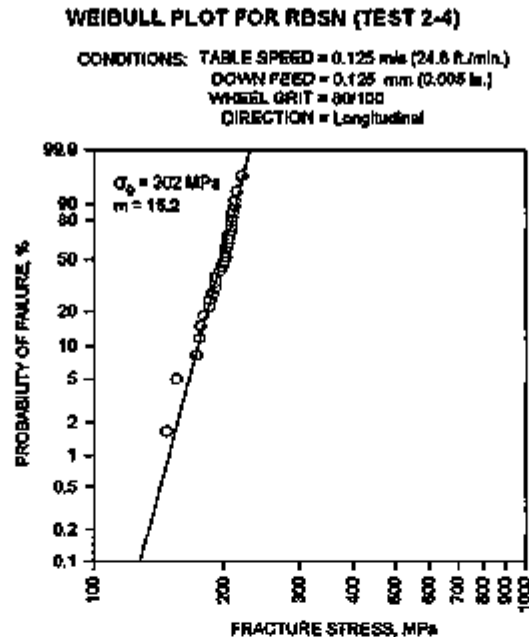
Figure 2. Weibull plot of strength data for the RBSN material for one combination of grinding conditions.

Figures 3 and 4 present a summary of the results obtained so far with respect to the influence of grinding conditions on flexural strength for the three silicon nitride materials studied. The grinding conditions plotted on the abscissa are designated by the numbers 1 and 2 which refer to values given in Table 1. The least severe combinations are located at the left end of the scale and the most severe conditions at the right. The final ranking of each combination of conditions will, of course, be determined by the outcome of the tests. Results for specimens ground in the longitudinal direction are shown in Fig. 3. For reference, the strength values for each material that were obtained using grinding conditions meeting specifications given in ASTM C1161 are also included in the graph. The ASTM procedure was designed to minimize the influence of grinding damage on flexural strength in order to permit the determination of the inherent strength of the material. The results show that for the longitudinal direction the grinding conditions chosen had essentially no effect on flexure strength.

For the transverse direction, the results shown in Fig. 4 indicate that there is a reduction in strength for all combinations of grinding conditions. None of the conditions or combinations of conditions appears to have a significantly stronger influence than the others. However, this outcome may change as more data is included and a more thorough statistical evaluation is carried out.
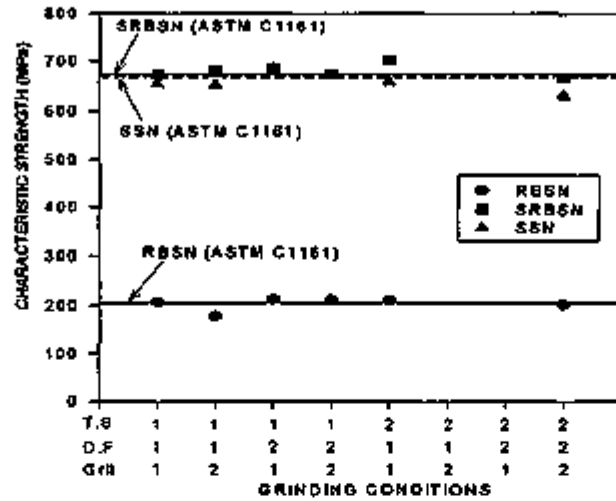
Figure 3. Characteristic strength values for silicon nitride materials ground in the longitudinal direction with different combinations of grinding conditions.
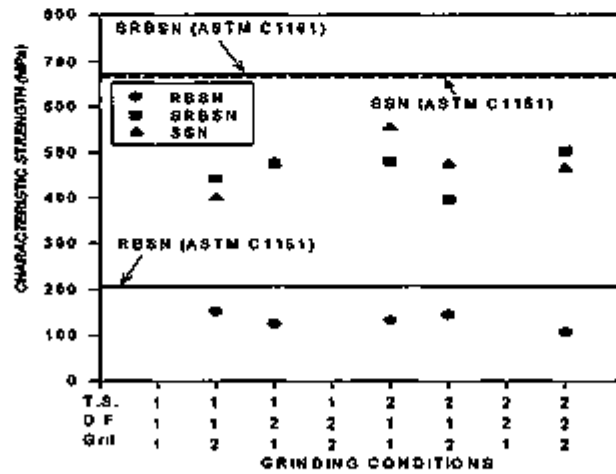
Figure 4. Characteristic strength values for silicon nitride materials ground in the transverse direction using different combinations of grinding conditions.

Grinding Force Measurements

In order to evaluate the grinding response of the three selected silicon nitrides in comparison with other types of silicon nitride materials, grinding forces were measured under controlled conditions. In these experiments the effect of grinding parameters and fluids on grinding forces were determined for five types of silicon nitrides: RBSN, SRBSN, SSN, HPSN, and HIPSN. Three commercial grinding fluids designated A, B, and C were used.

The average normal and tangential grinding forces per unit width for the five silicon nitride ceramics using grinding fluid B are plotted in Fig. 5 as a function of equivalent chip thickness. The data for each material was first analyzed statistically and straight lines were drawn through the data points using the least square method. The correlation coefficient R^2 ranged from 0.85 to 0.99. Statistical analysis of the force data confirmed that the grinding forces for SRBSN, SSN, HPSN, and HIPSN were essentially equivalent without significant difference at a 95% confidence level. The same analysis confirmed that the grinding forces for RBSN were consistently lower than for the other silicon nitrides. Figure 5 shows that, as expected, the grinding forces increase as the grinding severity, or the equivalent chip thickness, is increased.

The tangential grinding forces F_x were used to calculate the specific grinding energies u_c, defined as the total grinding energy per unit volume of removed material;

$$u_c = F_x / (b h_{aq})$$

where b = workpiece width and h_{aq} is the equivalent chip thickness. Plots of specific grinding energy versus the equivalent chip thickness indicated that the grinding energy decreases as the h_{aq} is increased. However, due to the scatter in the data, it was not possible to obtain a definite trend. Therefore, all the data for each material were used to obtain an average value for the specific grinding energy. Considering the average values and the standard deviations, it was concluded that the specific grinding energies for SRBSN, SSN, HPSN, and HIPSN are equivalent, but the specific grinding energy for RBSN is lower.

The grinding forces using fluid B are plotted in Fig. 6 to compare the force ratios, F_x/F_z where F_z is the normal force. Considering the scatter of the data in Fig. 6, it is concluded that the force ratios of the different silicon nitride ceramics are not significantly different and that the grinding conditions do not significantly affect the force ratio. The average force ratio for the silicon nitrides, given by the slope of the linear best fit curve to the data points, is approximately 0.12. According to Malkin[1] this ratio is equivalent to the friction coefficient for sliding of the abrasive particles against the workpiece. In agreement with Malkin's finding, the force ratio obtained from Fig. 6 is approximately equal to the friction coefficient for synthetic diamond films sliding against silicon nitride or silicon carbide at room temperature and in air, which has been found to range from about 0.08 to 0.20[2-4].
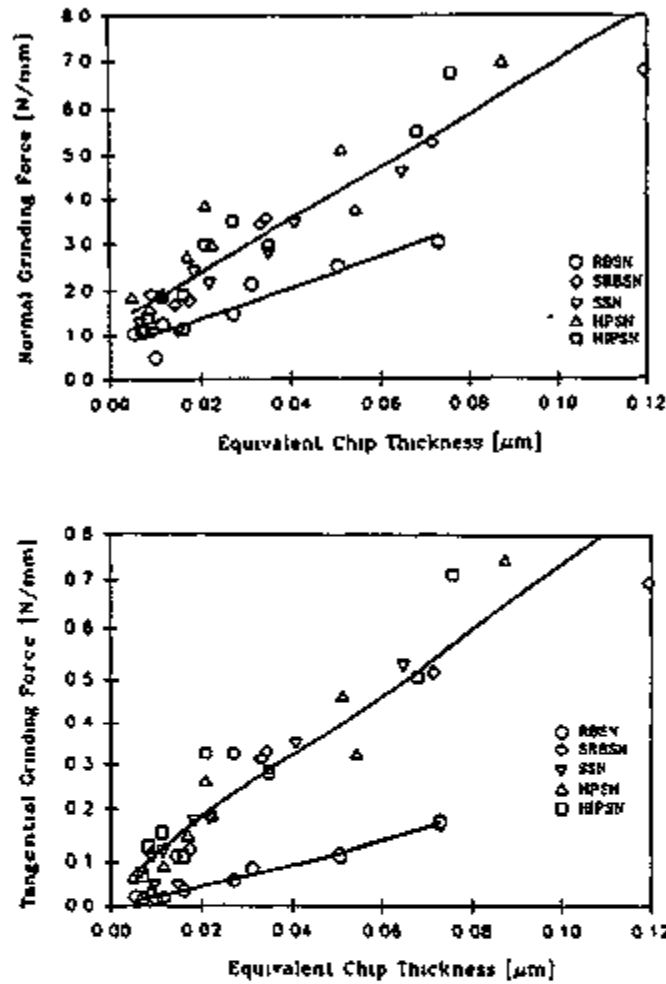
Figure 5. Normal and tangential force components for grinding of different silicon nitrides using grinding fluid B in down-grinding configuration.

A series of tests were conducted using a factorial design of experiments in which the table speed and depth of cut were used as the primary variables. The values of the coefficients for the main effects and the interaction effects were normalized with respect to the grand average for each material. The following conclusions were made: 1) The effects of both table speed and depth of cut are significant and increasing either parameter increases the magnitudes of the grinding force components. 2) The interaction effects between table speed and depth of cut are significant, but the interaction effects are not as large as the main effects. This implies that increasing both the depth of cut and table speed increases the grinding forces by a factor larger than associated with either of the parameters independently. 3) The interaction effects on the tangential force is equal to or greater than the interaction effects on the normal force.
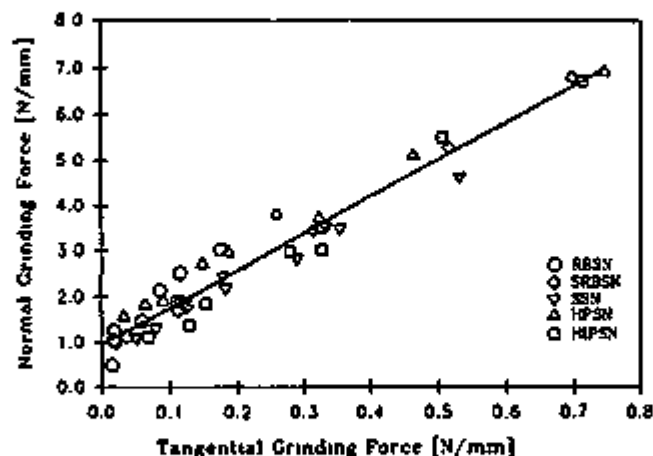
Figure 6. A plot of the normal grinding force versus the tangential grinding force for different silicon nitrides using grinding fluid B in down-grinding configuration.

It is important to note that the response of ceramic materials to grinding is strongly influenced by the type of grinding wheel and the condition of the abrasives in the wheel. For example, the type of bond, diamond type, grit size and concentration, bond porosity, and dressing and truing conditions are important parameters. Therefore, the results presented in this report may differ from those obtained under other conditions. For example, the magnitude of grinding forces increases readily as the diamond particles wear and become dull Spur[5]. Therefore, the sharpness of the diamond particles as they enter the grinding zone is an important parameter, which depends on the initial dressing condition, prior usage of the wheel, grinding parameters, grinding fluid, etc.

Thermal Wave Studies

The objective of this task is to evaluate the feasibility of the thermal-wave measurement technique for detecting and characterizing machining damage in ceramics. In general, three types of cracks can be produced in ceramics by grinding: lateral cracks (parallel to the surface), median and radial cracks (perpendicular to the surface), and small intergranular and transgranular microcracks.

The thermal-wave measurement technique is a powerful tool for evaluating the thermal properties of materials. The technique is based on the measurement of the temperature distribution (both in time and in space) generated by localized heating of the material being tested. It has the advantage of being both non-destructive and non-contact, and is capable of providing information on thermal properties as a function of depth below the surface. In the present study, the samples were heated locally by a modulated laser beam. The modulated heating generates a varying temperature field, i.e. thermal

wave, in the sample and in the medium (air in these experiments) above the sample. A modulation in the index of refraction is associated with the thermal wave in the air. A probe laser beam passing through the air near to the sample surface is deflected by the change in index of refraction, and can therefore be used to monitor the thermal wave as a function of both time and position. This method is sometimes referred to as the mirage-effect thermal wave technique. Since the presence of surface and near surface microcracks changes the local thermal flux, the thermal wave technique is capable, in principle, of detecting these defects.

In the work reported here, controlled damage was introduced into alumina specimens by a series of scratches made with a hardness indenter. The scratches were then analyzed both by the thermal wave measurement technique and by an ultrasonic detection method. The scratches were made at two loads (20 N and 40 N). Scratches using a single pass and multiple passes (up to 8) were introduced. Aluminas having two different grain sizes, 3 and 9 μm, were studied. For the thermal wave measurements, the radius of the heating beam was 10 μm and that of the probe beam was 15μm. A raster scan of specimens was performed to generate an image. The image consisted of a background level from the material, and peak signals from local temperature rise due to the reflection of thermal waves from defects, for example, cracks in the material.

The ultrasonic examination was performed on the samples immersed in water using a 100 MHz transducer. For these measurements, the normal incident compressional waves were used to detect scratches.

These and other results are currently being examined to distinguish the signals associated with the different types of damage produced by scratching, for example, surface topography changes, grain pull-out, subsurface cracks, intergranular microcracks, etc.

Status of Milestones

1. Prepare 300 specimens ground under "best in-house" conditions to establish bounds for a more extensive data program (9/1/92 completed).

2. Complete fracture testing, characterization, and preliminary statistical analysis of data (12/1/92 completed).

3. Evaluate feasibility of thermal wave measurement on selected flexure specimens ground under different conditions (4/1/93 completed).

4. Select grinding conditions based on statistical design of experiments, and distribute additional 2000 flexure bars for grinding (6/1/93 completed).

5. Develop a preliminary database structure to be used for data collected in this study and those collected from literature (9/1/93 completed).

6. Measure grinding forces, and evaluate the effects of down feed, table speed, wheel grit size, and grinding fluid (1/1/94 completed).

7. Characterize fracture strength and surface roughness of 2000 flexure bars prepared with three different silicon nitride materials (4/1/94 delayed until 10/1/94 completed).

8. Compare the results of thermal wave measurement with ultrasonic evaluation of the selected samples ground under different conditions (7/1/94 completed).

9. Evaluate the test results on fracture strength and surface roughness and develop guidelines for grinding optimization of selected materials (12/1/94).

10. Issue a final report on evaluation of machining damage by thermal wave and ultrasonic techniques (2/1/95).

11. Select three other types of ceramics for the next phase of the project and arrange for the billets from consortium members (4/1/95).

12. Add recent data to the database and arrange for testing of the prototype by the consortium members (8/1/95).

Publications

1. H. S. Ahn, L. Wei, and S. Jahanmir, "Non-destructive Detection of Damage Produced by a Sharp Indenter in Ceramics," manuscript accepted for publication in Proceedings of Symposium on Measurement and Inspection of Products and Processes, ASME Winter Annual Meeting, Chicago, IL, Nov 13-17, 1994.

2. S. Jahanmir, T. W. Hwang, E. Whitenton, L. Job, and C. Evans, "Measurement and Characterization of Forces in Grinding of Silicon Nitride," paper accepted for Tribology Symposium, ASME Energy and Environmental Expo 95, Houston TX, Jan 29 - Feb 1, 1995.

3. T. Strakna, S. Jahanmir, R. Allor, and K. Kumar, "Effect of Grinding Direction on Strength of Silicon Nitride," submitted for presentation and publication in *Transactions of NAMRI/SME*, May 24-26, 1995.

References

1. S. Malkin, *Grinding Technology*, John Wiley and Sons, New York (1989).

2. S. Jahanmir, D. E. Deckman, L. K. Ives, A. Feldman, and E. Farabaugh. "Tribological Characteristics of Synthesized Diamond Films on Silicon Carbide," *Wear*, Vol. 133, 73 - 81 (1989).

3. A. K. Gangopadhyay, and M. A. Tamor, "Friction and Wear Behavior of Diamond Films Against Steel and Ceramics," *Wear*, Vol. 169, 221 - 229 (1993).

4. M. N. Gardos, "Tribology and Wear Behavior of Diamond," in *Synthetic Diamond: Emerging CVD Science and Technology*, K. E. Spear and J. P. Dismukes (Eds.), John Wiley and Sons, New York, NY, 419 - 504 (1994).

5. G. Spur, C. Stark and T. H. Tio, "Grinding on Non-Oxide Ceramics Using Diamond Grinding Wheels," *Machining of Ceramic Materials and Components*, K. Subramanian and R. Komanduri (Eds.), American Society of Mechanical Engineers, PED - Vol. 17, 33 - 44 (1985).

Chemically Assisted Machining of Ceramics

S. M. Hsu, Y. N. Ying, and C. J. Hsu
(National Institute of Standard and Technology)

Objective/Scope

The ceramic industry has identified the lack of a rapid low cost ceramic machining technology as one of the major barriers for widespread use of ceramics. Current machining technology for ceramics is slow and labor intensive. Residual surface damage on machined surface and the characterization of such surface defects are the key industrial concerns. This project aims to increase the machining rate of ceramics using chemical reactions at the interface. The chemical reactions at the interface could change the hard ceramic surface into something softer hence reduce the contact stresses and damage. The reaction product layer produced could also change the conditions at the interface between the diamond abrasive and the ceramic surface reducing the wear of the diamond thus increasing the machining rate. Si_3N_4 is the main material of focus, but other materials such as SiAlON or SiC may be examined.

The project involves several subtasks including:

1. Development of a bench test simulation to allow screening of chemistries under well-controlled conditions.

2. Identify new chemistries that can significantly improve the machining rate of ceramics, especially for silicon nitrides.

3. Provide understanding on the working mechanisms of the chemistries identified and develop correlations with the surface quality of the machined surface.

4. Establish limits of performance and applicability of the chemistry on different material compositions and processes. Establish optimum machining conditions for each chemistry, material combinations.

5. Examine the environmental impact of the chemistry and work with industrial partners to optimize the chemistry and introduce the technology into practice.

Technical Progress

A two-prong approach has been taken: screening of chemicals on the small bench cutter; validate the results on the surface grinder. Additionally, nano-scratch tests and single diamond scratch tests are used to study the mechanisms when needed.

Bench Cutting Tests

Research on chemical screening and looking for chemical trends using the diamond cutting wheel on silicon nitride continues. Additional chemicals were screened and the correlation reported

last time was reexamined. The characteristic cutting curve for most fluids tested has a steep initial slope followed by a gradual leveling off in cutting rate. The steady state cutting rate was plotted against the surface tension divided by density on a log-log scale in Figure 1. A clear trend of increasing cutting rate with the decreasing ratio of surface tension to density can be seen. A low surface tension to density ratio may suggest the relative ease of the fluid to penetrate into the cutting edge.

In the course of screening of chemicals, we have noticed that the different blades sometimes influence the outcome. A new blade has a 127mm diameter and as the blade was used to cut ceramics, the blade becomes sharper as well as the diameter decreases. Figure 2 shows the result of a study using water as the cutting fluid with five used cutting blades. The steady state cutting rate can increase almost three fold when a new blade of 127.16 mm progresses to a worn blade of 124.24 mm. Profilometer traces of the leading edges of these blades are shown in Figure 3. The continuous change of the cutting blade introduces a systematic error in the data. To correct for this factor, a simple mechanical truing technique was developed to reshape the wheel after each experiment. The edges of the wheel were made square each time by counter-rotating the cutting wheel against a flat diamond wheel surface. A reference fluid was also used to periodically calibrate the MRR of the decreasing wheel diameter effect. This way, consistent steady state MRRs have been achieved.

The parametric correlation study on the silicon nitride cutting data suggested that the steady state material removal rate (SSMRR) increased with molecular weight, density, and decreased with surface tension. By selecting chemicals with these properties, we discovered a new chemical, AD6341. It is chemically inert, nonflammable, has high thermal stability, good lubricity, high dielectric strength, high density, low compressibility, good miscibility with common solvents, and nonpolar organic chemical. It has a SSMRR of approximately 0.1 mm^3/s. This is an order of magnitude faster than the mineral oil family, and two orders of magnitude faster than Meqqem, the commercial water based fluid. The chemical was tested on the surface grinder, the results were encouraging. However, a high pitch noise was produced during grinding. Upon closer examination, it was discovered that the fluid had a high volatility and caused cavitation at the exit zone of the contact. This produced the noise. From this result, we have incorporated additional requirements for the fluid screening.

Grinding tests

Several grinding tests were conducted under constant load using two fluids, 3% meqqem in tap water (a commercial grinding fluid) and a candidate fluid CM011. The purpose was to examine the relationship between the material removal rate and the grinding forces under these two fluids. The first group of test was conducted in 3% meqqem in tap water, the preset grinding depth was 1.016 mm, and the tangential load was 22, 27, 31, 36, 45, 67 N. The material ground was a silicon nitride supplied by Kennametal. The sample was 20.3 × 20.3 × 6.35 mm. Two of these samples were aligned together and the length of the test sample bed was 40.6 mm. The schematic diagram for the grinding experiment was shown in Fig. 4. Under different tangential loads, the speed of the sample moving relative to the grinding wheel varied somewhat. The measured forces in X and Z direction and sample traveled distance were recorded. The material

Cutting Experiment
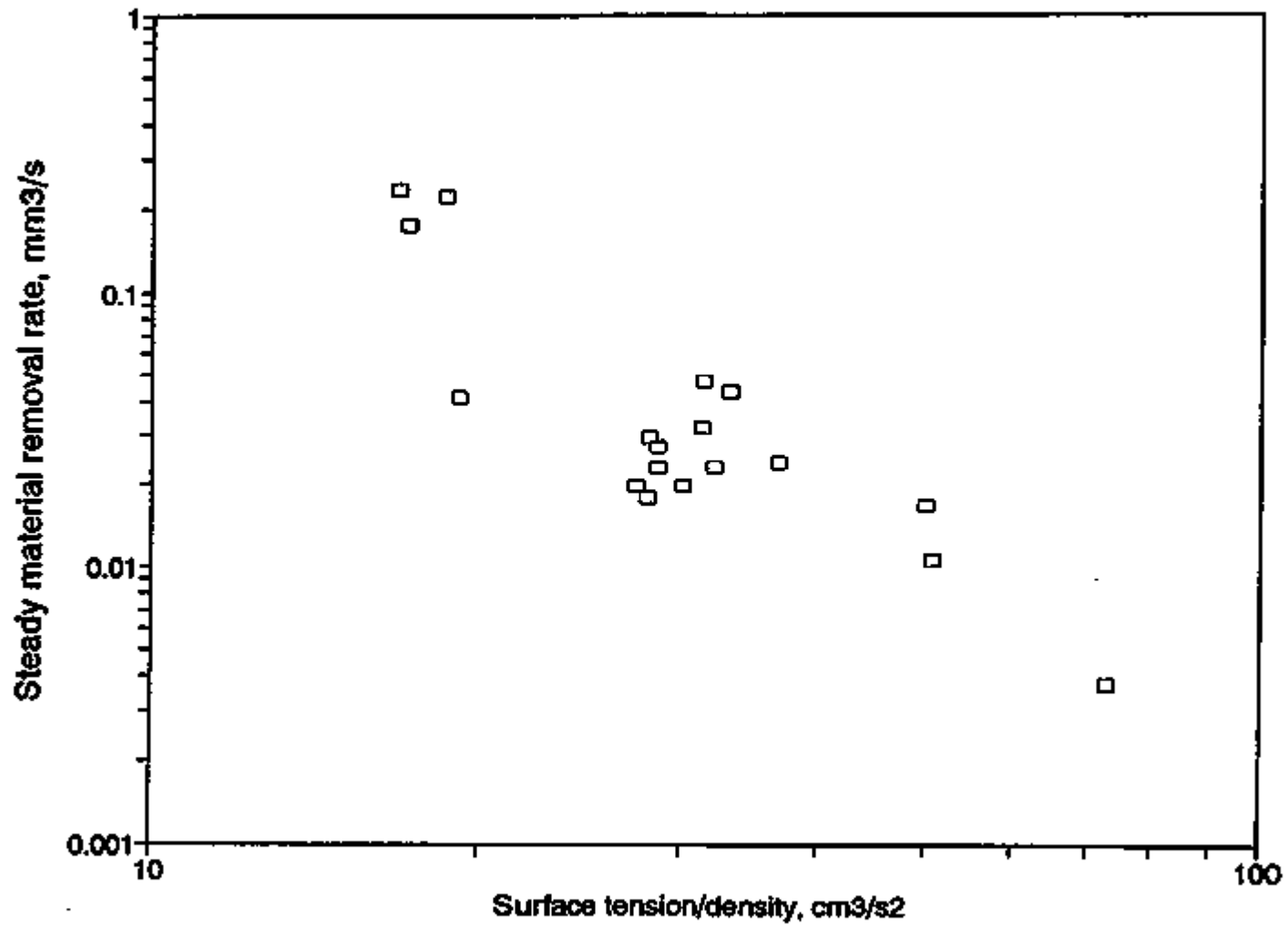
Fig. 1   Material removal rate is a function of surface tension and density.

Diamond Wafering Blade Wear
LECO 801-136, Cer096 Si3N4 sample
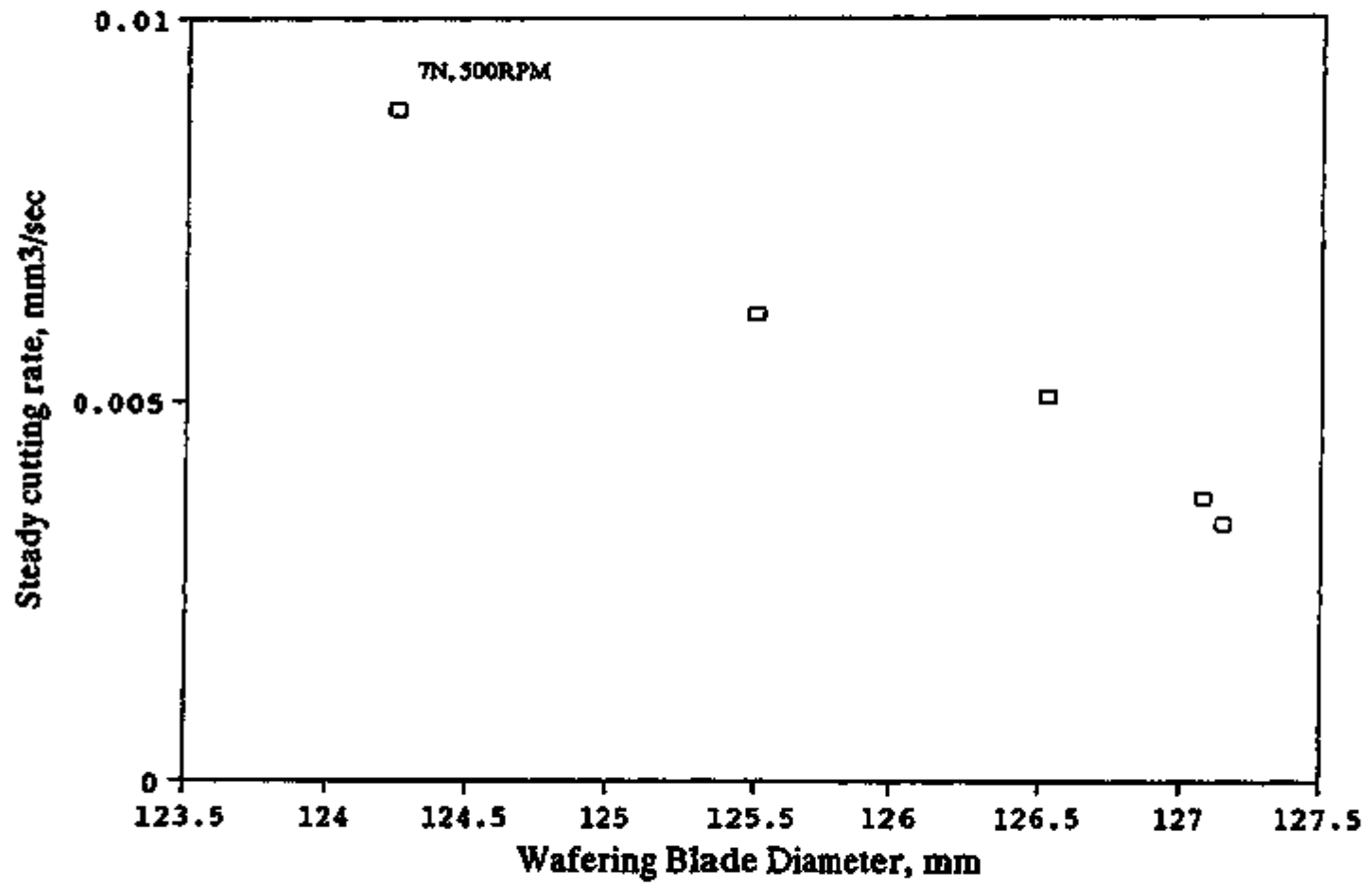
Fig. 2   Geometry of the cutting wheel affect on the material removal rate.

Profilometer probe tip

LECO diamond wafering blade

127.2 mm dia.

124.2 mm dia.
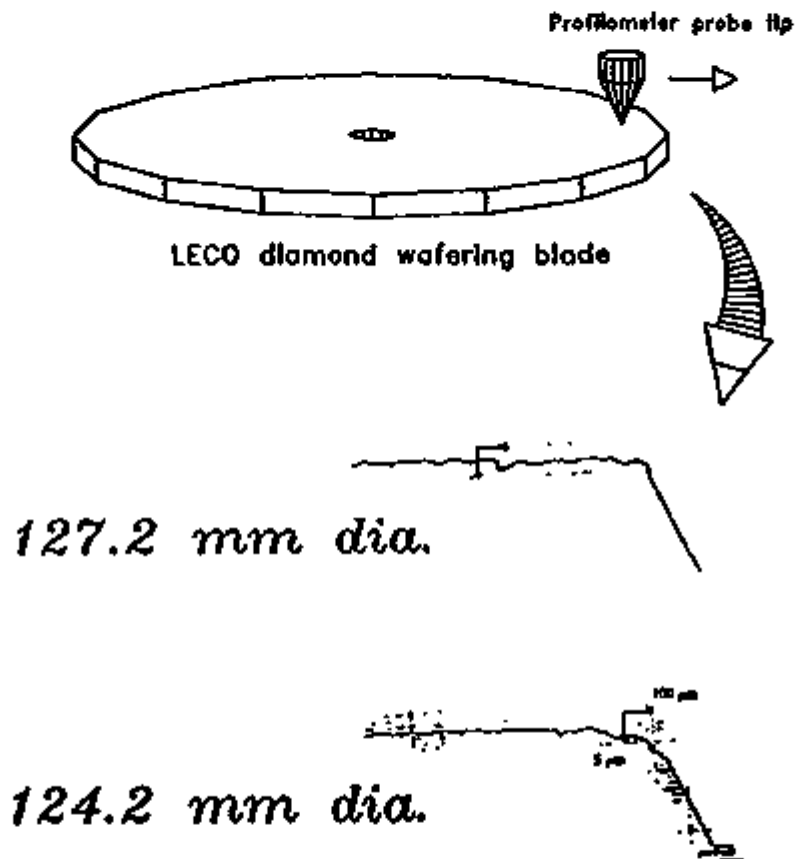
Fig. 3   Profile shapes of two cutting wheels.
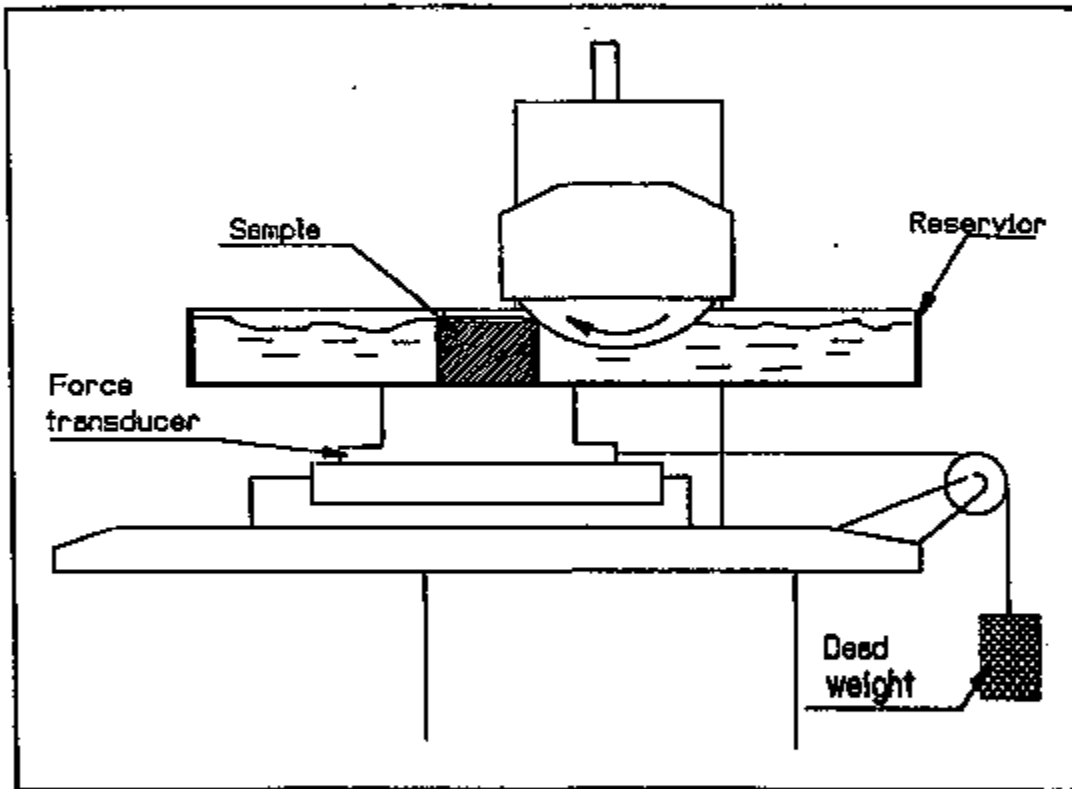
Fig. 4   Constant loading grinding schematic diagram.

removal rate for this experiment was calculated by the following equation

$$V=hwl \qquad \qquad (1)$$

where h is the grinding thickness (preset overlap, 1.016 mm); w is the width of the sample (6.35 mm); l is the sample length (40.6 mm). The volume removed divided by the grinding time gives the material removal rate.

The data for the 22 N load are plotted in Fig. 5. After few seconds of grinding, the wheel stops advancing forward, rotating but not removing any material from the sample. This is indicated by the displacement value. This trend repeats as the load is incresed until 36 N. Fig. 6 shows the force curve and the displacement. The grinding wheel continues and finishes the grinding under the constant tangential load. This is significant. This suggests that there is a transition load. When the load is lower than 36 N, the grinding wheel grinds into the material, after moving a little, the sample is stopped and no further material is removed even though the wheel is churning. At 36 N, the wheel grinds through. This load then can be defined as the **lower critical load** for fast grinding. This data and the comparison data for the candidate fluid CM011 are shown in Fig. 7 as a function of the tangential loads. For the candidate fluid, the transition load occurs at 9 N instead of 36 N and the material removal rate is much higher than the reference fluid.

At high preset overlap such as 1 mm, the contact area is relatively large and the average contact pressure could be relatively low. To investigate the effects of the fluids at high contact pressure, the preset overlap was reduced to 50 μm. At this overlap, the 67 N tangential load can result in much high contact pressure since only some of the diamond grit will scratch the surface. The material removal rate at this setting for both meqqem and CM011 are shown in Fig. 8. Under this condition, there appears to be a upper limiting load beyond which any increase in tangential loading does not increase the material removal rate. This load can be defined as the **upper critical load** for fast grinding.

This upper limit of the material removal rate is probably due to the reduction in grinding depth. The grinding depths were measured after each test. The depth is a function of the tangential load, especially when the preset overlap is small. Thus, the removal volume is calculated by multiplying the measured depth, h instead of the preset overlap. Two examples of measured depth of ground grooves are shown in Fig. 9 a and b. When the tangential load is 22 N, the average depth of the ground groove is 36 μm, and when the tangential load is 67 N, the depth is only 18 μm under the same preset overlap of 50 μm.

The test results show that for a grinding coolant, the material removal rate changes as a function of the tangential loading. There is a lower critical load L_1 and a upper critical load L_u. If the tangential load is below the lower critical load, the material removal rate is very small. If the tangential load is higher than the upper critical load, any increase in the tangential loads will not increase the material removal rate. What are the role of the additional pressure on the sample?

For a small overlap depth, the contact distance of the grinding wheel and the workpiece is short, and the mean contact pressure on the workpiece is high. The concentration of diamond

G62 3% Meqqem 1.016 mm thick
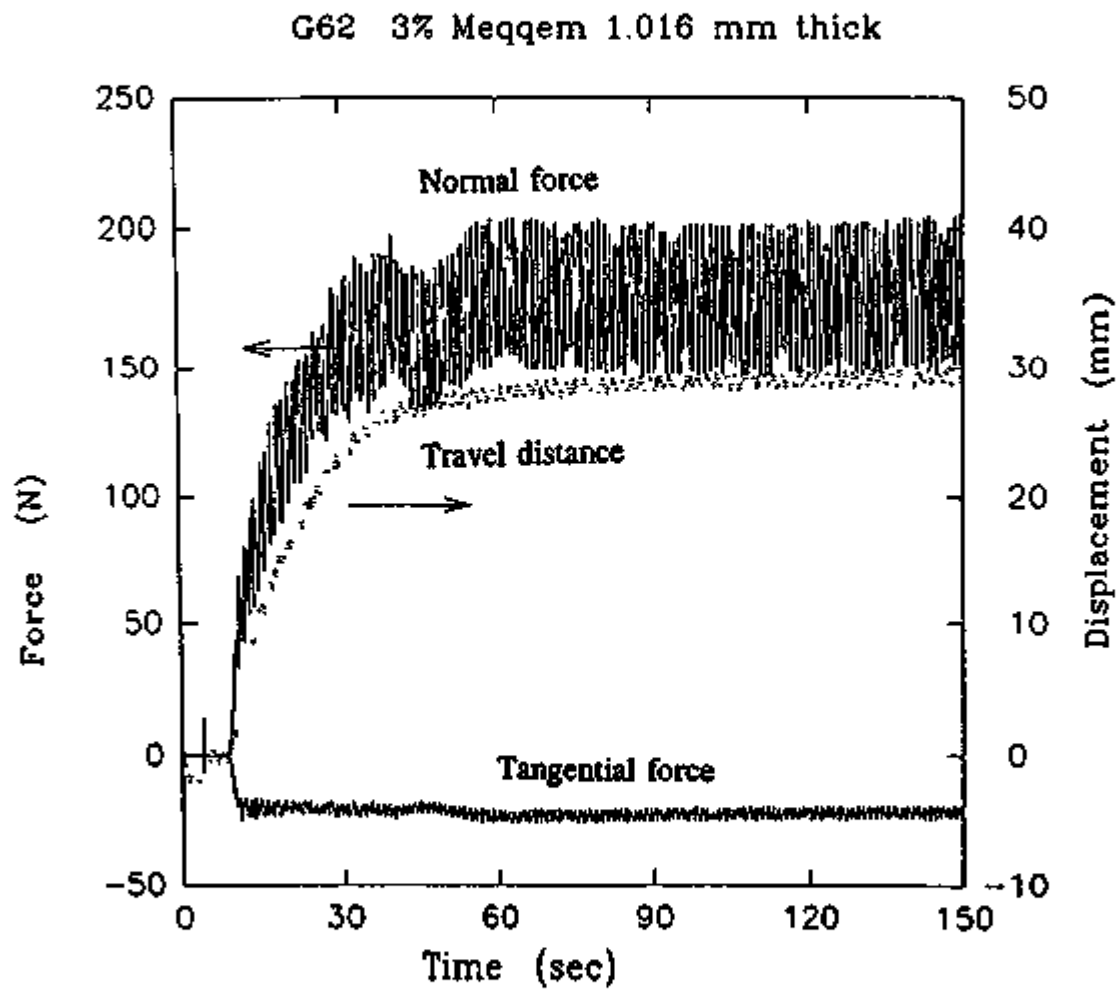
Fig. 5   The coolant used in grinding is 3% meqqem in tap water. Preset overlap is
1.016 mm.   When the tangential load is 22 N, the material removal rate is
zero after a few second grinding.

G74   3%   meqqem 1.016 mm thick
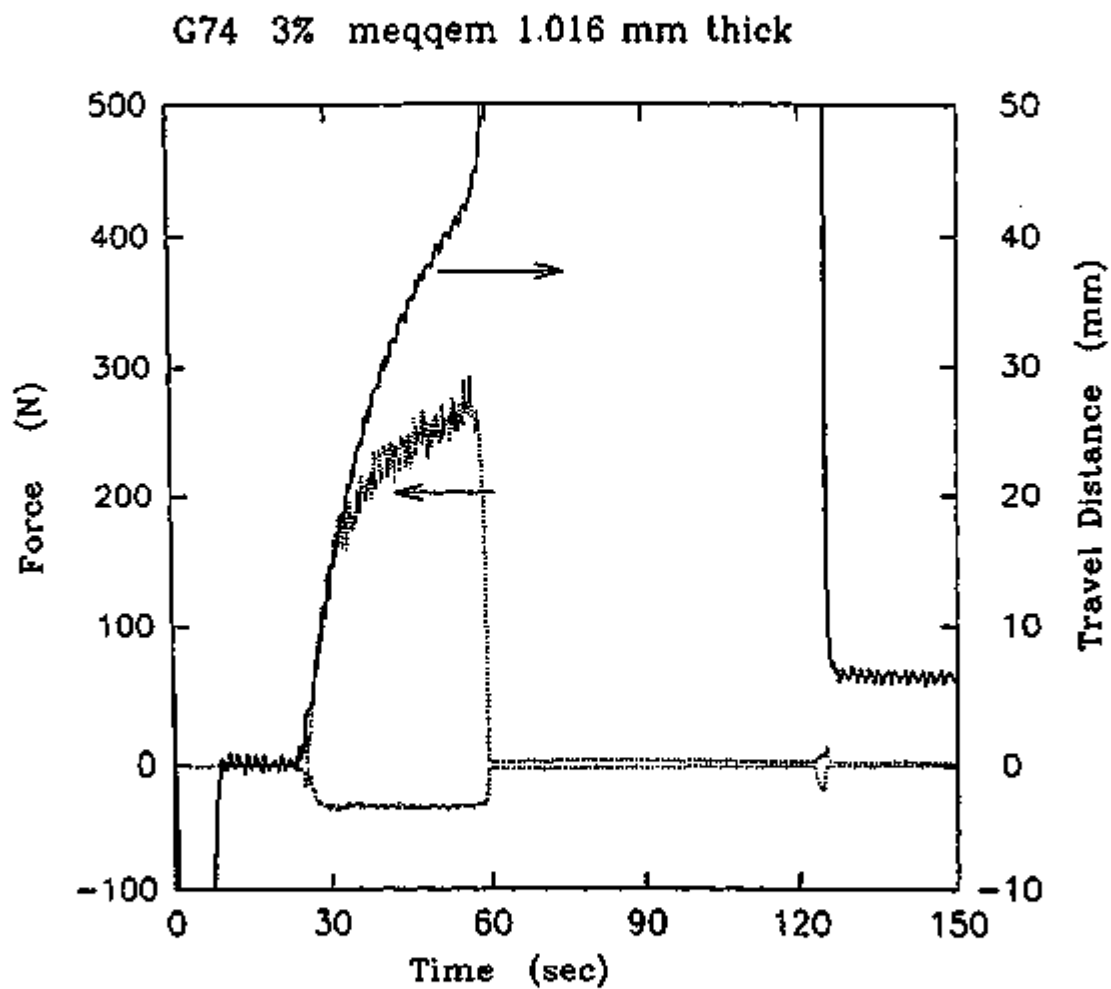
Fig. 6   When the tangential load is 36 N, the material removal rate keeps constant in the single pass grinding process.

Preset overlap 1.016 mm, Silicon Nitride
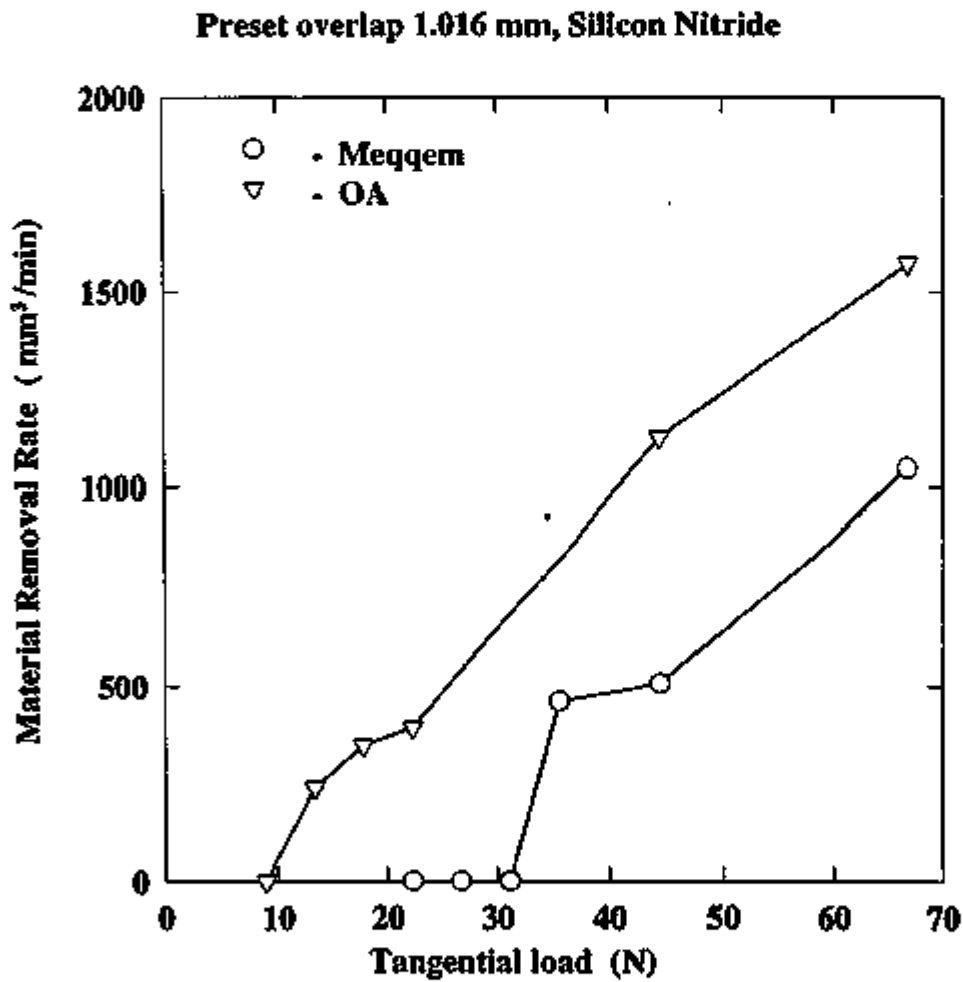
Fig. 7   The material removal rate versus tangential load with two coolants are compared. The low critical load of CM011 is less than that of Meqqem.

Preset overlap 0.05 mm, Silicon Nitride
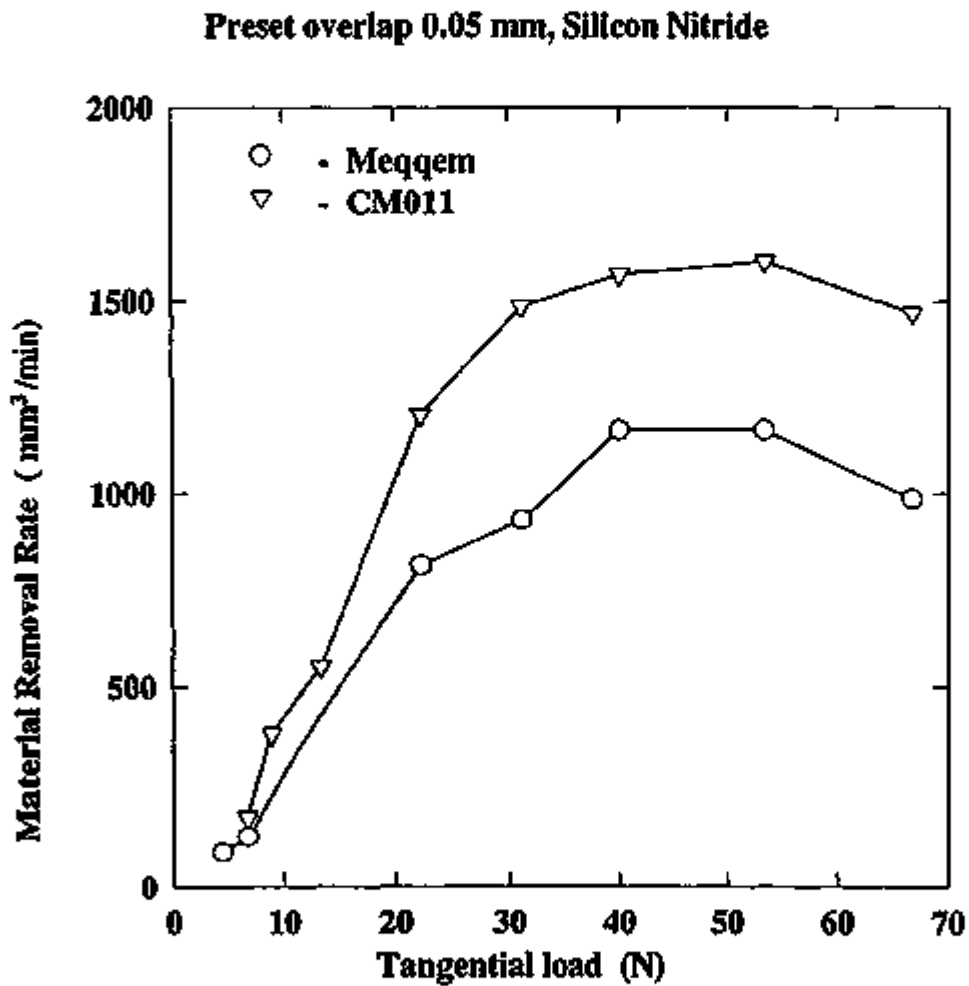
Fig. 8   The preset overlap is 0.05 mm. The material removal rate with CM011 is faster than the tangential load is higher than 31.2 N, the removal rates almost keep constant.
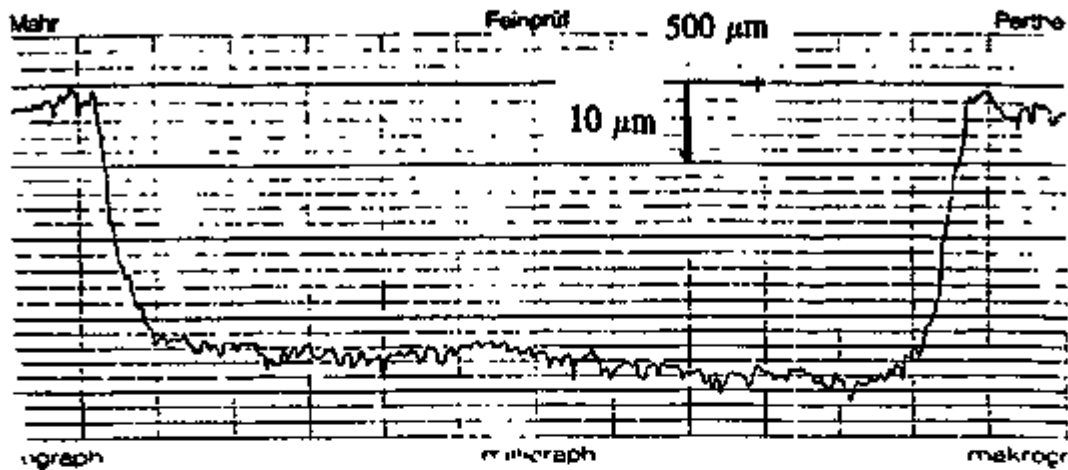
Fig. 9 a   The profile of the ground groove with a 22N tangential load and 0.05 mm preset overlap in meqqem coolant.
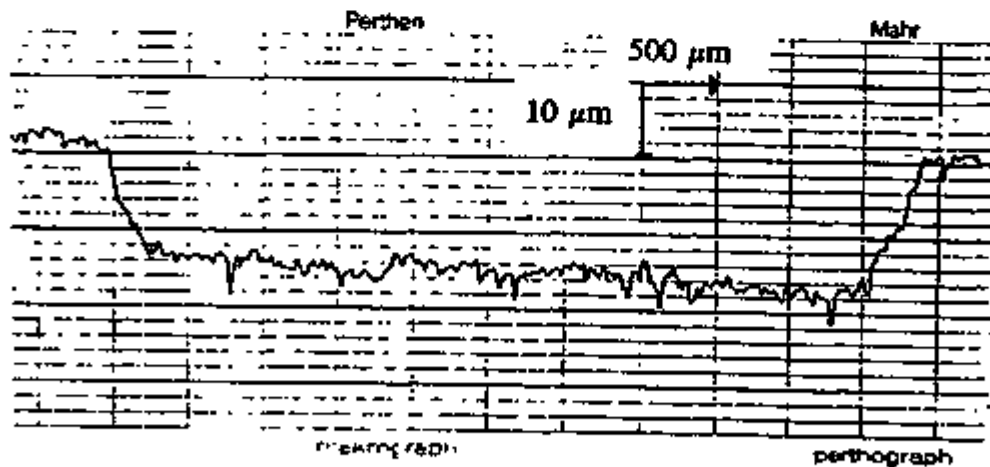
Fig. 9 b   In the same condition, when the tangential load increases to 67 N, the grinding depth is reduced.

abrasives on the wheel surface is about 30% based on direct observation on the SEM. The apparent contact area, A, is a function of the preset overlap, h, and the relationship between the two is shown by Equation 1.

$$A = wR \cos^{-1}(\frac{R-h}{R}) \qquad (2)$$

where R is the radius of the wheel, w is the width of the wheel, and h is the overlap. For different overlap, the contact distance and the apparent contact area calculated by Equation 1 are shown in Table 1.

Table 1   The apparent contact area under a given preset overlap

Overlap (mm)	Contact Distance (mm)	Apparent Contact Area (mm^2)
0.02	2.25	14.28
0.05	3.56	22.61
0.50	11.27	71.56
1.0	15.94	101.22
2.0	22.57	143.32

When the preset overlap is small, the contact distance is short. The temperatures on the tips of the diamond is relatively low, and the wear of the diamond is relatively low. Since the contact distance is short, the overall contact area is small, under the same load the mean contact pressure is high. There is a critical contact pressure above which all of the diamond particles will penetrate into the silicon nitride workpiece. If the contact pressure is higher than the critical pressure, the resin bonding will come into contact with the workpiece and will begin to share the load. The material removed per contact cycle therefore will not increase any further since all of the diamond particles are already fully penetrated into the workpiece. Any increase in the cutting forces will not increase the material removal rate.

When the preset overlap is large, the contact distance is long and the mean contact pressure is low. However, the temperatures at the tips of the diamond particles are high and wear of the diamond abrasives becomes an issue. When the tangential load is below a critical pressure, the diamond will not penetrate substantially into the workpiece. Depending onthe viscosity of the fluid, some elastohydynamic lift will come in. This is why below certain critical loads, the grinding wheel quickly establishes an equilibrium with the workpiece and no substantive material are removed.

In summary, the two fluids, Meqqem and CM011 each has separate low critical load and the upper critical load. This is important because it suggests that the chemical nature of the fluid significantly affects the mechanical processes.

This phenomeana also raises an interesting issue. Beyond the upper critical load, the material removal rate can have two different tangential loads, or the cutting force. This suggests that the energy dissipation process as well as the energy level during grinding may be different to produce the same volume of grinding particles. This warrents a closer examination.

Two surfaces are prepared by constant load grinding. For meqqem, the tangential load is 53 N and the preset overlap is 0.05 mm. For CM011 the tangential load is 27 N and the overlap is the same as meqqem. In both cases, the material removal rates are about the same. After grinding, both samples were examined by profilometry, thermal wave technique, ultrasonic microscope, and SEM.

The surface roughnesses of the ground surfaces with Meqqem and CM011 are shown in Fig. 10 a and b, respectively. Both surfaces have about the same roughness and the difference between the two R_a is less than 0.1 μm. Yet it does not mean that the surfaces have the same quality.

A thermal wave technique with which the surface thermal diffusivity can be measured is used to analyze the ground surfaces. The basic mechanism of the thermal wave technique is shown in Fig. 11. A laser beam is pulsed perpendicular to the sample surface to form a thermal field, another laser beam is set parallel to the surface and pass the field. Due to the rising temperature on the surface the horizontal laser beam will be deflected. Measuring the deflected angle, the surface thermal diffusivity can be estimated. If the sample moves in X and Y direction, a thermal diffusivity map can be obtained. The surface diffusivity map of sample ground with Meqqem is shown in Fig. 12 a and the mean value is 0.11 cm²/s. The dark points indicate low thermal diffusivity. The surface diffusivity map of the sample ground with CM011 is shown in Fig. 12 b and the mean value is about 0.18 cm²/s. These data indicate that the thermal wave travel faster in the surface ground by CM011 than that ground by Meqqem. There are more surface defects associated with the surface ground by Meqqem.

An ultrasonic microscopic technique is also used to measure the echo amplitude of pulsed elastic sound wave from the two ground surfaces. The ground surface is put under a ultrasonic microscope, the ultrasonic wave is focused on the surface, when the sound wave collides with a surface, it echoes back, and a sensor detects the amplitude of the echo wave. There are mainly two factors affect on the echo wave. Since a rough surface scatters the sound wave, the rougher the surface, the lower the amplitude of the echo. The amplitude of the echo also reflects the rigidity of the surface. The more rigid the surface, the higher the echo amplitude. The two echo amplitudes of two samples are shown in Fig. 13. Sample 1 is ground with Meqqem, and sample 2 is with CM011. The abscissa is the echo amplitude and the coordinate is the number of echoes at that amplitude. The figure is a histogram of the echo amplitude distribution. Since the measured surface roughnesses are the same, the difference of the echo amplitude distribution is primarily caused by the rigidity of the surface. From the two distributions, the rigidity of the surface ground with CM011 is better than that with Meqqem. This result agrees with the thermal diffusivity measurement.
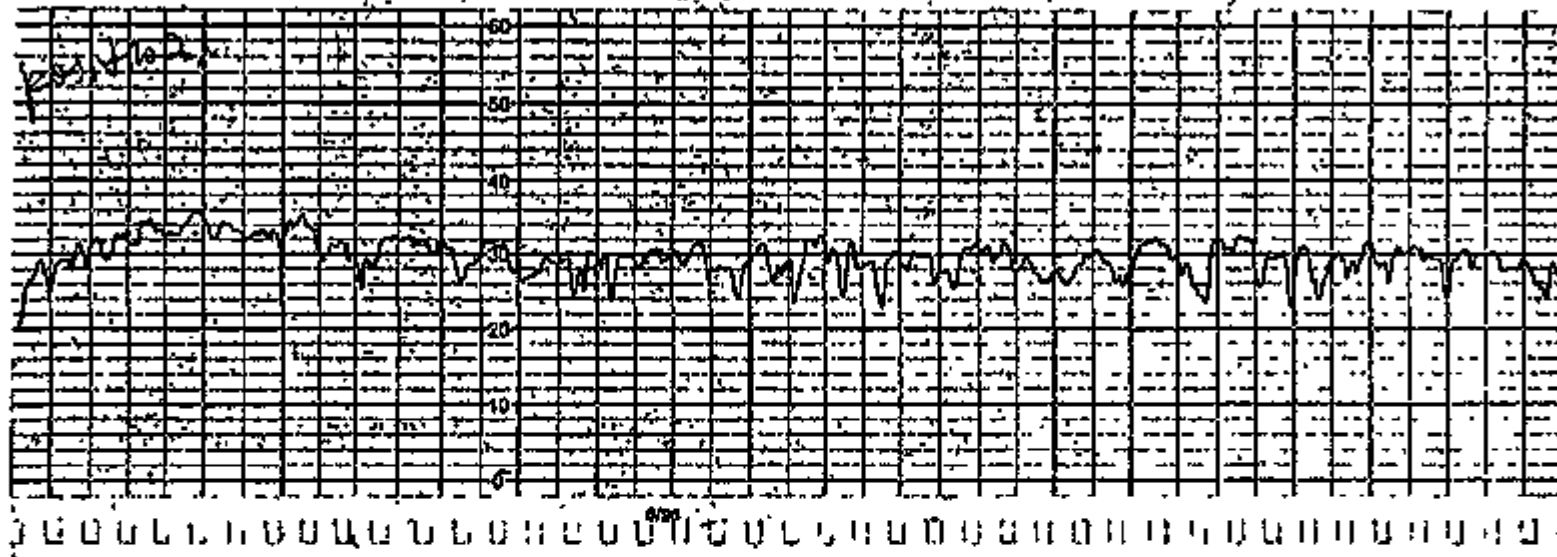
Fig. 10a   The surface roughness ground with 3 % Meqqem in tap water.
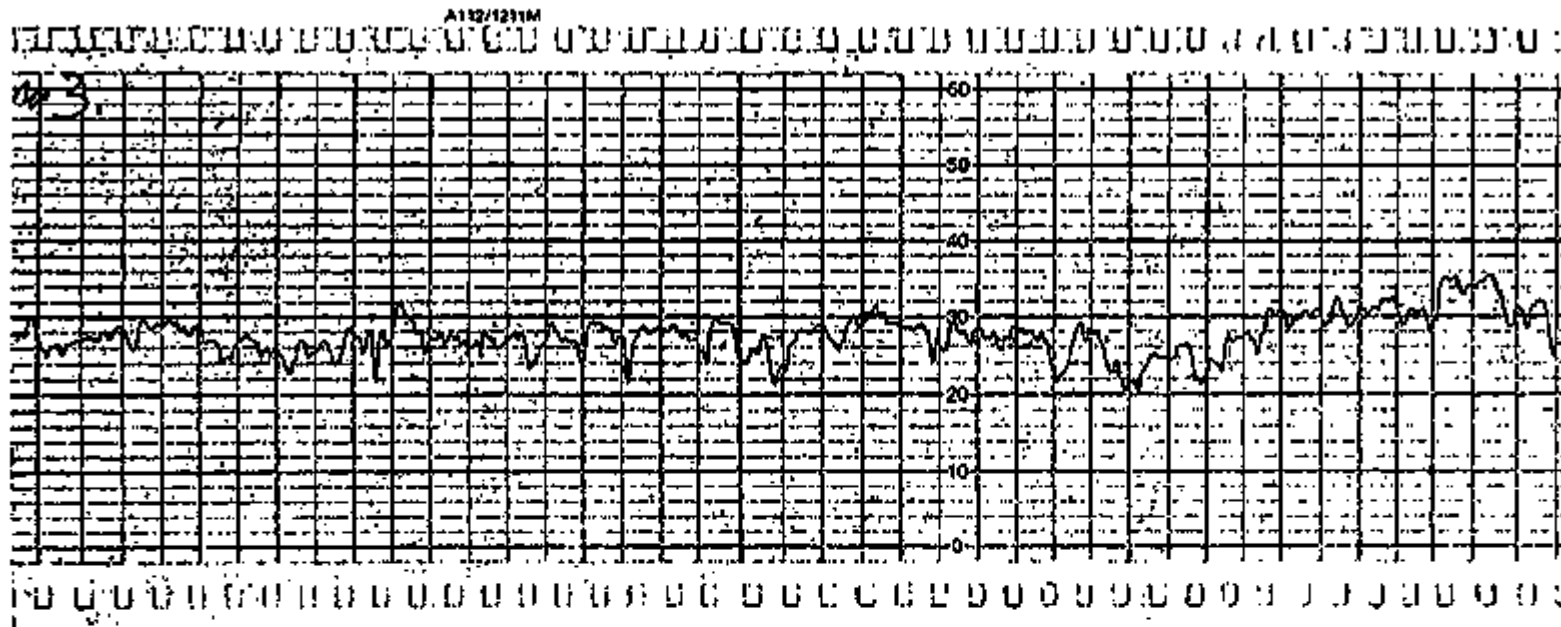
Fig. 10b   The surface roughness ground with CM011.
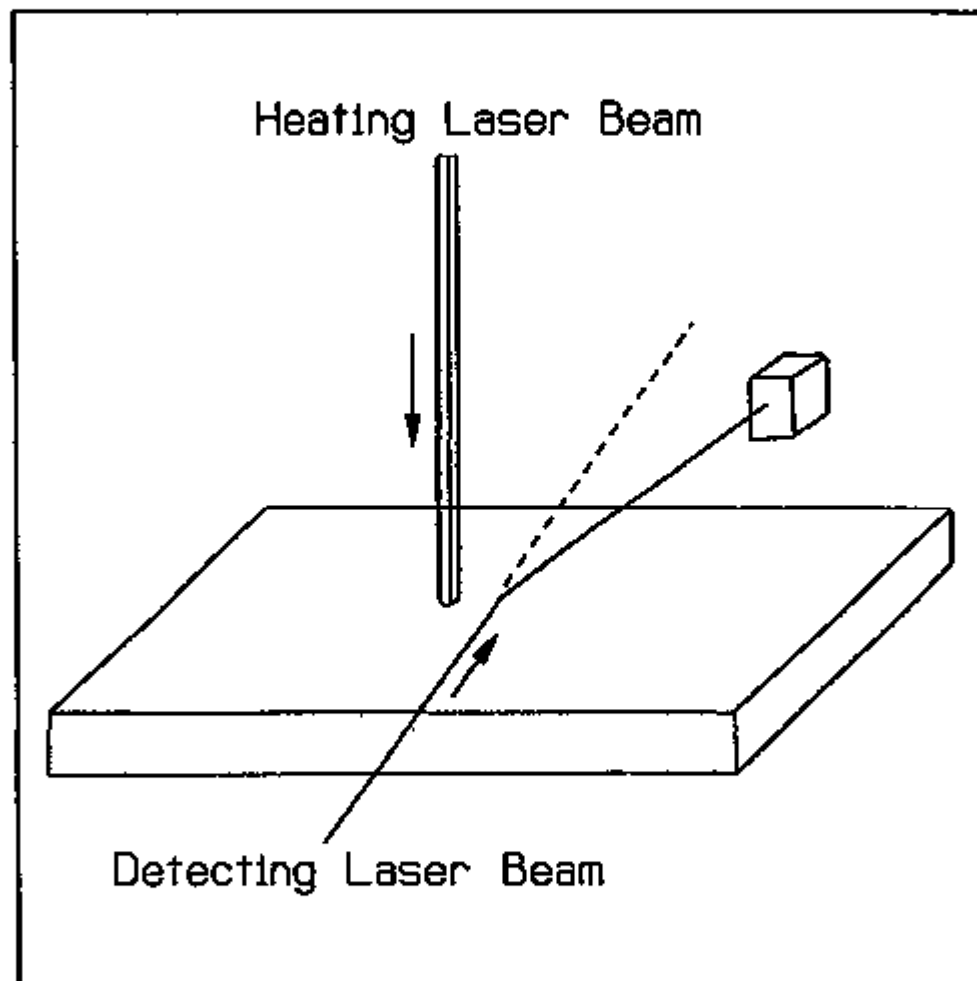
Fig. 11   Schematic diagram of thermal wave measurement.

Fig. 12a   Thermal diffusivity map of the sample surface ground with Meqqem, the mean
            value is 0.11 cm²/s.

Fig. 12b   Thermal diffusivity map of the sample surface ground with CM011, the mean
            value is 0.18 cm²/cm.

Silicon Nitride: YING
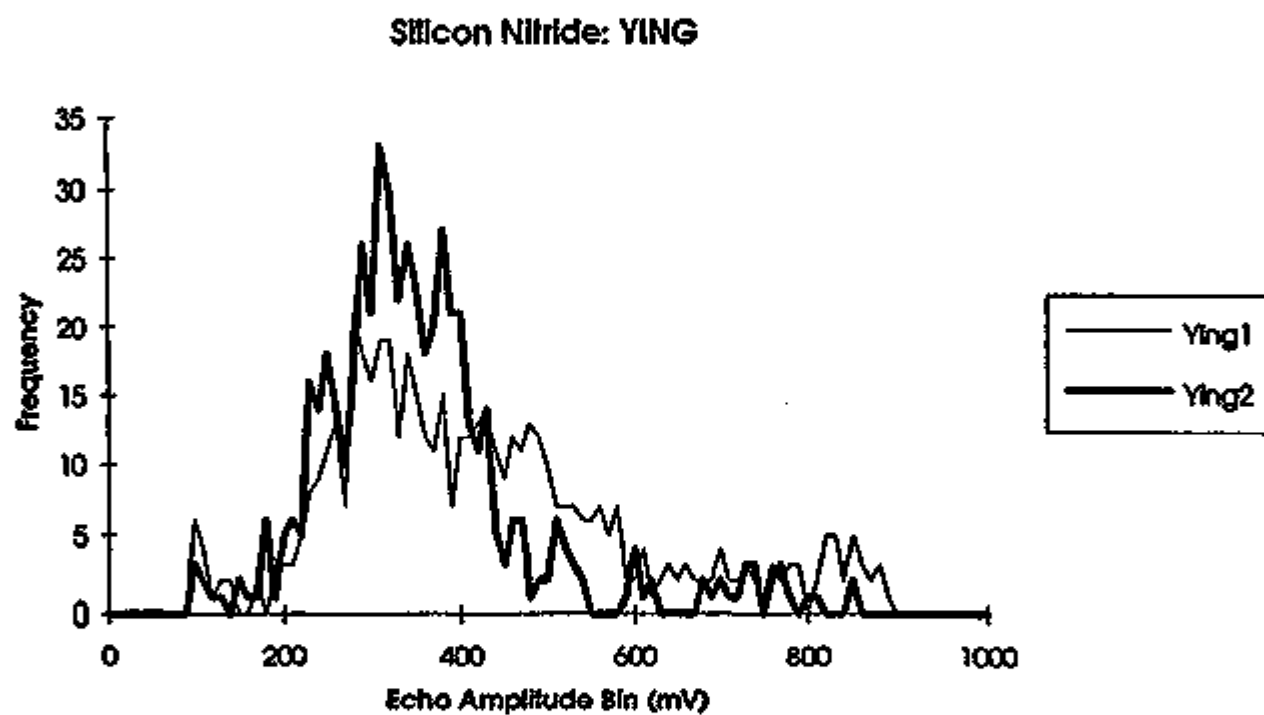
Fig. 13   The ultrasonic echo amplitude distribution of the two sample surfaces.

The SEM micro-photos of these two surfaces are shown in Fig. 14 a and b. At low magnification, the two surfaces look identical. At high magnification, Fig. 15 a and b, different surface morphologies are self-evident. Since the tangential load with Meqqem is twice as large as that with CM011, extra energy is dissipated during the grinding process. The extra energy is consumed by additional frictional between the surface on the wheel and silicon nitride surface. This results in more and finer wear particles as well as more micro-cracks left on the surface.

Development of a Coolant

We have demonstrated that chemistry had a profound influence on the machining rate as well as the surface quality. We developed a ball-on-inclined plane test technique that gave a reasonable indication of the quality of the as-machined surface. We developed test techniques to measure the effect of the chemicals on machining rate with a surface grinder. The next logical steps will be to develop a fully formulated grinding fluid for commercial grinding trials.

At the beginning of the project two years ago, we contacted the metal working fluid producers and additive suppliers and asked for their participation. No commercial coolant specifically designed for ceramic machining was available at that time. The industry agreed to supply existing chemicals for testing but would not agree to undertake special developmental effort to synthesize chemicals for this purpose. The reason given was primarily the lack of market for such products in the foreseeable future. We asked them this time for participation on the coolant formulation development, the answer remained the same, the lack of current market prohibited them from undertaking any significant effort.

The situation is different with ceramic suppliers and users of coolant. Based on our results to date, Kennemetal is sufficiently interested that they supplied us 300 samples for machining tests and the corrosion test procedures.

For the plant trial at Kennemetal, we have to select the form of the fluid for testing, the fluid could be oil-based, water-based, or emulsion-based. After reviewing the data, we settle on emulsions. Since the organics give several order of magnitudes higher machining rate than the water-based ones, but the water-based fluid offer advantages in more efficient cooling as well as ease of handling, a compromise would be to use emulsions to take advantage of the best qualities of both.

We consulted the metal-working industry and received guidance to formulate the emulsions. Several emulsions were successfully formulated. In an emulsion, the organic phase can vary from 20% to 50% depending on the emulsifiers used and the blending efficiency. A range of emulsions were prepared and checked for stability. The stable ones were tested on the cutter as well as on the surface grinder.
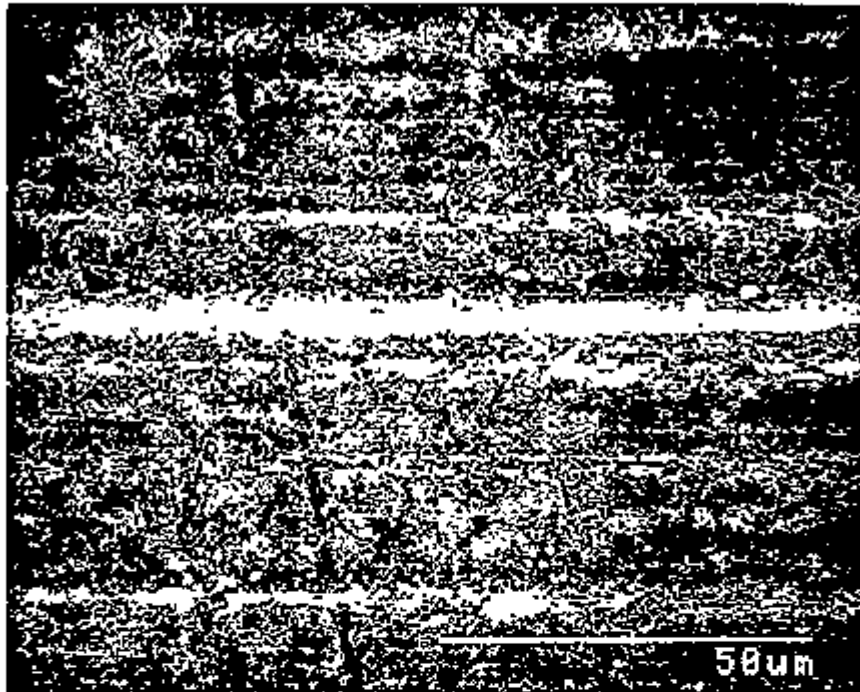
Fig. 14a   SEM micro-graph of the surface ground with Meqqem.
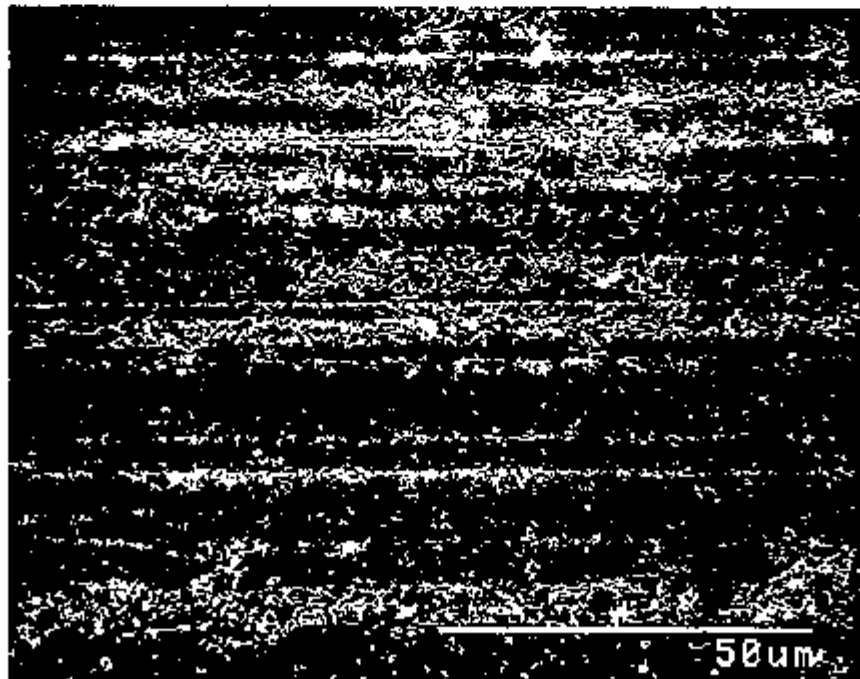
Fig. 14b   SEM micro-graph of the surface ground with CM011.
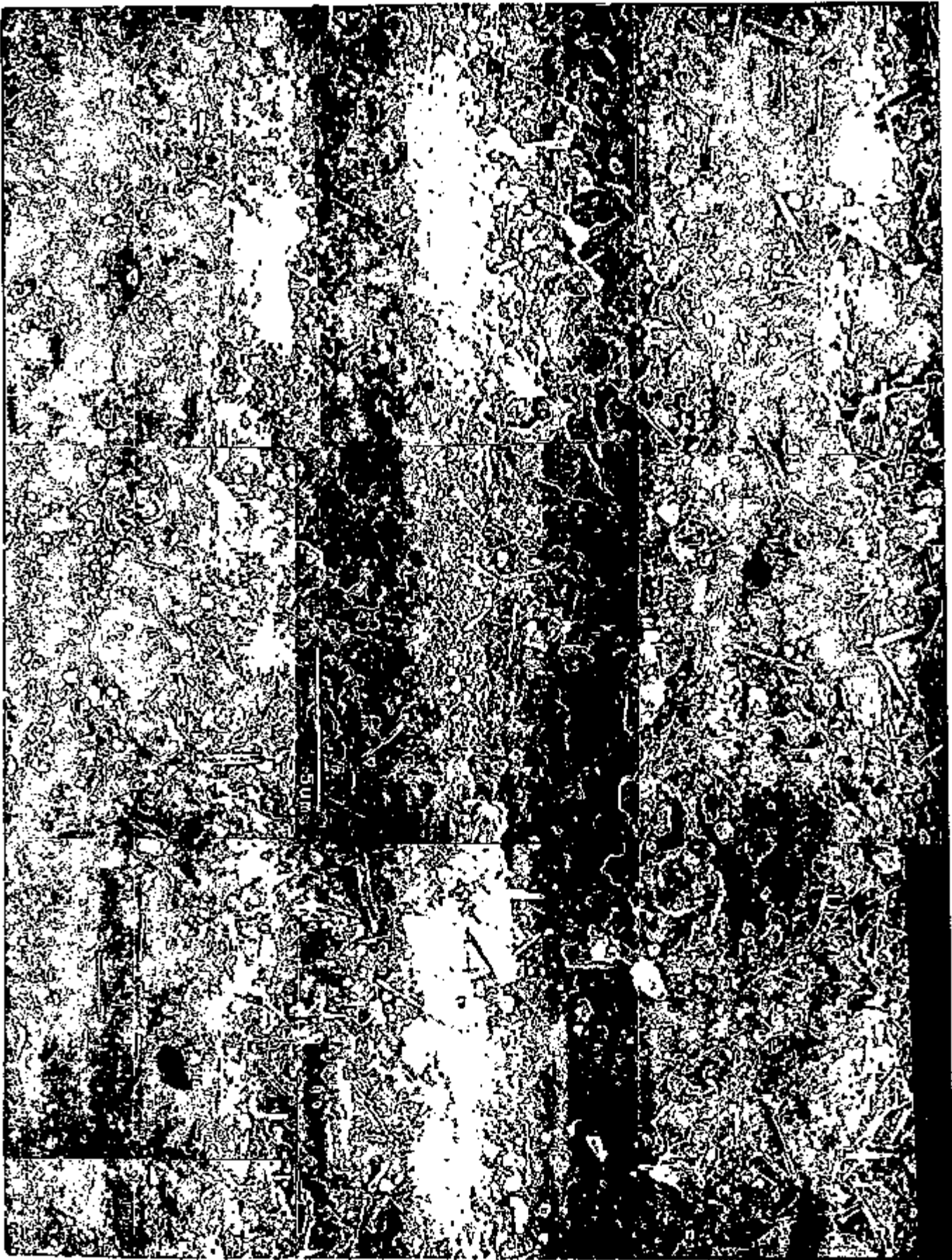
Fig. 15a   High magnification photo shows that there is layer of fine particles on the surface
            ground with Meqqem.
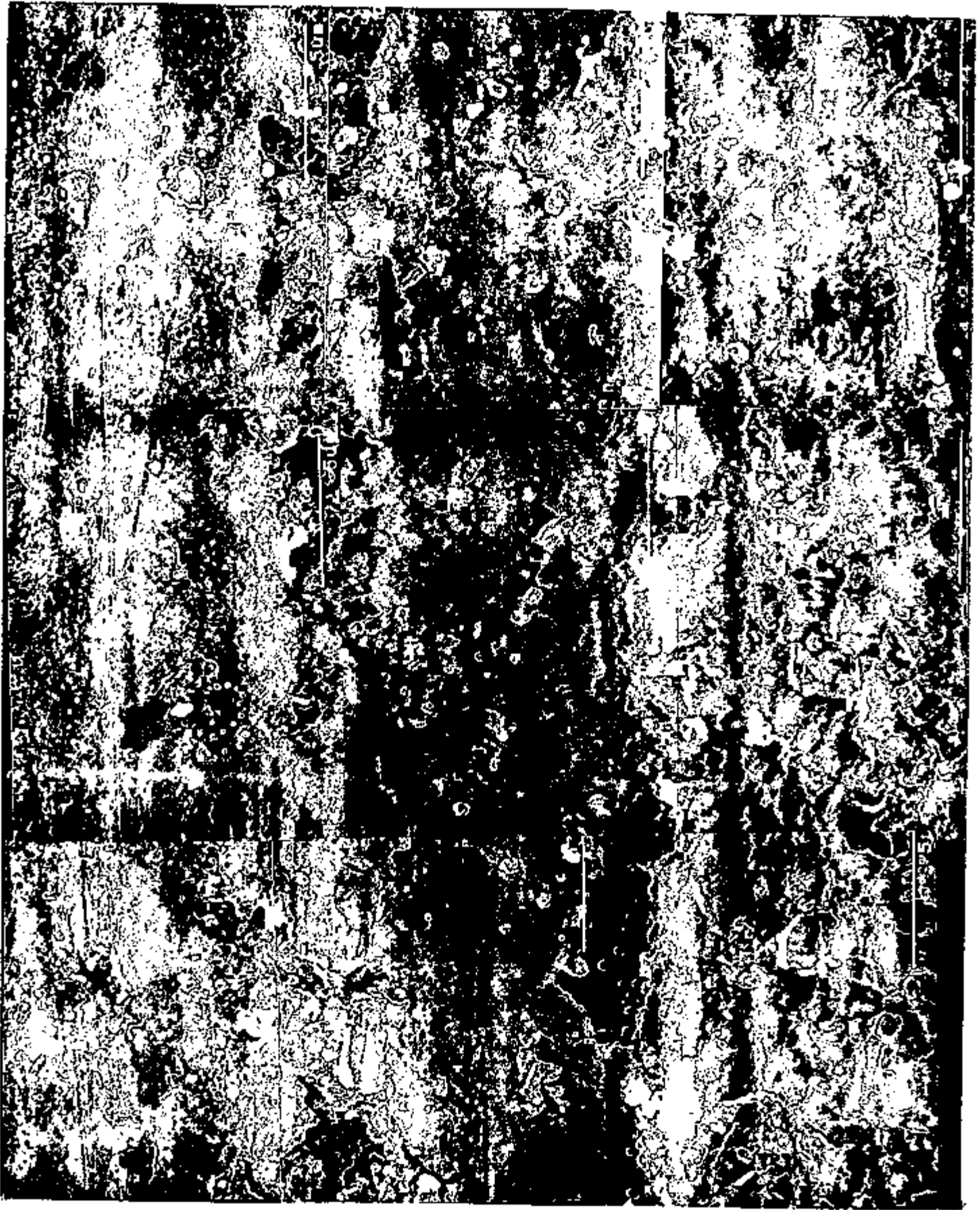
Fig. 15b   The density of and fine particles on the surface ground with CM011 is less than that with Meqqem.

<u>Water Soluble Coolants:</u>

Screening tests were conducted on the cutting machine with 100 cc of fluid. Promising candidates were tested on the surface grinder under the constant load testing procedure developed previously. For this purpose, multiple pass experiments were conducted to measure the effect of the fluids.

A baseline case comparing this technique with two well defined fluids was first conducted. The operating conditions were: 31N tangential load, 0.5 mm. overlap, 23 m/s speed, 180 grit diamond wheel. The sample was silicon nitride supplied by Kennametal. Three typical test curves are plotted in Fig. 16, 17, 18. The results of 3% Meqqem in tap water is shown in Fig. 16. Under the operating conditions, the grinding wheel ground through the sample on the first pass. The wheel was set back at the beginning position to start the second pass without changing the position of the sample. On the third pass, the grinding wheel advanced for about 30 mm into the horizontal distance then stopped. The grinding wheel just kept on sliding on the sample under a constant tangential load without removing further material. The total grinding distance for the three passes was 150 mm.

When CM011 was used, more material is removed, the total grinding distance is about 1000 mm. For direct comparison, the first 2,500 second data is plotted as the material removal rate for the fluids in Fig. 17. Comparing the two fluids, with the Meqqem, the material removal rate is low and CM 011 fluid can remove the material much faster.

CM011 is an organic fluid, although it is non-toxic and non-corrosive, Kennemetal prefers a water-based fluid. Thus, an emulsified fluid which contain 40% of CM011 was formulated. The test results are shown in Fig. 18 and the material removal rate is etween the Meqqem and the pure CM011. Although the emulsion improved the grinding distance over the pure water and the Meqqem, an operational problem occurred. During the grinding process, numerous fine particles were produced. These fine particles interfered with the emulsification and the emulsion became unstable. At this stage, we decided to concentrate on the water soluble fluid.

To change the solubility of CM011, a hydrophilic functional group was added on the CM011 molecule so as the CM011 structure can be soluble in water. This was successful, however, the presence of water retarded the grinding rate to a large extent. Other chemicals are needed to facilitate grinding. Several chemical classes were tested and these include: water soluble perfluorocarbon or fluoro-chloro carbons; sulfur-containing chemicals; phosphorous- containing chemicals; hindered phenols; and dispersants. Some improvements were achieved but they were on the order of 30-50% improvement over the Meqqem case.

Industrial cooperation

Coolants are application specific. Kennametal Co. uses a vertical grinding operation for their production line for ceramic inserts. In order to evaluate the chemicals under similar conditions, Kennametal decided to donate a vertical grinder similar to the machine they use on the production line. However, in order to measure the forces during grinding, we need to mount a force transducer and displacement sensor on the grinder. Parts have been ordered and after installation, tests will be conducted on that machine to validate results so far.

G120-122 meqqem overlap 0.5 mm 7 lbs
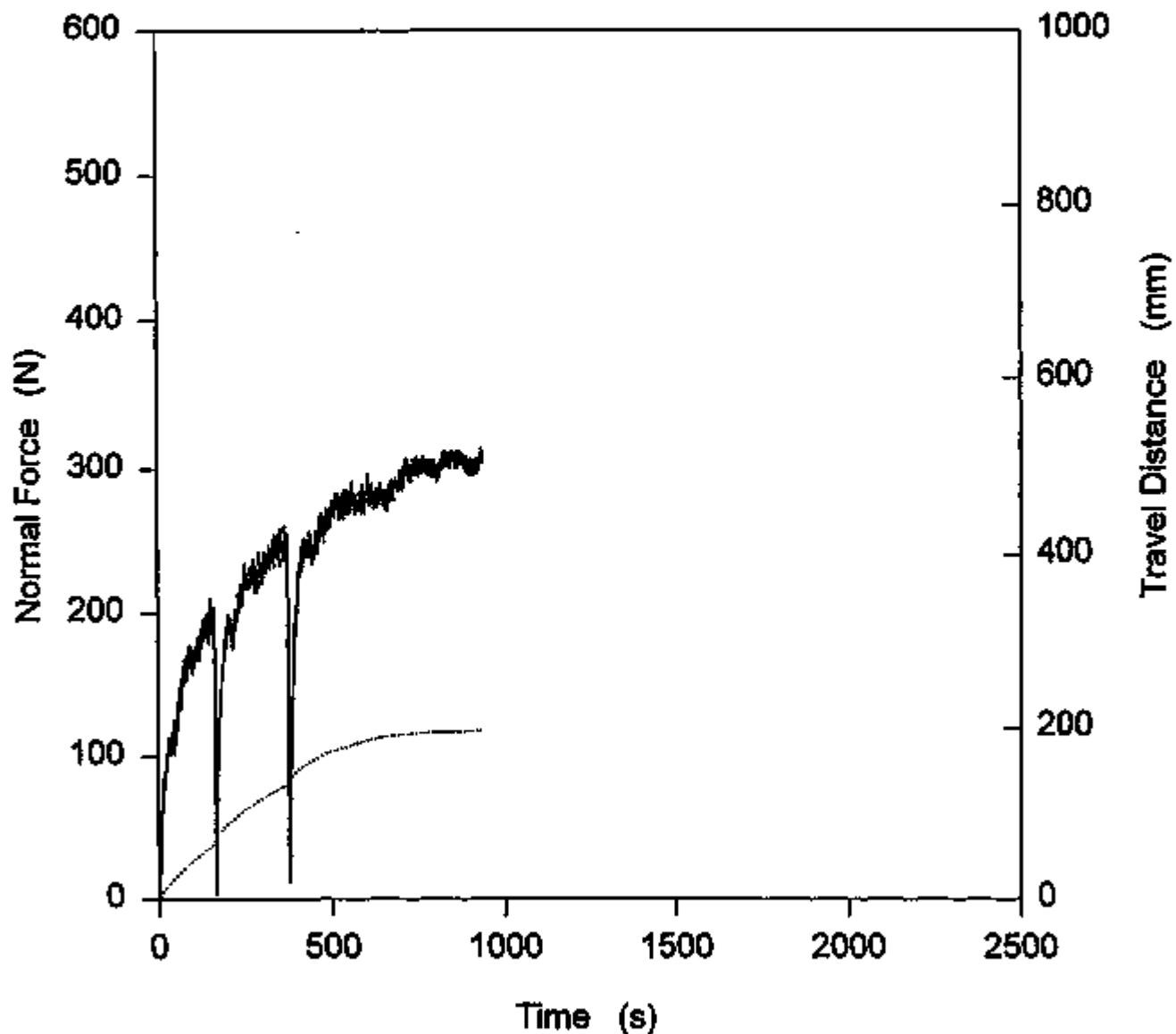
Fig. 16   The grinding distance and grinding forces with 3% Meqqem in tap water. Tangential load is 31 N and overlap is 0.5 mm. The grinding distance curve is similar with that in cutting test.

G128-145 CM011 overlap 0.5 mm 7 lbs
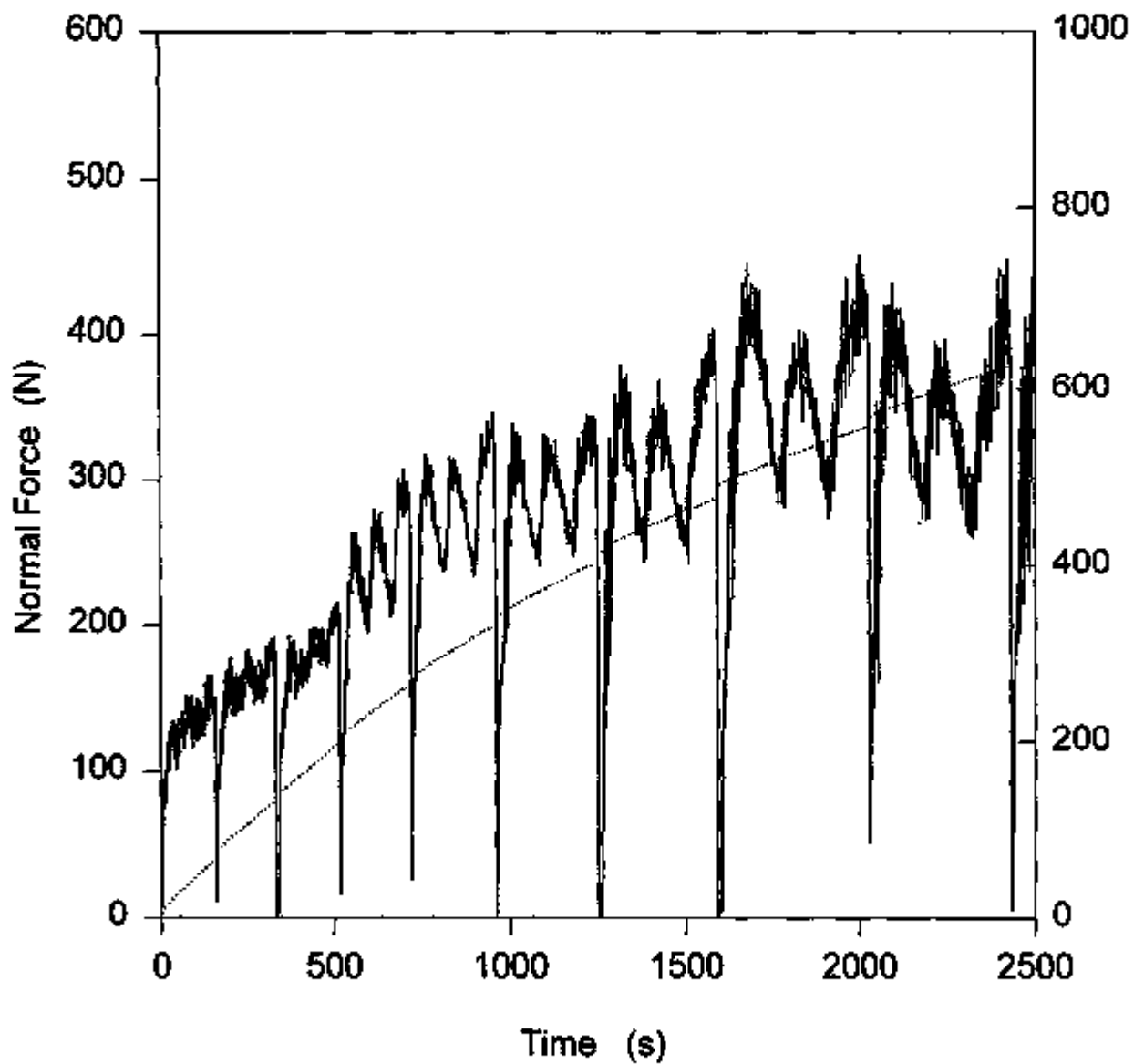
Fig. 17   Under the same condition with CM011, the grinding distance is increased to about 1000 mm.

G180-184 CM518 overlap 0.5 mm 7 lbs
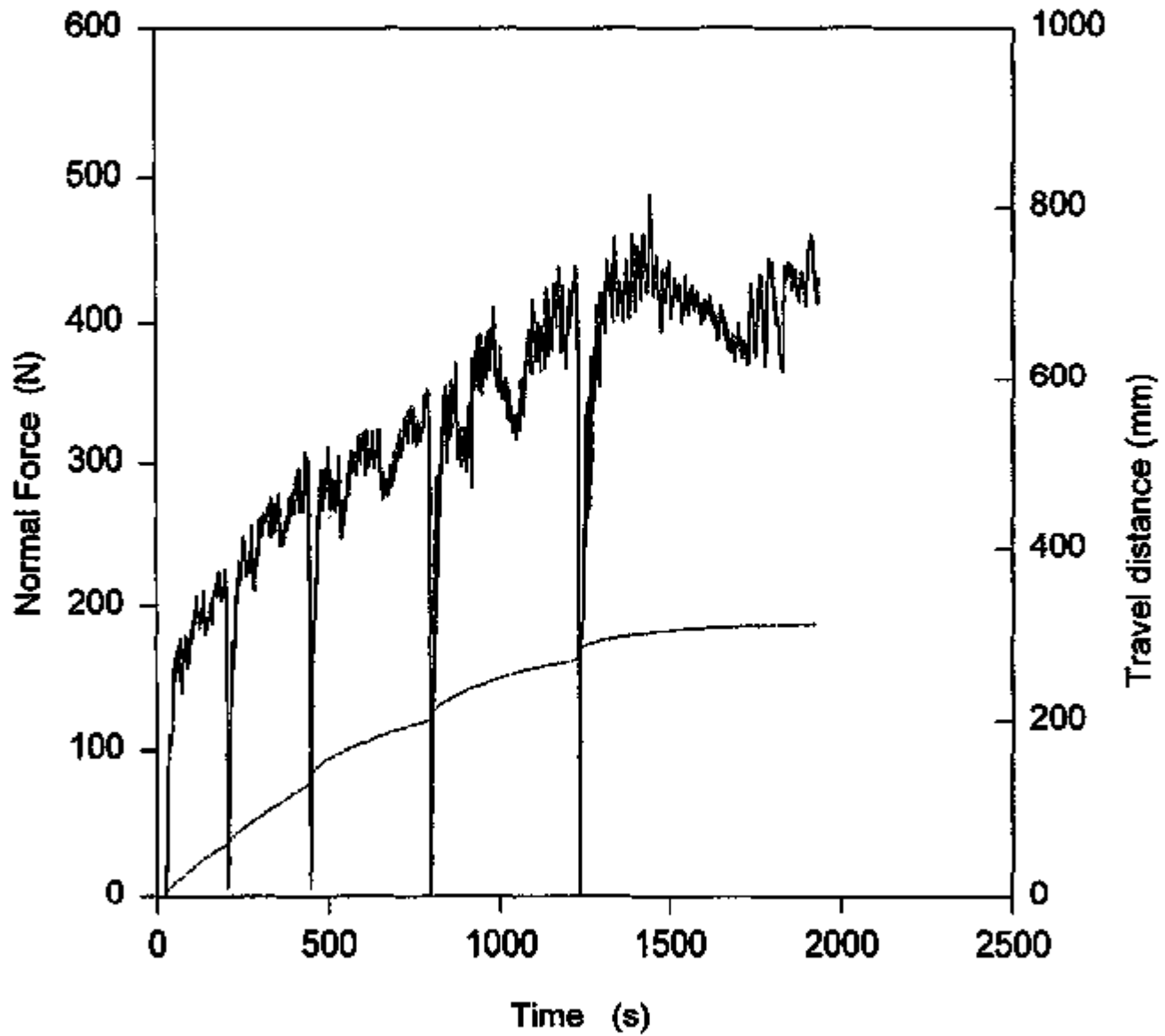
Fig. 18   With CM011 emulsion fluid, the grinding distance is improved a little.

Status of Milestones

On Schedule

Communications/Visits/Travel

S. M. Hsu visited Purdue University visiting Prof. Tom Ferris and Chandresaka and dicussed the machining technology. Information on wheel truing was discussed.

Solarex of Federick, Md visited NIST to explore cooperative research on cutting and grinding of brittle materials. Some samples were received from Solarex.

S. M. Hsu participated the second annual project review meeting at ORNL on Aug. 23-25, 1994 and presented a progress report of the project.

Kennametal Inc. donated a vertical grinder to NIST valued at $12,000 for examining the concept of the chemical assisted machining.

Problems Encountered

None

Publications

Two manuscripts have been prepared for publication and are currently undergoing NIST internal reviews.

Laser Scatter Methods for Detection of Subsurface Machining Damage in Ceramics – J. Scott Steckenrider, William A. Ellingson, George A. Forster (Argonne National Laboratory), Michael H. Haselkorn, Charles J. Anderson (Caterpillar Inc.)

Objective/scope

The primary objective of this program is to develop a laser scattering procedure that would provide a direct (near-real-time) indication of changes in the subsurface (and surface) during machining. These changes include machining-induced damage (such as median crack formation) and surface roughness. A second objective is to evaluate dye penetrant technology as an off-line indicator of surface-breaking cracks. The laser program is being executed in three steps. The first is evaluating optimization of the laser scattering procedure to examine specimens machined by innovative techniques. The second step will involve correlation of the laser scattering results with mechanical properties in "real" machined ceramic specimens. The final step will be to develop a prototype instrument to be evaluated for on-line implementation in a production environment. The investigation into dye penetrants for surface-defect detection is being conducted in three steps: review of literature, off-site visits to appropriate current users (e.g., Norton) and vendors (e.g., Sherwin, Inc.), and laboratory experiments.

Technical progress

The machining damage detection work accomplished during this period involved laser scatter and dye penetrants. In laser scatter, two primary achievements were made. First, initial comparisons were made of as-processed and machined surfaces using the 2-D scanning system discussed last period. However, because the test specimens planned for evaluation in this effort have not yet been acquired through Caterpillar (the current projection for their arrival is November 1994), the data presented below were taken from specimens obtained outside this program. Because of this delay, we have begun to address other work planned for the next year. Therefore, based on the results of these initial machined vs. as-processed comparisons, a system modification was designed and is being implemented to increase both sensitivity to median (rather than lateral) crack detection and acquisition speed.

The second area of machining damage detection this period was dye penetrant analysis. First, an initial literature review was conducted to determine the current state of the art in dye penetrant inspection with regard to ceramic materials. In conjunction with this search, ceramic manufacturers were contacted to determine the techniques currently employed on a regular basis. Finally, a comparison of three promising penetrant techniques was made on a thermally shocked SiAlON component known to contain cracks.

Part 1: Laser Scatter

A. Comparison of As-Processed and Machined Surfaces

Two experiments comparing as-processed and machined surfaces were conducted. The first of these was a comparison of laser scatter from several NT164 flexure bars that were received in machined and as-fired conditions. Figure 1 shows 2-D grayscale "images" generated

from scatter data. A focused laser beam (≈250 µm diameter) was rastered across the surface of several adjacent flexure bars, and a scatter measurement was taken every 200 µm in each direction. These data values were then assembled into an array to produce the images seen in Fig. 1. The figure shows laser scatter scans for 10 flexure bars (5 of each surface condition). Figure 1a shows the subsurface sensitive analysis, which indicates a significantly higher signal strength (i.e., more scatter) for 4 of the 5 machined bars. The fifth bar, on the other hand, appears to have a subsurface signature very similar to that of the 5 as-fired bars; the reason for this discrepancy is not yet known. However, because the current system is not focused on detection of median cracks (which are the dominant sources of machining damage), this result is not necessarily indicative of a difference between the one machined specimen and all other machined bars. Further examination of this discrepancy is planned (see subsection B below).
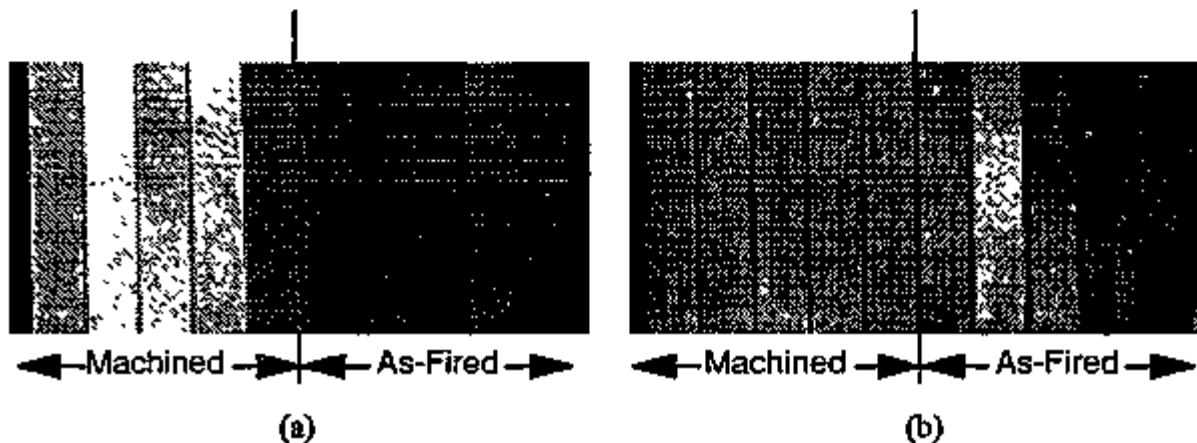
Figure 1.   Comparison of laser scatter images for 10 NT164 flexure bars with machined and as-fired surface conditions. Shown are (a) subsurface and (b) surface scans.

Figure 1b shows results of the surface sensitive analysis; several features are noticeable. First, the machined specimens show a vertically elongated texture, as would be expected from the highly directional surface roughness. However, because the surface is being scanned at only 200 µm resolution (owing to time constraints in the current system), the observed texture is not a specific representation of the exact texture of the surface, but rather is indicative of the general character of that region of the surface. A second feature evident from the figure is that the machined specimens have a far more uniform surface character not only within a given bar but also from bar to bar. The as-fired bars, on the other hand, show an overall nonuniformity that includes large regions of increased or decreased scatter (indicating possible changes in surface roughness, surface coating, etc.). Finally, the as-fired bars show several bright spots that correspond to dramatic increases in scatter intensity. Microscopic examination of these locations indicate the presence of "pools" which appear glassy and that range in diameter from less than 100 µm to just under 1 mm. Because these are only present in the surface scan of the as-fired material, one can expect that they are relatively transparent and thin enough to be removed in the machining process.

The second comparison of machined and as-processed surfaces is shown in Fig. 2. Once again, the examined material is NT164. In this case, a single specimen was examined under four conditions of surface preparation: as-processed, 180-grit machining, 320-grit machining, and

lapped. Several features are evident from the figure. First, as expected, the subsurface scan shows the highest amount of scatter (indicating the greatest amount of subsurface damage) in the two machined areas, less scatter from the as-processed region (indicating that the processing-induced subsurface damage is less severe than that produced by machining), and the least amount of scatter from the lapped area (where the near-surface damaged region has been polished away). A similar trend is seen in the surface scans, where the region of highest surface roughness (the 180-grit machined surface) shows the highest amount of scatter intensity. (While this correlation between surface roughness and surface scatter intensity holds for three of the four conditions, the lapped surface shows an increase in scatter intensity, resulting from saturation of the detection system at the center of the Fourier pattern. The texture seen in the lapped section is the result of chemical contamination of the surface.)

Another feature seen in Fig. 2 is the presence of localized defects. The first of these is in the as-processed region and is indicated by a single bright spot in the subsurface scan and two slightly less intense spots on either side of that location in the surface scan. The fact that these are not exactly coincident indicates that the effect of the subsurface defect is diffused and spread over a larger area as it reaches the surface. Furthermore, because the subsurface scan shows the defect with an increase in intensity, it is likely that the defect is either a subsurface ceramic/air discontinuity, as would be present in a pore or crack, or a second defect is seen in the lower left corner of the lapped region of the subsurface scan. Here, the defect is seen as a reduction in scatter intensity and is not visible in the surface scan. This is likely an iron inclusion, because such defects are common in the NT164 material and give this type of indication.

(a)   (b)
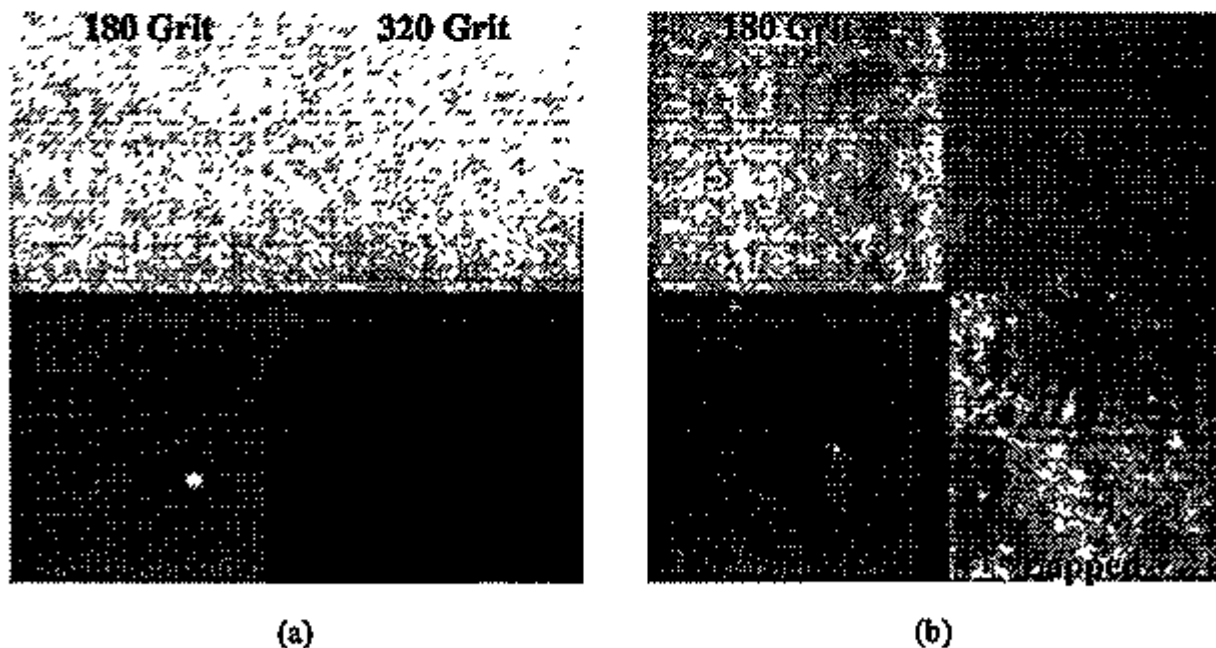
Figure 2.   Laser scatter images of a flat plate of NT164 with various machined and as-processed surface conditions. Shown are (a) subsurface and (b) surface scans.

B. System Modification

As presented above, the current laser scatter technique has proven capable of detecting subsurface (and surface) machining damage. However, the current system is designed for maximum sensitivity to lateral cracks (those parallel with the surface), while the most critical machining-induced cracks are median cracks (those perpendicular to the surface and parallel to the machining direction). The laser scatter indications seen with the current system therefore may not be the best indication of the machined component's mechanical strength. A system modification has therefore been designed to improve sensitivity to subsurface median cracks without sacrificing lateral crack detection. In addition, use of an imaging system rather than the current Fourier arrangement will improve acquisition speed (by using point detectors rather than the CCD array of the current setup). Hardware for this modified system has been installed. To take advantage of the improved detection speed, the system's translation stages also require greater velocity capabilities; they are being upgraded at the manufacturer. Once the translation stages are returned, software will be updated and acquisition will begin.

Part 2: Dye Penetrant

Dye penetrant detection of surface cracks has been improved by the addition of a microscope/video camera system for the observation and digitization of microcrack images. The system was calibrated so that the magnification (in pixels per micrometer) and aspect ratio was known for each microscope objective. (This manual calibration was necessary because of the inclusion of additional optical components to maximize resolution.) For the three magnifications, horizontal resolution was measured as 3.95, 0.96, and 0.24 μm/pixel. With a 5:4 horizontal-to-vertical aspect ratio, this corresponds to a vertical resolution of 3.12, 0.76, and 0.19 μm/pixel, respectively. Figure 3a is an example of the measurement of a crack with this system used at its highest resolution. The indent and associated crack were produced on a polished silicon nitride sample by a Vickers microhardness tester at a load of 20 kg. The crack measured 53.4 μm in length and had a diffraction-limited resolution of ≈1 μm.

Efforts continued this period to develop a monolithic ceramic microcrack standard. Figure 3b shows a Vicker's indent in a machined surface of an NBD200 silicon nitride material. Surface-roughness measurements in the machining direction and normal to the machining direction were measured and found to be 0.075 and 0.18 μm, respectively. The roughness values were measured with a wedge-shaped stylus of about 2.5 x 1 μm on a calibrated Rank-Taylor-Hobson Talysurf Model 6. A Nikon Optiphot optical microscope was retrofitted with a Sony XC57 CCD digital imaging camera coupled to a Data Translation frame-grabber in a 386/33 PC to allow digital image capture of the cracks at the indent. Cracks are faintly visible radiating from the corners of the indent, but are significantly less visible than on the polished surface of Fig. 3a. The indent is about 105 μm on each side. The indents were made after cleaning the surface with alcohol, and therefore the cracks were not exposed to solvents or contamination of any kind before the image was acquired.

(a)   (b)
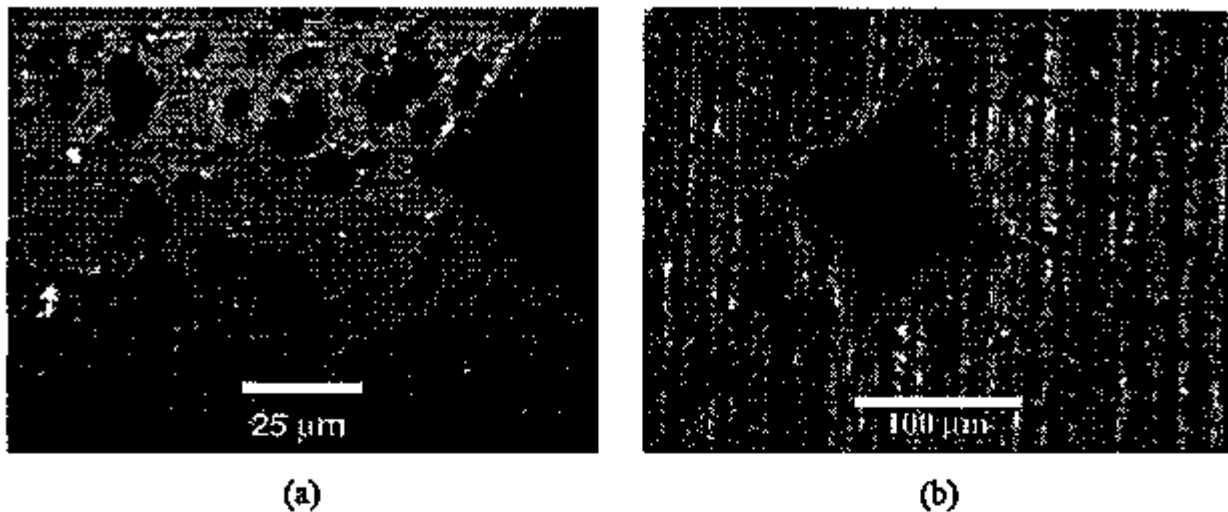
Figure 3.   Microscopic images of Vickers microhardness indents in (a) polished and (b) machined silicon nitride samples.

To complete our work on visible dye penetrants, attempts were made to enhance the visibility of the cracks using visible (red) dye penetrants, cleaners, and developers from several sources. No cracks were detected. The Statiflux technique reported earlier was also tried without success. Evidently, cracks of 1 to 2 μm width do not hold enough dye to adequately stain the developer powder or do not provide enough magnetic field variability to impact the Statiflux powder. However, fluorescent penetrants continue to hold high promise. An ultraviolet light source (a mercury lamp with optical filter) for our Nikon microscope was ordered, and several cracks similar to that described above were detected by using fluorescent penetrant with such a UV attachment. (Images of these cracks are unavailable because the system used to detect them was only a demonstration unit. The mercury light source we ordered is expected to arrive in early October, so we will provide fluorescent penetrant images in our next report.)

In our continued work, we intend to compare ASTM Level 4 high-sensitivity fluorescent penetrants for their ability to detect microcracks on various microstructure materials containing various surface machining conditions. Each machined surface will be characterized by the Talysurf. We have also purchased an ultrasonic cleaner. A protocol that we will develop will include:

1. Ultrasonic cleaning

2. Oven drying

3. Application of fluorescent penetrant

4. 10X → 40X observation using magnification

5. Ultrasonic removal of dye penetrant

Once we have established the exact protocol to use, i.e., time in ultrasonic cleaner, time in oven, setting time of penetrant, and best optical magnification, we will then begin to determine if automated digital imaging methods can be used to inspect components. In addition, we expect to begin initiation of a CRADA with an industrial penetrant vendor in the near future, because we have learned of significant industrial interest in this technology owing to its potential as a low-cost and effective detection method for surface-breaking cracks. However, concerns about EPA regulations for 1-1-1 trichlorethane as a surfactant remain and will need to be addressed.

Status of Milestones

Determine optical properties of SiAlON and GS-44 for optimal optical detection parameters (polarization, wavelength, angle of incidence, etc.).	Completed February 28, 1994
Conduct exploratory studies of dye penetrant on machined surfaces.	Completed May 31, 1994

With the exceptions noted below under "Problems Encountered," all other ANL milestones are on schedule.

Communications/Visits/Travel

W. A. Ellingson presented an invited paper titled "Nondestructive Characterization of Structural Ceramic Components" to the 5th International Symposium on Ceramic Materials and Components for Engines, Shanghai, China, May 29-June 1, 1994.

J. Scott Steckenrider attended and presented an update on the ANL work to the Cost-Effective Ceramic Machining Workshop, September 8, 1994 at Oak Ridge, TN.

Problems Encountered

The delay in obtaining machined specimens from Caterpillar continues. Current estimates indicate that these components will not be received until at least the end of November. In the meantime, to compensate for this delay in the overall execution of the project, future milestones (involving improvement of system capabilities with regard to speed and curved specimen inspection) are being preliminarily addressed ahead of schedule. Moreover, upon completion of translation-stage modification for the laser scatter system, a set of machined S/RBSN specimens that were analyzed and characterized in other portions of this project will be inspected.

Publications

Steckenrider, J. S., and Ellingson, W. A., Application of laser scattering to detection of surface and subsurface defects in Si_3N_4 components, <u>Ceramic Engineering and Science Proceedings Vol. 15: 18th Annual Conference on Composites and Advanced Ceramic Materials</u>, (Cocoa Beach, FL, January 9-14, 1994), American Ceramic Society, 382-389 (1994).

Stinson, M. C., Lee, O. W., Steckenrider, J. S., and Ellingson, W. A., Recognition of subsurface defects in machined ceramics by application of neural networks to laser scatter patterns, Ceramic Engineering and Science Proceedings Vol. 15: 18th Annual Conference on Composites and Advanced Ceramic Materials, (Cocoa Beach, FL, January 9-14, 1994), American Ceramic Society, 390-396 (1994).

Ellingson, W. A., Steckenrider, J. S., Sivers, E. A. and Ling, J. R., Nondestructive characterization of structural ceramic components, Proceedings of the 5th International Symposium on Ceramic Materials and Components for Engines, Shanghai, China, May 29-June 1, 1994 (in press).

Advanced Manufacturing Technology for Ceramic Heavy Duty Diesel Turborotors
E. Kraft, S. Roby, and J. McCormack (Kyocera Industrial Ceramics Corp.)

Objective / Scope

The objective of this program is to develop the cost effective manufacturing technology required for ceramic turbine rotors for use in turbochargers for heavy duty diesel truck and bus applications. A team, led by Kyocera (KICC, the ceramic component manufacturer) and including Schwitzer U.S., Inc. (the turbocharger manufacturer) and Caterpillar, Inc. (the diesel engine manufacturer) will develop and demonstrate production readiness for reliable, cost affordable turbochargers with ceramic turborotors. Program goals include a nominal order of magnitude reduction in cost over the present cost for small quantities, and process capability for critical component attributes which is adequate for the performance and reliability specifications of the application. Silicon nitride, SN 235, is the material of choice for this application. Program goals are to be achieved utilizing Kyocera's production proven Hybrid Molding, gas pressure sintering and cylindrical grinding processes. Yield, quality and cycle time improvements will be achieved through process modeling, statistical process control and intelligent processing.

Technical Progress

Task 1 Component Design and Specification

The objective of this task is to provide detailed design and specifications for a ceramic turbocharger rotor. An 80 mm diameter turbocharger rotor was jointly chosen for this application by Schwitzer and Caterpillar. It is sized to be applicable to the Caterpillar 3176 truck engine. This design has previously been produced in metal. Aerodynamic optimization of the blade geometry was performed by Schwitzer to maintain critical gas flowpath characteristics to accommodate the increased tip thickness of the rotor and change in materials. Electronic data transfer of rotor geometry was accomplished between Schwitzer and Kyocera, who added detail of the nose and shaft geometry. Finite Element Method (FEM) analyses by KICC using MARC Analysis, and by Schwitzer using ANSYS gave estimates of maximum stress within 4 MPa. Reliability analysis by KICC using CARES gave an estimated probability of failure at design speed of only 1.85×10^{-3} percent. This result is shown in Figure 1. If a spin proof test is utilized at 120% overspeed, 0.37% of the parts would be expected to fail. Design of the ceramic rotor to metal shaft joint was successfully completed, allowing the new rotor /shaft combination to be used within the existing metal housing. The Milestone 1 design package was submitted to ORNL on time and approved. Refinement of the ceramic to metal joint design was initiated, based on insights gained during preparation for the baseline process demonstration. The location of a lubrication groove corresponds with that of a weld line, causing concern for joint strength. Viable options for redesign have been identified and are being investigated with reference to the turbine housing configuration, and joint fabrication process. Experimental verification of joint strength is planned.

Task 2 Component Manufacturing Technology Development

Task 2.1 Cost Model

The original cost model was completely revised to reflect current cost factors, and recreated in Microsoft Excel and Microsoft Project. Studies of costs of prototype manufacturing were conducted and the model confirmed. This model was then applied to projections of the cost of prototype turbocharger rotor production. Figure 2 shows the breakdown of prototype costs by department for a run of 50 parts. This projection will be compared to actual cost data collected during the baseline process demonstration. A cost target will be established based on Schwitzer requirements and data from the baseline process demonstration.
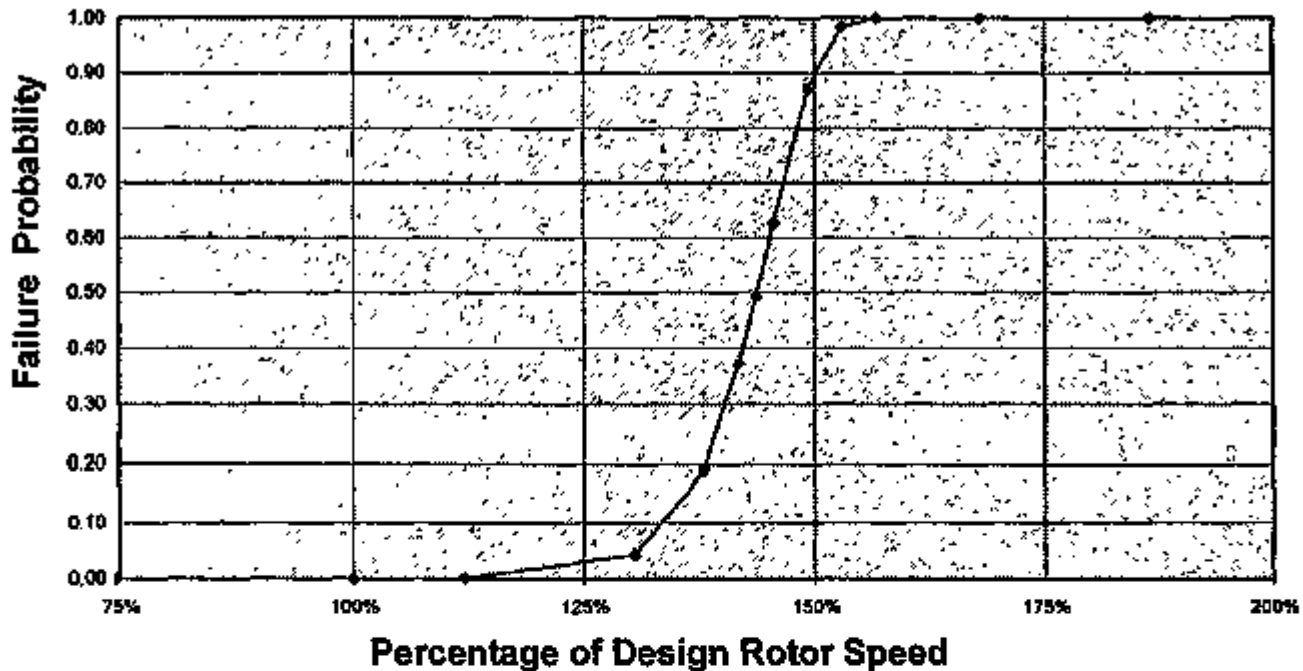
Figure 1. Estimated 80mm Ceramic Rotor Failure Probability

Case studies of prototype vs. production scale costs have been initiated. A production component and similar prototype part was selected and production cost data are being collected.
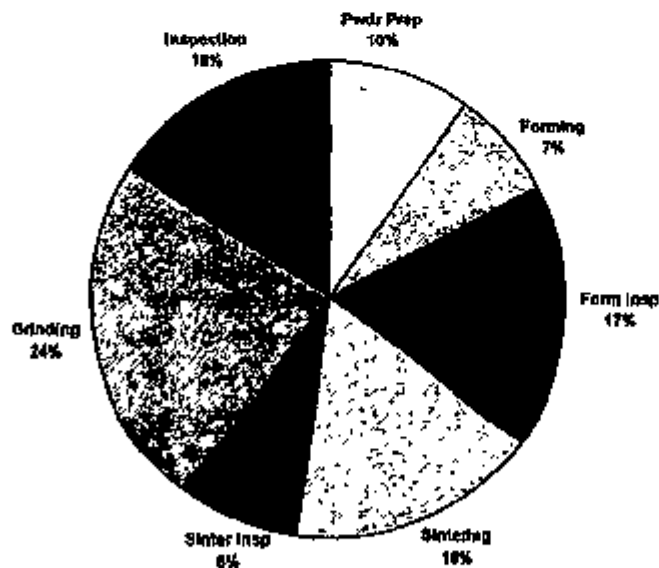
Figure 2. Baseline Cost Factor Prediction

Task 2.2 Environmental Safety and Health

A material balance was completed for processing of one rotor equivalent. This balance included all input materials and all product material, possible scrap and any emissions. Discarded material is being tested according to the Department of Ecology protocol at a certified laboratory. All gaseous effluents are passed through a burn-off furnace, for which flue gas analysis is scheduled.

Task 2.3 Process Control

Task 2.3.1 Statistical Process Control:

Studies of process control and process capability have been initiated on unit processes where sufficient data can be obtained. Control charting of the sintering process is ongoing as shown in Figure 3. In this case, the process capability (Cpk) for average MOR in sintering of a production component was found to be 1.65. In the case of centerless grinding of cylinders, discussed in Task 2.3.8, Cpk = 3.5 for diameter within cylinders and 0.8 between cylinders. The unacceptable latter value was traced to a deficiency in the chucking procedure, which has been corrected. Identification of other critical process parameters is continuing.
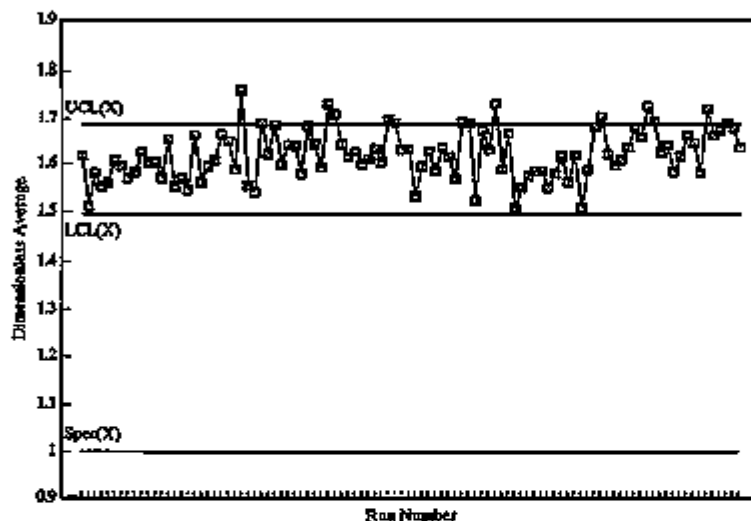
Figure 3. Control chart for flexural strenth in sintering runs

Task 2.3.2 Raw Material Preparation:

Sufficient Si_3N_4 and sintering aids were purchased for all process control and initial process demonstration tasks. These were ordered to KICC standard purchase specifications. Incoming inspection specifications for all raw materials have been completed, and the first lot of all materials inspected. Inspections include: particle size and surface area, C, N_2, and O_2 content, XRD, ICP, Si_3N_4 α/β ratio.

Characterization of mixed raw materials has begun using material at hand. Leco C, N_2 and O_2 analysis was performed on samples taken from 3 random locations in the container. Triplicate particle size analyses, using an L&N Microtrac, was performed on these same 3 random samples. There was no statistically significant difference in the results of these analyses. It is concluded, therefor, that there is no significant within-lot material variation. X-ray diffraction analysis on one sample showed all expected peaks and no extraneous peaks. Scanning Electron Microscopic examination of this sample showed no abnormal agglomeration or segregation.

Work has begun on analysis of sintering aid distribution and its effects in order to analyze the feasibility of reducing sintering cost through improved methods for distribution of the sintering aids. SEM and XRD analysis of samples from interrupted sintering experiments have shown that sintering aids introduced by the conventional process are completely dissolved in a liquid phase several hundred degrees below the sintering temperature. In addition, no voids greater than 20 µm could be detected from agglomerated sintering aids. Nevertheless, a plan is being formulated to investigate the effect of solution processing on the sintering cycle time and temperature, and high temperature mechanical properties. A literature search was performed and potential precursors identified for study of this solution processing approach.

Task 2.3.3 Slip Preparation:

One important process control consideration is the consistency of the molecular weight of the organic slip constituents. Several binder lots are currently available for use on the Hybrid Molding activities. A technique and vendor have been identified and initial measurements completed. Results to date indicate that the mixed organics exhibit a different molecular weight distribution than expected from the constituents. Initial slip preparation trials have been carried out to confirm critical parameter measurement methods and prepare slip for initial hybrid molding trials. DTA/TGA/FTIR characterization has begun.

Task 2.3.4 Forming:

The initial activity in this task is to model the hybrid molding process for turbocharger rotors. Technalysis, Inc. has been subcontracted to perform this analytical modeling. In this effort, they will perform the subtasks listed in Table 1. Drawings of appropriate molding machine parts have been prepared for FEM mesh generation and flow analysis.

Table 1   Technalysis Tasks

Subtask	Proposed Effort
1	Generation of 3-D Finite Element Mesh
2	Fluid Flow Analysis - Runner System
3	3-D Mold Filling Analysis
4	Postfilling Solidification Analysis
5	Design Change Analysis

Effort was initiated at Technalysis on modeling of the hybrid molding machine and process. A three dimensional finite element mesh, using hexahedral solid elements, of the flow control valve and slip injection passages was constructed for partial and full flow conditions. In addition, a two dimensional mesh was generated for the full flow configuration. Fluid flow was then simulated using the PASSAGE® program using slip properties and boundary conditions that would result in either laminar or turbulent flow. Pressure, velocity contours, velocity vectors and pressure convergence x-y plots from these analyses were produced for two sections of the injection passage and the valve. Examples of these results are shown in Figures 4 and 5.

The flow analyses of the full flow configuration do not indicate any danger of flow separation with the model boundary conditions and material properties. A critical zone is shown, however, at the injection tube exit location due to a high velocity gradient. This location will receive special attention in analysis with measured boundary conditions and material properties. In the partial flow configuration, however, flow separation is indicated in the valve. This area will also receive special attention in subsequent analyses. The measured material properties and boundary conditions have been supplied for these analyses, and this work has begun.

Initial hybrid molding trials were begun with a test plate mold to confirm critical parameters and provide test material for development of residual stress and green strength test procedures. A three point bend fixture in the x-ray diffraction machine is being used. Initial trials have shown that useable diffraction patterns of the binder in molded test bars can be obtained. The procedures for preparation of green strength test bars are being developed using the molded test plates.

Task 2.3.6 Binder Removal:

Thermal analysis of the binder constituents and system has been completed. Consistent with molecular weight distribution results, reported above, the thermal and gravimetric effects of heating the mixed binder constituents are not simply the sum of the individual results. Results do indicate the opportunity
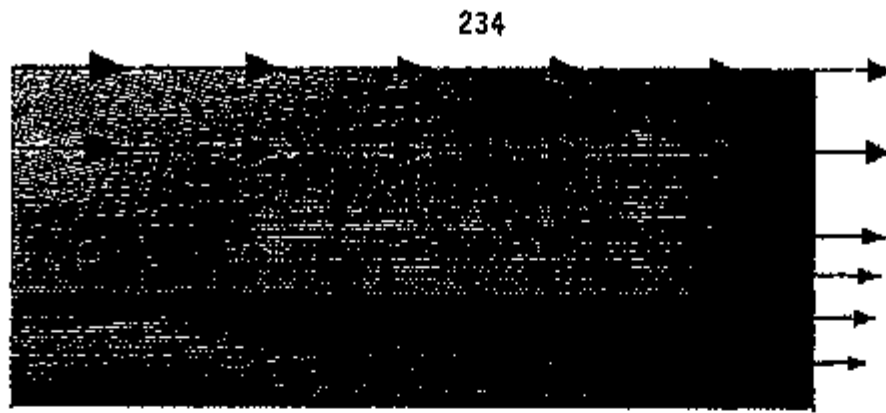
Inlet
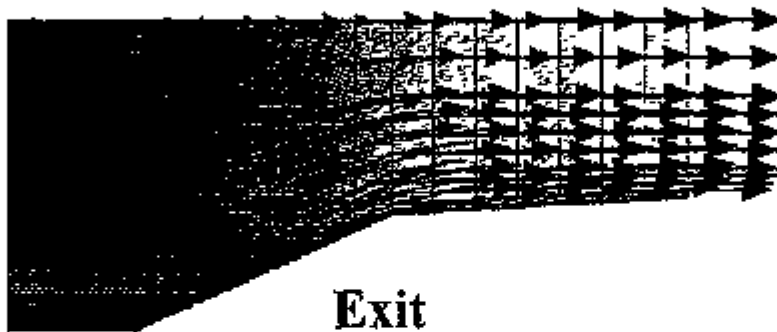
Exit

Figure 4.   Velocity contours and vectors for full flow configuration.
             (3-D and turbulence analysis)

Pressure (Pascal)
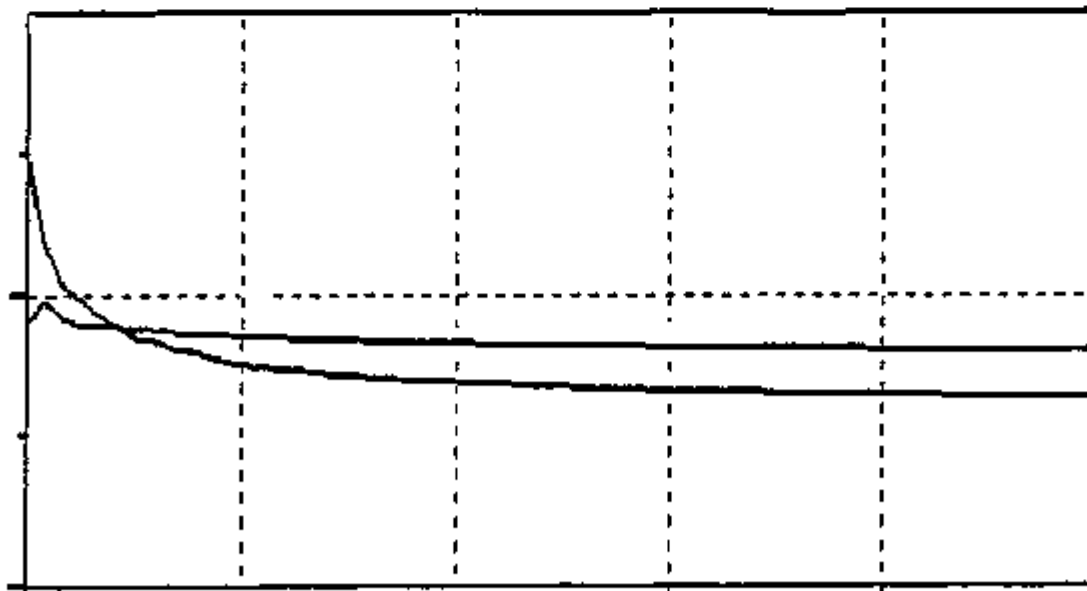
Time (Seconds)

Figure 5.   Convergence of pressure at two positions for full flow configuration.
             (3-D mesh and turbulence analysis)

setup was completed for in-situ weight loss and gas monitoring. However, initial testing of the gas monitoring setup showed the need for additional cleansing of the gas stream, and a modified design is in progress.

Task 2.3.7 Sintering Investigation:

The initial subtask in sintering process control was to measure the temperature uniformity within the gas pressure sintering furnace to be used in this program. Temperature uniformity measurement hardware, both type "C" thermocouples and independent IR measurement methods, are being employed. Use of this equipment on production runs in this furnace have shown temperature variation of less than 3 °C within the furnace volume. Run to run consistency is described above in Task 2.3.1.

Effort has begun on identification of in-process sensing systems for sintering atmosphere and shrinkage. SiO spectral data has been received, and limited sampling technique determined. Experimental setup designs for in-situ monitoring have been initiated. Data from the interrupted sintering studies described in Task 2.3.2 is being used to develop a phenomenological model of the sintering of this material.

Task 2.3.8 Grinding:

Initially in this task, cylindrical test specimens were fabricated by CIP (cold isostatic pressing) to determine the baseline of the current grinding procedure using SN235. CIP was utilized for ease of fabrication and to reduce tooling costs. 50 test specimens (.8" diameter X 2.75" length) were fabricated and sintered using the CIP molding process. The test matrix includes flexural strength at room temperature, surface roughness and dimensional evaluation. The grinding of 35 test cylinders using present equipment and setup is now complete. These baseline results are shown in Table 1.

Table 1:   Baseline Grinding Dimensional and Surface Roughness Results

	O.D.	Surface Roughness (Ra)	Surface Roughness (Rmax)	Strength
Average	14.321mm	0.463µm	4.590µm	541.9 MPa
Standard deviation	0.010mm	0.041µm	0.614µm	25.4
Weibull Modulus				25.6

Analysis of the dimensional results for process capability gave values for C_{pk} of 0.80 between bars and 3.55 within bars. The main sources of variation has been identified as due to rechucking procedure. While the typical average MOR of SN235 is 921 MPa, it must be recognized that the value above is for cylindrically ground and tested round bars, whereas typical MOR data is obtained from optimally, longitudinally ground flat bars. Nevertheless, this data will serve as a measure of baseline process capability, against which process improvements will be measured.

The sources of variation in the cylindrical grinding process are being studied. The first technique applied is multi-vari analysis, in which samples are pulled from a production process at regular intervals and measured. In this case, the process was simulated by cylindrically grinding cylinders under CNC control over 5 working days, with every bar being measured. The grinding wheel was dressed at the beginning and halfway through the experiment. The results for dimensional control are given in Figure 6 and for surface roughness in Figure 7.

Sources of variation are identifies as follows:

For dimensional control -
1. Rechucking is the largest source of variation
2. Diameter decreases following dressing

3. Diameter increases with time of day (specific correlation TBD)
4. There is a possible long term cycle
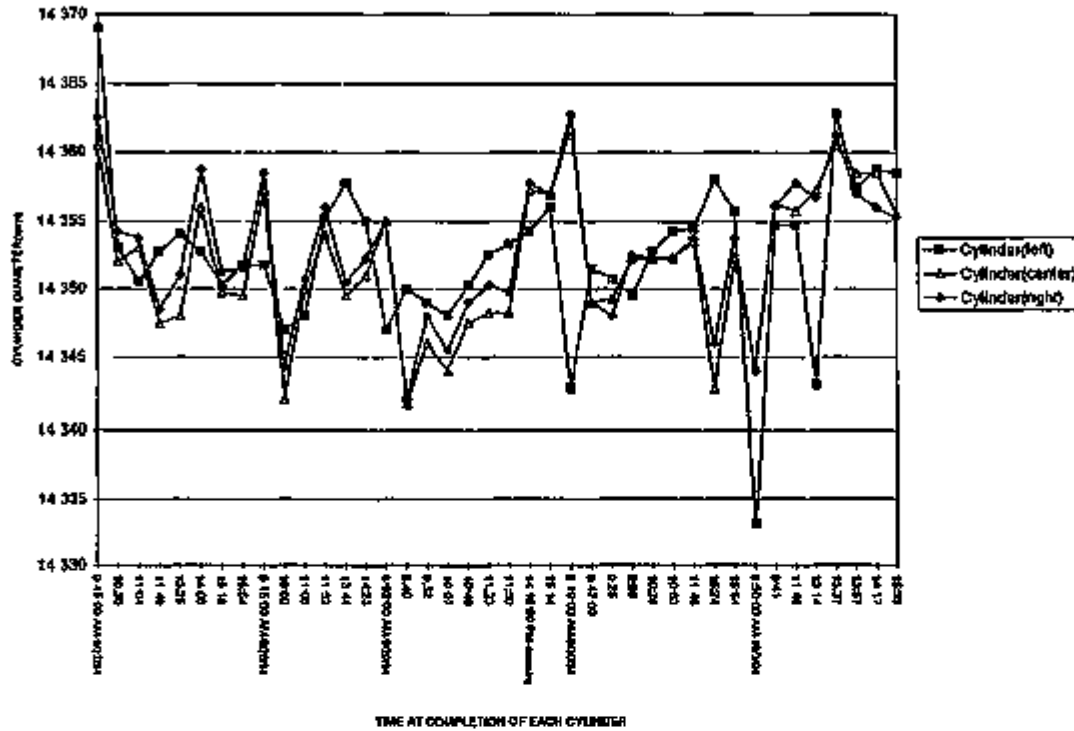
Figure 6. Multi-Vari Analysis of Dimensional Control
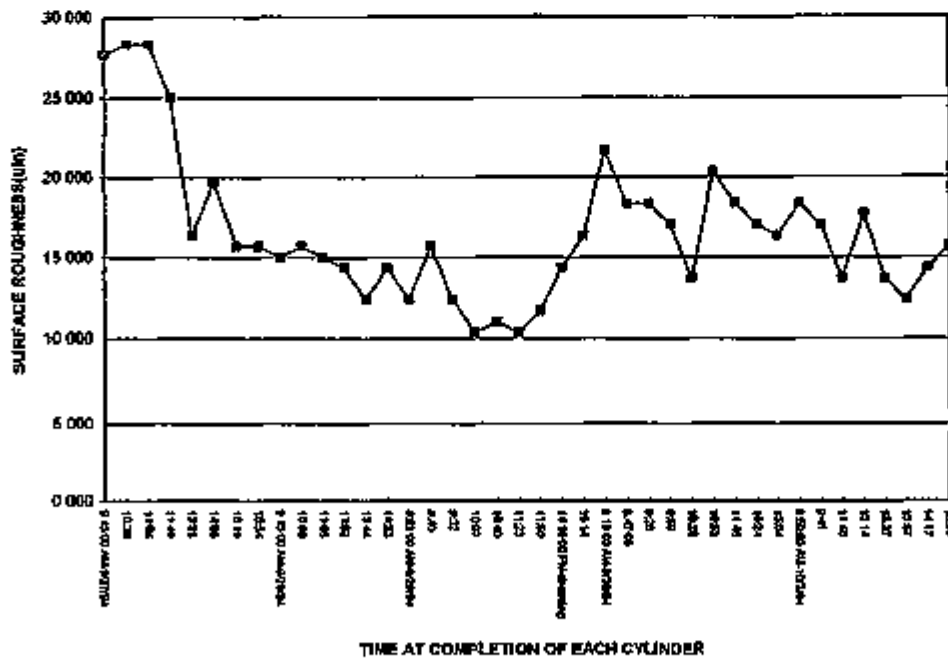
Figure 7. Multi-Vari Analysis of Surface Roughness Control

For surface roughness -
1. Dressing increases surface roughness
2. After dressing, roughness initially increases and then decreases

3. A sporadic, unknown event appears to cause roughness increase

A full factorial analysis of grinding parameters is underway to further identify those parameters and their interactions most important for surface roughness control. In process dimensional and surface roughness measurement, and electrolytic in-process dressing (ELID) are being investigated as methods to reduce variation.

Task 2.4 Intelligent Processing

Task 2.4.1 Slip preparation & Forming:

In-situ viscosity analyzers have been tested and found to provide faulty data for the slip system employed in hybrid molding. Conventional viscosity measurements are therefor being conducted to determine the extent of variation during molding.

The soft computing approach to optimization and control of the hybrid molding process has been developed. The fundamental elements of the plan are building of a hybrid system in which radial basis function neural networks (Figure 8), and fuzzy sets are combined with genetic algorithms. The RBF network will be used to model the parameters of the ceramic forming process, and will function as a simulator of these parameters. The simulator will then be used as an objective function generator for genetic optimization as outlined in Figure 9. Considerable work will go into data preprocessing, which involves both feature selection and data formatting such as data normalization, scaling, averaging. The hybrid system will utilize the process expert's
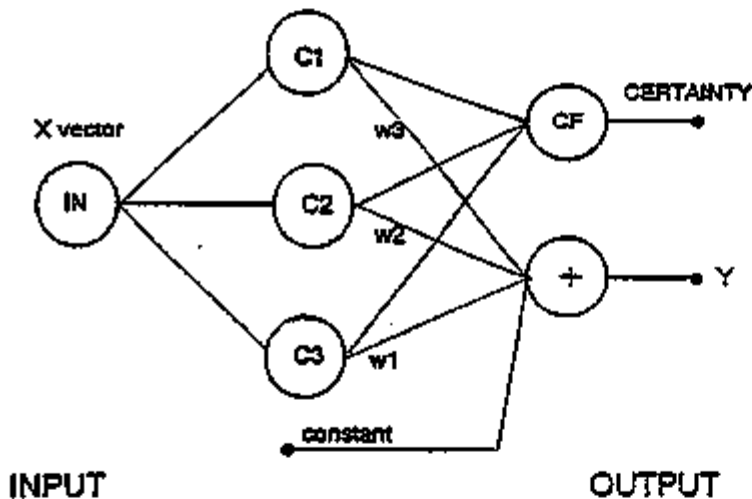
Figure 8. RBF neural network generating uncertainty factors.
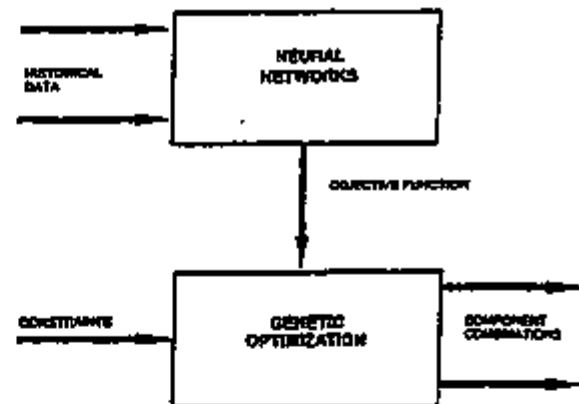
Figure 9. Proposed combination of soft computing and genetic algorithms.

knowledge in defining the fuzzy sets. A preliminary test matrix for generation of the neural network training data has been constructed, consisting of approximately 15 each of input and output variables. Ranges for these process variables have been set. This matrix will be further analyzed for possible compression to minimize the number of process runs required.

Task 3 Inspection and Test

Task 3.1 Rotor Inspection

The surface flaw detectability in ultrasonic inspection was evaluated using 15MHz, 25MHz and 50MHz immersion type probes for surface flaws. The most sensitive was a 50MHz probe, which can detect an approximately 50μm round shape and 35μin. width linear tool mark flaw. Subsurface flaw detectability tests have started and ASTM standards obtained. Preliminary evaluation of braze and shaft candidate materials shows that they have ultrasound velocities between 3,700 and 5300 m/sec. Since ultrasonic

inspection of metal joints may utilize the double probe method, we have prepared an equipment modification plan.

Spin test capability has been confirmed, with successful operation at 200,000 rpm. However, spin test setup investigation revealed deficiencies in the arbor design used for testing ceramic rotors of the size to be made in this program. The arbor has been redesigned and delivery is expected well within the allowed test setup schedule.

Status of Milestones

Milestone 1, Design Package, was completed and submitted on time. The design package was approved. No other milestones are due during this fiscal year, and all future milestones are expected to be met on schedule. The next milestone, due April 15 after completion of the baseline process demonstration, is establishment of process improvement goals.

Development of Advanced Ceramic Manufacturing Technology
E. Bright, C. Burk, S. A. Dynan, J. Ekatbar, B. J. McEntire (Norton Advanced Ceramics)
Y. Kalish, T. Kaushal (Detroit Diesel Corporation)
M. Hauptman, L. E. Mains (Deco Technologies, Inc.)
M. Tricard, J. Picone, K. Subramanian (Norton Superabrasives Division)
C. Miller (Centorr/Vacuum Industries)
V. K. Pujari, L. Sales, R. L. Yeckley (Saint-Gobain/Norton Industrial Ceramics Corp.)
L. Christodoulou (BDM Federal Incorporated)
J. Busch, A. E. Mascarin (Ibis Associates)
D. Whittmer (Whittmer Consultants)

Report Prepared by
Eric Bright
Saint-Gobain/Norton Industrial Ceramics Corporation
Norton Advanced Ceramics
10 Airport Park Road
East Granby, CT 06026

Objective/Scope

The objectives of this program are to design, develop, and demonstrate advanced manufacturing technology for the production of ceramic exhaust valves for a diesel engine. The ceramic material for this program is Norton Advanced Ceramic's NT451 SiAlON, and component to be developed and tested is the exhaust valve for DDC's Series 149 engine. Specific objectives are: (1) To reduce manufacturing cost by at least an order of magnitude over current levels; (2) To develop and demonstrate process capability values (C_{pk}) of 0.7 or less for all critical component attributes; and (3) To validate ceramic valve performance, durability, and reliability in rig and engine testing.

Technical Highlights

Task 1 - Component Design and Specification.

Task 1a - Preliminary Design.

Two dimensional finite element analysis of the valve seat angle and keeper groove geometry was completed by ORNL under an existing DDC-ORNL CRADA. The FEA results are summarized in DDC's Semiannual Technical Report for the reporting period provided in Attachment 1.

DDC has modified valve drawing DD-125232 to incorporate the lowest stress design.

Two ceramic valve part No's were created: DD-125232-D for a valve with a 30° seat angle; and DD-125233-ND for a 45° seat angle option. DDC has released valve drawing DD-125232 to NAC as the preliminary valve design. NAC has completed all shop drawings and technical specifications comprising the preliminary design package.

DDC material specification 15T-4/S149 "Engineering Product Approval Requirements for Experimental SiAlON Exhaust Valve" was completed during the reporting period. Mechanical properties of the most recent powder batches of NT451 SiAlON were analyzed and taken into consideration in preparing this document. This material specification has been included as part of the preliminary design package.

The preliminary design package comprising Milestone No. 1 was finalized and submitted by NAC during the reporting period.

Task 1b- Final Design Analysis.

No Activity to Report.

Task 2 - Component Manufacturing Technology Development.

Task 2a - Environmental Safety and Health.

No activity to report.

Task 2b - Process Cost Modeling.

A kickoff meeting to initiate the cost modeling effort was held between IBIS and NAC ACM team members. NAC's current and proposed cost effective process was outlined, and technical specifications for each operation were discussed. IBIS's first two subtasks, 1.1. (Technology Review) and 1.2 (Data Collection), were initiated during the reporting period. IBIS has initiated data collection and published literature research activity to provide background for each operation. Particular focus is being given to machining operations. Contacts for expert review of the model were made at Alfred University and commercial ceramic machining businesses. Data is being assembled in to a database for analysis in a subsequent data analysis subtask. Tony Mascarin form IBIS participated in a meeting with DECO Technologies to review development of the ceramic valve production machining process.

Task 2c- Process Control

Milling and Spray Drying Process Control - One test batch (SLX02) and two production batches (SPP01 and SLP02) have been milled and spray dried using Ube E-10 as the raw material source. Fifteen (15) Kg from batch SLP02 have been pressed into valve blanks and green machined to establish density and dimensional control capability of parts fired in the continuous sintering furnace at Centorr/Vacuum Industries (CVI). Batch SLP03 (35

Kg) is currently being milled for use in preparing valve blanks for the valve machining development effort.

Four additional batches (SLX15, SLX17, SLX18, and SLX19) have been milled and spray dried using silicon nitride provided by Kemanord, Shin-Etsu, Stark, and Ube. These materials behave differently during slurrying and milling and therefore, required some initial work to establish pH and viscosity controls. In particular, the Shin-Etsu powders could not be filtered due to a high viscosity and flocking even with a pH of 10.2. All of the powders resulted in reasonable spray dried powder properties, and are currently being pressed into tile and cylinders for evaluation of sintered properties by batch sintering at NRDC and continuous sintering at CVI.

Continuous Sintering - Continuous sintering activity was initiated during the reporting period in conjunction with Centorr/Vacuum Industries (CVI) and Wittmer Consultants. The CVI/Wittmer team has begun work on their Subtask 1.1 (Raw Material Process Control) and Subtask 1.2 (Dimensional Control). Sintering trials using sections of NT451 SiAlON DDC series 149 valve blanks were conducted during the reporting period under the Dimensional Control subtask. Valve stems readily sintered to full density. Valve heads had lower sintered densities than the stems for all sintering conditions explored.

Machining - The valve machining process development effort was initiated during the reporting period. This activity is being performed in conjunction with Norton Superabrasives Division and DECO Technologies. A kickoff meeting was held at NAC's East Granby plant on September 12, 1994. NAC transferred all of the technical specifications for the current valve machining process to DECO. A detailed work plan for Norton Superabrasives' valve machining development and technology transfer activity was reviewed wit DECO. DECO has prepared a corresponding work plan for receiving and demonstrating the valve production machining process technology. During the reporting period, DECO established contacts with various machine tool builders to obtain data and proposals for cost effective grinding of ceramic valves.

Norton Superabrasives personnel participated in a meeting with Arvid Pasto from ORNL to discuss possibilities of a user program to support the valve machining development effort. It was decided not to proceed with a user program until initial grinding wheel screening trials using small diameter wheels are completed. At that time, a user agreement could be initiated utilizing full scale grinding wheels on the centerless grinding equipment at the HTML.

Task 2c- Intelligent Processing

A work plan detailing the scope of BDM's effort under the intelligent processing effort was completed during the reporting period. BDM will perform the following activities:

(1) Conduct a literature search on modeling of the spray drying process.
(2) Code an expert system to tie into the control software.

(3) Provide guidance on the selection of sensors to monitor spray drying.

(4) Perform modeling of the dry bag isopressing process.

A similar effort is underway for intelligent processing of the milling operation. The sensors to be utilized in the milling process have been selected, and the sensor equipment will be acquired during the next reporting period.

Task 3 - Inspection and Testing

No Activity to Report.

Task 4 - Process Demonstration.

Task 4a.

NAC has received DDC's released preliminary design valve drawing, DD-125232. The corresponding shop prints for the pressed blank, green machined blank, and fired blank have been completed. A detailed routing for fabrication of NT451 SiAlON valves to this drawing has been completed as well. A total of 200 preliminary design valves are being fabricated - 100 with a 30° seat angle; and 100 with a 45° seat angle. A pre-production batch of 24 valves has been processed through batch sintering for to check stock condition and to set up finish grinding ceprations.

Task 4b.

No Activity to Report.

Status of Milestones

Milestone No. 2 is expected to be completed in January 1995. A partial delivery of 30 to 60 preliminary design valves is estimated for December 1994.

Communications/Visits/Travel

NAC hosted a kickoff meeting for its ACM Program on April 7, 1994. All of NAC's subcontractors attended the meeting to present and discuss their work plans for the program. Tours of the Northboro Research and Development Facility, Norton Superabraisives' World Technology Grinding Center, and NAC's East Granby, CT silicon nitride component production facility were conducted as well.

DDC held a quarterly CRADA review meeting at its facility on May 23, 1994. The purpose of this meeting was to coordinate activities between the DDC-ORNL CRADA and NAC's ACM program. It was decided in this meeting that ORNL will perform the 2-D FEM analysis on the Series 149 exhaust valve under its CRADA with DDC. This change has been incorporated into DDC's ACM program Statement of Work.

A design review meeting for the preliminary design valve was held at DDC on June 9, 1994. Topics of discussion included NAC's valve design recommendations, a review of NAC's current valve prototype manufacturing process, DDC's draft material specification, and NAC's fabrication schedule for 200 preliminary design valves. A technical approach to integrating machining development and cost sensitivity analyses under the ACMT program was discussed and adopted.

August 29, 1994 - IBIS-NAC process cost modeling kickoff meeting, NAC E. Granby, CT.

C.W. Miller traveled to Wittmer Consultants to discuss valve sintering and intelligent processing as related to the subcontract.

D.E. Wittmer traveled to CVI to discuss subcontract modifications and scheduling with CVI and NAC personnel.

D.E. Wittmer traveled to CVI to conduct sintering trials on valve sections and to discuss intelligent processing as related to the subcontract.

September 7-15, 1994 - Murray Hauptman from DECO Technologies attended the IMTS machine tool show in Chicago, IL to obtain information on machine tools for production ceramic valve grinding.

September 12, 1994 - DECO Technologies, IBIS, NAC valve production machining process development meeting, NAC E. Granby, CT.

September 30, 1994 - Norton Superabrasives, NRDC, NAC meeting with Arvid Pasto from ORNL to discuss possibilities for a user program to support valve machining development, SGNICC Northboro Research Center, Northboro, MA.

Problems Encountered

Delays were encountered in initiating subcontracts with Norton Superabraisives and BDM. These two subcontractors are now under contract, and have begun work.

Publications

None.

Attachment 1

Attachment 1

Development of Advanced Ceramic Manufacturing Technology
Yury Kalish (Detroit Diesel Corporation)

Objective/Scope

The objectives of the program are to design, develop and demonstrate advanced manufacturing technology for the production of ceramic exhaust valves for diesel engine. The ceramic valve for this program is Norton Advanced Ceramics' SiAlON material to be designed and tested in the DDC Series 149 engine. Specific objectives are (1) to reduce the manufacturing cost by an order of magnitude, (2) to develop and demonstrate process capability and reproducibility, and (3) to validate ceramic valve performance, durability and reliability in fixture rig and engine testing.

Technical Progress

According to the revised Statement of Work, DDC utilized finite element modeling (FEM) done by ORNL under CRADA for ACMT ceramic valve design. Preliminary valve design is based on the results of 2-D FEM and probability of survival (POS) calculations. Final design analysis will include 3-D FEM and POS and will consider translated seat and asymmetric temperature.

Baseline analysis using early insert and material properties has been completed. Each load combination that occurs during the valve cycle was analyzed. On the seat, the maximum principal stresses were significantly larger when the pressure (15.9 MPa), spring force (445 N), and thermal loading acting simultaneously (valve closed). Based on its results the fillet radius was increased from 0.5" (12.7 mm) on the metal valve to 0.75" (19.05 mm) on the ceramic valve.

Seat angle and keeper groove geometry were also considered. In addition to the production 30^0 seat angle, 45^0 option was modeled. The stress values are shown in Table 1.

Attachment 1

Table 1. Maximum principal stresses in the valve seat

Location	Stress, MPa	
	30^0 seat	45^0 seat
Seat radius (midway between the seat and the stem)	201.3	155.8
Seat (in insert contact region)	188.2	174.4

Since the mean strength of SiAlON NT451 at the temperature of interest is 780 MPa, the POS calculations gave a value of 1.00 for all cases. Fatigue and other factors may, however, reduce the strength significantly. The 45^0 valve has a 23% lower maximum tensile stress in the radius, and a 7% lower stress in the seat. The lower radius stress is probably due to the fact that the 45^0 valve can slide more easily on the insert. Therefore, the lower stress with the 45^0 seat angle will likely come at the expense of more wear. In order to investigate the stress-wear trade-off, it may be beneficial to have both 30^0 and 45^0 prototype valves made.

Four different keeper groove geometries were compared. They represent the groove configurations on the current production Series 149 valve, on the Series 60 exhaust valve, on the ceramic valve tested under ADECD program and one configuration proposed by Norton. Standard groove (the one currently used for the metal valve) has a 30^0 angle at the bottom. Option 1 has a 44^0 angle at the top, and Option 2 has both the 44^0 angle at the top and 30^0 angle at the bottom. Deeper groove was proposed by Norton and featured 0.2942" (7.47 mm) nominal keeper groove diameter compared to 0.2965" (7.53 mm) diameter on DDC designs. Proposed groove was also wider and had broken edges with 0.0075" (0.19 mm) radius. Keeper groove options were modeled with 1335 N closing force. The maximum calculated principal stresses are shown in Table 2.

Table 2. Maximum principal stresses in the keeper groove (MPa)

Case	Stress, MPa
Standard	106.2
Option 1	107.6
Option 2	108.2
Norton design	146.9

All of these maximum stresses are on the surface of the groove, upward from the groove center line. Based on these results, standard keeper groove design is recommended for the prototype ceramic valve.

Valve drawing DD-125232 was modified to incorporate the results of the ORNL finite element modeling. Figures I and II were removed, leaving only one keeper groove configuration on the drawing. Valve seat angle was charted to include both 30^0 and 45^0

Attachment 1

options on the same drawing. Following part numbers were assigned: DD-125232-D for a valve with a 30° seat, and DD-125233-ND for a valve with a 45° seat.

Work on the Series 149 valve train dynamic modeling has started. Model will be created using PC version of the ADAMS software.

A 15T-4 material specification "Engineering product approval requirements for experimental SiAlON exhaust valve" has been generated based on previous DDC experience with structural ceramic components. Unlike a 90K specification which is for production components, a 15T-4 specification is for development components with DD part numbers. The 15T-4 S149 ceramic valve specification is based on DDC experience with the design, analysis and testing of components from various suppliers other than Norton. DDC specifications are supplier and process specific. Therefore, a considerable amount of refinement is needed to this specification as Norton develops specific processes to manufacture ceramic valves. Characterization results from lots of SiAlON will provide the basis for these refinements. Properties must be developed from co-processed samples that are fabricated coincident with the parts for each lot of material. These refinements will also depend on DDC testing of valves on fixtures and engines.

Minimum requirements for material hardness, density, fracture toughness, MOR strength, Weibull modulus, porosity and microstructure are specified, as well as corresponding measurement standards.

Status of Milestones

One milestone was completed during the reporting period. Material specification for ceramic valve was finalized and released. All other milestones are on schedule.

Publications

None.

Advanced Ceramic Manufacturing Technology Program

J. Sibold, J. Stephan, G. Garvey, M. Ritland, and R. Weaver
(Golden Technologies, Inc.)

Objective/Scope

The purpose of this program is to develop a cost-effective advanced ceramic manufacturing technology capable of achieving:

- High volume production
- Prices competitive with current metals
- High Process Capability

to result in components *qualified* for installation in diesel engines.

Approach

The focus of the technical approach is the development of viable ceramic manufacturing technology for commercial introduction of selected ceramic components in diesel engines. Two components were selected by our two diesel engine companies. Both parts are of a similar geometry, leading to a whole family of parts that can be pursued in the near future. Hence, while the development effort will involve two product teams, two parts, two materials, the similarity of components and processes will provide Golden Technologies a common platform for problem solving through the application of the TQM process to program needs.

The technical challenges of the program (High volume, Low cost, High process capability) will be addressed through:

- Near-net shape processes will be developed to reduce the high cost of post-sintered machining

- Intelligent Processing will provide the technological edge needed to control processes at a level leading to high process yields that impact improvements in cost, and

- Selecting simple geometry parts, and using lower cost raw materials to satisfy product specifications and performance standards.

The manufacturing technology development effort will be an iterative process starting with the careful analysis of baseline operations to establish control and cost data for characterizing the processes. The principle of continuous process improvement will be applied to solve problems in achieving the highest yields as the key element required of cost-effective manufacturing. Total Quality Management will be emphasized to identify process deficiencies, design experiments, solve problems, and implement improvements. At each step of the way, process improvements will be monitored by Statistical Process Control and cost modeling to measure the effect of changes in processing operations.

Task 1. **Component Design and Specification**

Initial Cummins Component Design. Discussions with Cummins regarding their component were productive in defining meaningful test methods for acceptance. An underlying premise of this activity assumed that chemical corrosion properties and tribology were inherent in the composition chosen, independent of processing conditions. Critical properties chosen for TTZ in this application were flexural strength, coefficient of thermal expansion and density. The intent of the testing program defined by Cummins remains to test actual components with the approved design reflected by the component print.

Initial Detroit Diesel Component Design. A Design Failure Mode Analysis and Effects (FMEA) document was completed by the GTC/Eaton/DDC team. Two designs were addressed during this review including the standard solid cylinder and a hollow cylinder. The latter design was considered due to the cost reducing benefits of a hollow cylinder which facilitates debindering and nitriding. The standard design and DFMEA was supplied to Martin-Marietta as a Task 1 deliverable.

Nominal property data on thermal and mechanical properties of SRBSN has been completed by GTC. A preliminary material property specification has been completed, but material specifications will continue to be updated. The significant characteristics that have been identified for sampling each lot produced are: 1) Density, 2) MOR b-1 strength, 3) Weibull Modulus, 4) Surface porosity. Periodic sampling was considered for: 1) Fracture toughness, 2) Bulk composition, and 3) Microstructure grain size analysis. Elasticity, hardness and thermal properties were not considered essential for sampling. Sixty strength data values for a GTC standard SRBSN batch were supplied to DDC together with Weibull analysis to aid in upcoming finite element analysis.

Task 2.   **Component Manufacturing Development**

GTC-Cummins Transformation Toughened Zirconia (TTZ) Component. The primary processing technology chosen for component fabrication was determined be an extrusion process. The cross-sectional thickness of the component design was acceptable for extrusion processing. Although the fabrication of secondary geometric features is required for the component to function in the application, the high green strength afforded by GTC's extrusion process is an advantage in completing near-net shape forming. Other desirable attributes of GTC's extrusion process include: (1) sufficient plastic flow under pressure for shape generation; (2) post extrusion rigidity (yield point) to resist slumping during handling; (3) a smooth surface texture created by the extrusion die; and (4) a benign aqueous-based binder system that promotes particle distribution homogeneity under pressure for uniform density.

Development activity for the period has been focused on defining a baseline process for TTZ including mixing, extrusion and drying. The extrusion process chosen utilizes a standard binderless, spray dried powder procured from Coors Ceramics' Golden Plant. The baseline process has been used to produce test blanks for grinding studies at Coors Ceramics and Cummins. Additional sintering campaigns are intended to produce blanks for grinding studies at Eaton MTC. In anticipation of increased blank production for grinding trials, a precision, automatic cut-off saw has been ordered from an outside vendor for December, 1994, delivery. Also, a support fixture has been developed and implemented on a routine basis that minimizes deformation of the rod, when transferring it from the extrusion die to drying setter.

With the development of a viable extrusion-binder system for the baseline process from mixing through drying, current development activity is now more focused on achieving the highest level of component straightness in the as-sintered state. Kiln support refractory has been identified as a key concern affecting product quality. A porous line of refractory materials has been identified in a variety of support shapes for sintering trials that are being explored in firing trials in a production kiln.

Kiln sintering cycles have been evaluated for optimizing mechanical properties. Cooling cycle control is the key element in controlling precipitate formation in the microstructure which, in turn, determines material toughness and flexural strength. With time, implementation of an optimized sintering cycle will be achieved in the production

environment to ensure that all critical material properties conform to specifications.

GTC-DDC Sintered Reaction Bonded Silicon Nitride (SRBSN) Component

Milling Development. Several experiments were performed toward a goal of improving the standard operating procedure for milling for SRBSN. In one experiment the pH was maintained at a specific level throughout milling. A second experiment was performed during which pre-scheduled additions of deflocculant were added. Equivalent properties were achieved with pre-scheduled additions. The standard operating procedure was modified as appropriate.

Extrusion. This period activity has focused on forming process development for manufacturing the cylinder. Based on preliminary cost analysis and experience in forming process capability, GTC has focused on developing the extrusion process as the preferred forming technique. Three tasks have been pursued toward extrusion development, including: the production of a large standardized feed powder lot, development of a standard operating procedure for the milling process and extrusion process development.

A total of 1,220 pounds of SRBSN raw material has been prepared to data representing ten separate batches. This material was the feedstock for extrusion development and isopress part forming.

It was recognized that the impact of silicon powder processing upon mixing and extrusion variables is key to controlling the extrusion process. Key parameters during powder processing include surface area generated during milling and the deflocculant/dispersant used. These parameters influence the wetting behavior of the binder system during mixing. Mixing time appears to be a response variable to powder wetting resulting from changes in surface area and the dispersant used during milling. Mixing time is varied to achieve the desired state of mixing agglomeration as a requisite step for high quality extrusion. Viable binder formulations have been developed for extruding thick walled tubes and solid rod geometries. A basic format for capturing fundamental mixing data through drying has been implemented for future process control. Future changes for mixing, extruding, and drying processes will be predicated on feedback from downstream thermal processes-nitriding and sintering.

The flexural strength of dried, green rods and tubes was measured for extruded Si and TTZ. Using the three point bend method, flexural strength values in the range of 1,000 to 1,500 psi. were measured for TTZ. Correspondingly, flexural strengths for Si were in the range of

1,400 to 2,300 psi., depending on drying treatment and binder formulation. Load-deflection curves for TTZ indicated a large inelastic behavior up to the load to break. The inelastic region was present for extruded Si, but was relatively small compared to TTZ. Energy-to-break values were calculated from the area under the load-deflection curves for each material. Strength values for extruded TTZ and Si reflect a 1 to 1.5 order of magnitude increase over typical strengths for powder processed compacts formed by dry or isostatic pressing.

A total of 21 developmental extrusion runs were made during this period. Three subtasks were addressed including: binder composition development binder level optimization and process replication. These experiments resulted in elimination of visual flaws such as cracks, striations and voids. Typical optimized sintered densities were high (i.e. 3.38 g/cc). During this time drying process development was addressed. A preliminary standard operating procedure for extrusion and drying was determined.

In total, feed stock for over 12,000 components have been produced and over 1,500 finish sintered blanks have been completed. These parts have been or will be used for fixture tests, motor tests, static tests, destructive material property testing and machining development studies.

Thermal Processing. A series of experiments were performed to investigate debindering. an optimal thermal schedule/atmosphere combination resulted in a 70% reduction in cycle time.

Two campaigns of continuous sintering tests were performed at a commercial furnace manufacturer during which iso-press and extruded components were fired. A total of eleven time-temperature combinations were evaluated. None produced the high densities obtained using batch furnaces. Additional experiments are planned.

A series of experiments were performed to evaluate the effect of part size on thermal cycle times. Samples as large as 1.4 inches in cross section were successfully debindered and nitrided within 28 hours. Parts as thick as 0.35 inches were sintered to theoretical density.

Additional work has been completed evaluating several commercial refractory compositions and their applicability to thermal processing.

Material Properties. Initial strength test results have been completed for four independent batches of sintered extruded hollow parts. Average batch strengths have ranged from 71 ksi (490 MPa) to 93 ksi

(642 MPa). Fractography has been performed on many of these broken specimens and the data are being used in extrusion development.

Part Manufacture. GTC has prepared 48 components by isostatic pressing. Half of these components were supplied to DDC for fixture tests and half were supplied to Eaton, CoRD for material and dimensional characterization. All parts were characterized by GTC for both material and dimensional characteristics.

Task 2a.   Process Cost Modeling

Summit Solutions, Inc. has completed cost simulations for the production of both the Cummins engine and Detroit Diesel ceramic engine parts. The simulations support the identification of cost drivers in the production processes and the behavior of those drives under various operating scenarios. The simulations reflect the process flow for the production processes for each of the parts, and can be run with or without animation. Process cost data is included for all relevant process steps either in terms of cost per unit time, cost per volume, or cost per part. Output is provided graphically, in table form and in file format that can be manipulated in a spreadsheet or database. Output information for a given operating scenario includes production cost per part and total cost for the production run. The cost contribution of each process step to the total production cost is shown graphically as well as in data format. A graphical display of the contributing share of each cost element in a process step is shown for all process steps. Inspection costs, scrap costs and the breakdown of overhead costs are shown in the aggregate and for each process step. All key production process elements are included in the models as variables. The variable values can changed by the user at the start of a model run, which provides for doing "what if" analyses to determine the impact of changes in the production processes on production costs.

Task 2b.   Environmental Health & Safety

A subcontractor has been identified and its reviewing current processes and existing documentation (i.e., MSDS) to perform an assessment of EHS issues.

Task 2c/d.   Intelligent Processing and Process Control

After evaluating both manufacturing processes two primary areas of focus concerning intelligent processing and process control have been identified. First, a networked comprehensive database and a computerized information system is recognized as an essential

platform to carry-out and support intelligent processing, integrated process control, data acquisition, and SPC. This extensible and scaleable hardware and software platform will support both development and production level efforts and is being developed in parallel and in conjunction with other efforts. Second, process control and process modeling for individual operations and the overall manufacturing processes is being approached on a priority basis. The unit operations and overall process control schemes that are the most critical and have the greatest impact on component cost and quality are receiving the initial focus.

The RMH Group, Inc. is responsible for designing and implementing the database and information system which will gather and process data from all the critical processing steps. This system solution includes a wide area network(WAN), a large local area network(LAN) throughout the GTC buildings, an integrated and comprehensive data base and data server, a new supervisory control and data acquisition(SCADA) system, new sensors and transducers, data links into existing control systems, and man machine interface(MMI) stations including their operational software. The design is based on platforms which support the current and future needs of the project, for example, scaling to large production volumes and supporting possible future ISO 900X guidelines, documentation and audits. RMH has completed the first phase of the information system including recommendations for computer hardware, software, instruments and requirements for process monitoring and the database. Purchasing specifications for all standard hardware and software is complete. Major hardware components recommended include Compaq computers and Allen Bradley programmable controllers. Software recommendations include Wonderware with built in statistical processing capabilities for data monitoring and operator interfaces and Microsoft SQL Server for the data base manager. RMH has completed preliminary monitoring and database requirements for selected processes and documented in process block diagrams and spreadsheet tables. These preliminary efforts will be refined during the second phase into specifications for the process monitoring software and the prototype database. Process flow charts are nearly complete and process engineering and standard operating procedures are in progress. Additionally, training for design of experiments (DOE) and process capability (C_{pk}) is currently underway.

The second focus involves process engineering and process modeling for individual process steps as well as an overall process line model. Both engine component manufacturing processes were considered and evaluated for the most effective opportunity to initially apply process control and intelligent processing. Six major processing steps,

including; milling, spray drying, mixing, extruding, drying, and nitriding have been identified to receive the first attention. The modeling effort taken involves a blend of theoretical, heuristic, and empirical approaches. When available, theoretical models from the literature have been utilized as a starting point. Heuristic information (or rules of thumb) are then compiled and superimposed over the theoretical model and finally historical and empirical data is used to verify the models. Green shaping by extrusion was determined to be an area that plays a critical role to achieve the overall goal of significant cost reduction by producing a near-net-shape fired blank to final machining. The extrusion shaping process is common to both engine components and is the least understood. Within the green shaping process block the emphasis is further focused on quantifying the rheological parameters as a function of ceramic paste formulation. A process model for the extrusion process has been developed that utilizes a fully instrumented test cell that allows six quantifiable batch variables to be correlated against batch composition and product qualities. The test cell has been designed and it's construction is nearly complete. Initial results suggest that the model is appropriate A process model that describes the batch mixing operation is being developed. To support this model the mixer has been modified and instrumented to monitor mixing time, temperature, and torque. A process model that describes the drying of extruded stock has been initiated. Finally, a product model that describes the roundness, straightness, and cylindricity of the components as they move through the green shaping and firing processes is under development. A real-time in-line vision system will be used to characterize this geometric aspect of the components. An extension to this production vision system is being considered for final part dimensional measurement. Intelligent processing and expert system software is being evaluated as a tool and platform to develop the process models and simulate process variables. Gensym Corporation's G2 real-time expert system software has been identified as an appropriate tool for developing the process models. It supports real-time intelligent monitoring, rule-based reasoning, simulation, network connectivity, and system learning.

Task 3.   **Inspection and Testing**

GTC - Cummins Component
To determine the correlation of roundness and straightness measurements between GTC and Cummins, a precision instrument was delivered and installed on a trial basis in the metrology lab at Coors Ceramics. Measured results from this instrument on test components compared favorably for critical dimensions measured at both Eaton and Cummins using similar equipment.

GTC - DDC Component

Progress has been made in the area of part testing. For the initial pass, parts were manufactured at GTC by an iso-press forming process while extrusion was under development. These parts were machined to specification by Coors Ceramic Co. and independently tested for material properties and dimension at GTC and Eaton-CoRD. All specifications were met. Some of these of these parts were forwarded to Eaton for static fatigue testing. The remainder was set to DDC for rig testing.

Static rig testing has progressed largely through the effort of Eaton Corp. at the CoRD facility. Due to the nature of the mechanical stress experienced by the component, it was necessary to develop special static shear fixture. This test fixture has been completed. Replaceable bushings were used wherever wear surfaces were encountered. The static shear test fixture is flexible in design and can be converted to dynamic testing by inserting rod-end adapters. These adapters allow usage on an MTS cycling device.

DDC has modified a valve train rig apparatus for ceramic component testing. GTC parts have been installed and the test run is in progress. The test parameters were selected to be abusive and exceed normal load cycles anticipated in the field. At the time of this writing, GTC ceramic parts have racked up over 100 hours of run time. No failures have been detected to date. The test is scheduled to run about 1000 hours.

Task 4.   **Process Demonstration.**

A review of processing capital equipment has been performed to determine critical needs for future process scale-up. The focus of this activity has been to define equipment for extrusion mixing and grinding/finishing operations. Certain capital purchases are planned prior to year-end as this analysis continues and procurement measures are pursued.

Credits

2.0 MATERIALS DESIGN METHODOLOGY

INTRODUCTION

This portion of the project is identified as project element 2 within the work breakdown structure (WBS). It contains three subelements: (1) Modeling, (2) Contact Interfaces, and (3) New Concepts. The sub-elements include macromodeling and micromodeling of ceramic micro-structures, properties of static and dynamic interfaces between ceramics and between ceramics and alloys, and advanced statistical and design approaches for describing mechanical behavior and for employing ceramics in structural design.

The major objectives of research in Materials Design Methodology elements include determining analytical techniques for predicting structural ceramic mechanical behavior from mechanical properties and microstructure, tribological behavior at high temperatures, and improved methods for describing the fracture statistics of structural ceramics. Success in meeting these objectives will provide U.S. companies with methods for optimizing mechanical properties through microstructural control, for predicting and controlling interfacial bonding and minimizing interfacial friction, and for developing a property descriptive statistical data base for their structural ceramics.

2.2 CONTACT INTERFACES

2.2.2 Dynamic Interfaces

Development of Standard Test Methods for Evaluating the Wear Performance of Ceramics
P. J. Blau (Oak Ridge National Laboratory)

Objective/Scope

The goal of this effort is to improve consistency in reporting ceramic wear data by helping to develop one or more standard test methods for quantitatively determining the wear resistance of structural ceramics, in reciprocating sliding, a type of motion which is experienced by several types of automotive and truck engine wear parts. ORNL is working with the ASTM in meeting this objective. Wear-test development normally falls within the scope of ASTM's G-2 Committee on "Wear and Erosion," and in 1990, P. J. Blau was appointed chairman of a newly established Task Group G02.40.07, "Reciprocating Sliding Wear Testing," within the G-2 Committee. This report describes the continuing activities of the Task Group.

Technical Highlights

The draft standard was reballoted and discussed at the ASTM G-2 meeting in Montreal, Canada, in May 1994. A number of changes were suggested, but the subcommittee decided that upon successful review by the Editorial Subcommittee and contingent upon approval by the Subcommittee G02.40 Chairman, a joint subcommittee-main committee ballot would be conducted prior to the next meeting to move the standard into it final phase of completion. In addition, results of the interlaboratory wear-testing program on lubricated silicon nitride specimens were incorporated into the precision and accuracy statement of the standard.

Results of the joint ballot are expected by November or December 1994.

Future Plans

The next meeting of the G-2 Committee will be held in Phoenix, Arizona, on December 8-9, 1994. Plans are to address all negative votes on the joint subcommittee/main committee ballot and to prepare the draft standard for society-level balloting in 1995.

Status of Milestones

222206	Make revisions to the first ballot and submit to ASTM G-2.
222207	Complete reduction of data from the second set of round-robin wear tests. Completed December 1993.
222208	Revise and resubmit draft for subcommittee balloting. Completed January 1994.

222209   Address any negatives and comments on the subcommittee ballot and prepare for discussion at the G-2.40 meeting. Completed May 1994.

222210   Prepare and submit revised draft standard for Editorial and Subcommittee Chairman review. Completed August 1994.

222211   Address comments on joint main/subcommittee ballot. December 1994, (continuing).

Communications/Visits/Travel

P. J. Blau attended the ASTM G-2 Committee meeting in Montreal, Canada, in May 1994, to lead the Task Group G02.40.07 meeting on "Reciprocating Sliding Wear Testing." The traveler also chaired Subcommittee G02.91, "Wear and Erosion Terminology."

Publications/Presentations

None.

2.3 NEW CONCEPTS

Advanced Statistical Concepts of Fracture in Brittle Materials
C. A. Johnson and W. T. Tucker (General Electric Corporate)

Objective/Scope

The design and application of reliable load-bearing structural components from ceramic materials requires a detailed understanding of the statistical nature of fracture in brittle materials. The overall objective of this program is to advance the current understanding of fracture statistics, especially in the following four areas:

- Optimum testing plans and data analysis techniques.

- Consequences of time-dependent crack growth on the evolution of initial flaw distributions.

- Confidence and tolerance bounds on predictions that use the Weibull distribution function.

- Strength distributions in multiaxial stress fields.

The studies are being carried out largely by analytical and computer simulation techniques. Actual fracture data are then used as appropriate to confirm and demonstrate the resulting data analysis techniques.

Technical Highlights

Work has continued on the development of a rigorous justification of a multiaxial probability of failure from fundamentals. In earlier reports, the derivation of Batdorf and Heinisch (Ref. 1) and Lamon and Evans (Ref. 2) was contrasted with a development based on the Poisson distribution given by Thiemeier et. al. (Ref. 3). In a sense, the Lamon and Evans approach follows Weibull's first derivation in his 1939 paper (Ref. 4) based on the hazard function, while the Batdorf and Heinisch approach follows Weibull's second derivation in the 1939 paper. The approach in Ref. 3 treats flaws as individual failure sites with a corresponding probability of failure. These sites are then assumed to occur via a Poisson distribution. As shown earlier, the two approaches are not consistent with each other. The fact that the Batdorf and Heinisch (B-H) and Lamon and Evans (L-H) approaches may be treated as one follows from their equivalence shown in Ref. 5.

The continuing study has focused mainly on a development of the B-H and L-E approaches from a weakest link formulation. In a weakest link setup each "link" is considered to have at least one flaw: the failure producing flaw. This is shown most clearly in the derivation given by Batdorf and Heinisch. Assuming the weakest link hypothesis and statistical independence yields the probability of survival of a particular specimen under a given load environment as

$$P_S = \prod_i^n [1 - (\Delta P_F)_i] \tag{1}$$

where the subscripts S and F denote respectively survival and failure, $(\Delta P_F)_i$ gives the probability of failure of the ith increment in a sequence of divisions of the specimen denoted by Δ into ever decreasing division sizes, and the product follows from the assumption of statistical independence (cf., Ref. 1, Eq. 1). The product gives the probability that none of the individual increments fail. The assumption is made that as n approaches infinity P_S approaches a limit. However, even if a limit exists, Eq. 1 does not show how P_S is determined. Thus there are two central issues with Eq. 1: Under what conditions does a limit exist and when a limit exists how can it be evaluated.

Weibull's first approach can be adapted to demonstrate the method. Moreover, a solution is obtained in which both of the issues are answered. The key is that in a uniform loading of a homogeneous material with equal sized increments the probability of failure is the same for each such increment (of a given size). This greatly simplifies the development. Indeed classical extreme value theory can be employed. It can be shown that

$$P_S = \prod_i^n [1 - (\Delta P_F)_i] \to e^{-\tau} \tag{2}$$

if and only if

$$n(\Delta P_F)_i \to \tau \tag{3}$$

as Δ approaches zero when n approaches infinity. Eq.'s 2 and 3 are essentially contained in Ref. 6, Theorem 1.5.1, which treats the extreme value distribution of the maximum (the weakest link formulation treats the distribution of the minimum). Following Weibull, if it is assumed that $(\Delta P_F)_i$ is given by (the size scaled Weibull distribution)

$$(\Delta P_F)_i = 1 - \exp\left[-\frac{V}{n}\left(\frac{\sigma}{\sigma_0}\right)^m\right], \tag{4}$$

then τ is given by

$$\tau = V\left(\frac{\sigma}{\sigma_0}\right)^m. \tag{5}$$

In Eq.'s 4 and 5, σ is actually σ_i, but since the load is uniform all the σ_i are equal. Study of a generalization of Eq.'s 2 and 3 to include multiaxial effects and the hazard function employed in the B-H and L-E approaches is underway. It appears that with suitable assumptions such a generalization is possible.

The approach of Ref. 3 answers the two issues directly but may not be appropriate as a model of statistical failure in brittle materials: P_S is determined directly in the formulation, so there is no question about the existence of a limit or the value of P_S determined by this limit. The approach of Ref. 3 assumes that a probability of failure for a single individual flaw is defined for a particular specimen under a given load environment. In determining the probability of failure, the flaw is considered to be located at random within the specimen with a distribution of possible flaw sizes. Flaws are assumed to act independently of each other and their occurrence is assumed to follow a Poisson distribution with a given rate parameter. If the probability of failure is denoted by B, then the survival probability of a component containing exactly one flaw is given by

$$R_1 = 1 - B. \tag{6}$$

When there are k flaws present their overall survival probability is

$$R_k = (1-B)^k, \tag{7}$$

from the assumption of independence. Letting M denote the average number of flaws in the specimen in the Poisson distribution yields a specimen survival probability of

$$P_S = \sum_0^\infty p_k R_k \tag{8}$$

$$= \exp(-MB), \tag{9}$$

where

$$p_k = M^k e^{-M}/k! \tag{10}$$

and each term in the sum of Eq. 8 gives the joint probability that there are k flaws present and the specimen survives all k of them. Now Eq. 9 implies, as the failure stress (or load) approaches infinity, that P_S is not zero. (M is finite or otherwise the development based on the Poisson distribution is not defined.) With an infinite load B becomes one for typical flaw size distributions and Eq. 9 becomes

$$P_S = \exp(-M). \tag{11}$$

Eq. 11 gives the probability that a specimen with no flaws is produced. This possibility always exists with the Poisson distribution. However, observation of many brittle materials indicates that all specimens contain flaws and over a range of sizes the Weibull distribution fits observation very well. P_S being greater than zero with an infinite load does not seem to be consistent with observation.

The difficulty with the approach in Ref. 3 is in claiming that B and r are equal. In order for the approach using the Poisson distribution to be valid, B must be a probability. However, as indicated, it is possible to set up a derivation in which B is a probability. Clearly from Eq.'s 2 and 3, r is the value of a hazard function (and generally takes values greater than one). Thus B and r cannot be equivalent. The central issue relates to the possibility of making a specimen that contains no flaws. Under the Poisson setting this is possible. Under the weakest link setting this is not possible. In a sense, in the Poisson formulation flaws are "rare," while for a weakest link formulation flaws are "numerous."

References

1. S.B. Batdorf and H.L. Heinisch, "Weakest Link Theory Reformulated for Arbitrary Fracture Criterion," *J. Am. Ceram. Soc.*, 61, 7-8, 355-358, 1978.

2. J. Lamon and A.G. Evans, "Statistical Analysis of Bending Strengths for Brittle Solids: A Multiaxial Fracture Problem," *J. Am. Ceram. Soc.*, 66, 3, 177-182, 1983.

3. T. Thiemeier, A. Bruckner-Foit and H. Kolker, "Influence of the Fracture Criterion on the Failure Prediction of Ceramics Loaded in Biaxial Flexure," *J. Am. Ceram. Soc.*, 74, 1, 48-52, 1991.

4. W. Weibull, "A Statistical Theory of the Strength of Materials," *Royal Swedish Academy of Eng. Sci. Proc.*, 151, 1-45, 1939.

5. W.T. Tucker and C.A. Johnson, "The Multiaxial Equivalent of Stressed Volume," *Life Prediction Methodologies and Data for Ceramic Materials*, ASTM STP 1201, C.R.

Brinkman and S.F. Duffy, Eds., American Society for Testing Materials, Philadelphia, 1994.

6. M.R. Leadbetter, G. Lindgren, and H. Rootzén, *Extremes and Related Properties of Random Sequences and Processes*, Springer-Verlag, New York, 1983.

Status of Milestones

All milestones are on schedule.

Publications

None.

3.0 DATA BASE AND LIFE PREDICTION

INTRODUCTION

This portion of the project is identified as project element 3 within the work breakdown structure (WBS). It contains five subelements, including (1) Structural Qualification, (2) Time-Dependent Behavior, (3) Environmental Effects, (4) Fracture Mechanics, and (5) Nondestructive Evaluation (NDE) Development. Work in the Structural Qualification sub-element includes proof testing, correlations with NDE results and microstructure, and application to components. Work in the Time-Dependent Behavior subelement includes studies of fatigue and creep in structural ceramics at high temperatures. Research in the Environmental Effects subelement includes study of the long-term effects of oxidation, corrosion, and erosion on the mechanical properties and microstructures of structural ceramics. Work in the Fracture Mechanics subelement includes development of techniques for measuring the tensile strength and creep resistance of ceramic materials at high temperatures, and testing ceramic materials at high temperatures under uniaxial tension. Work in the NDE Development subelement is directed at identifying approaches for quantitative determination of conditions in ceramics that affect their structural performance.

Major objectives of research in the Data Base and Life Prediction project element are understanding and application of predictive models for structural ceramic mechanical reliability, measurement techniques for long-term mechanical property behavior in structural ceramics, and physical understanding of time-dependent mechanical failure. Success in meeting these objectives will provide U.S. companies with the tools needed for accurately predicting the mechanical reliability of ceramic heat engine components, including the effects of applied stress, time, temperature, and atmosphere on the critical ceramic properties.

3.1 STRUCTURAL QUALIFICATION

Microstructural Analysis of Structural Ceramics
B. J. Hockey and S. M. Wiederhorn
(National Institute of Standards and Technology)

Objective/Scope

The objective of this part of the program is to identify mechanisms of failure in structural ceramics subjected to mechanical loads at elevated test temperatures. Of particular interest is the damage that accumulates in structural ceramics as a consequence of high temperature exposure to stresses normally present in heat engines.

Design criteria for the use of ceramics at low temperature differ from those at high temperature. At low temperature ceramics are elastic and brittle; failure is controlled by a distribution of flaws arising from processing or machining operations, and the largest flaw determines the strength or lifetime of a component. By contrast, at high temperature where ceramics are viscoelastic, failure occurs as a consequence of accumulated, or distributed damage in the form of small cavities or cracks that are generated by the creep process. This damage effectively reduces the cross-section of the component and increases the stress that must be supported. Such increases in stress are autocatalytic, since they increase the rate of damage and eventually lead to failure as a consequence of loss in cross section. When this happens, the individual flaw loses its importance as a determinant of component lifetime. Lifetime now depends on the total amount of damage that has occurred as a consequence of the creep process. The total damage is now the important factor controlling lifetime.

Recent studies of high temperature failure of the non-oxide ceramics intended for use for heat engines indicates that for long term usage, damage accumulation will be the primary cause of specimen failure. Mechanical defects, if present in these materials, are healed or removed by high temperature exposure so that they have little influence on long term lifetime at elevated temperature. In this situation, lifetime can be determined by characterizing the damage and the rate of damage accumulation in the material at elevated temperatures. In ceramic materials such as silicon nitride and SiAlON, such characterization required high resolution analyses because of the fine grain size of these materials: hence the need for transmission electron microscopy as an adjunct to the mechanical testing of ceramics for high temperature applications is apparent.

In this project, the creep and creep-rupture behavior of several ceramic materials will be correlated with microstructural damage that occurs as a function of creep strain and rupture time. Materials to be studied include: SiAlON; hot-pressed silicon nitride; sintered silicon carbide. This project will be coordinated with WBS 3.4.1.3, Tensile Creep Testing, with the ultimate goal of developing a test methodology for assuring the reliability of structural ceramics for high temperature applications.

Technical Highlights

The processes involved in the creep of various grades of silicon nitride were studied. Most recent efforts were directed at determining whether plastic deformation of the silicon nitride grains by dislocation glide/climb processes occurs and contributes to high temperature creep. Comparative observations were made on samples of NT-154 crept in tension or compression as well as unstressed material. All three types of samples contained relatively dense tangles of dislocations, as well as dislocation sub-boundaries, within distributed silicon nitride grains. While the number density of grains containing dislocations appeared highest in the compressive sample and lowest in the unstressed material, indicating some stress induced dislocation activity, the relative differences between samples appeared too small to conclude dislocation processes play a significant role in tensile or compressive creep. At best, these processes may lead to localized stress relief, but under restricted conditions.

Additional results on the distribution of crystalline second phases produced in PY-6 and NT-154 were also obtained. In both, devitrification of the original "sintering" glass results in both nitrogen apetite (H-phase) and yttrium disilicate, which differ in yttrium to silicon concentration. For PY-6, the formation of nitrogen apetite (higher Y\Si) is significantly favored over yttrium disilicate (lower Y/Si), while for NT-154 the reverse holds. While this result can be traced to differences in yttria concentrations in the starting powders (6 w/o, PY-6 vs. 4 w/o, NT-154), it also suggests that, despite initial differences, the residual glass compositions become similar after heat treatment. In both materials, devitrification should result in a more silica-rich, and therefore more refractory, residual glass composition. As the residual glass remains only at narrow interfaces, this beneficial change in properties should contribute to the similar, high resistance to interfacial cavitation exhibited by both PY-6 and NT-154.

Experimental Technique

The results of this study were obtained by analytical transmission microscopy (ATEM). ATEM was used to examine samples of GTE PY-6 and Norton NT-154 silicon nitride which had been subjected to tensile or compressive creep under the tensile test task of this project (WBS 3.4.1.3). Standard ceramographic techniques were used to prepare specimens for ATEM analysis.

Results and Discussion

During the past six months, studies relating to the high temperature creep of silicon nitride were continued. One part of this effort was concerned with determining whether plastic deformation occurs and plays a role in the creep of NT-154, while in the other part additional studies on the microstructure of crept PY-6 and NT-154 were obtained.

The question of whether or not dislocation activity occurs and contributes to creep was raised, in part, by earlier compressive creep

test results on NT-154 (WBS 3.4.1.3). Specifically, the stress and strain rate dependencies for compression were distinctly different from those in tension. Moreover, the absence of cavitation was indicated by density measurements which revealed no significant change in density, even after strains exceeding 1%.

As part of this recent effort, TEM examination also failed to reveal any cavities, interfacial or interstitial, that could be attributed to compressive creep. This compressive sample, strained to over 1% at 1430 C., was also examined for evidence of dislocations within the silicon nitride grains. For comparison, similar observations were also made on various tensile samples strained from 0.12 to 1.4 %, an unstressed but heat treated sample, and as-received NT-154 material. In brief, all samples, regardless of thermo-mechanical history, exhibited individual grains that contained high densities of dislocations. These dislocations were often in the form of dense tangles (as opposed to well defined slip arrays or sub-boundaries) and exhibited line curvatures, indicative of stress, again regardless of sample history. At best, comparison of the results suggested a possible difference in total dislocation density (alternatively, the density of grains containing dislocations), with the compressive creep sample containing the highest density and as-received material the lowest density. Here, however, it should be noted that even after over 1% compressive strain, the dense tangles of dislocations are sparsely distributed. Thus, while dislocation processes do not appear to play a major, rate-limiting role in compressive or tensile creep, limited dislocation activity may occur to relieve localized stress concentrations.

As indicated above, additional studies were conducted on GTE PY-6 and Norton NT-154 silicon nitride samples which had been subjected to tensile creep. Part of this effort was concerned with determining whether the formation of discrete, lenticular cavities on narrow two-grain junctions in these two grades is accompanied by an increase in the width of the remaining interface. So far, results based on high resolution observations indicate no relative increase in interfacial width occurs; interface widths adjacent to the cavities are comparable to those for other, non-cavitated interfaces, roughly one nanometer or less.

Additional results were also obtained on the crystalline second phases that form in these materials due to devitrification of the original intergranular glass. Past results showed that both PY-6 and NT-154 contain nitrogen apetite (H-phase) and yttrium disilicate (alpha in NT-154 and delta in PY-6) within multigrain junctions after high temperature exposure. These two phases differ in both structure and composition, with one aspect being the yttrium to silicon concentration. The new results indicate that for PY-6 the formation of nitrogen apetite (higher Y/Si ratio) is significantly favored over yttrium disilicate (lower Y/Si ratio), while for NT-154 the reverse is true. Here, the relative difference in nitrogen apetite formed in these two grades of material can apparently be related to original amount of yttria additive (6 w/o for PY-6 versus 4 w/o for NT-154). Moreover, the results suggest that although the composition of glass in PY-6 and NT-154 is different during sintering, the residual glass compositions after devitrification may be similar. In both materials, the formation of yttria- rich

N-Apetite, in particular, will result in a more silica-rich residual glass, which is effectively more refractory. This may explain why both materials exhibit a similar high resistance to interfacial cavitation, even at temperatures of 1400 C. and above.

Status of Milestones

On schedule

Publications

"Fracture of Silicon Nitride and Silicon Carbide at Elevated Temperatures". S. Wiederhorn, B. Anne Fields, and B. Hockey. Materials Science and Engineering, A176, 51-60, 1994.

"Creep Damage Mechanisms in Silicon Nitride". S.M. Wiederhorn, W.E. Lueche, B.J. Hockey and G.G. Long. M.J. Hoffmann and G. Petzow (eds.), Tailoring of Mechanical Properties of Silicon Nitride Ceramics, 305-326. 1994 Kluwer Publishers.

"Cavitation Contributes Substantially to Tensile Creep in Silicon Nitride". W. Luecke, S. Wiederhorn, B. Hockey, R. Krause, Jr. and G. Long. In review, J. Amer. Ceram. Soc.

Mechanical Properties and Microstructural Characterization of Si₃N₄ Ceramics

Mechanical Properties and Microstructural Characterization of Si_3N_4 Ceramics
T. A. Nolan and K. L. More (Oak Ridge National Laboratory)

OBJECTIVE/SCOPE

The objective of the research is to use analytical and high-resolution electron microscopy to characterize the microstructures of several silicon nitride materials. This report will focus on the microstructural changes occurring during dynamic fatigue testing of a self-reinforced silicon nitride/SiAlON ceramic, NT-451, manufactured by Saint-Gobain Norton.

TECHNICAL HIGHLIGHTS

In the previous reporting period, the results of the microstructural characterization of portions of a billet and several reciprocating engine valves of NT-451 were reported. NT-451 is a principal candidate for manufacture of valves and other components for replacement in reciprocating engines in an effort to reduce mass and improve efficiency. Laboratory mechanical testing of NT-451 under various conditions has begun. Reported herein are the initial observations of the effects of dynamic fatigue testing.

NT-451 has a "typical" microstructure of a self-reinforced Si_3N_4; large acicular grains are surrounded by smaller, nearly equiaxed grains. Transmission electron microscopy (TEM) reveals that there are two principal constituents, single crystal grains of Si_3N_4 with amorphous material at "triple-point" pockets, and present as a thin film between grains. No evidence for any devitrification has been found. Energy dispersive X-ray analysis (EDS) reveals both aluminum and yttrium in the grain boundary glass. Thus, yttrium and aluminum compounds are used as sintering aids in the manufacture of this material. X-ray diffraction supports the above; only one crystalline phase with peaks close to those of β-Si_3N_4 has been identified. Quantitative scanning electron microscopy (SEM) of metallographically polished and plasma-etched specimens indicated about 15 vol % glass in NT-451. Considerable effort has been expended to determine to what degree NT-451 is a SiAlON. The X-ray diffraction data indicate that the major phase is "nearly" β-Si_3N_4 but with a very small peak shift toward the positions of a silicon-rich SiAlON structure $Si_{14}Al_3O_3N_{20}$. EDS analysis in the TEM and matching to calculated spectra give a composition of $Si_{2.85}Al_{0.15}O_{0.3}N_{3.7}$ or an aluminum-to-silicon ratio of approximately 1 to 20. No differences in structure or composition were found between the billet or the valves.

Dynamic fatigue tests at 800°C have been run on flexure bars cut from the shafts of several NT-451 valves. After failure, thin foils from near the tensile surface of the bars were prepared for TEM observation. Also, new fracture surfaces were created at room temperature in order to see in the SEM resulting changes in the microstructure. One phenomenon that was observed was the formation of microcracks. Figure 1(a) is an SEM of the new fracture surface about 25 μm below the tensile surface and shows several cracks resulting from grain movement during testing. TEM confirmed the presence of cracks close to the tensile surface [see Fig. 1(b)]. The cracks primarily follow grain boundaries.
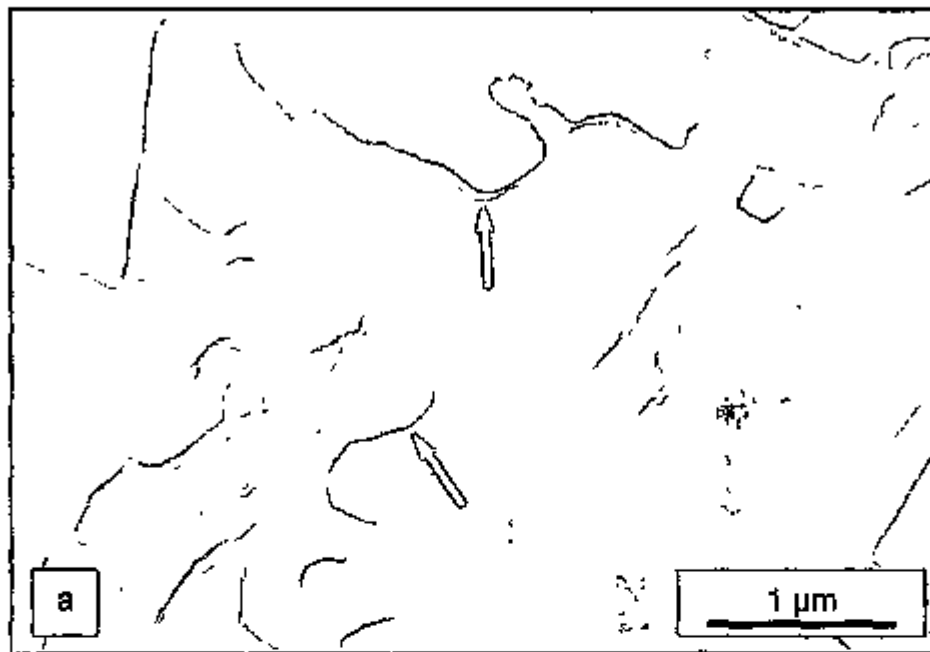
Fig. 1.   Both a scanning electron microscope image (*a*) of a new fracture surface approximately 25 μm below the original failure and a transmission electron microscope image (*b*) of a thin foil approximately 30 μm deep show cracks resulting from the dynamic fatigue testing (cracks were found only near the tensile surface).

Another phenomenon was the thickening of the amorphous grain boundary layers that separate grains near the original tensile surface. Figure 2(a) is an SEM of a new fracture surface about 10 μm below the original tensile surface that shows the cast of a large grain. On portions of the surface of the cast is a 20- to 30-μm layer of grain boundary material. In the as-manufactured material and away from the tensile surface of the tested samples, this layer is too thin to be directly observed by SEM. Again, TEM confirmed the presence of this thick amorphous layer near the tensile surface [see Fig. 2(b)]. Both the two-grain junction and the surface of the void have this film present. Considerable work remains to be done to determine changes in composition of this thick layer and to determine the relationship of depth below the tensile surface with thickness of the film.

STATUS OF MILESTONES

Program on schedule.

COMMUNICATIONS/VISITS/TRAVEL

1.   K. L. More, A. A. Wereszczak, M. K. Ferber, and R. Yeckley, "A Kinetic Study of the Formation of Voids in a Silicon Nitride Ceramic During High Temperature Creep Deformation," presented at The 96th Meeting of The American Ceramic Society, Indianapolis, Ind., April 24-28, 1994.
2.   T. A. Nolan, K. L. More, L. F. Allard, M. K. Ferber, and D. W. Coffey, "Microstructural Characterization of Silicon Nitride Intended for Use in Reciprocating Engines," presented at The 96th meeting of The American Ceramic Society, Indianapolis, Ind., April 24-28, 1994.

PROBLEMS ENCOUNTERED

None.

PUBLICATIONS

1.   K. L. More, D. A. Koester, and R. F. Davis, "Microstructural Characterization of a Creep-Deformed SiC Whisker-Reinforced Si_3N_4 Composite," *Ultramicroscopy* **37**, 263 (1991).
2.   K. L. More, D. A. Koester, and R. F. Davis, "The Role of Interfaces in the Creep-Deformation of a SiC Whisker-Reinforced Si_3N_4 Composite," p. 382 in *Electron Microscopy 1990*, Vol. 4, ed. L. D. Peachey and D. B. Williams, San Francisco Press, 1990.
3.   D. A. Koester, K. L. More, and R. F. Davis, "Deformation and Microstructural Changes in SiC Whisker-Reinforced Si_3N_4 Composites," *J. Mater. Res.* 6[12], 2735 (1991).
4.   K. L. More, "Defect Characterization in a CVD α-Si_3N_4," p. 936 in *Proceedings of the 49th Annual Meeting of the Electron Microscopy Society of America*, ed. G. W. Bailey, San Francisco Press, 1991.
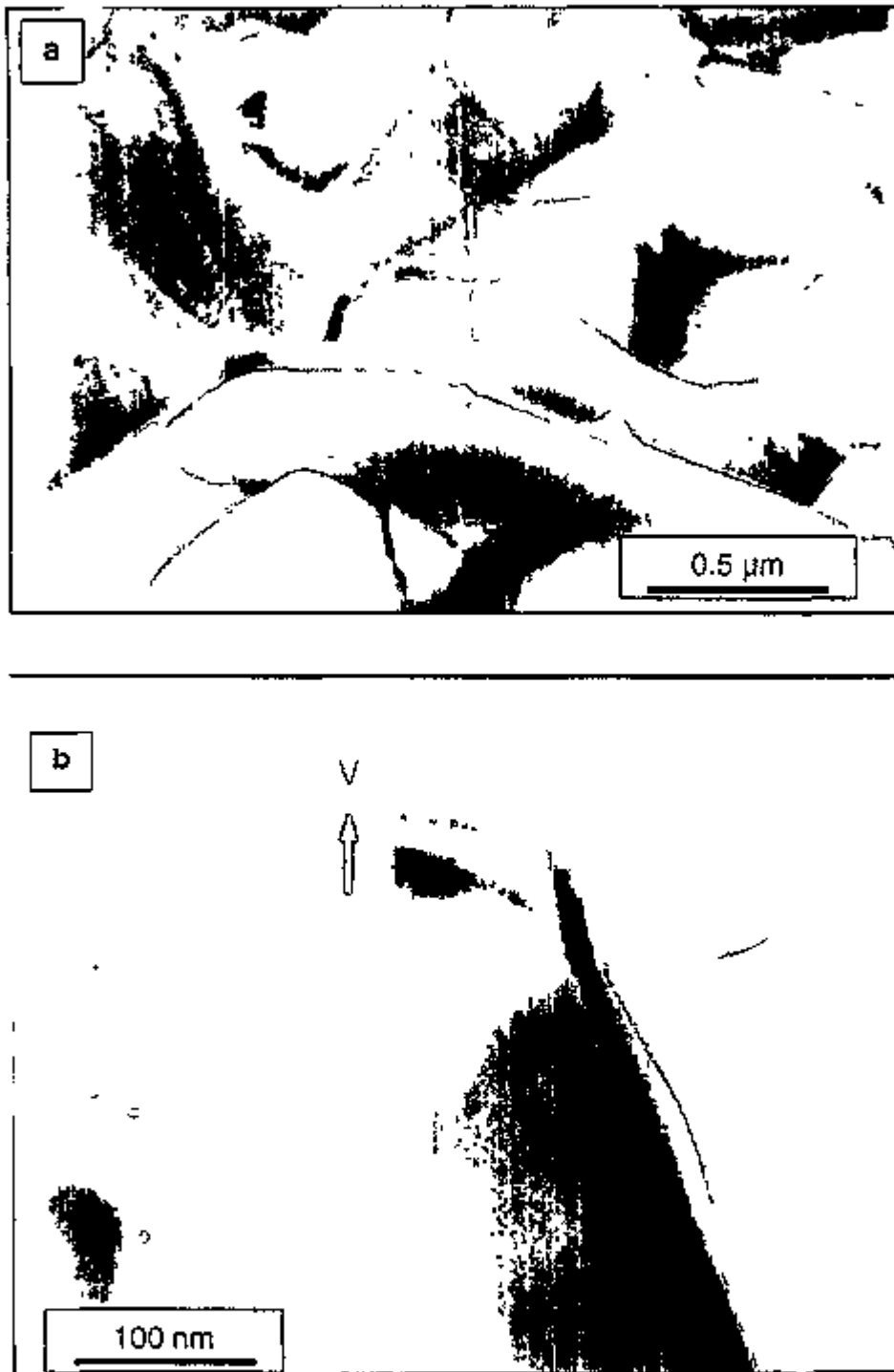
Fig. 2.   In the scanning electron microscope image of a new fracture surface (a) within 10 µm of the tensile surface, a cast of a large grain is visible. Covering portions of the cast is a 20- to 30-µm layer of grain boundary material.   The transmission electron microscope image (b) shows a two-grain junction and void with a thick layer of amorphous material in the junction and on the surface of the void.

5.   D. A. Koester, K. L. More, and R. F. Davis, "The High Temperature Creep of a SiC Whisker-Reinforced Si_3N_4 in an Air Ambient," submitted to *J. Mater. Res.*

6.   T. A. Nolan, L. F. Allard, D. W. Coffey, C. R. Hubbard, and R. A. Padgett, "Microstructure and Crystallography of Titanium Nitride Whiskers Grown by a VLS Process," *J. Am. Ceram. Soc.* 74[11], 2769 (1991).

Project Data Base
B. L. Keyes (Oak Ridge National Laboratory)

Objective/scope

The objective of this task is to develop a comprehensive computer database containing the experimental data on properties of ceramic materials generated in the total effort. This computer system should provide a convenient and efficient mechanism for the compilation and distribution of the large amounts of data involved. The database will be available in electronicfor to all project participants. In addition, periodic hard-copy summaries of the data, including graphical representation and tabulation of raw data, will be issued to provide convenient information sources for project participants.

Technical highlights

Work continued on conversion of the existing database to FoxPro™ from dBase IV™. Foxpro is a much more powerful program with a more versatile programming language for the developer. The primary reason for conversion is that the new database and software should be completely compatible across the PC/compatible-Macintosh platform lines, a major consideration in our multi-platform society. Foxpro also has some capabilities for handling graphics within the database, thus permitting incorporation of the existing photomicrograph database that currently resides on the Macintosh only. Conversion will continue as time permits. Versions for Windows 3.1, DOS, and the Macintosh are in progress.

New data input during this period included micrographs, test-related diagrams, tribology information and numerous results from modulus of rupture, tensile, stress-rupture, and creep tests. Creep curves as scanned-in graphic images are now being stored along with the time-strain points from those curves, because the understanding that can be gained from the curves was thought to be of sufficient importance. Users may plot the time-strain data using their own software.

Progress of a standard for computerization of ceramic material identification has been stalled due to a subgroup committee leadership change in ASTM E-49. A solution to the problem has now been identified, and the document should return to subcommittee ballot soon. During the spring committee meetings in Montreal, CAnada, B. L. Keyes agreed to become the liaison between E-49 and C-28 on Advanced Ceramics to facilitate ceramic-related standards development in E-49.

Efforts are under way to determine the feasibility of making the database accessible through the Ethernet locally and Internet for outside access. Only a limited number of files would be available initially, with more to be added as time permits. Current plans call for the first files to be accessible on or before February 1, 1995, depending on results from the initial trial runs.

Database personnel are again requesting that any particpant in the Ceramic Technology Project who has test data (especially from tests run in the last 3 years) please send a copy to the database administrator at ORNL. Data are acceptable on disk or in hard-copy form. Please identify the format (Lotus, Wordperfect, etc.) and platform (PC or Macintosh) in which the data are recorded if on a disk. Data in reasonable quantities may be sent via e-mail to "bip @ ornl.gov." All sources will be noted and preserved in the database.

The 1994 database summary will consist of old and new data, as test results and graphics, characterizing the major materials researched in the project. Organization of the report should be more useful than past formats, since each section will contain all the information in the database on the given material, rather than just the new data. Test background information will be available in a separate appendix in the report. Due to an unforeseen crisis, the completion data, through draft from, has been revised to December 1, 1994.

Communications/Visits/Travel

None.

Problems Encountered

Time allotted for work on the database was impacted by another crisis. This problem should be cleared up in the next month.

Status of Milestones

The database summary report scheduled for September 30, 1994, completion has been revised to December 1, 1994.

Publications

The Ceramic Technology for Advanced Heat Engines Project Database: September 1993 Summary Report, ORNL/M-3155, has been published.

3.2 TIME-DEPENDENT BEHAVIOR

Fracture Behavior of Toughened Ceramics
H. T. Lin, P. F. Becher, W. H. Warwick, and T. N. Tiegs
(Oak Ridge National Laboratory)

Objective /Scope

Ceramics with reinforcing microstructures and ceramic composites offer important advantages for heat engine applications. Chief among these is the improved fracture toughness that can be achieved by appropriate design of microstructural and material parameters. Previous studies show that these materials often exhibit substantial improvement in damage, thermal shock, and slow crack growth (SCG) resistances. However, design of such systems must also consider those factors influencing their performance at elevated temperatures.

In response to these needs, studies are conducted to determine the mechanical properties (e.g., creep, delayed failure, strength, and toughness) at elevated temperatures for these toughened ceramics. Particular emphasis is placed on understanding how microstructure and composition influence the mechanical performance at elevated temperatures and the stability of these properties for extended periods at these temperatures. The knowledge gained from these studies provides input on how to modify materials to optimize their mechanical properties for the temperature ranges of interest.

Technical Highlights

During this 6-month reporting period, research efforts were devoted into three parts. The first effort was the improvement of the stability and resolution of laser-based optical extensometers employed to measure the tensile creep displacements at elevated temperatures in air. The second effort was the evaluation of the effects of specimen size and the gripping system on the tensile creep of a hot-isostatically pressed (HIPed) silicon nitride. At last, the third effort was the study of the creep behavior of sintered reaction-bonded silicon nitride (SRBSN). The results achieved with the modification of laser extensometers were demonstrated with a HIPed silicon nitride containing 4 wt % Y_2O_3 as a sintering additive tested at 1370°C for up to 2000 h.

1. Modification of Laser-based Optical Extensometers

The laser extensometer system consists of a laser transmitter and a receiver, which is used to measure the tensile creep displacement for flat dog-bone-type specimens at elevated temperatures. It has been shown that the stability and resolution of a laser extensometer can be greatly influenced by fluctuations in air density, thus the refractive index of air present in the laser

beam path during creep.[1,2] Such air density fluctuations are a result of local changes in temperature along the laser beam path. Consequently, the local changes in the refractive index of air contribute to the scatter of the beam and, thus, in the displacement measurements.

Figure 1 shows the influence of ambient environment on the tensile creep displacements measured by a laser extensometer system (LaserMike Inc., Dayton, Ohio). The nominal resolution and stability of this laser system within its operating temperature limits (4 to 43°C) is ±0.5 μm, which is limited by its own analog output resolution of 0.0024 VDC (12 bits digital). Initially, the scatter in the displacement was quite large (at least ±5 μm), as seen in Fig. 1. Each data point in the present case is an average of 1000 scans (one data per 10 s). The large scatter in the displacement measurement is due to air convections present in the laser beam path and air seepage into the furnace, resulting in a large change in air density and thus refractive index. An improvement in the measurement accuracy to ~ ±2 to 3 μm can be achieved by simply cutting off the laboratory air circulation fan to reduce both the air seepage and air density fluctuations (see Fig. 1).

To further improve the stability of the laser system, an inverted, U-shaped, water-cooled copper shield for the laser path was designed and installed between the furnace surfaces and the laser and receiver. As a consequence, a stable air temperature (thus air refractive index) in the laser beam path was achieved, and a nominal displacement readout stability of ±0.5 μm was then maintained at elevated temperatures (see Figs. 1 and 2). Figure 2 shows a creep displacement versus time curve for a HIPed silicon nitride material with 4 wt % Y_2O_3 tested at 1370°C and at 125 MPa for up to 2000 h in air. The creep curve reveals a stable and smooth displacement with a minimum scatter of ±0.5 μm over the test time period by employing the water-cooled laser path shielding.

2. Creep of a HIPed Si_3N_4: Specimen Geometry and Gripping System Effects

Studies of the effects of the specimen geometry (and size) and the type of gripping system on the creep behavior of a HIPed Si_3N_4 were part of the research efforts in this reporting period. This study is a joint effort with WBS Element 3.2.1.6. (Rotor Data Base Generation). The HIPed Si_3N_4 (designated as NT164, Saint-Gobian/Norton Industrial Ceramics Corp.) contains 4 wt % Y_2O_3 as a sintering additive and has undergone a proprietary post-annealing procedure to crystallize the amorphous phase at grain boundary and at triple grain junction.

The flat dog-bone-shaped tensile specimen employed in the present study has a gage cross section of 2.54 by 2.54 mm with a gage length of 15.2 mm. The button-head type specimen used in WBS Element 3.2.1.6. has gage section dimensions of 6.35 mm diam and 35 mm gage length. The volume material ratio between button-head and dog-bone type specimens is ~ 11.3. In the present study, the entire dog-bone-type specimen and grips are located in the center of the hot zone (hot-grip design). On the other hand, the button-head specimens extend outside of a compact, two-zone, resistance-heated furnace and are gripped by water-cooled grips (cold-grip design).[3]

ORNL-DWG 95-5889
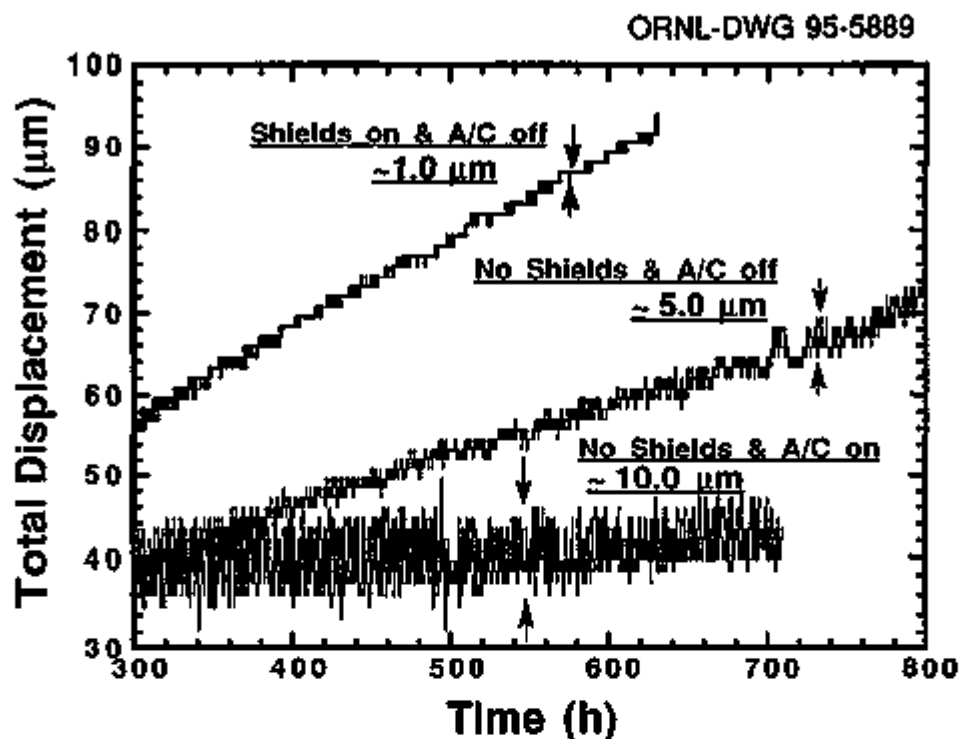
Fig. 1. Displacement versus time curves as a function of testing environment. Note that the application of laser path shielding reduces the scatter of the displacement measurements to ±0.5 μm.

ORNL-DWG 95-5890
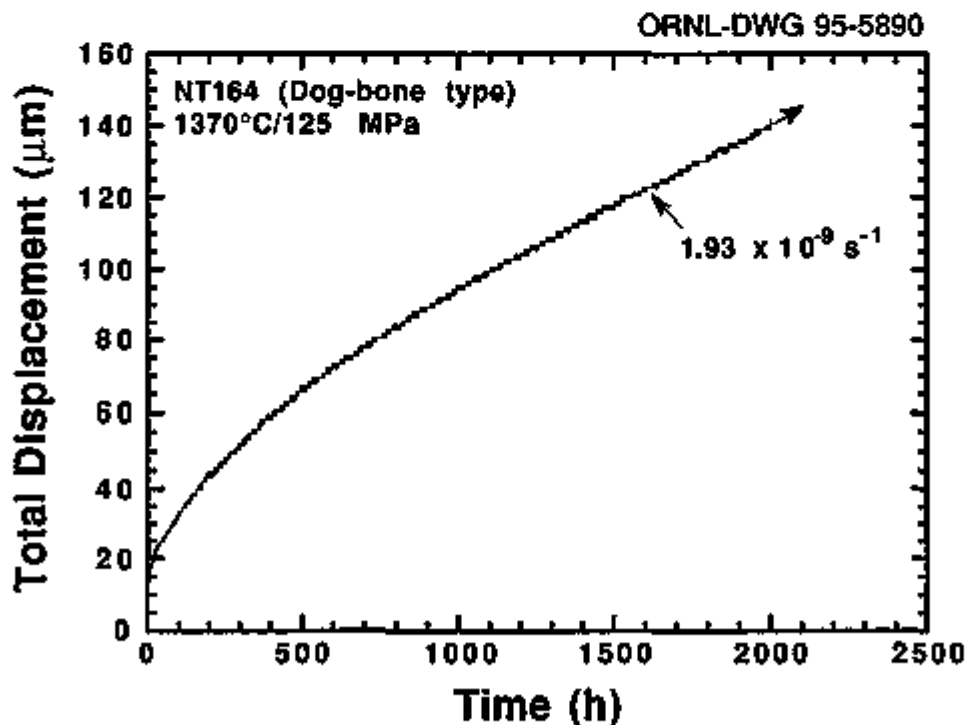
Fig. 2. Displacement versus time curve for a hot-isostatically pressed silicon nitride with 4 wt % Y_2O_3 tested at 1370°C showing a stable and accurate tensile displacement measurement.

Figure 3 shows the tensile strain versus time curves at 1370°C and at 150 MPa in air for NT164 Si_3N_4 material in small dog-bone or large button-head geometry. The creep curves for both specimen geometries are characterized by a limited primary creep stage followed by an extended transient creep. The transient creep behavior observed in Si_3N_4 materials is generally attributed to (1) a progressive devitrification of intergranular glassy phase and (2) the greater frequency of contacts between elongated grains with continued grain boundary sliding. Figure 4 summarizes the creep data [log (strain rate) versus log (applied stress)] obtained in this study and that from button-head specimens with a cold-grip system. The results show that the creep rates of this HIPed silicon nitride material are not sensitive to the specimen geometry (size) and gripping system (see Fig. 4). The independence of creep rate of the material volume indicates that the specimen geometry and gripping system employed in the present study apparently minimize bending stresses to levels comparable to those achieved with the cold-grip systems. In addition, a transition in creep stress exponent with the applied stress level was also observed similar to that reported for a similar HIPed silicon nitride (NT154) tested in tension at 1430°C (ref. 4). The observation suggests that creep data generated by using a small, flat dog-bone-shaped specimen are reliable and can provide accurate and meaningful inputs for improvements to ceramic materials that are under development for heat engine applications.

3. Sintered Reaction-Bonded Silicon Nitride

Flexural creep studies of the SRBSN were also conducted in this reporting period. The objective of this study is to evaluate the influences of the microstructure, Si powder purity, and processing method (microwave versus conventional process) on the creep behavior of SRBSN materials. The SRBSN materials were fabricated under W.B.S. Element 1.1.2.4 (Microwave Sintering of Silicon Nitride). This is part of a large effort to develop more cost-effective approaches to fabricate silicon nitride ceramics and to assess their application limits as structural materials.

The SRBSN materials investigated were fabricated by microwave (TM145X) or conventional (TM145Z) heating processes. The nominal composition of both TM145X and TM145Z materials after nitridation and sintering is Si_3N_4-3 wt % Al_2O_3-9 wt % Y_2O_3. The conventional processing for the SRBSN material (TM145Z) was conducted in a graphite-resistance heated furnace in a two-step process.[5] The X-ray analysis indicates that the sintered TM145X and TM145Z materials contain ß-Si_3N_4 plus a grain boundary glassy phase.

As indicated in the previous reports,[6] SRBSN specimens tested under a single-stress condition exhibited a threshold stress above which the SRBSN materials revealed higher creep rates accompanied by shorter creep lives. Scanning electron microscopy observations of the fracture surfaces indicated that the higher creep rate plus shorter creep life was associated with the SCG process induced by the presence of surface defects (i.e., pores). However, those specimens tested under sequential multiple-stress conditions can be loaded with stresses up to 250 MPa without the occurrence of any catastrophic
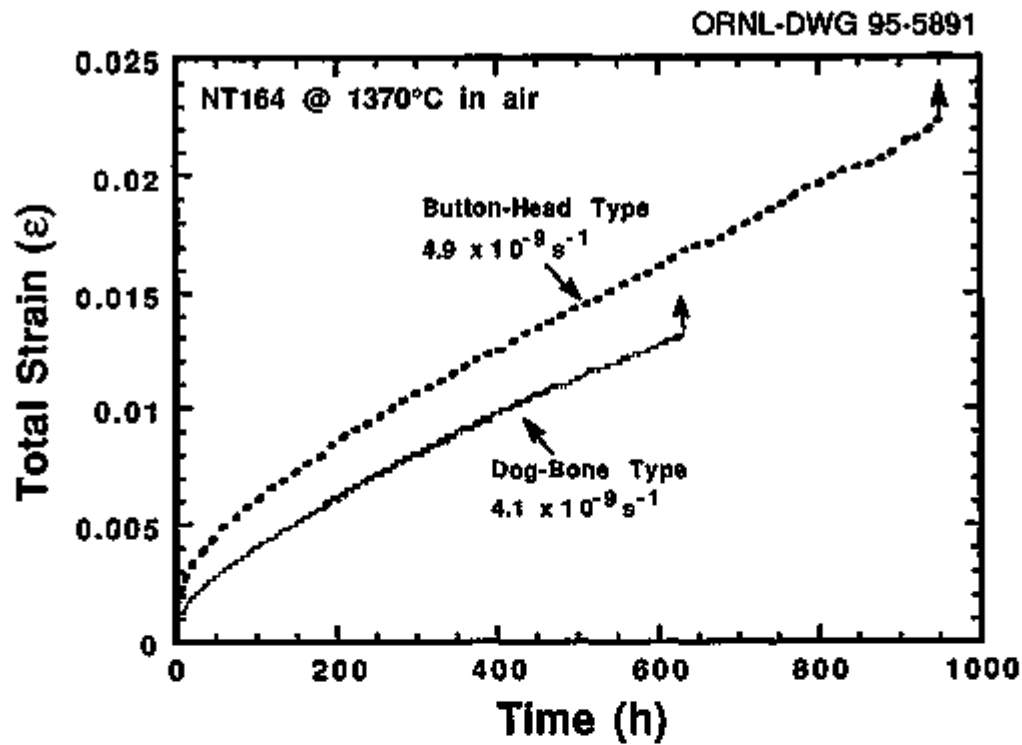
Fig. 3. Tensile strain versus time curves for NT 164 with button-head or dog-bone-type geometry.
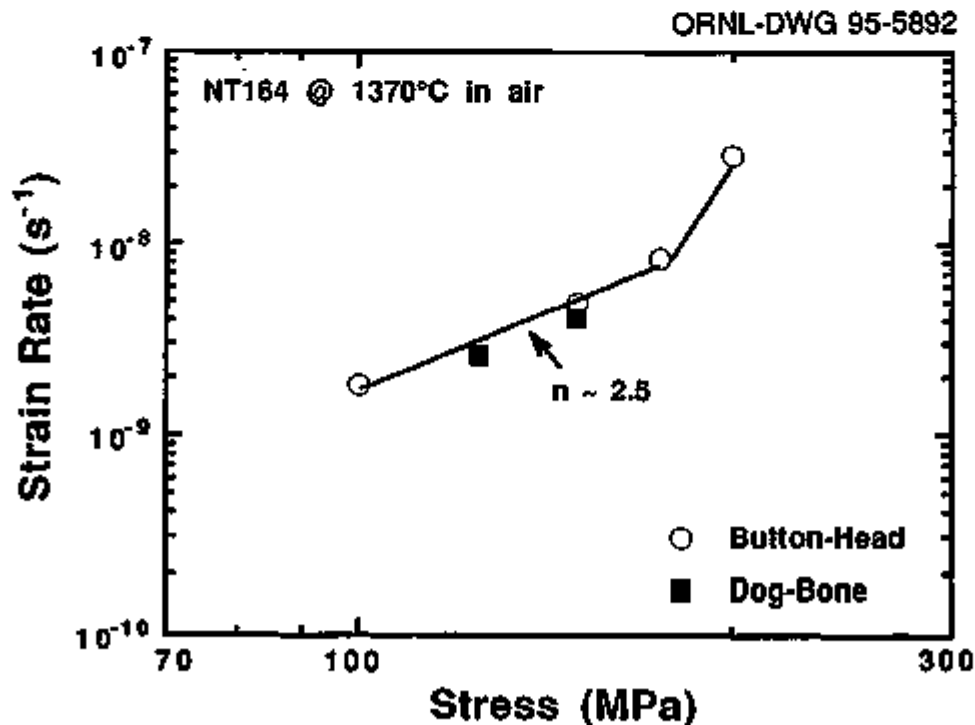
Fig. 4. Strain rate versus stress curves for NT164 with button-head or dog-bone-type geometry.

failure. A post-annealing at 1200°C for 100 h in air was therefore conducted to evaluate the effect of surface oxidation on the SCG susceptibility.

Figure 5 shows the creep results at 1200°C for the annealed specimens of TM145X and TM145Z under a single-stress condition. The creep results reported previously[6] for those as-received SRBSN materials are also included for comparison. The results indicate that an initial stress of up to 200 MPa can be applied on the annealed TM145X or TM145Z specimens without any specimen rupture. At the same time, the creep rates of annealed SRBSN materials are identical to those obtained under sequential multiple-stress tests for the as-received SRBSN materials. These observations suggest that the heat treatment at 1200°C in air prior to creep testing seals the surface and surface pores by formation of an SiO_2 layer, substantially reducing susceptibility to the SCG process.

ORNL-DWG 95-5893
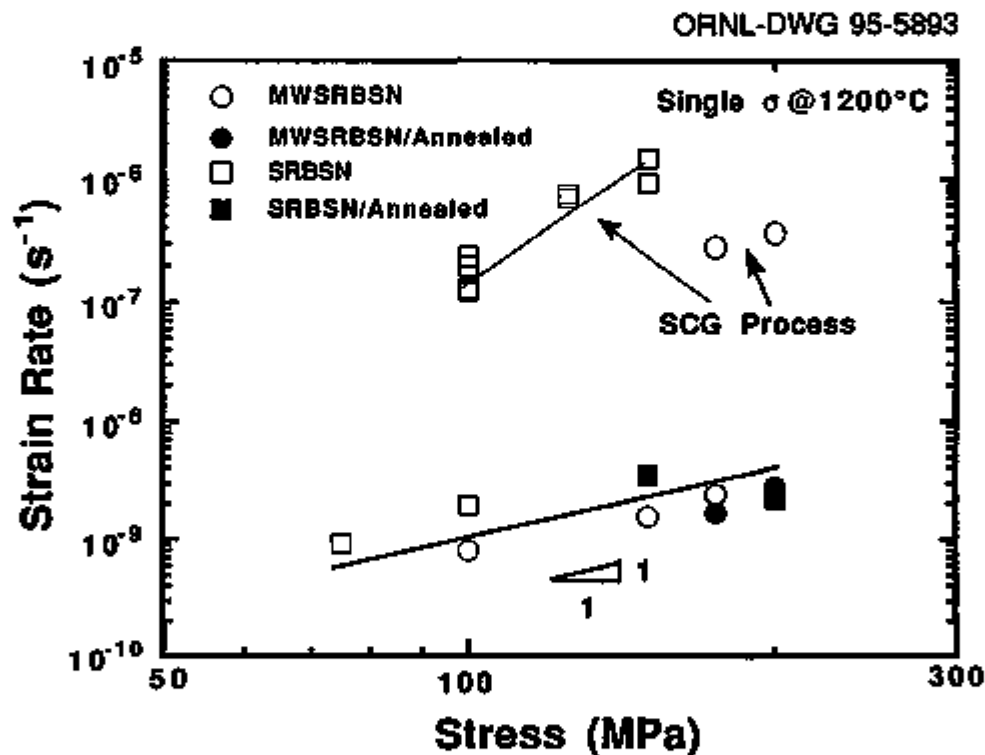
Fig. 5. Strain rate versus stress curves for sintered reaction-bonded silicon nitride ceramics at 1200°C under a single-stress condition.

Status of Milestones

Milestone No. 321317: Complete evaluation of static fatigue and creep behavior of gas-pressure-sintering Si_3N_4 ceramics will be further delayed until April 1995, due to the delay in receipt of materials from WBS Element 1.2.3.1 (Dispersion-Toughened Ceramic Composites) and, also, in machining of the tensile specimens.

Milestone No. 321318: Complete evaluation of effects of the tensile grip system and specimen size on the tensile creep rupture of promising Si_3N_4 ceramics was completed.

Publications

1. H. T. Lin, P. F. Becher, and M. K. Ferber, "Improvement of Tensile Creep Displacement Measurements," *J. Am. Ceram. Soc.* **77** [10], 2767-70 (1994).

2. H. T. Lin and P. F. Becher, "Creep Behavior in SiC Whisker-Reinforced Alumina Composites," in *Proceedings of Plastic Deformation of Ceramics*, ed. J. Routbort, R. C. Bradt, and C. Brooks, Plenum Publishing Corp., New York, in press.

3. P. F. Becher, C. H. Hsueh, H. T. Lin, K. B. Alexander, T. N. Tiegs, W. H. Warwick, and S. B. Waters, "Properties of Whisker-Reinforced Ceramics," in *Proceedings of Ceramic Matrix Composites Symposium*, ed. J. P. Singh, American Ceramic Society, Westerville, Ohio, 1994, in press.

4. T. N. Tiegs, J. O. Kiggans Jr., H. T. Lin, and C. A. Wilkins, "Comparison of Properties of Sintered and Sintered Reaction-Bonded Silicon Nitride Fabricated by Microwave and Conventional Heating," in *MRS Symposium Proceedings, Vol. 347: Microwave Processing of Materials IV*, San Francisco, 1994.

References

1. D. F. Carroll et al., "Technique for Tensile Creep Testing of Ceramics," *J. Am. Ceram. Soc.* **72** [9], 1601-14 (1989).

2. J. Sankar et al., "Testing and Evaluation of Advanced Ceramics at High Temperature in Uniaxial Tension," pp. 72-73 in *Ceramic Technology Project Bimonthly Report*, ORNL/CF-92/285, Martin Marietta Energy Systems, Inc., Oak Ridge Natl. Lab., 1992.

3. M. K. Ferber, M. G. Jenkins, T. A. Nolan, and R. L. Yeckley, "Comparison of the Creep and Creep Rupture Performance of Two HIPed Silicon Nitride Ceramics," *J. Am. Ceram. Soc.* **77** [3], 657-65 (1994).

4. W. E. Luecke and S. M. Wiederhorn, "Tension/Compression Creep Asymmetry in Si$_3$N$_4$," *Key Eng. Mater.* **89-91**, 587-92 (1994).

5. T. N. Tiegs, J. O. Kiggans, K. Ploetz, and P. A. Menchhofer, "Microwave Sintering of Silicon Nitride," pp. 2-6 in *Ceramic Technology Project Bimonthly Technical Progress Report, October-November 1992*, ORNL/CF-92/285, Martin Marietta Energy Systems, Inc., Oak Ridge Natl. Lab., 1992.

6. H. T. Lin, P. F. Becher, W. H. Warwick, and T. N. Tiegs, "Fracture Behavior of Toughened Ceramics," pp. 45-49 in *Ceramic Technology Project Bimonthly Technical Progress Report, December 1993-January 1994*, ORNL/CF-94/41, Martin Marietta Energy Systems, Inc., Oak Ridge Natl. Lab., 1994.

Cyclic Fatigue of Toughened Ceramics
K. C. Liu, C. O. Stevens, and C. R. Brinkman (Oak Ridge National Laboratory)

Objective/Scope

The objective of this task is multifold:

1. To develop, design, fabricate, and demonstrate the capability of performing cyclic fatigue in tension-tension/compression and static fatigue testing in uniaxial tension/compression on candidate structural ceramics at elevated temperatures. While significant progress has been made in several areas on the experimental front (such as specimen/grip alignment, specimen heating, and high-temperature extensometry), testing capabilities in fully reversed tension-compression cyclic fatigue and compression creep in the uniaxial direction remain to be further developed and demonstrated.
2. To develop baseline information on cyclic fatigue behavior of candidate ceramics and, in turn, to establish a design database.
3. To develop creep and creep-rupture databases for advanced heat-engines design applications in the 1150 to 1370°C range.
4. To evaluate and refine existing constitutive models based on the information generated above.
5. To develop new constitutive models to facilitate design analyses of high-temperature structural components and improve their reliability.

Technical Highlights

Tension/Compression Fatigue of Si_3N_4

Ceramic materials at high temperature are known to exhibit asymmetric behavior in fast fracture and creep under tension and compression. However, little or no information is currently available concerning the influence of the asymmetric mechanical behavior on cyclic fatigue life of ceramic materials subjected to different modes of loading. The following tests are intended to generate the information so that the risk of a catastrophic failure can be minimized for ceramic components that may be subjected to some deleterious loading conditions.

The new electrohydraulic universal testing machine has been checked out and is in operation. It is capable of testing an hourglass specimen with no buttonhead in the fully reversed, tension/compression, cyclic fatigue mode. Results of several alignment tests show that the bending stress occurring in the gage section was high (>3%) when the load crossed over from tension to compression and versus but decreased to ~1.5% when a specimen was loaded to approximately 30% of the fracture strength. The specimen is heated by an induction coil with a tubular SIC suscepter, 30 mm OD x 20 mm ID x 50 mm long, centered with the specimen. It should be noted that this heating configuration is different from that used in tension-tension fatigue testing of buttonhead specimens due to
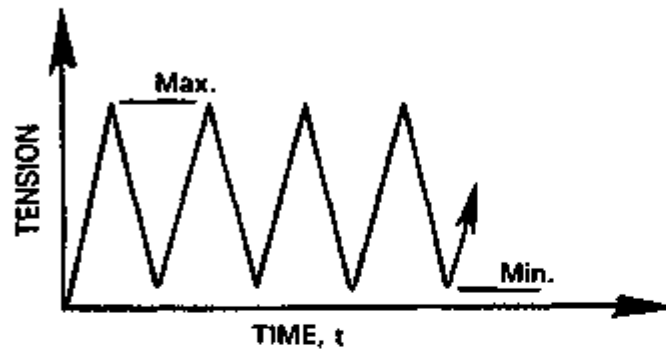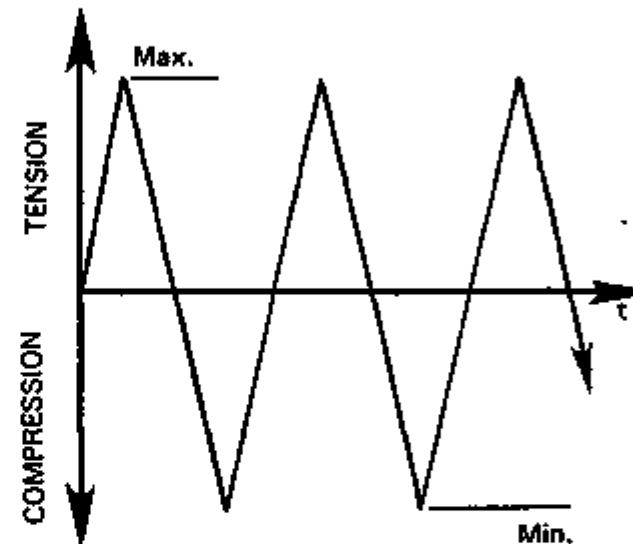
Fig. 1. (a) Wave form used in fully reversed tension-compression fatigue tests and (b) wave form used in tension-tension fatigue tests. Stress ratio R = minimum stress/maximum stress.

the limited space between the gripping heads. As a result, some differences in test temperature as well as temperature profile in the gage section may exist even though control thermocouples for both heating systems indicate the same values. An experimental effort is currently under way to investigate this problem.

Triangular wave forms, as shown in Fig. 1, with R (= minimum stress/maximum stress) = 0.05 were used in tension/tension (T/T) fatigue tests, and that with R = -1 was used in tension/compression (T/C) fatigue tests. It should be noted that the T/T mode is equivalent to cycling with an imposed mean stress as shown in Fig. 1. Since the same stressing rate was used in both cases and the compression cycle in T/C mode was assumed to be equally deleterious in fatigue damage as the intermittent tension cycle, one complete T/C cycle should be counted as two T/T cycles so that a comparison can also be made on the time basis as well.

Cyclic fatigue of GN-10 Si_3N_4 at 1200°C - Three hourglass specimens, numbered HG-1 to -3, were tested in the T/C mode. Test results are plotted in Fig. 2. Since the fatigue behavior in T/C was not known, the starting cyclic stress amplitude for each test was selected rather conservatively. Unfilled triangular symbols indicate the end of the starting cyclic period at the test condition indicated. Subsequently, the stress amplitude was increased in steps of 15 MPa as each time the specimen was cycled for a block of 1.0 to 2.5×10^5 cycles, until fatigue failure occurred at the test condition indicated by the filled triangular symbols. The dashed line interconnecting a pair of unfilled and filled triangles, also numbered to facilitate specimen identification, represents the intermittent cyclic fatigue steps.

An hourglass specimen (HG-4), made from the same tile, was tested at 1200°C in the T/T mode with an applied stress of 380 MPa. The specimen failed after completing 23,757 cycles, as indicated in Fig. 2. A comparison shows that specimen HG-3 tested in the T/C mode with the same stress amplitude significantly outperformed HG-4 tested in the T/T mode by two orders of magnitude in cyclic life. Two T/T fatigue data points, shown in Fig. 2 as filled circles, obtained previously for buttonhead specimens made from a tile of an earlier vintage, also indicate that cycling in T/T mode is more detrimental to fatigue resistance of GN-10 compared to that in T/C mode.

Four buttonhead specimens, made from different tiles but of the same lot as the hourglass specimens, were cycled in the T/T mode at various stress amplitudes of 360, 380, 400, and 420 MPa with fatigue lives of 42287, 19505, 9793, and 7970, respectively. The fatigue data are plotted in Fig. 2, using filled squares to differentiate from the filled circles. All the T/T data are bracketed between the two curves, which were determined visually to approximate the lower bounds of T/C fatigue and T/T fatigue curves. The tensile fast fracture was considered to have failed in a single cycle; therefore, the data point was plotted accordingly as 10^0 cycle. Overall, data appear to support the earlier finding, but more data are needed before the final conclusion can be made.

Cyclic fatigue of GS-44 Si_3N_4 at 1200°C - Four hourglass-shaped specimens of GS-44 were fatigued in the new T/C machine, three in T/C mode and one in T/T mode. The first specimen was cycled initially with a stress amplitude of 200 MPa, which was intentionally selected lower than 60% of the tensile strength, the procedure normally used to pick a
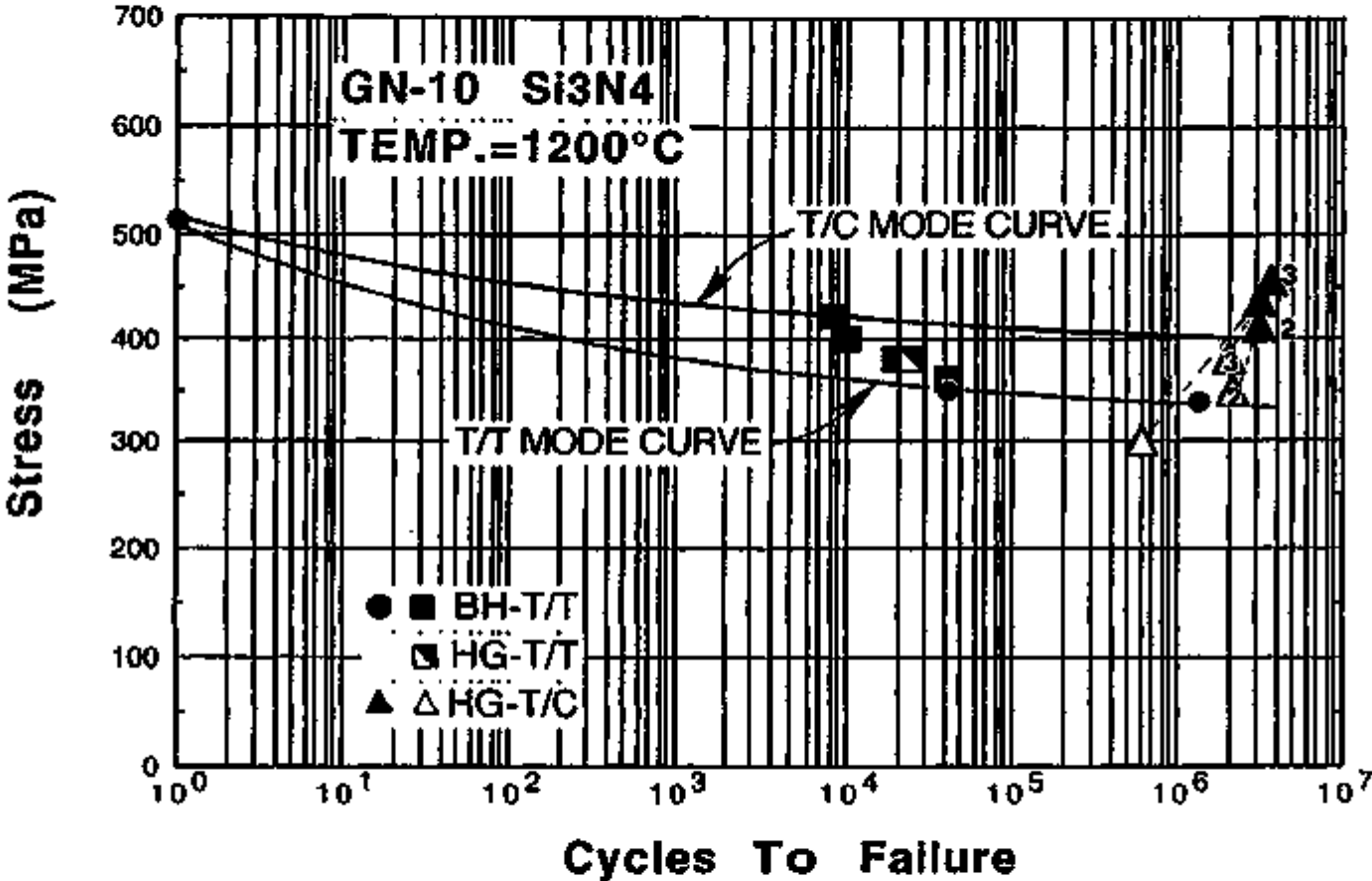
Fig. 2. Cyclic fatigue behavior of GN-10 Si_3N_4 tested at 1200°C. New data obtained in tension/tension mode are bracketed between two fatigue curves, the upper curve for T/C fatigue and the lower one for T/T fatigue.

starting stress amplitude in cyclic fatigue tests of new materials. Subsequently, the stress amplitude was stepped up intermittently in increments of 15 MPa as each time the specimen was cycled for ~2.5 × 10^5 T/C cycles (equivalent to 5 × 10^5 T/T cycles), until failure occurred under the maximum cyclic stress amplitude of 305 MPa with a total of 1.867 × 10^6 T/C cycles (or equal to 3.732 × 10^6 T/T cycles). Two tests followed, starting with a stress amplitude of 290 MPa in each case. After completing a block of ~4 × 10^5 T/C cycles at 290 Mpa, the stress amplitude was raised to 305 MPa. However, both specimens failed in less than 4200 cycles after the stress amplitude was raised. Data are plotted in Fig. 3, using triangular symbols. Open triangles indicate the starting stress amplitude and the number of cycles completed at the location indicated; filled triangles indicate rupture at the number of cycles indicated. The long series of open triangles indicates the intermittent cyclic lives at the stress amplitude indicated.

An hourglass specimen was tested in the T/T mode beginning with a stress amplitude of 290 MPa as was done in the T/C tests. After the specimen completed the first 10^6 cycles, the stress amplitude was raised to 305 MPa and cycled for 2 × 10^5 cycles without failure; however, the subsequent increase to 320 MPa led to fatigue failure after completing 9900 cycles. Test results are depicted by filled and unfilled circles. Results of the above four tests suggest that the mode of cyclic loading may play little or no significant role in fatigue behavior of GS-44. This observation, based on the limited information, is inconsistent with what was observed earlier for GN-10.

Three buttonhead specimens were tested on the T/T machine. Results are plotted in Fig. 3 using filled square symbols. With the aid of the tensile data being plotted as a single cycle, an approximate fatigue curve can be estimated for the sake of this discussion. This group of data indicates that this material is less resistant to cyclic fatigue in T/T mode compared to that in T/C mode, showing it to be in direct contradiction to the single T/T data point obtained from the hourglass specimen. If the test results are not biased due to the difference in testing machines, as was tentatively concluded based on the results of GN-10 tests, material variation is suspected to be the cause of the contradictory behavior because the buttonhead and hourglass specimens were fabricated from different tiles. Additional T/T fatigue tests on hourglass specimens are currently under way, and new results may help in resolving the issue.

Tensile testing of GS-44 Si₃N₄ at elevated temperatures

Five specimens in the as-sintered condition and seven specimens in microwave-annealed condition were tested in tension at elevated temperatures ranging from room temperature to 1200°C. Test results are summarized in Table 1, and data are plotted in Fig. 4. Modulus of rupture (MOR) data[1] (four-point) obtained at room temperature, 900, and 1100°C are also plotted in Fig. 4 for comparison.

Specimens that had been microwave annealed at temperatures below 1500°C were found to have somewhat lower tensile strengths compared to those of unannealed specimens. However, specimens annealed at 1600°C had elevated-temperature tensile strengths comparable to the unannealed specimens, suggesting that little or no significant beneficial effects were gained by microwave heating. Correspondingly, previous MOR tests[1] on GS-44 microwave annealed at 1700 and 1800°C also showed no beneficial effects
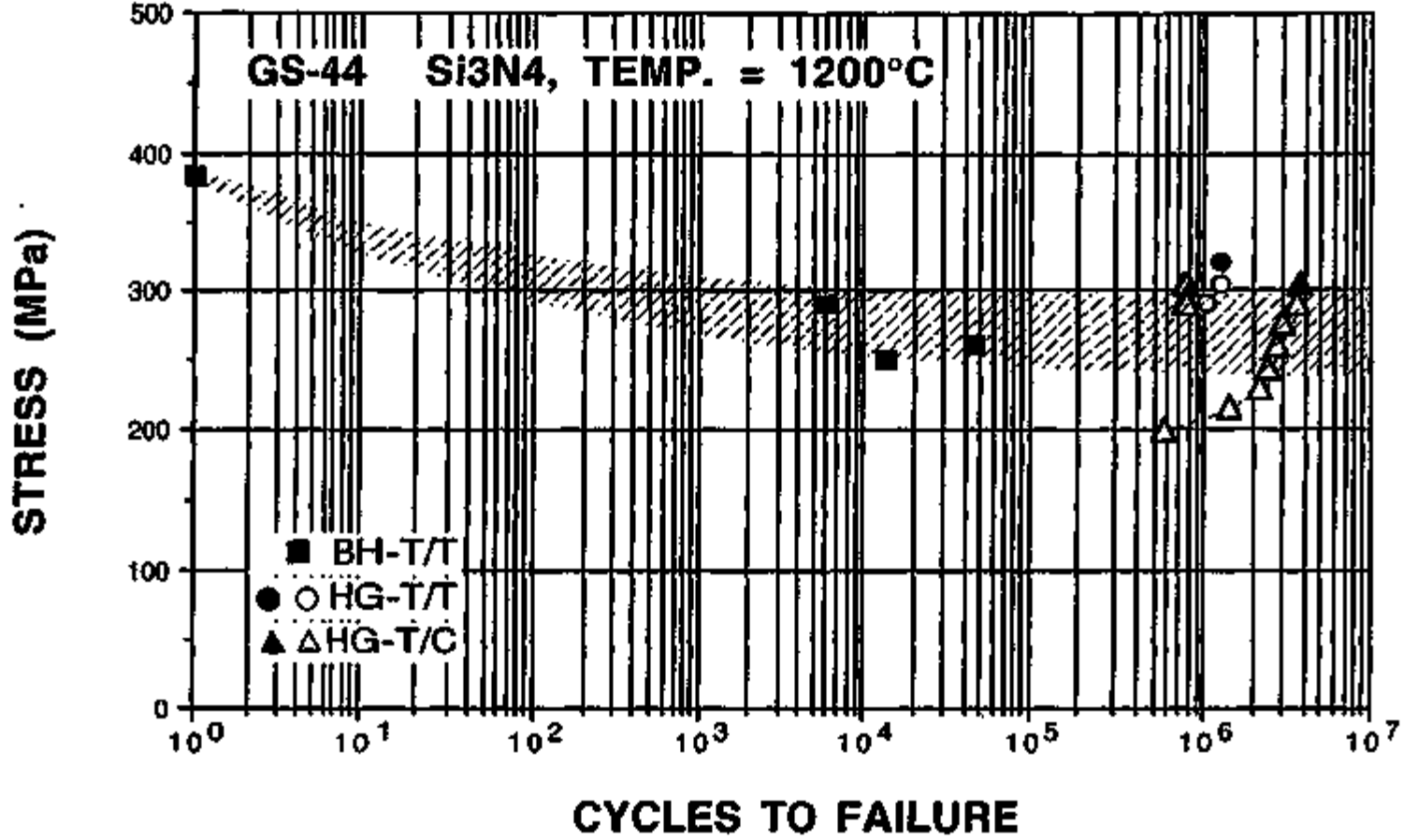
Fig. 3. Cyclic fatigue behavior of GS-44 Si_3N_4 tested at 1200°C. Test results also indicate that fatigue in tension-compression mode is less detrimental to that in tension-tension mode.

Table 1. Summary of tensile strengths of GS-44 Si_3N_4					
Temp. (°C)	MOR[a] (MPa)	As-Sint'd (MPa)	Microwave annealed (MPa)		
			1400°C/10 h	1500°C/10 h	1600°C/10 h
R. T.	961	596			
900	697	480		414	461
1000		438			
1100	434	388		310	435
1200		385	331	318	378

[a]Modulus of rupture (four-point) data are obtained from ref. 1.
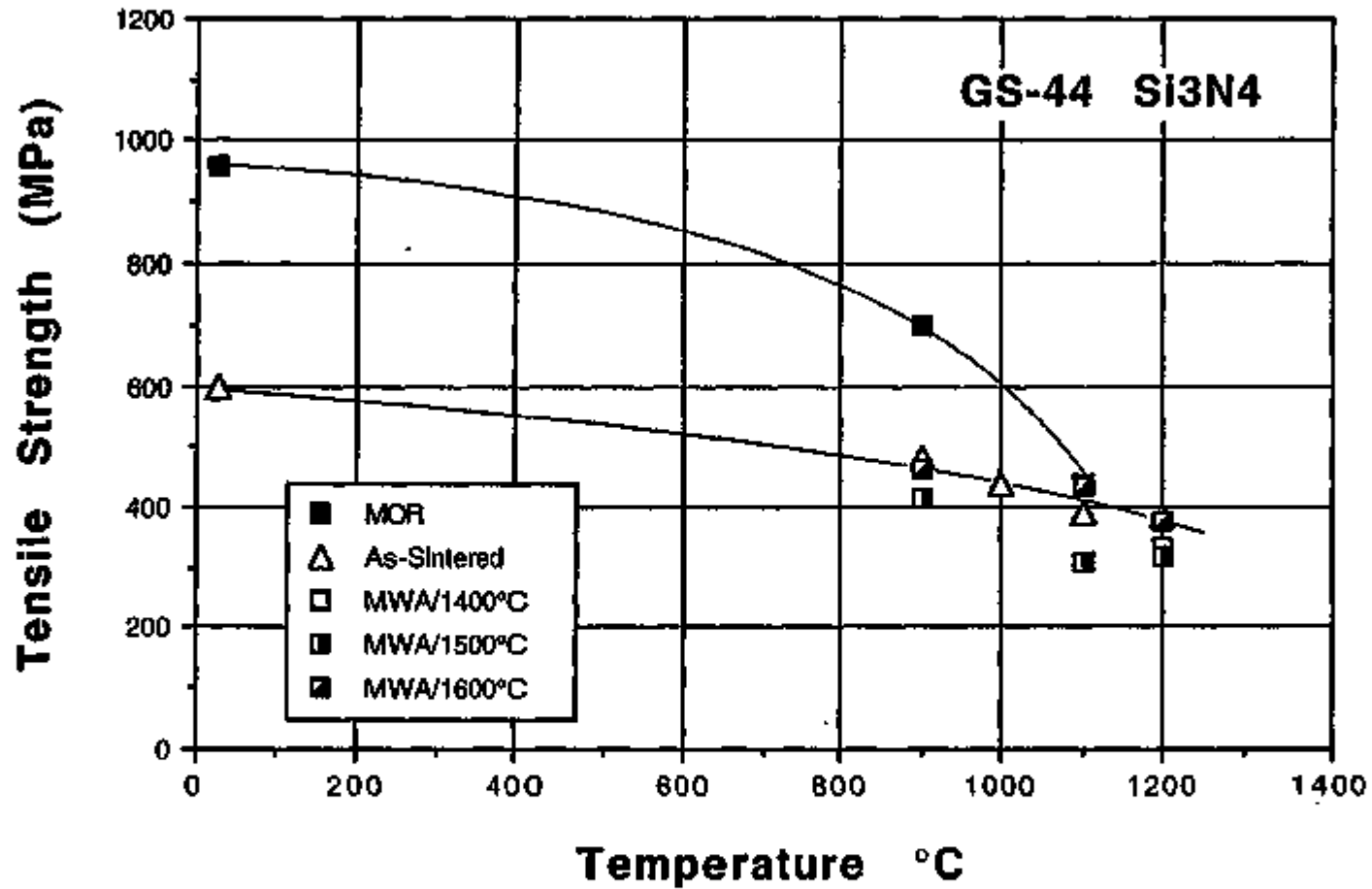
Fig. 4. Tensile fast fracture strengths of GS-44 Si_3N_4 tested at room and elevated temperatures. Specimens were tested in the as-received (or as-sintered) and microwave-annealed conditions as indicated. Four-point modulus of rupture data[1] are included for comparison with tensile data.

on MOR strength when compared with the baseline data obtained for unannealed material. However, the stress-rupture properties were shown to have been improved for the post-annealed GS-44 at 1600°C.

At room temperature, the tensile strength shown in Fig. 4 is about 40% below the MOR strength. The difference decreases slowly to 30% at 900°C but rather rapidly as test temperature increases. No MOR data are available to confirm whether the trend will be reversed or not at temperatures above 1200°C. The correlation between MOR strength and tensile strength is obviously complex at high temperatures in the creep range.

Predictions of tensile fast fracture of Si_3N_4 based on an in-house- developed viscoplastic model

A preliminary study was made using the above stated model to predict tensile stress/strain behavior and cyclic fatigue life of GN-10 Si_3N_4 at elevated temperatures. The model was originally developed for describing the creep behavior and predicting creep-rupture life of GN-10 Si_3N_4. Because of the flexibility in the state-variable approach to account for the material history, the model can describe the viscoplastic deformation of the material under general thermal-mechanical loading conditions and, in turn, predict the cyclic fatigue life.

Tensile behavior of GN-10 Si_3N_4 at elevated temperatures is simulated based on the model shown in Fig. 5. According to the results shown in Fig. 5(a), the stress-strain behavior at 1150°C is not sensitive to stressing rate, but viscoplastic behavior becomes obvious as temperature increases [see Fig. 5(d)]. Unfortunately, no GN-10 data of the kind are available for comparison with simulations at this time. However, the characteristic features of the viscoplastic behavior have been illustrated for reported test results[2] of NT-154 Si_3N_4 tested in tension under various stressing rates (see Fig. 6). Specimens made by cold-isostatically pressed processing are marked with a "CP" prefix, whereas a "PC" prefix indicates slip-casting. The viscoplastic effect was not clearly illustrated for NT-154 until the temperature was higher than 1200°C. Tensile data for GN-10 will be generated for comparison with the predictions.

Tensile-Rupture Testing of NT-154 Si_3N_4 in Support of the ATTAP Program

Stress-rupture tests for the phase II test program are near completion, with a total of 29 tests completed to date. Three remaining specimens are to be tested. Test results were periodically transmitted to AlliedSignal for reviewing and updating the database.

Creep testing of NT-154 Si_3N_4

Experimental efforts continued on three long-term creep tests of NT-154 specimens. All the specimens have been tested at 1250°C for periods ranging from 2.4 to 3.2 years. Updated creep curves for the three tests (see Figs. 7 through 9) indicate creep rates have been reasonably steady during the last 5000 h of testing. We are not aware of long-term creep tests having been reported with test durations in excess of 20,000 h on ceramic materials. In view of the current performance in creep rate, all three tests will probably continue indefinitely. Since no such data have been generated previously, the information
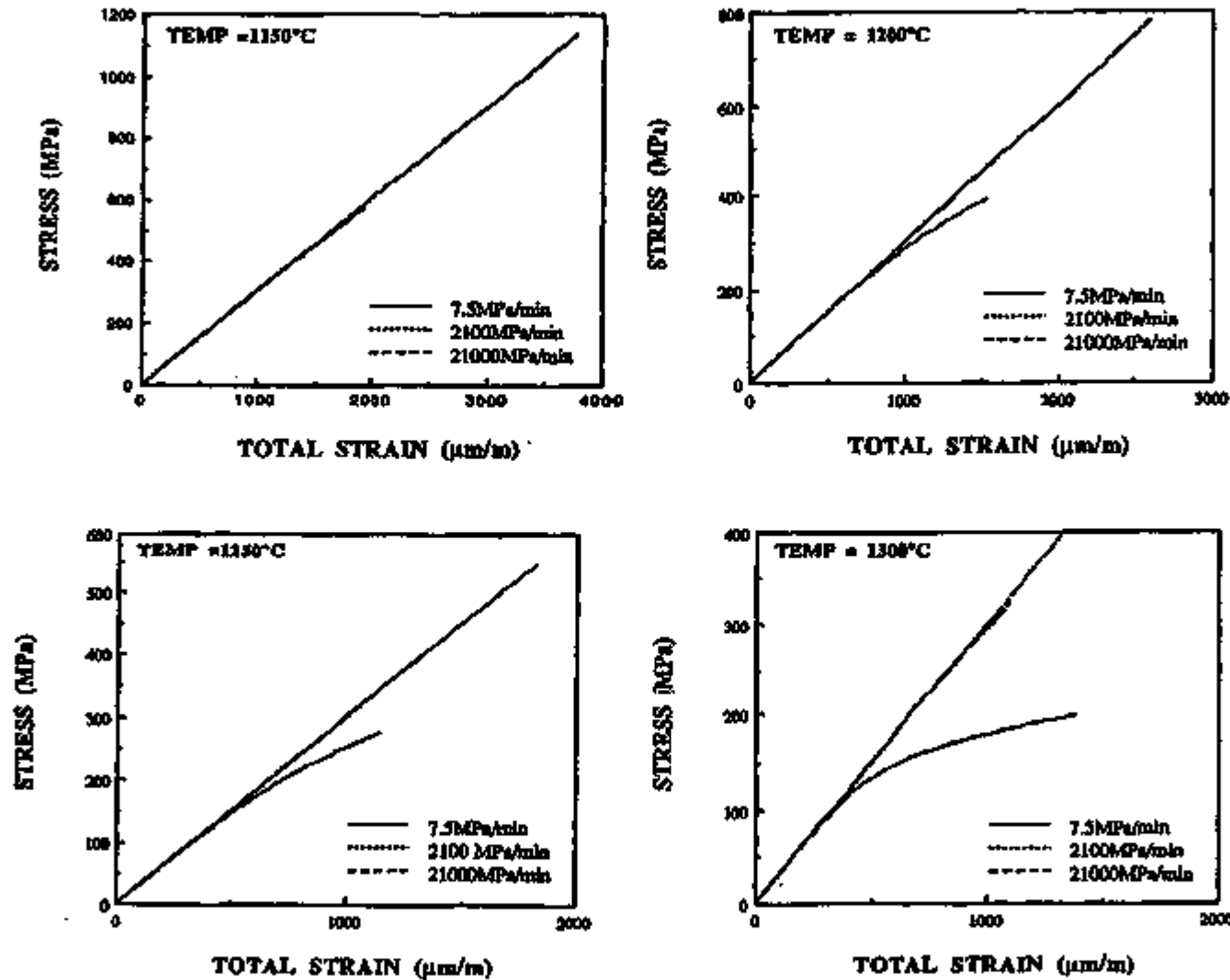
Fig. 5. Predictions of tensile behavior of GN-10 Si_3N_4 tested at elevated temperatures and various stressing rates, using the viscoplastic model developed at Oak Ridge National Laboratory.
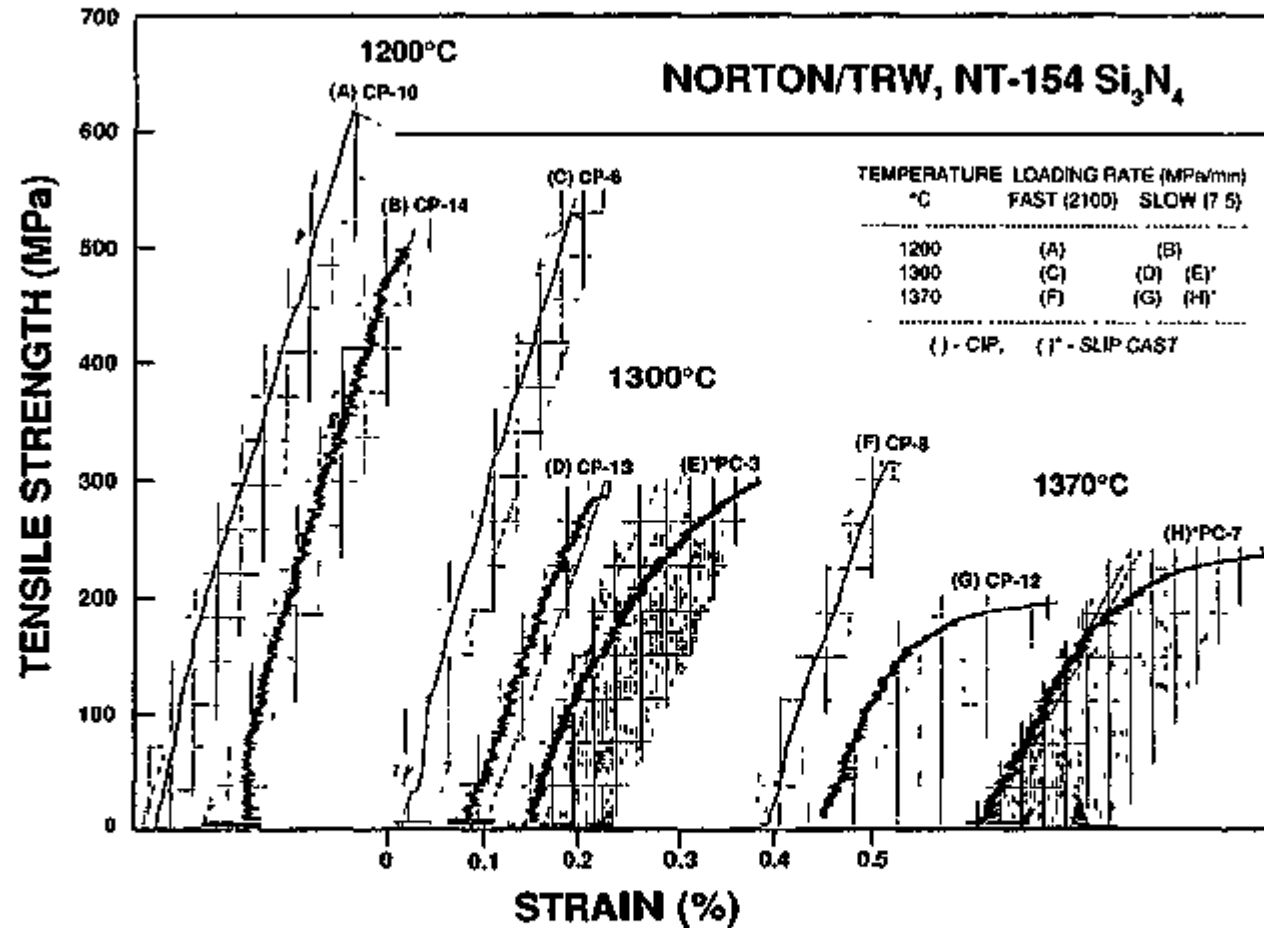
Fig. 6. Uniaxial tensile behavior of NT-154 Si₃N₄ tested at elevated temperatures with two different stressing rates. No visible viscoplastic effect was observed for specimens tested at 1200°C, but the stressing rate effects were clearly illustrated as the test temperature increased.
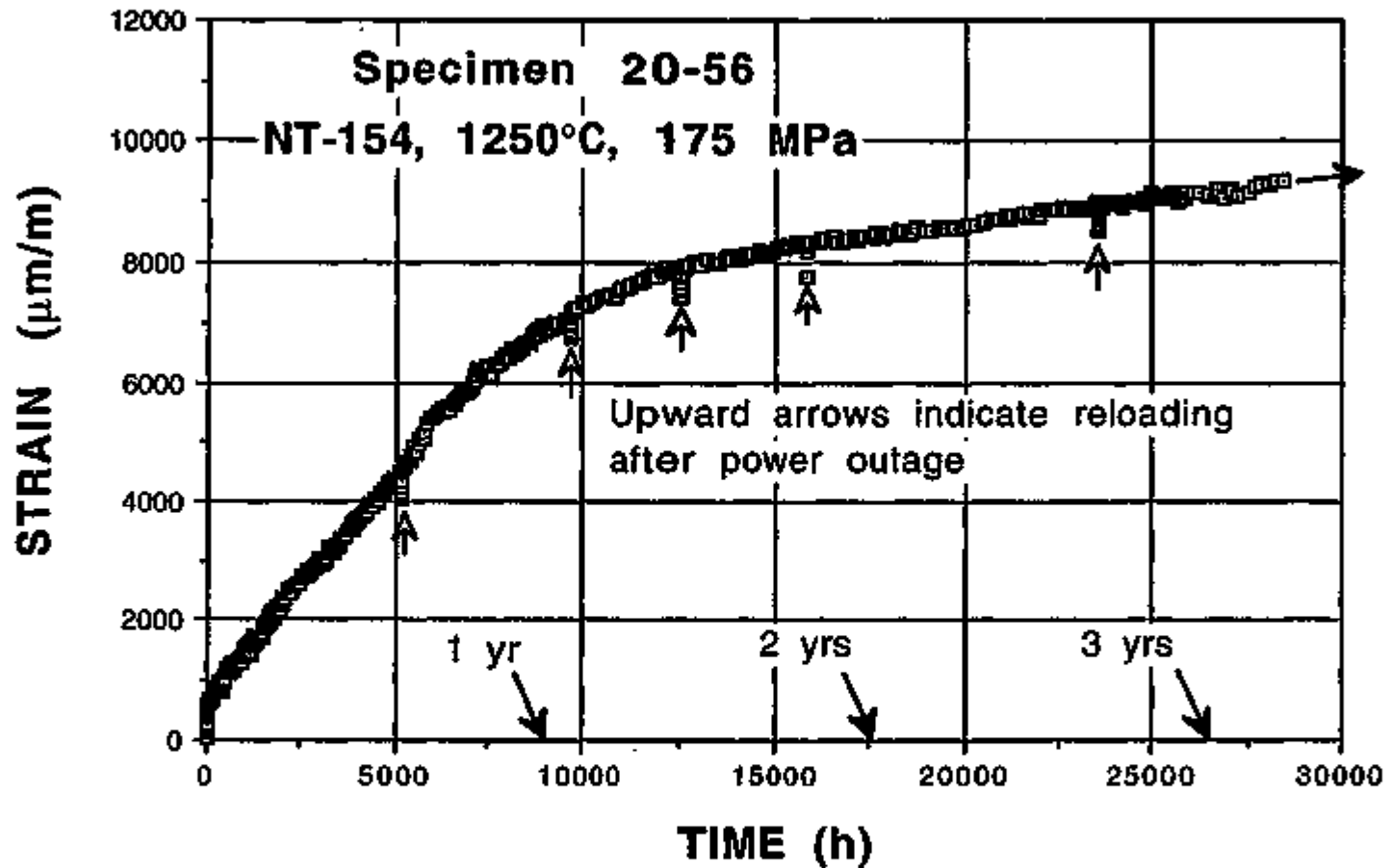
Fig. 7. Creep curve of NT-154 Si_3N_4 (specimen 20-56) tested at 1250°C and 175 MPa. Steady-state creep continued at a rate of about 2.3×10^{-11} s^{-1}. The specimen has accumulated a total of 28,500 h (or 3.25 years) of testing.
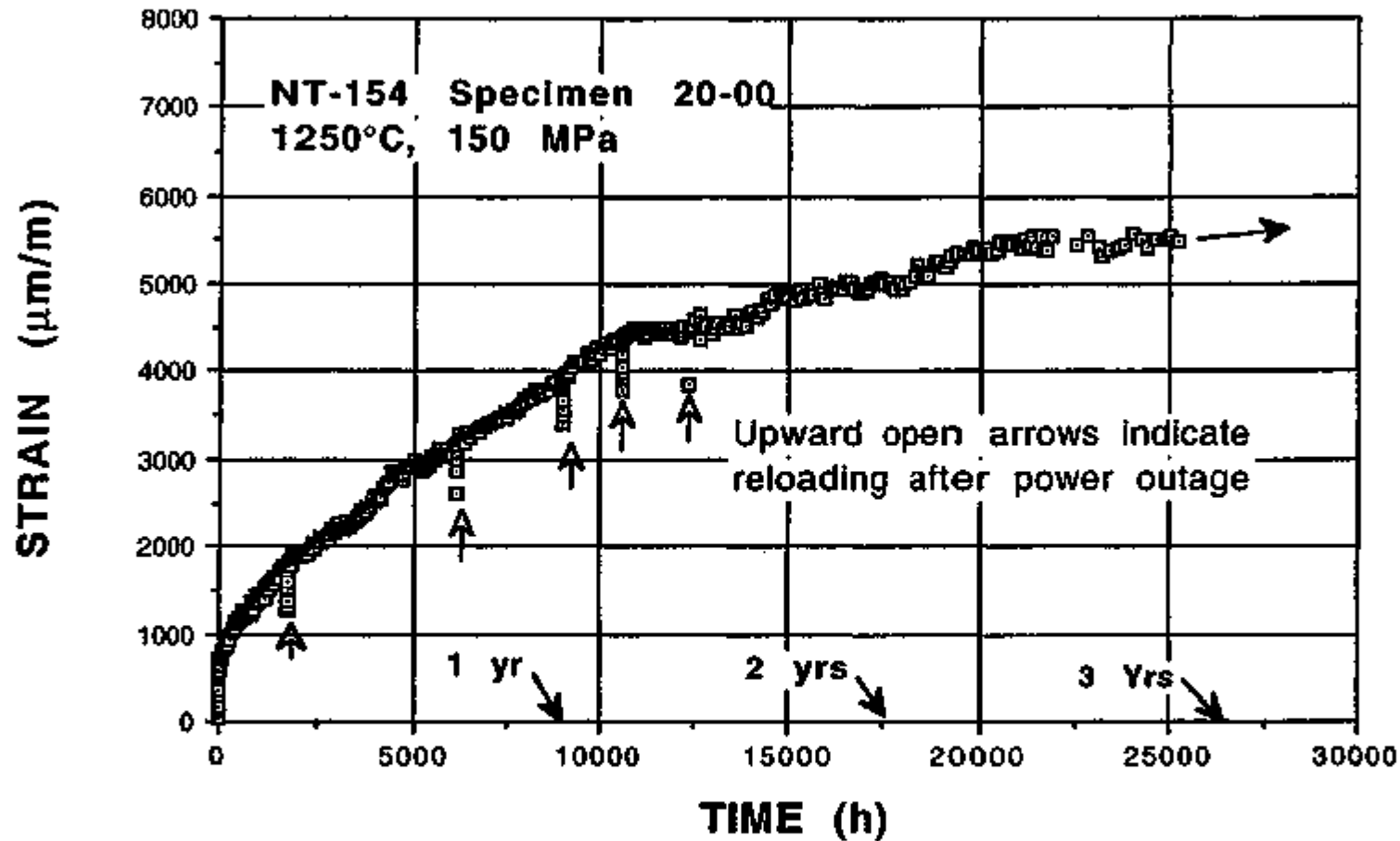
Fig. 8. Creep curve of NT-154 Si₃N₄ (specimen 20-00) tested at 1250°C and 150 MPa. The specimen appears to be in a steady-state creep phase although the behavior cannot be well defined as is the case shown in Fig. 1. A creep rate of about 1.56×10^{-11} s^{-1} is estimated from the data for the last 10,000 h of test. This specimen has accumulated a total of 25,000 h (or 2.85 years) of testing.
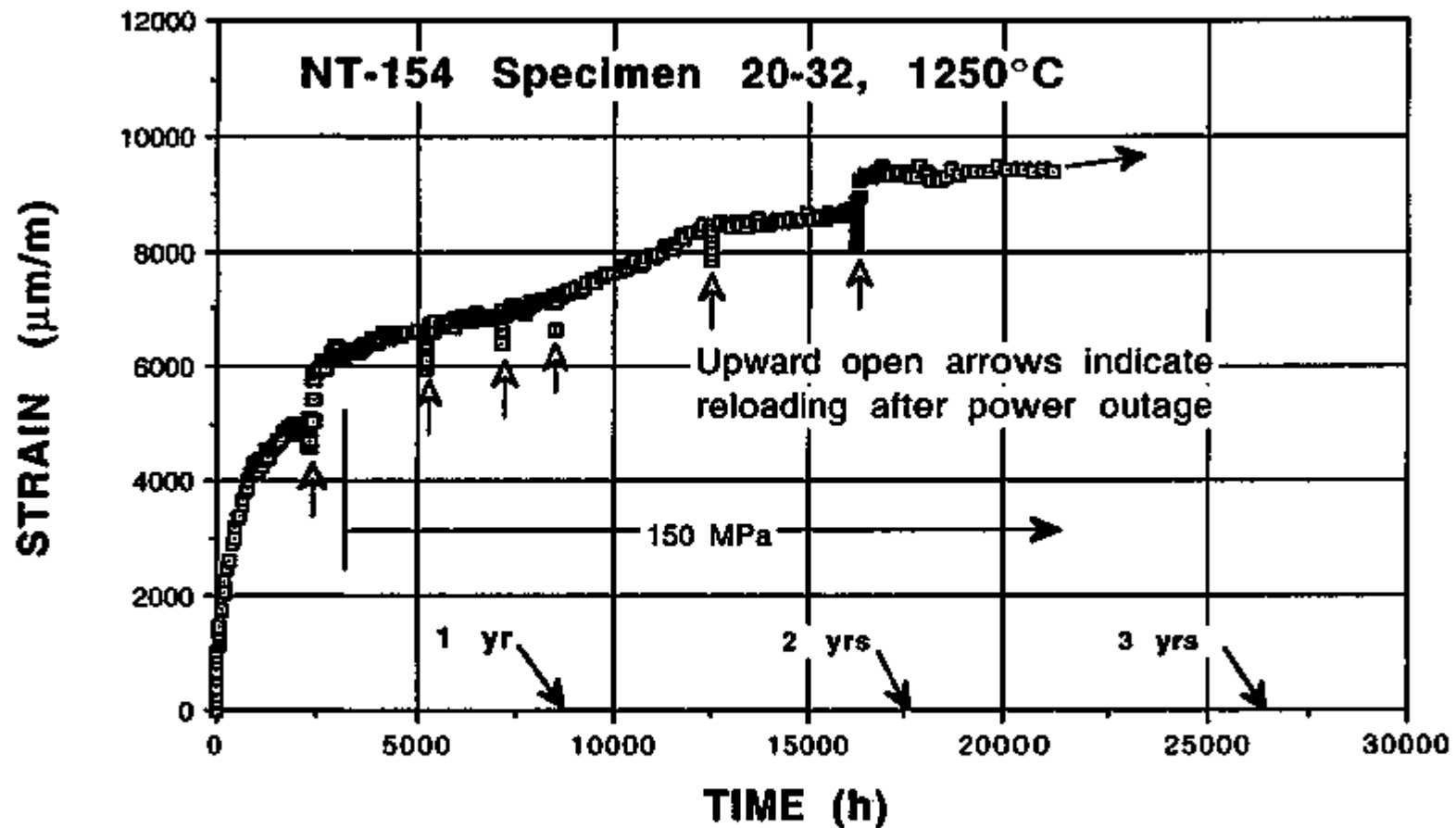
Fig. 9. Creep curve of NT-154 Si_3N_4 (specimen 20-32) tested at 1250°C and 150 MPa. This specimen was initially tested at 225, 200, and 175 MPa for 1000 h each before being reduced to the current level. After the most recent power outage, the creep rate decreased to about 1×10^{-11} s^{-1}. The specimen has accumulated a total of 21,000 h (or 2.4 years) of testing.

will provide extremely valuable insight into the behavior of this material. Hence, no decision has been made regarding the future direction of these tests.

Creep testing of GN-10 Si₃N₄

Two creep tests on GN-10 Si₃N₄ being tested with applied stresses at the low-stress end of the creep-rupture range (long-term tests) are still in progress. Testing of GN-10 at low temperatures and low applied stresses has been difficult due to the unstable creep behavior exhibited in Figs. 10 and 11. It is not known if the erratic behavior is real and typical in low- temperature/low-stress testing or attributed to signal drift of the mechanical extensometers under the influence of ambient temperature variations. The latter has tentatively been ruled out in view of good performance demonstrated by the others in the family of extensometers sharing the same master signal conditioning console. From the long-term testing perspective, optical extensometers are more reliable as illustrated in Figs. 7 through 9.

Creep testing of GS-44 Si₃N₄ in the as-sintered (or as-fabricated) and microwave-annealed conditions

To examine if microwave annealing was effective in enhancing the creep resistance of GS-44 Si₃N₄, creep tests were performed at 1200°C on three specimens in the as-sintered condition (specimen numbers designated with a prefix of "AS") and six microwave-annealed specimens (with a prefix of "MA"), which were annealed in three different heating schedules as indicated in Figs. 12 and 13. Results indicate that microwave annealing at temperatures above 1400°C did not only fail to enhance the creep resistance but made the material less resistant to creep. The situation was somewhat worse for creep tests at 100 MPa, as shown in Fig. 13, compared to that for tests at 80 MPa. Although not shown in Fig. 12, the creep behavior of specimen AS-8 tested at 120 MPa (shown in Fig. 14) was shown to be about the same as that of specimen MA15-7, indicating a significant downgrading in load-carrying capacity of about 50%. The creep behavior of the as-sintered specimens was consistent, as shown in Fig. 14.

A discussion was held with Terry Tiegs concerning the negative annealing effect described in the above section and the lowering of tensile strength resulting from microwave annealing. The causes of the negative annealing effects will not be known until X-ray diffraction analyses are completed. Tiegs suggested that we look into low-temperature annealing below 1400°C. Annealing by microwave has been completed for a tile subjected to a heating schedule of 1100 and 1200°C each for a period of 10 h. To compare the effect of furnace annealing, a tile was aged in a resistance furnace at 1200°C for a period of 100 h. Tensile creep specimens are now being fabricated.

Important Findings and Observations

Results of cyclic fatigue tests on GN-10 and GS-44 Si₃N₄ ceramics at 1200°C show that cyclic fatigue in tension/compression mode may be less detrimental to the fatigue resistance of the materials compared to that in tension/tension mode.
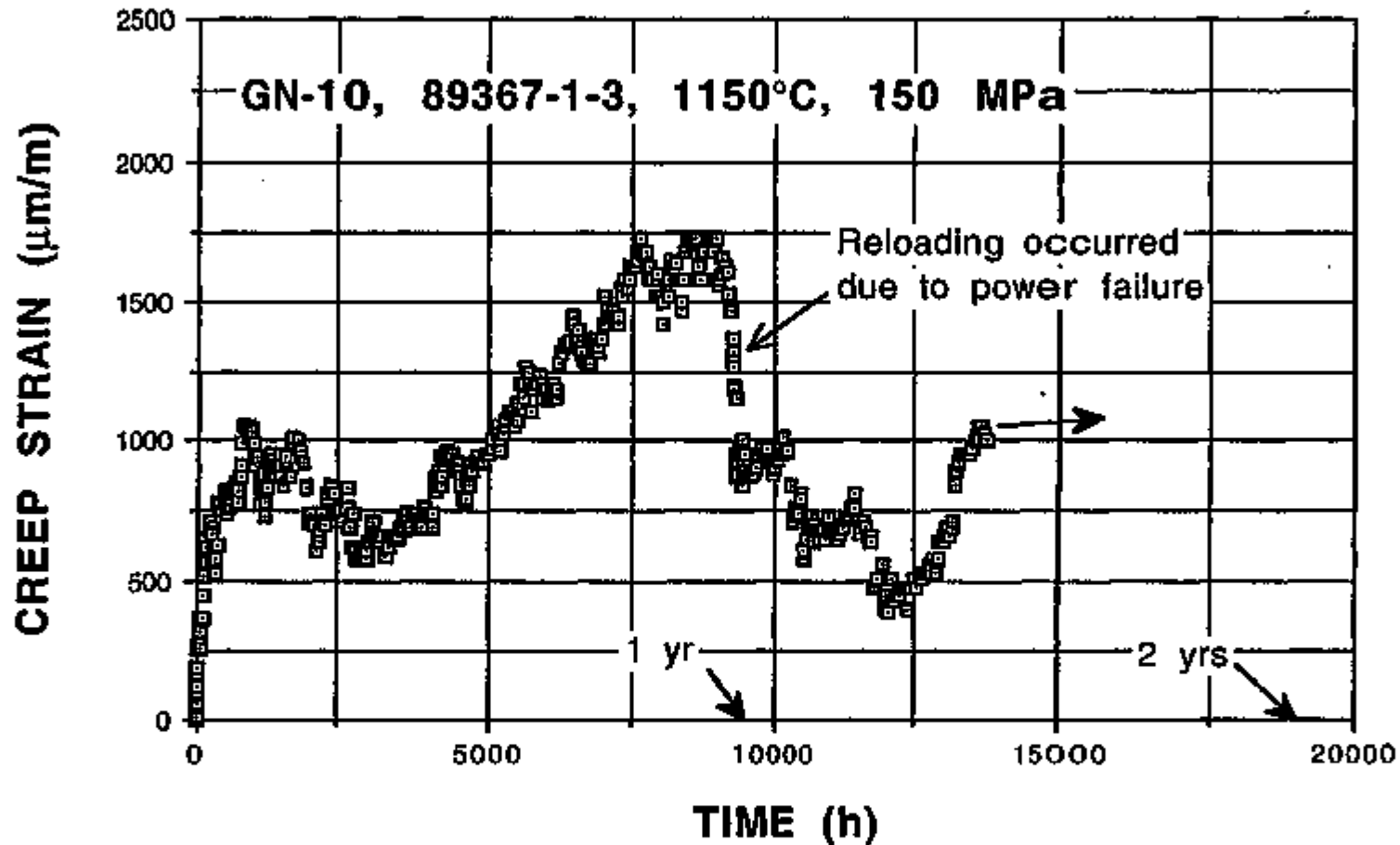
Fig. 10. Creep curve of GN-10 Si₃N₄ (specimen 89367-1-3) tested at 1150°C and 150 MPa. The decrease in creep strain, since the most recent test interruption due to a power outage, was more severe compared to the similar behavior observed earlier immediately after completing the first 2000 h of testing. Note that the maximum creep strain attained was less than 0.2%.
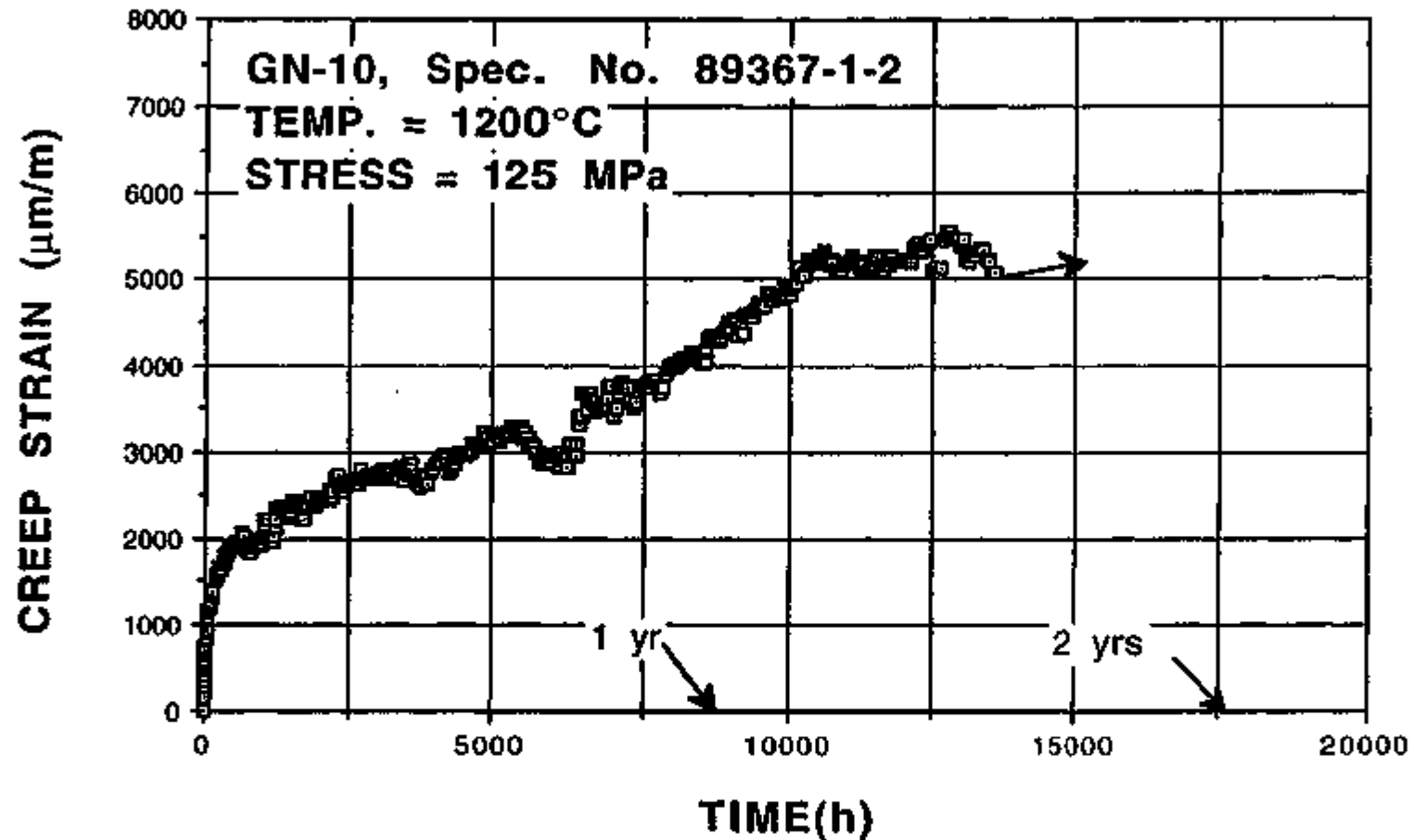
Fig. 11. Creep curve of GN-10 Si_3N_4 (specimen 89367-1-2) tested at 1200°C and 125 MPa. The creep behavior became less predictable after completing 10,000 h of testing. The specimen has accumulated a total of 13,300 h (1.5 years) of testing to date.
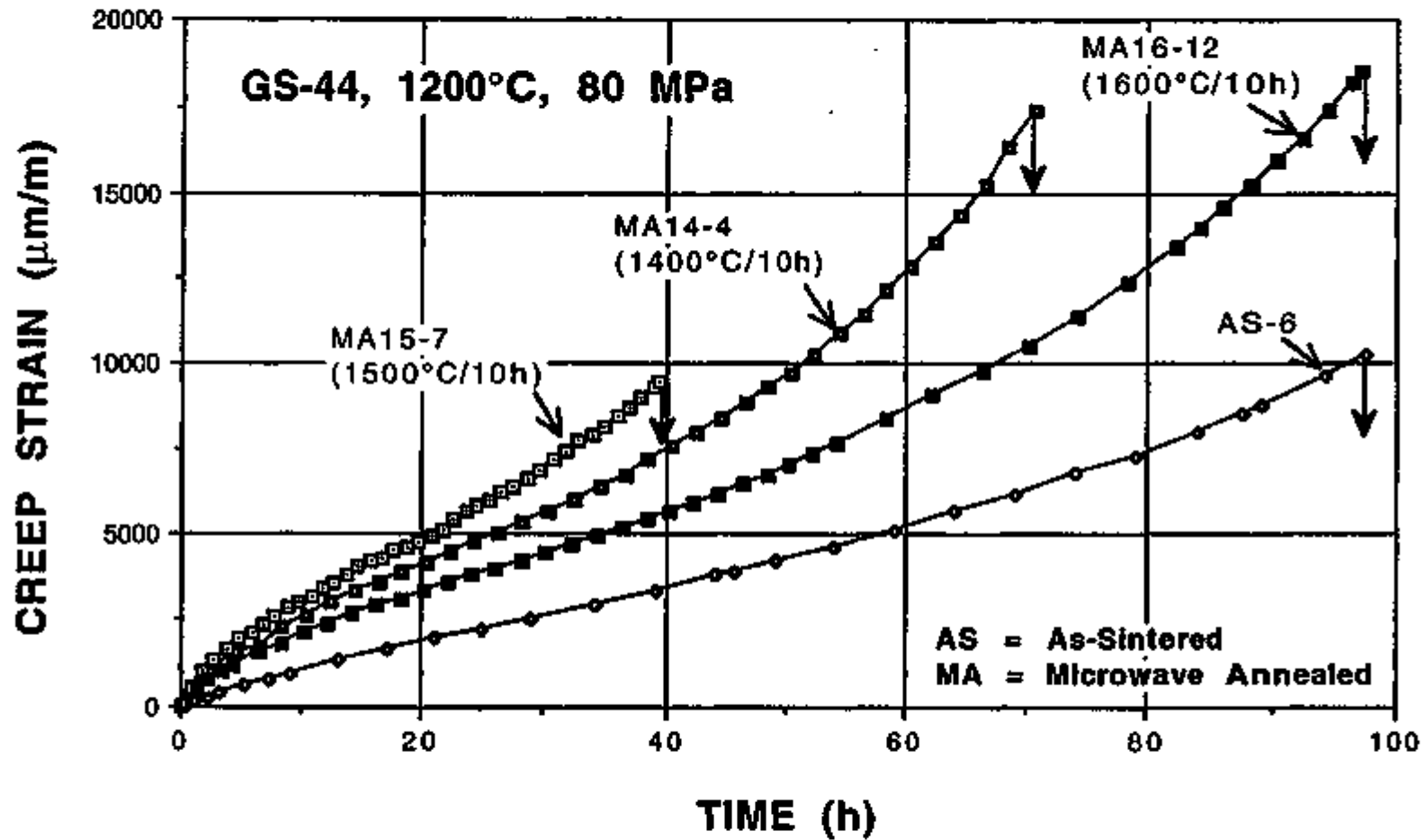
Fig. 12. Comparison of creep curves for microwave-annealed GS-44 Si₃N₄ specimens (conditions as indicated in parentheses) and unannealed ones tested at 1200°C and 80 MPa. Results show that creep resistance was reduced as a result of microwave annealing, contrary to what was observed for microwave-annealed SNW-1000 Si₃N₄.
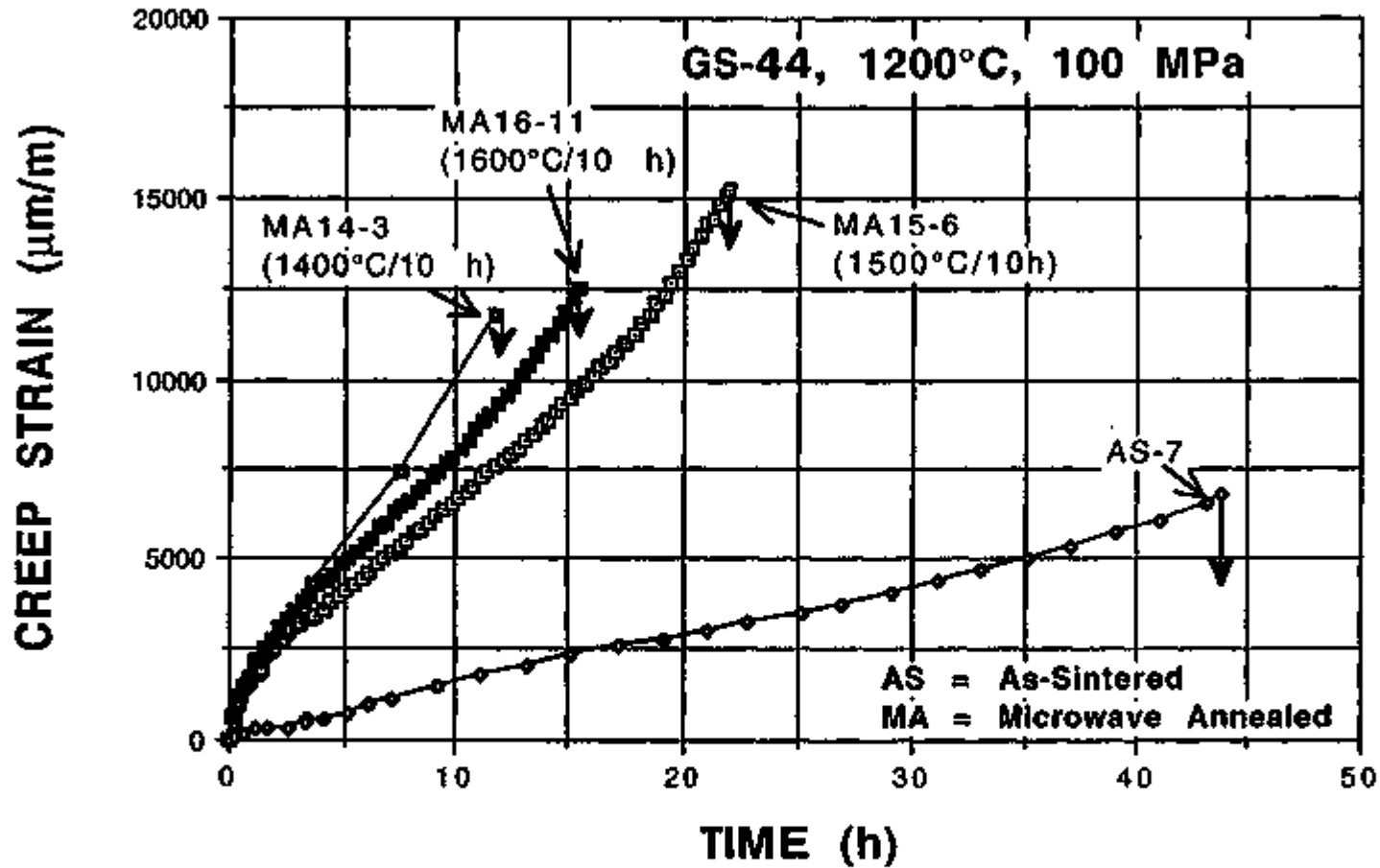
Fig. 13. Comparison of creep curves for microwave-annealed GS-44 Si_3N_4 specimens and unannealed ones tested at 1200°C and 100 MPa. Results show that creep resistance was significantly reduced as a result of microwave annealing.
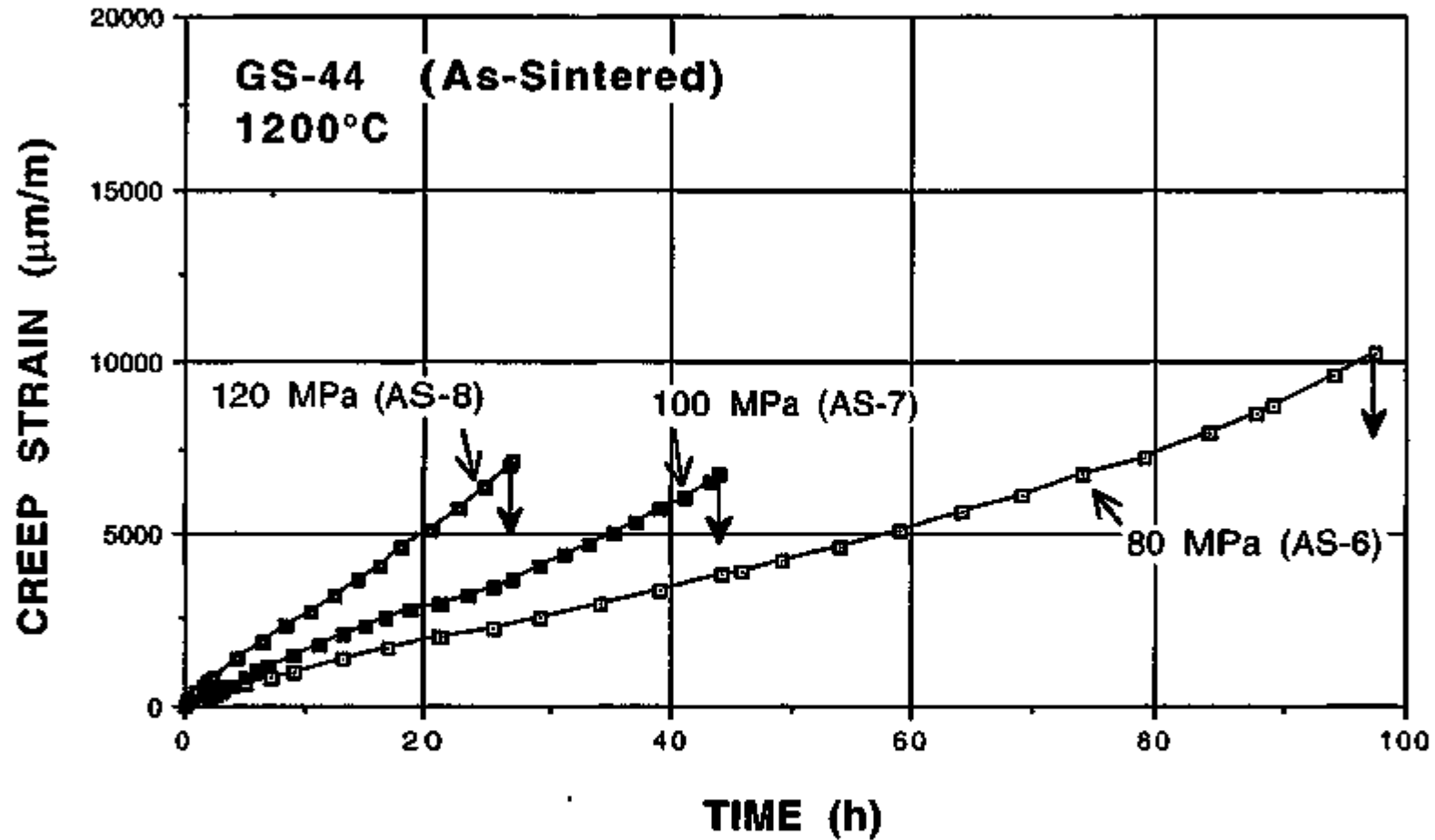
Fig. 14. Comparison of creep curves for GS-44 Si₃N₄ specimens tested in the as-sintered (unannealed) condition. Creep behavior was shown to be consistent with changes of the applied stresses.

Status of Milestones

Completed exploratory creep tests with stress and temperature histories for NT-154 Si_3N_4, including long-term creep tests (>10,000 to 30,000 h) at elevated temperatures - Milestone No. 321516, due on July 31, 1994.

Completed a draft report covering results of exploratory creep tests with stress and temperature histories for NT-154 Si_3N_4, including long-term creep tests (>10,000 to 30,000 h) at elevated temperatures - Milestone No. 321517, due on September 30, 1994.

Completed a preliminary study of high-temperature cyclic fatigue damage of ceramic materials using acoustic emission technique with waveguide - Milestone 321420, due on September 30, 1994.

Publications

1. J. L. Ding, K. C. Liu, and C. R. Brinkman, "A phenomenological high-temperature deformation and life prediction model for advanced silicon nitride ceramics," in the proceedings of the Symposium on Durability and Damage Tolerance, ASME Winter Annual Meeting, November 6-11, 1994, Chicago, Ill., Book No. G00940, American Society of Mechanical Engineers, New York.

2. K. C. Liu, C. O. Stevens, C. R. Brinkman, K. L. More, J. D. Kiggans, Jr., and T. N. Tiegs, "Enhancement of creep resistance of a sintered Si_3N_4 by microwave annealing," in the proceedings of the 5th International Symposium on Ceramic Materials and Components for Engines, Shanghai, China, May 29 - June 1, 1994 (in press).

3. K. C. Liu, C. O. Stevens, C. R. Brinkman, K. L. More, J. D. Kiggans, Jr., and T. N. Tiegs, "Enhancement of creep resistance of a sintered Si_3N_4 by microwave annealing," in the proceedings of the Science and Technology Alliance Materials Conference '93, North Carolina A & T State University, Greensboro, N.C., October 27-29, 1993 (in press).

References

1. T. N. Tiegs, J. O. Kiggans, P. A. Menchhofer, and K. L. Ploetz, "Microwave Sintering of Silicon Nitride," pp. 21-26 in Ceramic Technology Project Semiannual Progress Report for April 1992 through September 1992, ORNL/TM-12363, Martin Marietta Energy Systems, Inc., Oak Ridge Natl. Lab., July 1993.

2. K. C. Liu, C. O. Stevens, and C. R. Brinkman, "High Temperature Tensile and Fatigue Strengths of Si_3N_4," pp. 1261-65 in the proceedings of the Second European Ceramic Society Conference, September 11-14, 1991, Augsburg, Germany, Vol. 2, Structural Ceramics and Composition, Euro-Ceramics II, ed. G. Ziegler and H. Hausner, German Ceramic Society, 1993.

Life Prediction Verification

A. A. Wereszczak, H. Cai, T. P. Kirkland, and M. K. Ferber (ORNL)

<u>Objective/Scope</u>

There are three central goals of the proposed research program. High-temperature mechanical testing, microstructural characterization of failure phenomena, and the modeling of high-temperature deformation in candidate silicon nitrides are under investigation. The fundamental understanding of the evolution of damage, and ultimately the high-temperature mechanical performance and service life, is information that is critical for progress toward the implementation of structural ceramics as components in internal combustion and automotive gas turbine engines.

The systematic study of the high-temperature mechanical performance of silicon nitride is undertaken as a function of temperature and time. Two temperature regimes will serve as an independent parameter, $T \approx {<}1000°C$ and $T \approx {>}1000°C$, which are desired operating temperature ranges for internal combustion and automotive gas turbine engines, respectively. Tensile stress-rupture data will be generated by measuring fatigue life at a constant or cyclic stress. The time-dependent deformation will also be monitored during testing so that the extent of high-temperature creep may be ascertained.

The second goal is to characterize and understand the evolution and role of damage mechanisms associated with high-temperature deformation in silicon nitride. Tested specimens will be characterized using established ceramographic, scanning electron microscopy (SEM), transmission electron microscopy (TEM), and non-destructive acoustic techniques. Microstructural aspects of high-temperature failure will be examined and include:

1. extent of slow crack growth (SCG),
2. evolution of cavitation-induced damage and fracture,
3. transition between brittle crack extension and cavitation-induced growth,
4. crack blunting, and
5. the evolution and role of oxidation-assisted damage.

As the third goal, the resulting stress-rupture data will be used to examine the applicability of a generalized fatigue-life (SCG) and creep model. Refinements will be implemented to account for the damage mechanisms

listed. Consequently, the data generated in this program will not only provide a critically needed base for component utilization in Internal combustion and automotive gas turbine engines, but also facilitate the development of a design methodology for high-temperature structural ceramics.

<u>Technical Progress</u>

I. Lifetime Prediction Verification (temperatures < 1000°C)

During the present reporting period, work was initiated to examine the fatigue performance of a candidate structural ceramic material for conventional internal combustion engine components. Bend bars of a commercially available SiAlON material (NT451, Saint-Gobain/Norton Industrial Ceramics Corp.) were obtained and are being fatigue tested to address the verification of existing life-prediction methodologies. This is a β-sialon with yttria additive as sintering aid.[1] The microstructure consists of 0.6-μm grains with an aspect ratio of approximately six. There is 14 to 16% of glassy phase. Specimens are being dynamically loaded (i.e., dynamic fatigue) to determine fatigue parameters (e.g., fatigue crack growth exponent) as a function of temperature. Specimens were machined from the stems of failed SiAlON valves.

SiAlON ceramics were chosen because they are a candidate internal combustion engine valve material. They are much more cost effective than silicon nitrides because they can be fabricated by pressureless sintering like traditional ceramics.[2] Their ability to be joined makes SiAlON ceramics even more attractive. The grain boundary phase is not too refractory above 1000°C, so the mechanical performance degrades above this temperature; however, this does not present a problem for applications where the temperature is below 1000°C, such as in internal combustion engines.

The hardness of NT451 was determined using Vickers indentation on polished surfaces according to $H = 1.854P/d^2$, where P is indentation load and d is the diagonal of the impression. The indentation loads ranged from 1 to 5 kg. The average value from 20 measurements was 14.2 ± 0.3 GPa. The elastic constants were measured using a resonant ultrasound spectroscopic technique.[3] Specimens were rectangular parallelepipeds with a nominal size of 3 x 4 x 5 mm. The first 25 resonant frequencies (500 to 1500 kHz) were measured and used to fit the resonance model and compute the elastic

constants. A density of 3.23 g/cm^3 was used in the calculation. The shear modulus was calculated to be 116 GPa, the Young's modulus was 298 GPa, and the Poisson's ratio was 0.28.

The fracture toughness was evaluated using the modified indentation strength method. Three 5-kg Vickers indentations were made at the prospective tensile surface of each flexure bar. The bars were tested in four-point flexure to obtain the indentation strength. The crack lengths of the two surviving indentations were measured in an optical microscope. The fracture toughness is given by $T = (4y/3)\sigma_m\sqrt{c_m}$, where y is the indentation crack geometrical coefficient, σ_m is the indentation strength, and c_m is the crack radius of the surviving indentations. A controversy exists in the literature over what value should be used for y.[4] Because of this, the fracture toughness was computed using the original indentation strength method, in which the fracture toughness is given by $T = 0.59(E/H)^{1/8}(\sigma_m P^{1/3})^{3/4}$. With this, an average fracture toughness of 5.9 MPa$\sqrt{m}$ was obtained from six flexure specimens.

A brief survey of literature shows that very few studies have been done on the Weibull statistics and fatigue of SiAlON ceramics,[5] particularly at the intermediate temperature range relevant to engine applications. During this present reporting period, a dynamic fatigue curve was generated by testing at stressing rates of 10^{-3}, 10^{-2}, 10^{-1}, 10^0, 10^1, and 10^2 MPa/s and determining the flexure strength. For this purpose, a pre-production batch of 40 archive flexure specimens was obtained from R. L. Yeckley of Norton Advanced Ceramics.

The results are shown in Fig. 1, where the data points and error bars represent the average flexure strengths and standard deviations of four flexure tests in four-point bending. With the exception of the data point at stress rate of 10^2 MPa/s, this set of data shows no statistically significant susceptibility to dynamic fatigue. Variation in the flexure strength distribution overshadows any effect of the stress rate. The batch of the specimens consists of four sub-batches. The flexure strength versus the sub-batch number was examined, and no statistically significant dependence on the sub-batch number was found. Excluding the flexure strength data at the stressing rate of 10^2 MPa/s, qualitative Weibull statistics of the NT451 SiAlON material were obtained, as shown in Fig. 2, in which P_f and σ_f are the failure probability and strength, respectively. The Weibull modulus is 13, typical of conventional as-finished ceramics. The Weibull plot has three distinctive sections, perhaps indicative of different flaw
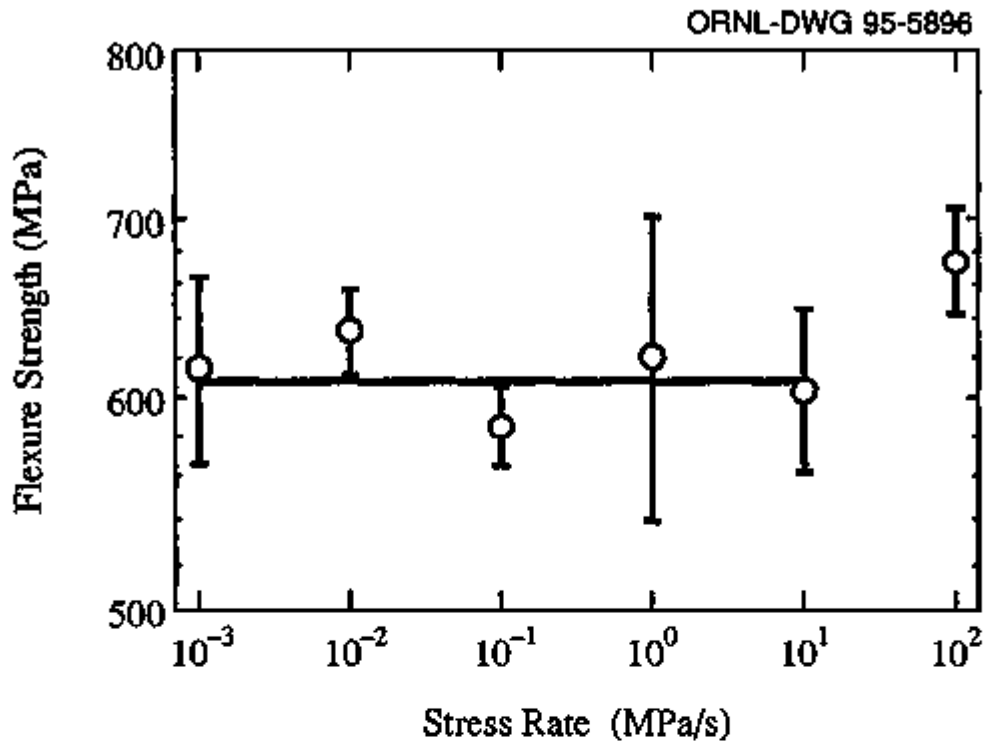
Fig. 1. Flexure strength of NT451 SiAlON as a function of stress rate. Tests were conducted in four-point flexure at 800°C in ambient air.
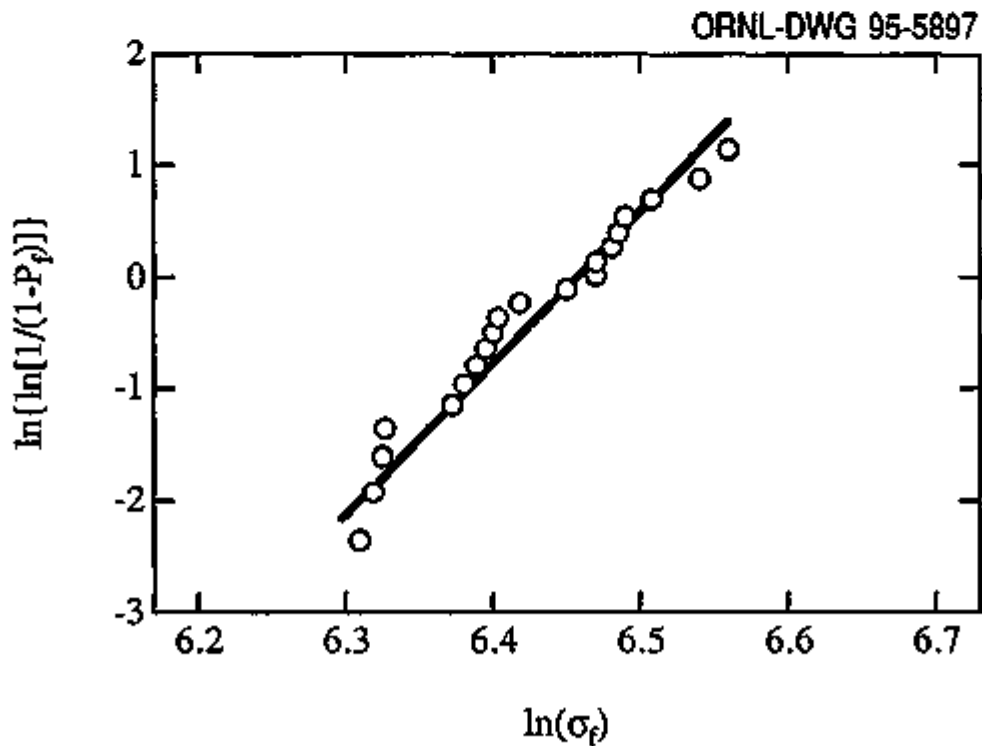
Fig. 2. Qualitative Weibull fracture statistics of NT451 SiAlON. Tests were conducted at 800°C in air. The Weibull modulus was calculated to be 13.

populations. Preliminary fractography examination using optical microscopy shows the data at the lower end of the flexure strength distribution are related to large pores, as indicated in Fig. 3. The reader should note that the material was a pre-production batch; it is expected that the current production batch has narrower strength distribution.

If the SiAlON is indeed very resistant to fatigue, then it would be even more attractive for applications such as engine components. Our present plan is to obtain a single, current production batch of NT451 SiAlON; to study the Weibull statistics and fracture modes; and to examine fatigue (dynamic, static, and cyclic) properties and mechanisms in detail.

A test matrix plan was designed so that the number of specimens and components needed for this project could be readily determined and a sufficient amount of material could be procured. In order to avoid batch-to-batch processing inconsistencies, all the specimens and components for this effort will be fabricated from the same batch of powder and additives and over the same processing/fabrication duration.

Planned experiments will include fracture toughness measurements and fast fracture strength tests in four-point flexure. Fracture modes will be

YPC-172

250 μm
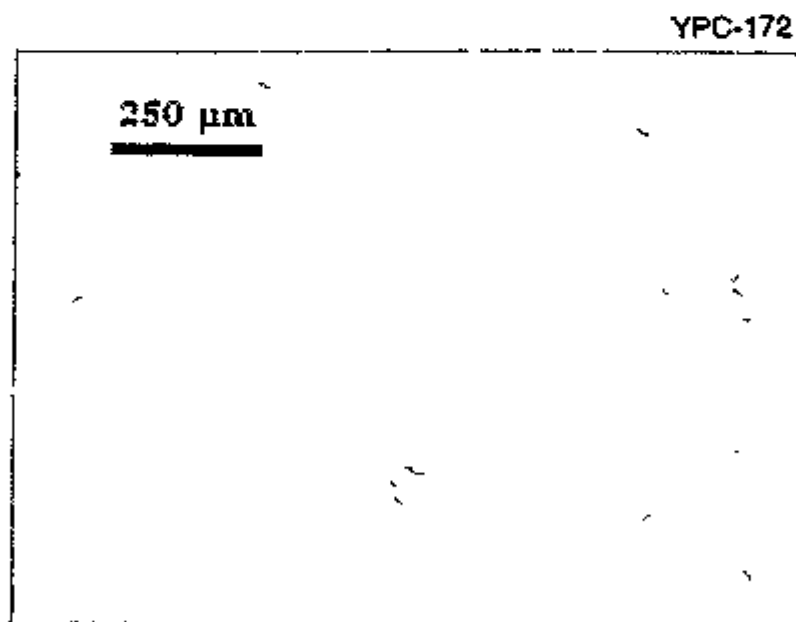
Fig. 3. The presence of large pores In NT451 SiAlON was consistently associated with low flexure strengths.

examined along with the generation of flexure strength data. Fatigue mechanisms and kinetics will be studied via static and dynamic fatigue tests in four-point flexure. Fatigue testing will also be conducted using rotating bending fatigue testing at a frequency of 100 Hz or greater. Tensile tests will be conducted to generate additional fast fracture and fatigue data and to confirm or compare the results from the flexure tests. Component confirmatory tests will be conducted on internal combustion engine valves also made from NT451. Tests will be carried out both at room temperature and at representative engine temperatures. Approximately 400 flexure bars, 46 rotating bending fatigue shank specimens, 37 buttonhead tensile specimens, and 44 valves will be required for the test matrix plan.

II. Lifetime Prediction Verification (temperatures > 1000°C)

The deleterious effects of "spotting" in NCX-5102 silicon nitride were described in a previous bimonthly report.[6] The nature of this spotting has been further complicated by the identification of additional types of spots;[7] however, the authors in the present study will refer to "spots" as those described in a previous bimonthly.[6] To further explore the nature of these spots and their effects on high-temperature mechanical performance, a comparison study has been initiated in collaboration with Saint-Gobain/Norton Industrial Ceramics Corporation, Northboro Research and Development Center (NRDC), Northboro, Massachusetts, manufacturers of this material. The test matrix is described in Table 1. A spotted and unspotted buttonhead tensile specimen will be tested at each of the 10 conditions described for a total of 20 specimens. The chosen temperatures are those which gas turbine engine components may be subjected to. To determine whether or not oxidation is causing the polarization in mechanical performance between the spotted and unspotted NCX-5102, two of the above conditions involve testing in the presence of a low partial pressure of oxygen. It is hoped that this test matrix, supplemented with post-testing X-ray diffraction, SEM, and TEM, will provide insight into the failure phenomena associated with the spotting in this material.

High-temperature tension-compression cyclic fatigue testing was initiated on NCX-5102 silicon nitride during the present reporting period. The motive of this effort is to determine a tension/compression cyclic stress-lifetime map

Table 1. Test matrix for NCX-5102 silicon nitride to be completed in collaboration with Saint-Gobain/Norton Industrial Ceramics Corp.

Condition	Atmosphere	Test type	Temp. (°C)	Stress (MPa)	Where to be tested
1	Inert	Static creep	1370	125	ORNL[a]
2	Inert	Static creep	1370	140	ORNL
3	Air	Static creep	1370	125	ORNL
4	Air	Static creep	1370	140	ORNL
5	Air	Static creep	1400	125	NRDC[b]
6	Air	Static creep	1450	80 to 100	NRDC
7	Air	Static creep	1500	30 to 50	NRDC
8	Air	Static creep	1260	220	ORNL
9	Air	ε or σ relaxation	1370	Varied	ORNL
10	Air	ε or σ relaxation	1260	Varied	ORNL

[a]ORNL = Oak Ridge National Laboratory, Oak Ridge, Tenn.
[b]NRDC = Saint-Gobain/Norton Industrial Ceramics Corporation, Northboro Research and Development Center, Northboro, Mass.

(i.e., S-N curve) while characterizing fatigue and creep interactions, the evolution of failure and its mechanisms, and grain boundary hardening behavior. Specimens were prepared with eight strain gages mounted on their gage sections, four each to monitor axial and concentric bending. Bending was reduced to less than 5%, and then tension-compression cyclic testing was initiated. The S-N relationship was unknown for this material at 1370°C. In order to gain insight, the first specimen was loaded with an initial peak-to-peak stress of ±100 MPa at 1370°C using a 1-Hz sinusoidal waveform. The motive with this specimen was to periodically increase the peak to peak stress until failure was produced. Once failure occurred, then another tension-compression cyclic test was to be initiated using that same ultimate peak-to-peak stress that caused fracture. For this first specimen, failure ultimately occurred at ±290 MPa, and the whole loading history is listed in Table 2. A second tension-compression test was initiated at 1370°C with the same waveform at ±290 MPa. Failure occurred after 2018 cycles. A third test was initiated at

Table 2. Summary of loading history of step-stressed tension-compression cyclic fatigue test at 1370°C on NCX-5102 silicon nitride (failure occurred at ±290 MPa)

Stress (MPa)	No. of cycles	Time (h)
±100	170701	47
±110	273587	76
±120	321616	89
±130	283164	79
±140	321125	89
±150	260645	72
±160	341521	95
±170	265263	74
±180	343954	96
±190	255256	71
±200	259403	72
±210	356328	99
±220	253334	70
±230	339139	94
±240	173250	48
±250	192777	54
±260	320995	89
±270	197301	55
±280	260132	72
±290	39054	11

±280, but failure occurred after only 81 cycles. A fourth test was initiated at ±250 MPa and is ongoing as of this writing. Fractography and microstructural analysis are under way to explain the mode and reason of failure in tension-compression cyclic fatigue at elevated temperatures.

The creep exponents for tensile and compressive creep of many structural ceramics have been shown to be different.[8,9] Any creep that occurs

during cyclic loading will be complicated by the reverse loading and its associated stress dependence. The tensile-compression cyclic performance of NCX-5102 will be compared with that from previous static and tension-tension cyclic tests at elevated temperatures generated as part of this subtask. The prediction of lifetime under the various loading histories is the goal. Refinements to a generalized creep model[10] that can take into account cyclic loading and relaxation phenomenon are continuing, and it is expected that sufficient data for the various loading histories (static, tension-tension, and especially tension-compression cyclic) will provide proper insight.

For the first tension-compression cyclic fatigue test, it appeared as though the increase in the step-stressing may have resulted in hardening behavior of the grain boundary phase and an increase in life; this behavior has been observed during incremental tension-tension cyclic testing.[11] Furthermore, cyclic loading (tension-tension) in general has been shown to be associated with longer lifetimes when compared with analogous static loading.[12] The tensile-compression cyclic performance of NCX-5102 will be compared with that from previous static and tension-tension cyclic tests at elevated temperatures generated as part of this subtask.

Static tensile creep testing of NCX-5102 silicon nitride in an argon environment at 1370°C continued during the present reporting period. Preliminary results show that this material creeps faster and has a shorter lifetime in argon than in ambient air, as shown in Fig. 4. This observation is consistent with findings from a study almost 20 years old where the creep of a hot-pressed silicon nitride was examined and compared in air and helium environments.[13] Comparisons of creep histories are shown in Fig. 5. Compared with creep tests in air, large reductions in the creep rate were not observed with specimens tested in argon. Testing is continuing and fractography and microstructural studies (SEM and TEM) are under way in an effort to explain the differences in creep performance. The role of long-term oxidation in ambient air creep is being sought; it is noted that creep testing in an inert environment removes its effect on the high-temperature mechanical loading.

316

ORNL-DWG 95-5898
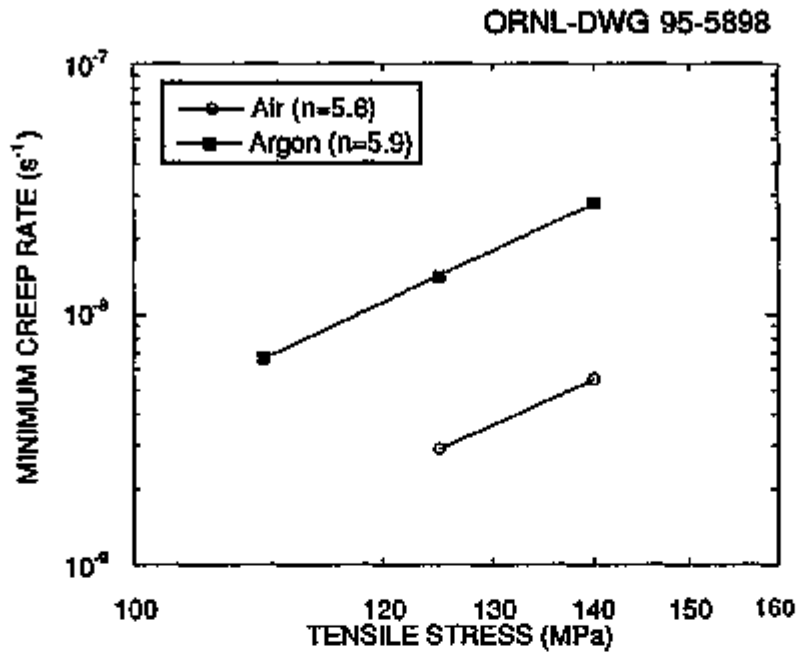
Fig. 4. NCX-5102 has a faster minimum creep rate in an inert environment than in air at 1370°C, while the creep exponents in the two environments are equivalent. Tests were conducted in tension on buttonhead specimens.

ORNL-DWG 95-5899
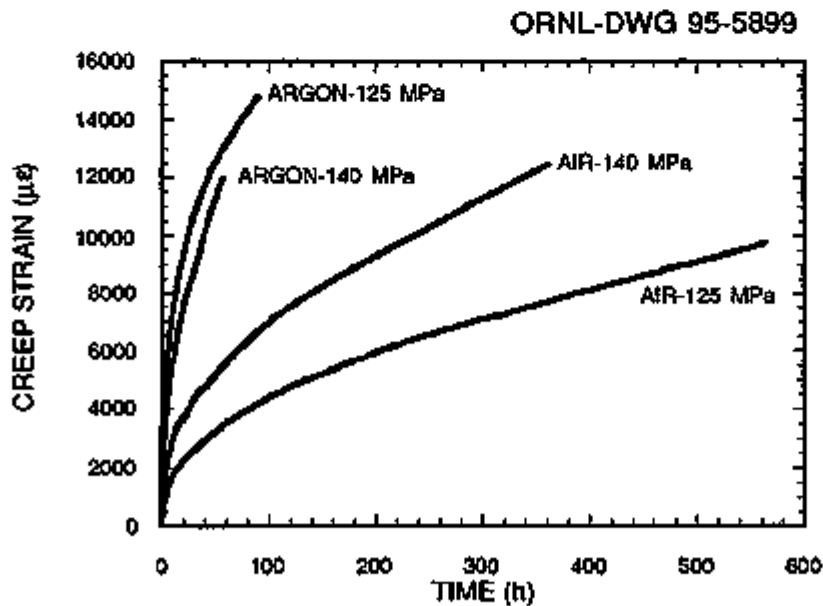
Fig. 5. Tensile creep histories of NCX-5102 tested in ambient air and argon environments at 1370°C.

Further comparisons of high-temperature mechanical performance of NCX-5102 in ambient air and inert environments included tensile dynamic fatigue testing at 1370°C. Specimens tested in argon at 1370°C had lower σ to ϵ proportional limits and greater strains to failure than those tested in ambient air, as shown in Fig. 6. Tests are continuing at slower stressing rates.

ORNL-DWG 95-5900
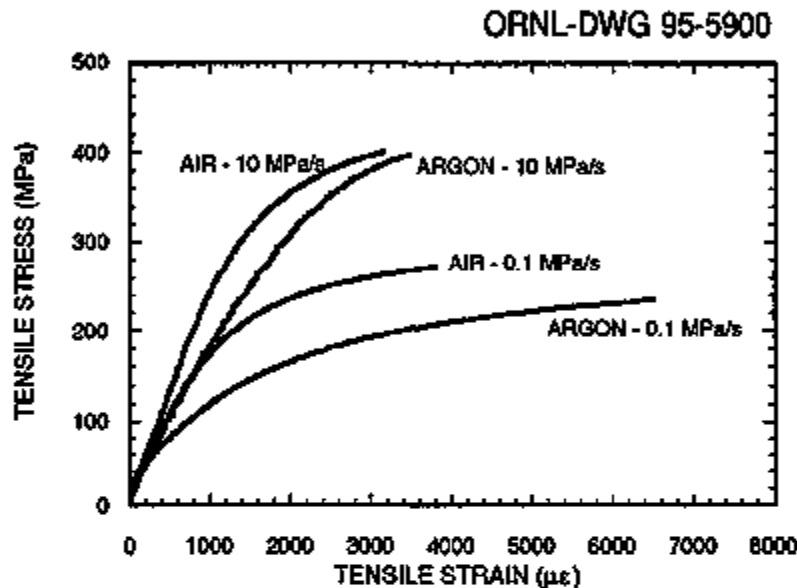
Fig. 6. Tensile dynamic fatigue histories of NCX-5102 tested in ambient air and argon environments at 1370°C. Preliminary results show strength to be decreasing with decreasing stressing rate.

Status of Milestones

A specification for a servohydraulic testing system was submitted to potential vendors for competitive bid. The servohydraulic test system will be capable of performing high-temperature reverse cyclic loading of a tensile specimen up to a frequency of 100 Hz. The system will be primarily used for cyclic tensile testing of materials that are candidates for internal combustion and gas turbine engine components. The choice from the competitive bidding process will be made and awarded before the November 1994 milestone; however, installation will not likely occur until early 1995.

An order has been placed for a rotating, bending fatigue machine. The instrument is manufactured by Fatigue Dynamics, Walled Lake, Michigan, and has capabilities of operating up to 1000°C at 10,000 rpm with a moment of 300 in.-lb.

All other milestones are on schedule.

Communications/Visitors/Travel

A. A. Wereszczak, H. Cai, and M. K. Ferber gave presentations at the 96th Annual Meeting and Exposition of the American Ceramic Society in Indianapolis, Ind., April 24-27, 1994.

M. K. Ferber visited R. L. Yeckley of Saint Gobain/Norton Industrial Ceramics Corp. to discuss work on candidate NT451 SiAlON material for engine components, July 25-26, 1994.

A. A. Wereszczak gave a presentation and submitted a supplementary manuscript at the Plastic Deformation of Ceramics conference, held August 7-12, 1994, at Snowbird, Utah. The article was entitled "Evolution of Oxidation and Creep Damage Mechanisms in HIPed Silicon Nitride Materials."

A. A. Wereszczak gave a presentation entitled "Creep and Oxidation Effects in Silicon Nitride" at the Ceramic Technology Project Quarterly Management Meeting, Washington, D.C., September 8, 1994.

M. K. Ferber traveled to AlliedSignal Engines in Phoenix, Arizona, to meet with David Wu to discuss AlliedSignal's life prediction program, September 20-22, 1994.

Problems Encountered

None.

Publications

An article entitled "Stress and Strain Relaxation Behavior in HIPed Silicon Nitrides" by A. A. Wereszczak, T. P. Kirkland, and M. K. Ferber was accepted for publication in *J. Mater. Sci. Lett.*

An article entitled "Evolution of Oxidation and Creep Damage Mechanisms in HIPed Silicon Nitride Materials," will be submitted for publication in the book *Plastic Deformation of Ceramics*, ed. R. Bradt, C. Brooks, and J. Routbort, Plenum Press, New York.

References

1. R. L. Yeckley, personal communication, 1994.
2. K. H. Jack, "Sialon Ceramics: Retrospect and Prospect," in *Mater. Res. Soc. Symp. Proc.* **287**, 15-27 (1993).
3. A. Migliori, J. L. Sarrao, W. M. Visscher, T. M. Bell, M. Lei, Z. Fisk, and R. G. Leisure, "Resonant Ultrasound Spectroscopic Techniques for Measurement of the Elastic Moduli of Solids," *Physica B* **183**, 1-24 (1993).
4. L. M. Braun, S. J. Bennison, and B. R. Lawn, "Objective Evaluation of Short-Crack Toughness-Curves Using Indentation Flaws: Case Study on Alumina-Based Ceramics," *J. Am. Ceram. Soc.* **75** [11], 3049-57 (1992).
5. R. R. Lee, B. E. Novich, G. Franks, D. Ouellette, M. K. Ferber, C. R. Hubbard, and K. More, "Mechanical Properties and Microstructure of Pressureless Sintered Duophase Sialon," pp. 459-67 in *4th International Symposium on Ceramic Materials and Components for Engines*, ed. by R. Carlsson, T. Johansson, and L. Kahlman, Elsevier Applied Science, London and New York, 1992.
6. A. A. Wereszczak, M. K. Ferber, and T. P. Kirkland, "Rotor Data Base Generation," pp. 65-73 in *Ceramic Technology Project Bimonthly Progress Report to DOE Office of Transportation Technologies, August-September 1993* .
7. Personal communication with Stephen Lombardo, Senior Research Engineer, Saint-Gobain/Norton Industrial Ceramics Corp., March 30, 1994.
8. M. K. Ferber, M. G. Jenkins, and V. J. Tennery, "Comparison of Tension, Compression, and Flexure Creep for Alumina and Silicon Nitride Ceramics," *Ceram. Eng. Sci. Proc.* **11** [7-8], 1028-45 (1990).
9. W. E. Luecke and S. M. Wiederhorn, "Tension/Compression Creep Asymmetry in Si_3N_4," *Key Eng. Mater.* **89-91**, 587-92 (1994).

10. M. K. Ferber, A. A. Wereszczak, and C.-K. Lin, "Rotor Data Base Generation," pp. 54-56 in *Ceramic Technology Project Bimonthly Technical Progress Report to DOE Office of Transportation Technologies, December 1992 - January 1993.*

11. K. C. Liu and C. R. Brinkman, "Dynamic Tensile Cyclic Fatigue of Si_3N_4," pp. 189-97 in *Proceedings of the 25th Automotive Technology Development Contractors' Coordination Meeting, P-209,* 1987.

12. C. -K. Lin, M. G. Jenkins, and M. K. Ferber, "Cyclic Fatigue of Hot Isostatically Pressed Silicon Nitride at Elevated Temperatures," *J. Mater. Sci.* **29**, 3517-26 (1994).

13. R. Kossowsky, D. G. Miller, and E. S. Diaz, "Tensile and Creep Strengths of Hot-Pressed Si_3N_4," *J. Mater. Sci.* **10**, 983-97 (1975).

Toughened Ceramics Life Prediction
Sung R. Choi, Jonathan. A. Salem, and John P. Gyekenyesi
(NASA Lewis Research Center)

Objective/Scope

The purpose of this research is to understand the room temperature and high temperature [≤ 1370°C (2500°F)] behavior of toughened ceramics as the basis for developing a life prediction methodology. A major objective is to understand the relationship between microstructure and mechanical behavior within the bounds of a limited number of materials. A second major objective is to determine the behavior as a function of time and temperature. Specifically, the room temperature and elevated strength and reliability, the fracture toughness, slow crack growth and the creep behavior will be determined for the as-manufactured material. The same properties will also be evaluated after long-time exposure to various high temperature isothermal and cyclic environments. These results will provide input for parallel materials development and design methodology programs. Resultant design codes will be verified.

Technical Highlights

The objective of this study is to analyze cyclic fatigue of both Griffith and as-indented flaw systems under sinusoidal loading conditions so that lifetime prediction from one fatigue (static) condition to another (cyclic) is readily feasible for either flaw system subjected to stress corrosion. For this purpose, the complete solution of the ratio of static to cyclic fatigue lives (h ratio) [1-3] was obtained numerically in conjunction with the fatigue parameter (n) and stress ratio (R-ratio) with a particular emphasis on as-indented crack system. The solution was compared with experimental data obtained from static and cyclic fatigue testing of both as-machined silicon nitride specimens at 1200°C and as-indented alumina specimens in room-temperature distilled water. The major assumptions made in this analysis are that the material exhibits a flat R-curve and that stress corrosion is a unique delayed failure mechanism.

I. ANALYSIS

In many cases slow crack growth of glass and ceramic materials under Mode I loading condition is described by the following empirical power-law relation

$$v = \frac{da}{dt} = A[\frac{K_I}{K_{IC}}]^n \tag{1}$$

where v, a, and t are crack velocity, crack size, and time, respectively. A and n are the material/environment parameters. K_I is the Mode I stress intensity factor, and K_{IC} is the Mode I critical stress intensity factor or fracture toughness of material with a flat R-curve. Since both Griffith (natural) flaws and microindentation flaws produced by a Vickers microhardness indenter have been frequently used to characterize fatigue behavior of brittle materials [4-9], both of the flaw systems are considered here for analysis.

(1) Griffith Flaws (Natural Flaws)

The corresponding Mode I stress intensity factor for this type of flaw system is

$$K_I = Y \sigma_a a^{\frac{1}{2}} \tag{2}$$

where Y is the crack geometry factor, and σ_a is the applied remote stress. Substituting Eq. (2) into Eq. (1) and solving the differential equation with some manipulations yields [10]

$$S_a^{n-2} = S_I^{n-2} - \frac{1}{B} \int_0^t [\sigma_a(t)]^n \, dt \tag{3}$$

where S_a is the degraded strength and S_i is the inert strength defined as $S_i - K_{IC}/(Y\sqrt{a_{ri}})$ with a_{ri} being a critical crack size with no slow crack growth. The parameter B is expressed

$$B = \frac{2 \, K_{IC}^2}{A Y^2 (n-2)} \tag{4}$$

In static fatigue testing a constant applied stress, $\sigma_a(t) - \sigma$, is employed. Noting that $n \geq 10$ for most glass and ceramics, one can derive the following static fatigue equation from Eq. (3) [10]

$$t_{fs} = B \, S_I^{n-2} \sigma^{-n} \tag{5}$$

where t_{fs} is the time to failure in static fatigue. In deriving Eq. (5), it was assumed that $(S_a/S_i)^{n-2} \approx 0$ since $n \geq 10$ for most glass and ceramics.

In cyclic fatigue testing a time-varying, periodic stress is applied

$$\sigma_a(t) = \sigma_{max} f(t) \tag{6}$$

where σ_{max} is the maximum applied stress, and $f(t)$ is a periodic function with a range of $0 \leq f(t) \leq 1$. Substituting Eq. (6) into Eq. (3) using $n \geq 10$, the time to failure in cyclic fatigue t_{fc} is obtained

$$t_{fc} = B \, S_I^{n-2} \, \sigma_{max}^{-n} \, \frac{1}{\frac{1}{t_f} \int_0^{t_f} [f(t)]^n \, dt} \tag{7}$$

For any periodic function with a constant mean and constant amplitude, the following mathematical relation holds

$$\frac{1}{t_f} \int_0^{t_f} [f(t)]^n \, dt = \frac{1}{\tau} \int_0^{\tau} [f(t)]^n \, dt \tag{8}$$

where τ is the period or the inverse of frequency $(1/f)$. Then, the cyclic fatigue equation yields

$$t_{fc} = B \; S_1^{n-2} \; \sigma_{max}^{-n} \; \frac{1}{\frac{1}{\tau}\int\limits_0^\tau [f(t)]^n \; dt} \tag{9}$$

The ratio of static fatigue to cyclic fatigue lives, h, with a condition of σ in static equal to σ_{max} in cyclic ($\sigma = \sigma_{max}$) can be obtained from Eqs. (5) and (9)

$$h = \frac{t_{fs}}{t_{fc}} = \frac{1}{\tau}\int\limits_0^\tau [f(t)]^n \; dt \tag{10}$$

with a condition of $0 < h \leq 1$.

The sinusoidal loading is the most common and popular wave form used in cyclic fatigue testing. The periodic function $f(t)$ for the sinusoidal wave (see Fig. 1) can be derived

$$f(t) = \frac{1+R}{2} + \frac{1-R}{2} \; sin\omega t \tag{11}$$

where R is the stress (or load) ratio, defined as $R = \sigma_{min}/\sigma_{max}$ with σ_{min} and σ_{max} being the minimum and maximum applied stresses, respectively. ω is the angular velocity. Hence, the h ratio for the sinusoidal wave becomes

$$h = \frac{1}{\tau}\int\limits_0^\tau [\frac{1+R}{2} + \frac{1-R}{2} \; sin\omega t]^n \; dt \tag{12}$$

Equation 12 can be solved either analytically or numerically. The h ratio for any other periodic loading configurations such as trapezoidal, triangular and square wave forms can be solved analytically with a straightforward procedure [1,11]. Equation 12 was solved analytically using the series expansion by Evans and Fuller [1]. Their analytical solution is expressed

$$h = \sum\limits_{k=0}^{n/2} \; [\frac{n!}{(n-2k)! \, (k!)^2}] \; [\frac{1-R}{2 \, (1+R)}]^{2k} (\frac{1+R}{2})^n \tag{13}$$
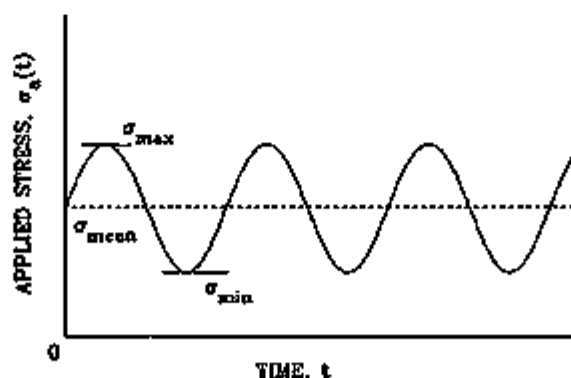
Figure 1. Sinusoidal wave form used in cyclic fatigue testing.

Equation (13) is still complicated to solve and valid only for integer values of n. Therefore, Eq. (12) must inevitably be solved numerically to cover integer or real values of n for a full range of R = 0 to 1.0, although only limited data exits on h ratio effects [1,2].

Figure 2 shows the results of the numerical solution of h ratio as a function of n for different R ratios from R = 0 to 1.0. In the figure log h was plotted against log n, and the solid lines represent the best-fit lines by regression. The h ratio increases with decreasing n and increasing R-ratio, and becomes unity at R = 1.0 (static fatigue). Since log h is almost a linear function of log n with the coefficients of correlation of $r_{coef} \geq 0.9966$, it is possible to obtain an approximate (but accurate) relation between log h and log n for a given R-ratio by using the regression analysis

$$log\ h = \alpha\ log\ n + \beta \qquad (14)$$

where α and β are the regression coefficients.

Table 1 shows the regression coefficients of α and β and r_{coef}'s thus obtained. Note that the coefficients of correlation are almost close to unity for R = 0 to 0.8. For $n \geq 10$, the maximum error associated in h ratio, compared to the exact solution, was 1.0 % for R = 0 to 0.7 and 4.5 % for R = 0.8 to 0.9. Therefore, this table gives a convenient means to determine the h ratio quickly and accurately for any given value of n, either integer or real. The complication of no simple analytical solution of Eq. (14) for real numbers can be eliminated with Eq. (14) and Table 1. The h ratio is independent of frequency, as can be mathematically demonstrated by manipulated of Eq. (12).
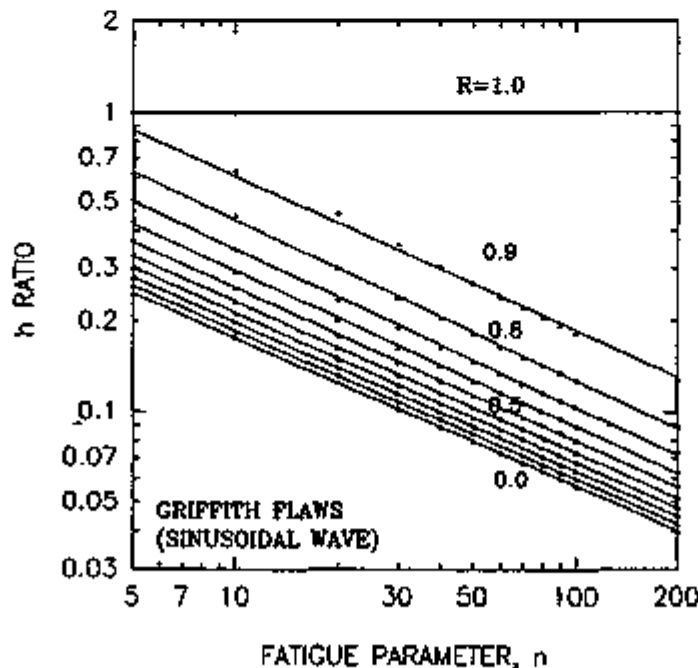
Figure 2. Numerical solution of the h ratio as a function of fatigue parameter (n) for different levels of R-ratio for Griffith flaw systems.

Table 1. Regression coefficient of h ratio (Eq. (14))
for Griffith flaw system

R	α	β	r_{coef}*
0.0	-0.4939	-0.2607	-1.0000
0.1	-0.4955	-0.2348	-1.0000
0.2	-0.4976	-0.2051	-1.0000
0.3	-0.5005	-0.1703	-1.0000
0.4	-0.5049	-0.1282	-1.0000
0.5	-0.5112	-0.0765	-0.9999
0.6	-0.5193	-0.0115	-0.9998
0.7	-0.5291	0.0705	-0.9997
0.8	-0.5353	0.1743	-0.9997
0.9	-0.5138	0.2977	-0.9966
1.0	0.0000	0.0000	-

* Coefficient of correlation.

(2) As-Indented Cracks

The dynamic and static fatigue analyses of as-indented cracks were developed numerically using indentation fracture mechanics [4,5]. Because an additional term appeared in the net stress intensity factor, due to residual contact stress produced by elastic/plastic indentation deformation [12], an analytical solution of cyclic fatigue for as-indented crack system is not feasible either. The solution should be made via numerical methods. To minimize having to specify several parameters, it is convenient to use a normalization scheme, as previously used for dynamic and static fatigue analyses [4-6,13]. With reference to the previous studies, the normalized variable are introduced as follow:

$$K^* = \frac{K_L}{K_{IC}}$$
$$J = \frac{A}{a_m} t$$
$$\sigma^* = \frac{\sigma_{max}}{\sigma_m}$$
$$C^* = \frac{a}{a_m}$$

(15)

where K^*, J, σ^* and C^* are, respectively, normalized stress intensity factor, normalized time, normalized maximum applied stress and normalized crack size. σ_m and a_m are, respectively, the strength and critical crack size in the inert condition. Using these variables, the crack growth rate of Eq. (1) and net stress intensity factor are expressed as follows:

$$\frac{dC^*}{dJ} = [K^*]^n$$
$$K^* = \frac{3}{4}\sigma_o^* C^{*\frac{1}{2}} + \frac{1}{4}C^{*-\frac{1}{2}}$$
$$\sigma_o^* = [\frac{1+R}{2} + \frac{1-R}{2} sin(\frac{\omega a_m}{A})J] \sigma^*$$

(16)

Note that the normalized net stress intensity factor consists of two terms: the first by remote applied stress and the second by residual contact stress [4,12]. The differential equation of Eq. (16) can be solved numerically using a fourth-order Runge-Kutta method. The initial condition was $C^* = 0.3967$ at $J = 0$ and the instability conditions were $K^* = 1$ and $dK^*/dC^* > 0$. The reason for the use of $C^* = 0.3967$ as an initial crack size is that an as-indented crack grows 2.52 times its initial crack size until instability via stable crack growth (not slow crack growth) due to the additional driving force by residual contact stress [4,12]. However, the solution was found to be insensitive to the initial crack sizes in a range of $C^* < 1.00$, as also noted previously [4].

The solution was initiated to determine the normalized time to failure (J_f) as a function of normalized maximum applied stress for the selected values of $n = 5-160$. This procedure was continued for the whole range of stress ratios from $R = 0.1$ to 1.0. Since the solution was independent of frequency (f) as far as $\omega a_m/A \geq 2\pi f$, any particular values of $\omega a_m/A$ satisfying $\omega a_m/A \geq 2\pi$ could be chosen. A value of $\omega a_m/A = 100$ was used in this analysis. The details regarding the influence of frequency on time to failure will be discussed in a later section.

Figure 3 shows a typical example of the normalized time to failure as a function of normalized maximum applied stress obtained for three different R-ratios of R =1.0, 0.5 and 0.1. Fatigue susceptibility increases with increasing R-ratio, yielding a maximum at R = 1.0 (static fatigue). Note that regardless of R-ratio the curves converge to $\sigma^* = 1.0$ in which the inert strength with no slow crack growth is attained. Similar to the static fatigue analysis [5], the slope in Fig. 3 is not representative of a 'true' fatigue parameter of n, due to the effect of residual contact stress. The slope in Fig. 3, which is called 'apparent' fatigue parameter (n'), was found to have the following relations
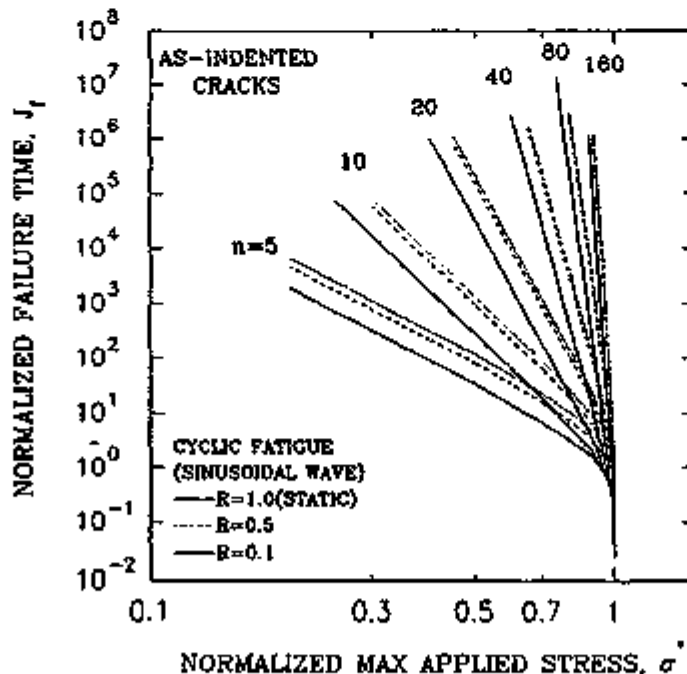
Figure 3. Typical examples of numerically obtained normalized fatigue time (J_f) as a function of normalized maximum applied stress (σ^*) for three different R-ratios of R = 0.1, 0.5 and 1.0 for as-indented flaw system.

$$n = 1.3347 \; n' - 0.7568 \quad \text{for } R = 1.0$$
$$n = 1.3340 \; n' - 0.7740 \quad \text{for } R = 0.5$$
$$n = 1.3341 \; n' - 0.7723 \quad \text{for } R = 0.1$$

with $r_{coef} = 1.0000$ for all the three cases. Therefore, the above results can be approximated with a reasonable accuracy as follows

$$n = 4/3 \; n' - 2/3 \tag{17}$$

which reduces to the relationship in static fatigue of as-indented cracks [5]. This indicates that the relationship between the true (n) and apparent (n') fatigue parameters is independent of R ratio, either static or cyclic. In fact, static fatigue is nothing more than one particular case (R = 1.0) of the generalized cyclic fatigue solutions (Eq. (16)).

The effect of frequency on time to failure can be seen in Fig. 4 with different n, σ^* and R. For the given R, n and σ^*, the normalized time to failure is independent of frequency, consistent with the case of Griffith flaw system.

Based on the results as shown in Fig. 3, h ratios for a given R can be determined for each n using the relation of $h = J_{fs}/J_{fc}$ ($= t_{fs}/t_{fc}$), where J_{fs} and J_{fc} are the normalized time to failure in static and cyclic fatigue, respectively. A value of h ratio for a given n was determined by averaging the individual h ratios obtained at a total of three to seven (depending on n values) different normalized maximum applied stresses. This repeated for other values of n and then R. It was found that the error in the h ratio thus obtained was negligibly small, considering the coefficients of variation in h ratio were less than 0.2 %.
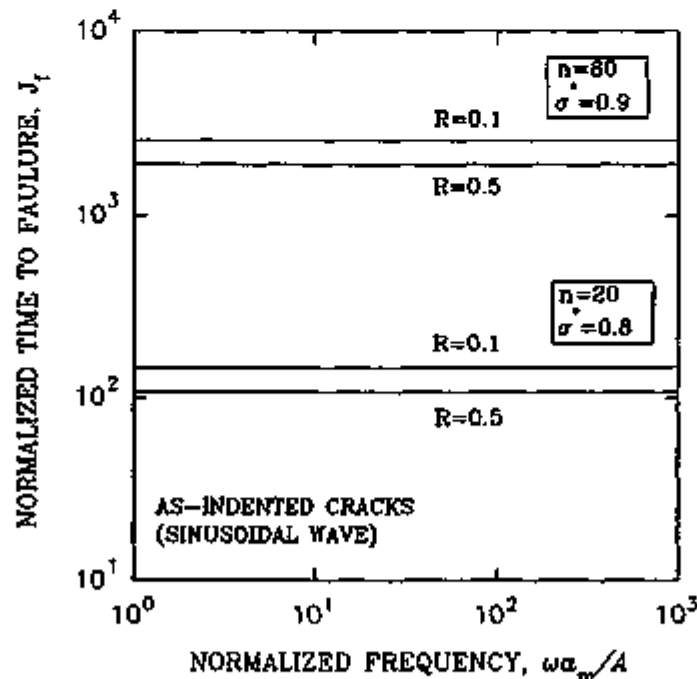
Figure 4. Effect of normalized failure time (J_f) on normalized frequency ($\omega a_m/A$) for different combinations of R, n and σ^* for as-indented flaw system.

Figure 5 shows a summary of the h ratio as a function of n for different levels of R-ratios from R = 0.1 to R = 1.0, where log h was plotted against log n in the same scheme as shown for Griffith flaw system (Fig. 2). The excellent curve fit allows one to obtain a relationship between log h and log n by using a linear regression analysis based on Eq. (14). The results of the regression analysis for α, β and r_{coef} are shown in Table 2. The coefficients of correlation are all close to unity except for R = 0.9, with a maximum error of about 4 % at R = 0.9 for $n \geq 10$, compared to the exact solution, so that Eq. (14) together with Table 2 provides an accurate solution of the h ratio for an as-indented crack system. Hence, lifetime prediction from one fatigue loading condition to another can be easily made using either Table 1 for Griffith flaw system or Table 2 for as-indented crack system.

(3) Evaluation of Fatigue Parameters

 (a) Griffith Flaws

The fatigue parameter n can be determined from the slope of fatigue data when log (time to failure) is plotted as a function of log (maximum applied stress) for either static or cyclic fatigue (see Eqs. (5) and (9)). From Eqs. (4) and (5), the fatigue parameter A in static fatigue is determined

$$A = \frac{2}{n-2} S_i^n a_{fi} \frac{1}{\lambda_s} \tag{18}$$
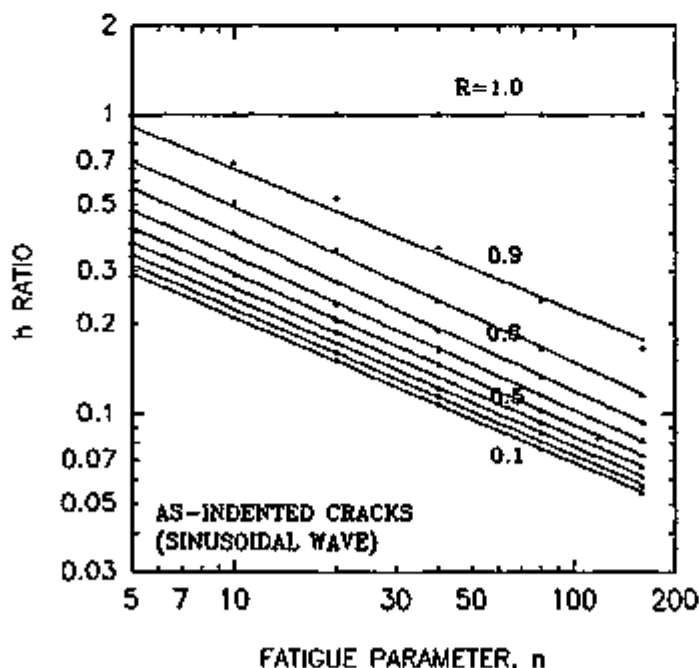
Figure 5. Numerical solution of the h ratio as a function of fatigue parameter (n) for different levels of R-ratio for as-indented flaw system.

Table 2. Regression coefficients of h ratio (Eq. (14))
for as-indented flaw system

R	α	β	r_{coef}*
0.1	-0.4856	-0.1925	-0.9999
0.2	-0.4885	-0.1612	-0.9999
0.3	-0.4925	-0.1240	-0.9999
0.4	-0.4977	-0.0804	-1.0000
0.5	-0.5049	-0.0268	-0.9999
0.6	-0.5126	0.0383	-0.9999
0.7	-0.5198	0.1172	-0.9999
0.8	-0.5173	0.2075	-0.9989
0.9	-0.4743	0.2932	-0.9911
1.0	0.0000	0.0000	.

* Coefficient of correlation.

where λ_s is the intercept of static fatigue data, expressed in $t_{fs}\sigma^n = \lambda_s$.
The fatigue parameter A in cyclic fatigue is obtained from Eqs. (4), (9)
and (10) as follows:

$$A = \frac{2}{n-2} S_f^n a_{fi} \frac{1}{\lambda_c h} \tag{19}$$

where λ_c is the intercept of cyclic fatigue data, expressed in $t_{fc}\sigma^n_{max} = \lambda_c$. The value of h can be determined using from Eq. (14) together with
Table 1.

(b) As-Indented Cracks

The 'true' fatigue parameter n for both static and cyclic fatigue can
be determined from Eq. (17) once the 'apparent' fatigue parameter n' is
determined from the slope of fatigue data. The fatigue parameter A in
static fatigue was determined previously [5]

$$A = (\frac{2\pi}{n'})^{\frac{1}{2}} \sigma_m^{n'} a_m \frac{1}{\lambda_s'} \tag{20}$$

where λ_s' is the intercept of static fatigue data, expressed in $t_{fs}\sigma^{n'} = \lambda_s'$. Since the following relation for as-indented flaw system holds

$$\frac{J_{fs}}{J_{fc}} = \frac{t_{fs}}{t_{fc}} = \frac{\lambda_s' \sigma^{-n'}}{\lambda_c' \sigma_{max}^{-n'}} = \frac{\lambda_s'}{\lambda_c'} = h \tag{21}$$

where λ_c' is the intercept of cyclic fatigue data in $t_{fc}\sigma^{n'} = \lambda_c'$. Hence,
from Eqs. (20) and (21), the parameter A in cyclic fatigue is obtained

$$A = (\frac{2\pi}{n'})^{\frac{1}{2}} \sigma_m^{n'} a_m \frac{1}{\lambda_c' h} \tag{22}$$

which is analogous to Eq. (19) for Griffith flaw system. The value of h
can be determined from Eq. (14) together with Table 2.

II. EXPERIMENT

Static and cyclic fatigue testing of silicon nitride (hot-pressed, NCX 34, Norton) flexure beam specimens (with Griffith flaw system) was conducted in ambient air at 1200°C. The detailed testing procedure is found elsewhere [14]. Briefly, the inner and outer spans of the SiC four-point bend fixture were 10 mm and 30 mm, respectively. The nominal dimensions of the test specimens were 3 mm by 7 mm by 35 mm, respectively, in height, width, and length. Stress levels applied in the static fatigue tests were 250 to 500 MPa. Cyclic fatigue test specimens were sinusoidally loaded with the maximum applied stress range from 300 to 500 MPa using a stress ratio of R = 0.5 at a frequency of f = 5 Hz. Each test specimen was preloaded with 20 N to maintain good alignment relative to the test fixture during heating to the test temperature.

Static and cyclic fatigue tests of as-indented alumina flexure (96 wt %, ALSIMAG 614, General Electrical Ceramics) beam specimens were carried out in room-temperature distilled water using a four-point bend fixture with 6.05 mm-inner and 19.05 mm-outer spans. The dimensions of the test specimens were 4 mm by 5 mm by 25 mm, respectively, in height, width, and length. The center (5 mm-side) of each specimen was indented in air for about 20 s using a Vickers microhardness indenter (Zwick, model 3212, Germany) with an indentation load of 49 N. Static fatigue test specimens were loaded with constant stress levels of 95 to 133 MPa. Cyclic fatigue test specimens were subjected to sinusoidal loading with a stress ratio of R = 0.5 at f = 5 Hz. The maximum applied stress range in cyclic fatigue was 100 to 130 MPa.

III. RESULTS AND DISCUSSION

The results of the static and cyclic fatigue testing at 1200°C for the silicon nitride specimens are shown in Fig. 6-a, where each solid line represents the best-fit line based on the appropriate fatigue equation. The decrease in time to failure with increasing applied stress, which represents fatigue susceptibility, was evident for both test conditions. For a given applied stress, fatigue susceptibility is higher in static fatigue than in cyclic fatigue, as reflected from Fig. (2). The fatigue parameter n was found to be n = 18.5 ± 2.8 and 20.8 ± 3.5, respectively, for static and cyclic fatigue. The results of the static and cyclic fatigue testing of the as-indented 96 wt% alumina specimens in room-temperature distilled water are depicted in Fig. 6-b. Consistent with the results shown in Fig. 6, fatigue is a little more susceptible in static loading than in cyclic loading within the experimental range used. The 'apparent' fatigue parameter was obtained from the data to be n' = 32.92 ± 6.01 and 35.37 ± 4.79, respectively, for static and cyclic fatigue.

The prediction of cyclic fatigue from static fatigue data for Griffith flaws can be made using Eqs. (10) and (14) together with Table 1. The best-fit static fatigue curve for the NCX 34 silicon nitride specimens was obtained to be

$$\log t_{fs} = -18.52 \log \sigma + 51.3172$$

where the units of t_{fs} and σ are in seconds and MPa, respectively. The corresponding h ratio can be obtained from Eq. (14) in conjunction with Table 1 for n = 18.52 and R = 0.5, which gives a value of h = 0.1886. Therefore, from Eq. (10) the predicted cyclic fatigue life is

$$\log t_{fc} = \log t_{fs} \cdot \log h$$
$$= -18.52 \log \sigma_{max} + 52.0416$$
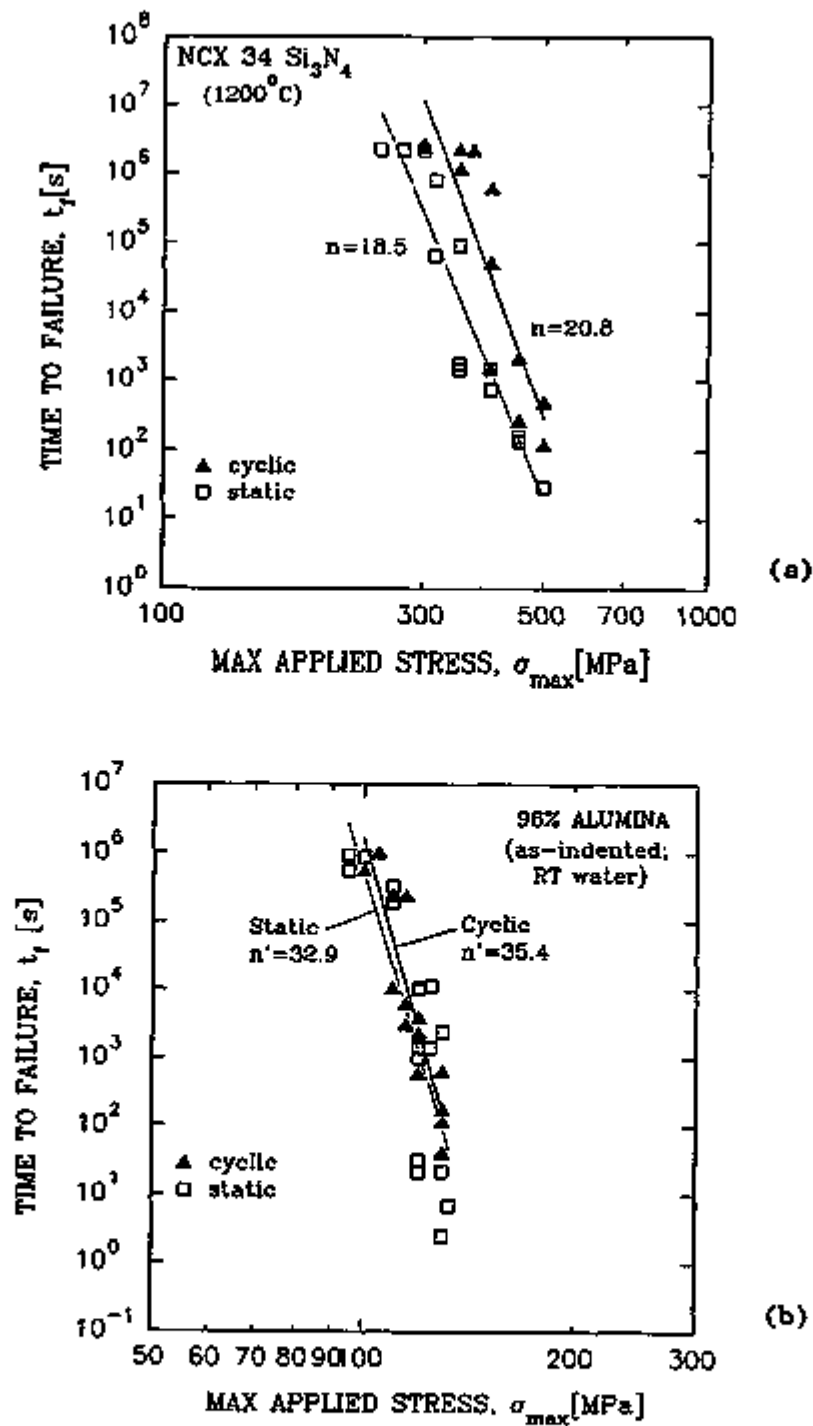
Figure 6. Results of static and cyclic fatigue testing obtained from the two materials: (a) NCX 34 silicon nitride flexure specimens tested at 1200°C [14]; (b) as-indented alumina flexure specimens tested in room-temperature distilled water.

In the same way, the prediction for the as-indented alumina specimens can be made. The best-fit static fatigue equation for the as-indented alumina specimens was determined to be

$$\log t_{fs} = -32.92 \log \sigma + 71.5612$$

Using the n'-n relation of Eq. (17), a true fatigue parameter of n = 43.23 was obtained. With the values of n = 43.23 and R = 0.5, the corresponding h ratio can be determined using Eq. (14) with Table 2, to give a value of h = 0.1404. Hence, the predicted cyclic fatigue life is

$$\log t_{fc} = -32.92 \log \sigma_{max} + 72.4142$$

The prediction thus made are shown in Fig. 7, where the cyclic fatigue data obtained from the experiments are included for comparison. The prediction underestimates somewhat the actual cyclic fatigue data for the silicon nitride specimens with Griffith flaws; whereas, it overestimates for the alumina specimens with as-indented cracks. However, considering the small number of test specimens used in this experiment, the overall agreement seems to be reasonable. In particular, the difference in fatigue parameter (n) between static (n = 18.5) and cyclic (n = 20.8) for the silicon nitride specimens and between static (n = 43.23) and cyclic (n = 46.49) for the as-indented alumina specimens is very small, thus implying that stress corrosion is a common, governing failure mechanism in both static and cyclic fatigue of each material.

It has been reported that for certain ceramic materials mechanisms such as damage accumulation and/or cyclic synergisms can be active in cyclic fatigue, resulting in more fatigue susceptibility in cyclic than in static loading [8,15-18]. If additional failure mechanisms or synergies such as damage accumulation, cyclic effects, and/or creep at elevated temperatures are involved simultaneously in cyclic fatigue, then the analysis given in this paper may not be valid. Notwithstanding, the analysis still provides some clues to pinpoint the prevailing failure mechanism associated with failure. In view of the reasonable agreement between the static and cyclic fatigue data shown here, it can be stated that fatigue parameters for these material systems can be obtained using either static or cyclic fatigue testing. In terms of testing economy, however, static fatigue is preferred because of the much high testing costs associated with cyclic fatigue testing.

As mentioned before, the analytical solution of the h ratio for other loading functions such as trapezoidal, triangular and square wave forms can be easily obtained for the Griffith flaw system because of its mathematical simplicity [1,11]. However, the conventional numerical solution for these loading functions may not be simple for as-indented crack system since the functions, unlike the sinusoidal wave, are not continuous but discontinuous in nature. In this case, each discontinuous periodic function should be converted into a continuous periodic function so that the numerical solution becomes feasible (see Eq. (16)). This will be done by using the Fourier analysis from which a discontinuous function can be approximated into a continuous function. This should be a future area of study.
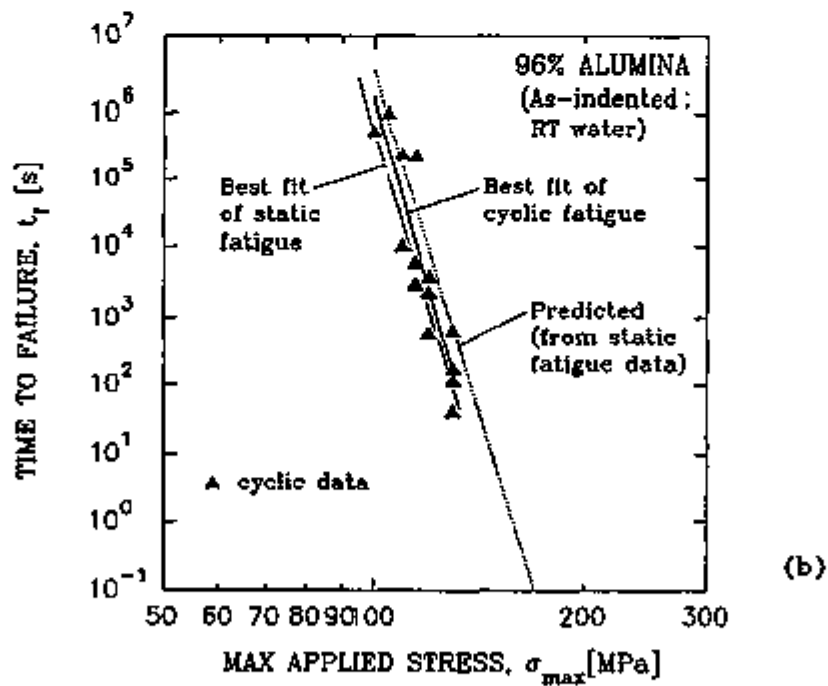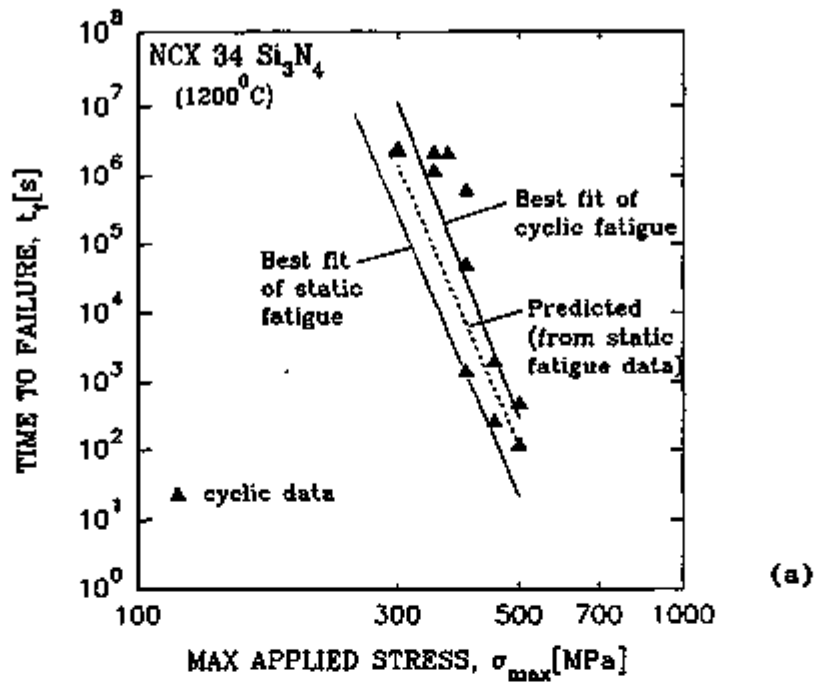
Figure 7. Prediction of cyclic fatigue lifetime from static fatigue data:
(a) NCX 34 silicon nitride specimens tested at 1200°C[14]; (b) as-indented
alumina specimens tested in room-temperature distilled water.

IV. CONCLUSIONS

The ratio of static to cyclic fatigue lives, h ratio, was obtained numerically for both Griffith and as-indented flaw systems subjected to sinusoidal loading conditions. The h ratio decreases with increasing n and decreasing R-ratio. Using this solution of the h ratio, lifetime prediction from static to cyclic fatigue was made based on static and cyclic fatigue data obtained from both silicon nitride (Griffith flaws) at 1200°C and as-indented alumina specimens in room-temperature distilled water. Reasonable agreement was observed between the analysis and experimental data, thus supporting the validity of the solution. Therefore, the solution provides a simple, quick lifetime prediction methodology from one fatigue condition to another for both Griffith and as-indented flaw systems whose governing failure mechanism is stress-corrosion.

REFERENCES

1. A. G. Evans and E. R. Fuller, "Crack Propagation in Ceramic Materials under Cyclic Loading Conditions," *Metall. Trans.*, 5[1] 27-33 (1974).

2. T. Kawakubo and K. Komeya, "Static and Cyclic Fatigue Behavior of a Sintered Silicon Nitride at Room Temperature, " *ibid*, 70[6] 400-405 (1987).

3. C.-K. J. Lin and D. F. Socie, "Static and Cyclic Fatigue of Alumina at High Temperatures," *J. Am. Ceram. Soc.*, 74[7] 1511-18 (1991).

4. B. R. Lawn, D. B. Marshall, G. R. Anstis, and T. P. Dabbs, "Fatigue Analysis of Brittle Materials Using Indentation Flaws, Part 1. General Theory," *J. Mater. Sci.*, 16 2846-2854 (1981).

5. E. R. Fuller, B. R. Lawn, and R. F. Cook, "Theory of Fatigue for Brittle Flaws Originating from Residual Stress Concentrations, " *J. Am. Ceram. Soc.*, 66[5] 314-21 (1983).

6. S. R. Choi, J. E. Ritter, and K. Jakus, "Failure of Glass with Subthreshold Flaws," *ibid*, 73[2] 268-74 (1990).

7. S. Lathabai, Y.-W. Mai, and B. R. Lawn, "Cyclic Fatigue Behavior of an Alumina Ceramic with Crack-Resistance Characteristics, " *J. Am. Ceram. Soc.*, 72 1760-63 (1989).

8. S. Horibe and R. Hirahara, "Cyclic Fatigue of Ceramic Materials: Influence of Crack Path and Fatigue Mechanisms," *Acta Metall. Mater.*, 39[6] 1309-1317 (1991).

9. R. H. Dauskardt, R. R. James, J. R. Porter, and R. O. Ritchie, "Cyclic Fatigue-Crack Growth in SiC Whisker-Reinforced Alumina Ceramic Composite: Long- and Small-Crack Behavior," *J. Am. Ceram. Soc.*, 75[4] 759-71 (1992).

10. a) J. E. Ritter, P. B. Oates, E. R. Fuller, and S. M. Wiederhorn, "Proof Testing of Ceramics, Part 1 Experiment," *J. Mater. Sci.*, 15[9] 2275-81 (1980).
    b) E. R. Fuller, S. M. Wiederhorn, J. E. Ritter, and P. B. Oates, "Proof Testing of Ceramics, Part 2 Theory," *ibid*, 15[9] 2282-95 (1980).

11. J. A. Salem and S. R. Choi, Bimonthly Progress Report, April/May 1994, Ceramic Technology Project, Oak Ridge National Laboratory, Oak

Ridge, TN (1994).

12.   B. R. Lawn, A. G. Evans, and D. B. Marshall, "Elastic/Plastic Indentation Damage in Ceramics: The Median/Radial Crack System," *J. Am. Ceram. Soc.*, 63 [9-10] 574-81 (1980).

13. S. R. Choi and J. A. Salem, "Effect of Preloading on Dynamic Fatigue Strength of Glass and Ceramics at Ambient Temperature," submitted to *J. Am. Ceram. Soc.*, (1994).

14.   a) S. R. Choi, J. A Salem, and J. L. Palko, "Comparison of Tension and Flexure to Determine Fatigue Life Prediction Parameters at Elevated Temperatures,"   pp. 98-111 in *Life Prediction Methodologies and Data for Ceramic Materials*, ASTM STP 1201, C. R. Brinkman and S. F. Duffy Eds., ASTM, Philadelphia (1994).
     b) S. R. Choi, J. A. Salem, N. Nemeth, and J. P. Gyekenyesi, "Elevated Temperature Slow Crack Growth of Silicon Nitride Under Dynamic, Static, and Cyclic Flexural Loading," *Ceram. Eng. Sci. Proc.*, 15[5] 597-604 (1994).

15.   D. A. Krohn and D. P. H. Hasselman, "Static and Cyclic Fatigue Behavior of a Polycrystalline Alumina," *J. Am. Ceram. Soc.*, 55[4] 208-211 (1972).

16. L. Ewart and S. Suresh, "Crack Propagation in Ceramics under Cyclic Loads," *J. Mater. Sci. Lett.*, 22[4] 1173-92 (1987).

17. M. J. Reece, F. Guiu, and M. F. R. Sammur, "Cyclic Fatigue Crack Propagation in Alumina Under Direct Tension-Compression Loading," *J. Am. Ceram. Soc.*, 72[2] 348-52 (1989).

18. R. H. Dauskardt, D. B. Marshall, and R. O. Ritchie, "Cyclic Fatigue-Crack Propagation in Magnesia-Partially-Stabilized Zirconia Ceramics," *ibid*, 73[4] 893-903 (1990).

Status of Milestones

Milestones are on time.

Communication/Visits/Travel

Problems Encountered

Availability of *in situ* toughened Si_3N_4's is limited.

Publications

1.   S. R. Choi and J. A. Salem,   "Creep Behavior of Silicon Nitride Evaluated by Deformation Curvature and Neutral Axis Shift Determinations," pp. 285-293 in *Silicon Based Structural Ceramics*, Ceramic Transaction, Vol 42, American Ceramic Society (1994).

2. V. Tikare, W. Sanders, and S. R. Choi, "Processing and Testing of High Toughness Silicon Nitride Ceramics," pp. 267-275, *ibid*.

Life Prediction Methodology
D. Wu (AlliedSignal Engines)

Objectives/Scope

AlliedSignal Engines has defined a program that builds on the progress made in Phase I of the Life Prediction Methodology for Ceramic Components of Advanced Heat Engines program. This Phase II program will develop the methodology required to adequately predict the useful life of ceramic components used in advanced heat engines. Phase II will concentrate on predictive methodology for time- and cycle-dependent failure modes, as well as proof testing and nondestructive evaluation (NDE) methodology that will enhance component reliability through screening of low-strength components.

The life prediction methodologies developed will be generic and hence will be applicable to ceramic components that operate under known temperature and stress conditions.

The technical effort has been organized into six objective-oriented tasks, as follows:

1. Material Baseline
2. Compressive Creep Methodology
3. Flaw Growth Methodology
4. Cyclic Fatigue Methodology
5. Proof Test Methodology
6. NDE Reliability Methodology

The planned test matrix is shown in Table 1.

Integration of the methodologies will be undertaken through continued development of the statistical and risk integration computer codes previously developed during the Phase I program.

Progress made under the Phase II objectives during the April through September, 1994 reporting period is described in the following sections.

TABLE 1. CERAMIC LIFE PREDICTION PHASE TEST MATRIX.

Test Objective	Test Description	Test Temperatures, F							
		RT	1300	2100	2200	2300	2400	2500	(TBD)
		No. of Specimens							
Baseline	Flexure MIL-B (Longitudinal Machined)	30	10	10	--	--	--	10	30
	Tensile FF (Longitudinal Machined)	--	--	10	10	--	--	10	--
	Tensile SR (Longitudinal Machined)	--	--	--	10	--	--	10	--
	Tensile SR (Transverse Machined)	--	--	--	10	--	--	10	--
	Tensile SR (As-Processed)	--	--	--	10	--	--	10	--
	Flexure MIL-B (As-Processed)	60	--	--	--	--	--	--	--
	Flexure Spin Disk Cut-Up	100	--	--	--	--	--	--	--
	Notch Specimen (Remachined)	10	--	--	--	--	--	--	--
Compressive Creep	Axial (Longitudinal Machined)	--	--	--	--	8	8	8	--
Flaw Growth	Flexure	--	--	5	5	5	5	--	--
Cyclic Fatigue	Tensile R = 0 (Longitudinal Machined)	--	16	--	16	--	--	--	--
	Tensile R = 0 (Longitudinal Machined), 60-Second Hold	--	8	--	8	--	--	--	--
	Tensile R = -1 (Longitudinal Machined)	--	10	--	10	--	--	--	10
	Flexure MIL-B (Longitudinal Machined)	15	15	25	25	--	--	--	--
	Flexure MIL-B (Transverse Machined)	--	25	15	--	--	--	--	--
	Flexure MIL-B (As-Processed)	--	--	15	15	--	--	--	--
Proof Testing	Machining Anisotropy	150	--	--	--	--	--	--	--
	Residual Strength (3-Pt/4-Pt)	30	--	--	--	--	--	--	--
	Residual Strength (RT/HT)	--	--	30	30	--	--	--	--
	Dynamic Fatigue								
	Proof Tested (Rate 1)	9	--	9	9	--	--	--	--
	Proof Tested (Rate 2)	9	--	9	9	--	--	--	--
	Non-Proof Tested (Rate 1)	9	--	9	9	--	--	--	--
	Non-Proof Tested (Rate 2)	9	--	9	9	--	--	--	--
	Non-Proportional Loading								
	Round Plate (Machined)	60	--	30	--	--	--	--	--
	Round Plate (As-Processed)	30	--	--	--	--	--	--	--
NDE POD	Square Plate (Machined)	4	--	--	--	--	--	--	--
	Square Plate (As-Processed)	4	--	--	--	--	--	--	--
	GTCP85 APU Stators (Machined)	55	--	--	--	--	--	--	--
	GTCP85 APU Stators (As-Processed)	55	--	--	--	--	--	--	--

FF = Fast Fracture. NDE = Nondestructive Evaluation. POD = Probability of Detection.

R = Stress Ratio. RT = Room Temperature. SR = Stress Rupture.

3-Pt/4-Pt = Proof testing in 3-point flexure followed by 4-point strength test.

RT/HT = Proof testing at RT followed by high-temperature (HT) strength test.

12025(00)-1

1.   **Material Baseline**

This task includes activities for:

a.   Procurement of NT154 silicon nitride specimens from Norton Advanced Ceramics in East Granby, Connecticut

b.   Specimen testing to determine the baseline material properties and establish a comparison with specimens used in Phase I

c.   Specimen testing to determine the strength and life characteristics of as-processed surfaces

d.   Specimen testing to complete the information acquired during Phase I dealing with surface condition and surface strength issues.

Care has been taken to ensure that the ceramic specimen material properties obtained in Phase II would be similar to those obtained in Phase I. This included relining the ball mill used for the ceramic powder with the same type of rubber as that used in Phase I.

Under activity 1(a), a powder contamination problem was discovered during powder qualification. An excessive number of failures in the flexure test bars were attributable to inclusions (as reported in the June-July bimonthly progress report). Fractography showed that the inclusions contained carbon, probably from the ball mill liner, and discrete iron particles. The inclusions are similar in composition to those found during Phase I, but are larger in size and higher in the frequency of occurance.

Powder reconditioning trials were defined, to determine the best method to eliminate the large inclusions. The reconditioning processes being evaluated include:

1. Dry magnetic separation
2. Dry magnetic separation + 600C oxidation treatment
3. Wet magnetic separation
4. Wet Magnetic separation + 600C oxidation treatment.

The magnetic separation processes employ magnetic fields as high as five times those used in the baseline process, and are intended to completely separate the iron-bearing inclusions. The oxidation treatment is intended to burn off any carbon found with the inclusions.

The powder reconditioning trials are nearing completion. Trial specimen mechanical testing will follow, to determine the efficacy of the reconditioning processes. The acceptance criteria for the reconditioned powder are based primarily on the proof testing requirements, explained further in Section 5.

2. Compressive Creep Methodology

This task includes generation of compressive creep data to support development of a compressive creep rate model. The data and model will complement the tensile creep data and model generated during Phase I.

The compressive creep test specimens have been machined from the buttonhead remains of the fast fracture tensile test specimens used during Phase I. The specimens are cylindrical, 5 mm in diameter and 10 mm in length. The specimens have been sent to the Oak Ridge National Laboratory High Temperature Materials Laboratory (ORNL-HTML) (Oak Ridge, Tennessee) for verification of compatibility with the compressive creep test apparatus.

3. Flaw Growth Methodology

This task includes generation of explicit crack growth rate data and comparing the data to crack growth parameters derived from stress rupture tests.

Professor R. Dauskardt of Stanford University has been contracted to perform the crack growth tests. The testing and analyses will be accomplished in three phases:

Phase I - Literature survey to identify potential testing techniques

Phase II - Preliminary experiments to optimize experimental techniques

Phase III - Core program to generate desired data.

Test variables include temperature, mode mixity (Mode I and mixed Mode I and II), crack size (long vs. inherent crack), and environment (air and nitrogen). Limited cyclic tests will also be conducted to determine the effects of cyclic loading.

4.   Cyclic Fatigue Methodology

The objective of this task is to develop a life prediction model for ceramic components subjected to cyclic loading. The effects of loading variables (stress ratio [R] and hold time) will be assessed using tensile test specimens. The effects of surface condition (longitudinal machined, transverse machined, and as-densified) will be assessed with flexure test specimens. Specimen/component size effects will be determined by comparison of the tensile and flexure test results from longitudinally-machined specimens.

A critical question is whether cyclic fatigue in ceramic components involves crack propagation from inherent defects in the material or whether it is a nucleation and propagation process. Crack growth behavior can be derived from fast fracture test data (which provides a measure of inherent defect distribution) and cyclic fatigue test results, if crack growth from inherent defects is assumed. This behavior can be compared to the explicitly obtained cyclic fatigue crack growth rate data, as described in Section 3.

5.   Proof Testing Methodology

The objective of this task is to develop the methodology to assess the effects of proof testing on the reliability of ceramic components for surface defects. As part of the objective, the shear sensitivity of the machining flaws in NT154 will be determined.

The proof testing test matrix is very sensitive to the powder contamination problem described in Section 1, since the tests will be conducted in the flexural mode. Excessive failures from inclusions would render the data analysis very difficult. As part of the powder reconditioning effort, a method to determine the acceptance criteria (in terms of allowable inclusion failures from flexure bars) for the reconditioned powder was defined.

Given that the surface and volume strength parameters are known for a given material, the ratio of the surface to volume flaws is calculated as follows. The survival probability for a system with two competing failure modes is given by:

$$S(x) = S_1(x)S_2(x) \tag{1}$$

The probability of failure is given by:

$$F(x) = 1 - S_1(x)S_2(x)$$ [2]

The probability density function for this system is obtained by differentiating Equation [2] to obtain:

$$f(x) = f_1(x)S_2(x) + S_1(x)f_2(x)$$ [3]

The first term in the right-hand side of Equation [3] represents the joint probability density of a specimen failing from the first mode and at strength x, and similarly, for the second mode, in the second term of the equation. Hence, the probability of failure from the first mode at or below strength x, is given by the integral from zero to x, and the proportion of total failures in a population is given by the integral from zero to infinity:

$$P_{f_1}(X) = \int_0^x f_1(x)S_2(x)dx$$ [4]

$$P_{f_1}(X) = \int_0^\infty f_1(x)S_2(x)dx$$ [5]

$$f_1(x) = \frac{I_1 V_1 m_1 (x)^{m_1-1}}{(\sigma_{o_1})^{m_1}} \exp\left[-I_1 V_1 \left(\frac{x}{\sigma_{o_1}}\right)^{m_1}\right]$$ [6]

$$S_2(x) = \exp\left[-I_2 V_2 \left(\frac{x}{\sigma_{o_2}}\right)^{m_2}\right]$$ [7]

$$P_{f_1}(X) = \int_0^X \frac{I_1 V_1 m_1 (x)^{m_1-1}}{(\sigma_{o_1})^{m_1}} \exp\left[-I_1 V_1 \left(\frac{x}{\sigma_{o_1}}\right)^{m_1}\right] \cdot \exp\left[-I_2 V_2 \left(\frac{x}{\sigma_{o_2}}\right)^{m_2}\right] dx \qquad [8]$$

Equation [8], does not have a closed-form solution for $m_1 \neq m_2$! Therefore, the equation must be solved numerically.

Equation [8], represents the proportion of failures for Failure Mode 1 that will fail in a population. If all specimens were tested to failure, X goes to infinity.

In the case of proof testing of a specimen population, only a proportion of the whole population will fail. Hence, the proportion of the population that fails due to Failure Mode 1 is given by the ratio of the number of failures of Mode 1 that can fail in the proof test to the total number of specimens that can fail in the proof test, which is:

$$ratio = \frac{\int_0^X f_1(x) S_2(x) dx}{\int_0^X \left[f_1(x) S_2(x) + S_1(x) f_2(x)\right] dx} \qquad [9]$$

Where: the different terms are given by Equations [6]. and [7], with the corresponding changes for the given Failure Mode.

The above equations were tried with the data obtained during Phase I. The results show excellent agreement with the Phase I data. Table 2 summarizes the results of the sample calculations.

TABLE 2. SAMPLE FAILURE PROBABILITY CALCULATION SUMMARY. (COMPARISON WITH PHASE I DATA).

Phase I Test Data	σ_0		m		Percent Volume Failures		Percent Surface Failures		Percent MIL-B Volume Failures	
	Vol	Surf	Vol	Surf	Actual	Predicted	Actual	Predicted	Actual	Predicted
MIL-E	67	104	8.0	8.1	15	14.8	50	51	8	5

12025(02)-2

6. NDE Reliability

The objective of this task is quantify the probability of detection (POD) of surface flaws in ceramics for various nondestructive evaluation (NDE) techniques, such that NDE can be fully integrated into life prediction methodology for ceramic components. The objective will be accomplished through a comprehensive reliability study.

Dr. A. Berens of the University of Dayton Research Institute (UDRI) in Dayton, Ohio has been contracted to provide consultation regarding the design of the reliability study, as well as statistical analysis tools for determining POD.

A procedure for documenting the defect population in the reliability study specimens was established and delivered to Norton Advanced Ceramics. This procedure will by used by the Norton personnel at their Northboro, Massachusetts facility to document the naturally-occurring defect populations in the reliability specimens prior to delivery to AlliedSignal Engines. Surface defects in the reliability specimens will be classified in accordance with American Society for Testing and Materials Specification ASTM F109 definitions using magnified visual inspection. Additional defect characterization will be performed by AlliedSignal Engines upon receipt of the specimens.

A PC Windows-based relational database has been created to catalog the defects in the specimens. The database facilitates easy input and retrieval of specimen information.

3.3 ENVIRONMENTAL EFFECTS

Environmental Effects in Toughened Ceramics*

G. A. Graves, Jr. (University of Dayton)

Objective/scope

Since December 1984, the University of Dayton has been involved in a five-phase project to investigate the effects of environment on the mechanical behavior of commercially available ceramics being considered for heat engine applications. In the first phase of this project, the effects of environment on the mechanical behavior of transformation-toughened ZrO_2 ceramics were investigated. In the second phase, two Si_3N_4 ceramics (GTE PY6 and Norton/TRW XL144) and one SiC ceramic (Hexoloy SA) were evaluated. In the third phase, the tensile, flexural, and fatigue strength of three SiC and six Si_3N_4 ceramics were evaluated at temperatures ranging from 20 to 1400°C. Microstructure, chemistry, and physical properties were also investigated. In the fourth phase, the flexural strength and fatigue behavior of two additional Si_3N_4 ceramics (Kyocera SN-260 and Garrett GN-10) were investigated. In addition, the fatigue behavior of one Si_3N_4 ceramic (Norton/TRW NT-154) was studied. In phase five, three newly developed SiC and five newly developed Si_3N_4 ceramics are planned. In addition, the effects of different machining processes on the mechanical behavior of selected SiC/Si_3N_4 ceramics will be studied.

During the past six months the project, a study to investigate the effects of various machining treatments on the flexural strength of Morton International (MI) SiC was completed. In addition, the evaluation of an Allied Signal, Ceramic Components Division, AS-800 material was initiated.

Technical progress

During this semiannual reporting period several limited studies were carried out on various heat engine candidate materials. The delayed or canceled delivery of specimens from suppliers has resulted in delays of the evaluation of materials selected for high-temperature strength and physical property characterization, and the planned effects of various machining techniques on strength study. Dow Corning recently informed UDRI personnel that they were discontinuing production of their βSiC and, therefore, they would not be delivering the specimens previously agreed upon. In addition, Kyocera is developing a new material presently designated as SN-X. They have requested that UDRI characterize this material instead of their SN253 and UDRI has agreed. The delivery of SN-X is expected in December 1994. A revised delivery schedule and test matrices are shown in Tables 1 through 4. Discussions have recently been held with Cummins Engine, Norton Advanced Ceramics, and Ceradyne Corporation representatives in an effort to obtain additional materials for study in the program. All three companies have agreed to work with

UDRI and furnish material they are interested in for heat engine applications. A formal test plan and delivery schedule with these companies will be developed and submitted to the ORNL program manager during the Oct/Nov 94 bimonthly reporting period.

Table 1. Milestone 331417 Status of Specimens Promised and Received

Supplier	Material	Flexure Bars	Due Date	Tensile Blanks	Due Date	Machined MOR	Due Date
Allied Signal	AS-800		10/94	140	10/94		
Kyocera	SN-253	20	12/94	40	12/94	165	7/15-30/94
Carborundum	Hexoloy SA-X	125	Received. 9/94	60	delayed		
	Totals	145		240		165	

Table 2. Milestone 331417 Planned Future Physical Property Measurements

	Physical Properties					
Intended Use for	E	α	H/ρ	K_{Ic}		
Candidate Ceramics	20-1350°C	20-1350°C	20°C	20°C	1000°C	1300°C
Turbine Engine Components Kyocera SN-253, Si$_3$N$_4$					5	5

*Number of specimens.
E = elastic modulus
α - thermal expansion
H/ρ = hardness/density
K_{Ic} = fracture toughness

Table 3. Milestone 331417 Planned Flexural Strength and Stress Rupture Measurements

Intended Use for Candidate Ceramics	Flexural Strength Measurements						Stress Rupture	
Temperature:	20°C		1250°C		1350°C		1350°C	
Loading Rate:	4x10^{-3}	4x10^{-5}	4x10^{-3}	4x10^{-5}	4x10^{-3}	4x10^{-5}	1/2σf	2/3σf
Turbine Engine Components								
APUs Carborundum Hexoloy SA-X	30		20	10	20	10		
Automotive Turbines Kyocera SNX Si$_3$N$_4$							5	5

*Number of specimens.

Table 4. Milestone 331417 Planned Tensile Stress Rupture and Cyclic Fatigue Measurements

Intended Use for Candidate Ceramics	Tensile Stress Rupture					Cyclic Fatigue	
	1000°C	1100°C	1200°C	1300°C	1350°C	1000°C	1300°C
Piston Engine Components Material B Allied Signal AS-800		10*	10	10	10		
Turbine Engine Components APUs Carborundum Hexoloy SA-X			10	10	10		5
Automotive Turbines Kyocera SNX, Si₃N₄					5		5

*Number of specimens.

A tension-compression cyclic fatigue study at room temperature was initiated for Norton NT-154 silicon nitride specimen. Due to the lack of experience in operating the Instron tension-compression system, considerable effort was expended while becoming familiar with its operation. A strain gaged specimen was used to monitor the alignment procedure to ensure that pure tension-compression loading was achieved (less than 3% bending). After proper specimen alignment was achieved, the Instron 1361 test machine controls were adjusted to obtain a sawtooth loading curve to attain the desired tension-compressive stress of 350 MPa (50 ksi). This stress was approximately 50% of the fast-fracture average tensile strength of NT-154 at room temperature. The specimen was tested for 450×10^3 cycles (approximately 100 hours) without failure, and the test was then terminated. Further testing on this and additional specimens was planned at elevated temperatures. During this test it was discovered that the present design of the Instron Short Furnace would not accommodate the Instron tension-compression fixture. A specially-designed furnace is being built by Instron to accommodate the tension-compression test fixture for operation at elevated temperatures. When delivered, tension-compression tests will be run on the NT-154 and other more recently developed materials.

In addition to the T/C redesign, a new Instron 1362 testing machine has been ordered for use in the program. It will have 8500 plus electronics package with a "piggybacked" series 9 data acquisition system. The new machine will have a much higher stiffness load frame giving us an improved capability, especially at the higher loading rates required for dynamic fatigue. In addition, the older Instron 1361 and the two benchtop Instron 1122 machines will have a state-of-the-art electronic control(s) that will be interfaced with the same computer controls as the 1362 testing machine. The upgrading of the machines presently in the laboratory was completed on 30 September 1994, making them available for use as the new materials are delivered. The cost to UDRI for the new machine and electronic control upgrades is approximately $255,000.

Tensile stress rupture studies were performed on Kyocera SN-253 buttonhead specimens. Eight specimens were tested at 1350°C under loading conditions that provide stresses that were 67, 58, and 50 percent of the average tensile strength of

the material at this temperature. The results shown in Table 5 indicate that the applied tensile stress on this material, for long duration use at 1350°C, would have to be kept well under 50% of the fast-fracture tensile strength. The surface-initiated failures indicate slow crack growth, probably aided by oxidation.

Table 5. Tensile Stress Rupture Results of Kyocera SN-253

Specimen Number	Test Stress (MPa)	Percent of Fast Fracture Strength	Time to Failure (hrs)	Fracture Origin
41	289	67	0.7	Surface
42	289	67	1.2	Surface
43	251	58	6.4	Surface
44	251	58	4.5	Surface
45	216	50	14.9	Surface
46	216	50	30.1	Surface
47	216	50	21.7	Surface
48	216	50	40.9	Surface

Note:
Test Temperature: 1350°C (2462°F)
Test Fixture: Instron Super Grips
Test Atmosphere: Air

Recently the improved material was delivered to UDRI, Carborundum's Hexoloy SA-Xy. The bulk material will be sent to Chand Kare Technical Ceramics for machining to obtain the required number of specimens (Table 1). The tests listed in Tables 2 through 4 will then be performed when machining is completed for each group of specimens (material type, specimen type).

In addition to the material characterization, numerous viewgraphs were prepared for Dr. M. Ferber, ORNL, for a presentation in Detroit, MI, which took place in June 1994. The viewgraphs summarized material property data obtained for the program over the past eight years, the types of tests and equipment used, and the program goals and objectives.

The baseline machining effects study on Morton International chemical vapor deposited silicon carbide (CVD SiC) was completed. The CVD SiC material was machined at Chand Kare Technical Ceramics, Inc. (CK) where they used six different sets of machining parameters (Table 6) to prepare flexure test specimens (type B). The specimens were then tested to failure at room temperature to determine if strength was affected by the various machining parameters. The flexural strength results are also shown in Table 6. The fractured material was then examined by Raman microprobe spectroscopy. Previous work at UDRI has shown that relatively minor surface disturbances (strain) caused by machining or residual stress can be detected by this technique as Raman line broadening or splitting. Although not a heat engine candidate material, the CVD SiC was chosen as the baseline material because of its consistent pore-free microstructure and high-purity making it very

sensitive to the Raman technique. In addition, it had been extensively characterized at UDRI in a previous study.

Table 6. Flexural Strength Machining Effects Study (Baseline Material - CVD SiC)

Test Group Grinding Wheel Type	Removal Rate[1] per Pass mm (in)	Total Amount Removed/Side mm (in)	Average Flexural Strength MPa, Std. Dev. (Ksi, St. Dev.)	Test Conditions Crosshead Speed mm/s (in/min)	 Temp. (°C)	No. Specimens Tested
[22] Norton SD 150 R75B99E-1/4	0.005 (0.0002)	0.025 (0.001)	352, 29 (51, 4.3) 340, 23 (49, 3.3)	0.04 (0.1) 0.0004 (0.001)	20 20	10 5
[23] Norton SD 320 R75B99E-1/4	0.005 (0.0002)	0.20 (0.008)	383, 23 (56, 3.4) 369, 15 (54, 2.1)	0.04 (0.1) 0.0004 (0.001)	20 20	10 5
[24] General Dia. CGD600 R75B-1/4	0.0025 (0.0001)	0.025 (0.001)	454, 17 (66, 2.5) 422, 52 (61, 7.6)	0.04 (0.1) 0.0004 (0.001)	20 20	10 5
[25] Norton SD 800 R50-1/32	0.0025 (0.0001)	0.025 (0.001)	389, 32 (56, 4.6) 432, 24 (63, 3.4)	0.04 (0.1) 0.0004 (0.001)	20 20	10 5
[26] Norton SD 800 R75B56-1/4	0.0025 (0.0001)	0.025 (0.001)	478, 52 (69, 7.6) 438, 91 (64, 13.2)	0.04 (0.1) 0.0004 (0.001)	20 20	10 5
[27] Norton D 3/6 mic R75B-1/4	0.0025 (0.0001)	0.025 (0.001)	297, 65 (43, 9.5) 337, 48 (48.9, 6.9)	0.04 (0.1) 0.0004 (0.001)	20 20	10 5

[1]All specimens were ground in the longitudinal direction.

Based on these preliminary results, a more comprehensive Raman spectroscopy study was initiated on specimens from the Chand Kare machining study. Pieces of fractured flexure specimens were selected from each of the six different groups of machined specimens for Raman microprobe spectroscopy analysis. Each specimen has been examined by scanning across the surface placed in tension during the four-point bend test and down the sides of the specimen.

A wide variety of data were taken on the CVD SiC specimens identified as SMG-93-2-gg-nn. The gg specification identifies the group and the nn value gives the specimen number in that group. The data presented herein represent the six finish grinding groups plus two of the groups after being etched. The etching removes the damaged surface layer and exposes the relatively unstrained bulk material. Group 23 was purposely chosen for one of these etched series because it had the highest level of strain due to the large number of passes with a relatively coarse grit. Group 27 was chosen because it was the least strained of the six groups. The etched specimens provided solid evidence for the sensitivity and reliability of the Raman measurements and clearly identified a reasonable baseline for ranking the six finish grinding groups.

These data were acquired using a new diode-laser pumped, doubled Nd:YAG laser. This laser provides 50 mW of highly stable CW power at 530.8 nm. It has a bandwidth of less than 2 MHz. To put that in perspective, the laser frequency is 5.6×10^8 MHz. This very narrow line width was responsible for increasing the signal level by more than five relative to a laser used previously. This allows for the acquisition of high-quality data in a relatively short time. Moreover, the system resolution was

limited only by the detection system, that is, the spectrometer resolution and the CCD array detector pixel size. The conditions for these measurements amounted to an effective system bandwidth of about 0.6 cm^{-1}. Three data points per cm^{-1} were recorded which permits the detection of very small changes in the widths of the Raman lines, typically less than 0.1 cm^{-1}. This claim is supported by the small standard deviations for the data from the etched specimens.

The laser probe spot size on the specimen was a line ~2 μm x 20 μm. Considerable care was taken to prevent any laser-induced damage to the specimen during the measurements. Examples of the spectra are shown in Figures 1 through 3. The measurement time for a typical spectrum was 5 to 10 minutes. The data has a high signal-to-noise ratio that allows very precise measurements of the full width at half maximum (FWHM), typically about 1%. This made it possible to detect very small changes in the width of the line due to the local residual surface stress. This is clearly illustrated by the two plots for specimens 26-2 (Figure 1) and 23-9 (Figure 2). Basically, the residual surface stress results from mechanical working of the material due to machining or polishing. These processes typically distort the crystalline lattice in the surface grains (i.e., introduce local strain) which effectively lowers the Q-factor of the lattice vibrations. This loss was recorded as broadening of the line, namely, as an increase in the FWHM. Theoretically, the shape of a Raman line for a good single crystalline specimen follows the Lorentzian function that is characterized by a sharp peak and slowly-decaying wings.

A good example of a minimally-disturbed line is the specimen shown for specimen 26-2 (Figure 1). These data were taken on the end of the specimen that was only cut by a diamond saw. The fit to the Lorentzian function is quite good with an uncertainty of <1% for the resulting FWHM value. In the data analyses, the amplitude, position, background, and FWHM were fit using a nonlinear regression procedure.

The effect of machining on the width is illustrated by the spectrum for specimen 23-9 (Figure 2). This specimen was submitted to 40 passes of the grinding wheel producing a considerable broadening of the line. Notice also that the fit is degraded. The observed spectra are essentially sums of contributions from the volumes of individual grains summed over several grains. These contributions would be expected to be essentially random, that is, normally distributed. When the disturbance is large, the line shape would then tend toward the Gaussian functional form with a blunt peak and faster-decaying wings. The spectrum for specimen 23-9 shows this postulated behavior.

Besides sensitivity to residual surface stress, the Raman spectrum of SiC can also reveal the presence of bulk stress. Because of the high symmetry of the lattice (cubic), the TO line is two-fold degenerate; that is, it is made up of two lattice vibrations that have the same vibration frequency in the pure single crystal form of the material. If the lattice symmetry of the grains in a local area of the specimen were strongly distorted during growth of the material, this would lower the lattice symmetry in that region. This could cause the TO line to split since the two-fold degeneracy can be supported only in lattices of high symmetry. The degree of splitting is some measure of the bulk stress; this splitting was observed in some earlier specimens of cubic CVD SiC
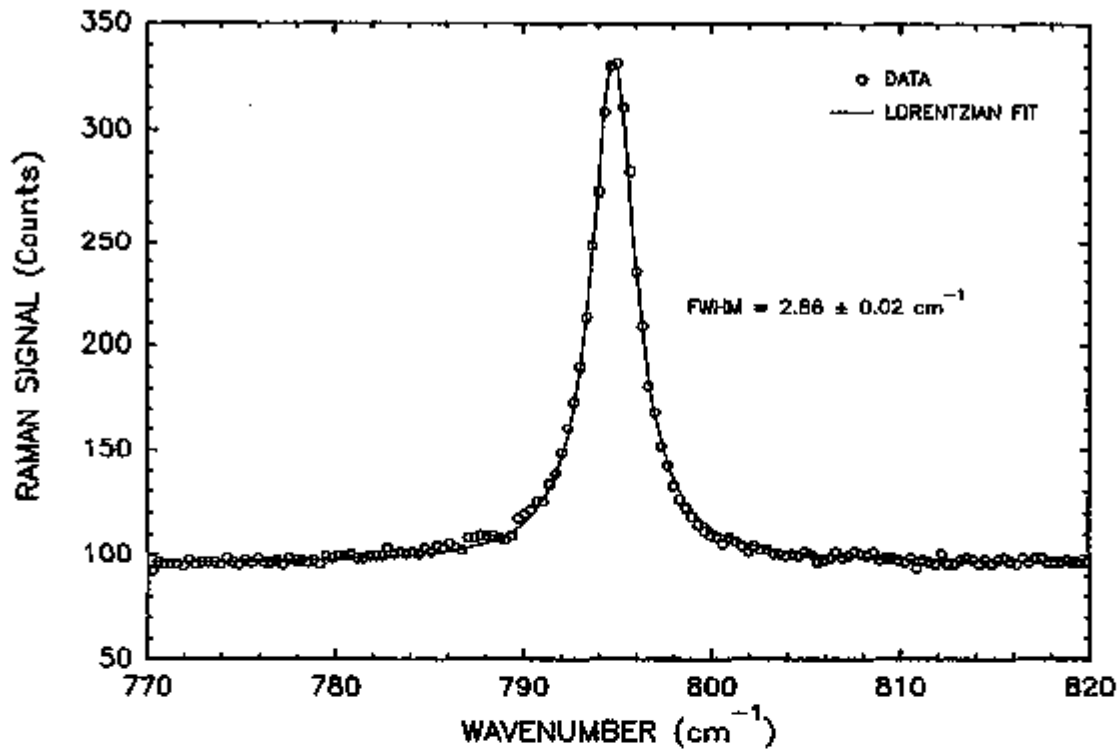
Figure 1. Raman Transverse-Optical Line of CVD SiC, Specimen SMG-93-2-26-2, on the Diamond Cut, Unpolished End.
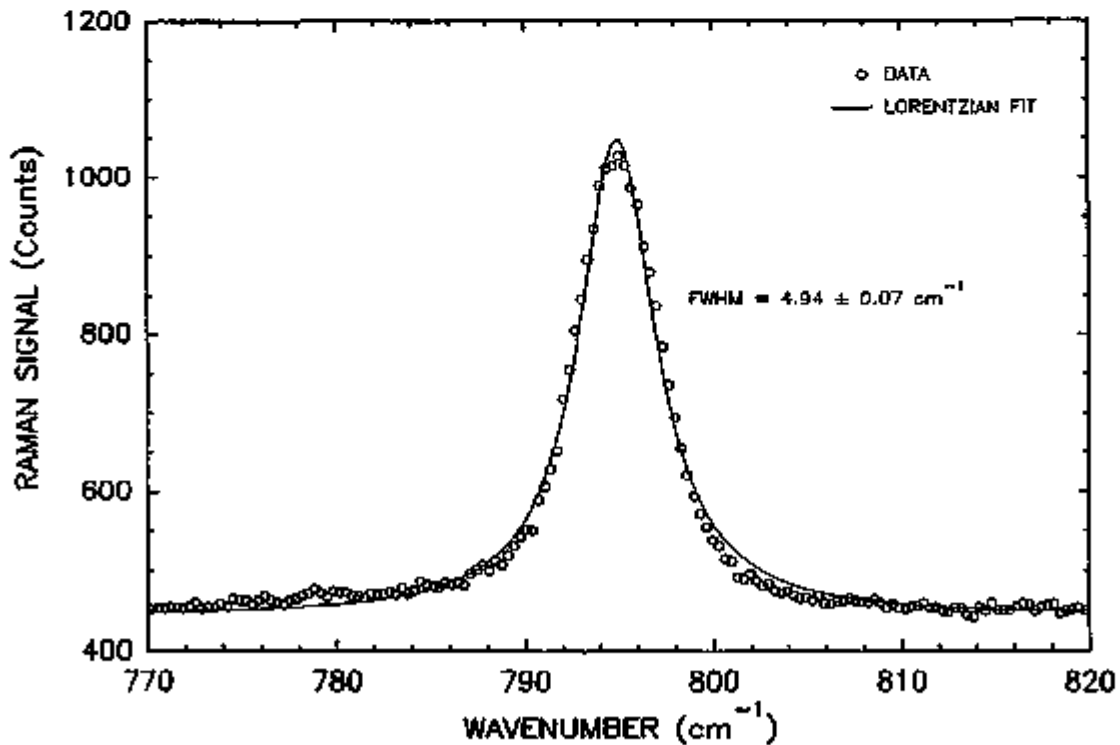
Figure 2. Raman Transverse-Optical Line of CVD SiC, Specimen SMG-93-2-23-9, on the Tension Side.

possibly due to layering during growth. In the 10 specimens of this study, splitting was observed on one edge of one end of every specimen. An example of this splitting is the spectrum for specimen 27-9 (Figure 3). Some studies of this splitting were made as a function of position to better characterize these data; however, the positions of the specimens in the original slab of material were not known. More information about the fabrication history of the specimens is required to interpret the results of these studies.
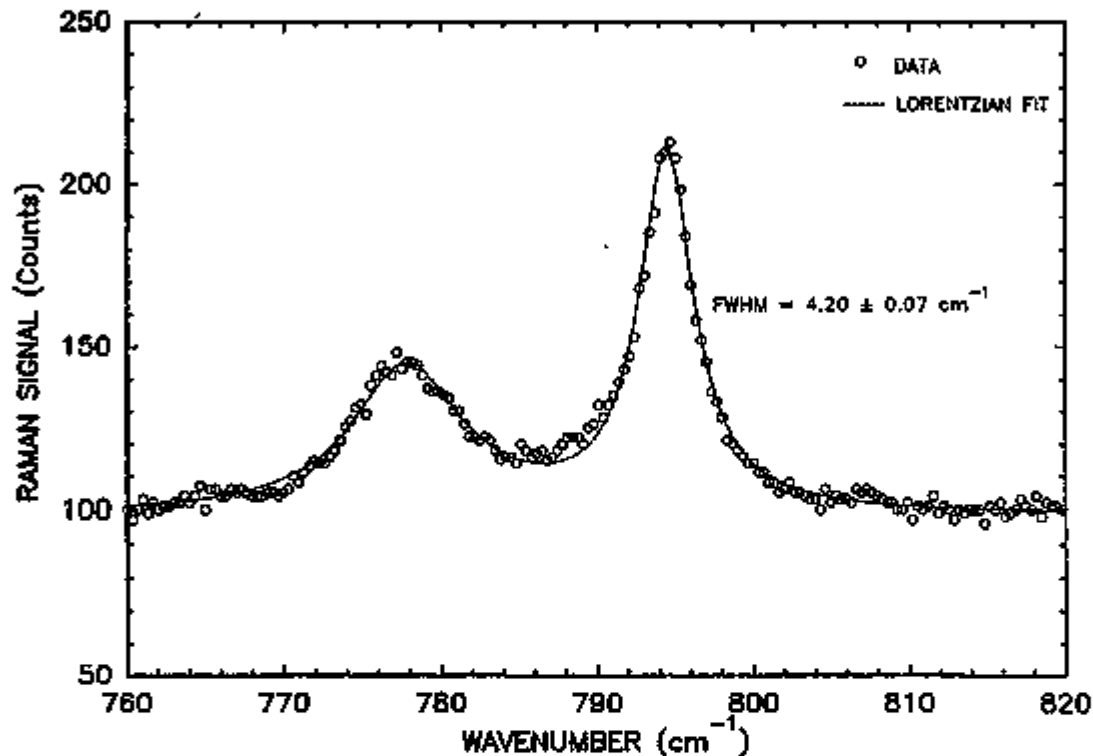
Figure 3. Raman Transverse-Optical Line of CVD SiC, Specimen SMG-93-2-27-9, Splitting Due to Bulk Stress Near One Side of the Specimen.

The most revealing results of these studies are presented in the bar graph (Figure 4) on which the mean values of the Raman line FWHM taken over all 12 specimens are plotted. Each specimen was scanned at 10 positions in a line spaced at five micron intervals on the tension side at approximately the same relative location. there were two specimens for each group. The 20 values of FWHM from these scans for each group were averaged and a standard deviation calculated. These mean values for the five groups are plotted as a bar graph with the standard deviation values included as error bars. The bars are plotted from left to right in the order of increasing fineness of the grinding wheel grit. Except for group 23, the mean values of FWHM fall as the grit size decreases as would be anticipated from the discussion in the above paragraphs. Group 23 is a special case because of the much larger number of passes used on these specimens. The 40 passes of the grinding wheel compared to the five and 10 passes used on the other groups clearly produced large residual stress in the specimen of this group. Some degree of correlation between the Raman line broadening and the strength variations can be seen by comparing Figures 4 and 5.
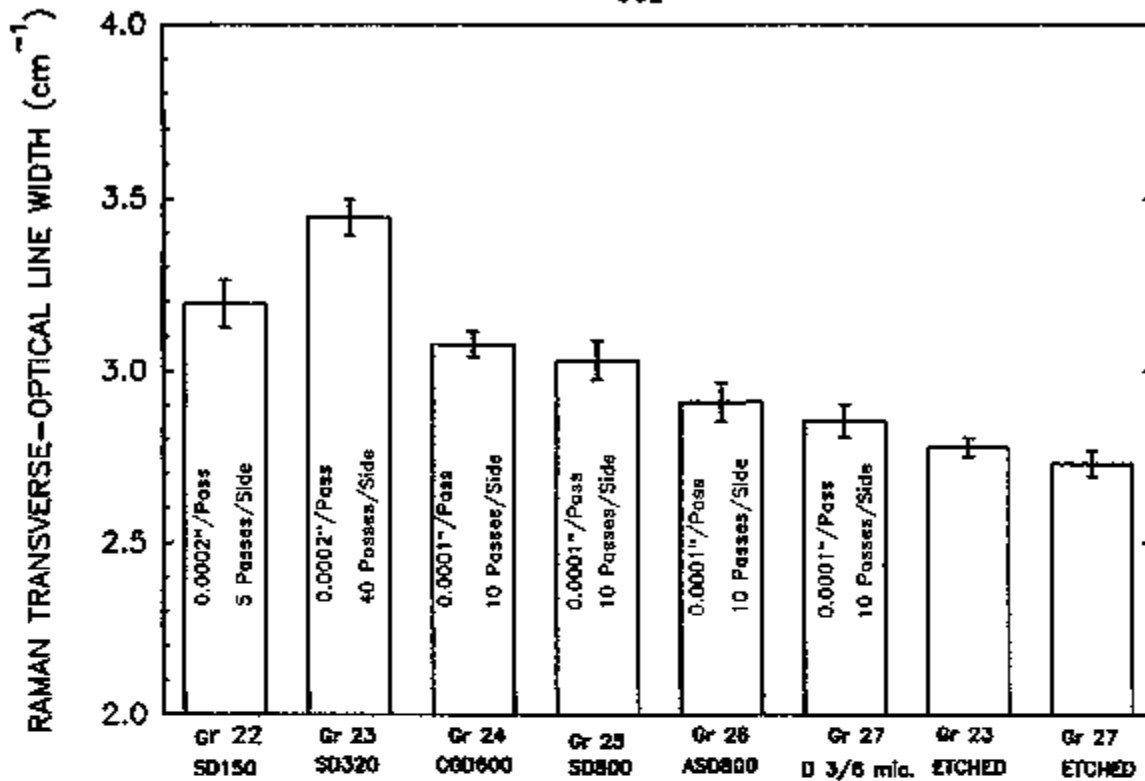
Figure 4. Relative Residual Surface Stress Due to Finish Grinding of CVD SiC.
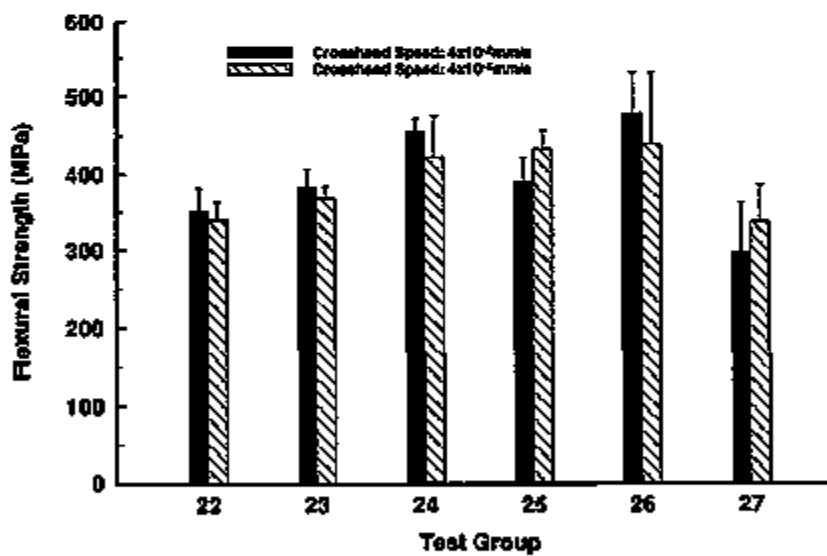
Figure 5. Flexural Strength Machining Effects Study.

Status of milestones

Milestone 331416 has been completed.
Milestone 331417 is in progress.

3.4 FRACTURE MECHANICS

Testing and Evaluation of Advanced Ceramics at
High Temperature in Uniaxial Tension
J. Sankar, A. D. Keller, and J. Neogi (North Carolina A&T State University)

Objective/Scope

The objective of this research is to test and evaluate the long-term mechanical reliability of a sintered and HIPed Si_3N_4 at temperatures upto 1300°C. The emphasis of this effort in the current year is to perform pure tensile and creep test on GS44 (Si_3N_4 ceramic) and below 1000°C creep test on GTE-PY6 (HIPed Si_3N_4 ceramic). The effort also includes microstructural/ microchemical analysis of the fracture surfaces using scanning electron microscopy (SEM), transmission electron microscopy (TEM) and energy dispersive spectral analysis (EDS).

Technical Highlights

During this reporting period the following tasks were carried out:

1. Procurement of machined GS44 tensile bars from Chand Associates, Inc., Worcester, MA 01603, 28 samples were received so far.

2. Pure tensile test were conducted on GS44 at room temperature.

3. Creep tests are being performed on GS44 at 1100°C at 80MPa and 100MPa.

4. Creep tests are also being performed on GTE-PY6 at various stress levels at temperature below 1000°C.

5. Bend fixture with 1600°C capability is being designed with Applied Test System, Inc., Butler, PA 16003.

Test Results and Discussions

Tensile tests were performed at room temperature. A stressing rate of ~ 50 MPa/sec (equivalent to a cross head speed of 0.004 cm/sec) was used in all the tests. The tensile tests were essentially conducted to compare the GS44 Si_3N_4 ceramic (Figure 1) with, previously tested Si_3N_4 ceramic GTE-PY6 and GTE SNW-1000. Table 1 lists the room temperature tensile strength of the three Si_3N_4 ceramic under consideration.
Figure 2 compares the room temperature tensile strength of the three material

under consideration. It can be observed that at room temperature, the GS44 is stronger than both PY6 and SNW-1000. The GS44 tensile specimens failed from both surface and volume flaws which was similar to earlier studies by Sankar et al. (1993, 1994) on sintered and HIPed Si_3N_4. Studies showed that at room temperature, the tensile specimens failed mostly from radial grind marks in the gage section produced by machining (Figure 3).

References

Sankar, J., Neogi, J., Neogi, S., Dixie, M. T. and Vaidyanathan, R., "Thermal and Loading Effects on Mechanical Properties of a Hot Isostatically Pressed Si_3N_4," accepted for publication in ASME Transactions.

Sankar, J., Krishnaraj, S., Vaidyanathan, R., and Kelkar, A. D., 1993, "Elevated temperature behavior of sintered silicon nitride under pure tension, creep and fatigue," *Life prediction methodologies and data for ceramic materials, ASTM STP 1201*, C. R. Brinkman and S. F. Duffy, eds., American Society for Testing Materials, Philadelphia, PA (in press).

Status of Milestones

On schedule

Communications/Visitors/Travel

None

Problems Encountered

None

Publications and Presentations

Sankar, J., Neogi, J., Neogi, S., Dixie, M. T. and Vaidyanathan, R., "Thermal and Loading Effects on Mechanical Properties of a Hot Isostatically Pressed Si_3N_4," accepted for publication in ASME Transactions. (paper presented at the International Gas Turbine and Aero engine Congress and Exposition, at The Hague, Netherlands, June 13-16, 1994).

Table 1. Room temperature tensile strength

Material	Average Room Temperature Tensile Strength (MPa)
GS44	631
GTE-PY6	621
GTE SNW-1000	492
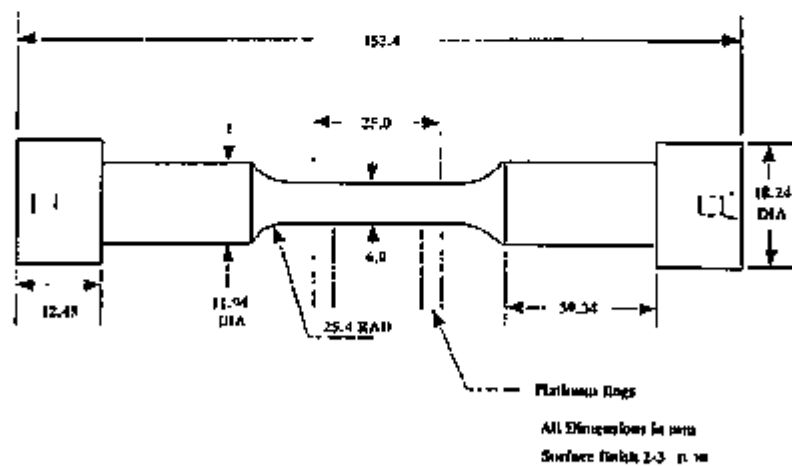
Figure 1. GS44 tensile specimen geometry
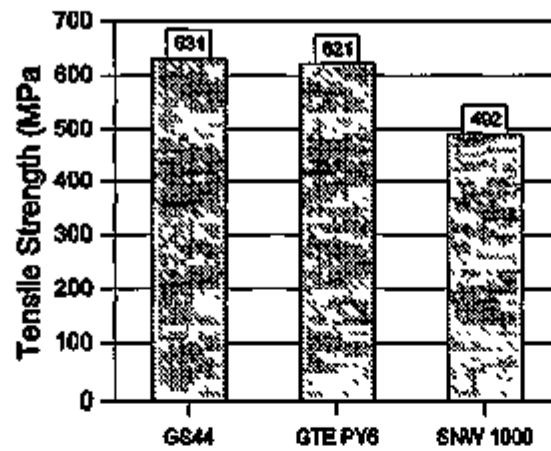
Figure 2. Comparison of room temperature tensile strength measurements for (a) GS44, (b) PY6, (c) SNW-1000. (All tests were conducted at N C A&T SU).

Figure 3. Tensile tested specimen at room temperature: Typical surface-flaw-initiated failure.

Standard Tensile Test Development

S. M. Wiederhorn, R. F. Krause, Jr., W.E. Luecke and J.D. French
(National Institute of Standards and Technology)

Objective/Scope:

This project is concerned with the development of test equipment and procedures to determine the tensile strength and creep resistance of ceramic materials at elevated temperatures. Inexpensive techniques for measuring the creep behavior and strength of structural ceramics have been developed and are being used to characterize the mechanical behavior of these materials. The ultimate goal of the project is to help develop a data base and a test methodology for the structural design of heat engines for vehicular applications.

Technical Highlights:

During the past six months we have focussed efforts on test development for flat dogbone specimen designs. In this regard we investigated the importance of pin friction to strength and creep data at elevated temperatures. Results of this study will improve test techniques used to collect data on flat dogbone type specimens. In addition to the studies of friction, a new, smaller dogbone specimen was developed for experimental billets which require specimens as small as 30 mm in length. Finally, an analysis of data collected earlier on NT154 was obtained in terms of two different stress functions to provide a better empirical fit to creep rupture data.

Results and Discussion:

Effect of lubrication and annealing on creep - We have now completed our lubrication and annealing studies on PY6 and NT154. Earlier studies had shown that lubrication strongly affected the elastic behavior of tensile test specimens at room temperature. Strain gauge measurements on tensile test specimens indicated a flexural strain of as much as 40% to 90% of the total tensile strain under tensile stresses of 100 MPa, figure 1. This flexure stress could be greatly reduced by lubricating the loading pins with paraffin, graphite foil, or teflon. All three lubricants reduced the flexural strain to about 3% to 6% of the total tensile strain, resulting in much better alignment during the tensile test. As a consequence of this finding, it was decided to lubricate all loading pins with paraffin prior to the tensile testing of dogbone specimens. Specimens were then partially loaded to set the alignment of the specimens prior to heating to elevated temperature. As there are no external forces on the load train during loading, it was assumed that specimens would retain their alignment as they were heated to the test temperature. This procedure is now adopted as standard practice for all specimens tested at NIST.

Alignment at room temperature does not, unfortunately, guarantee alignment at elevated temperature when creep is occurring. To investigate

Effect of Lubrication on Bending
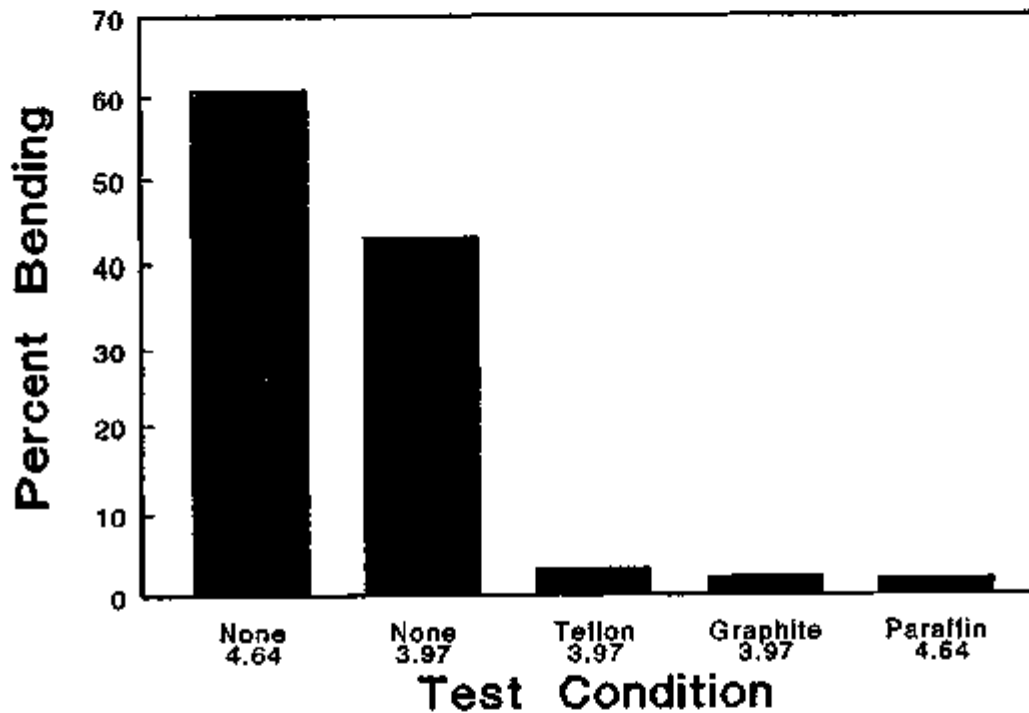
1. Importance of lubrication to the tensile stress in pin-loaded test
    specimens. The numbers on the abscissa give the diameter of the pin
    used to apply the load. The teflon and the graphite were applied in
    the form of foils; the paraffin was applied as a liquid.

the effect of room temperature alignment on temperature testing, specimens were crept at elevated temperatures both with and without paraffin lubrication. Some specimens were annealed prior to testing, others were tested in the unannealed state. Tests were conducted on 13 NT154 specimens and 15 PY6 specimens. NT154 specimens were annealed at 1400 °C for 700 h; PY6 specimens at 1350 °C for 1080 h. A statistical analysis of variance was carried out on the results using the method described by John Mandel (*The Statistical Analysis of Experimental Data*, Dover Publications) in his discussion of structured data. The analysis was conducted for both the time-to-failure, and the maximum creep rate data. Results are as follows: a) NT154 specimens indicate no significant effect of annealing on creep behavior ($p<0.9$); b) NT154 specimens indicate a low probability for an effect of lubrication on creep rate or failure time, suggesting that lubrication is not important to creep behavior ($0.9<p<0.95$ for failure time, $0.8<p<0.9$ for creep rate); c) PY6 specimens suggest no significant effect of lubrication on creep rate ($p<0.9$); d) PY6 specimens indicate a strong effect of annealing on creep rate ($0.95<p<0.99$). In contrast to the results at room temperature, lubrication does not seem to play an important role at creep temperatures. The misalignment that causes high stresses at room temperature are possibly relaxed by pin sliding at elevated temperatures. Investigations to clarify this finding will be pursued during the coming year on two new types of NIST specimens.

Small specimen development - Currently NIST uses three specimen geometries (30 mm, 50 mm and 75 mm overall length) for tensile creep and creep-rupture testing. Each has its use under specific ranges of test conditions. These designs have not, however been optimized, which limits their usefulness for testing purposes. The NIST 30 mm tensile creep specimen is being developed to provide creep and creep rupture information on specimens taken from actual components used at elevated temperatures. The small 30 mm specimen will enable the engineer to evaluate total remaining life in components that have been used for extensive periods. The existing specimen design developed at NIST is limited to low test loads, as head and pin failures occur at high loads. An elasticity analysis has been conducted on this type of specimen in collaboration with Dr. T.-J. Chuang of NIST and Dr. Z. Wang, Guest Worker from Shanghai China. The decision was made to have a specimen with a gauge section 1.5 mm by 2 mm, and an overall length of 30 mm. This specimen has a gauge length of 8 mm, which was considered to be the minimal length for strain measurements by laser extensometry. With these boundary conditions, the specimen shown in figure 2 was developed. For a stress in the gauge section of 250 MPa, the maximum stress in the holes is 375.8 MPa; the maximum stress in the neck is 281.1 MPa. This specimen will probably not be useful as a strength specimen because of the high stresses in the holes. It should, however, be of value for establishing the creep and creep rupture behavior at elevated temperatures, because lower loads are usually used for this purpose. A partial analysis of the specimen for other geometries is given in figure 3.

Analysis of Tensile Creep Data - The "steady state" creep rate of silicon nitride in tension is usually expressed in terms of a temperature modified Norton equation (a power law function in stress):

Small Tensile Specimen
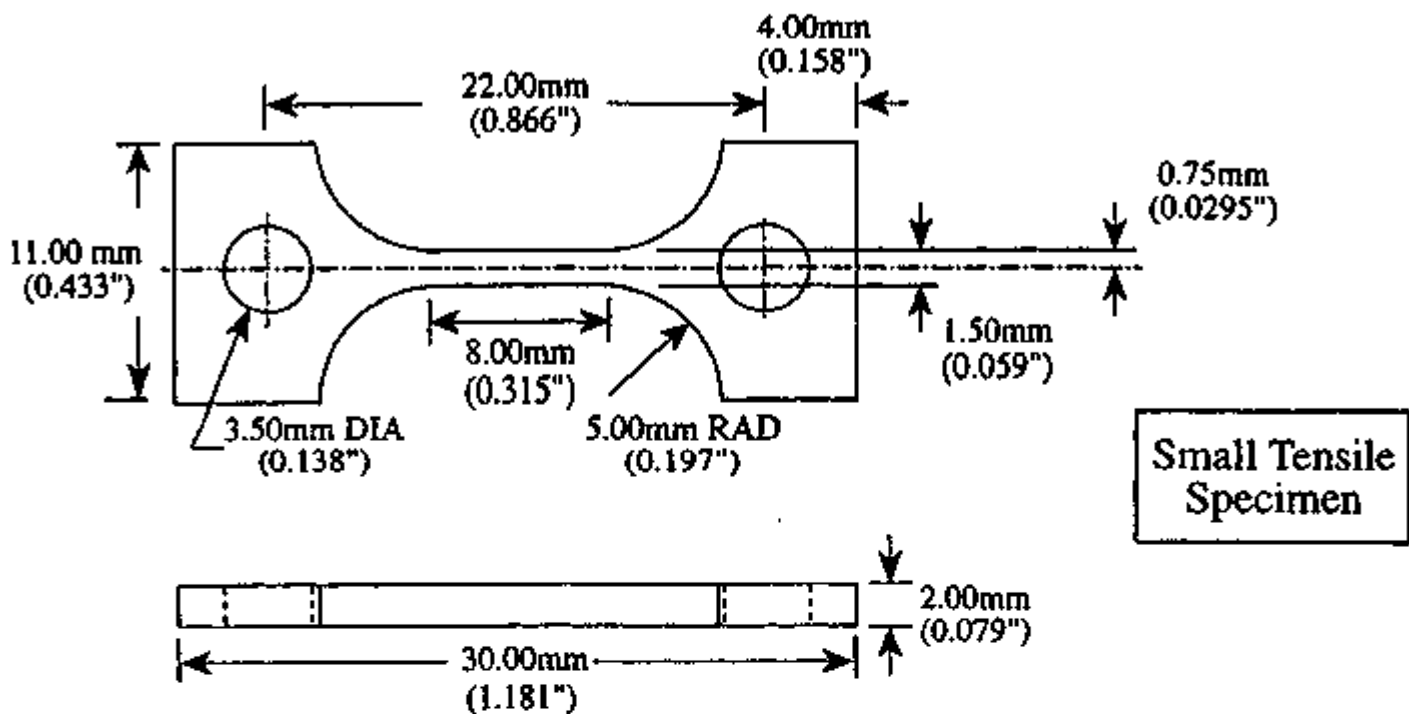
1. Holes and gauge length share the same center line, +/- 0.01mm (+/- 0.0005").

2. Hole tolerance : -0.0125mm, +0.025mm (-0.0005", +0.001").

3. All other tolerances +/- 0.025mm (+/- 0.001").

4. All longitudinal surfaces 0.0002mm (8 microinch) rms finish.

2.   Standard creep test specimen - dogbone design, 30 mm length.
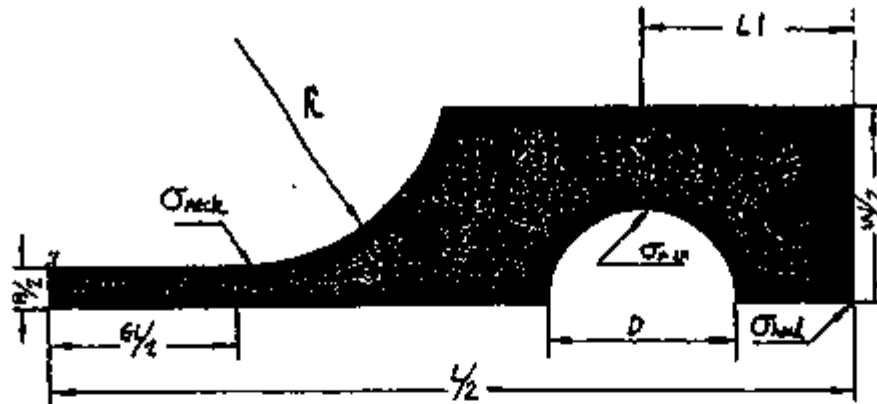
MAXIMUM STRESS ON SPECIMEN

Applied Stress = 250 Gauge area = 2.0 mm x 1.5 mm
L = 30 mm   D = 3.5 mm

(GL) Gauge Length, mm	(R) Neck Radius	(L1) Hole Location	(W) Flange Width	Maximum	Stresses Neck	Head
7.0	4.0	4.0	7.0	353.3	272.6	226.1
7.0	4.0	4.0	9.0	316.4	272.7	207.9
7.0	4.0	4.5	7.0	345.6	272.2	172.7
7.0	4.0	4.5	9.0	312.5	272.4	164.9
7.0	4.0	5.0	7.0	352.8	271.7	134.8
7.0	4.0	5.0	9.0	312.0	272.0	134.4
7.0	5.0	4.0	7.0	369.7	265.6	231.4
7.0	5.0	4.0	9.0	331.5	265.8	208.9
7.0	5.0	4.0	11.0	294.0	265.9	189.8
7.0	5.0	4.5	7.0	366.0	265.3	176.0
7.0	5.0	4.5	9.0	325.8	265.5	166.5
7.0	6.0	4.5	11.0	294.8	265.6	152.2
8.0	3.0	4.0	7.0	354.7	281.8	226.8
8.0	3.0	4.5	7.0	347.6	281.3	173.6
8.0	3.0	5.0	7.0	356.1	280.6	135.9
8.0	4.0	4.0	7.0	373.6	272.1	232.9
8.0	4.0	4.0	9.0	334.4	272.4	209.4
8.0	4.0	4.5	7.0	371.3	271.6	179.8
8.0	4.0	4.5	9.0	329.5	272.0	167.0
8.0	5.0	4.0	7.0	395.8	265.2	239.1
8.0	5.0	4.0	9.0	347.9	265.4	210.9
8.0	5.0	4.0	11.0	308.6	265.5	193.0
9.0	3.0	4.0	7.0	375.8	281.1	233.9
9.0	3.0	4.5	7.0	374.8	280.5	181.1
9.0	4.0	4.0	7.0	401.5	271.5	241.1
9.0	4.0	4.0	9.0	351.4	271.9	211.4

3.   Analysis of geometry for 30 mm tensile test specimen.

$$\dot{\epsilon} = A_1 \cdot \sigma^n \cdot \exp(-\Delta H/RT) \qquad (1)$$

where A_1, n and ΔH_1 are constants of the fit. n is the stress exponent of the creep rate, whereas ΔH_1 is an apparent activation energy for creep. When plotted in this manner, data on silicon nitride often shows a distinct curvature, suggesting that some other function of stress might be more appropriate to represent the creep behavior of this class of materials.

An alternate representation of creep data in terms of stress is a hyperbolic sine function rather than a power law function:

$$\dot{\epsilon} = A_2 \cdot \sinh(\sigma \cdot \Omega/RT) \cdot \exp(-\Delta \cdot H/RT) \qquad (2)$$

where A_2, Ω and ΔH_2 are constants of the fit. Ω is the apparent activation volume for the creep process; whereas ΔH_2 is an apparent activation energy for creep. This equation can be derived from reaction rate theory. For example, if it is assumed that the flow of the amorphous phase between grains of silicon nitride controls the creep process, then Ω should represent the activation volume for the deformation of the glass, while ΔH_2 represents the activation energy for the flow of the glass.

Creep data collected on a grade of silicon nitride containing 4 wght. % yttria as a sintering aid was fitted to equations 1 and 2 by first linearizing these equations and then applying the method of least squares. The apparent activation energies for the data were 1069 kJ/mol from the Norton equation and 1302 kJ/mol for the hyperbolic sine equation, figure 4. These values of ΔH lie within the range usually reported for the more modern grades of silicon nitride. The high value of ΔH is believed to be due to the sum of the activation energy for glass deformation, and the energy of solution of silicon nitride in the amorphous boundary layer. The difference of value between the two fits is probably not significant. The scatter in the data is slightly smaller for the fit of equation 2 to the creep data. Thus, the scatter along the ordinate in the data is approximately 0.5 for equation 2, and 0.9 for equation 1, i.e. the scatter seems to be about twice as large for equation 1.

A comparison of the stress dependence of equations 1 and 2 is given in figure 5. The stress exponent, n, for equation 1, 3.57, is similar to values of this parameter reported on other grades of silicon nitride. Comparing the individual data with the least squares line, data points from the lowest stresses or the highest stresses seem to scatter from the least squares fit. This type of scatter has been observed in other tensile stress experiments on silicon nitride. Sometimes the high stress portion of the data is ignored in obtaining the value of n. The use of a hyperbolic sine function appears to eliminate most of the scatter observed
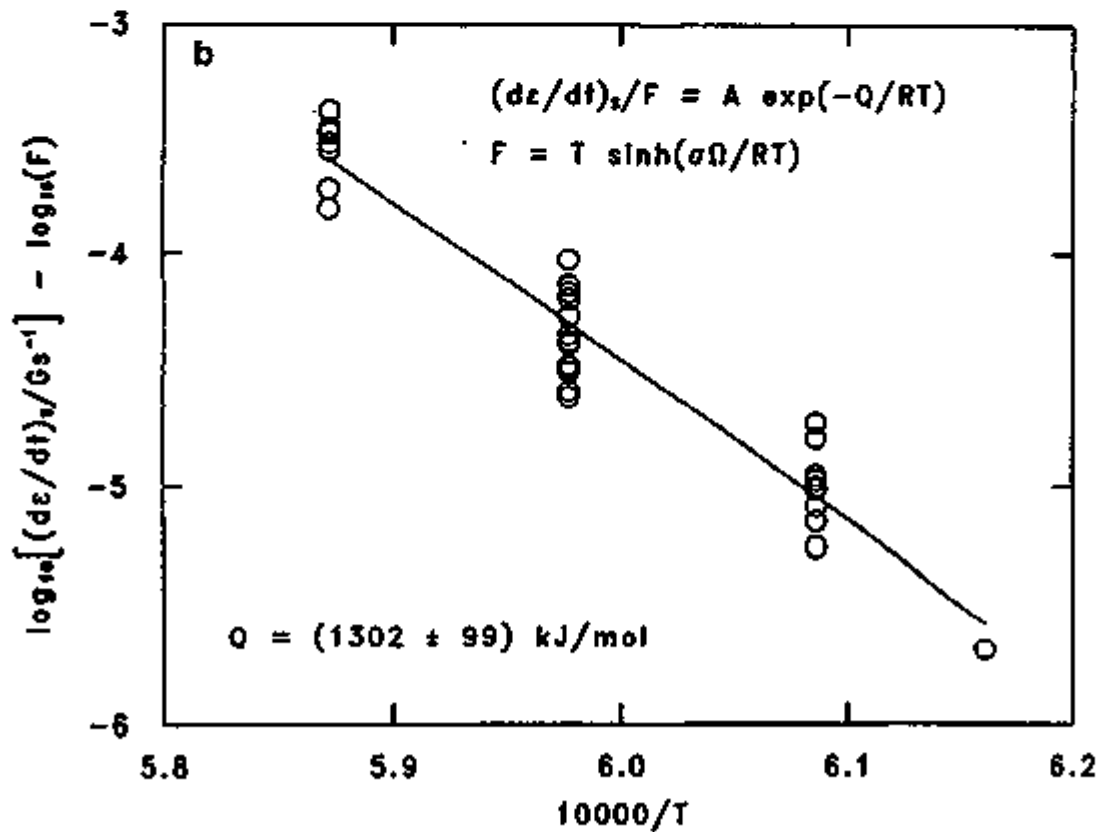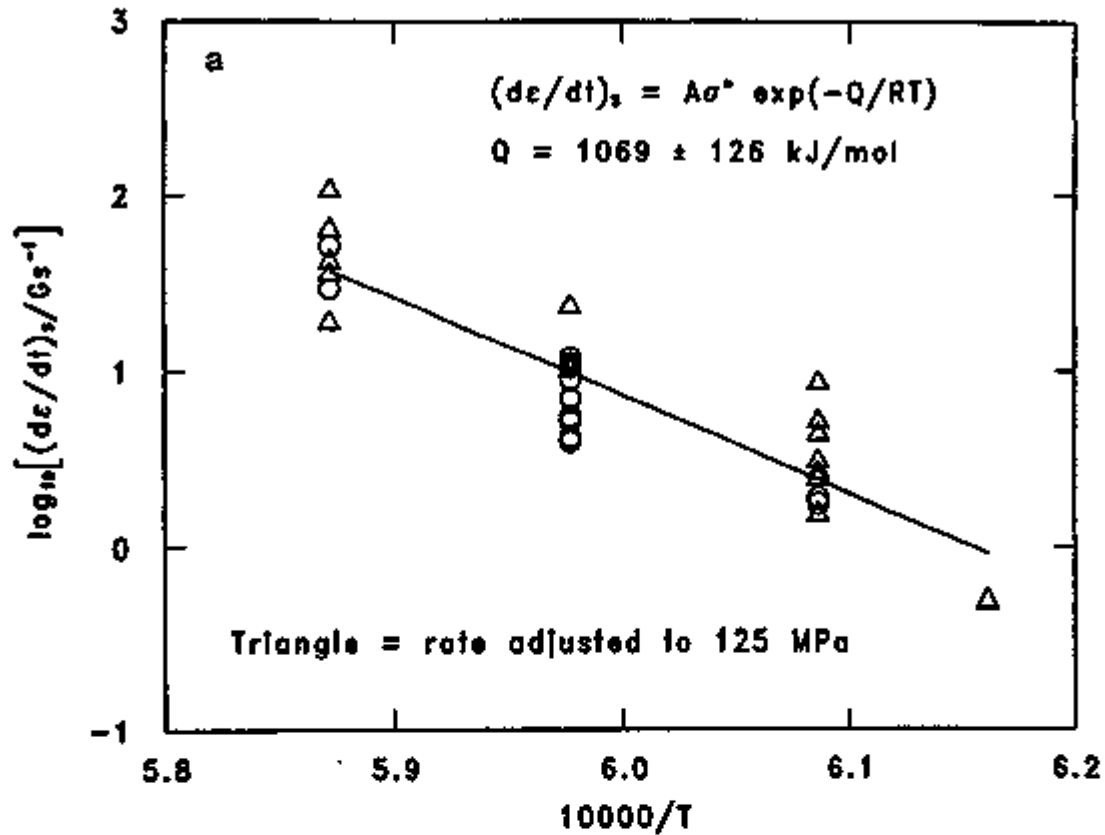
4. A comparison of fit: Temperature Modified Norton Equation (equation 1) versus Hyperbolic Sine Equation (equation 2). Temperature fit: (a) Norton Equation; (b) Hyperbolic Sine Equation.

$(d\varepsilon/dt)_s = A\sigma^n \exp(-Q/RT)$

$n = 3.57 \pm 0.46$

Triangle = 1370 c
Circle = 1400 c
Square = 1430 c

$\log_{10}[(d\varepsilon/dt)_s/Gs^{-1}]$

$\log_{10}(\sigma/MPa)$

a

$(d\varepsilon/dt)_s = AT \exp(-Q/RT) \sinh(\sigma\Omega/RT)$

$\Omega = (5.89 \pm 0.50)10^{-4} \; m^3/mol$

Triangle = 1370 C
Circle = 1400 C
Square = 1430 C

$\log_{10}[(d\varepsilon/dt)_s/Gs^{-1}]$

$\log_{10}[\sinh(\sigma\Omega/RT)]$

b
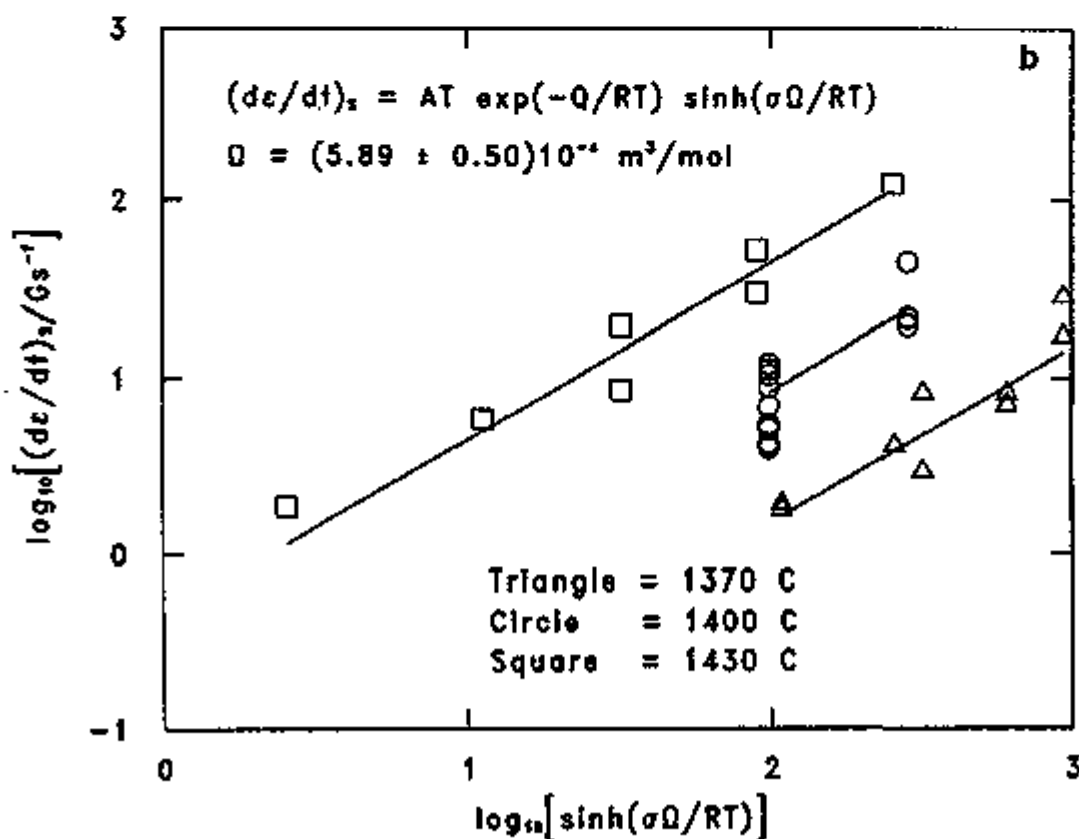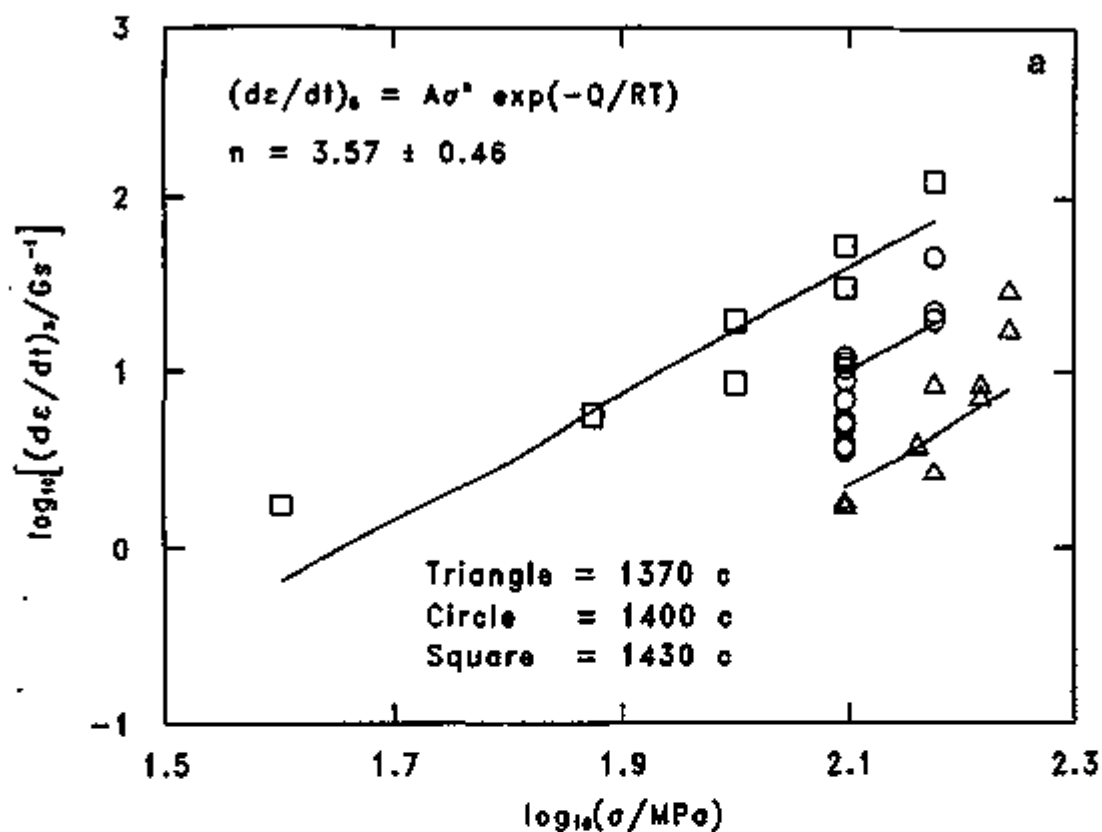
5. A comparison of fit: Temperature Modified Norton Equation (equation 1) versus Hyperbolic Sine Equation (equation 2). Stress fit: (a) Norton Equation; (b) Hyperbolic Sine Equation.

in the power law fit. The activation volume determined from this fit, 589 cc/mol, is, however, considerably larger than that expected from a unit step in glass deformation. The molar volume of glass is about 25 cc/mol, and one would expect the activation volume for glass deformation to be a fraction of this value. Never-the-less, it is worth noting that similar values of the activation volume are obtained on glass tested in the nonlinear viscous region. Until this phenomenon is understood, the use of equation 2 to fit creep data should be considered only as an empirical fit to the creep data.

Lectures Presented and Meetings Attended:

Sheldon M. Wiederhorn, Jonathan D. French and William E. Luecke, "High temperature reliability of structural ceramics," *Proceedings of the Symposium on Ceramic Materials and Components for High Temperature Engines*, Shanghai China, May 29 through June 1, 1994.

S.M. Wiederhorn and W.E. Luecke, "The importance of cavitation to the creep of structural ceramics," *Plastic Deformation of Ceramics*, Sponsored by the Engineering Foundation, Snowbird, Utah, August 7-12, 1994.

S.M. Wiederhorn, J.D. French, W.E. Luecke and J.S. Wallace, "Silicon nitride for heat engines," September 27, 1994, *Basic Science Division Meeting of the American Ceramic Society*, Louisville, KY.

Publications:

Sheldon M. Wiederhorn, B. Anne Fields and Bernard J. Hockey, "Fracture of Silicon Nitride and Silicon Carbide at Elevated Temperatures," Mat. Sci. and Engineering, <u>A176</u> 51-60 (1994).

Sheldon M. Wiederhorn, Jonathan D. French and William E. Luecke, "High temperature reliability of structural ceramics," to be published in the Proceedings of the Symposium on *Ceramic Materials and Components for High Temperature Engines*, Shanghai China, May 29 through June 1, 1994.

S.M. Wiederhorn and W.E. Luecke, "The importance of cavitation to the creep of structural ceramics," to be published in the Proceedings of the Conference on *Plastic Deformation of Ceramics*, Sponsored by the Engineering Foundation, Snowbird, Utah, August 7-12, 1994.

3.5 NONDESTRUCTIVE EVALUATION DEVELOPMENT

Nondestructive Characterization
D. J. McGuire (Oak Ridge National Laboratory)

Objective/Scope

The purpose of this program is to conduct nondestructive evaluation (NDE) development directed at identifying approaches for quantitative determination of conditions (including both properties and flaws) in ceramics that affect the structural performance. Those materials that have been seriously considered for application in advanced heat engines are all brittle materials whose fracture is affected by structural features whose dimensions are on the order of the dimensions of their microstructure. This work seeks to characterize those features using high-frequency ultrasonics and radiography to detect, size, and locate critical flaws and to measure nondestructively the elastic properties of the host material.

Technical Progress

Ultrasonics - W. A. Simpson, Jr.

We continued to explore uses of the new high-frequency (0.1- to 2-GHz) acoustic microscope. We previously presented images of scratch-induced cracking in both silicon nitride[1] and silicon carbide.[2] One of the more intriguing aspects of these images is the presence of "banding," i.e., alternating light and dark bands which generally parallel the scratch but which, in the vicinity of the induced cracks, tend to "stream" away from the crack in a manner that suggests a stress pattern. The acoustic microscope, in the upper portion of the stated frequency range, is known to be capable of revealing residual stress patterns.

We have now obtained some preliminary surface profilometry results on the silicon nitride sample which, surprisingly, do reveal surface upset amounting, in the extreme case, to almost 3 µm at the edges of the scratches. Unfortunately, the exact location on the sample at which these results were obtained is not known; hence, it is not possible to compare the profilometry and the acoustic results directly. In addition, the surface profiles do not intersect any of the scratch-induced cracks, and it is the profile in this vicinity which is of primary interest. We have asked for a two-dimensional surface profilometry analysis, but we have not yet received the results.

Even in the event that the profilometry trace is included in the area depicted in the acoustic microscope images, it is difficult to reconcile the results. There are two primary causes (other than stress or changes in the local elastic properties of the sample) of changes in the image contrast in the acoustic microscope. One of these is the response of the instrument to changes in the acoustic lens-to-sample separation. Because of the presence of an elastic surface wave in images generated by the acoustic microscope, the quasimonochromatic nature of the radiation leads to interference between this surface wave and the wave directly reflected from the specimen surface. This, in turn, means that

the contrast of a perfectly plane-reflecting surface will vary from light to dark as the lens-to-sample distance is varied. Indeed, the periodicity of the contrast with distance can be used to obtain the surface wave velocity of the sample; this response is known as the $V(z)$ response.

Although the variation in contrast with distance is not the simple half-wavelength relationship familiar from optics (i.e., the contrast does not go from maximum to minimum when the lens-to-sample distance is varied by a half wavelength), it is not difficult to show that the periodicity is given by:

$$\Delta z = \frac{\lambda}{2(1 - \cos\theta_R)} ,$$

where λ is the acoustic wavelength in the liquid coupling medium (usually water), θ_R is the Rayleigh angle for the sample, and Δz is the variation in lens-to-sample distance necessary to give a *full* 2π change in the contrast. Note that because the wave traverses the distance twice in reflection mode, the phase change is twice that for a one-pass path change.

This equation shows that, neglecting the Rayleigh angle term (i.e., $\cos\theta_R = 0$), the contrast would vary from minimum to maximum and back again as the lens-to-sample distance changed by a half wavelength, as intuition suggests. Because of the Rayleigh angle term, however, the distance must vary by a greater amount to yield the same 2π phase change.

Applying these results to the acoustic images, the observed contrast changes do not agree with the results of surface profilometry, nor is it likely that they would agree at any point if the surface upset is relatively uniform along the scratch. Until we obtain more complete surface profilometry results, it is difficult to assign the observed parallel "banding" to surface upset.

A second factor responsible for producing parallel banding in acoustic images of cracks and scratches is diffraction of the surface wave from the edges of the crack. The periodicity of this banding, however, does follow a simple half-wavelength path change relationship with the salient wavelength being that of the surface wave. In both silicon nitride and silicon carbide, this wavelength is about 6 µm at 1 GHz, and this figure is also in disagreement with the measured value in the acoustic image.

Finally, the "streaming" of the contrast around a crack tip and the relatively large area over which the contrast is constant—as well as the shape of that area—still suggests that the cause of the observed contrast is stress. We are hopeful that the two-dimensional surface profilometry will provide some resolution of this important question, but we still are inclined to believe that the observed patterns are due to stress.

We also obtained, earlier, an acoustic image of cracking produced by diamond pyramid indentation of silicon nitride. Unfortunately, the sample surface was in the as-fabricated condition, which means that the signal produced by grinding marks all but obscured that from the small cracks produced by indentation at the 1-GHz frequency used in obtaining the image. The sample was subsequently polished, revealing the cracks shown

in the acoustic image. This process also tended to reduce the signal from the cracks (at least when the microscope was focused on the surface) because of smearing of the sample surface. We have now produced a second sample, obtained by polishing the surface *before* indentation. The results, obtained at 1.2 GHz, were much better than those obtained previously. The more prominent cracks did not, in general, radiate from the center of the associated vertex but, rather, began well away from the sharp corner.

Subsurface images of these cracks show very strongly the banding described earlier produced by the diffraction of surface waves from the crack opening. The periodicity of these bands agrees very well with the calculated spacing based on the surface wave velocity of silicon nitride.

During the course of this reporting period, we obtained an independent, indirect confirmation of the imaging of the stress fields around scratch-induced cracking in polished silicon nitride. An independent group, working with scratch-induced cracking in glass, has observed virtually identical results with the acoustic microscope. In that study, the nature of the contrast variations was identified using both polarized light and scanning electron acoustic microscopy (SEAM) and definitively proven to be stress fields surrounding the cracks. It is therefore virtually certain that the same patterns detected by us in silicon nitride are attributable to stress as well. The utility of this observation is that the stress distribution on ceramic surfaces may be viewed directly, rapidly, and with a resolution of less than a micron at the highest frequency. No other technique, aside from SEAM, which is basically a complementary acoustic technique, can, to our knowledge, provide this information as rapidly and with such resolution.

We have also reexamined a few laser-drilled holes in silicon nitride which were previously used to quantify the detection limits of our older, lower-frequency (100-MHz) ceramic inspection system. The smallest of these holes was stated to be 10 μm in diameter, and using extremely careful gating techniques and maximum contrast enhancement, this standard was marginally detectable.[3] With the high-frequency system, however, the hole is not only detectable with extreme ease, but material melted by the laser beam may be seen lining the edge of the entry point. Figure 1 shows an image at 1 GHz (half the maximum operating frequency) and a magnification of 1250× of the hole. The very noticeable horizontal linear features are grinding marks (the surface was in an as-fabricated condition), and numerous voids and pits in the 1- to 2-μm range may be seen. In the original data, melt debris could be seen entirely surrounding the hole, but the fine detail may not reproduce well here. Most notable here is the imaging of numerous subsurface voids, detected by the acoustic surface wave, which cannot be seen in the optical images (not shown here).

We have also received a request to evaluate thin films (~10 μm) of alumina on a titanium substrate. These films are polycrystalline, non-oriented films having an optically smooth surface. The concern is for cracking in the film. Examining one such film acoustically at 1 GHz, it was immediately obvious that there were several surface scratches present. Recognizing that such defects might give rise to cracking, we examined the area adjacent to one of these scratches very carefully and did indeed find several extremely fine cracks. Figure 2 shows the scratch and surrounding area at relatively low power (250×). The scratch is evident; the crack produced by the scratch can be seen faintly to the left of
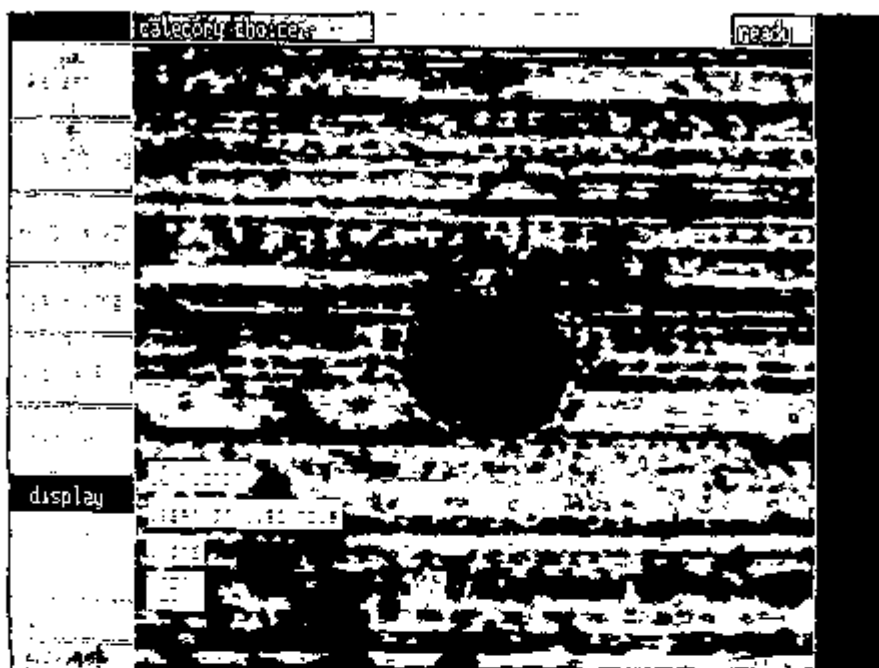
Fig. 1. Ultrasonic image at 1 GHz of a 10-µm laser-drilled hole in silicon nitride.
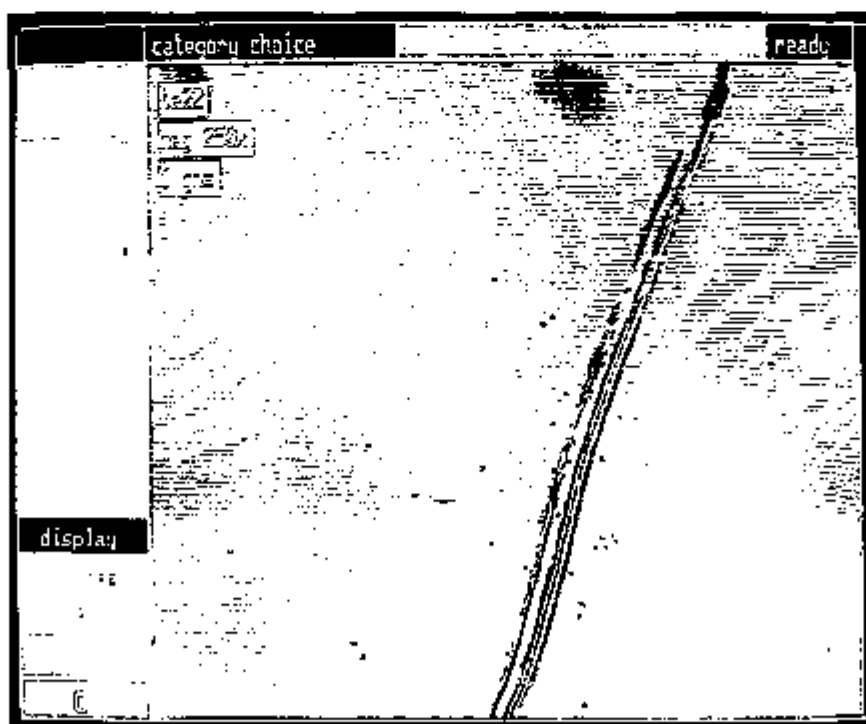
Fig. 2. Acoustic image at 1 GHz of a scratch and subsequent crack in an alumina film.

the scratch and in the lower half of the figure. The mottled areas scattered throughout the image may be variations in the local film acoustic properties or variations in the film-to-substrate bond (this particular film is about one surface acoustic wavelength thick; hence, the quality of the bond should affect the resulting image).

Figure 3 shows the crack at considerably higher power (1250×). The crack is readily seen, and the dark pointlike indications scattered around the image are small pores in the coating. The interference fringe patterns adjacent to the crack and surrounding each pore occur at multiples of half the acoustic surface wavelength (~6 μm at 1 GHz), and both surface and subsurface pores are imaged. Several other cracks were found acoustically, indicating that high-frequency acoustic microscopy is an excellent tool for detecting and characterizing cracks in thin ceramic films and coatings.

In producing these coatings, it is not uncommon to find small regions that are entirely disbonded. Because the alumina is virtually transparent in such thin layers, this condition has been noted optically from the resulting color fringes produced by interference in the layer. The films examined thus far did not possess such regions of
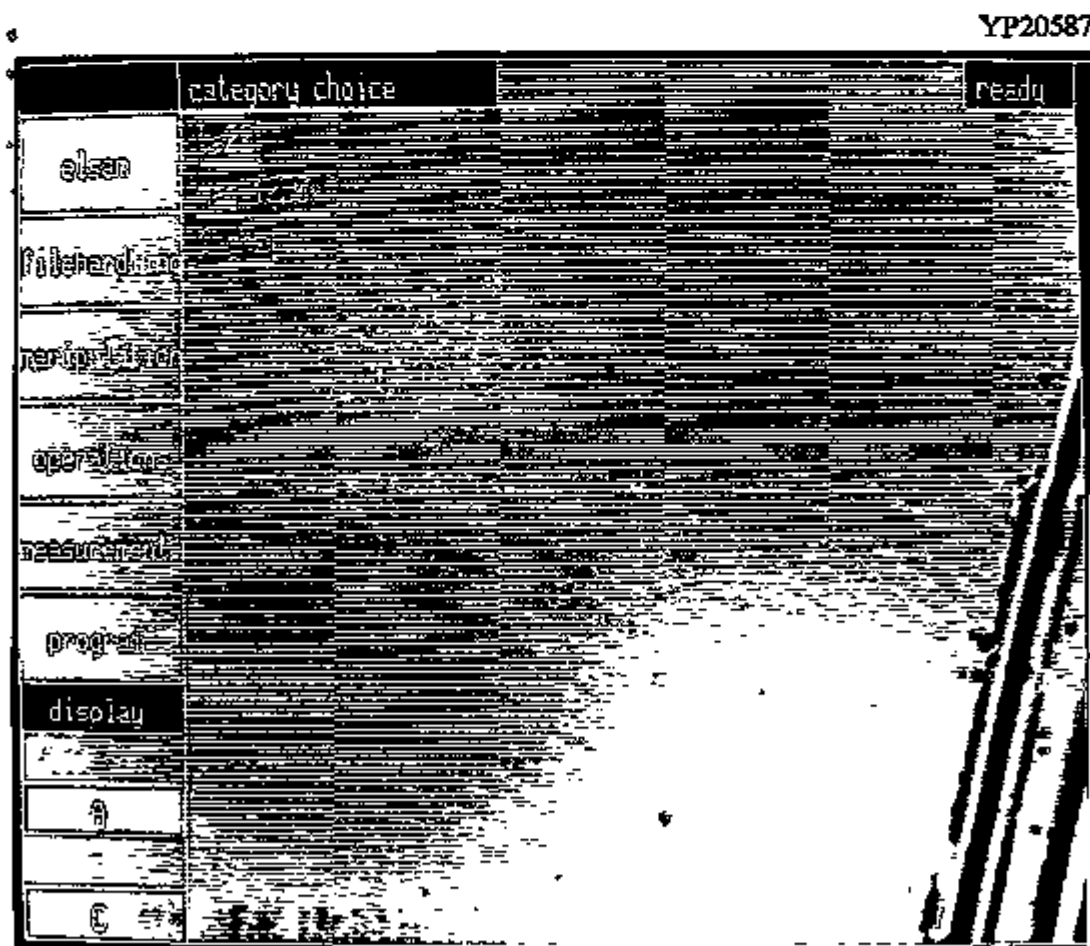
Fig. 3. Detailed acoustic image at 1 GHz of a crack in an alumina film.

disbonding, but the film manufacturer is interested in evaluating the capability of acoustic microscopy for detecting this condition as well. Several more coatings are being produced for examination.

We continue to examine the nonlinear behavior of ceramics as a likely tool for detecting and quantifying damage in monolithic and composite ceramics. In measuring the acoustic nonlinearity of materials, two approaches are possible. In the first, the second- and higher-order dependence of ultrasonic velocity on the sample nonlinearity may be measured. This requires detecting very small changes in the velocity. In the second approach, the acoustic nonlinearity causes a portion of the incident energy to be converted into the second and higher harmonics of the fundamental driving frequency, and this harmonic content is then detected and quantified. We have adopted the second of these two approaches, primarily because it is more closely related to techniques which we have already developed or pioneered and because it does not require interrogating the sample while under load. As we have mentioned previously, however, harmonic generation and detection require the use of high levels of ultrasonic excitation because the second harmonic content, while it is extremely sensitive to the state of fatigue (presence of microcracking) in monolithic systems and the degree of fiber-matrix bonding in composites, is still a very small quantity. This has necessitated the purchase of appropriate hardware for high-level excitation of high-Q, tuned transducers, and we have now received the high-power toneburst hardware necessary to conduct studies of the nonlinear behavior of ceramics. Previously, we have been limited to a power output of no more than 100 W (200 V p-p), sufficient to detect acoustic nonlinearity in materials which exhibit a high degree of anharmonicity but inadequate to establish changes with accumulated damage in the ceramics we have examined thus far. Using a 50-ohm resistive load, we have already measured a power output of 3600 W (1200 V p-p) with the new hardware. Since the acoustic nonlinearity increases quadratically with driving amplitude (voltage), the new hardware should increase the harmonic content by a factor of 36.

We have also specified the remainder of a system necessary to establish a viable procedure for measuring the nonlinearity of structural ceramics. An appropriate digital oscilloscope for acquiring data in a form suitable for computer analysis and a stepped, high-power attenuator remain to be purchased. Digital acquisition and storage of data are mandatory because we have already developed the software and procedures for extracting harmonic content for a two-transducer, 2:1 transmit/receive frequency ratio technique. We have also acquired undamped (high-Q) transducer elements for a 5-MHz transmit, 10-MHz receive configuration. Since the harmonic generation also increases quadratically with frequency, there is reason for going to still higher frequencies in monolithic ceramics, but the lower frequency will be more useful in some composites, for which the attenuation increases rapidly with frequency.

We have completed preliminary studies on the elastic nonlinearity behavior of structural ceramics. Using only the low-power system described above, we have succeeded in producing a weak nonlinear response in several materials. The results were sufficiently encouraging to warrant further development of the technique, and the new hardware should provide sufficient power to excite measurable nonlinearity in ceramics. Several researchers have shown that the nonlinearity parameter of metals and composites is an extremely sensitive indicator of the presence of damage, second phases, precipitates, and

the degree of bonding between fiber and matrix in numerous fiber-reinforced composites. The reasons for this correlation are unrelated to the specific material, and hence, the monitoring of elastic nonlinearity to quantify global damage should be equally applicable to both monolithic and composite ceramics.

Computed Tomography (CT) - B. E. Foster

An experimental exhaust manifold was received for CT evaluation. The sample had an inner cylinder of ceramic with a wall that was approximately 8 mm thick. This cylinder was wrapped with a compliant layer of some material unknown to us and then cast with an outer layer of aluminum that was about 10 mm thick. Figures 4 through 6 show a single CT slice at three different positions through the sample. In Fig. 4, the voids in the compliant layer are quite obvious, as well as porosity in the aluminum with diameters ranging from 0.1 to 0.6 mm. Note the crack-like indication in the ceramic at the 1 o'clock position. In Fig. 5, a crack-like indication is also noted at the 1 o'clock position, as well as even larger voids in the compliant layer. The porosity in the aluminum is more numerous up to 1 mm diam. In Fig. 6, there were no crack-like or linear indications noted in the ceramic. However, the large voids in the compliant layer are still obvious, and the porosity in the aluminum is up to 1.3 mm diam.
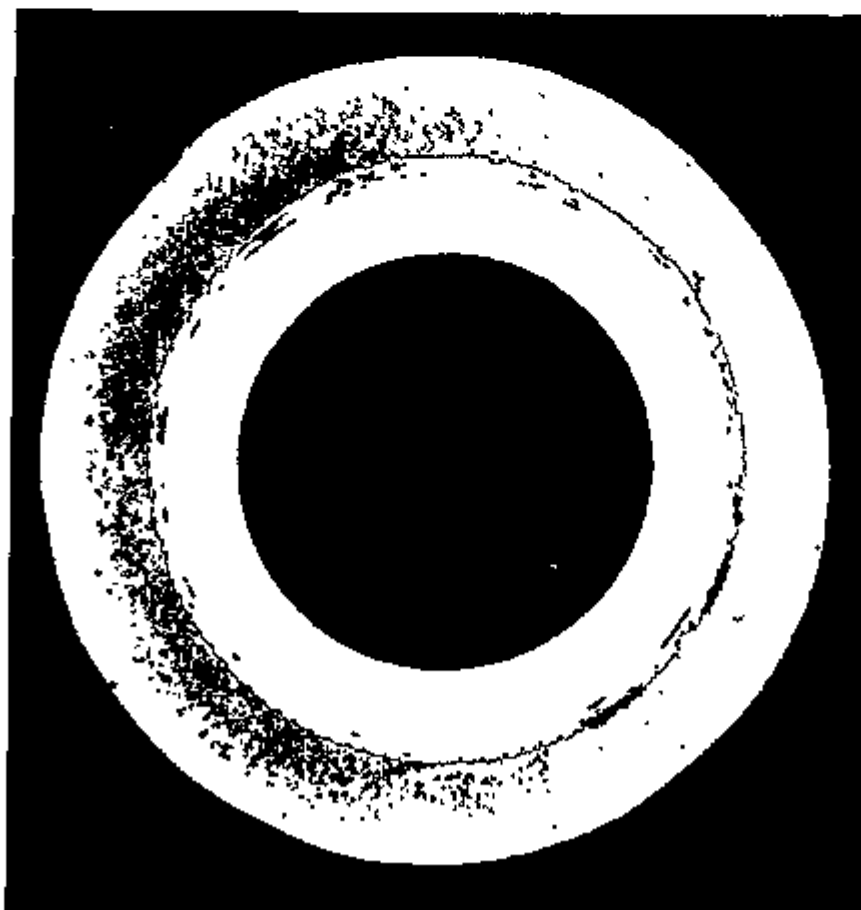
YP19787

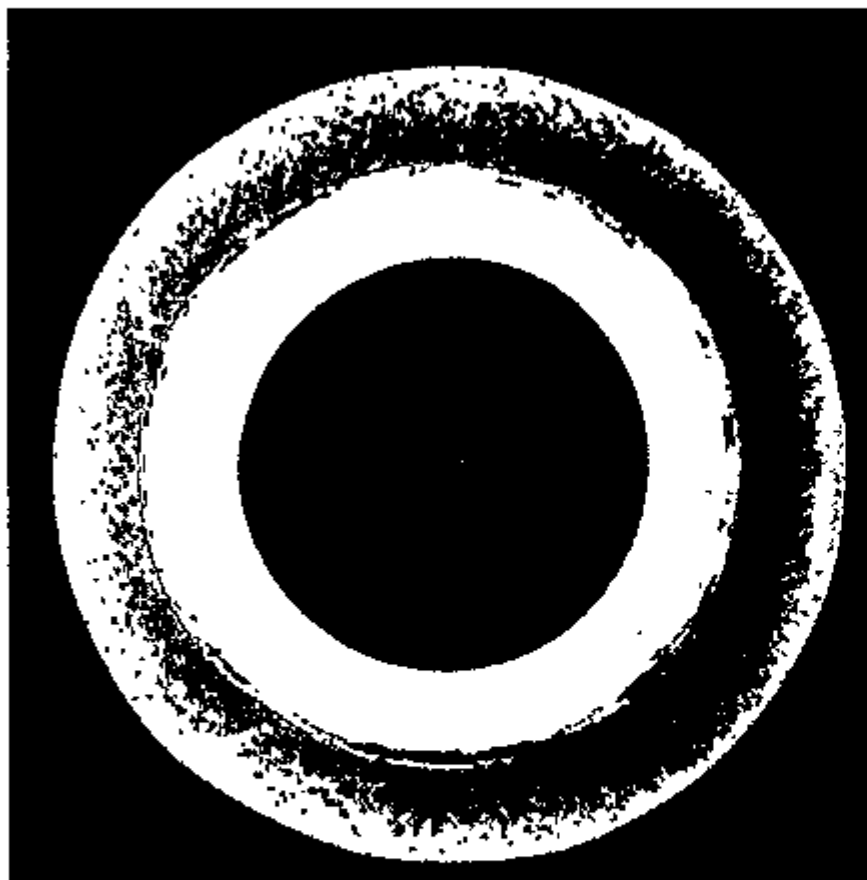Fig. 4.   CT slice (0.5 mm thick) of the exhaust manifold 25 mm
from the bottom end.

Fig. 5. CT slice (0.5 mm thick) of the exhaust manifold 77 mm from either end.
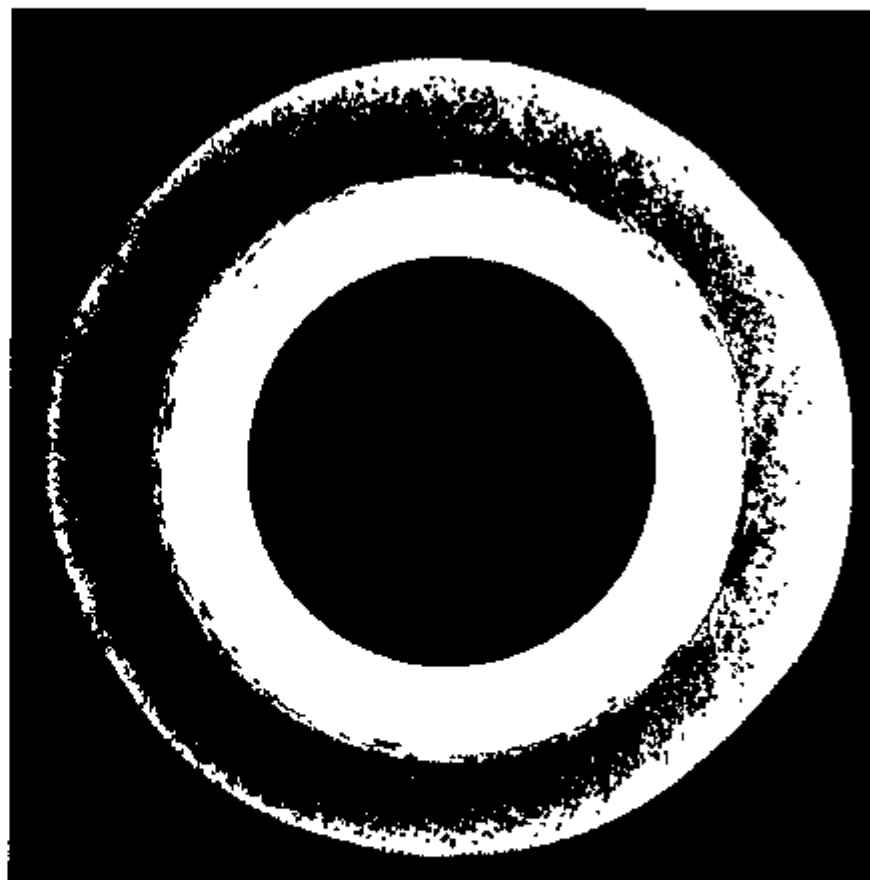
Fig. 6. CT slice (0.5 mm thick) of the exhaust manifold 129 mm from bottom end.

In addition, an all-ceramic conductive glow plug with enhanced electrical connection was received for evaluation. Figure 7 is a CT slice through the long axis of the glow plug. The left two-thirds of the image are not ceramic and will not be further described. The ceramic is the rod-shaped material in the right one-third of the image. Note the vertical dark line toward the left end of the rod. Another CT slice was made diametrically through that area and is shown in Fig. 8. Note the crack-like indication extending both right and left from the central hole in the ceramic. The rather bright ring in the image is the braze between the ceramic and metal material.

Scientific Measurement Systems, Inc. (SMS), has developed an area detector assembly for attachment to the existing 101B+ computed-tomography systems that permits spatial resolution in the range of 25 to 50 μm. The area detector assembly can be added to the present computed-tomography system with only minor changes to the primary collimator of the X-ray beam and a connecting software package. The upgrade can significantly improve the spatial resolution and reduce manpower requirements as well as provide better quality images. The major advantages of the upgrade to the existing CT system are noted to include:

1. order-of-magnitude speedups in data acquisition time with slice thicknesses as small as 20 μm;
2. at least a factor of two improvement in spatial resolution;
3. complete compatibility of data, command files, and user interfaces with the present system; and
4. full sharing of hardware peripherals between the units and easy interchange between detectors.

The disadvantage was the limitation of sample size to about 48 mm for this very high resolution.

B. E. Foster traveled to SMS in early July 1994 to evaluate the performance of the area detector on specific samples. The samples included: ceramic turbine blade, silicon nitride tensile specimen, line pair phantom, a ceramic glow plug, and a spark plug insulator. These samples had previously been scanned with the 101B+ CT system at ORNL.

The area detector at SMS was a laboratory prototype which was difficult to use because it was somewhat unstable and optimum focussing and alignment were problematical. However, several excellent images were obtained, and a good evaluation of the capabilities was assessed.

Referring once again to Fig. 7, which is a CT slice through the long axis of the ceramic glow plug using the 101B+ system, note the vertical dark line toward the left end of the rod. Many other CT slices had been made diametrically through that area without very much success in defining the nature of that dark line or band. One such diametral CT slice (made with the 101B+) was shown in Fig. 8. One of the area detector scans is shown in Fig. 9. The banding is clearly defined and may well be a density gradient without cracking.
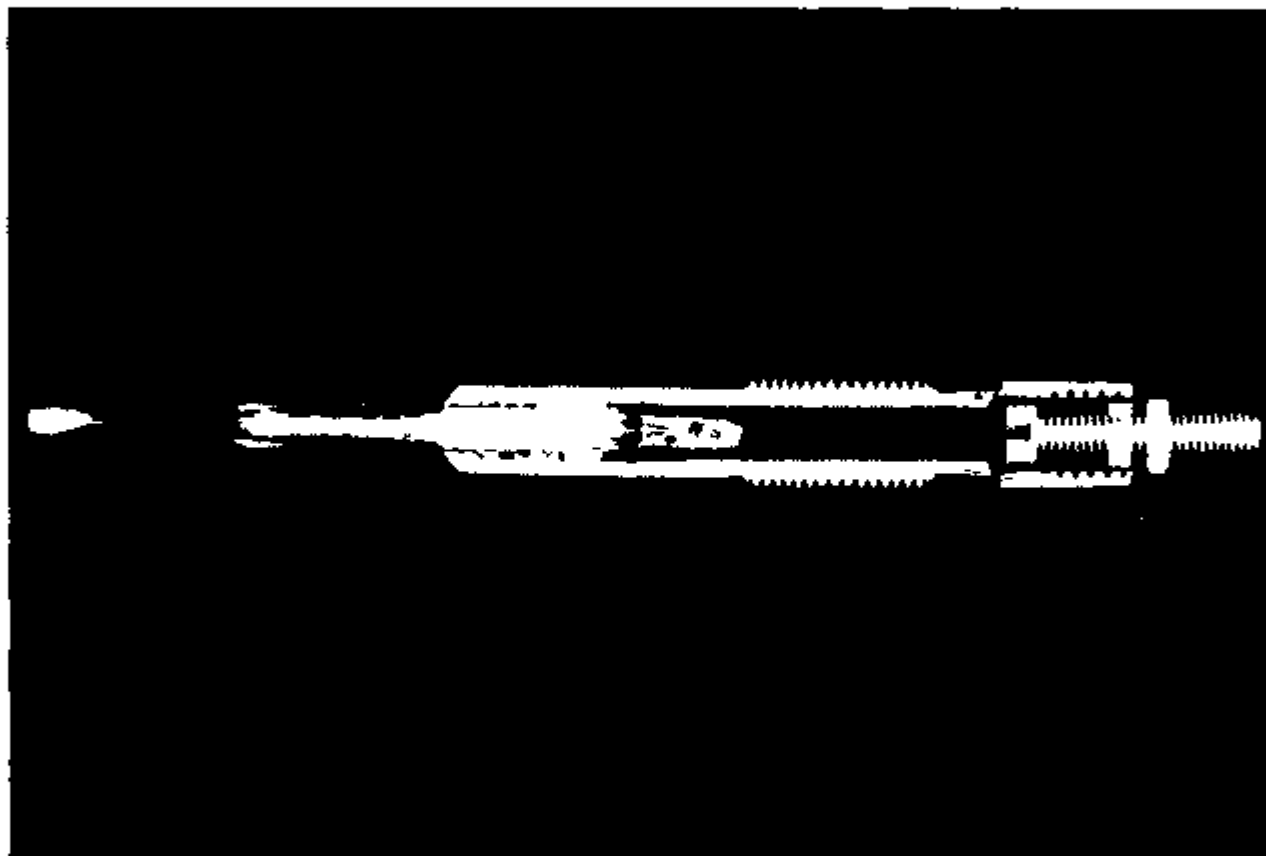
Fig. 7. CT slice (0.25 mm thick) of the ceramic glow plug through the long axis.
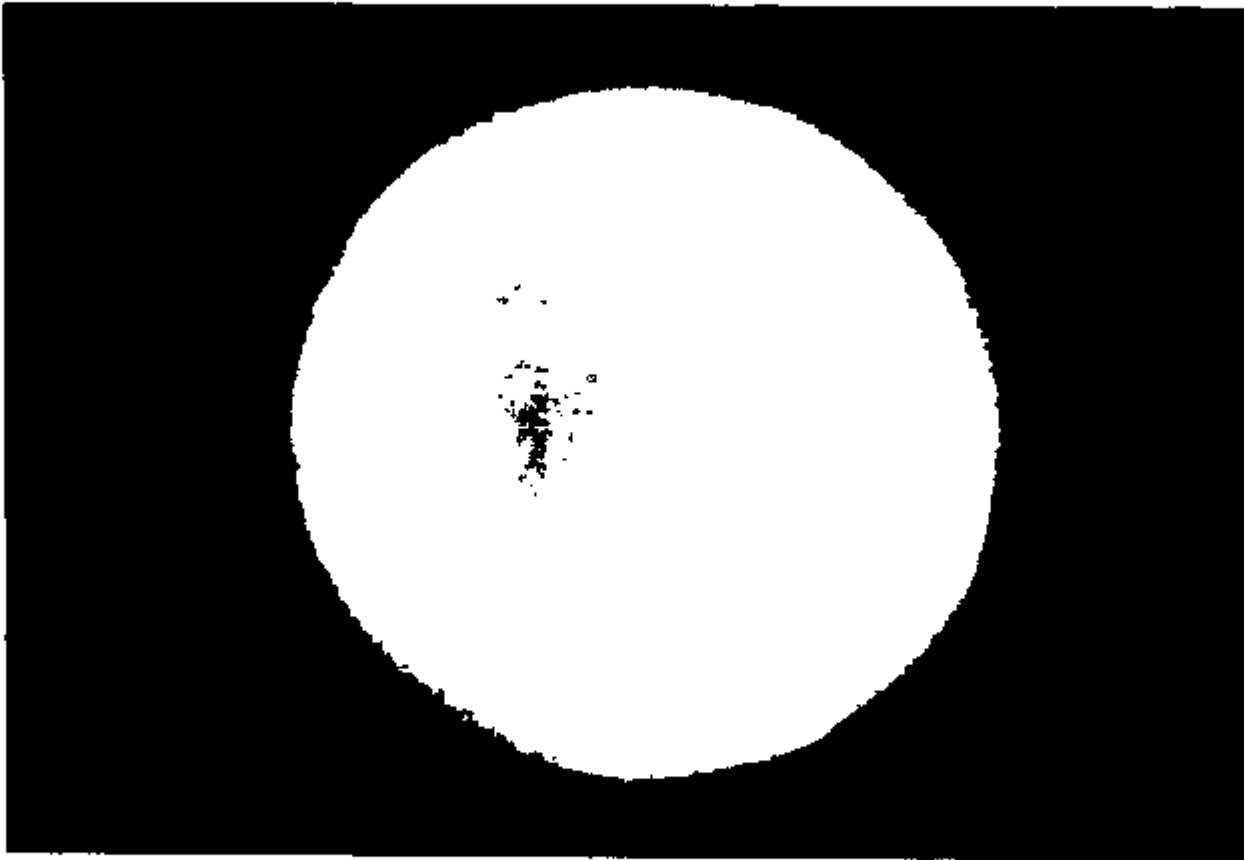
Fig. 8. CT slice (0.25 mm thick) of the ceramic glow plug through the diameter.
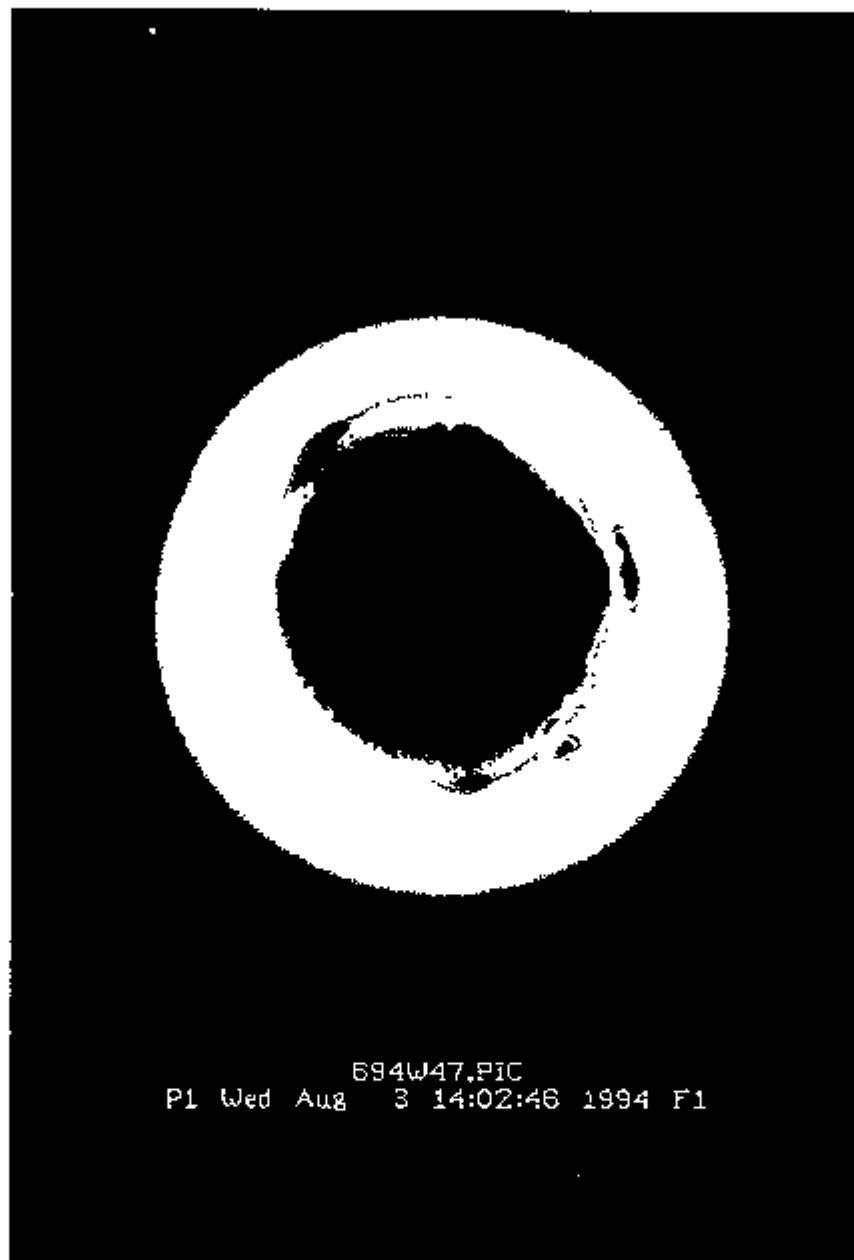
Fig. 9.   CT slice (0.25 mm thick) of the ceramic glow plug through
the diameter with the area detector.

On the surface of the tensile sample, there were grey-colored splotches that were
several millimeters in diameter. The images made with the 101B+ system did not show
any discontinuities in those areas. However, the area detector images showed density
variations and can be seen in Fig. 10.

378
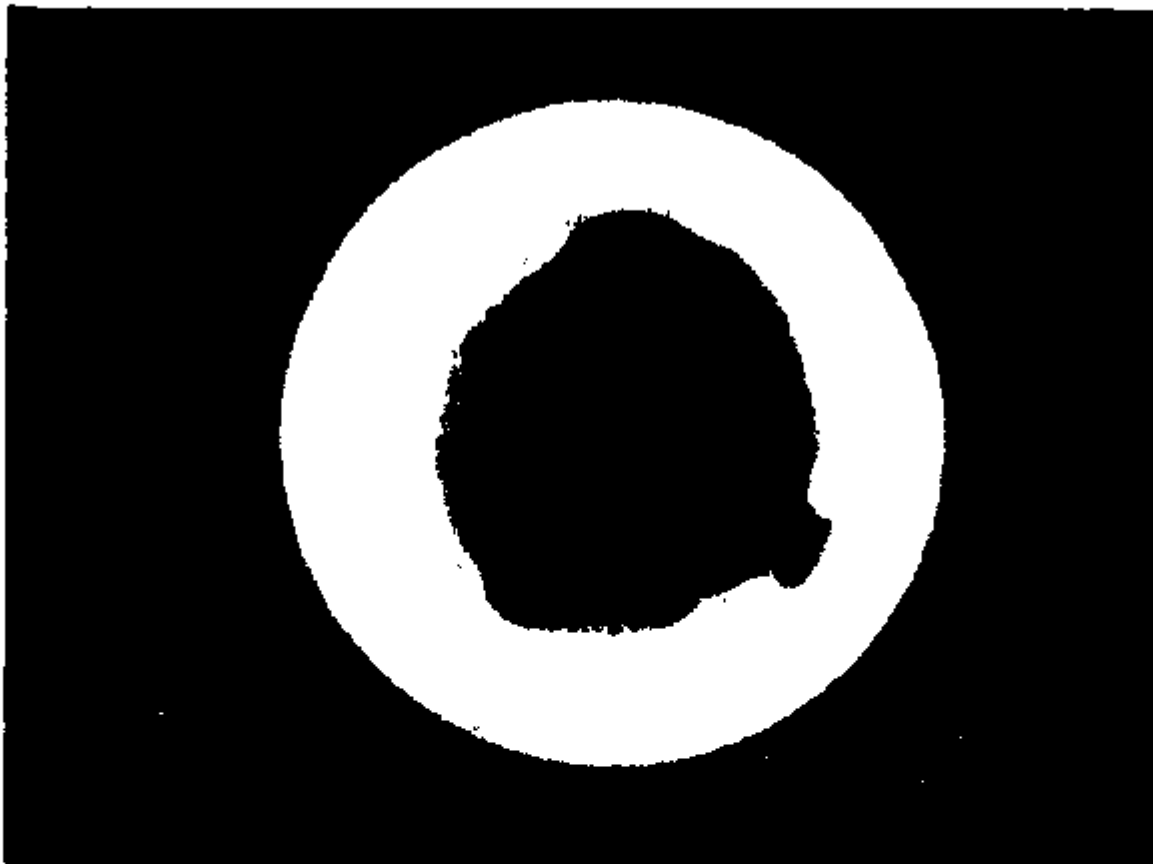
Fig. 10. CT slice (20 μm thick) of the ceramic tensile specimen through the diameter with the area detector.

The spark plug insulator had a tiny pinhole through the wall which had been caused by the plug manufacturer during a high-voltage test. This particular pinhole had not been successfully defined with the 101B+ system. Figure 11 shows one image made of that plug using the area detector. Note the crisp definition of the pinhole in the wall at the 6 o'clock position.

The images of the line pair phantom were also very crisp and sharp. The images from the ceramic turbine blade were quite disappointing. Stable alignment just was not achieved, and circular artifacts in the reconstructed images were unacceptable. Even filtering failed to significantly reduce the interference circles.

After return to ORNL, with further review of the images and discussions with program management, the decision was made to initiate procurement of the area detector assembly. The anticipated installation and acceptance testing is planned for early October 1994.
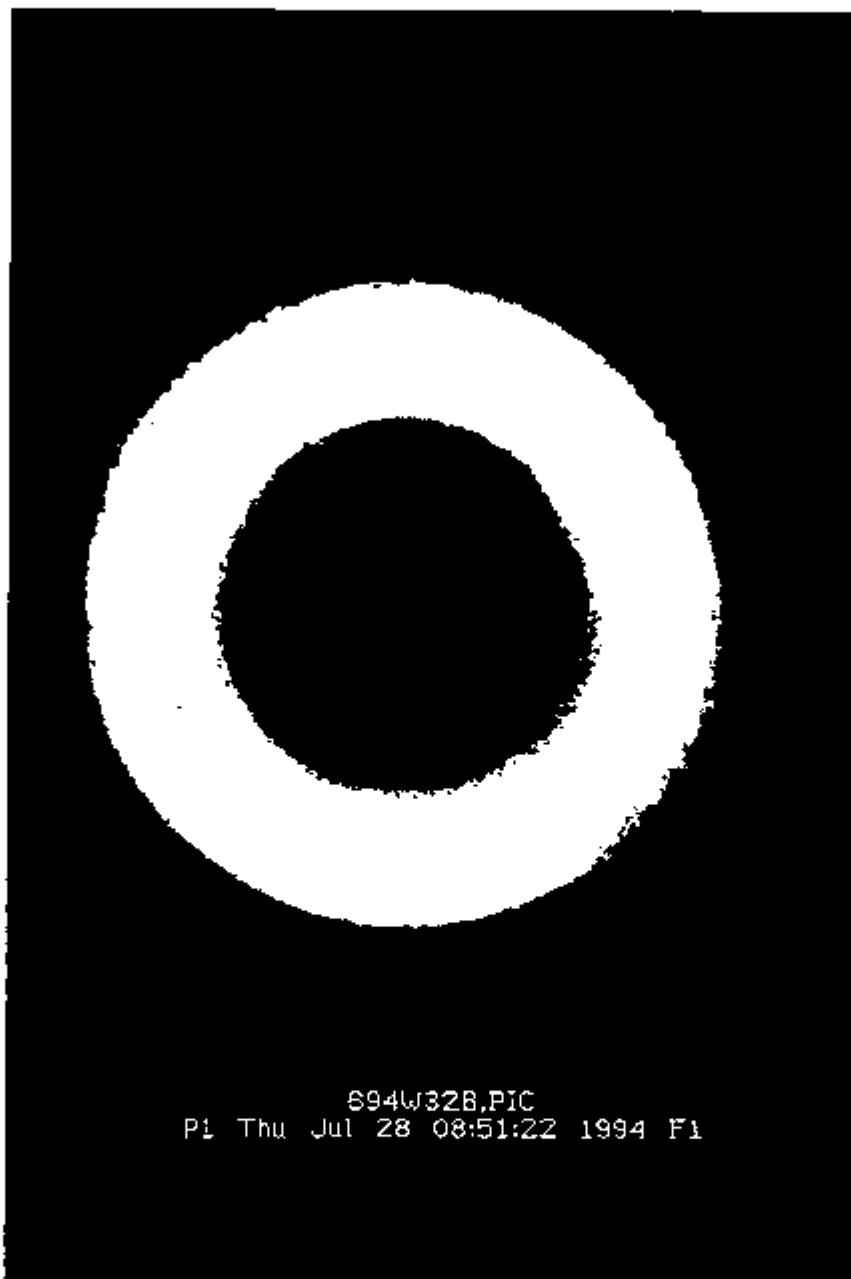
Fig. 11. CT slice (20 μm thick) of the ceramic spark plug insulator through the pinhole with the area detector.

Milestones

Milestone 351107 was completed on schedule.

Publications

None.

References

1. W. A. Simpson, Jr., "Nondestructive Evaluation Development," p. 59 in *Ceramic Technology Project Bimonthly Technical Progress Report, October-November, 1993.*

2. W. A. Simpson, Jr., "Nondestructive Evaluation Development," p. 63 in *Ceramic Technology Project Technical Progress Report, February-March, 1994.*

3. W. A. Simpson, Jr. "Nondestructive Evaluation Development," p. 39 in *Ceramic Technology Project Bimonthly Technical Progress Report, April-May, 1992.*

X-ray Computed Tomographic Imaging – W. A. Ellingson, E. A. Sivers,
D. L. Holloway (Argonne National Laboratory), in cooperation with
J. P. Pollinger and H. C. Yeh (AlliedSignal Ceramic Components)

Objective/Scope

The objectives of the Phase III work of this project are to (1) utilize 3-D X-ray micro-computed tomography techniques to study density distributions in composite green-state (as cast) pressure slip-cast Advanced Turbine Technology Application Program (ATTAP) rotors and (2) correlate destructive density analysis (to be conducted by AlliedSignal Ceramic Components) of the as-cast ATTAP rotors with the 3-D microtomography density data.

Technical Highlights

ATTAP Rotor Density Studies

Introduction

Initial results indicate that multiscan, three-dimensional X-ray CT (3D-XRCT) can be used successfully to image large ATTAP turbine rotors for the purpose of determining density variations and identifying anomalies. This process, which images a large rotor by scanning partial sections sequentially, effectively optimizes signal-to-noise and stretches the dynamic range of the scanner by maximizing X-ray flux through regions of similar thicknesses.

Data Collection

Figure 1 illustrates the geometry of the ANL 3D-XRCT system as used for multiscan data collection. The equipment is the same as that used for ordinary 3D-XRCT because it is necessary only to rotate and translate the turntable during the acquisition. Two-dimensional interpolation is used to combine individual data sets into a composite image.

Data Processing

Figure 2 illustrates the flow of data in multiscan processing. Figure 2a shows the steps used to calibrate the scanner for normal data acquisition. Because the area detector is an image intensifier (II), the initial two-dimensional (2-D) image exhibits spatial distortion. This distortion is removed by scanning an object having a precise, uniform distribution of small, dense spheres and building a table to interpolate a correspondingly uniform image. It is also necessary to determine the sample (pixel) spacing, the distance from the X-ray source to the object, and the projection of the axis of the turntable upon the II.

Figure 2b shows the steps used in initial data acquisition. The source-to-object distance, pixel size, and width of the object to be scanned determine the number of scans that must be taken and the position of the turntable during each scan. In addition to each of the individual scans, an unattenuated exposure (air scan), and a background noise scan (dark current) are required for source-strength calibration. As a result of light scattering (veiling glare) within the II, there will be a low-frequency offset on each image that must be removed before processing. This is measured by performing each scan twice: once in the normal way and once with intervening lead strips that are thick enough to stop all direct X-rays. The signals under the lead strips represent veiling glare, and a low-order curve can be fit to these readings to estimate them. Because it is necessary to take the natural logarithm of X-ray attenuation readings, any offset (such as veiling glare) that is not removed will cause a nonlinearity that results in radial density artifacts.

Figure 2c shows the primary steps used in data processing and reconstruction. The air scan and dark current are used to normalize the X-ray source distribution, and the natural logarithm of the data is computed. Partial scans can then be combined to produce a composite multiscan. It has been found that an imprecise measurement of the source-to-object (STO) distance can result in column misalignment in the composite scan. To refine the estimate of STO, a multiscan data acquisition of two metal pins separated by the diameter of the object is also made. Overlapping regions of this multiscan are cross-correlated to determine the amount of misalignment, and a new estimate of STO is generated for use in data combination. Finally, a single-material beam-hardening calibration is performed. Because material X-ray attenuation is energy-dependent and the X-ray source contains a distribution of energies, transmitted X-ray intensity will not be directly proportional to the product of the material density times the thickness penetrated. Compensation can be made by scanning known thicknesses of the material and building a calibration table to linearize readings. Nonlinearities in the data due to beam hardening also cause radial density anomalies and streaks between dense objects in reconstructed images. Before image reconstruction, a smoothing filter is applied to compensate for nonuniformity between detector elements in the CCD camera.

Results

Several multiscan data sets of the first ATTAP rotor have been taken and some initial images have been reconstructed. These images demonstrate the suitability of 3D-XRCT for the examination of ATTAP rotors and identify steps for further improvement. The objective is to map density variations within the rotors nondestructively to assist AlliedSignal in maintaining quality control. The first of two specially made rotors is being imaged in each of five 2-mm-thick slices to map X-ray attenuation values, which are proportional to density. When imaging is completed, the rotor will be diced into 2-mm-square sections, and density values will be computed for comparison.

For reference, Fig. 3 is a sketch of the first rotor, illustrating four of the five cross-sectional planes to be imaged. A slice will also be taken halfway down the 4.1-cm-diameter neck. Figure 4 is a digital radiograph of the midsection of this rotor, which illustrates the relative density values. Figure 5a shows a preliminary 913 x 913, single-scan, 3D-XRCT reconstructed cross section through the neck of the rotor and illustrates the presence of radial density variations. (Here, white represents the denser regions and black represents air.) Figure 5b is a line plot through the center of this slice. This shows that the center of the rotor neck is more dense than the edges.

Initially, three-scan data collection was used to image the L/5, 3L/5 and 4L/5 rotor sections. Figure 6 is a sinogram (line profile as a function of angle) of the plane from the 4L/5 region. Figure 7a is a 757 x 757 multiscan reconstruction of the 8-cm-diameter 4L/5 region, and Fig. 7b is an enlargement of the bottom of this image. (Here, black represents the more dense regions and white represents air.) The image shows radial density fluctuations, being less dense in the center and more dense at the edges. A line profile through the center of the reconstruction, identified in Fig. 8a, is given in Fig. 8b.

This image is also of sufficient quality that high-contrast voids, cracks, or inclusions would be seen if present. Its primary deficiencies are a high level of statistical noise caused by the extreme attenuation of the X-ray beam and some residual velling-glare scatter. A simulated beam-hardening correction was performed successfully on the data, as evidenced by the absence of "wagon wheel spokes" between the rotor blades. Primarily because of the high level of noise, it was decided to retake the data using five-scan data collection to improve the signal flux to the dense center of the rotor. Plans currently underway to improve processing are detailed below.

Noise
The advantage of multiscan data collection for the ATTAP rotors is the ability to use longer data-dcollection times to image thicker regions. Three separate scans were used to image the 4L/5 region, but the attenuation range in the inner region was too great to obtain good statistics. Five scans are being collected in the next data set to permit longer integration times through the center.

Beam Hardening
Beam-hardening calibration data taken from radiographs of a Si_3N_4 step wedge have not been processed yet. Instead, initial reconstructions were made with a set of simulated beam-hardening data using a representative 150 kVp X-ray "spectrum" and compiled charts of the X-ray mass-attenuation coefficients of Si_3N_4. This correction was successful in preventing streaks between the rotor blades and severe "cupping" in the image, but an experimental correction made from the step wedge may be even better and will be evaluated.

Veiling Glare/Constancy of X-ray Signal Strength
It has been determined that the intensity of the X-ray source strength varies, both during long data acquisition periods and between subsequent scans. This does not cause a problem in ordinary multiscan data collection because air readings in the outer scans are compared to normalize intensity during one scan and overlapping regions in adjacent scans are scaled to match. However, at present, the source intensity is not monitored in the lead blocker files used to compute veiling-glare/scatter profiles because the lead strips are mounted on a plastic sheet. Although the plastic sheet is thin, the percentage by which it changes the transmitted signal varies with the hardness of the X-ray beam. This will be remedied by hanging the lead strips on a frame so that signal strength can be compared through identical path lengths in lead blocker scans and unobstructed scans.

Accurate veiling-glare correction is essential because in scans of dense objects, veiling glare can be several hundred percent of the true signal. Figure 9 shows the raw data (solid line), raw data with lead blockers (solid line with "dips"), the fit veiling-glare curve (dashed line), and the veiling-glare-corrected data (bold line) for the center scan of the multiscan data set used to reconstruct Fig. 7. Because source intensity fluctuation was not corrected in this processing, the magnitude of the scatter profile was slightly different in some views, causing a mismatch that is evident at the right edge of one line plot from the multiscan composite data set shown in Fig. 10. Both the left and right edges should be zero, and the elevated right edge causes a low-density ring artifact to surround the core of the reconstructed rotor image.

Conclusions
In view of the preliminary nature of the present images, it is recommended that the destructive evaluation of the ATTAP rotor be delayed for 1-2 months until the best 3D-XRCT images can be obtained. Initial images suffer predominately from statistical noise and X-ray flux variability. Steps that are being taken to increase data collection times through the densest part of the rotor and measure the variability of the source in lead-blocker scans can be expected to improve image quality substantially.

The overall quality of multiscan 3D-XRCT images is very good. In a comparison between the images of an 8 in.-diameter Al_2O_3 combustor liner made on the ANL 3D-XRCT using five multiscans and those made on a 2-D medical system, the 3-D images were found to have comparable density resolution and almost twice the spatial resolution. Due to beam-hardening correction and veiling-glare correction on ANL multiscan data, the level of image artifacts was also comparable.

Status of Milestones

Work is proceeding according to schedule, with the exception that destructive analysis of the first rotor should be postponed until 3D-XRCT analysis is completed.

MILESTONE SCHEDULE (3.5.1.5)

		DATE DUE	REV DATE
3.5.1.5.10	Obtain region-of-interest image of large Si_3N_4 rotors as-cast.	12/15/92	Completed
3.5.1.5.11	Complete fabrication of calibration wedges.	2/28/94	Completed
3.5.1.5.12	Complete 3-D X-ray CT images of calibration wedges.	5/30/94	Completed
3.5.1.5.13	Complete fabrication of first rotor.	3/31/94	Completed
3.5.1.5.14	Complete 3-D X-ray CT study of first rotor with destructive analysis.	9/30/94	Delayed
3.5.1.5.15	Complete fabrication of second rotor.	10/31/94	
3.5.1.5.16	Complete 3-D X-ray CT study of second rotor with destructive analysis.	4/30/95	
3.5.1.5.17	Submit report on correlation between X-ray CT data and destructive analysis.	9/30/95	
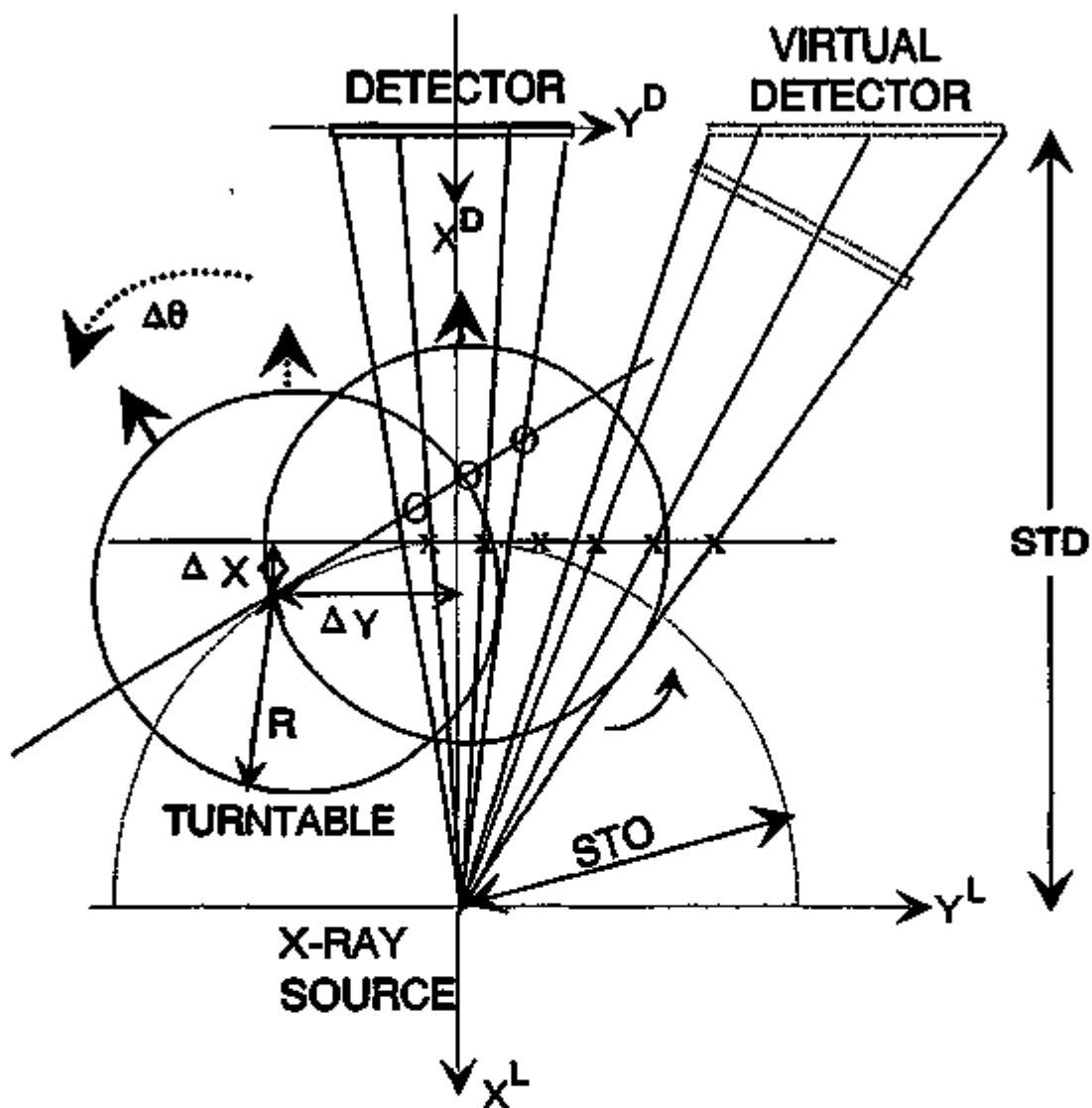
Fig.1. Sketch illustrating geometry of multiscan data acquisition.

DATA COLLECTION FOR MULTIPLE-SCAN COMBINATION
WITH SCATTER & BEAM HARDENING CORRECTIONS
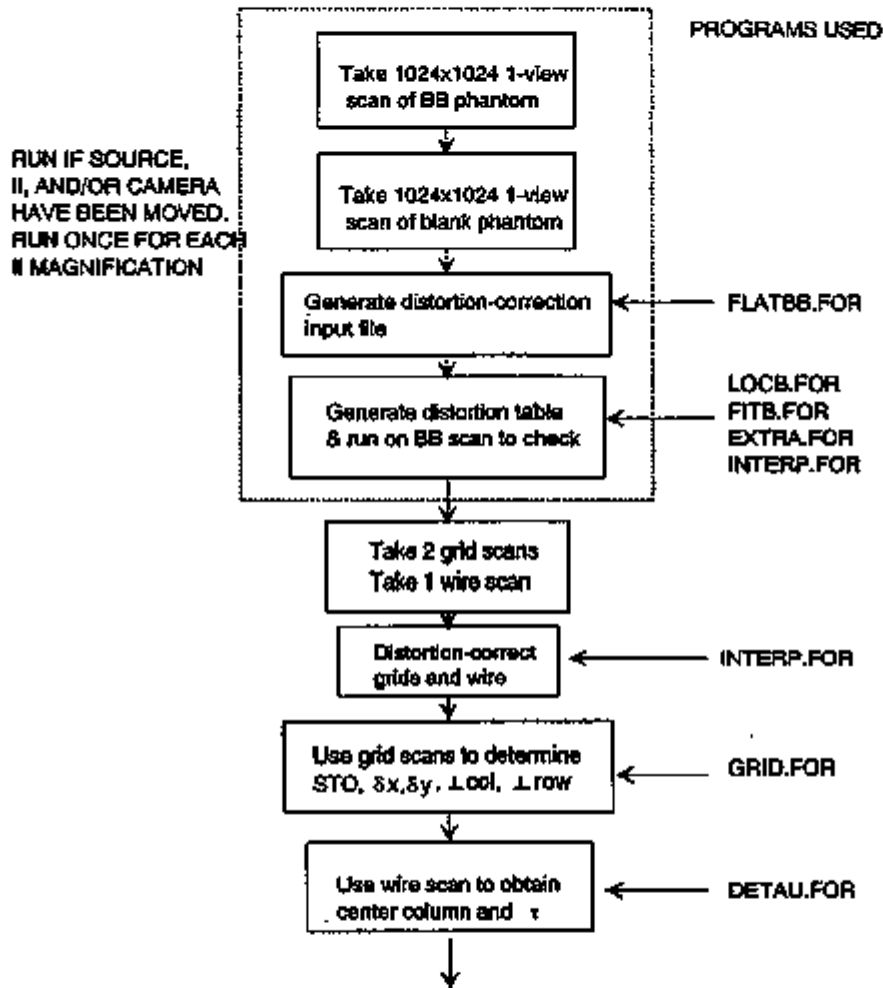
Fig. 2a. Diagram of calibration procedures for 3D-XRCT.

PROGRAMS USED

MOVEXY.FOR

Determine NSCAN, number of scans to take, the x,y positions of the turntable, ΔX, ΔY, and the initial angular orientations for each scan. The x and y increments (inches) and angular increments (degrees) between scans are stored in SCANn.POS. The increments needed to return to the origin are stored in RESET.POS. The file OFF.DAT contains the (x,y) coordinates (inches) and initial angles (radians) used by CORRM.FOR.

Take NSCAN scans with turntable at designated positions. Use the number of views appropriate to the usual scan diameter. If the object is dense, the scans should be repeated with lead blockers between the source and the object. Also, take NSCAN scans of the two-wire phantom.

Take one real air scan having approximately 63 views, with and without scatter blockers

Fit curves to Pb blocker scans and subtract from NSCAN object scans and air scan.

FITSCAT.FOR
SUBSCAT.FOR

Distortion-correct NSCAN object scans, NSCAN two-wire scans, and air scan.

INTERP.FOR

Fig. 2b. Diagram of steps used in initial data acquisition.

PROGRAMS USED

Subtract average dark current from
NSCAN scans and air scan, perform   ◄——— PREP.FOR
air calibration, and take logs.

2-Wire Scans

To make sure that OFF.DAT is current,
run MOVEXY.FOR again. Then, generate   ◄——— MOVEXY.FOR
composite data file of two-wire scans.   CORRM.FOR

Cross correlate sinograms of overlap
regions adjacent to center scan to   ◄——— XYCOREL.FOR
determine column shifts in 2-wire scans

Estimate new value for STO to   ◄——— STOEST.FOR
remove column misalignment.

Run CORRM.FOR on object data   ◄——— CORRM.FOR
using new value of STO.

Beam hardening correction.   ◄——— (POLYGEN.FOR)
                                                PGFIT.FOR
                                                POLY.FOR

Run ring-free correction   ◄——— RNGFRE.FOR

Reconstruct data   ◄——— ANLFELDK.FOR

Fig. 2c. Diagram of primary steps used in data processing and reconstruction.
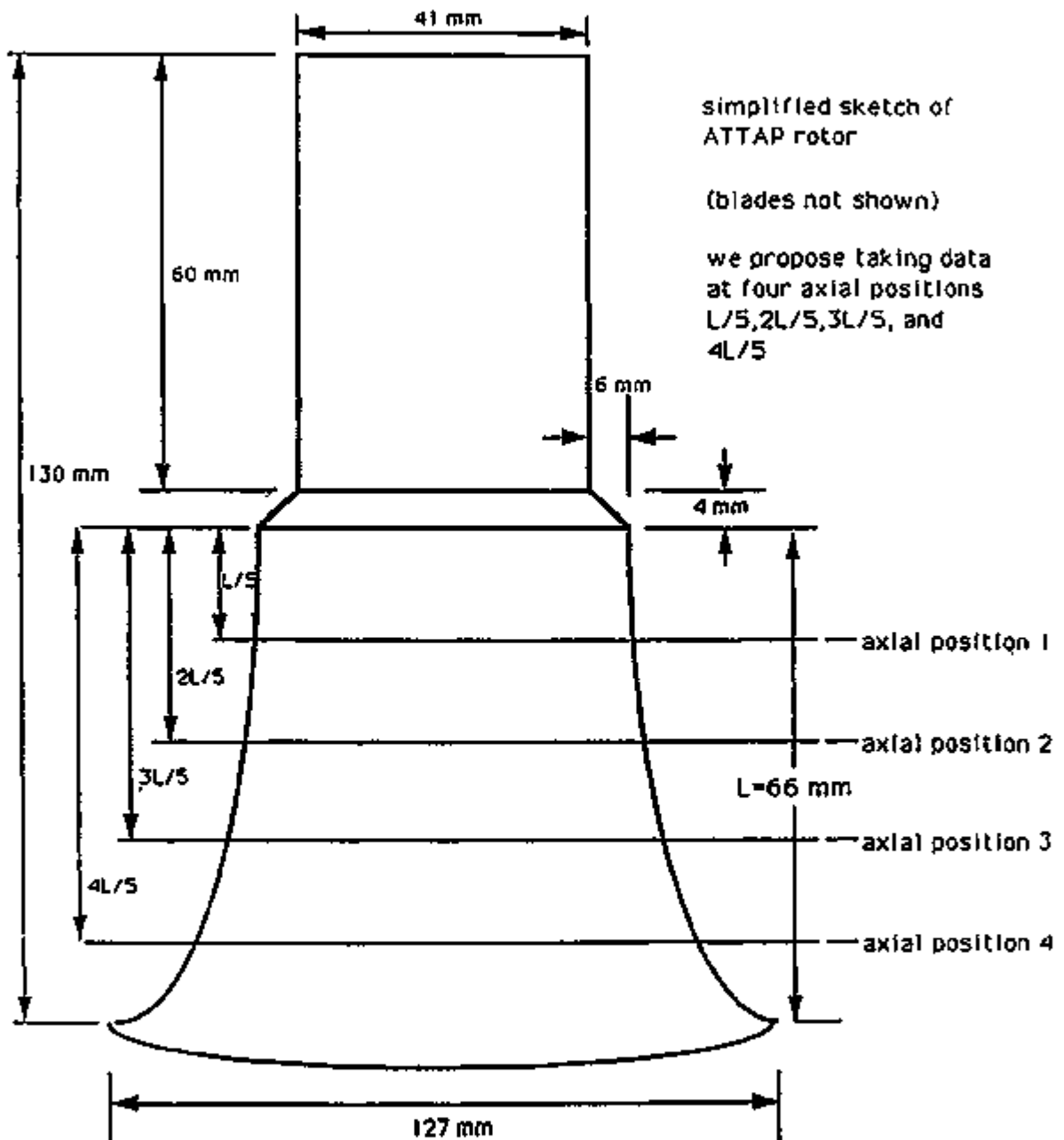
Fig. 3. Sketch Illustrating slice planes to be imaged ATTAP rotor.
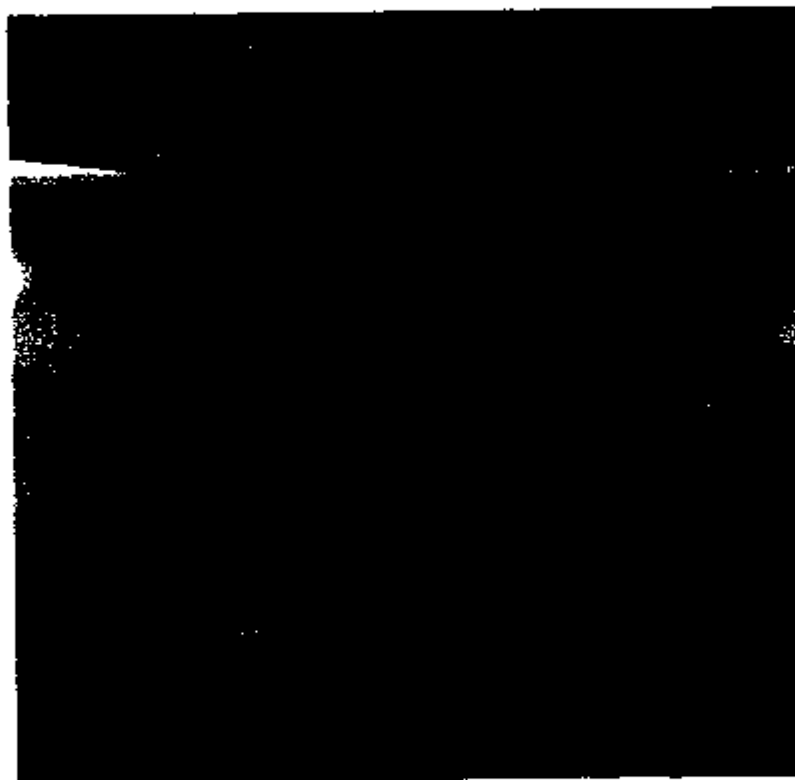
Fig. 4. Digital radiograph of ATTAP rotor inorientation of Fig. 3.
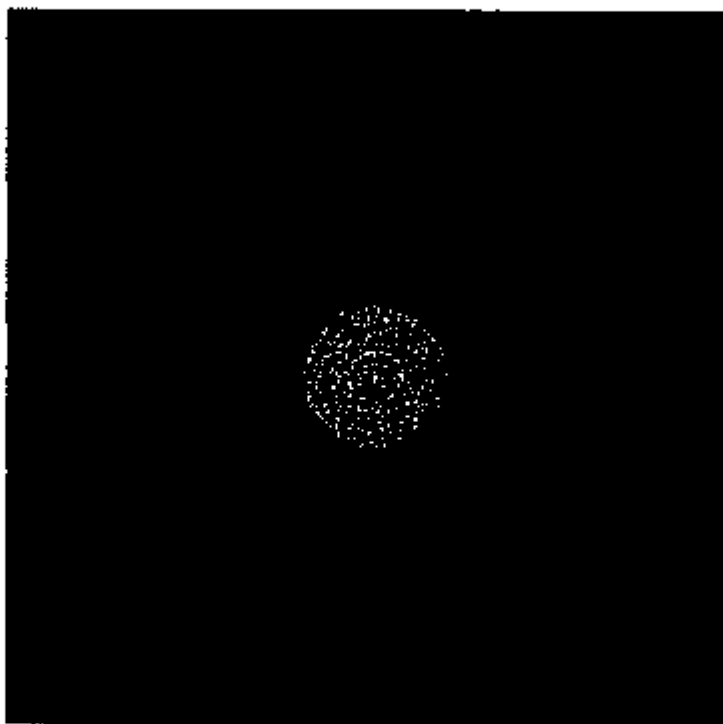
Fig. 5a. 913 x 913, single-scan, 3D-XRCT reconstruction of 4.1-cm-diameter region
halfway down neck of ATTAP rotor. Beam-hardening and veiling-glare
corrections were not performed on these data.
(Here, black represents high density and white represents air.)
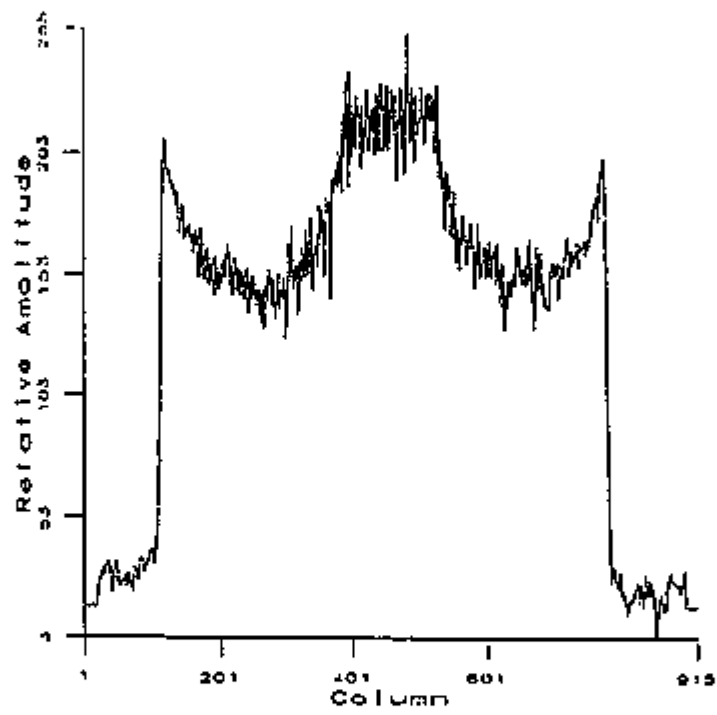
Fig. 5b. Line profile through center of the image of 4.1-cm-diameter rotor neck shown in Fig. 5a.
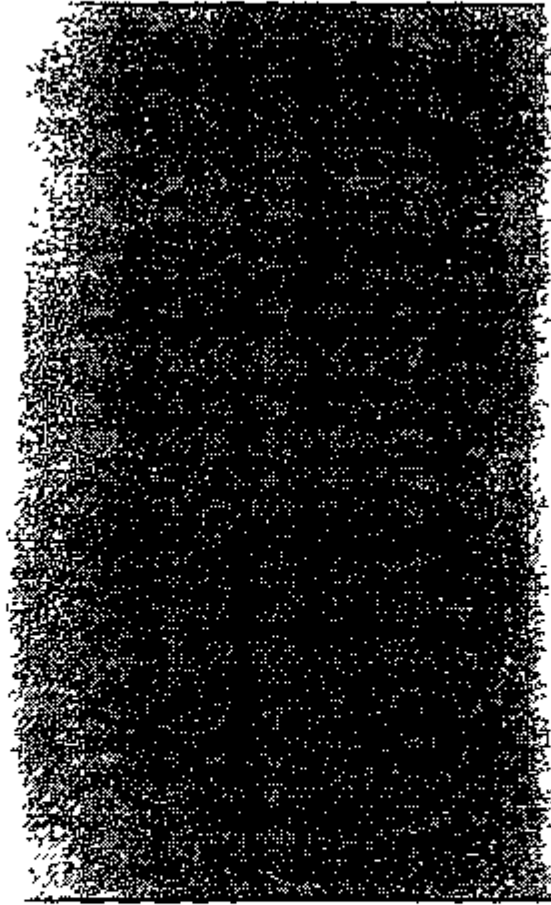
Fig. 6. Sinogram of multiscan line projection through 4L/5 plane of
ATTAP rotor as a function of view angle.

Masking tape roll →
used for marker →
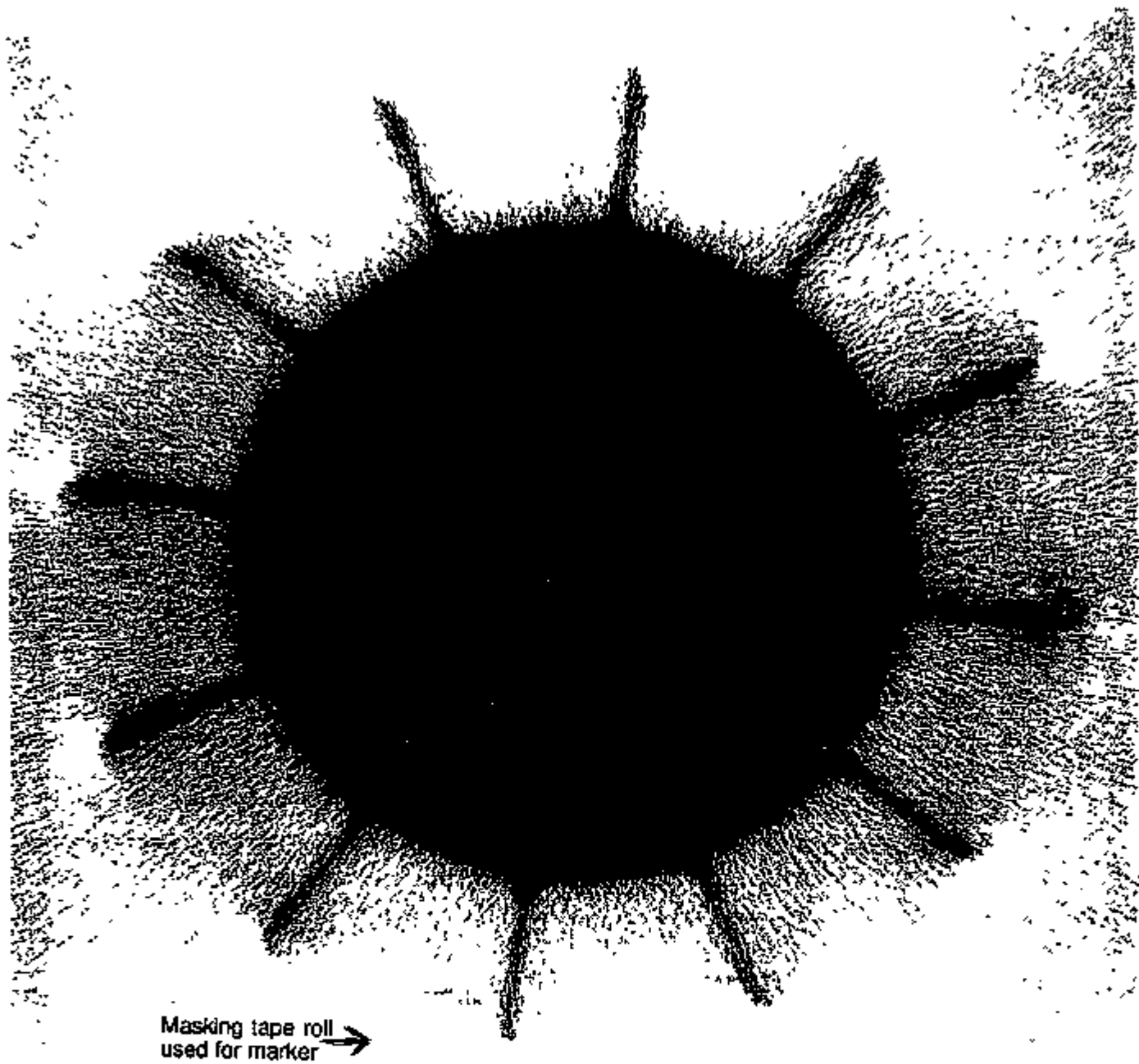
Fig. 7a. Reconstructed image of 4L/5 plane of ATTAP rotor. Circle at bottom is a roll of tape used for orientation. (Here black represents high density and white represents air.)
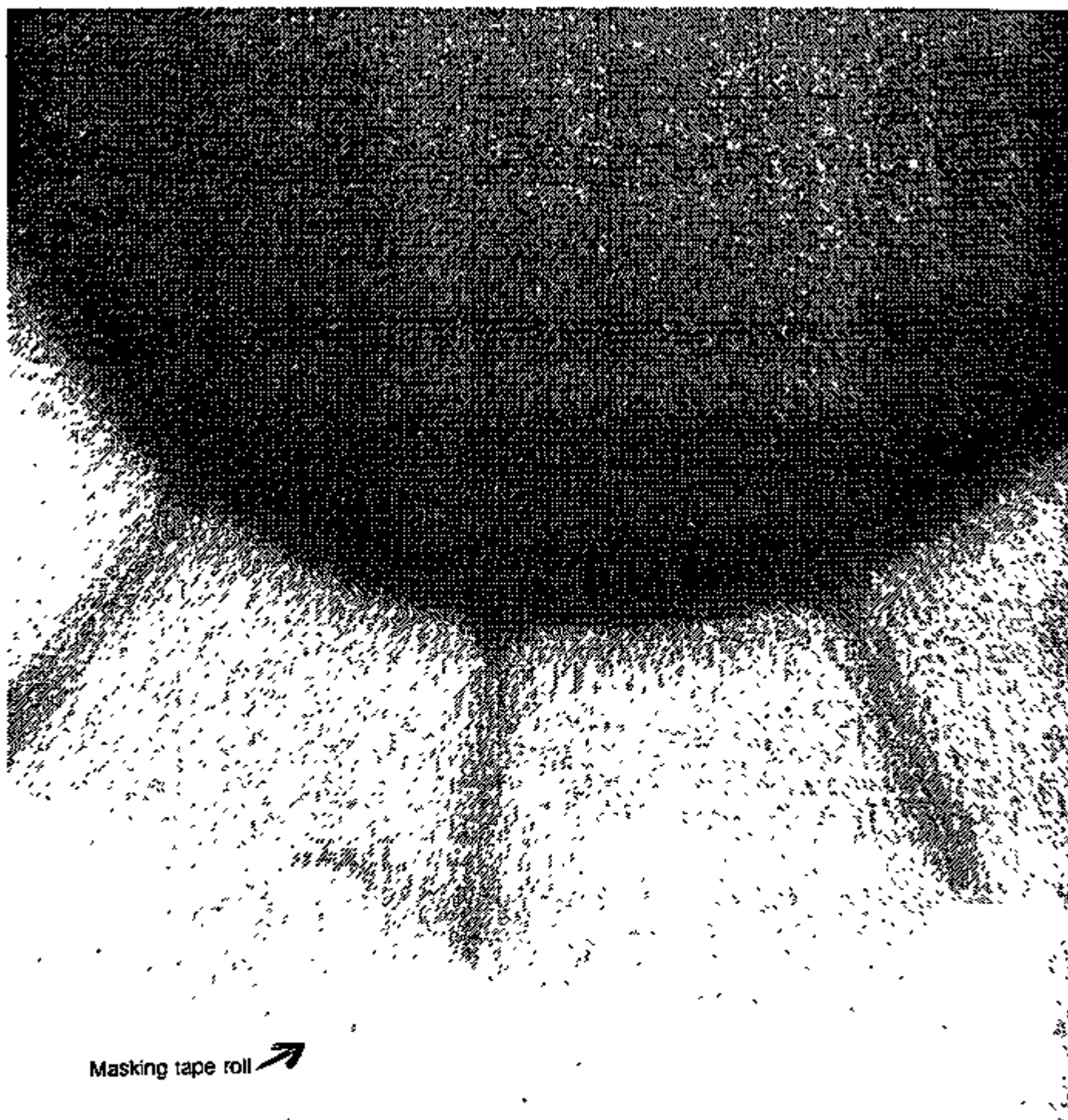
Masking tape roll

Fig. 7b. Enlarged section of Fig. 7a. (Note detection of masking tape used as a reference marker.)

Masking
tape roll
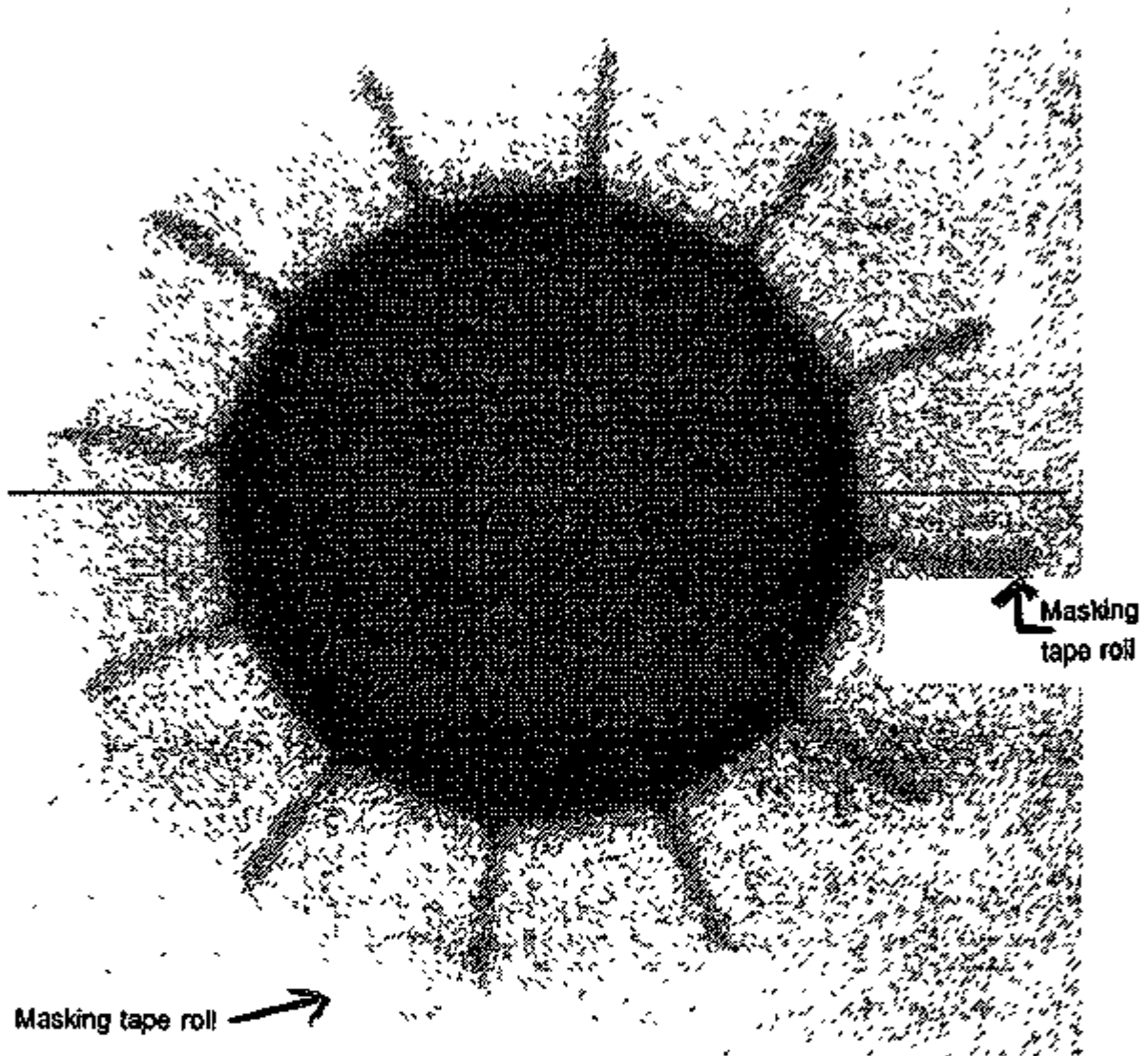
Masking tape roll

Fig. 8a. Horizontal line identifies line profile taken through center of reconstruction of 4L/5 section of ATTAP turbine rotor. (Again note detection of masking tape used to establish orientation.)

LINE PROFILE THROUGH CENTER OF
Si3N4 TURBINE ROTOR AT 4L/5
LEVEL (DIAMETER 8.15 CM)
0.025 CM PIXELS
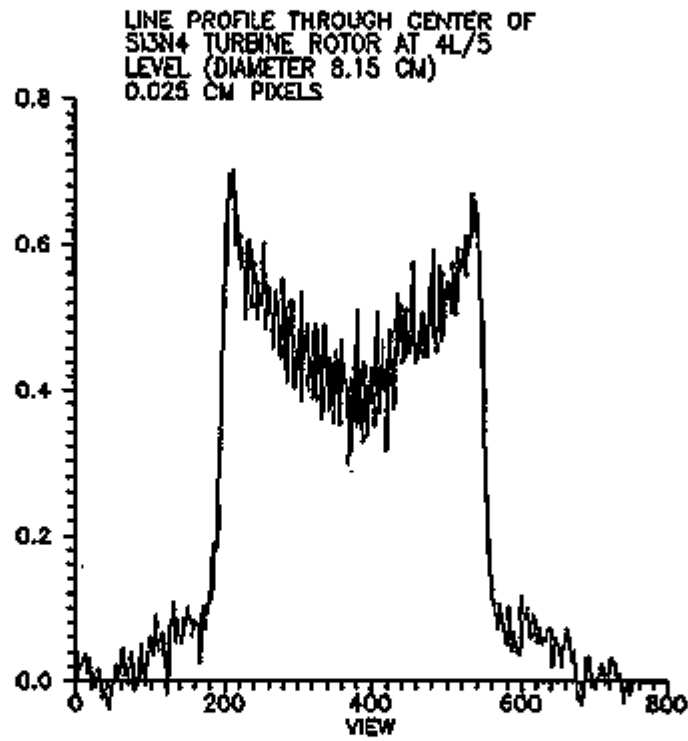
Fig. 8b. Line profile taken through center of reconstruction of 4L/5 section
of first ATTAP turbine rotor.

ROW 5, VIEW 148 OF ROT4C.DAT
ROT4CP8.DAT, AND ROT4CFIT.DAT (DASHED)
TAPES V AND W: ROW4CS.DAT IS STARRED
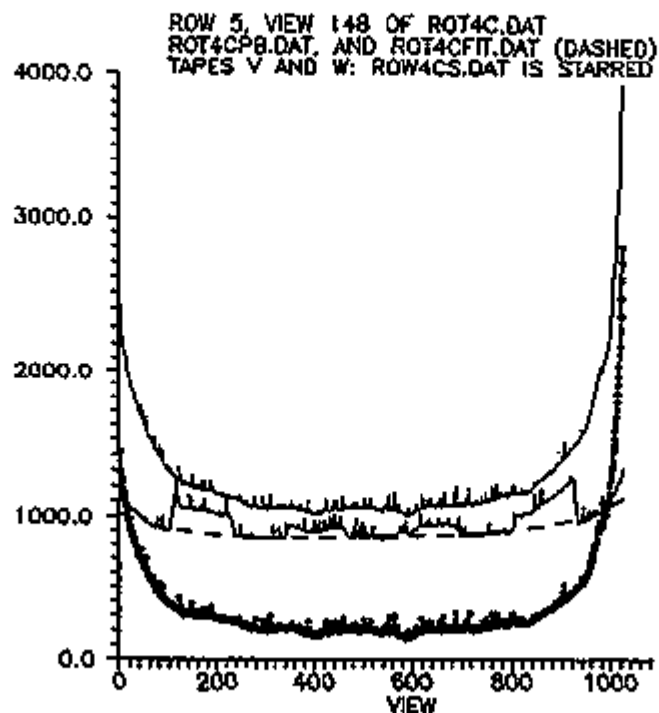
Fig. 9. Superposition at one view angle of line profiles of center portion of ATTAP rotor (solid), same profile with intervening lead blockers (solid with "dips"), fit profile of veiling-glare scatter (dashed), and veiling-glare-corrected profile (bold).

ROW4, VIEW 4 OF ROTCOMP.DAT
COMBINED 4L/5 ROTOR SLICE
TAPES V, W AND X
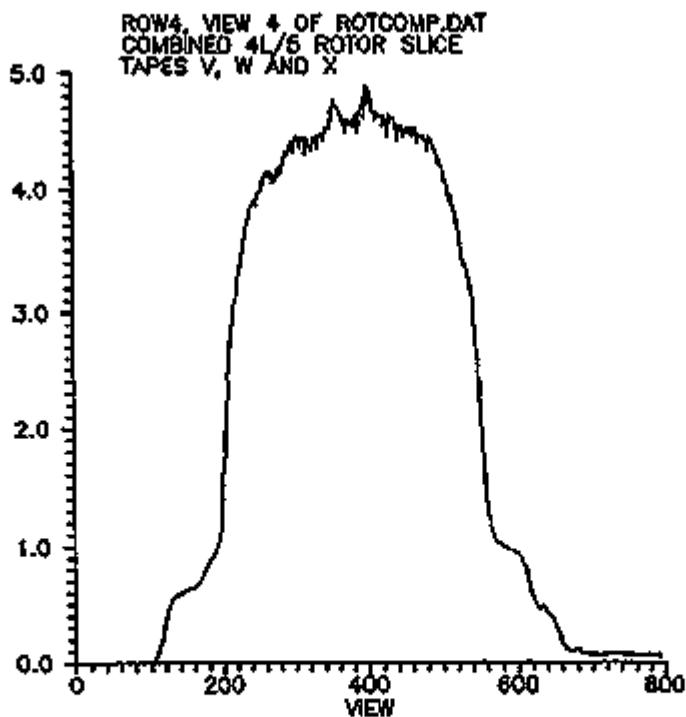
Fig. 10. Line profile at single view angle of multiscan data combination. Both right and left edges should be zero.

Nuclear Magnetic Resonance Imaging - S.L. Dieckman, S. Ahuja,
O. O. Omatete, A. C. Raptis, and W. A. Ellingson, Argonne National
Laboratory; Materials and Ceramics Division, Oak Ridge National
Laboratory

Objective/Scope

The purpose of this work is to evaluate the potential of NMR imaging to impact the
development and process control of near-net-shape gel-cast ceramic composites. The
specific objectives of this work are to determine the utility of NMR imaging for: (1) 3-D
mapping of polymerization homogeneity, (2) real-time imaging of the polymerization
process, (3) nondestructive evaluation of voids and flaws in the resultant components,
and (4) measurement of physical properties such as degree of polymerization, viscosity,
and specimen strength via correlation of these properties with measurable NMR
parameters (T_1, $T_{1\rho}$, and T_2). This work will be performed in conjunction with Dr.
Ogbemi O. Omatete of the Materials and Ceramics Division at Oak Ridge National
Laboratory.

Technical Highlights

[1]H nuclear magnetic resonance spectra have been evolved during polymerization of a
premix of soluble reactive methacrylamide (monomer) and N, N'-methylene
bisacrylamide (cross-linking molecules). The premix was polymerized by adding
ammonium persulfate (initiator) and Tetramethyl-ethylene-diamine (accelerator) to form
long-chain, cross-linked polymers. The time-varying spin-lattice relaxation times T_1
during the polymerization has been studied at 25 and 35°C, and the variation of spectra
and T_1 with respect to the extent of polymerization has been determined. To verify
homogeneous polymerization, multidimensional NMR imaging was utilized for in-situ
monitoring of the process. The intensities from the images were modeled and the
correspondence shows a direct extraction of T_1 data from the images. A Tecmag NMR Kit
II and Libra data acquisition system interacting with a CXP-100 spectrometer and a
Macintosh Quadra 950 computer was used. NMR images of the spatial distribution of the
standard MAM-MBAM (13.3 wt.% methacrylamide, 1.6 wt.% N,N'-methylene
bisacrylamide and 85.0 wt.% H_2O) copolymer premix with the initiator at a magnetic field
strength of 2.35 T were obtained via an in-house built probe tuned to the proton
resonance frequency of 100.13 MHz. The standard inversion recovery NMR pulse
technique was employed for measurement of T_1. An analysis of the images has been
conducted to relate the signal intensity to T_1 and the spin-spin relaxation time, T_2. NMR
spectra were studied as a function of the extent of MAA-MBAA polymerization.

The samples were prepared using the soluble reactive acrylamide (monomer) and N, N'
methylene bisacrylamide (cross-linking molecules), and the premix was made with water
as the solvent. The initiator 10% AP and the accelerator TEMED were then added to
begin the polymerization of the monomers, which formed long chain, cross-linked
polymers. For high resolution, 5 mm NMR sample tubes were used; for low resolution,
the solution was transferred to a 15 mm, cylindrical, flat-bottomed tube and quickly placed
in the probe for spectroscopy experiments. For low-resolution imaging experiments, it
was necessary to obtain a corresponding contrast between the polymerized and the
nonpolymerized specimen. For this reason, the sample geometry shown in Fig. 1 was
such that MAA-MBAA without the initiator was placed in a small inner tube (5 mm in dia)
that was immersed in a larger-diameter (15 mm) tube that contained polymerizing MAA-
MBAA (with the initiator). The time of the initial measurement was recorded, and careful
monitoring of the polymerization was conducted with respect to time. Times were

subsequently recorded at the end of an experiment and at the beginning of the next computer-controlled experiment.

A variation of the spin-lattice relaxation rates of the components as a function of reaction extent is also expected. ^{1}H NMR studies of T_1 were conducted on the individual standard MAA-MBAA copolymer premix at a magnetic field strength of 7.1 T. Spectra were acquired with D_2O as the solvent at 35°C to suppress the observable solvent resonance. The standard inversion recovery NMR pulse technique was employed for these studies. A stack plot of the resultant spectra for the copolymer premix is presented in Fig. 2. Variations in relaxation times are indicated by the rate of recovery from the inversion pulse. Studies suggest that as the reaction occurs, T_1 becomes longer.
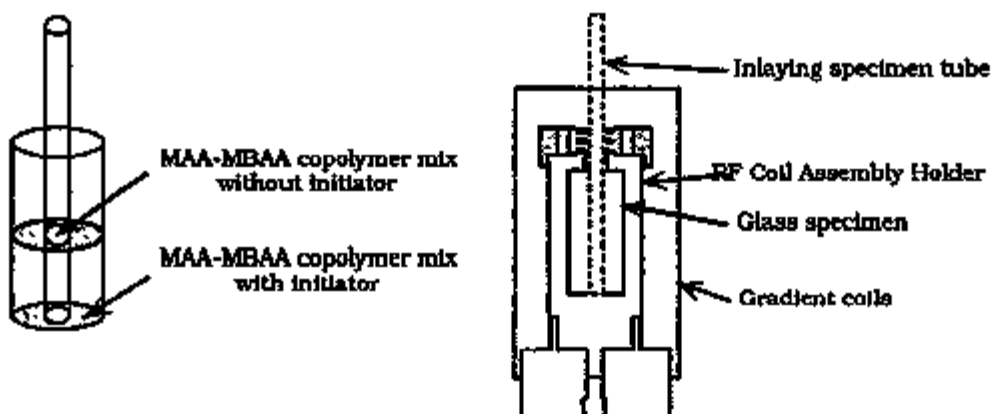
Fig. 1. Sample configuration and probe assembly used in imaging experiments
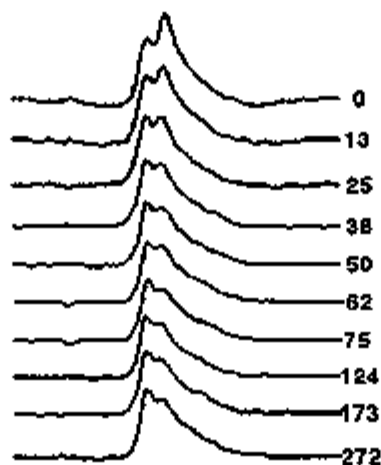
Fig. 2. Low-resolution ^{1}H NMR spectra evolved with time during polymerization process of MAA-MBAA due to AP and TEMED at 35°C. Time is in min.

NMR spectroscopy and imaging procedures were performed at 25 and 35°C to determine the variation in T_1's and whether the polymerization is homogeneous. Figure 2, obtained by low-resolution NMR spectrometry, shows the effect of polymerization on the intensity of the peaks with respect to time at the end of the inversion recovery sequence. It may be noted that the unchanged peak is that of the solvent, water, although T_1 of the solvent varied as the polymerization evolved. Also, the polymerizing peak encompasses several peaks that are not visible because of low-resolution analysis.

Figure 3 indicates the variation of relaxation time during polymerization, derived from

inversion recovery sequence results for the two peaks recorded at 25 and 35°C. High values of T_1, existing at the onset of polymerization in Fig. 3, indicate very slow relaxation. The measurements of T_1 reveal the effect of polymerization on methyl group, side chain, and main chain motions. T_1 measurements can be used to determine changes in molecular motion caused by polymerization. In Fig. 3, the value of T_1 decreases in accordance with the correlation time of the local motions that contribute to the relaxation. T_1 increases with temperature and decreases during polymerization. This indicates that the polymerization of MAA-MBAA with AP as the initiator and TEMED as the accelerator was more rapid at higher temperatures than at lower temperatures.
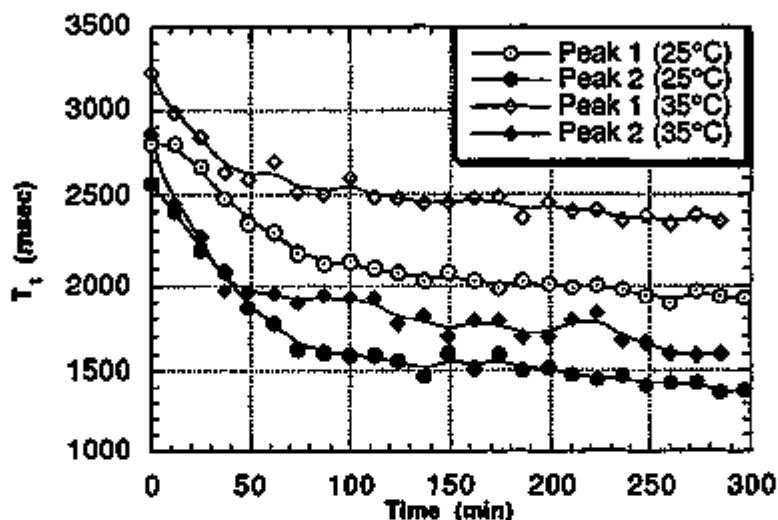
Fig. 3. Variation of spin-lattice relaxation time T_1 with time during polymerization of MAA-MBAAat 25 and 35°C.

NMR imaging was conducted on MAA-MBAA prepared in solvent water. During imaging, the obtained NMR signal was largely due to H_2O present in the premix and overwhelmed the signal due to other constituents in the premix. The standard inversion recovery NMR pulse technique, employed for the measurement of T_1, utilized a 180° pulse, followed by a time delay t, then another 90° pulse (180°-t-90°-acquire). Figure 4 shows a sequence of 2-D ^1H NMR images of the MAA-MBAA polymerization reaction with time. All images show the concentration gradient in the specimen. Figure 4(a) shows a 2-D ^1H image of the MAA-MBAA copolymer premix at 0.0 s. Here, polymerization has not begun because the initiator and the accelerator have not begun acting on the copolymer premix. During the process, at any temperature, no polymerizing front was observed with imaging techniques, and polymer gels formed homogeneously throughout the solution as seen in the images in Fig. 4. The sequence of images shows that because of the polymerization, the relaxation occurred more rapidly in the polymerizing MAA-MBAA (i.e., in the outer tube) while the relaxation in the inner tube remained constant. Because the images are individually scaled in intensity, it appears that the image intensity of the inner tube decreases. The variation of intensity has been indicated in Fig. 5 by a plot (solid line) of the intensity ratio (outside intensity/inside intensity, I_1/I_0) vs. time as the polymerization occurred.
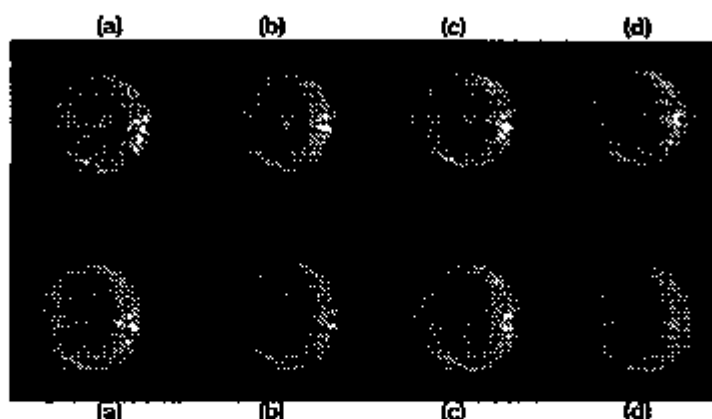
Fig. 4. 2-D ^{1}H NMR images at times from 0 to 139 min of standard MAA-MBAA polymerization reaction with initiator: (a) 0s, (b) 26 min, (c) 45 min, (d) 64 min (e) 83 min (f) 102 min (g) 120 min (h) 139 min)
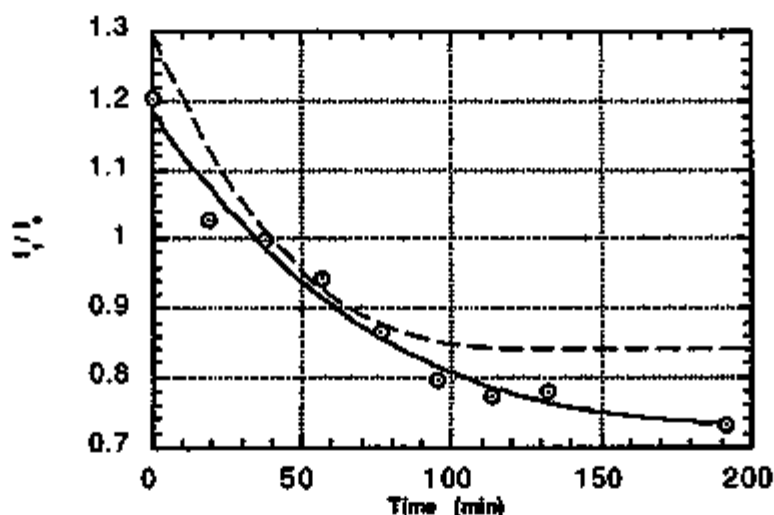
Fig. 5. Solid line is experimental plot of ratio of intensities of polymerizing MAA-MBAA (I_1)to uninitiated MAA-MBAA (I_0) vs. time derived from images in Fig. 7. Dashed line is theoretical plot of image intensity according to Eq. 4.

The intensity variation corresponds to that resulting from a simple spherical domain with an exterior sink. For the material to be inhomogeneous, the magnetization or intensity decay can be expected to be a composite sum of two exponentials. The intensity-vs-time plot for the MAA-MBAA system exhibits a curvature that strongly indicates an inhomogeneous system. Because the applied field M_0 is larger than the dipolar field, the shape of the decay of this spin-lattice relaxation depends on the small-scale morphology of the inhomogeneities. For spin diffusion into a sink,

$$M(t) = I(t) = \frac{2a^3}{\pi} \sum_{n=1}^{\infty} \frac{1}{2} \exp\left\{ -\left[K\left(\frac{n\pi}{a}\right)^2 + \frac{1}{T_1} \right] t \right\}, \tag{1}$$

where a is the atomic radius and K is a normalization constant.

Because the magnetization is directly related to the spin-echo intensity, it is possible to correlate the intensity obtained from the images to the magnetization. Considering that the fast inversion recovery pulse sequence was employed to determine T_1, the peak intensity as a function of time t can be written as

$$M(t) = M_o\left[1+e^{-\Delta/T_1}\right]e^{-t/T_1} \tag{2}$$

where M_0 is a normalization constant, D is the delay time, T_1 is the spin-lattice relaxation time, and the total delay time is the sum of the individual delays. More accurately, the intensity variation can be verified by using the inversion recovery sequence and the variation in the spin-lattice and the spin-spin relaxation times as a basis for calculation of the image intensities in each voxel. For the standard inversion recovery NMR pulse technique employed to measure T_1, the images were analyzed to relate the signal intensity to T_1 and the spin-spin relaxation time T_2. The signal intensity is

$$S \propto \rho e^{-\tau/T_2}\left[1-\left(1+e^{-\tau/T_2}\right)\right]\left[2e^{\tau/2T_1}-1\right]e^{-T_1/T_1}+e^{-\tau/T_2}\left[2e^{\tau/2T_1}-1\right]e^{-t_{tot}/T_1}, \tag{3}$$

where the recovery process is inspected with a 90° pulse applied at time T_1 following the inversion and t_{tot} is the total recovery time. Taking $T_2 \gg t$,

$$S \propto \left[2e^{\tau/2T_1}-1\right]\left[\rho e^{-T_1/T_1}+e^{-t_{tot}/T_1}\right] \tag{4}$$

This relationship shows the codependency of T_1 with the intensity of the obtained images. The dashed line in Fig. 5 is the plot of the intensity vs. time according to Eq. 4 for corresponding values of T_1. The decrease in intensity corresponds with the images shown in Fig. 4 and the intensity variation (solid line) shown in Fig. 5. The theoretical fit according to Eq. 4 breaks down with further passage of time because of the assumption $T_2 \gg t$. Because this assumption is valid only for high values of T_2 and therefore high values of T_1, a better fit can be obtained if T_2 is considered in the fitting analysis. Because this paper is restricted to variation of T_1, the T_2 values were not determined experimentally. Nevertheless, the above analysis demonstrates the capabilities and varying information that can be obtained with NMR imaging techniques. Equation 3 can be used to separately verify the spin-spin relaxation times T_2 if the intensities of the images and T_1 are known.

In the future, T_2 values will be determined and the fitting analysis recomputed to understand the differences between Eqs. 3 and 4. Additional studies are being conducted on the MAA-MBAA system as a function of reaction extent and temperature, and as a function of the concentration of individual reactants. This information is expected to provide details on molecular correlation times, sample viscosity, and reaction kinetics. Also, the nonaqueous organic gel systems that involve the addition of solid particles to the copolymer premix of MAA-MBAA will be imaged and the concentration differences will be analyzed to understand how the main quantity of comonomers becomes involved in the polymerization process.

Status of Milestones

Milestones are on schedule.

Trips/Communications/Visits

None.

Problems Encountered

Increased number of users on the system have limited the amount of time available on the NMR system in the Chemistry Building. A new NMR and imaging system has arrived at the Energy Technology Division and will be completely functional by the end of November.

MILESTONE SCHEDULE (3.5.1.6)

Phase 3:   Spectroscopy and Imaging of Gel-Cast Ceramic Components:

3.5.1.6.11   Complete spectroscopic studies of two gel systems.
Completed   11/15/93

3.5.1.6.12   Perform initial imaging studies on specimens
composed of the most appropriate gel system.
Completed   4/15/94

3.5.1.6.13   Complete real-time imaging studies of the
gelation process on specimens composed of the
most appropriate gel system. **Completed**   9/15/94

3.5.1.6.14   Report the conclusions of imaging studies of
as-cast, prefired, and fired components.   2/30/95

3.5.1.6.15   Submit topical report on application of NMR
to gel-cast ceramic processing.   5/15/95

4.0 TECHNOLOGY TRANSFER

4.1 TECHNOLOGY TRANSFER

4.1.1 Technology Transfer

Technology Transfer
D. R. Johnson (Oak Ridge National Laboratory)

Technology transfer in the Ceramic Technology Project is accomplished by a number of mechanisms including the following:

Trade Shows - A portable display describing the program has been built and has been used at numerous national and international trade shows and technical meetings.

Newsletter - A Ceramic Technology Newsletter is published regularly and sent to a large distribution.

Reports - Semiannual technical reports, which include contributions by all participants in the program, are published and sent to a large distribution. Informal bimonthly management and technical reports are distributed to the participants in the program. Open-literature reports are required of all research and development participants.

Direct Assistance - Direct assistance is provided to subcontractors in the program via access to unique characterization and testing facilities at the Oak Ridge National Laboratory.

Workshops - Topical workshops are held on subjects of vital concern to the ceramics community.

International Cooperation - This program is actively involved in and supportive of the cooperative work being done by researchers in West Germany, Sweden, the United States, Japan, and, most recently, Belgium under an agreement with the International Energy Agency. This effort is ultimately aimed at development of international standards and includes physical, morphological, and micro-structural characterization of ceramic powders and dense ceramic bodies, and mechanical characterization of dense ceramics.

IEA ANNEX II Management
V. J. Tennery (Oak Ridge National Laboratory)

Objective/scope

The purpose of this task is to organize, assist, and facilitate international research cooperation on the characterization of advanced structural ceramic materials. A major objective of this research is the evolution of measurement standards. This task, which is managed in the United States by ORNL, now includes a formal IEA Annex agreement identified as Annex II between the United States, Germany, Sweden, and Japan. The original annex included four subtasks: (1) information exchange, (2) ceramic powder characterization, (3) ceramic chemical and physical characterization, and (4) ceramic mechanical property measurements. In the United States, a total of 13 industrial and government laboratories have participated and contributed their resources to this research. The research in Subtasks 2, 3, and 4 is now complete. During CY 1990, agreements were reached for Japan to join the Annex, and for research in two new subtasks to be initiated. These included Subtask 5, Tensile and Flexural Properties of Ceramics, and Subtask 6, Advanced Ceramic Powder Characterization. The research in Subtasks 5 and 6 is now complete, and the reports have been distributed. In 1993, Belgium applied for membership in Annex II, and in 1994, the Executive Committee voted in favor of Belgium's membership. In addition, the Executive Committee has applied for an extension of Annex II to June 30, 1997, and this along with Belgium's membership has been submitted to the IEA in Paris, France, for final approval. Two new tasks, Subtask 7, on Ceramic Machining, and Subtask 8, on Ceramic Powder Characterization, were proposed in late FY 1993 and have now been accepted by all member countries; research is presently ongoing.

The next Executive Committee meeting will be held on October 21, 1994, in Mol, Belgium, in conjunction with the Ceramic Matrix Composites Conference, October 18-20, 1994, in Mons, Belgium.

Technical Highlights

Subtask 7, Machining Effects on Strength of Structural Ceramics

Minutes from the Subtask 7, IEA Annex II, Working Group Meeting held in Indianapolis, Indiana, on April 25, 1994, were sent to the international participants. Thomas Hollstein, Germany, could not attend (he supplied information from Germany by fax). The meeting agenda covered the following points: machining, flexure testing, strain gaging, fractography, billet exchange, specimen exchange, reporting, and time schedule.

Dr. Mizuno described the need for performing a fractography "round robin" in the first phase of Subtask 7, in order to provide researchers in each country with a common reference for the later fractography work in this task. The plan presented by Dr. Mizuno included Japan, Sweden, and the United States, each mounting 10 fractured specimens on a scanning electron microscopy (SEM) mount and with each participating country, including Germany and Belgium, performing fractography on the same specimens in turn. The fractography round-robin exercise was initiated, and the exercise is continuing. The U.S. silicon nitride (GS-44) specimens for the fractography analysis were mounted, and fractography was performed at ORNL. The specimen was then forwarded to Sweden

on June 17, 1994. Japan sent their specimen holder with 10 fractured specimens of SN-1 silicon nitride mounted on it to the United States (June 28, 1994). Fractographic analysis was performed at ORNL, and the specimens were forwarded to Sweden on July 8, 1994. Sweden will, in turn, forward both of these specimen sets to Germany. Japan forwarded the Swedish set of 10 fractured AC Cerama hot-isotatically pressed (HIPed) silicon nitride specimens mounted on an SEM holder (September 12, 1994). Fractography of this specimen set is presently ongoing at ORNL. Japan Fine Ceramics Center (JFCC) forwarded their results from the study of the U.S. fractography set (September 19, 1994). The results of the fractography study and other results will be compared at the upcoming technical meeting in Belgium (October 21, 1994). Two billets of AC Cerama AB silicon nitride and machining instructions were received in the United States from Sweden on June 23, 1994.

United States

Subtask 7

A summary of the results of the strength measurements of the five silicon nitrides evaluated for use was sent to the U.S. participants (April 4, 1994).

Work on the statistical experimental design for the Phase I machining parameter study on the instrumented grinder to be performed at the High Temperature Materials Laboratory (HTML) was initiated. Important independent and dependent variables have been identified, and a central composite design was selected. This design allows analysis of both main effects and interactions between the factors plus providing replication. Results from this work will form the basis for the specimen grinding to be done in the HTML by the U.S. participating teams. This is the first large-scale central composite design to be used for silicon nitride machining as far as we are aware.

Fourteen billets of GS-44 silicon nitride were received at ORNL on June 8, 1994, from AlliedSignal Ceramic Components. Final shipment of the GS-44 billets was received at ORNL on September 15, 1994. Upon receipt, the billets were inspected, measured, and photographed. Preliminary machining of the billets was initiated immediately; the top and bottom surfaces were trued by machining. Each billet was sliced into four quarters with approximate dimensions of 50 x 90 x 3.5 mm, and the sliced central surface was ground. From each quarter billet, 20 flexure specimens are being machined, with the experimental surface being cross machined for the flexure geometry before the specimens are sliced into flexure bars. In this manner, consistent measurements of the grinding forces for the tensile surfaces can be obtained for the experimental surface. The experimental surfaces of the 17 experimental runs in the statistical design have been completed. Data from the machining process have been collected, and a preliminary analysis of normal force data has been initiated. After the experimental surfaces were machined, each quarter billet was sliced into approximately 4-mm-wide flexure bars. After slicing, the flexure bars were machined longitudinally on the sides to bring the size of the bars to within the tolerances of the ASTM 1161 standard. Lastly, the flexure bars were chamfered according to ASTM 1161. All machining in these stages has been performed on the instrumented HARIG Grinder in the HTML. Presently, 90% of the flexure bars in the 17 experimental runs (a total of 340 specimens) are complete.

The main variables of the experiments are diamond grit size, grinding wheel rim speed, and depth of cut. The design required these to be used at three levels. The layout has one replicate, i.e., sets of 20 flexure bars will be manufactured first, the results analyzed, and then the entire matrix will be repeated to produce a set of 10 flexure bars such that there will be 30 flexure bars measured at each condition (needed for higher certainty in the Weibull m). During the experiment, the machining forces, acoustic emission, and spindle horsepower are continuously measured. After machining, the surface roughness and the room-temperature flexure strength and Weibull parameters are estimated using maximum likelihood estimation methods. Correlation is then made between the machining parameters and the mechanical properties.

Several other machining parameters are monitored but kept constant throughout the experiment (table speed, coolant flow, and coolant type). The grinding wheels are, with the exception for the grit size, all of the same type, i.e., the diamond type (DN, high friability), resin bond (type R), and a diamond concentration of 100. Several of the wheels have been trued such that their OD varies less than ± 0.004 mm around the circumference. The table speed has been optimized and will be kept constant at about 200 mm/s. Grinding of the first set of experimental surfaces is under way.

The completed flexure bars have been labeled and their dimensions measured and recorded. Four specimens in each completed set have been measured for surface roughness on the Rodenstock Laser Profilometer. When all flexure bars (340) are completed, the sets will be fractured in a fully randomized set. A study of the accuracy of the Rodenstock Laser Profilometer has been completed. Roughness standards were used to calibrate the instrument, and also analysis of machined and indented surfaces was performed. The results show that the Rodenstock profilometer produces a good representation of the machined surface at a vertical scale of a few micrometers to several micrometers.

Two flexure bars have been sent to HiTec Corporation for application of strain gages (September 22, 1994). Ten strain gages will be applied to each, and these specimens will be used to check the alignment of the flexure fixture before, during, and after flexure strength measurements of each set, similar to what was done in Subtask 5.

A technical working group meeting is scheduled to be held at the time of the Executive Committee meeting in Belgium on October 21, 1994.

Subtask 8, Ceramic Powder Characterization

Major responsibility for this subtask in the United States is at the National Institute of Standards and Technology (NIST), and a detailed report of progress on this subtask is provided in the section of this report submitted by NIST.

The primary activities during this period were preparing samples and conducting a U.S. participants meeting. By the end of May 1994, all six powders to be studied in this subtask had been received. Four out of the six powders have been homogenized in a cone blender. Each powder is a primary lot of 25 kg. From the primary lot, 1-kg samples have been prepared. The remaining powders will be prepared at a later stage. Some of the 1-kg samples were further divided. This task is about 50% complete for two of the four powders. In addition, we have tested a spray drying procedure for alumina

powder. The procedure and concentration of the binders was developed at NIST. All six powders have gone through homogenization, and large samples have been prepared. Further sub-division of these samples to 50 g has been completed for three powders. In addition, we have conducted studies to evaluate binder compositions for some of these powders. Based on these studies, a common composition has been developed for all powders except aluminum nitride. This composition of the binder is not the best, or optimum, for all powders. However, our purpose is to be able to produce homogeneous distribution of the known composition of binder components and to produce relatively good quality (nearly spherical, low amount of agglomerates, relatively high flowability, etc.) of the agglomerates. Spray drying of alumina, silicon nitride SNT, silicon nitride GP, silicon carbide, and zirconia powders was completed at NIRO Inc. in Columbia, Maryland. Most of the remaining activity in this area is on subdividing the powders for samples preparation. We are working diligently to meet the November 1994 target for mailing the samples to participants.

The U.S. participants of Subtask 8 met at NIST during May 18-19, 1994, to review and finalize procedures for analysis of powders. The participants had received from NIST a package of procedures which were developed at NIST and submitted by participants in the five countries. In most cases, we had very few choices to select procedures; however, the major task was to clarify the available procedures and develop questions for technical leaders to address. In addition, we studied the participation list for each procedure and ensured that a minimum level of participation exists for each. As a result, we had to request that some of the participants accept additional analyses. After the review of these procedures by the technical leaders in June 1994, the participants will have a second chance to provide input during August and September. A meeting of the technical leaders was held at NIST on June 6 and 7, 1994. Drs. George Nietfeld, M. Naito, R. Pompe, and R. Gillison attended the meeting. The purpose of this meeting was to review procedures and decide on one procedure for each measurement method. Consensus was reached on all procedures, though a number of them lacked details. One of the current activities at NIST has been to address the remaining details. We are continuing our efforts to test each procedure and identify sources of error. A draft version (No. 3) ["Compilation of Procedures -Primary and Secondary Properties of Ceramic Powders," IEA Annex 2, Subtask 8, Version 3 (DRAFT) by Subhas G. Malghan, NIST; Contributors: L.-S. H. Lum, NIST; R. Pompe, SCI, Sweden; M. Naito, JFCC, Japan; G. Nietfeld, HC Starck, Germany; and J. Erauw, VITO, Belgium; August 1, 1994] of the procedure compilation was sent to all participants to obtain their comments. The compilation contains approximately 20 new procedures for secondary properties of powders and 10 revised procedures for primary properties of powders. The participants in Japan held a meeting to consolidate their input, and consolidated review was sent to Dr. Naito, Japan's Technical Leader for Subtask 8. Responses have also been received from other participants in the United States, Germany, and Belgium. Currently, we are incorporating these comments in the procedures. A meeting of the technical leaders is scheduled in conjunction with that of the IEA Executive Committee in Belgium. The technical leaders will review the procedures and develop comments to be addressed at NIST. Therefore, a final review of the procedures is planned at NIST in November 1994.

Status of Milestones - Milestone 411516 (complete machining of specimens was changed from June 30, 1994, to October 31, 1994 - due to receiving the billets from the vendor late). Also, Milestone 411517 has been changed to March 1, 1995, since the previous item has caused the schedule to change. Other milestones are on schedule.

<u>Communications/Visits/Travel</u> - V. J. Tennery and Kristin Breder attended a working group meeting for the international participants held in conjunction with the American Ceramic Society 96th Annual Meeting, April 24-28, 1994, Indianapolis, Indiana, to discuss Subtask 7.

<u>Publications and Presentations</u> - None.

Characterization of Ceramic Powders
S. G. Malghan and L.-S. Lum
(National Institute of Standards and Technology)

Objective/Scope

Ceramics have been successfully employed in engines on a demonstration basis. The successful manufacture and use of ceramics in advanced engines depends on the development of reliable materials that will withstand high, rapidly varying thermal stress loads. Improvement in the characterization of ceramic starting powders is a critical factor in achieving reliable ceramic materials for engine applications. The production and utilization of such powders require characterization methods and property standards for quality assurance.

The objectives of the NIST program are: (1) to assist with the division and distribution of ceramic starting powders for an international round-robin on powder characterization; (2) to provide reliable data on physical (dimensional), chemical and phase characteristics of powders; and (3) to conduct statistical assessment, analysis and modeling of round-robin data. This program is directed toward a critical assessment of powder characterization methodology and toward establishment of a basis for the evaluation of fine powder precursors for ceramic processing. This work will examine and compare by a variety of statistical means the various measurement methodologies employed in the round-robin and the correlations among the various parameters and characteristics evaluated. The results of the round-robin are expected to provide the basis for identifying measurements for which Standard Reference Materials are needed and to provide property and statistical data which will serve the development of internationally accepted standards.

Technical Progress

The primary activities during this period were preparation of samples and procedures, and holding meetings to finalize procedures. Four out of the six powders have been homogenized in a cone blender. Each powder has a primary lot of 25.0 kg. From the primary lot, 1.0 kg samples were prepared. Some of the 1.00 kg samples were further divided. This task is about 90% complete.

One of the tasks is to distribute spray dried powders for preparation of green bodies and testing of procedures for green body evaluation. However, we would like as complete as possible information on the contents of the spray dried powders. Where possible, we will obtain commercially available powders. In certain cases, it is not possible to obtain information such as the type and concentration of sintering aids and binders. In such cases, we have decided to prepare spray dried powders with known type and concentration of binders. To accomplish this task, we have developed a system containing a polyethylene alcohol binder and a polyvinyl glycol lubricant. This system was tested for its suitability to produce spray dried powders

having a particle size distribution of d_{50} in the range of 50 micrometers. The spray drying of powders was conducted at a contract laboratory.

In addition, we have conducted studies to evaluate binder compositions for some of these powders. Based on these studies, a common composition has been developed for all powders except aluminum nitride. This composition of the binder is not the best or optimum for all powders. However, our purpose is to be able to produce homogeneous distribution of the known composition of binder components, and produce relatively good quality (nearly spherical, low amount of hard agglomerates, relatively high flowability, etc.) of agglomerates. Spray drying of alumina, silicon nitride SNT, silicon nitride GP, and silicon carbide powders was carried out at NIRO Inc. in Columbia, Maryland. A batch of spray dried aluminum nitride powder has been provide by Dow Chemical Company. This powder has been spray dried in non-aqueous medium to prevent oxidation.

The samples preparation process is continuing at a rapid pace. At present, 50.0 g samples of non-spray dried alumina, silicon nitride SNT, silicon nitride GP, and silicon carbide have been prepared. The samples from aluminum nitride and zirconia will be completed in the next two weeks. The spray drying of all powders except zirconia and aluminum nitride was only 2.0 kg from a 10.0 kg batch. This quantity is less than that needed for completion of the task. In addition, the zirconia powder could not be spray dried because the contractor ran out of time and work had to disscontributed to accommodate prior commitments of the spray drying facility. Therefore, currently we are trying to purchase additional SNT silicon nitride powder and spray dry both powders in the next few weeks.

The US participants of Subtask 8 met at NIST during May 18-19, 1994 to review and finalize procedures for analysis of powders. The participants had received from NIST a package of procedures which were developed at NIST and submitted by participants in the five countries. In most cases, we had very few choices to select procedures; however, the major task was to clarify the available procedures and develop questions for technical leaders to address. In addition, we studied the participation list for each procedure and assured that a minimum level of participation exists for each. As a result, we had to request some of the participants to accept additional analysis. After the review of these procedures by the technical leaders in June, the participants had a second chance to provide input during August and September.

A meeting of the technical leaders was held at NIST on June 6 and 7. Drs. George Nietfeld, M. Naito, R. Pompe, and R. Gillison attended the meeting. The purpose of this meeting was to review procedures and decide on one porcedure for each measurement method. Consensus was reached on all procedures, though a number of them lacked details. One of the major activities at NIST has been to address the remaining details. We continued our efforts to test each procedure and identify sources of error. The improved procedures were sent to participants in

all five countries to seek their input. At the next meeting of the technical leaders on October 17, 1994 in Belgium, these inputs will be reviewed and the final set of procedures will be prepared.

A draft version 3 of the procedure compilation was sent to participants in August for their review. We received comments from a significant number of participants. A number of these comments were related to requesting for additional information on the proposed steps in the procedures. The responses to these comments and additional improvements to the procedures are being incorporated. A revised version 4 of the procedure compilation was prepared for distribution to the participants. A meeting of the technical leaders is scheduled in Belgium on October 20th to review these procedures and provide final comments.

At the ASTM meeting in Montreal, Canada in June, the status of draft standards under C-28.05 Powders Characterization sub-committee was reviewed. One procedure on specific surface area has passed the final society ballot, the second draft on centrifugal sedimentation has passed the main committee ballot. The remaining two--one on gravity sedimentation for particle size distribution and the second on surface area by physical adsorption of gas--required additional improvements. Subsequent to the meeting, revisions were made and resubmitted for subcommittee ballot. We expect these to pass the final society ballot this year. That should bring the total to four standards adopted by ASTM.

In addition, we will start drafting other procedures from the IEA Subtask 6 compilation for submission to ASTM.

Status of Milestones
    On target.

Publications/Presentations

Variances in the Measurement of Ceramic Powder Properties, R. G. Munro, S. G. Malghan and S. M. Hsu, accepted by NIST Journal of Research, August 1994.

Communications/Visits

    None

Ceramic Mechanical Property Test Method Development
George D. Quinn
(National Institute of Standards and Technology)

Objective/Scope

This task is to develop mechanical test method standards in support of the Ceramic Technology Project and Advanced Turbine Technology Applications Programs. Test method development should meet the needs of the DOE engine community but should also consider the general USA structural ceramics community as well as foreign laboratories and companies. Emphasis will be placed on the needs of the DOE community.

Draft recommendations for practices or procedures shall be developed based upon the needs identified above and circulated within the DOE ceramics heat engine community for review and modification. Round-robins will be conducted as necessary, but shall be well-focussed, limited in scope and not interfere with ongoing IEA round-robins. Procedures developed in this program will be advanced for final standardization by ASTM or by the U.S. Army as possible MIL STD's.

Technical Highlights and Results

Earlier work in this project has contributed to the following completed standards:

1. ASTM C 1198-91 "Dynamic Young's Modulus, Shear Modulus, and Poisson's Ratio for Advanced Ceramics by Sonic Resonance," by S. Gonczy, Allied-Signal; G. Quinn, NIST; and J. Helfinstine, Corning.

2. ASTM C 1161-90 "Standard Test Method for Flexural Strength of Advanced Ceramics at Ambient Temperature," G. Quinn, NIST.

3. ASTM C 1211-92 "Standard Test Method for Flexural Strength of Advanced Ceramic at Elevated Temperature," by G. Quinn in cooperation with Mr. M. Foley, Norton; Mr. T. Richerson, Allied-Signal; and Dr. M. Ferber, ORNL.

4. MIL HDBK 790 "Fractography and Characterization of Fracture Origins in Advanced Structural Ceramics," with J. Swab and M. Slavin, U. S. Army, ARL.

5. ASTM C 1239-94a "Standard Practice for Reporting Strength Data and Estimating Weibull Distribution Parameters," by S. Duffy, NASA-Lewis; G. Quinn, NIST; and C. Johnson, G.E.

Weibull Analysis

The document: "Reporting Uniaxial Strength Data and Estimating Weibull Distribution Parameters for Advanced Ceramics," by S. Duffy, G. Quinn, and C. Johnson was adopted as an ASTM standard practice and designated C 1239. During this six month period, a few minor revisions were made to the standard. The revisions were approved by ballot and the revised standard has been designated C 1239-94a.

Also during this period, we received information regarding a draft Weibull analysis standard being prepared in Europe for CEN Technical Committee TC 184. The European standard seems to have been influenced by the ASTM work, but is limited to unimodal distributions. It uses the Maximum Likelihood Estimates for the Weibull parameters in much the same fashion as in C 1239. The same ranking estimator, and the same unbiasing and confidence bound factors are used. This is most gratifying and it now appears that the CEN and ASTM standards will be

very complementary. For unimodal, two-parameter strength distributions, the standards will produce the identical Weibull parameter estimates.

An innovation in the European standard is the inclusion (as an option) of polynomial expressions for the confidence bounds and unbiasing factors. The 4th order polynomials which express the factors as a function of sample size are amenable to simple spreadsheet or program analysis.

Fracture Toughness

Standardization of fracture toughness testing continues. Professor Isa Bar-on of Worcester Polytechnic Institute is now the overall coordinator of this activity as well as the C-28/E-8 committee liaison.

Work in this task has focussed on the surface crack in flexure (SCF) method (Figure 1) which is one of the three leading candidates for ASTM standardization. In the previous semiannual report, the primary results of the VAMAS 20 laboratory international round robin exercise were presented. The results were sufficiently favorable that it was decided that the SCF method warranted standardization. During this 6 months period, an intensive effort was made to document fully the results of the round robin. A comprehensive final report was published as VAMAS Report #17: "Fracture Toughness of Advanced Ceramics by the Surface Crack in Flexure Method: A VAMAS Round Robin," by Quinn, Kübler, and Gettings. Summary papers were presented at the Engineering Ceramics Meeting of the American Ceramic Society Cocoa Beach Meeting in January 1994, as well as at the 8th World Ceramics Congress (CIMTEC) conference in Florence, Italy in June 1994. A presentation was also made at the ASTM C-28 meeting at Cocoa Beach in January.

A complete rewrite of the SCF portion of the draft ASTM standard was prepared in May 1994, immediately prior to the C-28 meeting in Montreal, Canada. In addition, a list of symbols for the entire document was prepared as well as a number of revisions to the main body of the document. Unfortunately, none of these new elements were added or revisions made to the document and there was no input from the other task group members.

Hardness

Work continued at NIST on developing hardness standards for advanced ceramics. This is a two pronged program. There is an effort performed under this task to prepare ASTM Knoop and Vickers standard test methods. In addition, there is a separate NIST program to develop two standard reference materials (SRM's) for which the hardness values are certified.

All preliminary work on the NIST SRM program has been completed. A Kennametal tungsten carbide was selected for the Vickers SRM and Cerbec NBD-200 hipped silicon nitride as a Knoop SRM as shown in Figure 3. A nine laboratory international round robin was organized, conducted, and the results analyzed and documented during this 6 month period. The exercise was completely successful. NIST is scheduled to prepare 100 production SRM's each of the Vickers and Knoop ceramic SRM's in FY 1995.

In this CTAHE task, work was done to prepare the draft ASTM standards. Two preliminary hardness standards were written and presented to committee C-28 for evaluation. The responses were favorable and prompted us to prepare two draft

KNOOP INDENTATION - "TILT"

Use a 1/2° tilt on all specimens in this round robin. We recommend that a shim be used to support a simple platform that the specimen rests flat on. If you put a shim directly under the specimen, be careful that the specimen does not rock or move during the indentation.
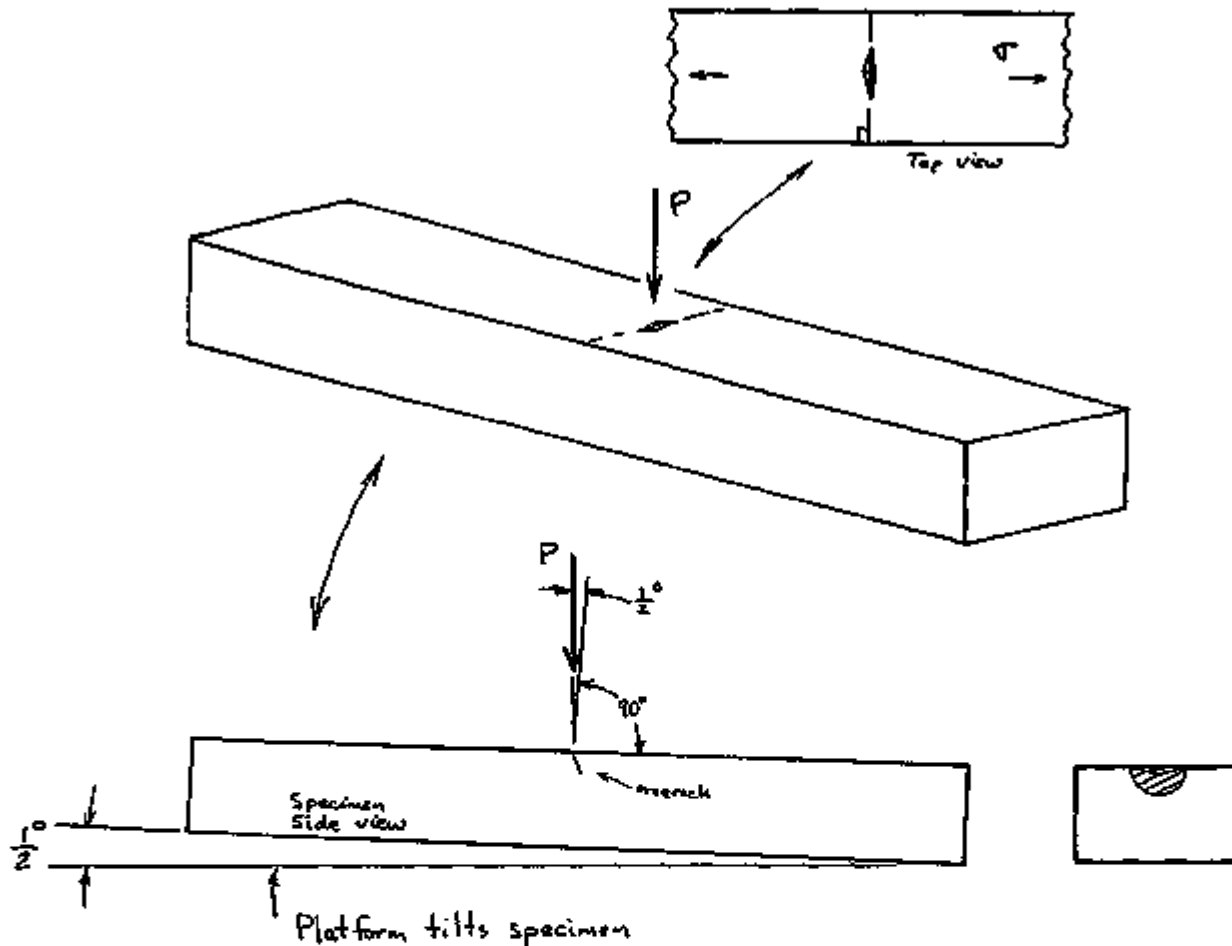
The $\frac{1}{2}^\circ$ tilt will cause the precrack to go in at an angle from $\frac{1}{2}^\circ$ - 5°. The stress intensity factor Y is not affected very much by such small tilt angles.

This technique is very useful since the precrack is at a slightly different angle than the final fracture surface. With low angle incident lighting, the difference in surfaces can be detected more easily. The different reflectivity can also help in ordinary microscopes or on an SEM. Note, even on specimens which are indented flat (without a tilt), sometimes the crack is a little off perpendicular which helps them to be detected.
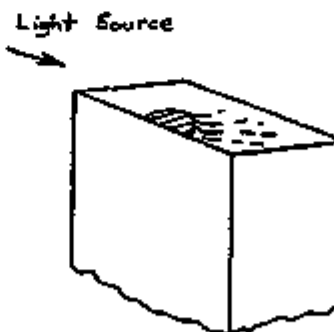
Figure 1   Schematic illustrating the surface crack in flexure (SCF) method for determination of fracture toughness. A Knoop indenter is used to create a semielliptical surface crack in a flexure bar. The fracture toughness is computed from the fracture strength and the size of the precrack.

SURFACE CRACK IN FLEXURE (SCF) METHOD

ADVANTAGES

* A simple flexure specimen is used.

* Conventional flexure test fixtures are used.

* Precrack size and shape can be controlled.

* The stress intensity shape factors are well-defined and can be controlled.

* Fracture toughness is measured at a microstructural level.

* Accurate and precise results are possible.
    $$K_{Ic} = Y \sigma \sqrt{a}$$

* Fractography is required.

DISADVANTAGES

* Precracking is a two or three step process:
    indent, lap or polish, (dye penetrate?).

* Some preliminary work may be needed to find a suitable indentation load.

* Fractographic analysis is required.

* The method does not work on all materials.

Figure 2 Advantages and disadvantages of the SCF method for fracture toughness determination.
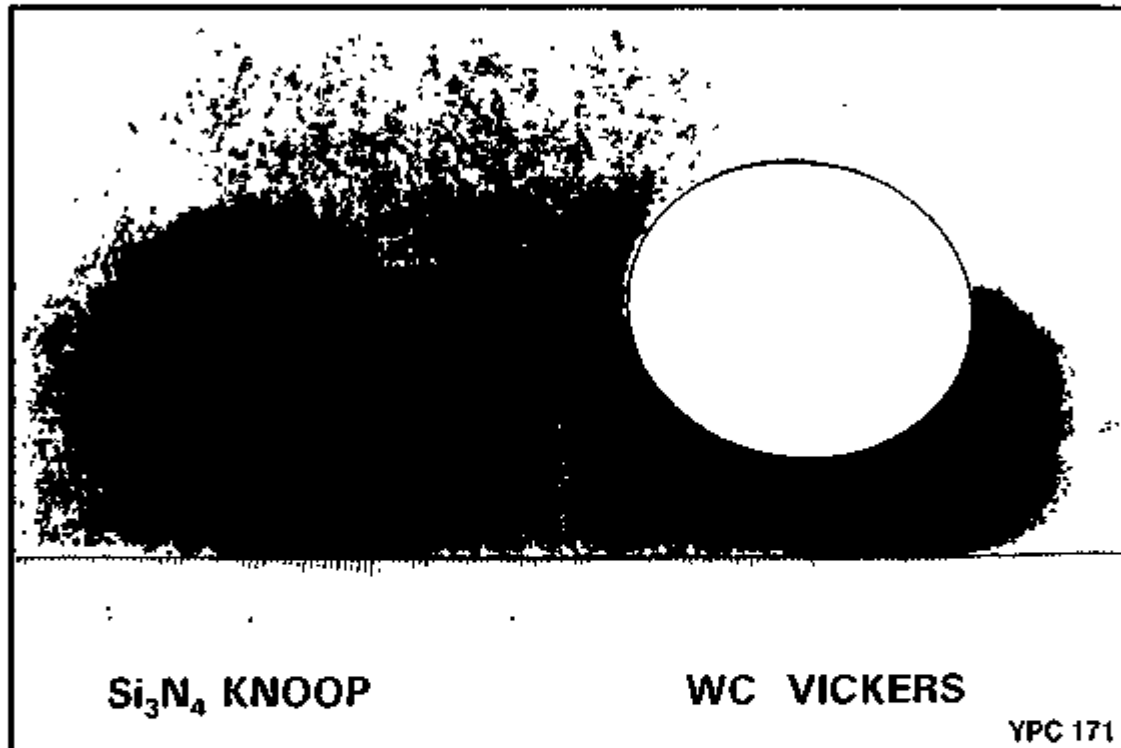
Figure 3 Prototype hardness standard reference materials. The silicon nitride disk will have 2 kg Knoop indentations that have been measured with a calibrated scanning electron microscope. The tungsten carbide disk will have 1 kg Vickers indentations, also measured by calibrated SEM.

standards for ballot. The results of the round robin on the prototype SRM's were used to prepare the precision and bias statements. In early 1994, we participated in a round robin organized by the German Materials Testing Office (MPA) in Dortmund, Germany. Six German ceramics were Knoop indented. We also took the opportunity to make some Vickers indentations in the same specimens for comparison. The Vickers indents were more heavily cracked in most specimens, making readings more difficult. A number of ceramics from the United States were tested at NIST using the draft procedures and it was determined that additional stipulations as to what constitute acceptable indentations had to be written into the draft standards. Figure 4 illustrates some of the criteria that will be used to specify the acceptability of Vickers indents. The Knoop standard will recommend the use of 2 kg load, but will allow the use of a 1 kg load. Figure 5 illustrates the approximate sizes of indents that will be created by the 2 and 1 kg loads.

The draft C-28 Knoop and Vickers standards were submitted to ASTM C-28 for a subcommittee C28.01 ballot. This ballot has been completed with one negative as well as a number of constructive comments from several balloters for each standard. These issues will be presented to the subcommittee at the next C-28 meeting in January 1995. It is anticipated that the documents will be reballoted early in 1995 in a concurrent main and subcommittee ballot.

Finally, we have noted with some consternation the increasing confusion in the ceramics literature over the correct formula to use to compute Vickers hardness. The *conventional, worldwide-adopted and standardized* formula is:

$$H_v = 1.854 \ P/d^2 \tag{1}$$

where H_v is the Vickers hardness (kg/mm^2 or GPa)
P   is the indentation load (kg or N)
d   is the indentation diagonal size (mm or m)

This formula represents the applied load divided by the idealized *contact area of the indenter*. The contact area is the area of contact of the four diamond pyramidal faces when in contact with the specimen at full load. Unfortunately, it has become fashionable in the ceramics indentation fracture community to compute an alternative, so-called "pressure hardness":

$$H = 2.0 \ P/d^2 \tag{2}$$

This is the hardness defined as load divided by the "projected surface contact area" of the indentation. This latter is the area that the indent impression makes as viewed (projected) on the specimen top surface. There is no fundamental reason why equation 2 is superior to equation 1. Some people in the ceramics indentation fracture community have used equation 2 in their work. (The alternative definition is used often in models of fracture associated with stress fields underneath indents. Equation 2 implies that the indenter applies a uniform pressure or stress over the indent area, but this is physically unreasonable. In any case, the fracture mechanics models and derivations inevitably roll up a group of constants into some overall "calibration constant" and it is a pity that the conventional definition of Vickers hardness was not used when contriving these models.) The difference in computed hardness is $2.0/1.854 = 7.9\%$ This is not a trivial difference and has caused the ceramics literature to be infested with contradictory and confusing hardness numbers. The

ACCEPTABLE INDENTATIONS

bowed edges

Porosity

UNACCEPTABLE INDENTATIONS

large tip
cracks

asymmetrical

spalled edges

tip region
displaced

chipping and
ragged edges

ragged edges
(grain displacement
pullouts)

Pore at tip
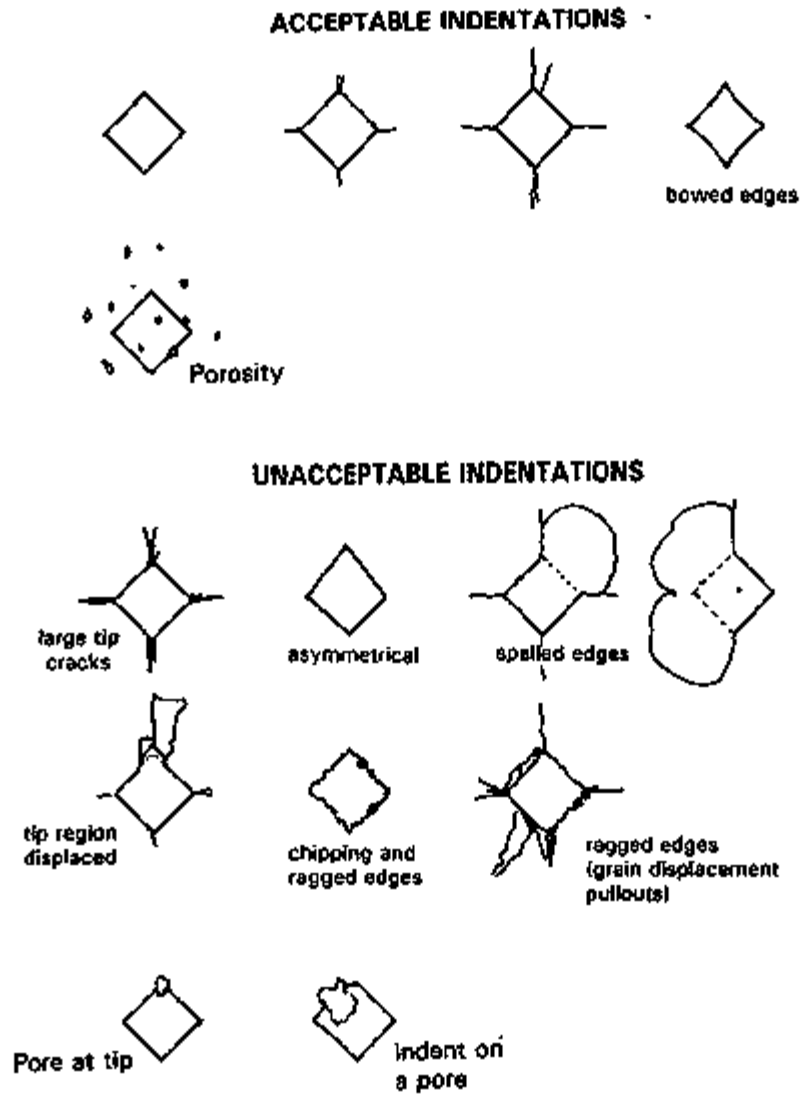
indent on
a pore

Figure 4   The Vickers draft standard includes criteria for the acceptability
            of Vickers indents.

**COMPARATIVE INDENTATION SIZES
FOR THE THREE ASTM KNOOP STANDARDS**

ASTM C-730	ASTM C-849	C-XXXX
Knoop Hardness of Glasses	Knoop Hardness of Ceramic Whitewares	Knoop Hardness of Advanced Ceramics
__100 g__	__1000 g__ (or less if cracking)	__Load Options:__
HKN 470-540	HKN 500-800	HKN 1000 - 2000

55 - 51 μm

168 - 133 μm

2 kg   168 - 119 μm

e.g.: S_3N_4 with HKN = 1450,

d = 140 μm

1 kg   119 - 84 μm

e.g.: S_3N_4 with HKN = 1450,

d = 99 μm

Figure 5   The Knoop standard for advanced ceramics will specify a 2 kg indentation load, with 1 kg as an option. The sizes of the indents at these loads in a silicon nitride are shown, as well as typical indent sizes for whitewares and glasses.

same confusion exists in the fracture toughness results reported by indentation methods. (The use of the wrong hardness leads to fracture toughness errors of 4% in the indentation fracture method, and 1% in the indentation strength method.)

In summary, *every standard test method (ASTM, ISO, DIN, etc) in the world that we are aware of uses equation 1 for computation of Vickers hardness*. There is no compelling reason why equation 2 is more fundamental or correct. Each formula is arbitrary, but equation 1 is the *worldwide consensus standard*.

Fractography
During this 6 months period, intensive work was done to adapt MIL HDBK 790, "Standard Practice for Characterizing Fracture Origins Limiting Defects in Advanced Structural Ceramics" into ASTM format as "Standard Practice for Fractography and Characterization of Fracture Origins in Advanced Ceramics." This work is a collaboration between G. Quinn of NIST and J. Swab of U. S. Army Research Laboratory (ARL).

A seventeen laboratory fractography round-robin that was organized under the auspices of the VAMAS collaboration has been completed. Emphasis was on the detection and characterization of machining damage, the detection and characterization of material processing related flaws, and fractographic techniques and analysis. The round-robin included the examination of photos and specimens. The exercise concluded in November 1993 and several months were spent in analyzing and documenting the results. A comprehensive report has been prepared as VAMAS Technical Report #19. A draft of this report has been reviewed by the participants and the U.S. ARL and NIST are in the process of making final revisions to the report. Summaries of the principal findings have been presented at ASTM C-28, VAMAS TWA #3, and American Ceramic Society meetings at Cocoa Beach in January 1994, at the C-28 meeting in Montreal, and at the 8th World Ceramics Congress (CIMTEC) in Florence, Italy.

Overall, the participants felt that the guidelines in the MIL HBK were adequate for characterization of fracture origins. Figure 6 illustrates the flaw characterization scheme that was used. There were a number of examples where the round robin participants were in general agreement on the flaw characterization, but an equal number of instances where there were sharp divergences. For example, most participants had no trouble in finding and identifying porosity flaws. In contrast, there was considerable variation in the characterization of machining damage.

Specifics are given in the final report, which is comprehensive and rather lengthy. This report should be available by late 1994. One key finding was that participants often did not use all of the available information in the assessment of the fracture origin. For example, many participants simply looked at the fracture surfaces and ignored the background information furnished with each specimen. (This was a single 3 or 4 sentence paragraph with strength fracture toughness, and material preparation or testing history.) Also, participants often looked at only one fracture half. If it was the specimen with the agglomerate origin, then it was pot luck whether they inspected the half with the agglomerate, or the half with a matching hole. In the latter instance, the participant was apt to characterize the origin as a pore. This was incorrect. Only a few participants made any effort to relate the observed origin size to

FLAW CHARACTERIZATION
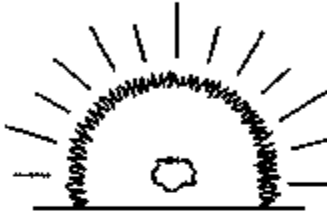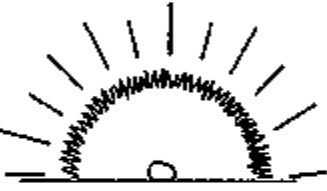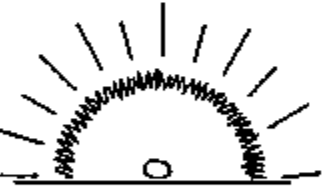
Specimen	1. Identity	2. Location	3. Size
#17	PORE VOLUME DIST.	VOLUME	~ 40 μm Diameter
#18	PORE VOLUME DIST.	SURFACE	~ 50 μm Diameter
#19	MACHINING DAMAGE SURFACE DIST.	SURFACE	~ 20 μm Deep × ~ 60 μm Long
#20	PORE VOLUME DIST.	NEAR SURFACE	~ 35μm Diameter
#21	LARGE GRAIN VOLUME DIST.	VOLUME	~ 20 μm × ~ 50 μm

Figure 6   Illustration of the flaw characterization scheme incorporated in the draft ASTM fractography standard practice.

fracture mechanics estimates. This should be a routine step to verify that a feature has been designated correctly as the strength-limiting flaw.

In brief, we learned that an experienced fractographer integrates all of the available information to make an evaluation as illustrated in Figure 7. The mixed successes that we had from the round robin respondents caused us to consider the intuitive, expert system procedures that a fractographer uses. We are now able to describe them more clearly. The new ASTM draft standard practice has benefitted a great deal from this experience round robin. This document has been prepared and sent to ASTM for a Subcommittee C28.05 (Characterization) ballot in November 1994.

Other Activities

Flexure strength of Referceram, a Japanese "Open Material" was evaluated by four-point flexure in accordance with ASTM standard test method C 1161 as well as by JIS R 1601. The "Open Materials" are intended to serve as stable, uniform materials that can be used in support of material standardization studies. We obtained a plate of Referceram alumina and fractured the specimens by the two standard methods in order to see if the results would be comparable. The results, illustrated in Figure 8, show that there is a systematic difference in the flexure strengths as measured by the two methods, but *neither set* gives an average flexure strength of 350 MPa as cited by the documentation accompanying the material. Further analysis of these results and fractographic analysis is planned.

A detailed review was made of a draft standard for "C" ring testing that Dr. Al. Segall of Penn State prepared for C-28 ballot.

Status of Milestones

412119   Prepare draft fractography standard for ASTM Committee C-28 (with U.S. ARL)
            Completed Oct 1994

All other milestones are on schedule.

Publications/Presentations

1.   G. Quinn, R. Gettings, and J. Kübler, "Fracture Toughness by the Surface Crack in Flexure (SCF) Method: Results of the VAMAS Round Robin," Ceram. Eng. and Sci. Proc., Vol. 15, 1994, pp. 846-855.

2.   J. J. Swab, and G. Quinn, "Results of a Round Robin Exercise on the Fractography of Advanced Structural Ceramics," idem, pp. 867-876.

3.   G. Quinn, J. Kübler, and R. Gettings, "Fracture Toughness of Advanced Ceramics: A New VAMAS Round Robin," to be publ. in Proceedings of the 8th World Ceramics Congress, CIMTEC, Florence, Italy, June 1994.

4.   J. Swab and G. Quinn, "Fractography and Characterization of Fracture Origins in Advanced Ceramics: A VAMAS Round Robin," idem.

General Crack Patterns

**Mating Halves of the
Primary Fracture Surface**

**Fracture
Mechanics
(K$_{Ic}$, Mirror Size)**

FRACTURE ORIGIN

**Background
Information**
(Processing,
Microstructure, exposure,
specimen preparation, test
conditions)

**Other Specimens
or Components**

**Other Surfaces of
the Specimen
or Component**
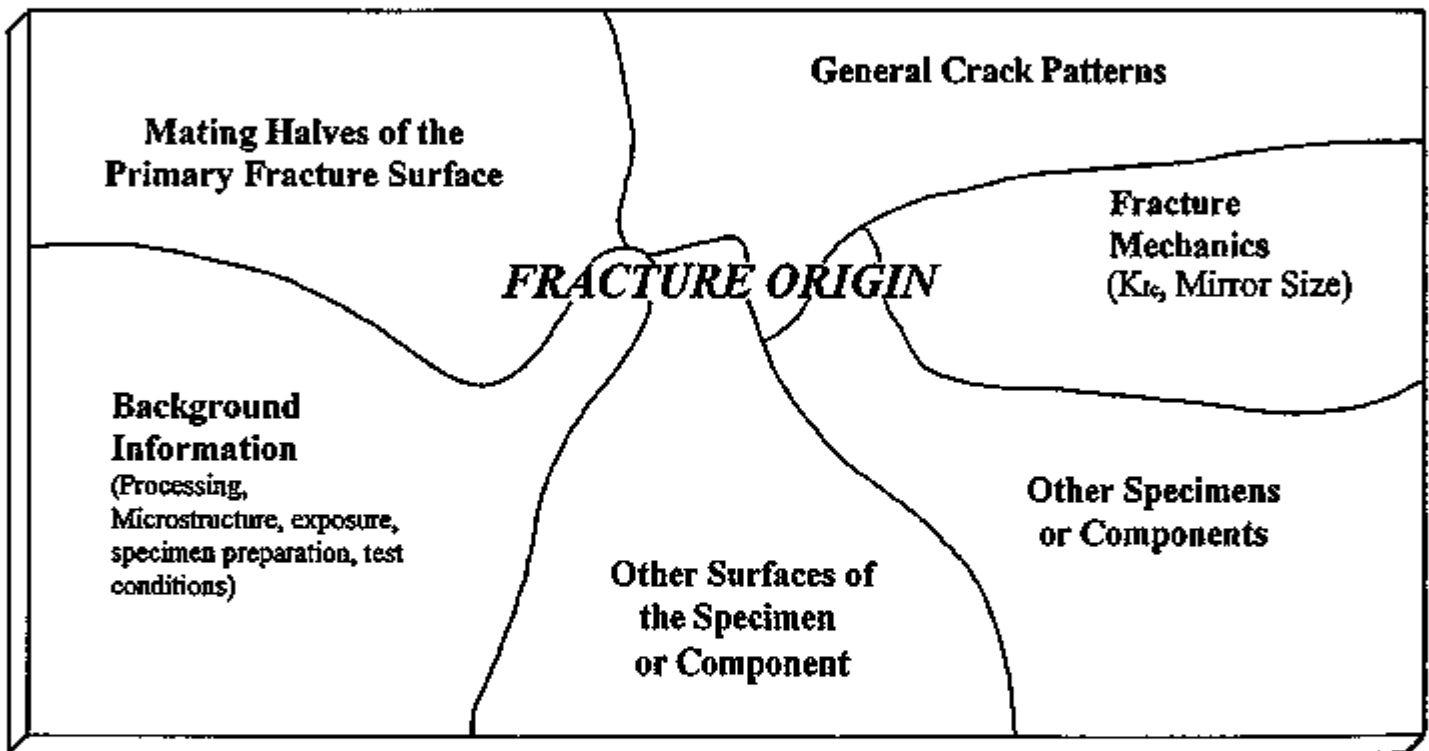
Figure 7   Fractographers must integrate all available information to make a
proper evaluation of a fracture origin in advanced ceramics.

REFERCERAM alumina
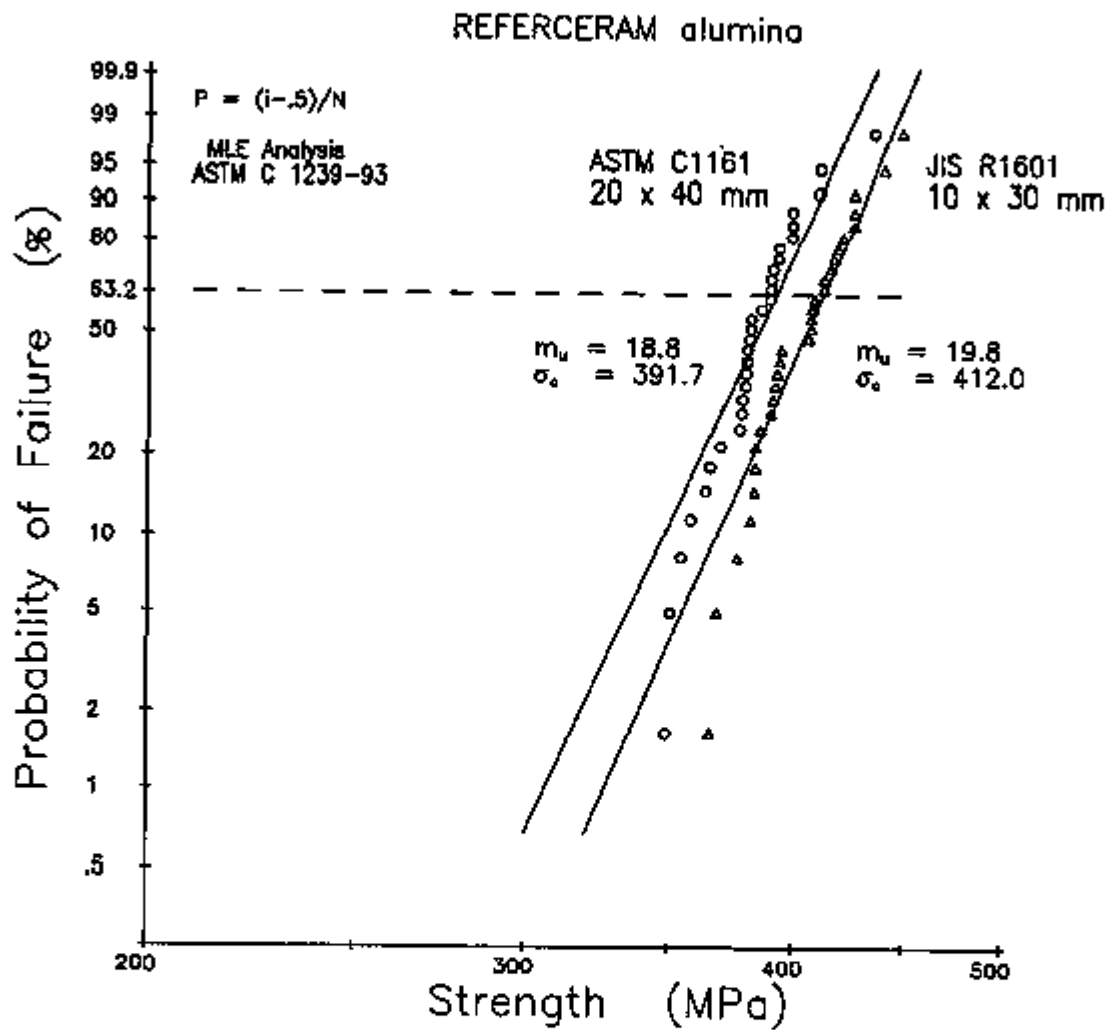
Figure 8   The four-point flexure strength of "Referceram" alumina as measured by JIS R1601 and C 1161. Weibull maximum likelihood parameter estimates are in accordance with ASTM C 1239, assuming a unimodal flaw population. Neither set of data agrees with the reported 350 MPa flexure strength for this material.

5. G. Quinn, J. Kübler, and R. Gettings, "Fracture Toughness of Advanced Ceramics by the Surface Crack in Flexure (SCF) Method: A VAMAS Round Robin," VAMAS Technical Report #17, NIST, June 1994.

Communications/Visits

1. G. Quinn and R. Gettings attended the ASTM C-28 meeting in Montreal in June 1994.

2. G. Quinn attended the 8th World Ceramic Congress, CIMTEC, in Florence, Italy in June 1994. The Italian Ceramics Research Center, CIRTEC in Faenza was visited. While there, Mr. Quinn encountered a meeting of the European CEN Technical Committee 184, Working Area #4, Ceramic Composites. An appeal was made for better cooperation between CEN and ASTM C-28 in matters of standard development.

3. A number of conversations were held with key personnel regarding the new ISO (International Standard Organization) Committee on Fine Ceramics, the secretariat for which is held by Japan. Mr. Edward Anderson of Alcoa will be the overall USA C-28 representative in ISO TC 206. G. Quinn was appointed by the ISO TC 206 steering committee as Convener of Working Group #2, flexure strength testing at room temperature. This was approved by C-28 in Montreal. G. Quinn was also designated by C-28 as the USA representative in ISO TC 206, Working Group #3, Hardness.

INTERNAL DISTRIBUTION

Central Research Library (2)
Document Reference Section
Laboratory Records Department (2)
Laboratory Records, ORNL RC
ORNL Patent Section
M&C Records Office (3)
L. F. Allard, Jr.
L. D. Armstrong
D. L. Balltrip
R. L. Beatty
P. F. Becher
T. M. Besmann
P. J. Blau
E. E. Bloom
R. A. Bradley
K. Breder
C. R. Brinkman
V. R. Bullington
H. Cai
G. M. Caton
S. J. Chang
D. D. Conger
R. H. Cooper, Jr.
S. A. David
J. H. DeVan
J. L. Ding
M. K. Ferber
R. L. Graves
D. L. Greene
H. W. Hayden, Jr.

E. E. Hoffman
C. R. Hubbard
M. A. Janney
D. R. Johnson (5)
F. W. Jones
R. R. Judkins
M. A. Karnitz
B. L. Keyes
H. D. Kimrey, Jr.
K. C. Liu
E. L. Long, Jr.
W. D. Manly
R. W. McClung
D. J. McGuire
J. R. Merriman
T. A. Nolan
A. E. Pasto
K. P. Plucknett
M. H. Rawlins
G. V. Rogers, Jr.
M. L. Santella
A. C. Schaffhauser
S. Scott
E. J. Soderstrom
D. P. Stinton
R. W. Swindeman
T. N. Tiegs
B. H. West
S. G. Winslow
J. M. Wyrick

EXTERNAL DISTRIBUTION

Pioneering Research Info. Ctr.
E.I. Dupont de Nemours & Co. Inc.
Experimental Station
P.O. Box 80302
Wilmington DE 19880-0302

Jeffrey Abboud
U.S. Advanced Ceramics Assoc.
1600 Wilson Blvd., Suite 1008
Arlington VA 22209

James H. Adair
University of Florida
Materials Science & Engineering
317 MAE Bldg.
Gainesville FL 32611-2066

Donald F. Adams
University of Wyoming
Mechanical Engineering Department
P.O. Box 3295
Laramie WY 82071

Andrzej Aeamski
Materials Conversion Group
236-B Egidi Drive
Wheeling IL 60090

Jalees Ahmad
AdTech Systems Research Inc.
Solid Mechanics
1342 N. Fairfield Road
Dayton OH 45432-2698

Yoshio Akimune
NISSAN Motor Co., Ltd.
Materials Research Laboratory
1 Natsushima-Cho
Yokosuka 237
JAPAN

Mufit Akinc
Iowa State University
322 Spedding Hall
Ames IA 50011

Ilhan A. Aksay
Princeton University
A313 Engineering Quadrangle
Princeton NJ 08544-5263

Charles Aldridge
Heany Industries, Inc.
249 Briarwood Lane
Scottsville NY 14546

Joseph E. Amaral
Instron Corporation
Corporate Engineering Office
100 Royale Street
Canton MA 02021

Edward M. Anderson
Aluminum Company of America
N. American Industrial Chemical
P.O. Box 300
Bauxite AR 72011

Norman C. Anderson
Ceradyne, Inc.
Ceramic-to-Metal Division
3169 Redhill Avenue
Costa Mesa CA 92626

Don Anson
BCL
Thermal Power Systems
505 King Avenue
Columbus OH 43201-2693

Thomas Arbanas
G.B.C. Materials Corporation
580 Monastery Drive
Latrobe PA 15650-2698

Frank Armatis
3M Company
Building 60-1N-01
St. Paul MN 55144-1000

Everett B. Arnold
Detroit Diesel Corporation
Mechanical Systems Technology
13400 Outer Drive West
Detroit MI 48239-4001

Bertil Aronsson
Sandvik AB
S-12680
Stockholm Lerkrogsvagen 19
SWEDEN

Dennis Assanis
University of Michigan
Dept. of Mechanical Engineering
321 W.E. Lay, N.C.
Ann Arbor MI 48109

V. S. Avva
North Carolina A&T State Univ.
Dept. of Mechanical Engineering
Greensboro NC 27411

Patrick Badgley
Sky Technologies, Inc.
2815 Franklin Drive
Columbus IN 47201

Sunggi Baik
Pohang Institute of Sci. & Tech.
P.O. Box 125
Pohang 790-600
KOREA

John M. Bailey
Consultant
Caterpillar, Inc.
P.O. Box 1875
Peoria IL 61656-1875

Bob Baker
Ceradyne, Inc.
3169 Redhill Avenue
Costa Mesa CA 92626

Frank Baker
Aluminum Company of America
Alcoa Technical Center
Alcoa Center PA 15069

Clifford P. Ballard
AlliedSignal Aerospace Company
Ceramics Program
P.O. Box 1021
Morristown NJ 07962-1021

B. P. Bandyopadhyay
ELID Team
Wako Campus
2-1 Hirosawa Wako-shi
Saitama 351-01
JAPAN

P. M. Barnard
Ruston Gas Turbines Limited
P.O. Box 1
Lincoln LN2 5DJ
ENGLAND

Harold N. Barr
Hittman Corporation
9190 Red Branch Road
Columbia MD 21045

Renald D. Bartoe
Vesuvius McDanel
510 Ninth Avenue
Box 560
Beaver Falls PA 15010-0560

David L. Baty
Babcock & Wilcox - LRC
P.O. Box 11165
Lynchburg VA 24506-1165

Donald F. Baxter, Jr.
ASM International
Advanced Materials & Processes
Materials Park OH 44073-0002

M. Brad Beardsley
Caterpillar Inc.
Technical Center Bldg. E
P.O. Box 1875
Peoria IL 61656-1875

John C. Bell
Shell Research Limited
Thornton Research Centre
P.O. Box 1
Chester CH1 3SH
ENGLAND

M. Bentele
Xamag, Inc.
259 Melville Avenue
Fairfield CT 06430

Larry D. Bentsen
BFGoodrich Company
R&D Center
9921 Brecksville Road
Brecksville OH 44141

Tom Bernecki
Northwestern University
1801 Maple Avenue
Evanston IL 60201-3135

Charles F. Bersch
Institute for Defense Analyses
1801 N. Beauregard Street
Alexandria VA 22311

Ram Bhatt
NASA Lewis Research Center
21000 Brookpark Road
Cleveland OH 44135

Deane I. Biehler
Caterpillar Inc.
Engineering Research Materials
P.O. Box 1875, Bldg. E
Peoria IL 61656-1875

John W. Bjerklie
Consolidated Natural Gas Service
 Co. Inc.
Research Department
Pittsburgh PA 15222-3199

William D. Bjorndahl
TRW, Inc.
One Space Park, MS:R6-2188
Building 01, Room 2040
Redondo Beach CA 90278

Keith A. Blakely
Advanced Refractory Technologies,
 Inc.
699 Hertel Avenue
Buffalo NY 14207

Edward G. Blanchard
Netzsch Inc.
119 Pickering Way
Exton PA 19341

Bruce Boardman
Deere and Company Technical Ctr.
3300 River Drive
Moline IL 61265

Lawrence P. Boesch
EER Systems Corp.
1593 Spring Hill Road
Vienna VA 22182-2239

Donald H. Boone
Boone & Associates
2412 Cascade Drive
Walnut Creek CA 94598-4313

Tom Booth
AlliedSignal, Inc.
AiResearch Los Angeles Division
2525 West 190th Street
Torrance CA 90509-2960

Raj Bordia
University of Washington
Roberts Hall
Box 35212
Seattle WA 98195-2120

Tibor Bornemisza
Energy Technologies Applications,
 Inc.
5064 Caminito Vista Lujo
San Diego CA 92130-2846

J.A.M. Boulet
University of Tennessee
Engineering Science and Mechanics
Knoxville TN 37996-2030

Leslie J. Bowen
Materials Systems
53 Hillcrest Road
Concord MA 01742

Steven C. Boyce
Air Force Office of Scientific
 Research
AFOSR/NA Bldg. 410
Bolling AFB DC 20332-6448

Gary L. Boyd
Ceramic Engineering Consulting
328 Sneath Way
Alpine CA 91901

Steve Bradley
UOP Research Center
50 E. Algonquin Road
Des Plaines IL 60017-6187

Michael C. Brands
Cummins Engine Company, Inc.
P.O. Box 3005, Mail Code 50179
Columbus IN 47201

Raymond J. Bratton
Westinghouse Science & Technology
1310 Beulah Road
Pittsburgh PA 15235

John J. Brennan
United Technologies Corporation
Silver Lane, MS:24
East Hartford CT 06108

Terrence K. Brog
Golden Technologies Company
4545 McIntyre Street
Golden CO 80403

Gunnar Broman
317 Fairlane Drive
Spartanburg SC 29302

Alan Brown
P.O. Box 882
Dayton NJ 08810

Jesse J. Brown
VPI & SU
Ctr. for Advanced Ceram Materials
Blacksburg VA 24061-0256

Sherman D. Brown
University of Illinois
Materials Science and Engineering
105 South Goodwin Avenue
Urbana IL 61801

S. L. Bruner
Ceramatec, Inc.
2425 South 900 West
Salt Lake City UT 84119

Walter Bryzik
U.S. Army Tank Automotive Command
R&D Center, Propulsion Systems
Warren MI 48397-5000

S. J. Burden
2572 Devonwood
Troy MI 48098

Curt V. Burkland
AMERCOM, Inc.
8928 Fullbright Avenue
Chatsworth CA 91311

Bill Bustamante
AMERCOM, Inc.
8928 Fullbright Avenue
Chatsworth CA 91311

Oral Buyukozturk
Massachusetts Institute of
 Technology
77 Massachusetts Ave., Room 1-280
Cambridge MA 02139

David A. Caillet
Ethyl Corporation
451 Florida Street
Baton Rouge La 70801

Roger Cannon
Rutgers University
P.O. Box 909
Piscataway NJ 08855-0909

Scott Cannon
P.O. Box 567254
Atlanta GA 30356

Harry W. Carpenter
1844 Fuerte Street
Fallbrook CA 92028

David Carruthers
Kyocera Industrial Ceramics
 Company
P.O. Box 2279
Vancouver WA 98668-2279

Calvin H. Carter, Jr.
Cree Research, Inc.
2810 Meridian Parkway
Durham NC 27713

J. David Casey
35 Atlantis Street
West Roxbury MA 02132

Jere G. Castor
J. C. Enterprise
5078 N. 83rd Street
Scottsdale AZ 85250

James D. Cawley
Case Western Reserve University
Materials Science & Engineering
Cleveland OH 44106

Thomas C. Chadwick
Den-Mat Corporation
P.O. Box 1729
Santa Maria CA 93456

Ronald H. Chand
Chand Kare Technical Ceramics
2 Coppage Drive
Worcester MA 01603-1252

Robert E. Chaney
EG&G Idaho, Inc.
Idaho National Engineering Lab
P.O. Box 1625
Idaho Falls ID 83415-3525

Frank C. Chang
U.S. Army Materials Technology
AMTL-EMM
405 Arsenal Street
Watertown MA 02172

Nam S. Chang
Chrysler Corporation
12000 Chrysler Drive
Highland Park MI 48288-0001

William Chapman
Williams International Corp.
2280 W. Maple Road
Walled Lake MI 48390-0200

Ching-Fong Chen
LECO Corporation
3000 Lakeview Avenue
St. Joseph MI 49085

Frank Childs
EG&G Idaho, Inc.
Idaho National Engineering Lab
P.O. Box 1625
Idaho Falls ID 83415-3527

William J. Chmura
Torrington Company
59 Field Street
Torrington CT 06790-4942

Tsu-Wei Chou
University of Delaware
201 Spencer Laboratory
Newark DE 19716

R. J. Christopher
Ricardo Consulting Engineers
Bridge Works
Shoreham-By-Sea W. Sussex BN435FG
ENGLAND

Joel P. Clark
Massachusetts Institute of
  Technology
Room 8-409
Cambridge MA 02139

Giorgio Clarotti
Commission of the European Comm
DGXII-C3, MO75, 1-53;
  200 Rue de la Loi
B-1049 Brussels
BELGIUM

W. J. Clegg
ICI Advanced Materials
P.O. Box 11, The Heath
Runcorn Cheshire WA7 4QE
ENGLAND

William S. Coblenz
Adv. Research Projects Agency
3701 N. Fairfax Drive
Arlington VA 22203

Gloria M. Collins
ASTM
1916 Race Street
Philadelphia PA 19103

William C. Connors
Sundstrand Aviation Operations
Materials Science & Engineering
4747 Harrison Avenue
Rockford IL 61125-7002

John A. Coppola
Carborundum Company
Niagara Falls R&D Center
P.O. Box 832
Niagara Falls NY 14302

Normand D. Corbin
Norton Company
SGNICC/NRDC
Goddard Road
Northboro MA 01532-1545

Douglas Corey
AlliedSignal, Inc.
2525 West 190th Street, MS:T52
Torrance CA 90504-6099

Keith P. Costello
Chand/Kare Technical Ceramics
2 Coppage Drive
Worcester MA 01603-1252

Ed L. Courtright
Pacific Northwest Laboratory
MS:K3-59
Richland WA 99352

Anna Cox
Mitchell Market Reports
P.O. Box 23
Monmouth Gwent NP5 4YG
UNITED KINGDOM

J. Wesley Cox
BIRL
1801 Maple Avenue
Evanston IL 60201-3135

Art Cozens
Instron Corporation
3414 Snowden Avenue
Long Beach CA 90808

Mark Crawford
New Technology Week
4604 Monterey Drive
Annandale VA 22003

Richard A. Cree
Markets & Products, Inc.
P.O. Box 14328
Columbus OH 43214-0328

Les Crittenden
Vesuvius McDanel
Box 560
Beaver Falls PA 15010

William J. Croft
U.S. Army Materials Technology
405 Arsenal Street
Watertown MA 02172

M. J. Cronin
Mechanical Technology, Inc.
968 Albany-Shaker Road
Latham NY 12110

Gary M. Crosbie
Ford Motor Company
20000 Rotunda Drive
MD-2313, SRL Building
Dearborn MI 48121-2053

Floyd W. Crouse, Jr.
U.S. Department of Energy
Morgantown Energy Technology Ctr
P.O. Box 880
Morgantown WV 26505

John Cuccio
AlliedSignal Engines
P.O. Box 52180, MS:1302-2Q
Phoenix AZ 85072-2180

Raymond A. Cutler
Ceramatec, Inc.
2425 South 900 West
Salt Lake City UT 84119

Stephen C. Danforth
Rutgers University
P.O. Box 909
Piscataway NJ 08855-0909

Sankar Das Gupta
Electrofuel Manufacturing Co.
9 Hanna Avenue
Toronto Ontario MGK-1W8
CANADA

Frank Davis
AlliedSignal Aerospace Company
7550 Lucerne Drive, #203
Middleburg Heights OH 44130

Robert F. Davis
North Carolina State University
Materials Engineering Department
P.O. Box 7907
Raleigh NC 27695

George C. DeBell
Ford Motor Company
Scientific Research Lab
P.O. Box 2053, Room S2023
Dearborn MI 48121-2053

Michael DeLuca
RSA Research Group
1534 Claas Ave.
Holbrook NY 11741

Gerald L. DePoorter
Colorado School of Mines
Metallurgical & Materials Engr
Golden CO 80401   .

J. F. DeRidder
Omni Electro Motive, Inc.
12 Seely Hill Road
Newfield NY 14867

Nick C. Dellow
Materials Technology Publications
40 Sotheron Road
Watford Herts WD1 2QA
UNITED KINGDOM

L. R. Dharani
University of Missouri-Rolla
224 M.E.
Rolla MO 65401

Douglas A. Dickerson
Union Carbide Specialty Powders
1555 Main Street
Indianapolis IN 46224

John Dodsworth
Vesuvius Research & Development
Technical Ceramics Group
Box 560
Beaver Falls PA 15010

B. Dogan
Institut fur Werkstofforschung
GKSS-Forschungszentrum Geesthacht
Max-Planck-Strasse
D-2054 Geesthacht
GERMANY

Alan Dragoo
U.S. Department of Energy
ER-131, MS:F-240
Washington DC 20817

Jean-Marie Drapier
FN Moteurs S.A.
Material and Processing
B-4041 Milmort (Herstal)
BELGIUM

Kenneth C. Dreitlein
United Technologies Research Ctr
Silver Lane
East Hartford CT 06108

Robin A.L. Drew
McGill University
3450 University Street
Montreal Quebec H3A 2A7
CANADA

Winston H. Duckworth
BCL
Columbus Division
505 King Avenue
Columbus OH 43201-2693

Bill Durako
Materials Engineering, Inc.
P.O. Box 43
Virgil IL 60182

Ernest J. Duwell
3M Abrasive Systems Division
3M Center
St. Paul MN 55144-1000

Chuck J. Dziedzic
GTC Process Forming Systems
4545 McIntyre Street
Golden CO 80403

Robert J. Eagan
Sandia National Laboratories
Engineered Materials & Processes
P.O. Box 5800
Albuquerque NM 87185-5800

Jeffrey Eagleson
Lanxide Corporation
1001 Connecticut Avenue, N.W.
Washington DC 20036

Harry E. Eaton
United Technologies Corporation
Silver Lane
East Hartford CT 06108

Harvill C. Eaton
Louisiana State University
240 Thomas Boyd Hall
Baton Rouge LA 70803

Christopher A. Ebel
Carborundum Company
Technology Division
P.O. Box 832
Niagara Falls NY 14302-0832

J. J. Eberhardt
U.S. Department of Energy
Office of Transportation Matrl's
CE-34, Forrestal Building
Washington DC 20585

Jim Edler
Eaton Corporation
26201 Northwestern Highway
P.O. Box 766
Southfield MI 48037

G. A. Eisman
Dow Chemical Company
Ceramics and Advanced Materials
52 Building
Midland MI 48667

William A. Ellingson
Argonne National Laboratory
Energy Technology Division
9700 S. Cass Avenue
Argonne IL 60439

Anita Kaye M. Ellis
Machined Ceramics
629 N. Graham Street
Bowling Green KY 42101

Glen B. Engle
Nuclear & Aerospace Materials
16716 Martincoit Road
Poway CA 92064

Jeff Epstein
Ceramic Technologies, Inc.
12739 Ashford Knoll
Houston TX 77082

Kenneth A. Epstein
Dow Chemical Company
2030 Building
Midland MI 48674

Art Erdemir
Argonne National Laboratory
9700 S. Cass Avenue
Argonne IL 60439

E. M. Erwin
Lubrizol Corporation
17710 Riverside Drive
Lakewood OH 44107

John N. Eustis
U.S. Department of Energy
Industrial Energy Efficiency Div
CE-221, Forrestal Building
Washington DC 20585

W. L. Everitt
Kyocera International, Inc.
8611 Balboa Avenue
San Diego CA 92123

Gordon Q. Evison
332 S. Michigan Avenue
Suite 1730
Chicago IL 60604

John W. Fairbanks
U.S. Department of Energy
Office of Propulsion Systems
CE-322, Forrestal Building
Washington DC 20585

Tim Fawcett
Dow Chemical Company
Advanced Ceramics Laboratory
1776 Building
Midland MI 48674

Robert W. Fawley
Sundstrand Power Systems
Div. of Sundstrand Corporation
P.O. Box 85757
San Diego CA 92186-5757

Jeff T. Fenton
Vista Chemical Company
900 Threadneedle
Houston TX 77079

Larry Ferrell
Babcock & Wilcox
Old Forest Road
Lynchburg VA 24505

Raymond R. Fessler
BIRL
1801 Maple Avenue
Evanston IL 60201

Ross F. Firestone
Ross Firestone Company
188 Mary Street
Winnetka IL 60093-1520

Sharon L. Fletcher
Arthur D. Little, Inc.
15 Acorn Park
Cambridge MA 02140-2390

Michael Foley
Norton Company
Goddard Road
Northboro MA 01532-2527

Thomas F. Foltz
Textron Specialty Materials
2 Industrial Avenue
Lowell MA 01851

Renee G. Ford
Materials and Processing Report
P.O. Box 72
Harrison NY 10528

John Formica
Supermaterials
2020 Lakeside Avenue
Cleveland OH 44114

Edwin Frame
Southwest Research Institute
P.O. Drawer 28510
San Antonio TX 78284

Armanet Francois
French Scientific Mission
4101 Reservoir Road, N.W.
Washington DC 20007-2176

R. G. Frank
Technology Assessment Group
10793 Bentley Pass Lane
Loveland OH 45140

David J. Franus
Forecast International
22 Commerce Road
Newtown CT 06470

Marc R. Freedman
NASA Lewis Research Center
21000 Brookpark Road, MS:49-3
Cleveland OH 44135

Douglas Freitag
Bayside Materials Technology
17 Rocky Glen Court
Brookeville MD 20833

Brian R.T. Frost
Argonne National Laboratory
9700 S. Cass Avenue, Bldg. 900
Argonne IL 60439

Lawrence R. Frost
Instron Corporation
100 Royall Street
Canton MA 02021

Xiren Fu
Shanghai Institute of Ceramics
1295 Ding-xi Road
Shanghai 200050
CHINA

J. P. Gallagher
University of Dayton Research
 Institute
300 College Park, JPC-250
Dayton OH 45469-0120

Garry Garvey
Golden Technologies Company Inc.
4545 McIntyre Street
Golden CO 80403

Richard Gates
NIST
Materials Bldg., A-256
Gaithersburg MD 20899

L. J. Gauckler
ETH-Zurich
Sonneggstrasse 5
CH-8092 Zurich 8092
SWITZERLAND

George E. Gazza
U.S. Army Materials Technology
Ceramics Research Division
405 Arsenal Street
Watertown MA 02172-0001

D. Gerster
CEA-DCOM
33 Rue De La Federation
Paris 75015
FRANCE

John Ghinazzi
Coors Technical Ceramics Company
1100 Commerce Park Drive
Oak Ridge TN 37830

Robert Giddings
General Electric Company
P.O. Box 8
Schenectady NY 12301

A. M. Glaeser
University of California
Lawrence Berkeley Laboratory
Hearst Mining Building
Berkeley CA 94720

Joseph W. Glatz
510 Rocksville Road
Holland PA 18966

W. M. Goldberger
Superior Graphite Company
R&D
2175 E. Broad Street
Columbus OH 43209

Allan E. Goldman
U.S. Graphite, Inc.
907 W. Outer Drive
Oak Ridge TN 37830

Stephen T. Gonczy
Allied Signal Research
P.O. Box 5016
Des Plaines IL 60017

Robert J. Gottschall
U.S. Department of Energy
ER-131, MS:G-236
Washington DC 20585

Earl Graham
Cleveland State University
Dept. of Chemical Engineering
Euclid Avenue at East 24th Street
Cleveland OH 44115

John W. Graham
Astro Met, Inc.
9974 Springfield Pike
Cincinnati OH 45215

G. A. Graves
U. of Dayton Research Institute
300 College Park
Dayton OH 45469-0001

Robert E. Green, Jr.
Johns Hopkins University
Materials Science and Engineering
Baltimore MD 21218

Alex A. Greiner
Plint & Partners
Oaklands Park
Wokingham Berkshire RG11 2FD
UNITED KINGDOM

Lance Groseclose
Allison Engine Company
P.O. Box 420, MS:W-5
Indianapolis IN 46206

Thomas J. Gross
U.S. Department of Energy
Transportation Technologies
CE-30, Forrestal Building
Washington DC 20585

Mark F. Gruninger
Union Carbide Corporation
Specialty Powder Business
1555 Main Street
Indianapolis IN 46224

Ernst Gugel
Cremer Forschungsinstitut
 GmbH&Co.KG
Oeslauer Strasse 35
D-8633 Roedental 8633
GERMANY

John P. Gyekenyesi
NASA Lewis Research Center
21000 Brookpark Road, MS:6-1
Cleveland OH 44135

Nabil S. Hakim
Detroit Diesel Corporation
13400 Outer Drive West
Detroit MI 48239

Philip J. Haley
Allison Engine Company
P.O. Box 420, MS:T12A
Indianapolis IN 46236

Judith Hall
Fiber Materials, Inc.
Biddeford Industrial Park
5 Morin Street
Biddeford ME 04005

Y. Hamano
Kyocera Industrial Ceramics Corp.
5713 E. Fourth Plain Blvd.
Vancouver WA 98661-6857

Y. Harada
IIT Research Institute
10 West 35th Street
Chicago IL 60616

Norman H. Harris
Hughes Aircraft Company
P.O. Box 800520
Saugus CA 91380-0520

Alan M. Hart
Dow Chemical Company
1776 Building
Midland MI 48674

Pat E. Hart
Battelle Pacific Northwest Labs
Ceramics and Polymers Development
P.O. Box 999
Richland WA 99352

Michael H. Haselkorn
Caterpillar In.
Technical Center, Building E
P.O. Box 1875
Peoria IL 61656-1875

Debbie Haught
U.S. Department of Energy
Off. of Transportation Materials
EE-34, Forrestal Bldg.
Washington DC 20585

N. B. Havewala
Corning Inc.
SP-PR-11
Corning NY 14831

John Haygarth
Teledyne WAA Chang Albany
P.O. Box 460
Albany OR 97321

Norman L. Hecht
U. of Dayton Research Institute
300 College Park
Dayton OH 45469-0172

Peter W. Heitman
Allison Engine Company
P.O. Box 420, MS:W-5
Indianapolis IN 46206-0420

Robert W. Hendricks
VPI & SU
210 Holden Hall
Blacksburg VA 24061-0237

Thomas P. Herbell
NASA Lewis Research Center
21000 Brookpark Road, MS:49-3
Cleveland OH 44135

Marlene Heroux
Rolls-Royce, Inc.
2849 Paces Ferry Road, Suite 450
Atlanta GA 30339-3769

Robert L. Hershey
Science Management Corporation
1255 New Hampshire Ave., N.W.
Suite 1033
Washington DC 20036

Hendrik Heystek
Bureau of Mines
Tuscaloosa Research Center
P.O. Box L
University AL 35486

Robert V. Hillery
GE Aircraft Engines
One Neumann Way, M.D. H85
Cincinnati OH 45215

Arthur Hindman
Instron Corporation
100 Royall Street
Canton MA 02021

Shinichi Hirano
Mazda R&D of North America, Inc.
1203 Woodridge Avenue
Ann Arbor MI 48105

Tommy Hiraoka
NGK Locke, Inc.
1000 Town Center
Southfield MI 48075

Fu H. Ho
General Atomics
P.O. Box 85608
San Diego CA 92186-9784

John M. Hobday
U.S. Department of Energy
Morgantown Energy Technology Ctr
P.O. Box 880
Morgantown WV 26507

Clarence Hoenig
Lawrence Livermore National Lab
P.O. Box 808, Mail Code L-369
Livermore CA 94550

Thomas Hollstein
Fraunhofer-Institut fur
 Werkstoffmechanik
Wohlerstrasse 11
D-79108 Freiburg
GERMANY

Richard Holt
National Research Council Canada
Structures and Materials Lab
Ottawa Ontario K1A OR6
CANADA

Woodie Howe
Coors Technical Ceramics Company
1100 Commerce Park Drive
Oak Ridge TN 37830

Stephen M. Hsu
NIST
Gaithersburg MD 20899

Hann S. Huang
Argonne National Laboratory
9700 S. Cass Avenue
Argonne IL 60439-4815

Gene Huber
Precision Ferrites & Ceramics
5576 Corporate Drive
Cypress CA 90630

Harold A. Huckins
Princeton Advanced Technology
4 Bertram Place
Hilton Head SC 29928

Fred R. Huettic
Advanced Magnetics Inc.
45 Corey Lane
Mendham NJ 07945

Brian K. Humphrey
Lubrizol Petroleum Chemicals Co.
3000 Town Center, Suite 1340
Southfield MI 48075-1201

Robert M. Humrick
Dylon Ceramic Technologies
3100 Edgehill Road
Cleveland Heights OH 44118

Michael S. Inoue
Kyocera International, Inc.
8611 Balboa Avenue
San Diego CA 92123-1580

Joseph C. Jackson
U.S. Advanced Ceramics Assoc.
1600 Wilson Blvd., Suite 1008
Arlington VA 22209

Osama Jadaan
U. of Wisconsin-Platteville
1 University Plaza
Platteville WI 53818

Said Jahanmir
NIST
Materials Bldg., Room A-237
Gaithersburg MD 20899

Curtis A. Johnson
General Electric Company
P.O. Box 8
Schenectady NY 12301

Sylvia Johnson
SRI International
333 Ravenswood Avenue
Menlo Park CA 94025

Thomas A. Johnson
Lanxide Corporation
P.O. Box 6077
Newark DE 19714-6077

W. S. Johnson
Indiana University
One City Centre, Suite 200
Bloomington IN 47405

Walter F. Jones
AFOSR/NA
110 Duncan Ave., Ste. B115
Washington DC 20332-0001

Jill E. Jonkouski
U.S. Department of Energy
9800 S. Cass Avenue
Argonne IL 60439-4899

L. A. Joo
Great Lakes Research Corporation
P.O. Box 1031
Elizabethton TN 37643

A. David Joseph
SPX Corporation
700 Terrace Point
Muskegon MI 49443

Adam Jostsons
Australian Nuclear Science &
 Technology
New Illawarra Road
Lucas Heightss New South Wales
AUSTRALIA

Lyle R. Kallenbach
Phillips Petroleum
Mail Drop:123AL
Bartlesville OK 74004

Nick Kamiya
Kyocera Industrial Ceramics Corp.
25 Northwest Point Blvd., #450
Elk Grove Village IL 60007

Roy Kamo
Adiabatics, Inc.
3385 Commerce Park Drive
Columbus IN 47201

Chih-Chun Kao
Industrial Technology Research
 Institute
195 Chung-Hsing Road, Sec. 4
Chutung Hsinchu 31015 R.O.C.
TAIWAN

Keith R. Karasek
AlliedSignal Aerospace Company
50 E. Algonquin Road
Des Plaines IL 60017-5016

Martha R. Kass
U.S. Department of Energy
Oak Ridge Operations
Building 4500N, MS:6269
Oak Ridge TN 37831-6269

Robert E. Kassel
Ceradyne, Inc.
3169 Redhill Avenue
Costa Mesa CA 92626

Allan Katz
Wright Laboratory
Metals and Ceramics Division
Wright-Patterson AFB OH 45433

R. Nathan Katz
Worcester Polytechnic Institute
100 Institute Road
Worcester MA 01609

Tony Kaushal
Detroit Diesel Corporation
13400 Outer Drive, West
Detroit MI 48239-4001

Ted Kawaguchi
Tokai Carbon America, Inc.
375 Park Avenue, Suite 3802
New York NY 10152

Noritsugu Kawashima
TOSHIBA Corporation
4-1 Ukishima-Cho
Kawasaki-Ku Kawasaki, 210
JAPAN

Lisa Kempfer
Penton Publishing
1100 Superior Avenue
Cleveland OH 44114-2543

Frederick L. Kennard, III
AC Rochester
1300 N. Dort Highway
Flint MI 48556

David O. Kennedy
Lester B. Knight Cast Metals Inc.
549 W. Randolph Street
Chicago IL 60661

George Keros
Photon Physics
3175 Penobscot Building
Detroit MI 48226

Thomas Ketcham
Corning, Inc.
SP-DV-I-9
Corning NY 14831

Pramod K. Khandelwal
Allison Engine Company
P.O. Box 420, MS:T10B
Indianapolis IN 46206

Jim R. Kidwell
AlliedSignal Engines
P.O. Box 52180
Phoenix AZ 85072-2180

Shin Kim
The E-Land Group
19-8 ChangJeon-dong
Mapo-gu, Seoul 121-190
KOREA

W. C. King
Mack Truck, Z-41
1999 Pennsylvania Avneue
Hagerstown MD 21740

Carol Kirkpatrick
MSE, Inc.
P.O. Box 3767
Butte MT 59702

Tony Kirn
Caterpillar Inc.
Defense Products Department, JB7
Peoria IL 61529

James D. Kiser
NASA Lewis Research Center
21000 Brookpark Road, MS:49-3
Cleveland OH 44135

Max Klein
900 24th Street, N.W., Unit G
Washington DC 20037

Richard N. Kleiner
Golden Technologies Company
4545 McIntyre Street
Golden CO 80403

Stanley J. Klima
NASA Lewis Research Center
21000 Brookpark Road, MS:6-1
Cleveland OH 44135

Albert S. Kobayashi
University of Washington
Mechanical Engineering Department
Mail Stop:FU10
Seattle WA 98195

Shigeki Kobayashi
Toyota Central Research Labs
Nagakute Aichi, 480-11
JAPAN

Richard A. Kole
Z-Tech Corporation
8 Dow Road
Bow NH 03304

Joseph A. Kovach
Eaton Corporation
32500 Chardon Road
Willoughby Hills OH 44094

Kenneth A. Kovaly
Technical Insights Inc.
P.O. Box 1304
Fort Lee NJ 07024-9967

Edwin H. Kraft
Kyocera Industrial Ceramics Corp.
5713 E. Fourth Plain Boulevard
Vancouver WA 98661

Ralph G. Kraft
Spraying Systems Company
North Avenue at Schmale Road
Wheaton IL 60189-7900

Arthur Kranish
Trends Publishing Inc.
1079 National Press Building
Washington DC 20045

A. S. Krieger
Radiation Science, Inc.
P.O. Box 293
Belmont MA 02178

Pieter Krijgsman
Ceramic Design International
 Holding B.V.
P.O. Box 68
Hattem 8050-AB
THE NETHERLANDS

Waltraud M. Kriven
University of Illinois
105 S. Goodwin Avenue
Urbana IL 61801

Edward J. Kubel, Jr.
ASM International
Advanced Materials & Processes
Materials Park OH 44073

Dave Kupperman
Argonne National Laboratory
9700 S. Cass Avenue
Argonne IL 60439

Oh-Hun Kwon
North Company
SGNICC/NRDC
Goddard Road
Northboro MA 01532-1545

W. J. Lackey
GTRI
Materials Science and Tech. Lab
Atlanta GA 30332

Jai Lala
Tenmat Ltd.
40 Somers Road
Rugby Warwickshire CV22 7DH
ENGLAND

Hari S. Lamba
General Motors Corporation
9301 West 55th Street
LaGrange IL 60525

Richard L. Landingham
Lawrence Livermore National Lab
P.O. Box 808, L-369
Livermore CA 94550

James Lankford
Southwest Research Institute
6220 Culebra Road
San Antonio TX 78228-0510

Stanley B. Lasday
Business News Publishing Co.
1910 Cochran Road, Suite 630
Pittsburgh PA 15220

S. K. Lau
Carborundum Company
Technology Division
P.O. Box 832, B-100
Niagara Falls NY 14302

J. Lawrence Lauderdale
Babcock & Wilcox
1850 "K" Street, Suite 950
Washington DC 20006

Jean F. LeCostaouec
Textron Specialty Materials
2 Industrial Avenue
Lowell MA 01851

Benson P. Lee
Technology Management, Inc.
4440 Warrensville Rd., Suite A
Cleveland OH 44128

Burtrand I. Lee
Clemson University
Olin Hall
Clemson SC 29634-0907

June-Gunn Lee
KIST
P.O. Box 131, Cheong-Ryang
Seoul 130-650
KOREA

Stan Levine
NASA Lewis Research Center
21000 Brookpark Road, MS:49-3
Cleveland OH 44135

David Lewis, III
Naval Research Laboratory
Code 6370
Washington DC 20375-5343

Ai-Kang Li
Materials Research Labs., ITRI
195-5 Chung-Hsing Road, Sec. 4
Chutung Hsinchu 31015 R.O.C.
TAIWAN

Robert H. Licht
Norton Company
SGNICC/NRDC
Goddard Road
Northboro MA 01532-1545

E. Lilley
Norton Company
SGNICC/NRDC
Goddard Road
Northboro MA 01532-1545

Chih-Kuang Lin
National Central University
Dept. of Mechanical Engineering
Chung-Li 32054
TAIWAN

Laura J. Lindberg
AlliedSignal Aerospace Company
Garrett Fluid Systems Division
P.O. Box 22200
Tempe AZ 85284-2200

Hans A. Lindner
Cremer Forschungsinstitut
 GmbH&Co.KG
Oeslauer Strasse 35
D-8633 Rodental 8866
GERMANY

Ronald E. Loehman
Sandia National Laboratories
Chemistry & Ceramics Dept. 1840
P.O. Box 5800
Albuquerque NM 87185

Bill Long
Babcock & Wilcox
P.O. Box 11165
Lynchburg VA 24506

L. A. Lott
EG&G Idaho, Inc.
Idaho National Engineering Lab
P.O. Box 1625
Idaho Falls ID 83415-2209

Raouf O. Loutfy
MER Corporation
7960 S. Kolb Road
Tucson AZ 85706

Lydia Luckevich
Ortech International
2395 Speakman Drive
Mississauga Ontario L5K 1B3
CANADA

James W. MacBeth
Carborundum Company
Structural Ceramics Division
P.O. Box 1054
Niagara Falls NY 14302

George Maczura
Aluminum Company of America
3450 Park Lane Drive
Pittsburgh PA 15275-1119

David Maginnis
Tinker AFB
OC-ALC/LIIRE
Tinker AFB OK 73145-5989

Frank Maginnis
Aspen Research, Inc.
220 Industrial Boulevard
Moore OK 73160

Tai-il Mah
Universal Energy Systems, Inc.
4401 Dayton-Xenia Road
Dayton OH 45432

Kenneth M. Maillar
Barbour Stockwell Company
83 Linskey Way
Cambridge MA 02142

S. G. Malghan
NIST
I-270 & Clopper Road
Gaithersburg MD 20899

Lars Malmrup
United Turbine AB
Box 13027
Malmo S-200 44
SWEDEN

John Mangels
Ceradyne, Inc.
3169 Redhill Avenue
Costa Mesa CA 92626

Murli Manghnani
University of Hawaii
2525 Correa Road
Honolulu HI 96822

Russell V. Mann
Matec Applied Sciences, Inc.
75 South Street
Hopkinton MA 01748

William R. Manning
Champion Aviation Products Div
P.O. Box 686
Liberty SC 29657

Ken Marnoch
Amercom, Inc.
8928 Fullbright Avenue
Chatsworth CA 91311

Robert A. Marra
Aluminum Company of America
Alcoa Technical Center
Alcoa Center PA 15069

Steve C. Martin
Advanced Refractory Technologies
699 Hertel Avenue
Buffalo NY 14207

Kelly J. Mather
William International Corporation
2280 W. Maple Road
Walled Lake MI 48088

James P. Mathers
3M Company
3M Center, Bldg. 201-3N-06
St. Paul MN 55144

Ron Mayville
Arthur D. Little, Inc.
15-163 Acorn Park
Cambridge MA 02140

F. N. Mazadarany
General Electric Company
Bldg. K-1, Room MB-159
P.O. Box 8
Schenectady NY 12301

James W. McCauley
Alfred University
Binns-Merrill Hall
Alfred NY 14802

Louis R. McCreight
2763 San Ramon Drive
Rancho Palos Verdes CA 90274

Colin F. McDonald
McDonald Thermal Engineering
1730 Castellana Road
La Jolla CA 92037

B. J. McEntire
Norton Company
10 Airport Park Road
East Granby CT 06026

Chuck McFadden
Coors Ceramics Company
600 9th Street
Golden CO 80401

Thomas D. McGee
Iowa State University
110 Engineering Annex
Ames IA 50011

James McLaughlin
Sundstrand Power Systems
4400 Ruffin Road
P.O. Box 85757
San Diego CA 92186-5757

Matt McMonigle
U.S. Department of Energy
Improved Energy Productivity
CE-231, Forrestal Building
Washington DC 20585

J. C. McVickers
AlliedSignal Engines
P.O. Box 52180, MS:9317-2
Phoenix AZ 85072-2180

D. B. Meadowcroft
"Jura," The Ridgeway
Oxshott
Leatherhead Surrey KT22 OLG
UNITED KINGDOM

Joseph J. Meindl
Reynolds International, Inc.
6603 W. Broad Street
P.O. Box 27002
Richmond VA 23261-7003

Michael D. Meiser
AlliedSignal, Inc.
Ceramic Components
P.O. Box 2960, MS:T21
Torrance CA 90509-2960

George Messenger
National Research Council of
 Canada
Building M-7
Ottawa Ontario K1A OR6
CANADA

D. Messier
U.S. Army Materials Technology
SLCMT-EMC
405 Arsenal Street
Watertown MA 02172-0001

Arthur G. Metcalfe
Arthur G. Metcalfe and
 Associates, Inc.
2108 East 24th Street
National City CA 91950

R. Metselaar
Eindhoven University
P.O. Box 513
Endhoven 5600 MB
THE NETHERLANDS

David J. Michael
Harbison-Walker Refractories Co.
P.O. Box 98037
Pittsburgh PA 15227

Ken Michaels
Chrysler Motors Corporation
P.O. Box 1118, CIMS:418-17-09
Detroit MI 48288

Bernd Michel
Institute of Mechanics
P.O. Box 408
D-9010 Chemnitz
GERMANY

D. E. Miles
Commission of the European Comm.
rue de la Loi 200
B-1049 Brussels
BELGIUM

Carl E. Miller
AC Rochester
1300 N. Dort Highway, MS:32-31
Flint MI 48556

Charles W. Miller, Jr.
Centorr Furnaces/Vacuum
 Industries
542 Amherst Street
Nashua NH 03063

R. Minimmi
Enichem America
2000 Cornwall Road
Monmouth Junction NJ 08852

Michele V. Mitchell
AlliedSignal, Inc.
Ceramic Components
P.O. Box 2960, MS:T21
Torrance CA 90509-2960

Howard Mizuhara
WESGO
477 Harbor Boulevard
Belmont CA 94002

Helen Moeller
Babcock & Wilcox
P.O. Box 11165
Lynchburg VA 24506-1165

Francois R. Mollard
Concurrent Technologies Corp.
1450 Scalp Avenue
Johnstown PA 15904-3374

Phil Mooney
Panametrics
221 Crescent Street
Waltham MA 02254

Geoffrey P. Morris
3M Company
3M Traffic Control Materials
Bldg. 209-BW-10, 3M Center
St. Paul MN 55144-1000

Jay A. Morrison
Rolls-Royce, Inc.
2849 Paces Ferry Road, Suite 450
Atlanta GA 30339-3769

Joel P. Moskowitz
Ceradyne, Inc.
3169 Redhill Avenue
Costa Mesa CA 92626

Brij Moudgil
University of Florida
Material Science & Engineering
Gainesville FL 32611

Christoph J. Mueller
Sprechsaal Publishing Group
P.O. Box 2962, Mauer 2
D-8630 Coburg
GERMANY

Thomas W. Mullan
Vapor Technologies Inc.
345 Route 17 South
Upper Saddle River NJ 07458

Theresa A. Mursick-Meyer
Norton Company
SGNICC/NRDC
Goddard Road
Northboro MA 01532-1545

M. K. Murthy
MkM Consultants International
10 Avoca Avenue, Unit 1906
Toronto Onntario M4T 2B7
CANADA

David L. Mustoe
Custom Technical Ceramics
8041 West I-70 Service Rd. Unit 6
Arvada CO 80002

Curtis V. Nakaishi
U.S. Department of Energy
Morgantown Energy Technology Ctr.
P.O. Box 880
Morgantown WV 26507-0880

Yoshio Nakamura
Faicera Research Institute
3-11-12 Misono
Sagamihara, Tokyo
JAPAN

K. S. Narasimhan
Hoeganaes Corporation
River Road
Riverton NJ 08077

Robert Naum
Applied Resources, Inc.
P.O. Box 241
Pittsford NY 14534

Malcolm Naylor
Cummins Engine Company, Inc.
P.O. Box 3005, Mail Code 50183
Columbus IN 47202-3005

Fred A. Nichols
Argonne National Laboratory
9700 S. Cass Avenue
Argonne IL 60439

H. Nickel
Forschungszentrum Juelich (KFA)
Postfach 1913
D-52425 Juelich
GERMANY

Dale E. Niesz
Rutgers University
Center for Ceramic Research
P.O. Box 909
Piscataway NJ 08855-0909

Paul W. Niskanen
Lanxide Corporation
P.O. Box 6077
Newark DE 19714-6077

David M. Nissley
United Technologies Corporation
Pratt & Whitney Aircraft
400 Main Street, MS:163-10
East Hartford CT 06108

Daniel Oblas
50 Meadowbrook Drive
Bedford MA 01730

Don Ohanehi
Magnetic Bearings, Inc.
1908 Sussex Road
Blacksburg VA 24060

Hitoshi Ohmori
ELID Team
Itabashi Branch
1-7 13 Kaga Itabashi
Tokyo 173
JAPAN

Robert Orenstein
General Electric Company
55-112, River Road
Schenectady NY 12345

Richard Palicka
Cercom, Inc.
1960 Watson Way
Vista CA 92083

Joseph N. Panzarino
Norton Company
SGNICC/NRDC
Goddard Road
Northboro MA 01532-1545

Pellegrino Papa
Corning Inc.
MP-WX-02-1
Corning NY 14831

Terry Paquet
Boride Products Inc.
2879 Aero Park Drive
Traverse City MI 49684

E. Beth Pardue
MPC
8297 Williams Ferry Road
Lenior City TN 37771

Soon C. Park
3M Company
Building 142-4N-02
P.O. Box 2963
St. Paul MN 55144

Vijay M. Parthasarathy
Caterpillar/Solar Turbines
2200 Pacific Highway
P.O. Box 85376
San Diego CA 92186-5376

Harmut Paschke
Schott Glaswerke
Christoph-Dorner-Strasse 29
D-8300 Landshut
GERMANY

James W. Patten
Cummins Engine Company, Inc.
P.O. Box 3005, Mail Code 50183
Columbus IN 47202-3005

Robert A. Penty
Penty & Associates
38 Oakdale Drive
Rocester NY 14618

Robert W. Pepper
Textron Specialty Materials
2 Industrial Avenue
Lowell MA 01851

Peter Perdue
Detroit Diesel Corporation
13400 Outer Drive West,
Speed Code L-04
Detroit MI 48239-4001

John J. Petrovic
Los Alamos National Laboratory
Group MST-4, MS:G771
Los Alamos NM 87545

Frederick S. Pettit
University of Pittsburgh
Pittsburgh PA 15261

Richard C. Phoenix
Ohmtek, Inc.
2160 Liberty Drive
Niagara Falls NY 14302

Bruce J. Pletka
Michigan Technological University
Metallurgical & Materials Engr.
Houghton MI 49931

John P. Pollinger
AlliedSignal, Inc.
Ceramic Components
P.O. Box 2960, MS:T21
Torrance CA 90509-2960

P. Popper
High Tech Ceramics International
 Journal
22 Pembroke Drive - Westlands
Newcastle-under-Lyme
 Staffs ST5 2JN
ENGLAND

F. Porz
Universitat Karlsruhe
Institut fur Keramik Im
 Maschinendau
Postfach 6980
D-76128 Karlsruhe
GERMANY

Harry L. Potma
Royal Netherlands Embassy
Science and Technology
4200 Linnean Avenue, N.W.
Washington DC 20008

Bob R. Powell
General Motors Corporation
Metallurgy Department
Box 9055
Warren MI 48090-9055

Stephen C. Pred
Biesterfeld U.S., Inc.
500 Fifth Avenue
New York NY 10110

Karl M. Prewo
United Technologies Research Ctr.
411 Silver Lane, MS:24
East Hartford CT 06108

Bert H. Probst
NASA Lewis Research Center
21000 Brookpark Road
Cleveland OH 44135

Vimal K. Pujari
Norton Company
SGNICC/NRDC
Goddard Road
Northboro MA 01532-1545

Fred Quan
Corning Inc.
Sullivan Park, FR-02-08
Corning NY 14831

George Quinn
NIST
Ceramics Division, Bldg. 223
Gaithersburg MD 20899

Ramas V. Raman
Ceracon, Inc.
1101 N. Market Boulevard, Suite 9
Sacramento CA 95834

Charles F. Rapp
Owens Corning Fiberglass
2790 Columbus Road
Granville OH 43023-1200

Dennis W. Readey
Colorado School of Mines
Metallurgy and Materials Engr.
Golden CO 80401

Wilfred J. Rebello
PAR Enterprises, Inc.
12601 Clifton Hunt Lane
Clifton VA 22024

Harold Rechter
Chicago Fire Brick Company
7531 S. Ashland Avenue
Chicago IL 60620

Robert R. Reeber
U.S. Army Research Office
P.O. Box 12211
Research Triangle Park NC
   27709-2211

K. L. Reifsnider
VPI & SU
Engineering Science and Mechanics
Blacksburg VA 24061

Paul E. Rempes
McDonnell Douglass Aircraft Co.
P.O. Box 516, Mail Code:0642263
St. Louis MO 63166-0516

Gopal S. Revankar
John Deere Company
3300 River Drive
Moline IL 61265

K. Y. Rhee
Rutgers University
P.O. Box 909
Piscataway NJ 08854

James Rhodes
Advanced Composite Materials Corp
1525 S. Buncombe Road
Greer SC 29651

Roy W. Rice
W. R. Grace and Company
7379 Route 32
Columbia MD 21044

David W. Richerson
2093 E. Delmont Drive
Salt Lake City UT 84117

Tomas Richter
J. H. France Refractories
1944 Clarence Road
Snow Shoe PA 16874

Michel Rigaud
Ecole Polytechnique
Campus Universite De Montreal
P.O. Box 6079, Station A
Montreal, P.Q. Quebec H3C 3A7
CANADA

John E. Ritter
University of Massachusetts
Mechanical Engineering Department
Amherst MA 01003

W. Eric Roberts
Advanced Ceramic Technology, Inc.
990 "F" Enterprise Street
Orange CA 92667

Y. G. Roman
TNO TPD Keramick
P.O. Box 595
Einhoven 5600 AN
HOLLAND

Michael Rossetti
Arthur D. Little, Inc.
15 Acorn Park
Cambridge MA 01240

Barry Rossing
Lanxide Corporation
P.O. Box 6077
Newark DE 19714-6077

Steven L. Rotz
Lubrizol Corporation
29400 Lakeland Boulevard
Wickliffe OH 44092

Robert Ruh
Wright Laboratory
WL/MLLM
Wright-Patterson AFB OH 45433

Robert J. Russell
17 Highgate Road
Framingham MA 01701

Jon A. Salem
NASA Lewis Research Center
21000 Brookpark Road
Cleveland OH 44135

W. A. Sanders
NASA Lewis Research Center
21000 Brookpark Road, MS:49-3
Cleveland OH 44135

J. Sankar
North Carolina A&T State Univ.
Dept. of Mechanical Engineering
Greensboro NC 27406

Yasushi Sato
NGK Spark Plugs (U.S.A.), Inc.
1200 Business Center Drive, #300
Mt. Prospect IL 60056

Maxine L. Savitz
AlliedSignal, Inc.
Ceramic Components
P.O. Box 2960, MS:T21
Torrance CA 90509-2960

Ashok Saxena
GTRI
Materials Engineering
Atlanta GA 30332-0245

David W. Scanlon
Instron Corporation
100 Royall Street
Canton MA 02021

Charles A. Schacht
Schacht Consulting Services
12 Holland Road
Pittsburgh PA 15235

Robert E. Schafrik
National Materials Advisory Board
2101 Constitution Ave., N.W.
Washington DC 20418

James Schienle
AlliedSignal Engines
P.O. Box 52180, MS:1302-2P
Phoenix AZ 85072-2180

Gary Schnittgrund
Rocketdyne, BA05
6633 Canoga Avenue
Canoga Park CA 91303

Mark Schomp
Lonza, Inc.
17-17 Route 208
Fair Lann NJ 07410

Joop Schoonman
Delft University of Technology
P.O. Box 5045
2600 GA Delft
THE NETHERLANDS

Robert B. Schulz
U.S. Department of Energy
Office of Transportation Matrls.
CE-34, Forrestal Building
Washington DC 20585

Murray A. Schwartz
Materials Technology Consulting
30 Orchard Way, North
Potomac MD 20854

Peter Schwarzkopf
SRI International
333 Ravenswood Avenue
Menlo Park CA 94025

William T. Schwessinger
Multi-Arc Scientific Coatings
1064 Chicago Road
Troy MI 48083-4297

W. D. Scott
University of Washington
Materials Science Department
Mail Stop:FB10
Seattle WA 98195

Nancy Scoville
Thermo Electron Technologies
P.O. Box 9046
Waltham MA 02254-9046

Thomas M. Sebestyen
U.S. Department of Energy
Advanced Propulsion Division
CE-322, Forrestal Building
Washington DC 20585

Brian Seegmiller
Coors Ceramics Company
600 9th Street
Golden CO 80401

T. B. Selover
AICRE/DIPPR
3575 Traver Road
Shaker Heights OH 44122

Charles E. Semler
Semler Materials Services
4160 Mumford Court
Columbus OH 43220

Thomas Service
Service Engineering Laboratory
324 Wells Street
Greenfield MA 01301

Kish Seth
Ethyl Corporation
P.O. Box 341
Baton Rouge LA 70821

William J. Shack
Argonne National Laboratory
9700 S. Cass Avenue, Bldg. 212
Argonne IL 60439

Peter T.B. Shaffer
Technical Ceramics Laboratories,
4045 Nine/McFarland Drive
Alpharetta GA 30201

Richard K. Shaltens
NASA Lewis Research Center
21000 Brookpark Road, MS:302-2
Cleveland OH 44135

Robert S. Shane
1904 NW 22nd Street
Stuart FL 34994-9270

Ravi Shankar
Chromalloy
Research and Technology Division
Blaisdell Road
Orangeburg NY 10962

Terence Sheehan
Alpex Wheel Company
727 Berkley Street
New Milford NJ 07646

Dinesh K. Shetty
University of Utah
Materials Science and Engineering
Salt Lake City UT 84112

Masahide Shimizu
New Ceramics Association
Shirasagi 2-13-1-208, Nakano-ku
Tokyo, 165
JAPAN

Thomas Shreves
American Ceramic Society, Inc.
735 Ceramic Place
Westerville OH 43081-8720

Jack D. Sibold
Coors Ceramics Company
4545 McIntyre Street
Golden CO 80403

Johann Siebels
Volkswagen AG
Werkstofftechnologie
Postfach 3180
Wolfsburg 1
GERMANY

George H. Siegel
Point North Associates, Inc.
P.O. Box 907
Madison NJ 07940

Richard Silberglitt
FM Technologies, Inc.
10529-B Braddock Road
Fairfax VA 22032

Mary Silverberg
Norton Company
SGNICC/NRDC
Goddard Road
Northboro MA 01532-1545

Gurpreet Singh
Department of the Navy
Code 56X31
Washington DC 20362-5101

Maurice J. Sinnott
University of Michigan
5106 IST Building
Ann Arbor MI 48109-2099

John Skildum
3M Company
3M Center
Building 224-2S-25
St. Paul MN 55144

Richard H. Smoak
Smoak & Associates
3554 Hollyslope Road
Altadena CA 91001-3923

Jay R. Smyth
AlliedSignal Engines
111 S. 34th Street, MS:503-412
Phoenix AZ 85034

Rafal A. Sobotowski
British Petroleum Company
Technical Center, Broadway
3092 Broadway Avenue
Cleveland OH 44115

S. Somiya
Nishi Tokyo University
3-7-19 Seijo, Setagaya
Tokyo, 157
JAPAN

Boyd W. Sorenson
DuPont Lanxide Composites
1300 Marrows Road
Newark DE 19711

Charles A. Sorrell
U.S. Department of Energy
Advanced Industrial Concepts
CE-232, Forrestal Building
Washington DC 20585

C. Spencer
EA Technology
Capenhurst Chester CH1 6ES
UNITED KINGDOM

Allen Spizzo
Hercules Inc.
Hercules Plaza
Wilmington DE 19894

Richard M. Spriggs
Alfred University
Center for Advanced Ceramic
 Technology
Alfred NY 14802

Charles Spuckler
NASA Lewis Research Center
21000 Brookpark Road, MS:5-11
Cleveland OH 44135-3191

M. Srinivasan
Material Solutions
P.O. Box 663
Grand Island NY 14702-0663

Gordon L. Starr
Cummins Engine Company, Inc.
P.O. Box 3005, Mail Code:50182
Columbus IN 47202-3005

Tom Stillwagon
AlliedSignal, Inc.
Ceramic Components
P.O. Box 2960, MS:T21
Torrance CA 90509-2960

H. M. Stoller
TPL Inc.
3754 Hawkins, N.E.
Albuquerque NM 87109

Paul D. Stone
Dow Chemical USA
1776 "Eye" Street, N.W., #575
Washington DC 20006

F. W. Stringer
Aero & Industrial Technology Ltd.
P.O. Box 46, Wood Top
Burnley Lancashire BB11 4BX
UNITED KINGDOM

Thomas N. Strom
NASA Lewis Research Center
21000 Brookpark Road, MS:86-6
Cleveland OH 44135

M. F. Stroosnijder
Institute for Advanced Materials
Joint Research Centre
21020 Ispra (VA)
ITALY

Karsten Styhr
30604 Ganado Drive
Rancho Palos Verdes CA 90274

T. S. Sudarshan
Materials Modification, Inc.
2929-P1 Eskridge Center
Fairfax VA 22031

M. J. Sundaresan
University of Miami
P.O. Box 248294
Coral Gables FL 33124

Patrick L. Sutton
U.S. Department of Energy
Office of Propulsion Systems
CE-322, Forrestal Building
Washington DC 20585

Willard H. Sutton
United Technologies Corporation
Silver Lane, MS:24
East Hartford CT 06108

J. J. Swab
U.S. Army Materials Technology
Ceramics Research Division,
SLCMT-EMC
405 Arsenal Street
Watertown MA 02172

Robert E. Swanson
Metalworking Technology, Inc.
1450 Scalp Avenue
Johnstown PA 15904

Yo Tajima
NGK Spark Plug Company
2808 Iwasaki
Komaki-shi Aichi-ken, 485
JAPAN

Fred Teeter
5 Tralee Terrace
East Amherst NY 14051

Monika O. Ten Eyck
Carborundum Microelectronics
P.O. Box 2467
Niagara Falls NY 14302-2467

David F. Thompson
Corning Glass Works
SP-DV-02-1
Corning NY 14831

Merle L. Thorpe
Hobart Tafa Technologies, Inc.
20 Ridge Road
Concord NH 03301-3010

T. Y. Tien
University of Michigan
Materials Science and Engineering
Dow Building
Ann Arbor MI 48103

D. M. Tracey
Norton Company
SGNICC/NRDC
Goddard Road
Northboro MA 01532-1545

Marc Tricard
Norton Company, WGTC
1 New Bond Street
Worcester MA 01615-0008

L. J. Trostel, Jr.
Box 199
Princeton MA 01541

W. T. Tucker
General Electric Company
P.O. Box 8, Bldg. K1-4C35
Schenectady NY 12301

Masanori Ueki
Nippon Steel Corporation
1618 Ida
Nakahara-Ku Kawasaki, 211
JAPAN

Filippo M. Ugolini
ATA Studio
Via Degli Scipioni, 268A
ROMA, 00192
ITALY

Donald L. Vaccari
Allison Gas Turbines
P.O. Box 420, Speed Code S49
Indianapolis IN 46206-0420

Carl F. Van Conant
Boride Products, Inc.
2879 Aero Park Drive
Traverse City MI 49684

John F. Vander Louw
3M Company
3M Center, Bldg. 60-1N-01
Saint Paul MN 55144

Marcel H. Van De Voorde
Commission of the European Comm.
P.O. Box 2
1755 ZG Petten
THE NETHERLANDS

O. Van Der Biest
Katholieke Universiteit Leuven
Dept. Metaalkunde en Toegepaste
de Croylaan 2
B-3030 Leuven
BELGIUM

Michael Vannier
Washington University, St. Louis
510 S. Kings Highway
St. Louis MO 63110

Stan Venkatesan
Southern Coke & Coal Corporation
P.O. Box 52383
Knoxville TN 37950

V. Venkateswaran
Carborundum Company
Niagara Falls R&D Center
P.O. Box 832
Niagara Falls NY 14302

Dennis Viechnicki
U.S. Army Materials Technology
405 Arsenal Street
Watertown MA 02172-0001

Ted Vojnovich
U.S. Department of Energy, ST-311
Office of Energy Research, 3F077P
Washington DC 20585

John D. Volt
E.I. Dupont de Nemours & Co. Inc.
P.O. Box 80262
Wilmington DE 19880

John B. Wachtman
Rutgers University
P.O. Box 909
Piscataway NJ 08855

Shigetaka Wada
Toyota Central Research Labs
Nagakute Aichi, 480-11
JAPAN

Janet Wade
AlliedSignal Engines
P.O. Box 52180, MS:1303-2
Phoenix AZ 85072-2180

Richard L. Wagner
Ceramic Technologies, Inc.
537 Turtle Creek South Dr., #240
Indianapolis IN 46227

J. Bruce Wagner, Jr.
Arizona State University
Center for Solid State Science
Tempe AZ 85287-1704

Daniel J. Wahlen
Kohler, Co.
444 Highland Drive
Kohler WI 53044

Ingrid Wahlgren
Royal Institute of Technology
Studsvik Library
S-611 82 Nykoping
SWEDEN

Ron H. Walecki
AlliedSignal, Inc.
Ceramic Components
P.O. Box 2960, MS:T21
Torrance CA 90509-2960

Michael S. Walsh
Vapor Technologies Inc.
6300 Gunpark Drive
Boulder CO 80301

Chien-Min Wang
Industrial Technology Research
 Institute
195 Chung-Hsing Road, Sec. 4
Chutung Hsinchu 31015 R.O.C.
TAIWAN

Robert M. Washburn
ASMT
11203 Colima Road
Whittier CA 90604

Gerald Q. Weaver
Carborundum Specialty Products
42 Linus Allain Avenue
Gardner MA 01440-2478

Kevin Webber
Toyota Technical Center, U.S.A.
1410 Woodridge, RR7
Ann Arbor MI 48105

Karen E. Weber
Detroit Diesel Corporation
13400 Outer Drive West
Detroit MI 48239-4001

James K. Weddell
Du Pont Lanxide Composites Inc.
P.O. Box 6100
Newark DE 19714-6100

R. W. Weeks
Argonne National Laboratory
MCT-212
9700 S. Cass Avenue
Argonne IL 60439

Ludwig Weiler
ASEA Brown Boveri AG
Eppelheimer Str. 82
D-6900 Heidelberg
GERMANY

James Wessel
Dow Corning Corporation
1800 "M" Street, N.W., #325 South
Washington DC 20036

Robert D. West
Therm Advanced Ceramics
P.O. Box 220
Ithaca NY 14851

Thomas J. Whalen
1845 Cypress Pointe Court
Ann Arbor MI 48108

Ian A. White
Hoeganaes Corporation
River Road
Riverton NJ 08077

Sheldon M. Wiederhorn
NIST
Building 223, Room A329
Gaithersburg MD 20899

John F. Wight
Alfred University
McMahon Building
Alfred NY 14802

D. S. Wilkinson
McMaster University
1280 Main Street, West
Hamilton Ontario L8S 4L7
CANADA

James C. Williams
General Electric Company
Engineering Materials Technology
One Neumann Way, Mail Drop:H85
Cincinnati OH 45215-6301

Steve J. Williams
RCG Hagler Bailly, Inc.
1530 Wilson Boulevard, Suite 900
Arlington VA 22209-2406

Thomas A. Williams
National Renewable Energy Lab
1617 Cole Boulevard
Golden CO 80401

Craig A. Willkens
Norton Company
SGNICC/NRDC
Goddard Road
Northboro MA 01532-1545

Roger R. Wills
Ohio Aerospace Institute (OAI)
22800 Cedar Point Road
Brook Park OH 44142

David Gordon Wilson
Massachusetts Institute of
 Technology
77 Massachusetts Ave., Room 3-455
Cambridge MA 02139

J. M. Wimmer
AlliedSignal Ceramic Components
Department 27000, MS:T21
2525 W. 190th Street
Torrance CA 90509

Matthew F. Winkler
Seaworthy Systems, Inc.
P.O. Box 965
Essex CT 06426

Gerhard Winter
Hermann C. Starck Berlin GmbH
P.O. Box 25 40
D-3380 Goslar 3380
GERMANY

William T. Wintucky
NASA Lewis Research Center
Terrestrial Propulsion Office
21000 Brookpark Road, MS:86-6
Cleveland OH 44135

Thomas J. Wissing
Eaton Corporation
Engineering and Research Center
P.O. Box 766
Southfield MI 48037

James C. Withers
MER Corporation
7960 S. Kolb Road
Building F
Tucson AZ 85706

Dale E. Wittmer
Southern Illinois University
Mechanical Engineering Department
Carbondale IL 62901

Warren W. Wolf
Owens Corning Fiberglass
2790 Columbus Road, Route 16
Granville OH 43023

Egon E. Wolff
Caterpillar Inc.
Technical Center
P.O. Box 1875
Peoria IL 61656-1875

George W. Wolter
Howmet Turbine Components Corp.
Technical Center
699 Benston Road
Whitehall MI 49461

James C. Wood
NASA Lewis Research Center
21000 Brookpark Road, MS:86-6
Cleveland OH 44135

Wayne L. Worrell
University of Pennsylvania
3231 Walnut Street
Philadelphia PA 19104

John F. Wosinski
Corning Inc.
ME-2 E-5 H8
Corning NY 14830

Ruth Wroe
EROC
Capenhurst Chester CH1 6ES
ENGLAND

Bernard J. Wrona
Advanced Composite Materials Corp
1525 S. Buncombe Road
Greer SC 29651

Carl C. M. Wu
Naval Research Laboratory
Ceramic Branch, Code 6373
Washington DC 20375

David C. Wu
AlliedSignal Engines
P.O. Box 52181, MS:301-227
Phoenix AZ 85072-2181

John C. Wurst
U. of Dayton Research Institute
300 College Park
Dayton OH 45469-0101

Neil Wyant
ARCH Development Corp.
9700 S. Cass Avenue, Bldg. 202
Argonne IL 60439

Roy Yamamoto
Texaco Inc.
P.O. Box 509
Beacon NY 12508-0509

John Yamanis
AlliedSignal Aerospace Company
P.O. Box 1021
Morristown NJ 07962-1021

Harry C. Yeh
AlliedSignal, Inc.
Ceramic Components
P.O. Box 2960, MS:T21
Torrance CA 90509-2960

Hiroshi Yokoyama
Hitachi Research Lab
4026 Kuji-Cho
Hitachi-shi Ibaraki 319-12
JAPAN

Thomas N. Yonushonis
Cummins Engine Company, Inc.
P.O. Box 3005, Mail Code 50183
Columbus IN 47202-3005

Thomas J. Yost
Corning Inc.
Technical Products Div., 21-1-2
Corning NY 14831

Jong Yung
Sundstrand Aviation Operations
4747 Harrison Avenue
Rockford IL 61125

C. S. Yust
106 Newcrest Lane
Oak Ridge TN 37830

A. L. Zadoks
Caterpillar Inc.
Technical Center, Building L
P.O. Box 1875
Peoria IL 61656-1875

Avi Zangvil
University of Illinois
104 S. Goodwin Avenue
Urbana IL 61801

Charles H. Zenuk
Transtech
6662 E. Paseo San Andres
Tucson AZ 85710-2106

Carl Zweben
General Electric Company
P.O. Box 8555, VFSC/V4019
Philadelphia PA 19101

Department of Energy
Oak Ridge Operations Office
Assistant Manager for Energy
   Research and Development
P.O. Box 2001
Oak Ridge, TN 37831-8600

Department of Energy (2)
Office of Scientific and Technical
   Information
Office of Information Services
P.O. Box 62
Oak Ridge, TN 37831

   For distribution by microfiche
   as shown in DOE/OSTI-4500,
   Distribution Category UC-332
   (Ceramics/Advanced Materials).